YUKON
EXPLORATION & GEOLOGY

2013

Edited by
K.E. MacFarlane, M.G. Nordling,
and P.J. Sack

Yukon Geological Survey
Energy, Mines and Resources
Government of Yukon

Published under the authority of the Department of Energy, Mines and Resources, Government of Yukon ***http://www.emr.gov.yk.ca.***

Printed in Whitehorse, Yukon, 2014.

Publié avec l'autorisation du Ministères de l'Énergie, des Mines et des Ressources du gouvernement du Yukon, ***http://www.emr.gov.yk.ca.***

Imprimé à Whitehorse (Yukon) en 2014.

© Department of Energy, Mines and Resources, Government of Yukon

ISSN 1718-8326 (on-line version)

This, and other Yukon Geological Survey publications, may be obtained from:
Yukon Geological Survey
102-300 Main Street
Box 2703 (K-102)
Whitehorse, Yukon, Canada Y1A 2C6

phone (867) 667-3201, e-mail ***geology@gov.yk.ca***

Visit the Yukon Geological Survey website at ***www.geology.gov.yk.ca.***

In referring to this publication, please use the following citation:
Yukon Exploration and Geology 2013. K.E. MacFarlane, M.G. Nordling, and P.J. Sack (eds.), 2014. Yukon Geological Survey, 232 p.

Papers are available in colour and can be obtained from the Yukon Geological Survey website.

Front cover photograph: Looking south across the Dezadeash Ranges. Photo by Steve Israel.

PREFACE

Yukon Exploration and Geology (YEG) and the Yukon Exploration and Geology Overview continue to be the main publications of the Yukon Geological Survey (Energy, Mines and Resources, Government of Yukon). Individual YEG papers, with colour images, are available in digital format only and can be downloaded from our website. The YEG Overview is available in a digital format (colour), as well as in a limited print run (black and white).

YEG 2013 contains up-to-date information on mining and mineral exploration activity, studies by industry, and results of recent geological field studies. Information in this volume comes from prospectors, exploration and government geologists, mining companies, and students who are willing to contribute to public geoscience for the benefit of the scientific community, general public, and mineral and petroleum industries of Yukon. Their efforts are appreciated.

Monica Nordling has returned again this year to work with me through Christmas, and into the New Year, in order to complete YEG. She enjoyed basking in the glory as our YEG 2012 volume received the first (in what we hope will be many) EMRIE Award for “Best EMR Publication” of 2013. The prized trophy is seen on the back cover of this issue. I would like to thank my Yukon Geological Survey colleagues for their comments and critiques of manuscripts; Patrick Sack and Charlie Roots helped with several papers, and thanks also to Don Murphy, Steve Israel, Maurice Colpron, David Moynihan, and Matt Hutchison.

We welcome any input or suggestions that you may have to improve future YEG publications. Please contact me at (867) 667-8519, or by e-mail at karen.macfarlane@gov.yk.ca.

Karen MacFarlane

Yukon Geological Survey staff: (front row, left to right) Monica Nordling, Carolyn Relf, Tiffani Fraser, and Lara Lewis; (back row, left to right) Sarah Laxton, Sam Darling, Panya Lipovsky, Lee Pigage, Bailey Staffen, Aubrey Sicotte, Matt Hutchison, Karen MacFarlane, David Moynihan, Robert Deklerk, Patrick Sack, Maurice Colpron, Steve Israel, Don Murphy, Charlie Roots, Midori Kirby, Derek Torgersen. Missing from photo: Sue Roy, Olwyn Bruce, Rosie Cobbett, Sydney van Loon, Kristen Kennedy, Jeff Bond, and Johann Slam.

YUKON GEOLOGICAL SURVEY

TABLE OF CONTENTS

Preliminary stable isotope and geochemical investigation of carbonate in the Klondike district.
M.M. Allan, J.K. Mortensen, and N. Cook 1

Pathfinder signatures in placer gold derived from Au-bearing porphyries.
R.J. Chapman, M.M. Allan, M.K. Grimshaw, J.K. Mortensen, T.M. Wrighton, and S. Casselman 21

Preliminary observations on the geology of the Anvil Lake area (parts of NTS 105K/11 and 12), central Yukon.
R.N. Cobbett 33

Field descriptions of the Middle-Upper Devonian Canol Formation on Trail River, east Richardson Mountains, Yukon.
T. Fraser 53

Geology and jade prospects of the northern St. Cyr klippe (NTS 105F/6), Yukon.
S.J. Isard and J.A. Gilotti 69

Preliminary investigation into the geologic relationships in the Granite Lake area, parts of NTS 115A/10, 11, 14, and 15, southwest Yukon.
S. Israel and R. Kim 79

The early Neoproterozoic Chandindu Formation of the Fifteenmile Group in the Ogilvie Mountains.
M. Kunzmann, G.P. Halverson, F.A. Macdonald, M. Hodgskiss, P.D. Sansjofre, D. Schumann, and R.H. Rainbird 93

A four stage evolution of the White Channel gravel: Implications for stratigraphy and palaeoclimates.
R.I. Lowther, J. Peakall, R.J. Chapman, and M.J. Pound 109

Structural controls on alteration and mineralization at the Coffee gold deposits, Yukon.
D. MacKenzie, D. Craw, and C. Finnigan 119

U-Pb age, whole-rock geochemistry and radiogenic isotopic compositions of Late Cretaceous volcanic rocks in the central Aishihik Lake area, Yukon (NTS 115H).
G.A. Morris, J.K. Mortensen, and S. Israel 133

Bedrock Geology of NTS 106B/04, Eastern Rackla Belt.
D. Moynihan 147

Geochemistry and U-Pb zircon geochronology of mid-Cretaceous Tay River suite intrusions in southeast Yukon.
L.C. Pigage, J.L. Crowley, C.F. Roots, and J.G. Abbott 169

Sedimentary pyrite as a gold-source in sediment-hosted gold occurrences in the Selwyn basin area, eastern Yukon.
P.J. Sack, L.V. Danyushevsky, R.R. Large, S. Gilbert, and D. Gregory 195

Bathymetric and geophysical surveys of the southern end of Kluane Lake, Yukon.
D.H. Shugar 221

Preliminary stable isotope and geochemical investigation of carbonate in the Klondike district

Murray M. Allan[1], James K. Mortensen, and Natalie Cook
Mineral Deposit Research Unit, The University of British Columbia, Vancouver, B.C.

Allan, M.M., Mortensen, J.K., and Cook, N., 2014. Preliminary stable isotope and geochemical investigation of carbonate in the Klondike district. *In:* Yukon Exploration and Geology 2013, K.E. MacFarlane, M.G. Nordling, and P.J. Sack (eds.), Yukon Geological Survey, p. 1-20.

ABSTRACT

Carbonate is an important component of gold-bearing quartz veins in the Klondike district, and also makes up an under-recognized proportion of the Klondike schist host rocks. The predominantly metavolcanic Klondike schist contains carbonate as disseminated porphyroblasts and as coarse quartz-carbonate segregations, and contains rare layers of marble. Chemical staining and LA-ICP-MS analyses reveal that, irrespective of paragenesis, carbonate is dominated by Mg-Fe-Mn calcite. Laser spectroscopic analyses of C and O isotopes reveal that marble is a ^{13}C-enriched isotopic reservoir compared to carbonate in micaceous schist. Carbonate in gold-stage veins has a similar isotopic signature to carbonate in metamorphic segregations and porphyroblasts in the host rocks. We tentatively interpret these results to indicate that the CO_2 component of vein carbonate has been remobilized from local sources during brittle deformation. The results of this study may bear on interpreting the scale of rock-fluid interaction during orogenic gold mineralization in the area.

[1] *mallan@eos.ubc.ca*

INTRODUCTION

The rich placer gold fields of the Yukon's Klondike district are underlain primarily by the Klondike schist – a strongly deformed, Late Permian assemblage of metamorphosed volcanic, volcaniclastic and associated meta-intrusive rocks that make up part of the Yukon-Tanana terrane (Fig. 1). The placer deposits are derived from erosion of orogenic quartz-carbonate-pyrite-gold veins of Late Jurassic age that crosscut the Klondike schist. Auriferous veins in the Klondike formed during regionally widespread brittle-ductile to brittle deformation (D_4 deformation event described by MacKenzie *et al.*, 2008b), an event which is also responsible for the numerous deposits and gold occurrences of the White Gold district (Allan *et al.*, 2013). Several aspects of Klondike vein mineralization have been studied, such as their age (Hunt and Roddick, 1992; Breitsprecher and Mortensen, 2004; J. Mortensen, unpublished data, 2012), fluid conditions and water source (Rushton *et al.*, 1993), structural style (MacKenzie *et al.*, 2008a), and metal sources (Mortensen *et al.*, 2006; J. Mortensen, unpublished data). However, little attention has been paid to the carbonate component of gold-bearing veins in the Klondike. In particular, what is the origin of the carbon, how is it redistributed during hydrothermal and deformation events, and what role may CO_2 play in the transport and precipitation of gold?

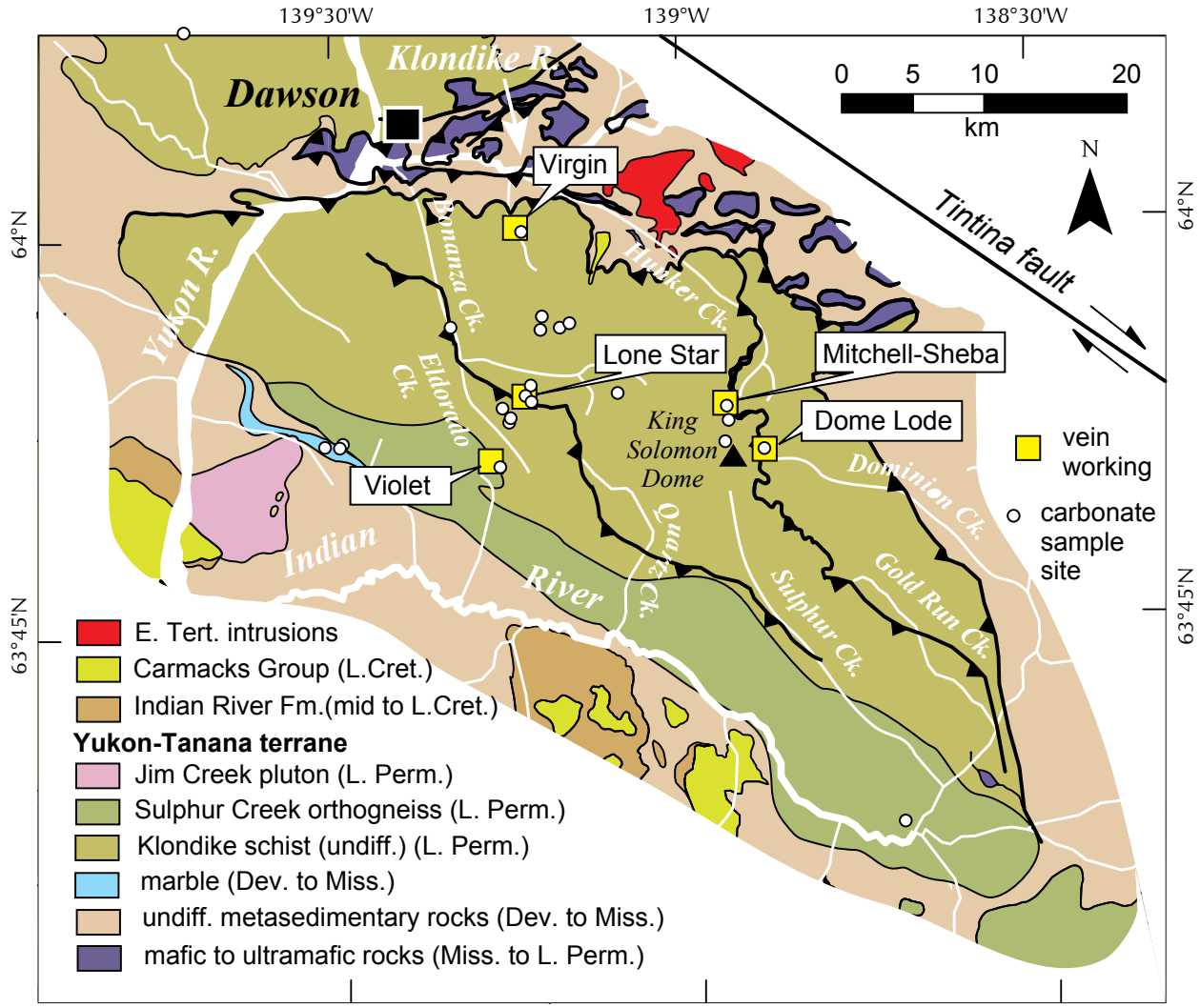

***Figure 1**. Simplified geologic map of the Klondike district, showing the location of carbonate samples and gold-bearing quartz vein workings.*

Carbon dioxide is a ubiquitous component of hydrothermal fluids that form orogenic gold deposits (*e.g.*, Groves *et al.*, 2003). It is recognized directly in fluid inclusions trapped in vein quartz, and is inferred from carbonate alteration haloes in the wallrock of veins. Stable isotopes may be useful in interpreting carbon sources in orogenic gold deposits. Carbon isotopic signatures of fluid inclusions and carbonate minerals in orogenic gold deposits globally range from $\delta^{13}C_{VPDB}$ = -26 to +13 ‰, with distinct modes at $\delta^{13}C_{VPDB}$ = -22 ‰ and -5 ‰ (Beaudoin, 2011) (VPDB = Vienna Pee Dee Belemnite C-isotope standard; VSMOW = Vienna Standard Mean Ocean Water O-isotope standard). More negative $\delta^{13}C$ values are typical of some Phanerozoic deposits hosted in metasedimentary rocks that contain reduced organic carbon (*e.g.*, Kontak and Kerrich, 1997), and more positive values are typical of deposits hosted in volcanic rocks. Although magmatic and mantle sources of carbon have been proposed for some volcanic-hosted orogenic gold systems, the overall distribution of isotopic signatures clearly demonstrates an influence of country rocks on the isotopic geochemistry.

During recent regional investigations of the Late Jurassic gold mineralization in west-central Yukon, we noted that carbonate is an under-recognized component of the Klondike schist. Because carbonate is so efficiently leached in the weathering environment – especially in the presence of acid-generating pyrite – it is commonly not preserved at surface. Instead, it is inferred in surface rock exposures from vuggy cavities or travertine coatings. Regardless, unweathered carbonate is found in many road cuts, trench exposures, and mine workings, and in some localities constitutes a significant rock-forming mineral.

Because carbonate minerals constitute not only a component of gold-bearing quartz veins, but also a locally significant component of the Klondike schist protolith, they provide an opportunity to test whether country rocks are a carbon source during gold mineralization. If so, can variations in isotopic signatures provide insight into the scale of rock-fluid interaction?

In this paper, we present the paragenesis, geochemistry, and carbon and oxygen isotopic signature of carbonate from the Klondike schist, in addition to the stratigraphically and structurally underlying Nasina assemblage. Carbon as graphite was not analyzed in this study, but is an obvious avenue of future work. In the Klondike schist, three modes of carbonate occurrence were sampled and analyzed: (1) "matrix" – carbonate as an essential rock-forming mineral, comprising part of the Late Permian protolith; (2) "segregation" – carbonate concentrated during ductile deformation into foliation-parallel, quartzose segregations; and (3) "vein" – carbonate occurring in late-stage veins that crosscut the dominant metamorphic fabric. The results are discussed in the context of orogenic gold mineralization in the Klondike district.

BACKGROUND

GEOLOGY OF THE KLONDIKE

The Late Permian Klondike assemblage is a thrust-imbricated sequence of metamorphosed arc rocks that underlies most of Klondike gold fields. The Klondike assemblage is composed of metavolcanic rocks of the Klondike schist, and age-equivalent metaplutonic rocks of the Sulphur Creek orthogneiss (Fig. 1). A component of the Klondike schist is quartz ± feldspar augen quartz-feldspar-muscovite ± chlorite ± biotite schist, interpreted as a felsic to intermediate metaporphyry. The Klondike schist ranges in composition from mafic (chloritic schist and minor metagabbro) to felsic (quartz-feldspar-muscovite schist), with rare exposures of impure marble and graphitic schist on the ridge between Eldorado and upper Bonanza creeks (Fig. 1; near the historic Lone Star gold mine, Yukon MINFILE 115O 072). Locally, the Klondike schist is strongly pyritic, and also contains showings of syngenetic, VMS-style galena-chalcopyrite ± gold mineralization (Mortensen, 1990; Mortensen *et al.*, 2006).

The Klondike assemblage is structurally and stratigraphically underlain by variably carbonaceous metasiliciclastic rocks and minor marble of the Devonian to Mississippian Nasina assemblage. These rocks are age-equivalent to volcanic rocks of the Finlayson assemblage, which represent the first phase of arc magmatism in the Yukon-Tanana terrane.

Rocks in the Klondike district have a penetrative metamorphic foliation S_2, which transposes an earlier S_1 fabric. This foliation was developed during the Late Permian Klondike orogeny, when the Yukon-Tanana terrane collided with, and overrode the North American margin (Beranek and Mortensen, 2011). The most common prograde metamorphic assemblage in the Klondike schist is quartz-feldspar-muscovite-chlorite, suggesting greenschist facies peak metamorphic conditions. A superimposed metamorphic fabric, consisting of asymmetric crenulations and a locally pervasive axial planar fabric (S_3), is commonly developed (Fig. 2). This deformation event has been linked to regional thrust faulting in the Early Jurassic (MacKenzie *et al.*, 2008b). A later generation of steep-dipping reverse faults,

angular kink folds, shears, and discordant quartz veins (S_4) is attributed to a subsequent phase of Jurassic deformation (MacKenzie *et al.*, 2008a). Orogenic gold mineralization in the Klondike is closely associated with this deformation phase. Subsequent geologic events include Late Cretaceous to Paleogene magmatism and normal faulting, but these are not relevant to this study.

***Figure 2**. Sample of Klondike schist, showing an F_3 fold with an accumulation of quartz and calcite in the hinge zone. Clots of partially leached calcite are indicated by the white arrows. Quartz and calcite are interpreted to have migrated into low-strain fold hinges during D_3 deformation, potentially from pre-existing, D_2-generation segregations.*

CARBONATE OCCURRENCES IN THE KLONDIKE

Nasina assemblage: A belt of marble is exposed as road rubble north of the mouth of the Indian River (Fig. 1). Rocks in this area include calcite marble as well as calcite and graphite-bearing quartz-muscovite schist and tremolite schist. Discordant calcite veins cutting the metamorphic foliation are common.

Klondike schist: Where preserved, carbonate in Klondike schist occurs as tan to orange-weathering clots in coarse-grained segregations along the S_1/S_2 metamorphic foliation (Fig. 3). Where carbonate is leached, the rocks contain vuggy cavities lined with a fine black, manganiferous coating. The coarsest accumulations of carbonate occur in the hinges of F_3 folds (Fig. 2), suggesting that quartz and carbonate were mobilized by dynamic recrystallization during ductile deformation. More rarely, carbonate occurs as 1 to 5-mm porphyroblasts in the silicate matrix. The metaporphyry member of the Klondike schist, well exposed in a reclaimed trench near the Violet gold mine (Yukon MINFILE 115O 073; Fig. 1), contains rare, pink, coarse-grained carbonate in foliation-parallel, quartz-rich segregations (Fig. 3C-D).

Klondike schist - marble: Blocks of tan-weathering marble are observed east of the Lone Star gold mine (Figs. 1 and 4), in a reclaimed trench near the 7 Pup of Victoria Gulch. Muscovite and quartz together comprise 20 to 60 % of the rock volume. Foliation-parallel, coarse carbonate-quartz segregations are observed.

D_4-Stage Veins: Carbonate-bearing veins are commonplace in steep, D_4 deformation zones in the Klondike schist, and more rarely in the Sulphur Creek orthogneiss and Nasina assemblage metasediments. In all cases, veins are discordant to the penetrative metamorphic schistosity. Carbonate is a common component of quartz veins, occurring either on the selvages or interiors of veins as a primary hydrothermal mineral (Fig. 5), or in the immediately surrounding wallrock as an alteration phase. Only hydrothermal carbonate from vein material was sampled in this study. Vein carbonate is typically blocky in quartz-carbonate veins, and blocky to fibrous in carbonate-only veins. Where preserved, carbonate is creamy white to brown to orange-weathering.

METHODS

SAMPLING

Carbonate-bearing samples were collected from outcrop, subcrop, historic exploration and mine workings, and drill core. The samples contained carbonate either as a component of the rock matrix, within coarse-grained, quartz-rich segregations parallel to the metamorphic foliation, or in crosscutting veins. Rock samples that had coatings of travertine, iron/manganese oxides, or lichen were sandblasted to expose fresh surfaces without removing excessive amounts of carbonate. Sample locations and lithology are listed in Table 1.

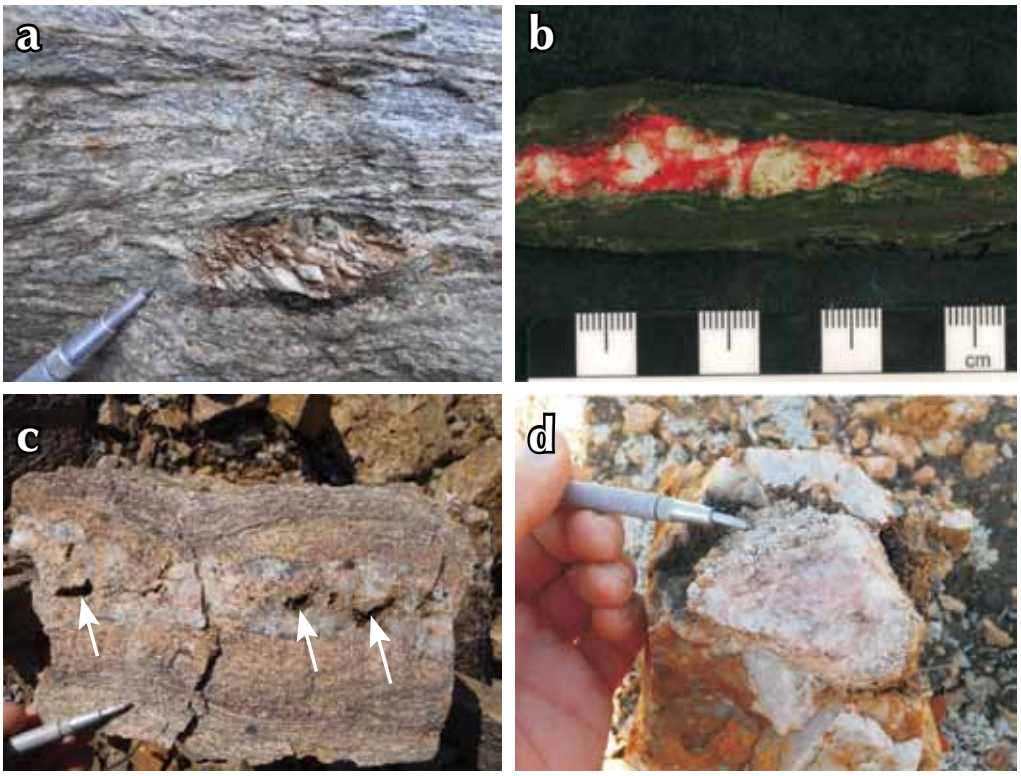

Figure 3. *Examples of carbonate-bearing segregations in Klondike schist: (a) lensoid calcite segregation in quartz-feldspar-muscovite-chlorite schist (Dome Lode; Yukon MINFILE 115O 067); (b) chloritic schist with a coarse quartz-calcite segregation, calcite stained by alizarin red S (Dome Lode); (c) boudinaged quartz-carbonate segregation in feldspathic metaporphyry (Violet); and (d) coarse clot of pink calcite within a quartz segregation (Violet).*

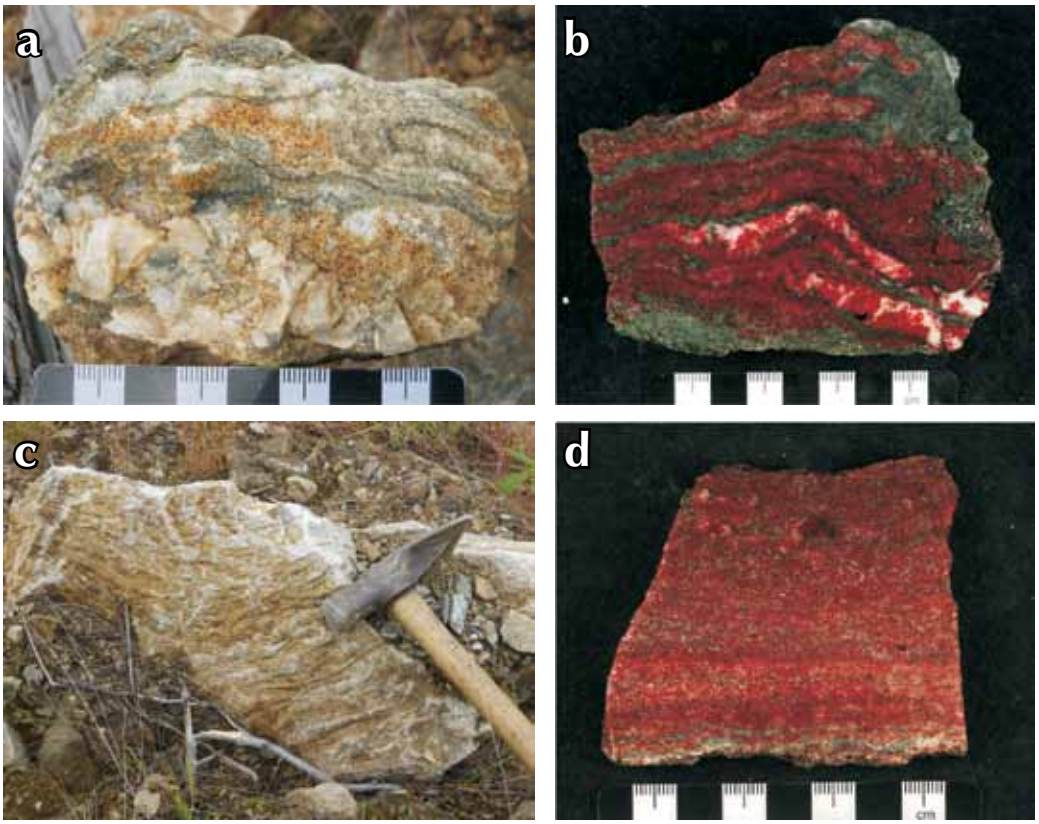

Figure 4. *Rare examples of marble from the Klondike assemblage: (a) folded quartz-muscovite-calcite schist with coarse quartz-calcite segregation; (b) same sample as in (a), calcite stained with alizarin red S; (c) sample of banded marble, with quartz and muscovite as the main impurities; and (d) same sample as in (c), calcite stained with alizarin red S.*

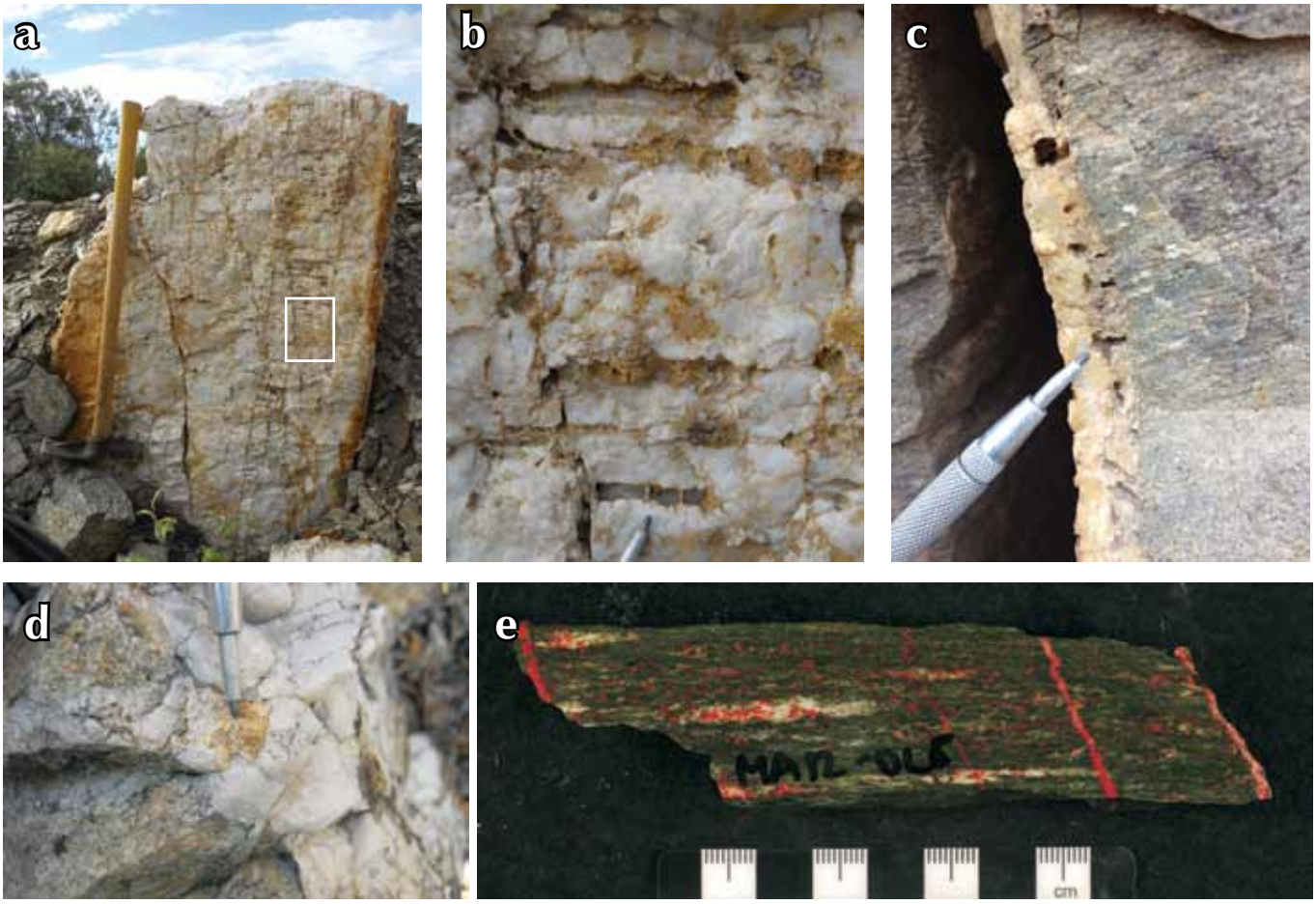

***Figure 5**. Examples of carbonate-bearing veins from the Klondike district: (a-b) milky quartz-carbonate vein of the Mitchell-Sheba vein system (Yukon MINFILE 115O 068). Carbonate is strongly leached; inset (b) shows columnar growth of quartz and carbonate (inferred from leached pits) perpendicular to the vein margins; (c) quartz vein with leached pits after blocky calcite. The vein is hosted by Sulphur Creek orthogneiss; (d) coarse calcite at the margin of a quartz vein (Virgin; Yukon MINFILE 116B 007); and (e) sample of Klondike schist with three modes of calcite occurrence: disseminated grains, quartz-calcite segregations, and discordant veins (Dome Lode).*

STAINING

Cut rock slabs and the curved, outer surfaces of halved drill core samples were treated with a sequential carbonate staining technique (modified from Hitzman, 1999) to determine the carbonate minerals present. Samples were pre-etched in 5% HCl v/v for 30 to 60 s, depending on how vigorously the carbonate reacted, and rinsed in water. A calcite-sensitive staining solution was prepared by dissolving 2.0 g of alizarin red S (sodium 3,4-dihydroxy-9,10-dioxo-2-anthracene sulphonate) in 250 mL of 2% v/v HCl. A second solution, sensitive to ferrous iron in carbonate, was prepared by dissolving 2.0 g of potassium ferricyanide ($K_3Fe^{III}(CN)_6$) in 250 mL of 2% HCl v/v. Samples were soaked in a 5-mm deep basin of alizarin red S solution for 30 s, rinsed in water, blotted dry, and photographed. Samples that stained bright red were interpreted to contain nearly pure calcite, whereas samples that stained wine red, red-brown, or purple were interpreted to contain impure calcite. Samples that were either unreactive with alizarin red S or stained very pale pink were interpreted to be dolomite. Samples were then stained in the potassium ferricyanide solution for 60 s, rinsed, blotted, and photographed. Carbonate samples that reacted to produce a blue, indigo, or purple stain were interpreted to contain ferrous iron.

MICROSAMPLING

Carbonate microsampling was required for two analytical procedures: (1) carbon and oxygen isotopic analysis by laser spectroscopy; and (2) compositional analysis by laser ablation – inductively coupled plasma mass spectrometry (LA-ICP-MS).

***Table 1**. Sample descriptions.*

Sample	Area	Sample Type	Location (NAD83/ UTM Zone 7N)		Rock Name	Group	Carbonate Type		
			Easting (m)	Northing (m)			Matrix	Seg'n	Vein
KLONDIKE ASSEMBLAGE SAMPLES									
05-LS-25_73.4m	Lone Star Ridge	drill core	586849	7086318	qtz-fs-ms schist	felsic	fcc	fcc*	
05-LS-25_75.0m	Lone Star Ridge	drill core	586849	7086318	qtz-fs-ms schist	felsic	fcc	fcc (2)	
06-LS-19_68.0m	Lone Star Ridge	drill core	586595	7086500	qtz augen schist	metaporphyry	(1)		
06-NZ-01_65.7m	Oro Grande Gulch / Eldorado Creek	drill core	584955	7085697	qtz augen schist	metaporphyry	fcc* (1)		
06-NZ-01_65.8m	Oro Grande Gulch / Eldorado Creek	drill core	584955	7085697	qtz augen schist	metaporphyry		fcc (1)	
BU-07-02_108.3m	Gay Gulch / Eldorado Creek	drill core	585473	7084751	qtz-fs-ms-chl schist	felsic			fcc* (1)
BU-07-02_114.6m	Gay Gulch / Eldorado Creek	drill core	585473	7084751	qtz-fs-ms-chl schist	felsic			fcc* (1)
BU-07-02_146.2m	Gay Gulch / Eldorado Creek	drill core	585473	7084751	qtz-fs-ms-chl schist	felsic	fcc		fcc (1)
BU-07-03_64.0m	Gay Gulch / Eldorado Creek	drill core	585539	7084949	qtz-fs-ms schist	felsic			fcc* (1)
BU-07-03_78.6m	Gay Gulch / Eldorado Creek	drill core	585539	7084949	qtz-fs-ms schist	felsic			fcc* (1)
BU-07-03_83.1m	Gay Gulch / Eldorado Creek	drill core	585539	7084949	qtz augen schist	metaporphyry			fcc* (1)
BU-07-03_91.7m	Gay Gulch / Eldorado Creek	drill core	585539	7084949	qtz-fs-ms schist	felsic			fcc* (1)
BU-07-04_100.5m	Gay Gulch / Eldorado Creek	drill core	585557	7085000	qtz-fs-ms schist	felsic			fcc* (1)
DDH-04-03_283.0m	Upper Bonanza / Last Chance Ridge	drill core	589201	7091349	qtz-fs-ms schist	felsic			fcc* (1)
DDH-04-04_106.5m	Upper Bonanza / Last Chance Ridge	drill core	589799	7091698	qtz-fs-ms schist	felsic			fcc (1)
DDH-04-04_108.5m	Upper Bonanza / Last Chance Ridge	drill core	589799	7091698	qtz-fs-ms schist	felsic	fcc		fcc (1)
DDH-04-04_135.8m	Upper Bonanza / Last Chance Ridge	drill core	589799	7091698	qtz-fs-ms schist	felsic			cc* (1)
DDH-04-04_87.0m	Upper Bonanza / Last Chance Ridge	drill core	589799	7091698	qtz augen schist	metaporphyry			fcc* (1)
DDH-04-05_149.3m	Upper Bonanza / Last Chance Ridge	drill core	587776	7091264	qtz augen schist	metaporphyry			fcc* (1)
DDH-04-05_265.0m	Upper Bonanza / Last Chance Ridge	drill core	587776	7091264	qtz augen schist	metaporphyry			fcc* (1)
DDH-04-05_314.5m	Upper Bonanza / Last Chance Ridge	drill core	587776	7091264	qtz augen schist	metaporphyry			fcc* (2)
DDH-04-05_320.5m	Upper Bonanza / Last Chance Ridge	drill core	587776	7091264	qtz augen schist	metaporphyry			fcc* (1)
DDH-04-05_322m	Upper Bonanza / Last Chance Ridge	drill core	587776	7091264	qtz augen schist	metaporphyry			fcc* (1)
DDH-04-05_332.4m	Upper Bonanza / Last Chance Ridge	drill core	587776	7091264	qtz augen schist	metaporphyry			fcc* (2)
DDH-04-05_333.6m	Upper Bonanza / Last Chance Ridge	drill core	587776	7091264	qtz augen schist	metaporphyry	fcc		fcc* (1)
DDH-04-06_281.3m	Upper Bonanza / Last Chance Ridge	drill core	587778	7092124	qtz augen schist	metaporphyry			fcc* (1)
DDH-04-06_32.0m	Upper Bonanza / Last Chance Ridge	drill core	587778	7092124	qtz augen schist	metaporphyry			fcc (1)
K70	7 Pup / Victoria Gulch	trench	587020	7087280	ms marble	marble	fcc (1)		
K71	7 Pup / Victoria Gulch	trench	587023	7087287	ms marble	marble	fcc* (1)		
K72	7 Pup / Victoria Gulch	trench	587026	7087297	ms mable	marble	fcc (2)		
MA12-DL1	Hunker Dome (Dome Lode)	trench	602646	7084060	qtz-fs-ms schist	felsic		* (3)	
MA12-DL2	Hunker Dome (Dome Lode)	trench	602646	7084060	qtz-fs-ms schist	felsic		fcc (1)	
MA12-DL3	Hunker Dome (Dome Lode)	trench	602646	7084060	qtz-fs-ms schist	felsic		* (2)	
MA12-DL4	Hunker Dome (Dome Lode)	trench	602646	7084060	qtz-fs-ms schist	felsic		cc (2)	
MA12-DL5	Hunker Dome (Dome Lode)	trench	602646	7084060	qtz-fs-ms schist	felsic			* (1)
MA12-DL6	Hunker Dome (Dome Lode)	trench	602646	7084060	chl schist	mafic	fcc (1)	fcc* (1)	fcc* (2)
MA12-DL7	Hunker Dome (Dome Lode)	trench	602646	7084060	chl schist	mafic		fcc* (1)	fcc* (1)
MA12-DL8	Hunker Dome (Dome Lode)	trench	602646	7084060	chl schist	mafic	cc (2)	fcc	fcc* (1)
MA12-DL9	Hunker Dome (Dome Lode)	trench	602646	7084060	chl schist	mafic			* (2)
MA12-K03	Top of the World Hwy.	outcrop	562595	7112051	qtz-fs-ms schist	felsic	fcc/cc*		cc
MA12-K05	Top of the World Hwy.	outcrop	562595	7112051	chl-tlc schist	mafic		cc* (2)	

***Table 1**. continued.*

Sample	Area	Sample Type	Location (NAD83/ UTM Zone 7N)		Rock Name	Group	Carbonate Type		
			Easting (m)	Northing (m)			Matrix	Seg'n	Vein
MA12-K07	7 Pup / Victoria Gulch	float	586913	7087144	ms marble	marble	fcc* (4)		
MA12-K08	7 Pup / Victoria Gulch	float	586913	7087144	ms marble	marble	fcc* (2)		
MA12-K09	7 Pup / Victoria Gulch	float	586913	7087144	ms marble	marble	fcc* (2)	fcc* (1)	
MA12-K10	7 Pup / Victoria Gulch	float	586913	7087144	ms marble	marble	fcc* (3)		
MA12-K11	7 Pup / Victoria Gulch	float	586913	7087144	ms marble	marble	fcc (1)		
MA12-K12	7 Pup / Victoria Gulch	float	586913	7087144	ms marble	marble	fcc* (2)		
MA12-K14	Bonanza Creek (near Magnet Gulch)	outcrop	581393	7091468	chl schist	mafic		fcc (2)	
MA12-K16	Upper Bonanza road	outcrop	593129	7086755	chl schist	mafic		fcc (1)	
MA12-K17	King Solomon Dome	outcrop	600775	7083353	chl schist	mafic	fcc* (2)		
MA12-K19	Scriber Creek (mouth)	outcrop	613377	7056823	qtz-fs-ms schist	felsic			(1)
MA12-K20	Hunker Dome (Mitchell)	trench	600790	7085848	chl schist	mafic	fcc* (2)		fcc (1)
MA12-K21	Hunker Dome (Mitchell)	trench	600790	7085848	chl schist	mafic	fcc* (1)		fcc (1)
MA12-SH1	Hunker Dome (Sheba)	outcrop	601000	7085000	chl schist	mafic		fcc* (4)	
MA12-SH2	Hunker Dome (Sheba)	outcrop	601000	7085000	chl schist	mafic		fcc* (3)	
MA12-SH3	Hunker Dome (Sheba)	outcrop	601000	7085000	chl schist	mafic	fcc (1)		fcc* (1)
MA12-VG1	Bear Creek (Virgin)	mine dump	586282	7098104	qtz augen schist	metaporphyry			* (1)
MA12-VG2	Bear Creek (Virgin)	mine dump	586282	7098104	qtz augen schist	metaporphyry			* (1)
MA12-VG3	Bear Creek (Virgin)	mine dump	586282	7098104	qtz augen schist	metaporphyry			* (1)
MA12-VG4	Bear Creek (Virgin)	mine dump	586282	7098104	qtz augen schist	metaporphyry			* (1)
MA12-VG5	Bear Creek (Virgin)	mine dump	586282	7098104	qtz augen schist	metaporphyry			* (1)
MA12-VG6	Bear Creek (Virgin)	mine dump	586282	7098104	qtz augen schist	metaporphyry			* (1)
MA12-VL5	Violet Ridge	trench float	584905	7081545	qtz-fs-bt schist	metaporphyry			* (2)
MA12-VL6	Violet Ridge	trench float	584905	7081545	qtz-fs-bt schist	metaporphyry		(3)	
MA12-VL7	Violet Ridge	trench float	584905	7081545	qtz-fs-bt schist	metaporphyry			fcc* (2)
MA12-VL8	Violet Ridge	trench float	584905	7081545	qtz-fs-bt schist	metaporphyry			* (2)
NASINA ASSEMBLAGE SAMPLES									
MA12-NAS5	near Jim Creek pluton	float	573633	7083041	cc-grph schist	calcareous schist	fcc (1)		
MA12-NAS6	near Jim Creek pluton	float	573633	7083041	cc-grph schist	calcareous schist	* (1)		* (3)
MA12-NAS7	near Jim Creek pluton	float	573633	7083041	grph-trem schist	calcareous schist	fcc (3)		
MA12-NAS8	near Jim Creek pluton	float	573633	7083041	cc-grph schist	calcareous schist		* (1)	
MA12-NAS9	near Jim Creek pluton	float	572526	7082873	cc marble	marble	fcc* (2)		
MA12-NAS10	near Jim Creek pluton	float	572526	7082873	cc marble	marble	fcc* (4)		
MA12-NAS11	near Jim Creek pluton	float	573562	7082892	cc marble	marble	* (1)		
MA12-NAS12	near Jim Creek pluton	float	573577	7082904	cc marble	marble	* (2)		

NOTES

qtz= quartz; ms = muscovite; fs = feldspar; chl = chlorite; bt = biotite; cc = calcite; grph = graphite; trem = tremolite

Under the heading "Carbonate Type":

cc = calcite (interpreted from staining)

fcc = ferroan calcite (interpreted from staining)

* = carbonate analyzed by LA-ICP-MS

(#) = number of C and O isotopic analyses

Samples of paragenetically distinct carbonate were removed from rock samples with a Dremel® rotary tool equipped with a tungsten carbide bit. Approximately 35 to 100 mg of powdered carbonate was collected on weigh paper and transferred to glass vials. Where silicate minerals could not be avoided during microsampling, sample sizes were scaled up accordingly. The tungsten carbide bit was cleaned in 10% HCl v/v followed by ethanol between samples. For some uncut samples, a clean stainless steel mortar and pestle were used to crush coarse fragments of carbonate to a powder.

For compositional analysis by LA-ICP-MS, single carbonate fragments between 1 and 4 mm were selected. For each paragenetic occurrence or composition of carbonate identified, a single grain was carefully sampled using a stainless steel point and placed in a grid on double-sided tape. Samples were mounted in epoxy, ground on 400 and 600 grit sandpaper, and polished sequentially using 6µm, 3µm, and 1 µm diamond, each for 4 minutes with 6 lb pressure.

CHEMICAL ANALYSIS BY LA-ICP-MS

Epoxy-mounted carbonate grains were analyzed at The Pacific Centre for Isotopic and Geochemical Research of UBC using a Resonetics® RESOlution M-50-LR 193-nm ArF excimer laser system, coupled to an Agilent 7700x quadrupole ICP-MS. Samples were ablated in the presence of helium carrier gas, which was delivered to the ICP-MS via polytetrafluoroethylene tubing equipped with a "squid" dispersion device to smooth out the resulting ICP-MS signal. Each carbonate grain was ablated five to ten times with a 24 µm diameter laser spot, pulsed at 10 Hz and having 100 mJ of energy. Each spot was ablated for 40 seconds, followed by 40 seconds of instrument flush time. The analytical sequence consisted of up to 60 spot analyses, and was bracketed by two analyses each of NIST 610 and 612 glass external standards. The NIST 610 and 612 external standards were also inserted between every 10 and 20 spot analyses, respectively. The isotopes analyzed were (dwell times in milliseconds): ^{23}Na (15), ^{25}Mg (100), ^{27}Al (15), ^{29}Si (15), ^{39}K (100), ^{43}Ca (40), ^{55}Mn (30), ^{57}Fe (30), ^{66}Zn (100), ^{88}Sr (30), ^{89}Y (100), ^{137}Ba (30), ^{139}La (30), ^{143}Nd (100), ^{208}Pb (30), and ^{238}U (30). Aluminum, silicon, potassium, and sodium were primarily analyzed as tracers of silicate contaminant material.

Time-resolved ICP-MS signals were background-corrected and converted from count ratios into mass ratios using background-corrected signals from the NIST 610 and NIST 612 external standards. Background corrections, signal integrations, drift corrections, and concentration calculations were carried out with the Matlab®-based computer program SILLS (Allan *et al.*, 2010), which allows individual portions of time-resolved signals to be selected. For each 40-second carbonate signal, the first 1-2 seconds of signal was discarded due to possible surface contamination, and the final 20 seconds was rejected due to possible element fractionation at greater ablation depths. Signals for ^{29}Si and/or ^{27}Al, ^{39}K, or ^{23}Na signals were interpreted as silicate contamination, in which case either the analysis was rejected or the carbonate-only portion of the time-series signal was integrated.

The major to trace element composition of each carbonate sample is expressed as the average of all spot analyses. Errors in element concentration are expressed as the standard deviation of the five to ten separate determinations, which significantly exceeds the analytical error associated with an individual measurement. The most significant cations (Ca, Mg, Fe, and Mn) are expressed as a molar ratio of the total cations. Trace element concentrations are expressed in µg/g on the basis of the molar weight of (Ca, Fe, Mg, Mn)CO_3, which is individually determined for each sample.

C AND O ISOTOPIC ANALYSIS BY LASER SPECTROSCOPY

Powdered carbonate samples were analyzed for $^{13}C/^{12}C$ and $^{18}O/^{16}O$ ratios, using off-axis integrated cavity output spectroscopy (OA-ICOS), closely following the technique of Barker *et al.* (2011). Between 35 and 100 mg of powdered carbonate was weighed and put into a clean borosilicate glass test tube and sealed with a butyl rubber septum. Between 0.2 and 0.3 mL of 85 % H_3PO_4 was injected into the sample tube, the tube was placed in an aluminum heating block, and left to react with the carbonate sample for 1 h at 72 °C. Prior to introducing the carbon dioxide reaction product to the analyzer, the OA-ICOS instrument (Los Gatos Research, model 908-0021) was flushed with dry laboratory air, and pumped down to pressure below 0.5 kPa. The carbon dioxide analyte, up to this point contained within a sealed test tube, was passed via tubing through a glass cold trap contained within a -78 °C bath of dry ice and ethanol to remove any water vapor. The dry CO_2 sample was then introduced via stainless steel tubing into to the OA-ICOS instrument, where carbon and oxygen isotope ratios of the CO_2 were recorded from the absorption spectra of isotopologues $^{12}C^{16}O^{18}O$, $^{13}C^{16}O^{16}O$, and $^{12}C^{16}O^{18}O$ in the near-infrared wavelength region.

Samples that generated sulphurous gas in the isotope analyzer revealed contamination by pyrite at the microdrilling stage, and were rejected due to spectral interferences. Samples contaminated by silicate material (*e.g.*, quartz or muscovite) are unaffected because only the carbonate component reacts with phosphoric acid.

In-house calcite standard BN13 ($\delta^{13}C_{VPDB}$ = 1.84‰; $\delta^{18}O_{VSMOW}$ = 13.64‰) was inserted into the analytical sequence every five unknowns to calculate errors and assess instrument drift. Analytical reproducibility ranged from 0.2 to 1.8 ‰ for $\delta^{13}C$ (±1σ) and 0.5 to 1.0‰ for $\delta^{18}O$ (±1σ). Higher than expected $\delta^{13}C$ errors for some samples were attributed to unusually warm lab conditions.

Sample duplicates, obtained by microdrilling the same geologic feature twice, were inserted every twentieth sample, and showed good correlations. Analytical duplicates, obtained by splitting the carbonate powder into two aliquots, were run every fifth sample, and show excellent correlations. The instrument was calibrated prior to analysis using calcite standards of known isotopic composition (Barker *et al.*, 2011).

RESULTS

CARBONATE CHEMISTRY

The alizarin red S and potassium ferricyanide staining indicated that the vast majority of carbonate, regardless of host rock lithology or mode of carbonate occurrence, is Fe-bearing calcite. In a small number of cases, samples produced only a very weak pink stain with alizarin red S, and the potassium ferricyanide produced a bright blue stain; in these cases, ferroan dolomite or ankerite was interpreted to be present. No distinguishing feature (*e.g.*, rock type) appears to control where ferroan dolomite is likely to occur. A small number of samples reacted only to alizarin red S, indicating a nearly pure calcite composition. These compositions are more typical of marble and calcareous schist of the Nasina assemblage.

Within a given sample, the colour and intensity of stain was generally consistent. This observation indicates little compositional zoning, and supports the approach of analyzing small representative grains by LA-ICP-MS.

The LA-ICP-MS results are reported in Appendix 1. Of 63 samples analyzed, 54 are "impure" calcite, containing subequal molar quantities of Mg, Fe, and Mn. In these samples, auxiliary cations comprise 0.7 to 6.4% of the cation inventory on a molar basis. In these samples, the other elements analyzed by LA-ICP-MS are in significantly lower abundance (median concentrations shown in parentheses): Sr (1001 µg/g); Y (22.3 µg/g); Ba (13.1 µg/g); Pb (9.6 µg/g); Nd (3.4 µg/g); Zn (3.0 µg/g); La (1.2 µg/g); and U (0.02 µg/g). Concentrations of these elements are similar in Mg-Fe-Mn calcite and ferroan dolomite samples, although the latter contains one to two orders of magnitude more Zn.

The concentrations of Mg and Fe show a good correlation, whereas the correlation of Mn to these elements is weaker. Sr and Y also show a reasonable correlation. A close correlation between La and Nd is observed over four orders of magnitude concentration variation (Fig. 6).

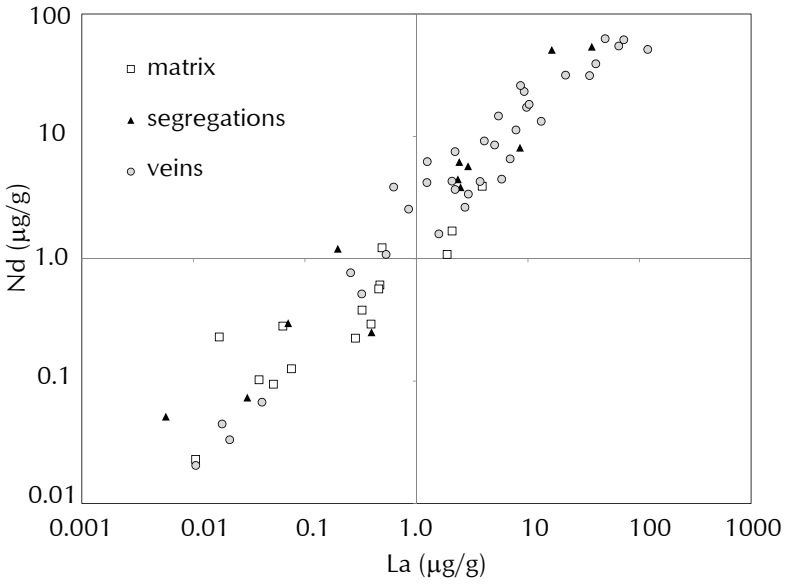

Figure 6. *La vs. Nd concentrations in Klondike schist carbonate samples. Data are divided into matrix (porphyroblasts), segregations, and veins. Data points represent the average La and Nd concentration of several point LA-ICP-MS spot analyses per sample. Errors bars are omitted for clarity.*

CARBON AND OXYGEN ISOTOPES

Carbon and oxygen isotope determinations for Klondike carbonate samples are presented in Appendix 2. Figure 7A shows the dataset coded by lithologic subunits, which include the felsic, mafic, metaporphyritic, and marble variants of the Klondike schist, as well as calcareous schist and marble variants of the Nasina assemblage.

Calcite marble of the Nasina assemblage forms a distinct data cluster with $\delta^{13}C_{VPDB}$ values of -2 to 4‰ and $\delta^{18}O_{VSMOW}$ values of +11 to +17‰. Relative to the Nasina marble, the calcareous, graphitic schist of the Nasina assemblage is shifted to lower $\delta^{13}C_{VPDB}$ (-10 to -6‰) and has similar, but more variable $\delta^{18}O_{VSMOW}$ values (+9 to +21‰).

The Klondike schist samples form two main isotopic populations. The Mg-Fe-Mn calcite marble samples cluster around $\delta^{13}C_{VPDB}$ = +1 to +5‰ and $\delta^{18}O_{VSMOW}$ = +5 to +10‰, which is ^{18}O-depleted by ~5 ‰ relative to the Nasina marble samples. In contrast, the remaining Klondike schist carbonate samples plot at much lower $\delta^{13}C_{VPDB}$ values (generally between -13 and -4‰), and over a much wider range of $\delta^{18}O_{VSMOW}$ values (-8 to +15‰). The range in C and O isotopic compositions between the mafic, felsic, and metaporphyry subunits of the Klondike schist overlap, with the exception of a few anomalously positive $\delta^{13}C_{VPDB}$ values in the mafic schist.

The extreme outlier at $\delta^{13}C_{VPDB}$ = -36‰ in Figure 7 is a sample of pink calcite in a quartz-rich segregation within quartz augen schist near the Violet gold occurrence (Fig. 4D). The sample had a chalky alteration rind which was avoided during microdrilling, but the interior of the sample was neither visibly altered nor unusual in chemical composition. Furthermore, the sample was microdrilled and analyzed in triplicate to rule out random sampling or analytical error. The Klondike assemblage's stratigraphy is dominated by meta-igneous rocks, so influence from a ^{13}C-depleted, organically-derived local carbon source is unlikely. Intrusive units of the Klondike assemblage are typically oxidized, so carbonate is unlikely to have inherited its extremely light $\delta^{13}C$ signature from intrusion-related CH_4. Our preferred explanation is that such low $\delta^{13}C_{VPDB}$ values are the result of extreme open-system Rayleigh fractionation behaviour during metamorphism.

Figure 7B discriminates between carbonate occurring as rock matrix, in segregations, and in veins. The isotopic composition of carbonate in segregations and veins strongly overlap (most hosted in Klondike schist). The significance of this observation is discussed in the following section.

DISCUSSION

Five important points emerge from this study:

1. Origin of Marble: Marble of the Klondike schist and Nasina assemblage is isotopically distinct from the silicate Klondike schist samples, with slightly positive $\delta^{13}C_{VPDB}$ values (+1 to +5‰) and a much narrower range of $\delta^{18}O_{VSMOW}$ values (+5 to +10‰). The $\delta^{13}C_{VPDB}$ isotopic signatures of both Klondike and Nasina marble are consistent with marine carbonate found in the Late Permian and Devono-Mississippian geologic record, respectively (Saltzman and Thomas, 2012). However, pristine limestone from the Late Permian Klondike assemblage and Devono-Mississippian Nasina assemblage would both be expected to have significantly heavier $\delta^{18}O_{VSMOW}$ signatures of ~+18 to +22‰ (Grossman, 2012). Rayleigh fractionation during open-system metamorphic degassing of CO_2 could produce a similar effect in $\delta^{18}O$. However, this effect would also shift $\delta^{13}C$ to lower values, which is not observed. The discrepancy may instead be explained by interaction with ^{18}O-depleted fluids during diagenesis. In addition, some degree of isotopic exchange with Yukon's modern ^{18}O-depleted meteoric water cannot be excluded ($\delta^{18}O_{VSMOW}$ ~-18 to -25‰; Bowen and Wilkinson, 2002).

   Relative to calcite marble of the Nasina assemblage, calcite in graphite-bearing schist of the Nasina assemblage is distinctly $\delta^{13}C$-depleted. The presence of tremolite in parts of the Nasina assemblage stratigraphy indicates CO_2 degassing via the reaction $5\ CaMg(CO_3)_2 + 8\ SiO_2 + 1\ H_2O = 1\ Ca_2Mg_5Si_8O_{22}$ (tremolite) $+ 3\ CaCO_3 + 7\ CO_2$. In open system degassing, fractionation of isotopically heavy CO_2 would drive the calcite reaction product to isotopically lower values of both $\delta^{13}C$ and $\delta^{18}O$. Alternatively, a depleted $\delta^{13}C$ signature may indicate the formation of calcite via the oxidation of isotopically light, organic-derived graphite.

2. C isotopes in the Klondike schist: Carbonate within the Klondike schist, regardless of paragenesis, shows a fairly narrow $\delta^{13}C_{VPDB}$ range of -13 to -2‰. This range of values is typical of carbonate in many orogenic gold camps worldwide (Nesbitt, 1991). The data also preclude any influence from externally-sourced sedimentary organic matter, *i.e.*, from the underlying Nasina assemblage, or from rare graphitic schist contained within the Klondike assemblage. The Klondike carbonate contrasts with other Phanerozoic examples of orogenic gold mineralization in which ^{13}C-depleted hydrothermal carbonate is sourced from reduced, biogenic sources of carbon in the wallrock (*e.g.*, gold deposits of Meguma terrane in Nova Scotia; Kontak and Kerrich, 1997).

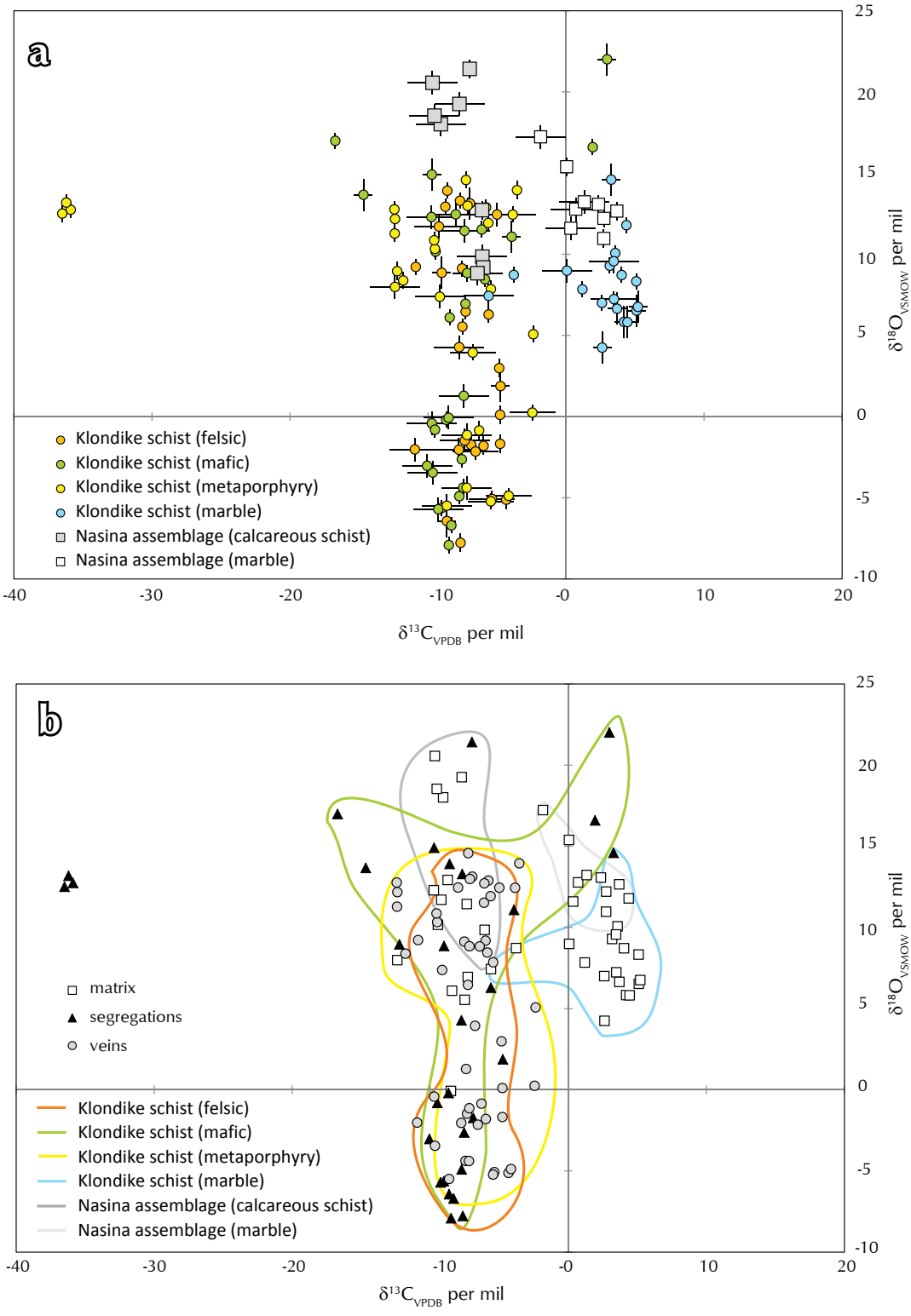

***Figure 7**. Carbon and oxygen isotopic ratios for Klondike carbonate samples; (a) plot of $\delta^{13}C_{VPDB}$ vs. $\delta^{18}O_{VSMOW}$, samples coloured by host rock lithology; and (b) sample plot as in (a), with data organized by mode of carbonate occurrence.*

3. O isotopes in the Klondike schist: The Klondike schist samples show a significant variation in $\delta^{18}O_{VSMOW}$, with no systematic difference between the different modes of carbonate occurrence. Some variation in oxygen isotopes is expected due to rock-fluid interaction during metamorphism, or by temperature-dependent fractionation of ^{18}O between minerals and CO_2 during hydrothermal activity. However, excursions to negative $\delta^{18}O_{VSMOW}$ values as low as -8‰ are not readily explained by these processes.

   Two main possibilities are considered. Rushton *et al.* (1993) collected δD data from fluid inclusions and hydrothermal minerals associated with gold-bearing veins in the Klondike, and argued that the 300 to 350°C fluids responsible for mineralization had a modified meteoric signature. However, the oxygen isotopic composition of hydrothermal carbonate is strongly rock-buffered, so a preserved meteoric signature is unlikely. The second possibility is interaction in the weathering environment with modern, ^{18}O-depleted meteoric water. Although care was taken to select only fresh, unaltered carbonate samples, relatively little exchange between calcite and meteoric water would be required to produce negative shifts in $\delta^{18}O_{VSMOW}$.

4. Origin of carbonate segregations: Textural observations indicate that segregations accumulate carbonate in the same manner as quartz, *i.e.*, migration by dynamic recrystallization during progressive deformation. Disseminated porphyroblasts of calcite, observed in some exposures of chloritic Klondike schist, are the most likely source of this remobilized carbonate. Both segregation carbonate and porphyroblastic ("matrix") carbonate yield $\delta^{13}C_{VPDB}$ values in the range from -15 to -3‰. These data are consistent with the preservation of C-isotopic signatures during ductile deformation, indicating closed-system behaviour (Appendix 2).

5. Origin of vein carbonate: The C and O isotopic signature of carbonate in D_4-stage veins maps remarkably well onto the signature of matrix and segregation carbonate in the Klondike schist host rocks. Although there are temperature and kinetic factors that can complicate interpretations of these signatures, these veins formed at mid-crustal levels in the absence of magmatism, and therefore, under pseudo-isothermal conditions. Rushton *et al.* (1993) concluded from fluid inclusion studies that most gold-stage veins in the Klondike formed at 300 to 350°C. Furthermore, vein carbonate in the Klondike shows no textural evidence for rapid precipitation, so hydrothermal conditions probably approximated isotopic equilibrium. Therefore, it is reasonable to suggest that the C isotopic signature of vein carbonate reflects the CO_2 from which it was derived. Although the range of measured $\delta^{13}C_{VPDB}$ values in vein carbonate from the Klondike (-12 to -2‰) are typical of volcanic-hosted orogenic gold deposits (Nesbitt, 1991), the data do not reveal an unambiguous source of CO_2. A number of sources could be considered, including: (1) metamorphic devolatization, especially of mafic rocks; (2) magmatic CO_2, either of crustal or mantle origin; or (3) CO_2 derived from a combination of ^{13}C-depleted and ^{13}C-enriched sources.

   A likely explanation for the source of carbonate in D_4-stage veins is that they derived their C isotopic signature from the local wallrock. This inference is supported by comparable $\delta^{13}C_{VPDB}$ values in veins and background (matrix or segregations) within the same sample (*e.g.*, see data for sample MA12-DL8 in Appendix 2). The strength of this relationship could be verified by targeting samples with a wider range of $\delta^{13}C_{VPDB}$ values, to test the hypothesis that carbon cycling between wallrock and hydrothermal fluids is a local phenomenon.

   The strong Nd-La correlation in Klondike schist carbonate may also support the notion that vein carbonate is locally derived. Figure 6 demonstrates that the Nd/La ratio in carbonate is consistent over orders of magnitude for matrix (porphyroblasts), segregations, and veins. This observation suggests that the system has been essentially closed with respect to rare earth elements since formation of the Klondike schist's volcanic protolith. Furthermore, absolute concentrations of Nd and La in carbonate from veins and segregations reach concentrations in the 10s of µg/g (ppm by weight), whereas concentrations in the matrix reach a maximum of a few µg/g. This may suggest that rare earth elements are progressively concentrated by carbonate remobilization into segregations, or by hydrothermal redistribution of carbonate into brittle structures.

CONCLUSIONS

Based on our field observations and preliminary isotopic evidence, we suggest the following sequence of events:

1. Carbonate was incorporated into the igneous protolith of the Klondike schist as alteration and/or veins during magmatic-hydrothermal activity in the Late Permian. During this time, small carbonate deposits formed at the seafloor, and later metamorphosed to form quartz-muscovite bearing marble.
2. Carbonate was segregated into quartz-rich layers during Late Permian D_1-D_2 deformation, during which it preserved its C-isotopic signatures.
3. Carbonate was re-concentrated into quartzose segregations during Early Jurassic D_3 deformation.
4. In the Late Jurassic, the onset of brittle D_4 deformation allowed aqueous hydrothermal solutions to leach carbonate stored by wallrock in segregations or in the rock matrix, to enter into fracture systems, and to precipitate quartz, carbonate, pyrite, and gold in veins.

The results of our study are consistent with $\delta^{13}C$ carbonate signatures being preserved in the Klondike schist during each of the above stages. Most importantly, carbonate in gold-bearing veins has a C-isotopic signature consistent with local host rock derivation of CO_2. Similarly, host rock derivation of gold and other vein components is a viable hypothesis.

This carbonate study is part of ongoing structural, geochemical, and geochronological studies of orogenic gold mineralization in Yukon. Further work on carbonate geochemistry should consider:

1. Integrating carbonate geochemistry with bulk rock compositional data;
2. Integrating carbonate geochemistry with stable (S, O, H) and radiogenic (Sr, Pb) isotopic studies of other minerals, to improve constraints on the source(s) of volatiles and metals;
3. Evaluating possible effects of surface weathering on stable isotopes.

ACKNOWLEDGEMENTS

This research was supported by MDRU's Yukon Gold Project – an industry-funded collaboration with sponsor companies Aldrin Resource Corp., Barrick Gold Corp., Full Metal Minerals Corp., Gold Fields Canada Exploration, Northern Freegold Resources Ltd., Kinross Gold Corp., Radius Gold Inc., Silver Quest Resources Ltd., Taku Gold Corp., Teck Resources Ltd., and Underworld Resources Inc. The Yukon Gold Project also benefitted from a NSERC Collaborative Research and Development grant. We thank Klondike Gold Corp. for allowing access to drill core and for providing collar coordinates, and Tim Liverton for providing additional samples.

We gratefully acknowledge Dr. Andreas Beinlich for guidance with stable isotope analysis, and Dr. Marg Amani for assistance with laser ablation ICP-MS measurements.

The manuscript benefited from a thoughtful review by Dave Craw from the University of Otago.

REFERENCES

Allan, M.M., Meier, D., and Guillong, M., 2010. SILLS: Signal Integration for Laboratory Laser Systems, v.1.1.0, Matlab program.

Allan, M.M., Mortensen, J.K., Hart, C.J.R., Bailey, L.A., Sánchez, M.G., Ciokiewicz, W., McKenzie, G.G., and Creaser, R.A., 2013. Magmatic and metallogenic framework of west-central Yukon and eastern Alaska. *In*: Tectonics, metallogeny, and discovery: the North American Cordillera and similar accretionary settings, M. Colpron, T. Bissig, B.G. Rusk, and J.F.H. Thompson (eds.), Society of Economic Geologists, Special Publication 17, p. 111-168.

Barker, S.L., Dipple, G.M., Dong, F., and Baer, D.S., 2011. Use of laser spectroscopy to measure the $^{13}C/^{12}C$ and $^{18}O/^{16}O$ compositions of carbonate minerals. Analytical Chemistry, vol. 83, no. 6, p. 2220-2226.

Beaudoin, G., 2011. The stable isotope geochemistry of orogenic gold deposits, *In:* 11th SGA Biennial Meeting, Antofagasta, Chile, 26-29 September, 2011. Society for Geology Applied to Mineral Deposits, Program with Abstracts, p. 556-558.

Beranek, L.P. and Mortensen, J.K., 2011. The timing and provenance record of the Late Permian Klondike orogeny in northwestern Canada and arc-continent collision along western North America. Tectonics, vol. 30, p. TC5017.

Bowen, G.J. and Wilkinson, B., 2002. Spatial distribution of $\delta^{18}O$ in meteoric precipitation. Geology, vol. 30, p. 315-318.

Breitsprecher, K. and Mortensen, J.K., 2004. Yukonage 2004: A database of isotopic age determinations for rock units from Yukon Territory. Yukon Geological Survey, CD-ROM.

Grossman, E.L., 2012. Oxygen isotope stratigraphy. *In*: The Geologic Time Scale 2012, F.M. Gradstein, J.G. Ogg, M. Schmitz, and G. Ogg (eds.), Elsevier, Boston, p. 181-206.

Groves, D.I., Goldfarb, R.J., Robert, F., and Hart, C.J.R., 2003. Gold deposits in metamorphic belts: Overview of current understanding, outstanding problems, future research, and exploration significance. Economic Geology, vol. 98, p. 1-29.

Hitzman, M., 1999. Routine staining of drill core to determine carbonate mineralogy and distinguish carbonate alteration textures. Mineralium Deposita, vol. 34, p. 794-798.

Hunt, P.A. and Roddick, J.C., 1992. A compilation of K-Ar ages: Report 21. Geological Survey of Canada Paper 91-2, p. 207-261.

Kontak, D.J. and Kerrich, R., 1997. An isotopic (C, O, Sr) study of vein gold deposits in the Meguma Terrane, Nova Scotia; implication for source reservoirs. Economic Geology, vol. 92, p. 161-180.

MacKenzie, D., Craw, D., and Mortensen, J.K., 2008a. Structural controls on orogenic gold mineralisation in the Klondike goldfield, Canada. Mineralium Deposita, vol. 43, p. 435-448.

MacKenzie, D., Craw, D., and Mortensen, J.K., 2008b. Thrust slices and associated deformation in the Klondike goldfields, Yukon. *In*: Yukon Exploration and Geology 2007, D.S. Emond, L.R. Blackburn, R.P. Hill, and L.H. Weston(eds.), Yukon Geological Survey, p. 199-213.

Mortensen, J., 1990. Geology and U-Pb geochronology of the Klondike District, west-central Yukon Territory. Canadian Journal of Earth Sciences, vol. 27, p. 903-914.

Mortensen, J.K., Dusel-Bacon, C., Hunt, J., and Gabites, J., 2006. Lead isotopic constraints on the metallogeny of middle and late Paleozoic syngenetic base-metal occurrences in the Yukon-Tanana and Slide Mountain/ Seventymile terranes and adjacent portions of the North American miogeocline. *In*: Paleozoic Evolution and Metallogeny of Pericratonic Terranes at the Ancient Pacific Margin of North America, Canadian and Alaskan Cordillera, M. Colpron, and J.J. Nelson(eds.), Geological Association of Canada Special Paper 45, p. 261-279.

Nesbitt, B., 1991. Phanerozoic gold deposits in tectonically active continental margins. *In*: Gold Metallogeny and Exploration, R.P. Foster(ed.), Blackie and Sons, Glasgow, p. 104-132.

Rushton, R.W., Nesbitt, B., Muehlenbachs, K., and Mortensen, J.K., 1993. A fluid inclusion and stable isotope study of Au quartz veins in the Klondike District, Yukon Territory, Canada; a section through a mesothermal vein system. Economic Geology, vol. 88, p. 647.

Saltzman, M.R., and Thomas, E., 2012. Carbon isotope stratigraphy. *In*: The Geologic Time Scale 2012, F.M. Gradstein, J.G. Ogg, M. Schmitz, and G. Ogg(eds.), Elsevier, Boston, 207-232.

Yukon MINFILE, 2010. Yukon MINFILE - A database of mineral occurrences. Yukon Geological Survey, <*http://data.geology.gov.yk.ca*> [accessed November 16, 2013].

APPENDIX 1. LA-ICP-MS data.

Sample	Carb. Type	Ca	Mg	Fe	Mn	Mineral	Zn	1σ	Sr	1σ	Y	1σ	Ba	1σ	La	1σ	Nd	1σ	Pb	1σ	U	1σ
		mol %	mol %	mol %	mol %		µg/g		µg/g		µg/g		µg/g		µg/g		µg/g		µg/g		µg/g	
K71	M	97.90	0.98	0.66	0.40	Mg-Fe-Mn cc	4.6	2.1	340	18	5	5	5.4	2.1	0.28	3.09	0.22	2.92	7.02	2.51	0.01	0.04
MA12-K03	M	99.73	0.02	0.06	0.15	cc	1.2	0.5	280	48	20	8	2.4	4.1	0.33	2.43	0.38	1.70	1.01	3.77	0.02	0.01
MA12-K07	M	97.97	1.04	0.66	0.26	Mg-Fe-Mn cc	4.6	3.1	276	202	15	8	13.1	22.4	0.39	9.14	0.29	7.00	9.65	5.35	0.05	0.02
MA12-K08	M	98.15	0.95	0.65	0.22	Mg-Fe-Mn cc	2.6	2.2	388	223	11	2	13.4	6.6	0.08	0.76	0.13	0.57	8.56	3.25	0.01	0.00
MA12-K09	M	97.58	1.18	0.85	0.36	Mg-Fe-Mn cc	3.3	1.3	515	434	13	6	15.4	5.4	0.49	2.31	1.23	2.93	16.97	7.82	0.06	2.20
MA12-K10	M	98.34	0.85	0.56	0.22	Mg-Fe-Mn cc	3.0	2.1	294	74	9	5	11.4	3.8	0.47	0.66	0.61	0.68	5.73	1.76	0.03	0.05
MA12-K12	M	98.42	0.78	0.54	0.22	Mg-Fe-Mn cc	3.4	1.8	428	116	14	6	7.3	5.4	0.05	1.25	0.09	0.75	6.27	2.43	0.01	0.01
MA12-K17	M	95.12	1.81	1.55	1.57	Mg-Fe-Mn cc	4.6	0.6	168	20	4	3	1.5	0.3	0.04	0.33	0.10	0.66	4.00	0.71	BD	
MA12-K20	M	95.39	1.81	1.53	1.22	Mg-Fe-Mn cc	2.5	0.6	187	328	7	4	12.2	2.8	0.06	0.59	0.28	0.80	4.10	7.28	0.01	0.00
MA12-K21	M	95.74	1.55	1.54	1.25	Mg-Fe-Mn cc	3.1	0.7	191	43	5	1	12.1	1.5	0.01	0.01	0.02	0.04	5.14	0.54	BD	
MA12-NAS6	M	96.17	3.27	0.22	0.06	Mg cc	4.1	3.0	2536	182	6	1	23.5	28.1	3.88	2.81	3.91	2.40	4.61	2.65	0.03	0.12
MA12-NAS9	M	96.45	2.56	0.77	0.12	Mg-Fe cc	15.8	3.2	362	14	7	1	5.2	0.9	0.02	0.32	0.23	0.34	1.88	0.11	0.01	0.00
MA12-NAS10	M	96.85	2.16	0.82	0.13	Mg-Fe cc	19.4	2.3	400	63	10	8	9.4	12.2	0.46	9.61	0.57	9.20	3.54	0.27	0.01	0.01
MA12-NAS11	M	99.02	0.44	0.35	0.07	cc	5.7	0.5	1021	37	6	1	4.5	0.7	2.08	0.25	1.69	0.19	7.83	1.06	BD	
MA12-NAS12	M	99.56	0.23	0.08	0.05	cc	4.2	0.3	706	38	4	0	33.4	2.5	1.88	0.11	1.08	0.09	1.39	0.15	0.01	0.03
05-LS-25_73.4m	S	54.77	39.68	4.47	0.85	Fe dol	230.8	37.1	371	66	8	17	5.6	2.2	8.49	22.46	8.08	18.25	12.48	3.29	0.14	0.03
MA12-DL1	S	97.02	0.99	0.59	1.08	Mg-Fe-Mn cc	1.5	4.8	235	216	29	8	16.1	18.9	2.42	1.22	6.17	1.93	21.07	2.33	0.11	0.10
MA12-DL3	S	93.45	2.75	2.02	1.61	Mg-Fe-Mn cc	4.4	1.1	800	61	29	6	6.1	8.9	0.03	0.02	0.07	0.08	40.48	4.89	0.26	0.78
MA12-DL6	S	96.71	1.46	0.66	1.01	Mg-Fe-Mn cc	2.0	2.0	1352	98	14	6	131.7	23.2	2.90	1.07	5.70	1.77	37.39	5.63	0.20	0.08
MA12-DL7	S	72.96	6.38	13.38	6.83	Fe-Mg-Mn cb			3808	1477	44	48	8000	10490	37.32	1.87	54.03	2.70	462	465	6.12	0.31
MA12-K05	S	98.95	0.35	0.26	0.38	Mg-Fe-Mn cc	5.1	0.6	537	36	72	3	16.3	1.1	0.07	0.09	0.30	0.07	21.35	2.30	BD	
MA12-K09	S	98.14	0.84	0.63	0.34	Mg-Fe-Mn cc	1.5	0.8	765	245	8	4	10.2	3.8	0.40	0.75	0.25	0.67	10.43	7.05	0.01	0.01
MA12-K14	S	51.62	41.20	6.57	0.44	Fe dol	130.3	51.9	314	140	33	6	6.0	3.6	2.49	0.69	3.84	1.00	22.20	47.51	0.07	0.15
MA12-K16	S	95.61	1.83	1.44	0.97	Mg-Fe-Mn cc	2.0	0.4	1281	33	9	0	6.1	1.0	0.01	0.00	0.05	0.01	37.32	4.80	BD	
MA12-NAS8	S	98.07	0.58	0.38	0.61	Mg-Fe-Mn cc	1.7	0.2	3045	165	48	5	17.9	1.0	0.20	0.03	1.21	0.13	5.72	0.36	0.01	0.02
MA12-SH1	S	94.45	2.95	0.82	1.64	Mg-Fe-Mn cc	21.9	9.7	1349	350	72	41	50.5	5.6	16.36	9.38	50.90	32.26	2.93	0.43	0.10	0.05
MA12-SH2	S	52.02	39.10	8.05	1.08	Fe dol	148.4	10.0	1103	80	11	4	88.0	9.7	2.35	0.99	4.46	2.11	6.19	2.12	0.02	0.02
BU-07-02_108.3m	V	96.20	2.28	0.75	0.59	Mg-Fe-Mn cc	8.4	24.7	1583	1651	15	17	14.2	5262.5	2.22	5.09	3.69	5.04	5.09	9.16	0.12	1.21
BU-07-02_114.6m	V	97.00	0.47	0.42	1.97	Mg-Fe-Mn cc			1152	504	168	38	20.1	39.2	65.06	59.74	54.78	23.82	0.16	0.04	0.01	0.00
BU-07-03_640m	V	95.88	1.17	0.97	1.76	Mg-Fe-Mn cc	1.0	0.4	1698	441	117	34	89.5	27.9	21.69	8.64	31.67	14.20	0.92	0.37	0.02	0.03
BU-07-03_78.6m	V	97.19	0.31	0.30	1.91	Mg-Fe-Mn cc	0.3	0.1	2165	668	21	14	72.8	33.1	2.92	1.98	3.38	3.53	0.14	0.05	0.07	0.04
BU-07-03_83.1m	V	97.45	0.30	0.30	1.81	Mg-Fe-Mn cc	0.3	0.0	1073	393	65	7	5.9	5.8	118.37	37.18	51.38	11.58	0.06	0.02	0.00	0.00
BU-07-03_91.7m	V	97.84	0.29	0.42	1.07	Mg-Fe-Mn cc			3345	575	44	4	88.6	27.9	13.12	2.14	13.28	1.09	0.19	0.06	0.02	0.00
BU-07-04_100.5m	V	97.13	0.57	0.78	1.09	Mg-Fe-Mn cc	0.4	0.2	3647	585	119	9	150.4	48.5	40.53	5.69	39.22	3.99	0.23	0.07	0.15	0.15
DDH-04-03_283.0m	V	95.16	1.64	1.20	1.67	Mg-Fe-Mn cc	0.8	0.1	2941	394	31	44	7.8	4.0	1.24	12.64	4.20	17.87	4.01	1.15	0.09	0.13
DDH-04-04_135.8m	V	98.42	0.19	0.29	0.85	Mg-Fe-Mn cc	0.6	0.5	666	350	97	42	12.3	4.8	72.17	53.07	61.58	28.47	3.09	28.77	0.04	0.15
DDH-04-04_87.0m	V	98.08	0.65	0.55	0.51	Mg-Fe-Mn cc	5.9	0.5	1800	253	28	4	27.2	4.4	0.32	1.29	0.52	1.18	45.31	5.48	0.16	0.13
DDH-04-05_149.3m	V	97.51	0.52	1.22	0.68	Mg-Fe-Mn cc	0.3		473	295	56	29	14.2	7.1	7.79	6.51	11.29	3.46	0.42	0.95	0.08	0.03
DDH-04-05_265.0m	V	98.86	0.11	0.13	0.85	Mg-Fe-Mn cc	0.4	0.2	357	167	218	95	2.0	1.6	49.11	31.22	62.89	32.38	0.27	0.13	0.01	0.03
DDH-04-05_314.5m	V	98.93	0.10	0.20	0.63	Mg-Fe-Mn cc			788	418	166	82	3.1	5.8	9.70	11.90	17.27	11.95	0.38	0.58	0.02	0.03
DDH-04-05_320.5m	V	70.85	20.41	8.08	0.50	Fe dol	188.2	52.4	648	717	69	60	25.0	69.5	35.64	40.34	31.39	40.39	20.61	12.98	0.19	0.14

APPENDIX 1. continued.

Sample	Carb. Type	Ca	Mg	Fe	Mn	Mineral	Zn	1σ	Sr	1σ	Y	1σ	Ba	1σ	La	1σ	Nd	1σ	Pb	1σ	U	1σ
		mol %	mol %	mol %	mol %		µg/g		µg/g		µg/g		µg/g		µg/g		µg/g		µg/g		µg/g	
DDH-04-05_322m	V	97.93	0.78	0.45	0.68	Mg-Fe-Mn cc	2.7	3.6	1765	531	16	10	16.0	6.8	2.72	3.37	2.63	3.42	17.03	3.44	0.10	0.13
DDH-04-05_332.4m	V	98.37	0.49	0.30	0.63	Mg-Fe-Mn cc	2.5	0.4	1713	481	8	3	33.0	6.2	0.02	0.03	0.04	0.05	40.14	9.87	BD	
DDH-04-05_333.6m	V	99.04	0.08	0.10	0.56	cc	0.5	0.1	2066	273	94	9	14.8	2.3	10.22	2.84	18.30	3.66	1.15	0.99	BD	
DDH-04-06_281.3m	V	97.75	0.41	0.82	0.65	Mg-Fe-Mn cc	2.7	15.3	3704	1474	20	43	15.5	8.9	1.59	1.77	1.60	2.67	18.13	6.71	0.42	0.35
MA12-DL5	V	98.27	0.62	0.43	0.58	Mg-Fe-Mn cc	0.8	0.3	864	62	10	2	6.0	0.8	0.04	0.04	0.07	0.07	26.71	2.00	0.01	0.01
MA12-DL6	V	96.51	1.73	0.61	0.90	Mg-Fe-Mn cc	3.4	4.2	1285	195	29	23	109.1	54.8	5.02	8.55	8.51	10.44	31.93	14.36	0.12	3.16
MA12-DL7	V	98.84	0.42	0.18	0.55	Mg-Fe-Mn cc	1.8	2.7	399	386	15	9	3.1	3.7	3.72	2.84	4.28	3.44	11.52	74.85	0.05	0.29
MA12-DL8	V	98.16	0.62	0.46	0.65	Mg-Fe-Mn cc	1.3	0.3	838	63	8	3	5.7	2.7	0.02	0.01	0.03	0.03	26.13	1.89	0.01	0.01
MA12-DL9	V	98.34	0.48	0.43	0.64	Mg-Fe-Mn cc	0.9	0.2	800	74	5	2	4.5	0.9	0.01	0.27	0.02	0.27	17.70	2.58	0.06	0.00
MA12-NAS6	V	99.56	0.19	0.13	0.05	cc	1.1	0.7	974	641	12	3	23.8	15.8	5.80	2.51	4.47	1.62	0.04	0.04	0.02	0.01
MA12-NAS6	V	98.32	0.17	1.23	0.17	Mg-Fe-Mn cc	109.6	52.5	240	126	22	18	17.1	9.8	6.91	9.54	6.55	10.71	0.76	0.90	0.32	0.14
MA12-SH3	V	96.81	0.86	0.47	1.06	Mg-Fe-Mn cc	0.5	1.0	1001	515	42	27	2.8	20.0	1.25	0.56	6.22	4.72	0.34	0.19	BD	
MA12-VG1	V	97.43	0.54	1.45	0.15	Mg-Fe-Mn cc	49.1	7.4	3984	724	52	9	2.3	1.4	4.05	0.73	9.18	0.87	610.10	155.86	8.61	1.12
MA12-VG2	V	97.34	0.04	1.15	0.46	Mg-Fe-Mn cc	3.2	0.2	8277	1173	522	146	29.2	8.6	2.22	0.69	7.51	2.65	62.98	11.37	0.01	0.00
MA12-VG3	V	96.40	0.50	1.31	0.68	Mg-Fe-Mn cc	4.7	1.4	9309	678	266	56	12.5	4.0	9.23	26.26	23.28	17.84	13.60	1.44	0.02	0.03
MA12-VG4	V	98.45	0.66	0.55	0.15	Mg-Fe-Mn cc	7.4	2.5	952	214	6	13	0.6	0.8	0.26	0.83	0.77	0.69	140.29	110.12	6.81	4.94
MA12-VG5	V	98.14	0.03	1.07	0.37	Mg-Fe-Mn cc	2.2	5.0	4072	250	143	52	8.5	3.7	0.62	3.36	3.86	3.80	71.91	20.03	0.01	1.15
MA12-VG6	V	96.20	0.35	2.45	0.19	Mg-Fe-Mn cc	3.3	0.4	6578	1085	247	88	10.6	5.3	8.56	2.85	26.04	7.97	52.32	20.17	0.05	0.09
MA12-VL5	V	96.90	0.56	0.81	1.04	Mg-Fe-Mn cc	4.4	1.2	5987	2689	31	10	149.0	91.2	2.08	5.70	4.31	5.39	61.04	13.38	0.02	0.00
MA12-VL6	V	98.69	0.22	0.39	0.07	Mg-Fe-Mn cc	3.4	0.5	5641	762	8	4	13.1	3.5	0.85	0.39	2.54	1.04	60.92	8.59	BD	
MA12-VL7	V	97.50	0.38	0.47	0.83	Mg-Fe-Mn cc	3.6	1.8	7134	924	78	29	119.4	207.4	5.43	11.23	14.68	12.87	64.42	18.67	0.02	0.27
MA12-VL8	V	98.35	0.41	0.62	0.53	Mg-Fe-Mn cc	4.4	0.5	791	128	28	3	30.5	6.8	0.53	0.77	1.09	0.80	98.23	13.93	0.01	0.01

NOTES

cc = calcite; dol = dolomite; cb = generic carbonate

BD = below detection

APPENDIX 2. CO isotopes.

Sample	Carb. Type	$\delta^{13}C_{VPDB}$ (per mil)	1σ	$\delta^{18}O_{VSMOW}$ (per mil)	1σ
Klondike schist (felsic)					
05-LS-25_75.0m	S	-6.88	0.23	-1.73	0.57
	S	-7.64	0.23	-7.77	0.57
BU-07-02_114.6m	V	-4.34	0.23	-5.12	0.57
BU-07-02_146.2m	V	-10.95	1.80	-2.02	0.72
BU-07-03_64.0m	V	-4.78	0.23	0.11	0.57
BU-07-03_78.6m	V	-4.78	0.23	-1.67	0.57
BU07-03_91.7m	V	-5.98	0.23	-1.80	0.57
BU-07-04_100.5m	V	-4.84	0.23	2.99	0.57
DDH-04-03_283.0m	V	-7.76	1.80	-2.04	0.72
DDH-04-03_322m	V	-6.55	1.64	-2.15	0.48
DDH-04-04_106.5m	V	-7.34	1.80	-1.47	0.72
DDH-04-04_108.5m	V	-5.00	1.80	12.45	0.72
DDH-04-04_135.8m	V	-5.36	1.64	-5.07	0.48
MA12-DL1	S	-4.75	0.66	1.88	0.99
	S	-5.61	0.26	6.29	0.49
	S	-7.74	1.80	4.28	0.72
MA12-DL2	S	-7.69	0.26	13.29	0.49
MA12-DL3	S	-8.60	0.26	13.92	0.49
	S	-9.01	0.66	8.86	0.99
MA12-DL4	S	-8.64	0.66	-6.43	0.99
	S	-9.02	0.26	-5.63	0.49
MA12-DL5	V	-6.96	0.66	13.13	0.99
MA12-K19	V	-10.89	0.26	9.22	0.49
MA12-K20	M	-7.51	0.26	5.54	0.49
	M	-9.21	1.80	11.71	0.72
	V	-7.28	0.26	6.47	0.49
MA12-K21	M	-8.75	0.26	12.93	0.49
	V	-7.53	0.26	9.13	0.49

M = Matrix

S = Segregation

V = Vein

Sample	Carb. Type	$\delta^{13}C_{VPDB}$ (per mil)	1σ	$\delta^{18}O_{VSMOW}$ (per mil)	1σ
Klondike schist (metaporphyry)					
06-NZ-01_65.7m	M	-12.39	1.80	7.99	0.72
06-NZ-01_65.8m	S	-12.24	0.23	8.96	0.57
BU-07-03_83.1m	V	-6.30	0.23	-0.85	0.57
DDH-04-04-87.0m	V	-3.55	0.23	13.95	0.57
DDH-04-05_149.3m	V	-8.64	1.80	-5.49	0.72
DDH-04-05_314.5m	V	-5.45	1.64	-5.22	0.48
	V	-7.20	1.80	-4.39	0.72
DDH-04-05_320.5m	V	-6.76	1.64	3.95	0.48
DDH-04-05_332.4m	V	-3.86	1.64	12.45	0.48
DDH-04-05_333.6m	V	-4.16	1.64	-4.88	0.48
	V	-7.18	1.80	-1.13	0.72
DDH-04-06_281.3m	V	-9.14	1.80	7.38	0.72
DDH-04-06_32.0m	V	-2.44	1.64	0.25	0.48
MA12-VG1	V	-2.38	0.17	5.07	0.51
MA12-VG2	V	-5.63	0.17	11.93	0.51
MA12-VG3	V	-5.80	0.26	12.89	0.49
MA12-VG4	V	-5.45	0.17	7.85	0.51
MA12-VG5	V	-7.25	0.17	14.58	0.51
MA12-VG6	V	-7.13	0.17	12.99	0.51
MA12-VL5	V	-11.80	0.17	8.39	0.51
	V	-12.44	0.26	12.77	0.49
MA12-VL6	S	-35.88	0.26	12.74	0.49
	S	-36.21	0.26	13.19	0.49
	S	-36.50	0.17	12.51	0.51
MA12-VL7	V	-12.39	0.17	12.18	0.51
	V	-12.41	0.26	11.28	0.49
MA12-VL8	V	-9.50	0.26	10.33	0.49
	V	-9.55	0.17	10.87	0.51

M = Matrix

S = Segregation

V = Vein

APPENDIX 2. continued.

Sample	Carb. Type	$\delta^{13}C_{VPDB}$ (per mil)	1σ	$\delta^{18}O_{VSMOW}$ (per mil)	1σ
Klondike schist (mafic)					
BU-07-02_108.3m	V	-7.41	1.80	1.28	0.72
MA12-DL6	M	-7.29	0.26	6.95	0.49
	S	-7.73	0.26	-4.90	0.49
	V	-9.66	1.80	-3.45	0.72
	V	-9.72	1.80	-0.42	0.72
MA12-DL7	S	-9.73	0.66	14.91	0.99
	V	-7.16	0.17	8.84	0.51
MA12-DL8	M	-7.36	1.80	11.45	0.72
	M	-8.43	0.26	6.11	0.49
	V	-7.99	1.80	12.46	0.72
MA12-DL9	V	-5.87	0.26	8.46	0.49
	V	-6.11	0.17	11.53	0.51
MA12-K05	S	-14.68	0.66	13.67	0.99
	S	-16.72	0.26	16.99	0.49
MA12-K14	S	2.97	0.66	22.01	0.99
	S	1.93	0.26	16.60	0.49
MA12-K16	S	-3.94	0.66	11.09	0.99
MA12-K17	M	-9.45	0.26	10.17	0.49
	M	-9.75	1.80	12.30	0.72
MA12-SH1	S	-7.55	0.17	-2.63	0.51
	S	-8.31	0.26	-6.70	0.49
	S	-8.68	0.26	-0.20	0.49
	S	-9.26	1.80	-5.71	0.72
MA12-SH2	S	-8.49	0.17	-7.91	0.51
	S	-9.49	0.26	-0.80	0.49
	S	-10.06	1.80	-3.03	0.72
MA12-SH3	M	-8.51	1.80	-0.07	0.72
	V	-7.45	0.23	-4.38	0.57

M = Matrix

S = Segregation

V = Vein

Sample	Carb. Type	$\delta^{13}C_{VPDB}$ (per mil)	1σ	$\delta^{18}O_{VSMOW}$ (per mil)	1σ
Klondike schist (marble)					
K70	M	0.06	1.80	8.99	0.72
K71	M	3.47	1.64	7.24	0.48
K72	M	-3.79	0.26	8.73	0.49
	M	-5.61	1.80	7.44	0.72
MA12-K07	M	5.10	0.66	6.53	0.99
	M	4.19	0.66	5.84	0.99
	M	4.03	0.26	8.72	0.49
	M	3.57	0.26	10.08	0.49
MA12-K08	M	3.70	0.66	6.65	0.99
	M	3.17	0.26	9.29	0.49
MA12-K09	M	2.61	0.66	4.25	0.99
	M	1.19	0.26	7.84	0.49
	S	3.27	0.66	14.60	0.99
MA12-K10	M	5.21	0.66	6.76	0.99
	M	4.37	0.26	11.79	0.49
	M	3.45	1.80	9.57	0.72
MA12-K11	M	2.60	0.26	7.00	0.49
MA12-K12	M	5.08	0.26	8.33	0.49
	M	4.44	0.66	5.82	0.99

M = Matrix

S = Segregation

V = Vein

APPENDIX 2. continued.

Sample	Carb. Type	$\delta^{13}C_{VPDB}$ (per mil)	1σ	$\delta^{18}O_{VSMOW}$ (per mil)	1σ
Nasina assemblage (calcareous schist)					
MA12-NAS5	M	-7.73	1.80	19.26	0.72
MA12-NAS6	M	-6.06	1.80	9.85	0.72
	V	-6.00	0.23	9.19	0.57
	V	-6.09	0.23	12.72	0.57
	V	-6.42	1.80	8.84	0.72
MA12-NAS7	M	-9.07	1.80	18.01	0.72
	M	-9.53	1.80	18.54	0.72
	M	-9.68	1.80	20.57	0.72
MA12-NAS8	S	-6.98	0.23	21.42	0.57
Nasina assemblage (marble)					
MA12-NAS9	M	3.68	0.23	12.66	0.57
	M	0.71	1.80	12.78	0.72
MA12-NAS10	M	2.74	0.23	12.21	0.57
	M	2.73	0.23	10.97	0.57
	M	1.32	1.80	13.23	0.72
	M	0.35	1.80	11.60	0.72
MA12-NAS11	M	2.35	0.23	13.08	0.57
MA12-NAS12	M	0.04	0.23	15.39	0.57
	M	-1.84	1.80	17.23	0.72

M = Matrix

S = Segregation

V = Vein

Pathfinder signatures in placer gold derived from Au-bearing porphyries

Rob Chapman[1], Matt Grimshaw
Placer Minerals Group, School of Earth and Environment, University of Leeds

Murray Allan, Jim Mortensen, Tim Wrighton
Mineral Deposits Research Unit, School of Earth, Ocean and Atmospheric Sciences, University of British Columbia, Vancouver

Scott Casselman
Casino Mining Corporation, Vancouver, BC

Chapman, R.J., Allan, M.M., Grimshaw, M.K., Mortensen, J.K., Wrighton, T.M., and Casselman, S., 2014. Pathfinder signatures in placer gold derived from Au-bearing porphyries. *In*: Yukon Exploration and Geology 2014, K.E. MacFarlane, M.G. Nordling, and P.J. Sack (eds.), Yukon Geological Survey, p. 21-31.

ABSTRACT

Porphyry and epithermal mineralization of early Late Cretaceous (*ca.* 76-74 Ma) at Casino, Revenue/Nucleus, and Sonora Gulch areas in the central and eastern Dawson Range in west-central Yukon is spatially related to numerous placer gold mining areas. Placer-lode relationships have been established through study of gold alloy compositions and associated mineral inclusion assemblages.

At Casino, hypogene gold grains are liberated by erosion and pass into the placer system without compositional modification, as evidenced by the common alloy signatures and a mineral association of Au, (Bi-Pb-Te-S) minerals and chalcopyrite. A second signature of higher-Ag, chalcopyrite-poor gold has been identified in placer populations, but this gold type also exhibited the Bi-Pb-Te-S signature. The results suggest that the placers contain a mixture of gold derived from the porphyry and peripheral or shallow level epithermal mineralization.

The Bi-Pb-Te-S association evident at Casino was also recorded at Revenue/Nucleus and Sonora Gulch. This generic signature of gold in Cu-Mo (-Au) porphyry deposits and their associated distal epithermal manifestations could be applied to exploration in areas where placer-lode relationships are unclear.

[1] *r.j.chapman@leeds.ac.uk*

INTRODUCTION

Porphyry mineralization commonly contains various resistive minerals which persist into the secondary environment. Several studies have sought to utilize the occurrence of these mineral grains in stream and glacial sediments to aid in exploration (*e.g.*, Celis *et al.*, 2012). In some cases, the suite of indicator minerals contains native gold (*e.g.*, Kelley *et al.*, 2011), but while Au-bearing porphyries may be spatially associated with placer gold districts, they are also commonly found in areas of complex geology where there may be more than one style of Au-bearing mineralization contributing to the placer inventory. Consequently, the presence of detrital Au may not necessarily invoke a porphyry source.

This paper describes an investigation into the relationship between placer and lode gold surrounding three Au-bearing porphyry systems in the Yukon. The aims of the project were twofold: i. to investigate whether the mineralogical characteristics of gold grains from hypogene porphyry ore persist into grains recovered from the placer environment; and ii. to identify any generic mineralogical signatures within placer gold populations that are diagnostic for this style of mineralization.

Porphyry style copper-gold mineralization has been identified at three localities in the Dawson Range: Nucleus-Revenue, Sonora Gulch, and Casino (Fig. 1). Recent geochronological studies have shown that intrusions and associated mineralization in all three of these localities were formed during an episode of early Late Cretaceous magmatism (76-74 Ma) (Bennett *et al.*, 2010; Allan *et al.*, 2013). A summary of the characteristics of these three systems is provided in Table 1.

While the three intrusive systems share some common metallogenic features, there are important differences in the ore mineralogy (such as the presence of hypogene pyrrhotite at Nucleus), which may be a consequence of a more reduced oxidation state at Revenue-Nucleus and Sonora Gulch, in comparison with Casino.

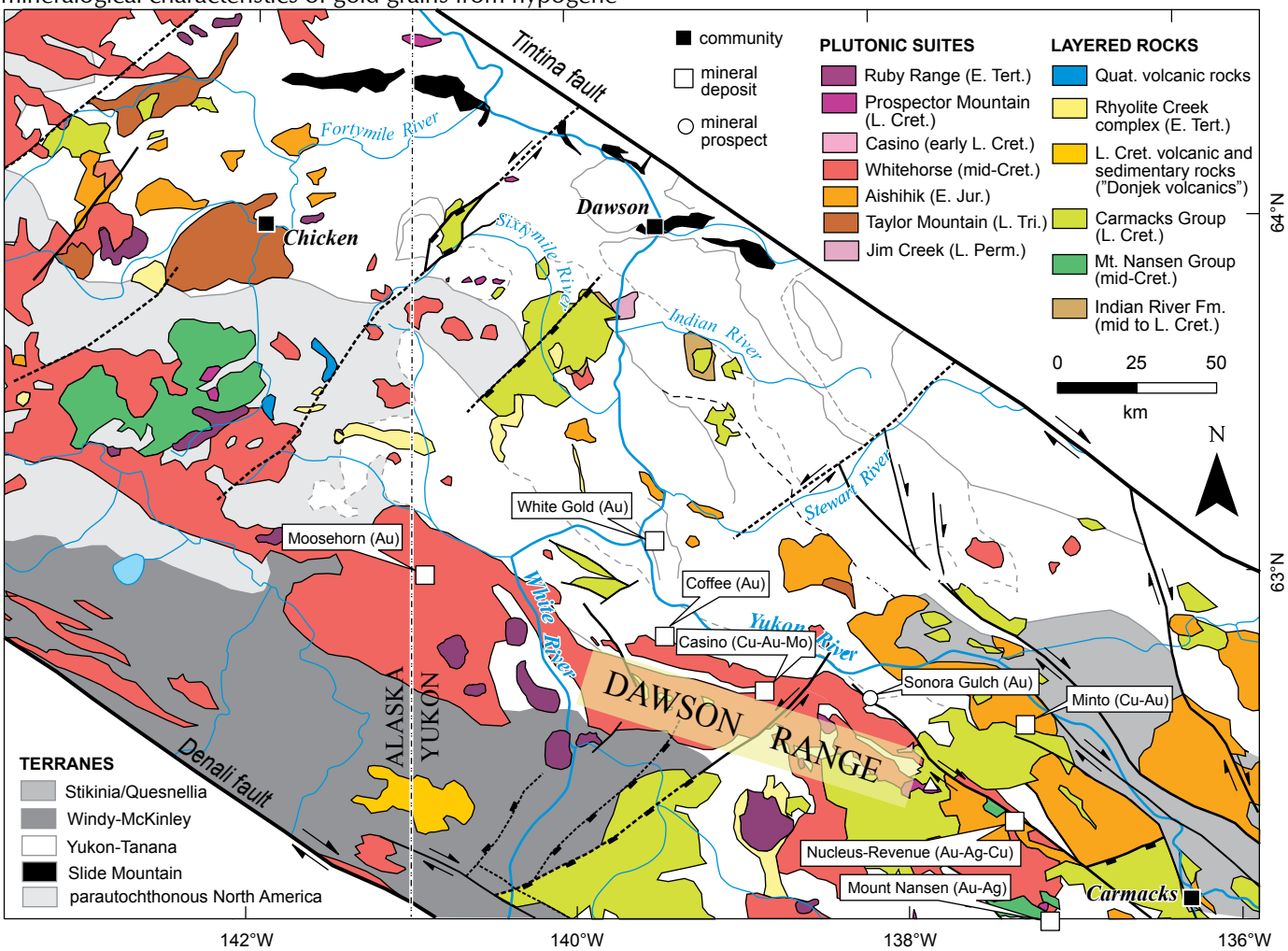

Figure 1. *Geological setting of intrusive rocks in southwest Yukon (adapted from Allan et al., 2013).*

Table 1. *Overview of lithology and mineralogy at the three early Late Cretaceous porphyry systems at Casino, Revenue/Nucleus, and Sonora Gulch.*

Porphyry system	Lithological Description	Mineralogy
Casino	Highly brecciated units of the Dawson Range batholith and the Coffee Creek granite, intruded by the Patton Porphyry[1]	Cpy, Py, Ap, An, Mo, Bi-bearing
Revenue/Nucleus	Revenue breccia complex and related porphyry dike swarm intruding Jurassic to mid-Cretaceous granitoids and Paleozoic metasediments[1]	Py, Po, Cpy, Mo, Ma, Ars
Sonora Gulch	Feldspar porphyry dykes and quartz-feldspar porphyry stocks[2]	i. Tetr, Ars ii. Py, Cpy
[1]Allan *et al*. (2013), [2]Bennett *et al*. (2011)		
Abbreviations used in all Tables and Figures: *An=anhydrite, Ap = apatite, Ars = arsenopyrite, Bi-bearing: unspecified Bi-bearing minerals regardless of stoichiometry and the presence of other elements (principally Pb, Te, S, Sb), Cpy = chalcopyrite, G = galena, Hs = hessite, Ma = marcasite, Mo = molybdenite, Mz = monazite, Po = pyrrhotite, Py = pyrite, Sch = scheelite, Sp = sphalerite Tet = tetrahedrite, Tetr = tetradymite.*		

Each of these centres of bedrock gold mineralization is within a region of placer deposit localities. Placer-lode relationships in the Nucleus-Revenue area were studied by Allan *et al*. (2012) who identified a distinctive suite of Bi-Pb-Te minerals present as inclusions within populations of placer gold grains. In addition to the sample suite from Nucleus-Revenue, small samples of placer gold from Sonora Gulch and Canadian Creek (which drains the Casino deposit area) were studied. Both additional samples exhibited the Bi-Pb-Te association previously recorded at Nucleus-Revenue. The present project was designed to establish whether placer gold derived from these porphyry systems exhibited a distinctive, generic signature. To this end, samples of core, placer, and eluvial gold were collected from the Casino orebody and environs.

FIELDWORK

A suite of placer and lode samples were collected and these are described in Table 2a and b. Placer sample locations are provided in Figure 2. Samples of placer gold were collected using a 'Le Trap River Robber' portable sluice. Material was screened at 1" prior to sluicing. Samples collected from the leached cap were clay-rich and required dispersion in water prior to sluicing to reduce Au grain loss through entrainment. Placer gold grains were isolated from the heavy sediment concentrates collected in the sluice by hand panning. Sample collection at Casino Creek yielded only a very small number of grains and this sample is not considered further.

ANALYTICAL PROCEDURES AND DATA PRESENTATION

Both placer gold grain populations and polished thin sections of auriferous ore were studied in each of the three areas. Analysis of gold grain particles and gold grains identified in polished thin sections was carried out at the University of Leeds (UoL) to generate the 'microchemical signature', which comprises a combination of data relating to gold alloy composition and mineral inclusion suite. A full description of this methodology is provided in Chapman *et al.* (2010a). Alloy compositions were determined at UoL using a Jeol 8230 Superprobe, and the inclusion suite was established at UoL using the EDS facility of a FEI Quanta 650 FEG-SEM.

The Ag content of populations are presented as cumulative percentile *vs.* increasing Ag plots (*e.g.*, Fig. 5). This approach permits the direct comparison of Ag ranges of populations which contain different numbers of grains. Inclusion suites are defined by the numbers of grains in a population which contain a particular mineral inclusion. Inspection of the inclusion suite usually reveals mineralogical criteria by which different populations may be compared. Data are presented on ternary diagrams (*e.g.*, Fig. 9).

Table 2a. *Placer and elluvial Au collected during fieldwork at Casino (P = placer; E = eluvial).*

Sample	Easting*	Northing*	Site Description	Gold Description
Upper Canadian Creek (P)	609928	6959026	Virgin gravel.	0.5-2 mm mostly rough Au
Potato Gulch (P)	611503	6965042	Side pay on bedrock.	Rough gold grains to 3 mm
Lower Canadian Creek (P)	614300	6965200	Sample donated.	Fine grained gold, mixed morphologies
Casino Creek (P)	612189	6958179	Active channel.	<10 grains to 50 µm
Casino Creek tributary (P)	612160	6958178	Active channel.	10 grains to 50 µm
Rude Creek (P)			Active placer	Many flaky grains
Oxidized Leached Cap (E)	610882	6958295	Material dug from leached cap.	c. 50 grains 50 µm micron - 1 mm
*UTM Zone 7N, NAD83				

Table 2b. *Core samples selected for production of polished sections.*

Drill Hole	Depth (m)		Zone	Mineralogy	
	From	To		Early	Late
94-185	161.54	165.59	Supergene	Cpy, Mo	
CAS 060	160.62	163.62	Hypogene	Bi-bearing in py, Sch, Py, Ap, An	G, Au, Bi- bearing, Cpy, Tet

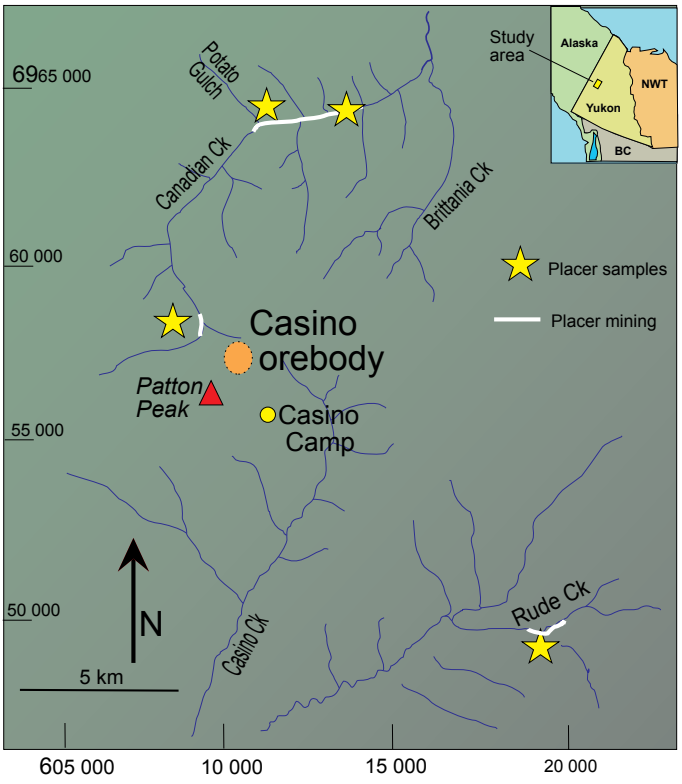

RESULTS

Gold grain compositions and mineral inclusions are presented in Table 3. The samples are considered firstly in terms of the mineralogy observed in polished thin sections and secondly in terms of the alloy and associated inclusion suites within populations of gold grains for the placer and eluvial environment.

GOLD IN SITU

Gold grains were observed in polished thin sections prepared from core in drill hole CAS 060 (hypogene zone) and drill hole 94-185 (supergene zone; Table 2b). Gold grains in the supergene sample were extremely small, and the quantitative data comprised (Au+Ag) totals of much less than 100%. Consequently these data were not included in the interpretation of gold compositions presented below.

Figure 2. *Details of sampling locations in the Casino area. The locations of hole CAS 060 and the leached cap are within the limits of the Casino orebody. UTM according to NAD83.*

Table 3. *Sample characteristics.*

Sample	No. grains	Cu mean (%)	Hg-bearing (%)*	Inclusions observed in polished section							
				Py	G	Sp	Cpy	Ars	Tetr	All Bi-bearing	Hs
Leached Cap (E)	34	0.05	0	3			1		1	2	
Upper Canadian Creek(P)	134	0.06	0	5	4	1	8	1	4	5	2
Lower Canadian Creek (P)	39	0.03	0	2	4			1	3	6	2
Potato Gulch (P)	40	0.05	7		7					4	3
Rude Creek (P)	166	0.04	0	5	2		3	1		5	
Gold grains in hole CAS 060	12	0.1	0	N/A							

**'Hg-bearing (%)' refers to the percentage of grains which contain Hg to above the detection limit of 0.3%. See Table 1 for list of mineral name abbreviations. P = placer; E = elluvial*

The mineralogy of the ore from CAS 060 (Fig. 3) suggests at least two paragenetic stages. Inclusions of anhydrite, apatite, and monazite were observed in pyrite. Gold, galena, and Bi-bearing minerals occurred either infilling the pyrite or as discrete grains within the surrounding quartz.

ELUVIAL GOLD AND PLACER

Details of the morphology and size range of the placer gold samples are presented in Table 2a and images of the different populations are provided in Figure 4. Gold from Rude Creek was mainly flaky, but all other populations contained gold grains which were predominantly rough.

The range of Ag content is depicted in Figure 5, rather than in Table 2, because simple statistical measures are ineffective for comparing the characteristics of different populations. All populations contained small amounts of Cu, commonly above the detection limit of 0.02%. Mercury was largely absent, and is not considered further.

The Ag plots for gold from the hypogene core sample and the grains collected from the leached cap show a very similar range of Ag values (Fig. 5a), with the majority of grains range from 6 to 12% Ag. The sample from upper Canadian Creek comprises three sub populations, one of which conforms to the 6-12% Ag range recorded in the sample from the leached cap. The other two populations contain grains in the Ag ranges 12-17% and 18-26%.

The placer populations from the two Canadian Creek localities and Rude Creek have similar ranges of Ag content, but only one grain in the sample from Potato Gulch returned a value of less than 12.5% Ag.

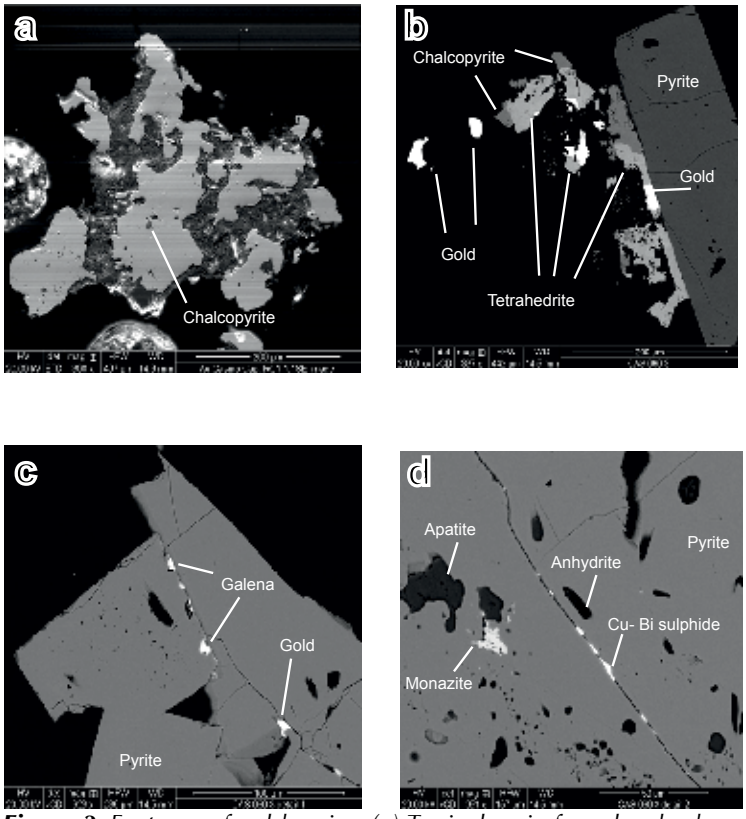

Figure 3*. Features of gold grains. (a) Typical grain from leached cap, with coating of Fe oxide. Inclusion (center) is chalcopyrite. (b) Assemblage in hole CAS 060. Chalcopyrite, tetrahedrite, and Au postdate the pyrite. (c) Galena and Au postdates the pyrite in hole CAS 060. (d) Apatite, anhydrite, and monzanite coeval with pyrite; Bi-Cu sulphide postdates the pyrite.*

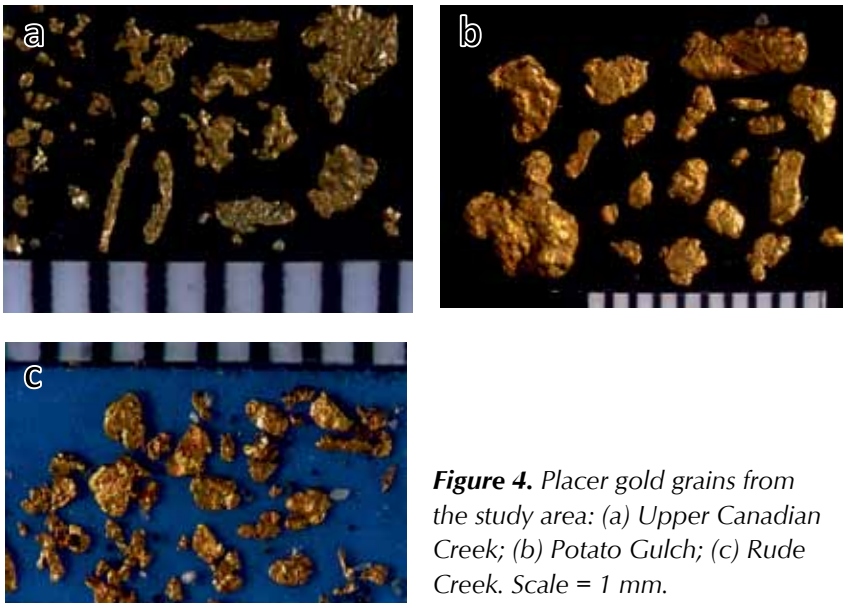

Figure 4. *Placer gold grains from the study area: (a) Upper Canadian Creek; (b) Potato Gulch; (c) Rude Creek. Scale = 1 mm.*

The abundance of mineral inclusions varied widely between samples, but they were more abundant in populations of placer grains from upper Canadian Creek and Potato Gulch. This is probably a consequence of the limited degree of fluvial transport, indicated by the morphology of the grains (Fig. 4). One grain from upper Canadian Creek contained an inclusion of Bi-Pb-Ag sulphosalt and another contained Sn within a Cu-Fe sulphide. Examples of inclusion species recorded in the placer samples are presented in Figure 6. Table 3 shows that all the placer populations contain Bi-bearing minerals as inclusions, although the presence of Bi tellurides at Rude Creek remains to be confirmed. The high incidence of chalcopyrite inclusions in the sample from upper Canadian Creek was not observed in any other of the placer samples.

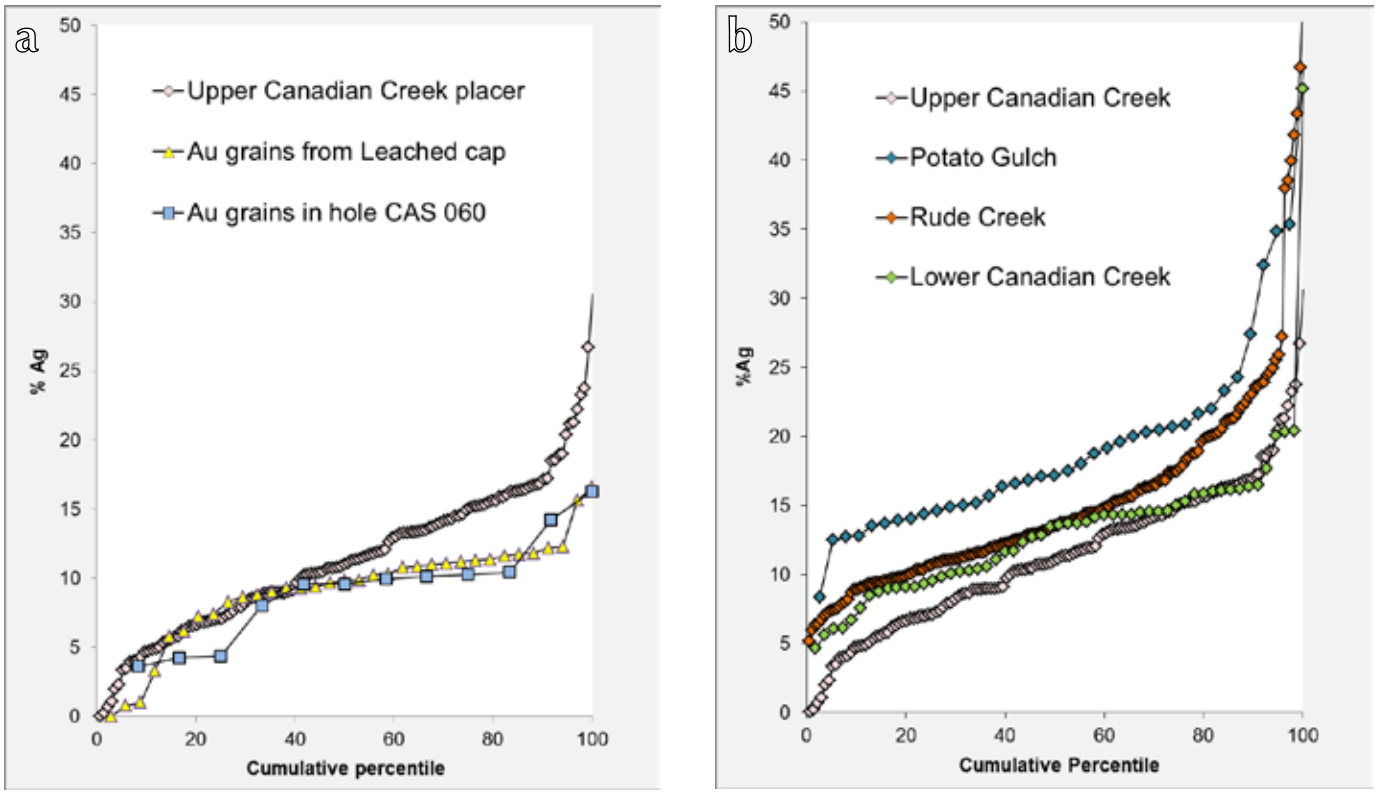

Figure 5. *Silver contents of gold grain populations. A: Casino area: comparison of Ag signatures of gold from the hypogene ore, the leached cap and a nearby placer in upper Canadian Creek. B: comparison of signatures from different placer localities in the study area.*

DISCUSSION

RELATIONSHIP BETWEEN HYPOGENE, ELUVIAL, AND PLACER GOLD IN CANADIAN CREEK

The alloy composition of gold grains from the hypogene ore corresponds to those obtained from the leached cap. This compositional range is also evident in the placer sample from upper Canadian Creek, where it is augmented by a separate population of gold containing Ag values over 11.9%. This cutoff has been identified by a slight break in the slope of the curve, which is highlighted in Figure 5.

Examination of a limited number of thin sections of hypogene mineralization suggests that gold, chalcopyrite, galena, bismuth minerals, and sulphosalts comprise a second paragenetic stage. This association was also observed within the inclusion assemblages of eluvial grains from the leached cap and in placer grains from upper Canadian Creek. Considered together, these data show that the composition of hypogene gold grains is unaffected by supergene processes or residence within the placer.

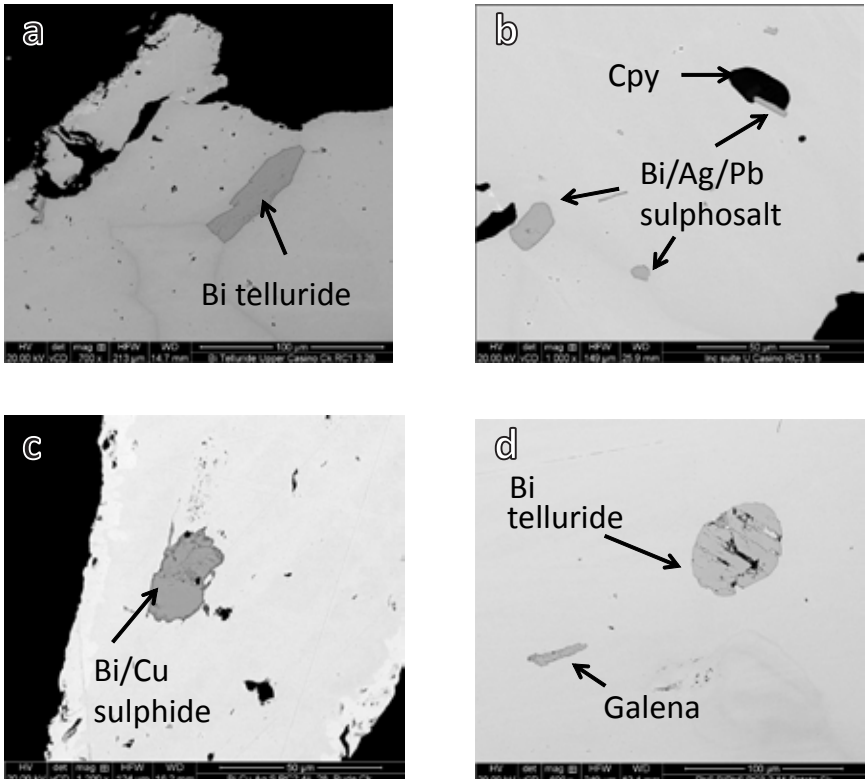

Figure 6. *Examples of mineral inclusions in placer samples from the study area: (a) and (b) Placer grains from upper Canadian Creek; (c) Grains from Rude Creek; (d) Grain from Potato Gulch.*

The alloy compositions depicted in Figure 5 suggest that two different sources contribute to the placer. In cases such as this, it is informative to examine the compositional range of gold grains according to the contained inclusion species. Figure 7 shows the Ag contents of sub populations of the upper Canadian Creek sample which contain inclusions of chalcopyrite, galena, and Bi-bearing minerals, respectively. The majority of chalcopyrite-bearing grains conform to the lower range of alloy composition, *i.e.*, that observed in the hypogene ore, where chalcopyrite is paragenetically linked with Au. The Bi-bearing minerals and galena, however, are equally abundant across the Ag compositional range. These data strongly suggest that there are two related compositional ranges of gold contributing to the placer inventory of upper Canadian Creek, with a second type entering the surficial system between the leached cap and the upper reaches of the Creek. Bennett *et al.* (2010) described two vein systems form Sonora Gulch, one of which comprises Au-tetradymite mineral assemblages. Placer gold compositions suggest that those similar vein systems are present around the Casino porphyry and contribute Au to the placer inventory. Placers in upper Canadian Creek have been exploited for wolframite (Yukon Placer database 2325, Lebarge, 2007) which occurred with magnetite and hematite particles up to 4cm in diameter. The abundance of these heavy minerals decreased downstream.

ORIGINS OF PLACER GOLD IN LOWER CANADIAN CREEK

The Canadian Creek placers were exploited in two discrete areas, one near the headwaters and the other downstream from the confluence with Potato Gulch (Fig. 2). The abundance of placer gold upstream of this confluence declined significantly (L. Olynek, 2013, pers. comm.), which corresponds to the decrease in concentration of heavy minerals described above. Consequently, it is very unlikely that much, if any, of the gold in the lower section has been transported from the headwaters. The sample from Potato Gulch comprised coarse rough grains (Fig. 3), which, together with the small size of this catchment,

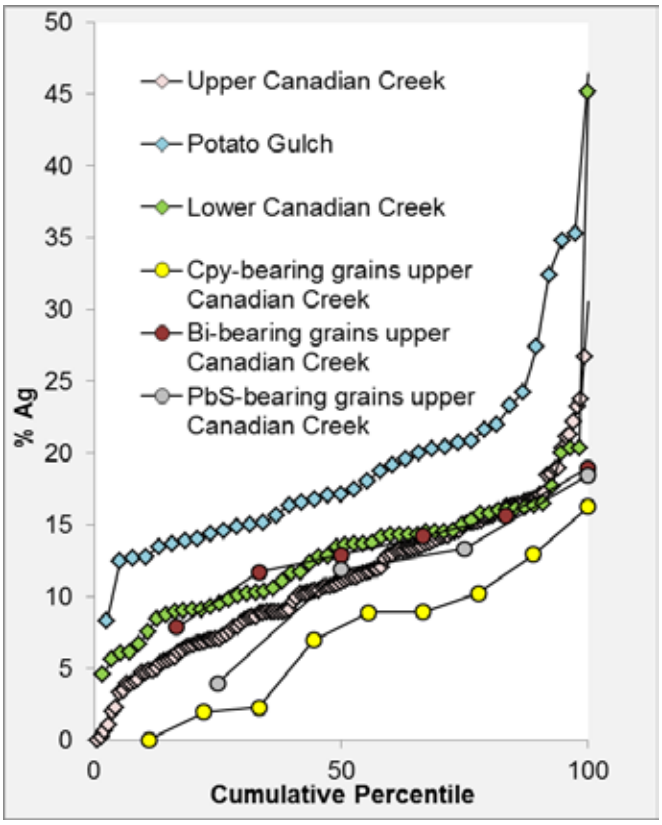

Figure 7. *Analyses of placer gold from upper Canadian Creek in terms of inclusion assemblages and associated alloy compositions.*

suggest a very local source. The relatively narrow range of Ag values is very similar to that observed in the Ag-rich fraction of the placer gold from upper Canadian Creek (described above), and inclusion assemblages of both samples contain galena and Bi-bearing minerals, whereas chalcopyrite is rare or absent in lower Canadian Creek samples. These data are interpreted as indicative of gold influx from sources near the lower placer workings, which are similar and possibly genetically related to the Casino orebody.

Barkhov *et al*. (2008) studied Sn-bearing hematite and associated W-Bi minerals present in the placer deposits in lower Canadian Creek and ascribed their origin to local magmatic hydrothermal systems. It is possible that this hypothesis could also account for Au mineralization in the lower Canadian Creek area. The coarse particle size of gold in Potato Gulch provides a further similarity with gold occurring in the tetradymite vein at Sonora Gulch.

The data presented in this study can be used to develop a hypothesis for placer formation in the Canadian Creek drainage. Gold in upper Canadian Creek is derived from the weathered porphyry, but is augmented by a second type, which appears to be present only in the periphery of the intrusion. The microchemical signature of placer gold from these (inferred) peripheral sources strongly suggests a genetic link with the porphyry mineralization, and it seems likely that they represent related epithermal veins. In situ gold in lower Canadian Creek appears to be wholly derived from such vein mineralization. The degree of transport of gold from the upper to lower sections of the creek is probably small, as evidenced by the absence of placer mining in the middle reaches of the creek and the abrupt influx of coarse gold at Potato Gulch.

ORIGINS OF PLACER GOLD IN RUDE CREEK

The population of placer gold from Rude Creek exhibits a similar range of Ag as the placer samples from Canadian Creek (Fig. 5b) and an inclusion assemblage which contains Bi-bearing minerals, galena, and chalcopyrite. The gold particles are relatively flat (Fig. 4c) and have probably originated some distance upstream of the present placer operation. Consequently, the population could represent gold from multiple sources, and the alloy and inclusion signatures show characteristics of all the populations observed in Canadian Creek. These data suggest that there are undiscovered gold sources feeding the Rude Creek drainage which are very similar to the Casino mineralization. However, the transport distance of the Rude Creek placer gold is greater than that between the Casino orebody and the upper Canadian Creek placers as evidenced by the morphology of gold grains at each locality. Consequently, there may be more placer gold deposits in the Rude Creek drainage of potential economic importance.

RELATIONSHIP TO SIGNATURES OF PLACER GOLD DERIVED FROM OROGENIC MINERALIZATION

Regional surveys of the compositions of placer gold grains have been undertaken in the Klondike (Chapman *et al*., 2010a,b) and the Indian River/Blackhills Creek drainages (Chapman *et al*., 2011). In addition, Wrighton (2013) characterized gold from the Sixtymile and White Gold districts. These studies have permitted characterization of gold grain signatures associated with orogenic gold formed during a widespread episode of mineralization in the middle to Late Jurassic (Allan *et al*., 2013). Two major

groups of signatures were recorded, characterized by the presence or absence of Te or As-bearing minerals in the inclusion suites. Only a small number of localities yielded samples in which both elements were present within the inclusions. The large majority of Te-bearing inclusions were (Au+Ag) tellurides and the incidence of Bi tellurides was confined to one tributary of Henderson Creek (White Gold district). The signature of all gold samples from the Casino area including Rude Creek are clearly distinct from the regional orogenic types.

RELATIONSHIP OF AU SIGNATURES AT CASINO WITH THOSE FROM PLACERS NEAR OTHER AU-BEARING PORPHYRIES

Figure 8 shows the relationships between Ag contents of placer samples from the environs of the Revenue-Nucleus Cu-Au porphyry and the Sonora Gulch porphyry compared to that of the gold grains collected from the Casino leached cap. There is a similarity between the Ag contents of the various populations of gold grains from these localities. Furthermore, sample populations of placer gold from the Nucleus/Revenue area and Sonora Gulch contain low, but measurable amounts of Cu (all average 0.04%), in contrast with gold from orogenic sources in which Cu concentrations are typically below detection limit (0.02%) in the large majority of cases. In addition, the Bi-Pb-Te-S signature, which was clearly evident in the placer gold from the Nucleus/Revenue area and Sonora Gulch, was observed in all populations of gold from Casino. Figure 9 shows the proportions of grains which contained Bi-bearing minerals, galena, and chalcopyrite. The low-Ag gold type observed in core, which forms part of the placer inventory in upper Canadian Creek, is characterized by the relatively high incidence of chalcopyrite inclusions. Chalcopyrite is far less abundant in all other samples. The Bi signature is present in all cases, however Pb mineral inclusions were not recorded at Sonora Gulch, but this may be a consequence of the very low sample size.

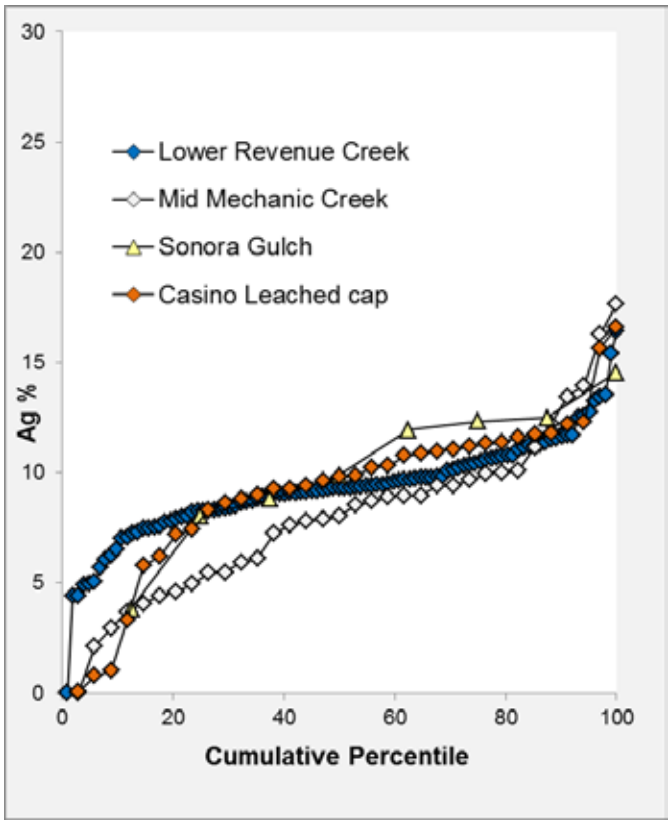

Figure 8. *Ag contents of placer samples from Revenue Creek and Mechanic Creek (which drain the Revenue and Nucleus deposits respectively), and Sonora Gulch, compared to the Ag signature of gold from the leached cap at Casino.*

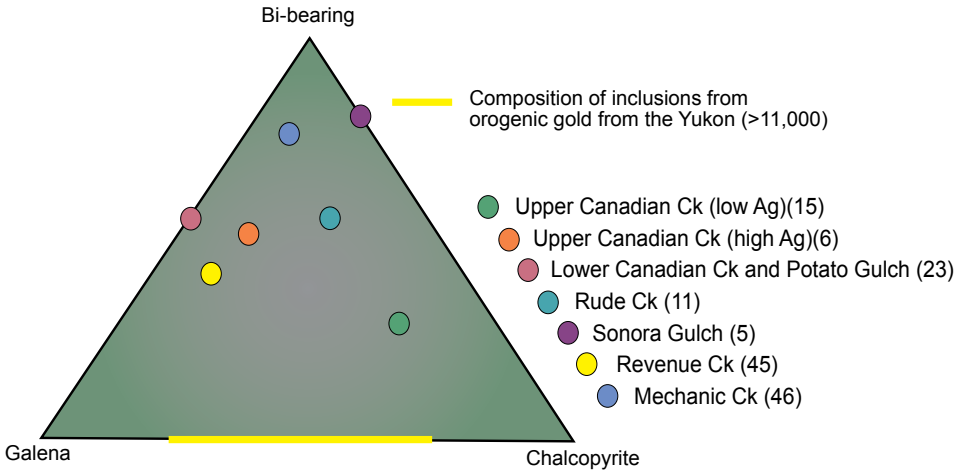

Figure 9. *Ternary plot illustrating abundance of different inclusion species in the sample suite. See methods section for explanation of the derivation of data. The sample from upper Canadian Creek has been subdivided according to Ag range. 'High Ag' refers to values of >11.9% (see Fig. 5). The compositional range of orogenic gold lies along the galena-chalcopyrite tie line. The values in parentheses following each locality refer to the number of inclusions contributing to the plot.*

IMPLICATIONS FOR EXPLORATION

The suite of mineral occurrences associated with early Late Cretaceous intrusions in the eastern and central Dawson Range in Yukon all yield gold particles which exhibit a very similar signature in terms of alloy composition and mineral inclusions. The presence of tetradymite and other minerals in the Bi-Pb-S-Te system are clear indicators for gold derived from these systems and this mineralogical signature is present within both the porphyry mineralization and associated shallow epithermal veins. This clear Bi-Pb-Te-S signature in the inclusion suite distinguishes this gold type from regional orogenic types, which exhibit varying proportions of S-As-Te in their inclusion suites. While Bi-bearing minerals have been recorded in four grains (in around 10 000 analysed) in regions of orogenic gold mineralization (Chapman *et al.*, 2011), their incidence in gold derived from Au-bearing porphyry deposits is far higher. In addition, the association with Pb, which manifests either from a high incidence of galena inclusions or Pb-Bi sulphides, provides a further discriminator.

The synthesis of data describing alloy compositions and mineral inclusions appears to discriminate between gold derived from a porphyry environment and that originating from peripheral vein mineralization. The high incidence of chalcopyrite in the gold grains from the leached cap and gold of corresponding composition in the placer is consistent with the mineralogy of the hypogene ore studied here.

The mineral inclusion signatures described herein may find application in an exploration context. Examination of gold grains collected during reconnaissance could yield information on the style of mineralization of the source. Two examples are provided in this report. Firstly, placer gold from Rude Creek clearly exhibits a signature similar to that of the placer gold from upper Canadian Creek; however, the source of this placer gold is currently unclear. Secondly, there is strong evidence for the presence of epithermal mineralization in lower Canadian Creek, which to date has not been the subject of exploration.

CONCLUSIONS

1. Gold associated with porphyry style mineralization at Casino was largely emplaced during a second phase of the paragenesis and is coeval with chalcopyrite, galena, and Bi sulphides and tellurides.
2. The gold signature in the hypogene ore corresponds to that observed in gold grains collected from the leached cap.
3. This signature persists into the placer gold present in upper Canadian Creek where it is augmented by another relatively Ag-rich gold type in which chalcopyrite is absent.
4. Further evidence of two different Au sources in the study area is provided by the signature of gold from Potato Gulch, which corresponds to the 'high Ag' component of the upper Canadian Creek sample. It is proposed that the two signatures relate to gold derived from the Casino porphyry and that originating in widespread epithermal veins.
5. Gold in the lower Canadian Creek placer is derived from local sources and is not a distal manifestation of the placer in upper Canadian Creek.
6. There are undiscovered, in situ sources of gold in Rude Creek and lower Canadian Creek.
7. The signature of gold from Canadian Creek shows a close similarity with the signatures of gold from placers surrounding other porphyry deposits of the same age elsewhere in the Dawson Range. Consequently the Bi-Pb-S-Te inclusion signature may be viewed as diagnostic for this style of porphyry mineralization in the Yukon and raises the possibility that a similar approach to define porphyry gold signatures may find value in exploration for porphyries elsewhere.

ACKNOWLEDGEMENTS

This work was made possible through support from the Yukon Geological Survey and the MDRU Yukon Gold Project. We are particularly indebted to the Casino Mining Corporation and Northern Freegold Resources who provided excellent logistical support during the sampling program. Lee Olynek kindly donated samples from lower Canadian Creek and allowed us to collect placer samples in his license areas. Andre Fournier and Dennis Ouellette are thanked for the donation of placer gold samples from Rude Creek and Sonora Gulch respectively.

REFERENCES

Allan, M.M., Hart, C.J.R., and Mortensen, J.K. (eds.), 2012. Yukon Gold Project Final Technical Report. Mineral Deposit Research Unit, University of British Columbia, 196 p.

Allan, M.M., Mortensen, J.K., Hart, C.J.R., Bailey, L.A., Sánchez, M.G., Ciolkiewicz, W., McKenzie, G.G., and Creaser, R.A., 2013. Magmatic and metallogenic framework of west-central Yukon and eastern Alaska. *In*: Tectonics, Metallogeny, and Discovery: The North American Cordillera and Similar Accretionary Settings, M. Colpron, T. Bissig, B. Rusk, and J. Thompson (eds.), Society of Economic Geologists, Special Publication 17, p. 111-168.

Barkov, A.Y., Martin, R.E., LeBarge, W., and Fedourthouk, Y., 2008. Oscillatory zoning in stanniferous hematite and associated W- and Bi-rich minerals from Canadian Creek, Yukon, Canada. Canadian Mineralogist, vol. 46, p. 59-72.

Bennett, V., Schulze, C., Ouellette D., and, Pollries, B., 2010. Deconstructing complex Au-Ag-Cu mineralization, Sonora Gulch project, Dawson Range: a Late Cretaceous evolution to the epithermal environment, *In:* Yukon Exploration and Geology 2009, K.E. MacFarlane, L.H. Weston, and L.R. Blackburn (eds.), Yukon Geological Survey, p. 23-45.

Celis, M.A., Hart, C.J.R., Bouzari, F., Bissig, T., and Ferbey, T., 2013. Porphyry Indicator Minerals (PIMs) from alkalic porphyry coppergold deposits in south-central British Columbia (NTS 092, 093). *In*: Geoscience BC Summary of Activities 2012, Geoscience BC, Report 2013-1, p. 37–46.

Chapman, R., Mortensen, J., Crawford, E., and Lebarge, W., 2010a. Microchemical studies of placer and lode gold in the Klondike district, Yukon, Canada: 1. evidence for a small, gold-rich, orogenic hydrothermal system in the Bonanza and Eldorado Creek area. Economic Geology, vol. 105, p. 1369-1392.

Chapman, R.J., Mortensen, J.K., Crawford, E.C., and LeBarge, W.P., 2010b. Microchemical studies of placer and lode gold in the Klondike District, Yukon, Canada: 2. Constraints on the nature and location of regional lode sources. Economic Geology, vol. 105, p. 1393–1410.

Chapman, R., Mortensen, J., and LeBarge, W., 2011. Styles of lode gold mineralization contributing to the placers of the Indian River and Black Hills Creek, Yukon Territory, Canada as deduced from microchemical characterization of placer gold grains. Mineralium Deposita, vol. 46, p. 881-903.

Kelley, K.D., Eppinger, R.G., Lang, J., Smith, S.M., and Fey, D.L., 2011. Porphyry Cu indicator minerals in till as an exploration tool: example from the giant Pebble porphyry Cu-Au-Mo deposit, Alaska, USA. Geochemistry: Exploration, Environment, Analysis, vol. 11, p. 321-334.

LeBarge, W.P. (compiler), 2007. Yukon Placer Database 2007 - geology and mining activity of placer occurrences. Yukon Geological Survey, CD-ROM.

Wrighton, T.M., 2013. Placer gold microchemical characterization and shape analysis applied as an exploration tool in western Yukon. Unpublished MSc Thesis, University of British Columbia, 140 p.

Preliminary observations on the geology of the Anvil Lake area (parts of NTS 105K/11 and 12), central Yukon

Rosie Cobbett[1]
Yukon Geological Survey, Whitehorse, YT

Cobbett, R.N., 2013. Preliminary observations on the geology of the Anvil Lake area (parts of NTS 105K/11 and 12), central Yukon. *In:* Yukon Exploration and Geology 2013, K.E. MacFarlane, M.G. Nordling, and P.J. Sack (eds.), Yukon Geological Survey, p. 33-51.

ABSTRACT

The Anvil Lake area consists of mostly contact-metamorphosed siltstone and sandstone having lesser interbedded volcanic and carbonate units that belong to the Early Paleozoic Selwyn basin, thrust northward over the Devono-Mississippian Earn Group and Carboniferous to Triassic formations. These are intruded by the mid-Cretaceous Anvil batholith. The mapped area surrounds the Keg, a disseminated silver-base metal deposit of current interest; new bedrock information will increase the efficiency of exploration of silver bearing veins noted along stratigraphic and structural contacts regionally. It is the first season of an investigation aiming to provide more detailed revision of regional maps, with further paleontology, geochronology, and structural analysis.

[1] *rosie.cobbett@gov.yk.ca*

INTRODUCTION

Grassroots mineral exploration, north and northwest of the town of Faro, has expanded regionally from the Keg deposit (MINFILE 105K 078; discovered in 1966, assessed through the 1970s). Since 2010, a trend of high-grade silver-bearing occurrences has been delineated, roughly parallel to a NW-trending fold-thrust belt that includes the Keg deposit.

Bedrock maps of the region stem from field work in the 1980's (Gordey, 2013a,b; at scales of 1:100 000 and 1:250 000). The mapped area lies immediately north of a regional compilation of the Anvil district (Pigage, 2004). More thorough coverage of the bedrock exposure will add structural and stratigraphic detail, and may elucidate the setting of these occurrences. In 2013 the Yukon Geological Survey initiated detailed revision mapping surrounding the Keg occurrence. The results of paleontology, geochronology, compositional, and structural analyses are pending; the intent is to continue mapping along the structural trend to the northwest.

GEOLOGICAL FRAMEWORK

The Anvil Lake area is located in the center of Yukon, 30 km north of the previously mined Faro deposit (Fig. 1). The mapped area is the heart of Selwyn basin, a broad region underlain by mostly lower Paleozoic deep water clastic, cherty and less common thin carbonate strata (Gabrielse, 1967; Gordey and Anderson, 1993; Gordey, in prep). The Selwyn basin depocenter ceased by middle Devonian. Devono-Mississippian greywacke, conglomerate, and siltstone, sourced primarily from the northwest (Abbott *et al.*, 1986; Gordey and Anderson, 1993) were unconformably deposited on the lower Paleozoic strata. The Anvil Lake area also preserves, in down faulted blocks and in the foot wall of thrusts, remnants of the Carboniferous through Jurassic shelf succession, also dominantly clastic. Regional unconformities separate these successions, although they are not exposed in the mapped area.

Central Yukon is in the Omineca structural province that is characterized by north and northeast-verging folds and thrust faults, some of which can be traced across the mapped area (Fig. 2). These reflect northeastward shortening generally accepted to have resulted from collision of continental fragments and arc assemblages with the western margin (present coordinates) of Laurentia in Middle Jurassic (Colpron *et al.*, 2006; Mair *et al.*, 2006). Remnants of the subducted exotic terrains (Yukon Tanana, Slide Mountain; Fig.1) lie 25 km south of the mapped area. In the late Early Cretaceous, granitic plutons, including the 60-km-long Anvil batholith, perforated the structurally telescoped and thickened Selwyn basin strata; those exposed in the mapped area belong to the Selwyn plutonic suite (Gordey and Anderson, 1993; Rasmussen, 2013). The Tintina fault, a northwest trending structure, along which 430 km dextral slip has occurred since mid-Cretaceous, lies 25 km southwest of the mapped area (Gabrielse *et al.*, 2006; Roddick, 1967). No systematic fault offset or brittle features related to it are recognized in the mapped area.

In summary the southern half of the mapped area consists of Cambrian to Silurian Selwyn basin strata that have been thrust over Devonian to Triassic strata in the northern half. Tight folds in the Devonian to Triassic strata are kinematically linked to northwest-striking thrust faults. Granitic plugs and the Anvil batholith intrude both successions and thrust faults, imposing a contact metamorphic aureole several kilometres wide.

STRATIGRAPHY

The Anvil Lake area is underlain by Selwyn basin strata of Lower Cambrian to Silurian age. These are: Mount Mye formation, Vangorda formation, and Menzie Creek formation, and an as-yet uncorrelated limestone unit of probable pre-Devono-Mississippian age. These are unconformably overlain by a Devonian through Triassic sequence including several lithologic divisions of the Earn Group, the Tay Formation, an as-yet uncorrelated sandstone of probable Carboniferous to Permian age, the Mount Christie Formation, and Jones Lake Formation (Fig. 3).

UPPER PROTEROZOIC TO SILURIAN ROCKS

Clastic and volcanic strata in the southern half of the mapped area, interpreted to be upper Proterozoic to Silurian, were designated as Gull Lake Formation, Rabbitkettle Formation, and overlying Menzie Creek formation on reconnaissance maps (Gordey, 2013a,b). Currently, however, local workers use the informally named Mount Mye formation (uPCMM), Vangorda formation (COV), and Menzie Creek formation (OSMC) (Jenning and Jilson, 1986; Pigage, 2004) for the same strata within the Anvil District. This informal terminology has been adopted to describe most of the rocks in the north part of the Anvil district.

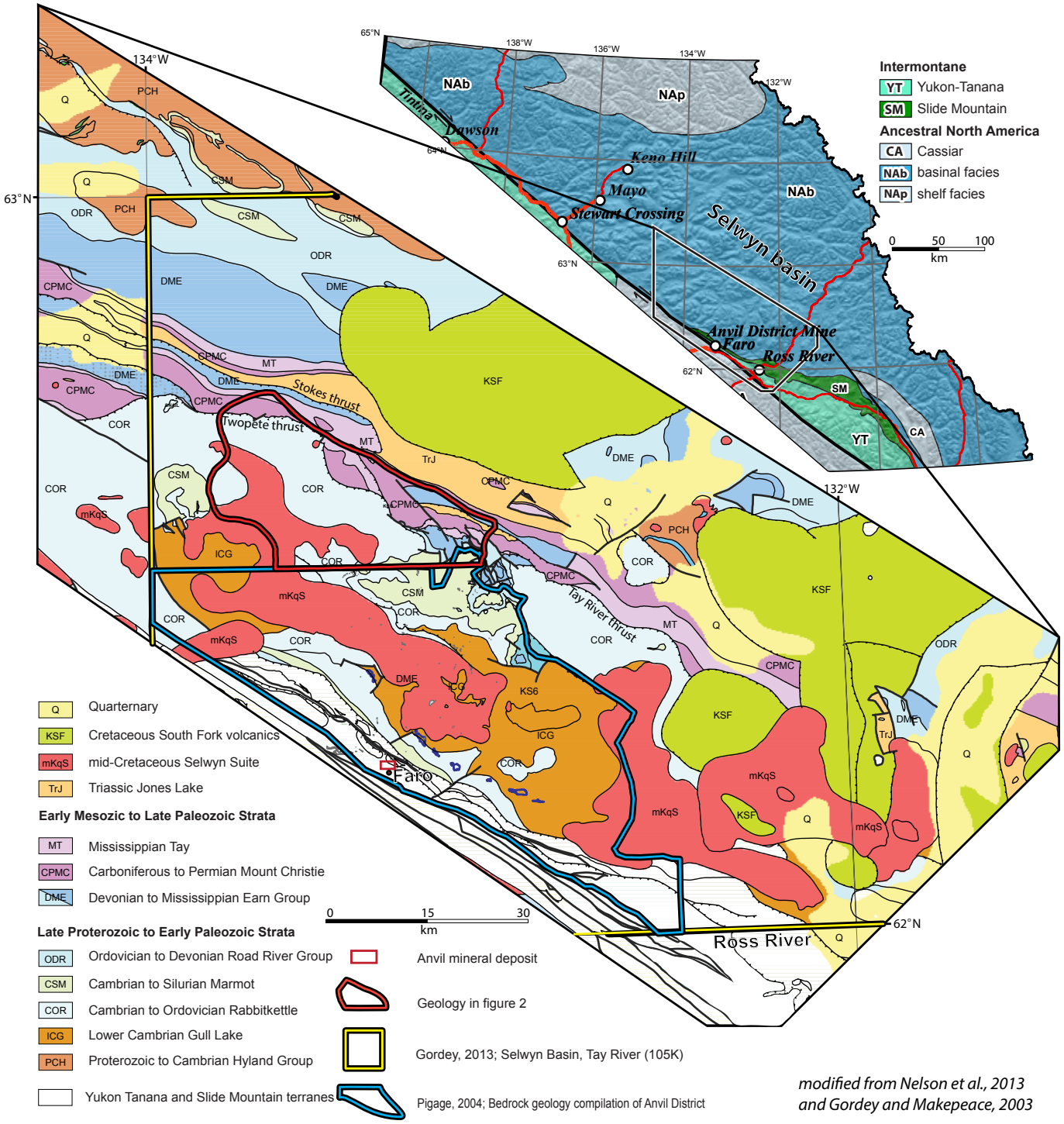

Figure 1. *Geological terranes (from Nelson et al., 2013) shown in top right map; mapped area lies in Selwyn basin. Larger map shows geology of the Anvil district (modified from Gordey and Makepeace 2003) with colored lines delineating regional mapping by Gordey, 2013 (yellow), Pigage, 2004 (blue), and this study (red).*

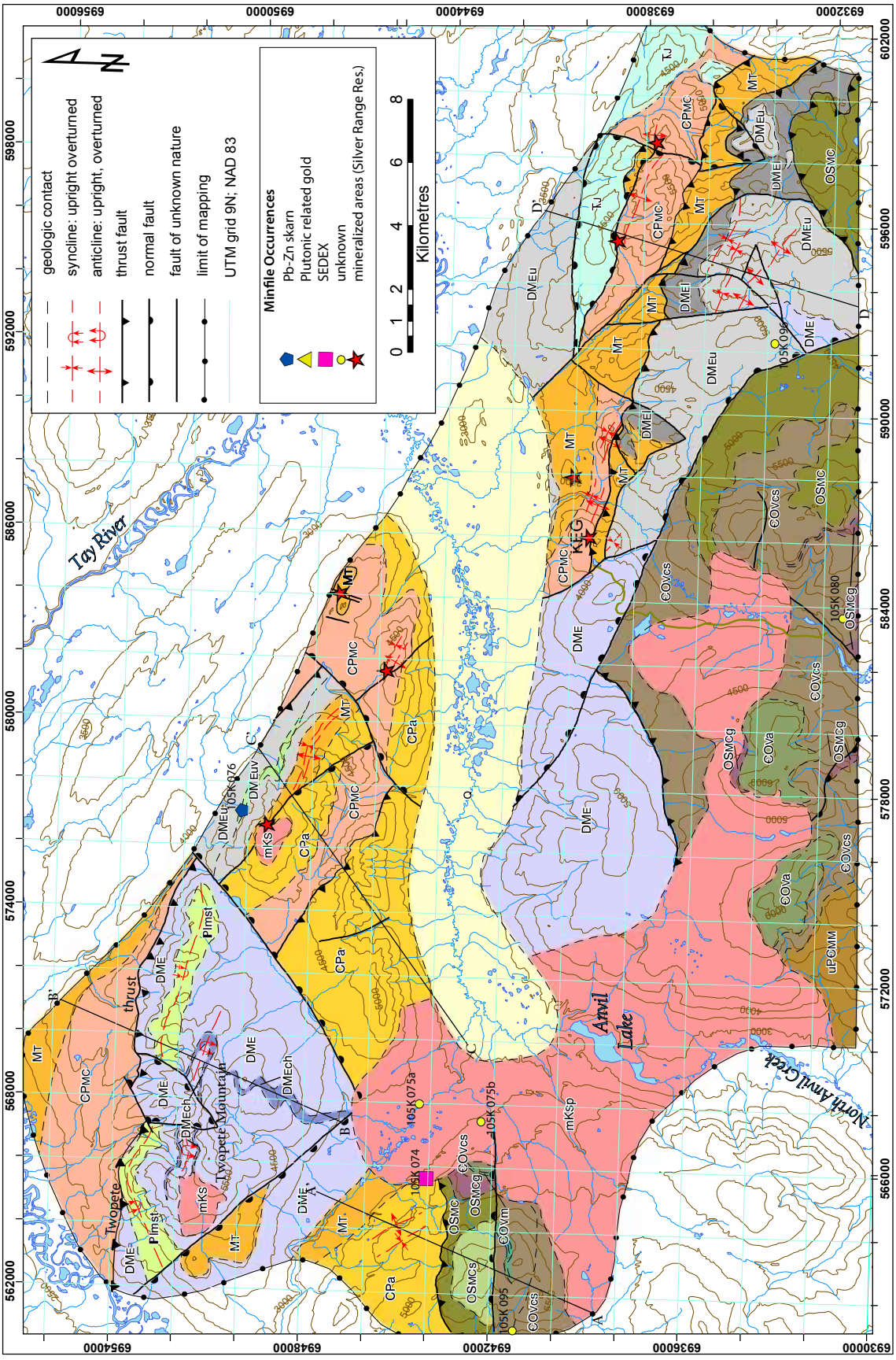
geologic contact
syncline: upright overturned
anticline: upright, overturned
thrust fault
normal fault
fault of unknown nature
limit of mapping
UTM grid 9N; NAD 83
Minfile Occurrences
Pb-Zn skarn
Plutonic related gold
SEDEX
unknown
mineralized areas (Silver Range Res.)
Kilometres
Tay River
Twopete Mountain
Amil Lake
North Amil Creek
thrust
105K 074
105K 075a
105K 075b
105K 076
105K 095
105K 096
105K 080
KEG

LEGEND

QUATERNARY

Q — glacial, glaciofluvial and glaciolacustrine deposits

INTRUSIVE ROCKS

MID CRETACEOUS

mKs — ANVIL BATHOLITH: biotite +/- hornblende granodiorite

mKsp — ANVIL BATHOLITH: porphyritic biotite +/- hornblende granodiorite

ORDOVICIAN AND SILURIAN

OSMCg — MENZIE CREEK gabbro: medium grained, dark green pyroxene bearing gabbro sills and dikes

LAYERED ROCKS

MIDDLE TO UPPER TRIASSIC

TJ — JONES LAKE FORMATION: light grey, calcareous sandstone, locally cross laminated; grey limestone and silty limestone

CARBONIFEROUS TO PERMIAN

CPMC — MOUNT CHRISTIE FORMATION: rusty orange to brown weathering, grey, green, maroon and black bedded chert with siltstone interbeds

CPa — Arenite: light grey quartz arenite, locally interlayered with dark grey siltstone and beige weathering, calcareous arkose; black weathering chert

MISSISSIPPIAN

MT — TAY FORMATION: grey-brown siltstone interbedded with calcareous sandstone, locally fossiliferous; dark grey siltstone interbedded with silty limestone

DEVONIAN AND MISSISSIPPIAN

EARN GROUP

DME — UNDIFFERENTIATED: sandstone and siltstone rhythmically bedded and may belong to DMP

DMEch — UNDIFFERENTIATED chert: black chert; siliceous siltstone

DMEuv — UPPER FORMATION volcanics: grey-green feldspar +/- pyroxene-phyric andesitic flows

DMEu — UPPER FORMATION: recessive dark grey and black, variably carbonaceous shale; sandstone; chert conglomerate; local volcanic and volcaniclastic interbeds

DMEl — LOWER FORMATION: recessive dark grey and black, variably carbonaceous shale; medium bedded black chert and siltstone

ORDOVICIAN AND SILURIAN

OSMCs — MENZIE CREEK FORMATION sandstone: dark weathering greywacke; grey-brown weathering siltstone and sandstone; buff weathering siltstone

OSMC — MENZIE CREEK FORMATION: dark green amygdaloidal basalt, locally pillowed; basalt breccia, heterolithic volcanic conglomerate, tuffaceous siltstone and tuffaceous sandstone

UPPER CAMBRIAN AND ORDOVICIAN

Plmst — Limestone: light grey limestone and calcareous sandstone; hetergeneous limestone boulder conglomerate

ЄOVa — VANGORDA FORMATION amphibolite: dark green amphibolite with lesser interlayered with calc-silicate hornfels and schist

ЄOVm — VANGORDA FORMATION marble: light brown-grey marble and calcareous sandstone

ЄOVcs — VANGORDA FORMATION calc-silicate schist: green, purple and beige striped calc-silicate hornfels and schist

UPPER PROTOERZOIC TO CAMBRIAN

uPЄMM — MOUNT MYE FORMATION: porphyroblastic (dominantly cordierite) biotite-muscovite schist

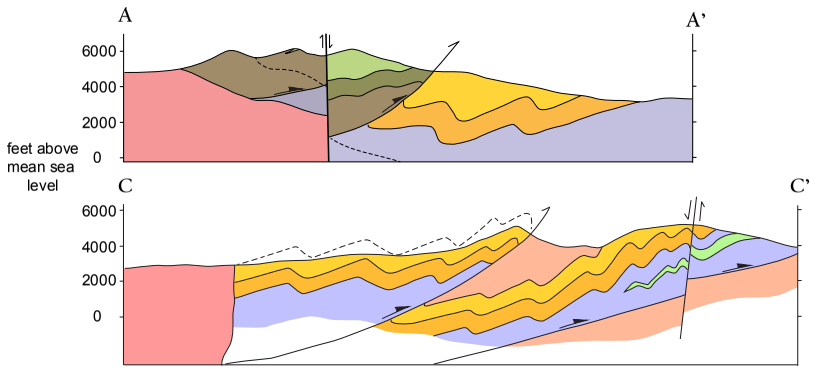

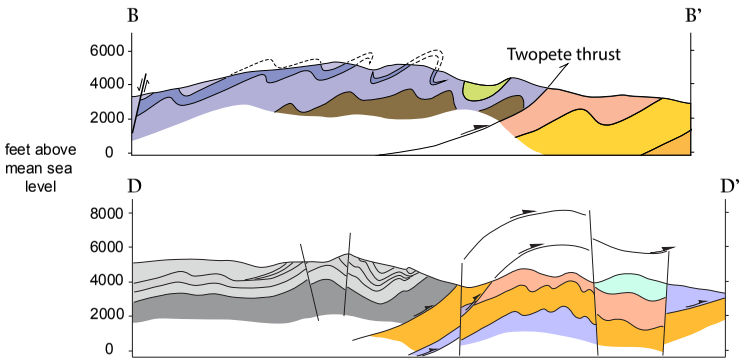

Figure 2. *Geologic map, cross sections, and legend for the Anvil Lake area.*

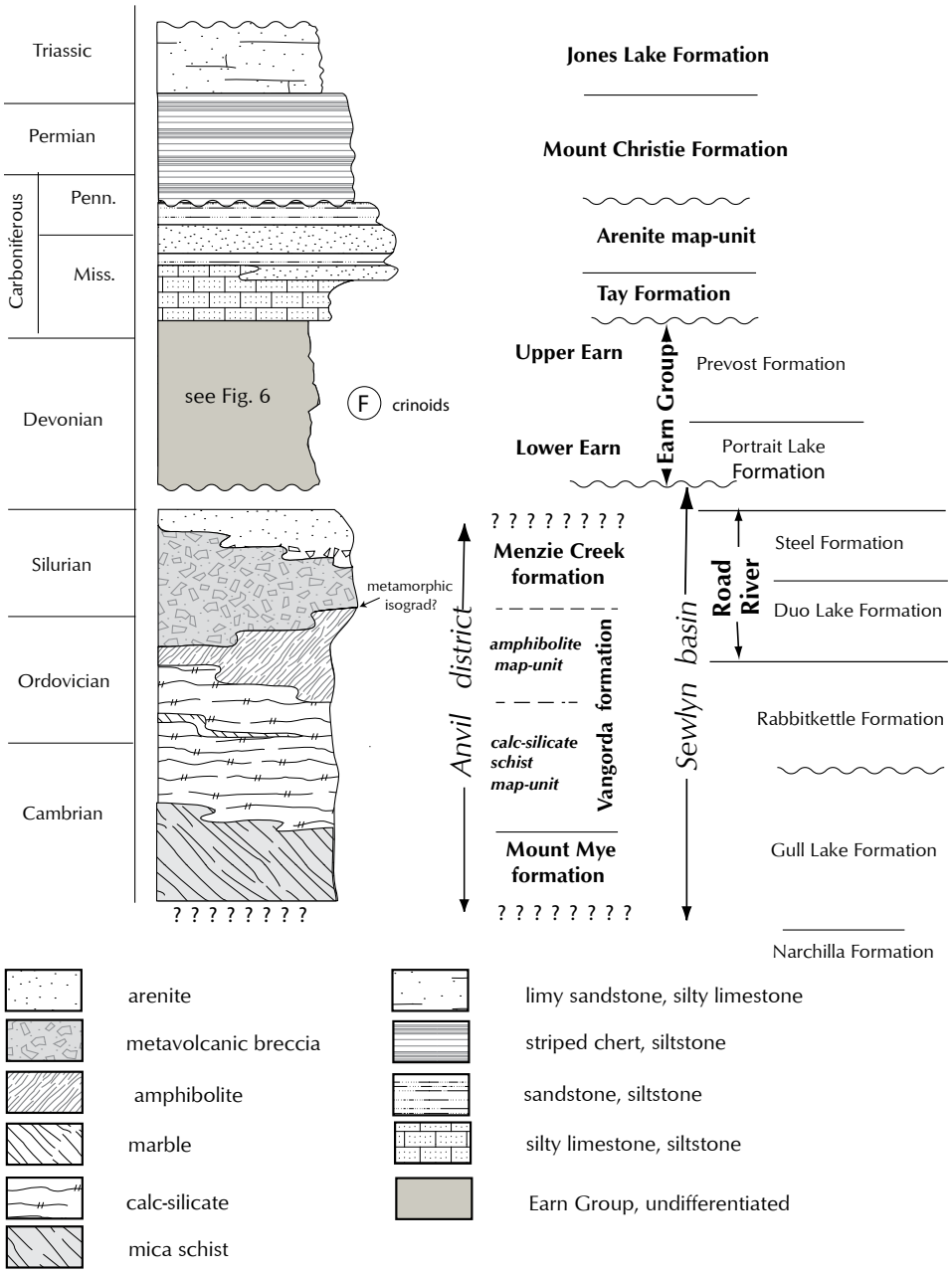

Figure 3. *Lithostratigraphy of Anvil Lake area; units in bold face are used in this paper. Names from Gordey and Anderson (1993), Pigage (2004), and Gordey (2013a,b).*

MOUNT MYE FORMATION

Biotite-muscovite schist, containing porphyroblasts of cordierite up to 1 cm across, is exposed in the southwestern part of the mapped area (Fig. 2). Brown weathering, fine and medium-grained schist (Fig. 4a) is interlayered with calc-silicate schist at the top of the Mount Mye formation, forming a gradational boundary with the overlying Vangorda formation. The top of the Mount Mye formation at its contact with the overlying Vangorda formation is exposed to a thickness of approximately 100 m at the base of a line of cliffs (Fig. 4b). The lower contact of the schist is not exposed within the mapped area and therefore an estimate of total thickness is not possible. The current thickness is greater than 100 m assuming the unit is not internally folded. The outcrops of this unit are within 2 km of exposed Anvil batholith and reflect its contact metamorphism.

This rock unit is presumed to extend south of the mapped area, where it was assigned to the Rabbitkettle Formation (Twopete facies) by Gordey (2013a), and interlayered Menzie Creek and Vangorda formations by Pigage (2004). The observed lithology however, more closely resembles that of the Mount Mye formation as described by Pigage (2004). If so, this unit is of upper Proterozoic to Cambrian age.

VANGORDA FORMATION

Calc-silicate (COVcs)

Purple, green, and beige striped, fine-grained calc-silicate schist and hornfels dominate this unit in the south-central part of the map area, as well as in a hill near the western edge. Rare purplish-grey, calcareous phyllite crops out near the upper part of the succession. The lower contact with the Mount Mye formation is gradational. The upper contact with Menzie Creek volcanics is gradational and characterized by thickly interlayered volcanic and volcaniclastic rocks with calc-silicate schist. The thickness of the calc-silicate schist varies from an estimated 150 m in the southwest corner of the map area, where it sits conformably between Mount Mye formation and Vangorda amphibolite, to an estimated greater than 500 m in other parts of the mapped area. Except for the southwest exposure, the base of the Vangorda formation

is not exposed. The lack of basal exposure and internal folding make a true thickness impossible to ascertain.

The calc-silicate rocks contain quartz, temolite-actinolite, plagioclase, biotite ± diopside ± calcite ± epidote (Jennings and Jilson, 1986).

In color and lithology these exposures match the description of the more highly metamorphosed variety of the Vangorda formation described by Pigage (2004). No age data have been attributed to this unit although it must be older than Early to Middle Ordovician Menzie Creek formation that overlies it.

Amphibolite (COVa)

Dark green and brown, fine-grained amphibolite ± biotite schist and phyllite, commonly cut by garnet-pyroxene ± calcite veins, are interlayered with calc-silicate schist (Fig. 4c). In the south-central part of the map area a very distinct, medium-grained, meta-igneous (?) rock and stretched porphyroclasts (?) are interlayered with amphibolite-biotite schist.

Minor, waxy, dark green to black weathering, amphibolite schist has a well-developed foliation defined by aligned feldspar grains. Light green, sub-spherical features, 3 to 8 mm across, occur rarely in streaks and patches (Fig. 4d) within massive amphibolite. These small structures are similar in appearance to amygdules in volcanic rock.

An exposed thickness of this unit is greater than 200 m. The lower contact is gradational with Vangorda calc-silicate schist and an upper contact with younger rocks is not exposed.

The metamorphosed mafic rock occurs within the upper part of the Vangorda formation. A similar unit is widely exposed south of the Anvil batholith where it contains 15-20% chloritic phyllite and amphibolite (Jennings and Jilson, 1986). The hilltop exposures in the Anvil Lake area are sufficiently large and coherent

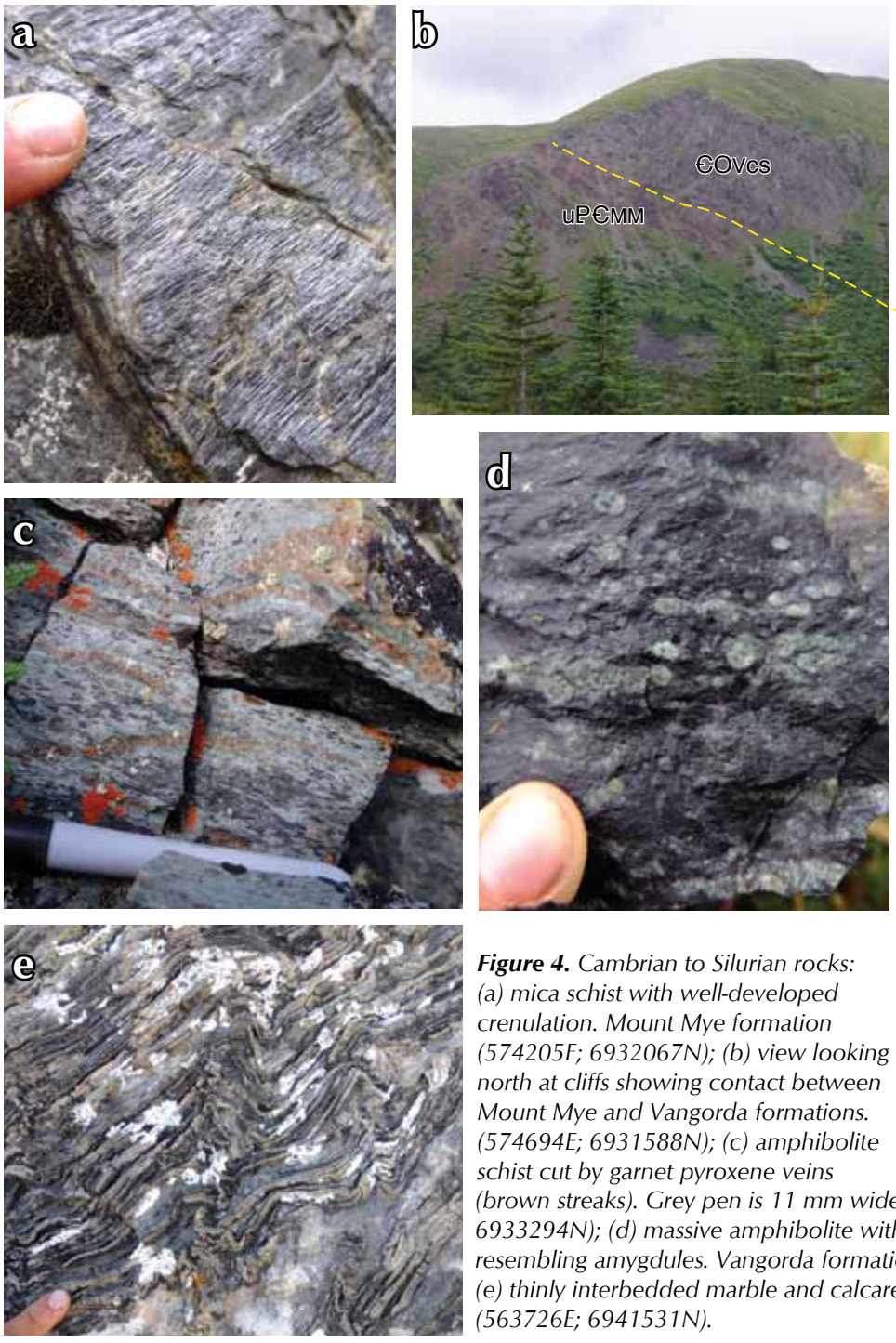

Figure 4. *Cambrian to Silurian rocks: (a) mica schist with well-developed crenulation. Mount Mye formation (574205E; 6932067N); (b) view looking north at cliffs showing contact between Mount Mye and Vangorda formations. (574694E; 6931588N); (c) amphibolite schist cut by garnet pyroxene veins (brown streaks). Grey pen is 11 mm wide. Vangorda formation (580602E; 6933294N); (d) massive amphibolite with light green spherical features resembling amygdules. Vangorda formation (579177E; 6932331N); and (e) thinly interbedded marble and calcareous sandstone. Vangorda formation (563726E; 6941531N).*

enough to warrant being mapped as a separate unit, but is considered coeval with it.

Marble (COVm)

Well bedded marble crops out in the far western part of the mapped area. Light brownish-grey weathering, thinly interbedded marble, and fine-grained, calcareous sandstone occur as a narrow horizon within calc-silicate schist (Fig. 4e). The upper and lower contact with calc-silicate schist was under cover and therefore not examined. The marble reaches a thickness of 80 m, however, it is deformed by polyphase folding suggesting the true thickness may be significantly less. The marble pinches out to the west.

PALEOZOIC LIMESTONE:

Limestone conglomerate, that grades upwards into a very thinly interbedded limestone and calcareous sandstone, cores an east trending anticline in the northwest corner of the map area (Fig. 2). It sits topographically above a hornfelsed, laminated siltstone unit of undifferentiated Earn Group. The contact between the limestone conglomerate and siltstone is exposed for approximately 20 m northeast of Twopete Mountain and is undulating and irregular (Fig. 5a). The thickness of the conglomerate and the limestone together is estimated to be 200 to 250 m.

The conglomerate contains pebble to boulder sized clasts of limestone, calcareous sandstone, and chert, floating in a muddy to sandy matrix that has flow textures (Fig. 5b). It is always matrix-supported and very poorly sorted. This unit grades upwards into a moderately sorted limestone conglomerate and is capped by thinly interbedded limestone and calcareous, fine-grained sandstone (Fig. 5c).

Thin bedded limestone has been described elsewhere in the Selwyn basin within the Rabbitkettle Formation (Fig.3) (Gordey and Anderson, 1993; Cecile, 2000). Gordey (2013b) assigned all rocks that crop out on Twopete Mountain (this unit together with undifferentiated Earn Group in Figure 2) to the Twopete facies of the Rabbitkettle Formation. However, he does not include the rocks described here in his regional description of Rabbitkettle.

The structural interpretation presented in Figure 2 (cross section B-B′), including the contact shown in Figure 5a, suggests the Paleozoic limestone stratigraphically overlies parts of the Earn Group. Correlation of the Paleozoic limestone unit to a regional formation is pending until further studies are complete.

MENZIE CREEK FORMATION

Interbedded with the upper parts of the Vangorda formation are mafic volcanic and volcaniclastic rocks. Monolithic basalt breccia, vesicular and amygdaloidal basaltic flows, and minor pillow basalts are interbedded with minor tuffaceous sandstone and siltstone and lesser conglomerate (Fig. 5d). The most notable exposures of these rocks are in the immediate hanging wall of thrust faults in both the easternmost and westernmost parts of the map area. A rounded ridge in the western part of the map area is underlain by dark grey-green weathering, thin bedded, medium-grained greywacke; grey-brown weathering, thin-bedded to laminated siltstone; buff weathering, laminated, mildly hornfelsed, fine-grained sandstone; and siltstone (OSMCs). This exposure is topographically higher than Menzie Creek volcanic rocks. The contact with Menzie Creek volcanic rocks is not exposed but, if conformable, this section is part of an upper, clastic phase of Menzie Creek formation. In the south-central part of the map area, contacts with Menzie Creek and Vangorda formation are nowhere exposed. Based on the map pattern, Menzie Creek formation is very thickly interlayered with Vangorda schist, and is estimated to be up to 300 m thick. In the western part of the map area, contact with Vangorda schist is obscured by a grabbo body.

The sequence described above is assigned to the Menzie Creek formation (Jennings and Jilson, 1986). Fossils found in the Menzie Creek formation, northeast of the Anvil batholith indicate an age of Ordovician to Silurian (Pigage, 2004). The Vangorda amphibolite schist occurs above and interlayered with Vangorda calc-silicate schist and has rare volcanic-like textures suggesting it may be a higher metamorphic grade equivalent of Menzie Creek formation.

EARN GROUP

Fine to coarse clastic sediments, interbedded locally with volcanic and volcaniclastic rocks, underlie the southeastern part of the mapped area (Fig. 2). The best exposure is a south-trending ridge where a limestone lens within shale contains two-holed crinoid fossils.

The bedrock exposure and relatively straightforward structure along this ridge allows a crude stratigraphic section to be constructed (Fig. 6). The lowest unit is a dark grey to black, variably carbonaceous siltstone. It is overlain by quartz-feldspar-phyric, intermediate, crystal tuff (Fig. 7a), hereafter referred to as the ‘lower volcanic unit’. Above is a dark grey to black, carbonaceous shale that has black chert horizons and uncommon limestone beds

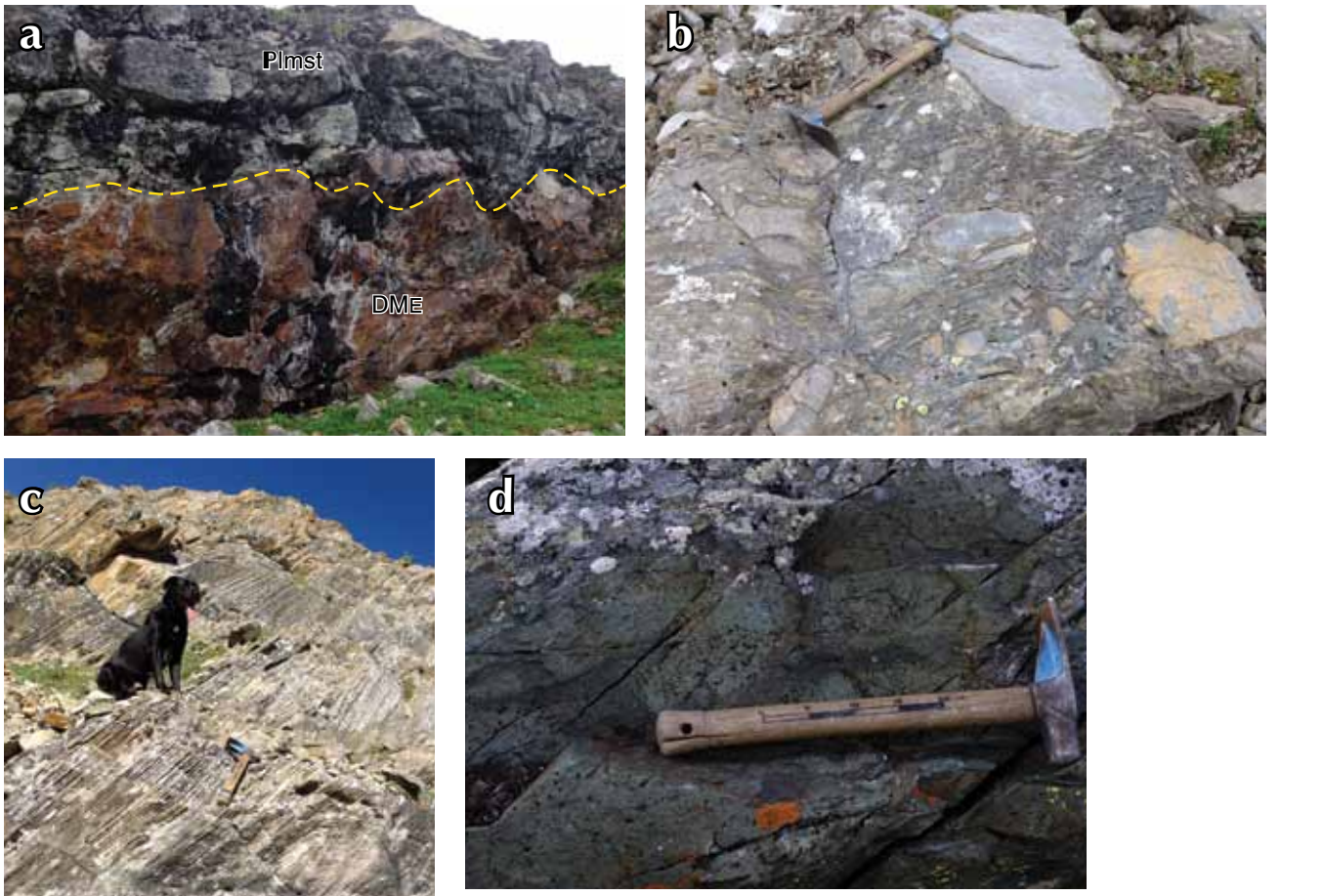

Figure 5. *(a) Contact between limestone conglomerate and hornfelsed siltstone. Unnamed Paleozoic limestone (Plmst) stratigraphically overlying Earn Group (DME). (570830E; 6952561N). (b) Poorly sorted limestone conglomerate. Unnamed Paleozoic limestone (Plmst). (570830E; 6952561N). (c) Thinly bedded limestone and calcareous sandstone. Unnamed Paleozoic limestone (Plmst). (565819E; 6953233N). (d) Monolithic basalt breccia, provisionally assigned to Menzie Creek formation (OSMC). (588040E; 6931926N).*

containing two-holed crinoids (Fig. 7b). It is succeeded by laterally discontinuous, resistant, dark grey weathering, chert conglomerate that grades upwards into coarse-grained, cross–bedded, quartz rich sandstone (Fig. 7c). The conglomerate ranges in thicknesses from 0 to 50 m across a couple kilometres. Several thick but lenticular beds of quartz arenite stratigraphically overlie the conglomerate, succeeded by an orange-brown weathering siltstone interbedded with fine-grained sandstone and minor fossiliferous dolomitic siltstone (Fig. 7d). The siltstone/sandstone is characterized by soft sediment deformation such as ball-and-pillow and flame structures. The highest unit in the succession is a medium-grained tuff of intermediate composition, and lesser felsic-to-intermediate, amygdaloidal flows (Fig. 7e), here termed the 'upper volcanic unit'.

Exposures in the western half of the mapped area lack stratigraphic context. Buff-weathering, variably hornfelsed, fine-grained sandstone, thinly interbedded with muddy siltstone are commonly rhythmically bedded with local massive cherty sections. A useful marker is a black, medium-bedded chert with minor dark grey siltstone (DMEch) within the rhythmically bedded fine clastic rocks: it outlines large scale folds within Twopete Mountain, and ranges in estimated thickness from 20 to 100 m (Fig.2, cross section B-B').

Two-hole crinoid fossils are diagnostic of the late Early Devonian to early Middle Devonian (Emsian-Eifelian; Johnson and Lane, 1969; Fig. 7b). This known age within the stratigraphy is depicted in Figure 6; the dark, dominantly clastic lithology and presence of volcanic rock, all point toward an Earn Group succession. In the eastern

half of the mapped area, Earn Group reveals a lower, siltstone-dominated succession, and an upper coarse clastic, limestone and volcanic succession (Fig. 2).

In the western part of the mapped area, areas assigned to undifferentiated Earn Group (Fig. 2) were previously interpreted as Rabbitkettle Formation (*c.f.*, Gordey, 2013a). The younger designation suggested within this paper is based on local occurrences of foliated crystal tuffs that look very similar to the lower volcanic unit, and relative stratigraphic position above the Paleozoic limestone unit.

TAY FORMATION

Grey and brown weathering, medium-bedded, variably fossiliferous, silty limestone evenly interbedded with dark grey, variably siliceous siltstone is exposed across the northern half of the map area (Fig. 2). In the eastern part of the map area the Tay Formation unconformably overlies the lower Earn Group or is bounded by thrust faults. This unit has an estimated minimum thickness of 350 m.

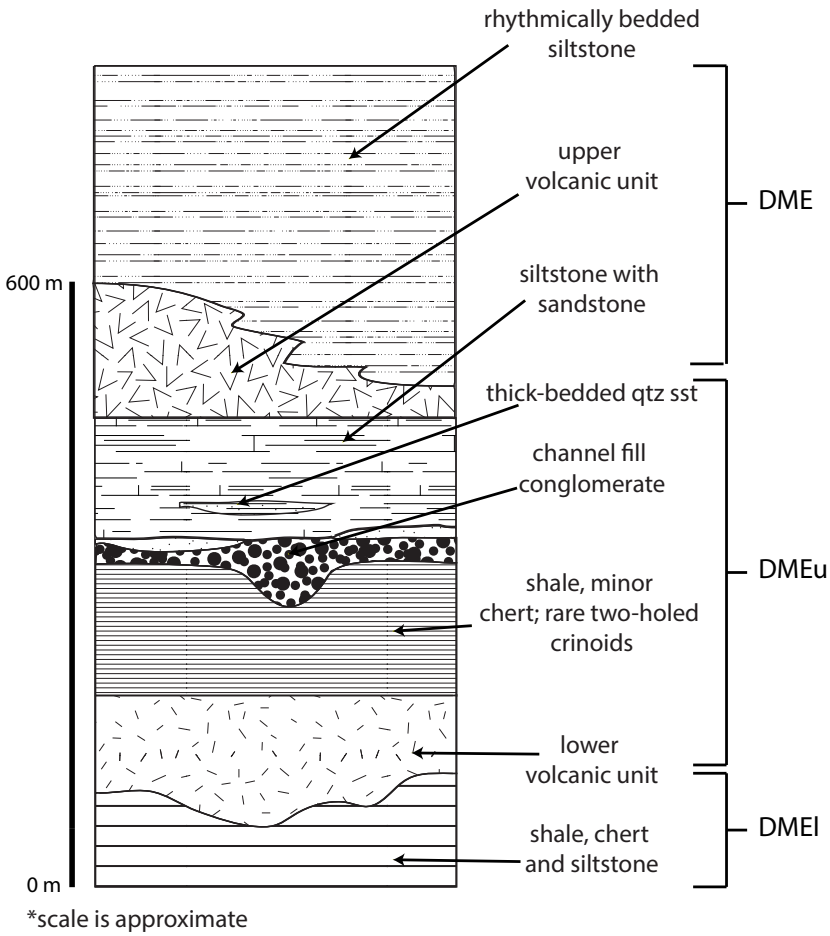

Figure 6. *Schematic stratigraphy of Earn Group. Section constructed from exposures in the southeast part of the mapped area, near 594000E; 6934500N.*

Southwest of Twopete Mountain this unit unconformably overlies the Earn Group. Fossils are common within limestone beds and rare within siltstone beds, and include coral, bivalves, and crinoids.

Numerous fossil occurrences in the eastern half of the map area constrain the Tay Formation to the Mississippian. Western exposures are correlated with the Tay Formation based on its similarities in lithology and stratigraphic position beneath the younger Mount Christie Formation.

CARBONIFEROUS TO PERMIAN (?) ROCKS (CPA)

Resistant, thick-bedded quartz arenite (Fig. 8a) interbedded with mildly carbonaceous, dark grey, variably fossiliferous siltstone; dark grey siliceous siltstone; medium-bedded black chert; and beige weathering, calcareous arkosic sandstone form prominent ridges and steep walls of deep canyons in the east and center of the map area (Fig. 8b). An internal stratigraphic section for this group of rocks is difficult to construct due to lack of continuous outcrop and folding. Locally, 30 m of black weathering, medium-bedded chert sit topographically below dark grey weathering, fine-grained, vitreous quartz arenite that forms beds several metres thick (Fig. 8c). A dark and light grey weathering, thin-bedded quartzose siltstone to fine-grained sandstone that is locally burrowed, crops out at the top of a short south trending ridge. Further south along this ridge (and conformably underlying the siltstone) is mildly carbonaceous siltstone containing rare plant stem and bivalve fossils. A thick bed (at least 1 m thick) of beige weathering, medium–grained, calcareous arkose, made up of well-rounded quartz and feldspar grains cemented by calcite, crops out down section to the south and is succeeded by light grey and beige weathering, thick-bedded quartz arenite. The overall thickness of this group of rocks is difficult to ascertain, but based on construction of cross sections has a crudely estimated minimum thickness of 1000 m.

Based upon its distribution, this unit is stratigraphically above the Tay Formation and overlain by a distinctive lithology assigned to the Mount Christie Formation. If correct, the unit must be of Carboniferous to early Permian age, and therefore cannot be Rabbitkettle Formation, as previously mapped (Gordey, 2013a,b). Micro and macrofossil collections

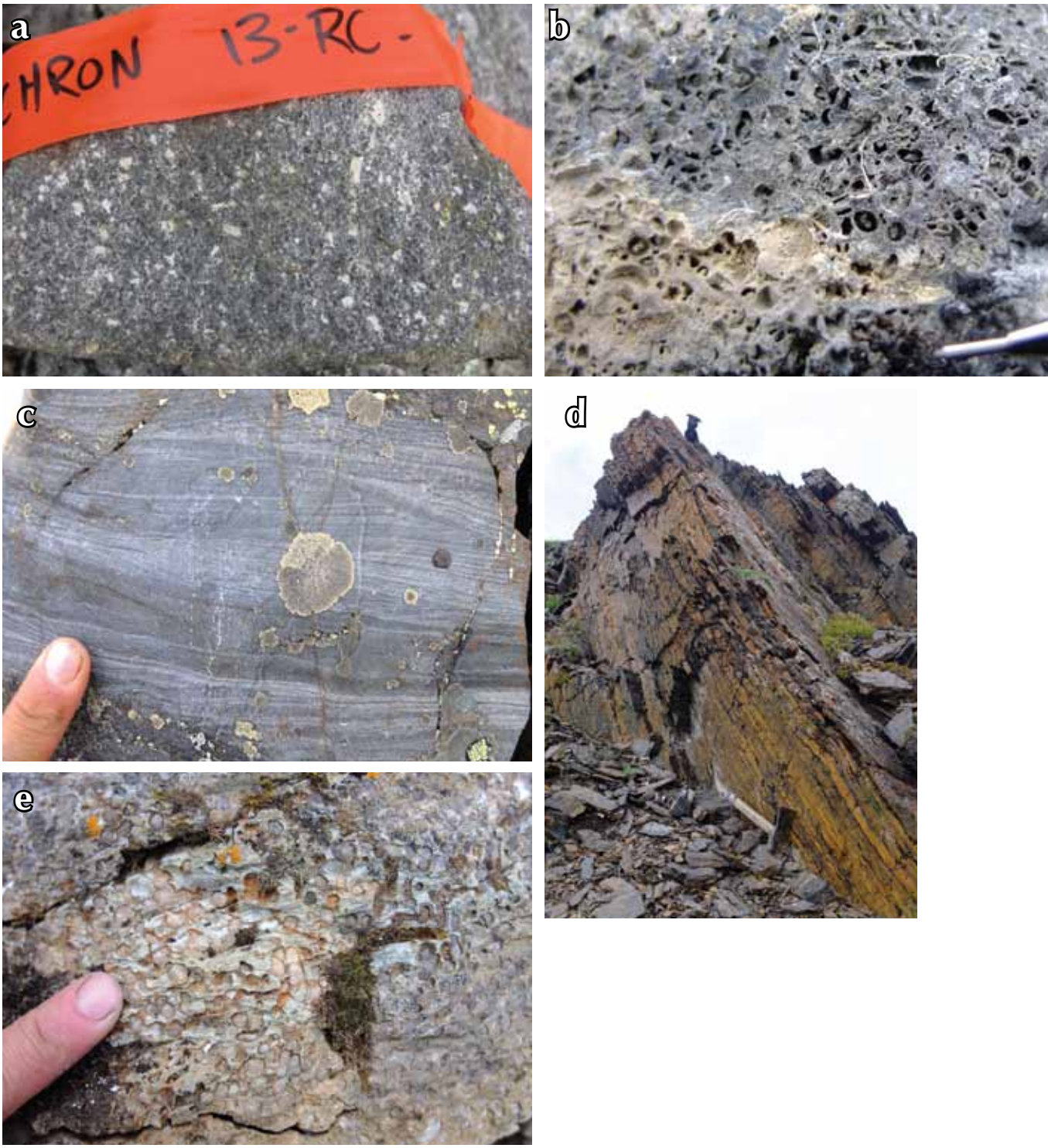

Figure 7. *Earn Group rocks: (a) quartz-feldspar-phyric crystal tuff. Orange tape is 2 cm wide. Lower volcanic unit (DMEu). (590189E; 6936759N); (b) limestone within shale of unit DMEu; contains two-holed crinoids. Steel cylindrical tip of pencil at lower right, is 5 mm long. (594786E; 6933413N); (c) coarse-grained, quartz-rich, cross-bedded sandstone of unit DMEu. Note that the cross-beds indicate stratigraphic tops are towards the top of the photograph which is taken of an outcrop that is sitting in place. (577736E; 6949337N); (d) interbedded fine-grained sandstone and muddy siltstone, unit DMEu. Figure on top is 0.5 m high. (594762E; 6934938N); and (e) amygdaloidal felsic flow in upper volcanic unit (DMEu), (593059E; 6931859N).*

have been submitted to attempt to constrain the age of this unit.

These rocks are provisionally assigned unit CPa, pending better understanding of their age. Correlation with other quartz-rich strata is yet to be determined. A similar succession of rocks in the Lansing map area (about 120 km north northwest of the mapped area) contains Early Carboniferous and Permian microfossils (Roots, 2003). The Heritage Trail Formation (Cecile, 2000) consists of grey-white quartzite and minor shale, and calcareous quartzite beds, and is probably of early Mississippian age. In the southeastern part of Selwyn basin, Gordey and Anderson (1993) describe the Carboniferous Tsichu formation as grey and white weathering, resistant quartz sandstone interbedded with recessive black shale and siliceous shale.

MOUNT CHRISTIE FORMATION

Rusty orange to brown weathering, grey, grey-green, maroon, and black, thin-bedded chert (Fig. 8d) interbedded with light grey siltstone, is well exposed in the northeast part of the mapped area. In the northwest, east of Twopete Mountain, minor grey limestone with thin interbeds of dark grey siltstone, and cross-bedded calcareous sandstone occur as 5 to 10 m sections within chert. The upper contact with the Jones Lake Formation was not examined during this study, but is regionally mapped as conformable (Gordey, 2013a,b). A lower contact, exposed in the north central part of the map area, places well bedded grey-green chert conformably on light grey weathering, massive quartz arenite (CPa). The chert is commonly tightly folded and in fault contact with other units making estimates of thickness difficult. A crudely estimated minimum thickness for this unit is 250 m.

Several fossil occurrences, located in the far northwest corner and the northeast part of the map area, bracket this formation to the Carboniferous or Early Permian. On the basis of the fossil ages and distinctively colored chert, this package is assigned to the Mount Christie Formation (Gordey, in press; Gordey and Anderson, 1993). Areas of the map assigned to Mount Christie Formation that do not have fossil age control are based upon lithologic similarities to known Mount Christie Formation aged rocks and a conformable contact with the Tay Formation. Numerous samples of chert were collected for microfossil analysis in an attempt to better constrain the age of this unit and its spatial distribution across the mapped area.

JONES LAKE FORMATION

Light grey weathering, fossiliferous, silty limestone and calcareous sandstone with cross-bedding (Fig. 8e) are exposed only along the eastern edge of the mapped area. Very limited exposure was examined during this study; snail-like fossils (spiral in cross section) were found in these outcrops. A minimum thickness of 80 m is estimated for this unit; however, nowhere are both the upper and lower bounds exposed.

The friable, nondescript lithology, and several fossil occurrences indicate a good match for the Jones Lake Formation (Gordey and Anderson, 1993). Fossil collections elsewhere from this unit constrains the age as Middle to Upper Triassic.

INTRUSIVE ROCKS

PRE-CRETACEOUS INTRUSIVE ROCKS

Several bodies, ranging in width from approximately 50 to 500 m and extending in length up to several kilometres, of dark green pyroxenite bearing gabbro are exposed near the southern limit of mapping; they extend further south and match well with previous mapping (Pigage, 2004). They intrude Cambrian to Silurian strata, and were not mapped in younger strata. One small exposure of an intermediate plagioclase-phyric intrusion was observed on the south side of Twopete Mountain. The body is approximately 100 by 500 m (too small to show on Fig. 2). Its purplish color and induration may be attributed to contact metamorphism of the nearby Anvil batholith.

ANVIL BATHOLITH

Light grey, medium-grained porphyritic (potassium feldspar) biotite ± hornblende granodiorite is a prominent feature in the central part of the mapped area (Fig. 2). Its contact with layered rocks is highly irregular and commonly shallowly dipping based on its relation to topography. Several smaller, non-porphyritic biotite granodiorite bodies occur north of the batholith and are presumed to be coeval.

These exposures are part of a much larger body called the Anvil batholith (Tempelman-Kluit, 1972). Within the Anvil batholith two phases have been mapped and are distinguished based on lithology, petrography, and geochemistry (Pigage and Anderson, 1985; Pigage

Figure 8. *Carboniferous to Triassic strata: (a) thick-bedded to massive quartz arenite. Unnamed CPa unit. (580882E; 6945316N); (b) steeply dipping, thick-bedded quartz arenite interbedded with dark grey quartzose siltstone and fossiliferous siltstone. Small bump on the highest peak is a person. Unnamed CPa unit. (575521E; 6946775N); (c) thick-bedded, vitreous quartz arenite of unnamed CPa unit; (d) Ribbon banded, black chert. Mount Christie Formation. (582013E; 6945328N); and (e) Cross-bedded, calcareous sandstone interbedded with silty limestone. Pen width is 7 mm. Jones Lake Formation (TrJ). (~600700E; 6937100N).*

2004). The extent of the Anvil batholith, shown in Figure 2, is similar to the Orchay phase (necessitating a jog in the contact projected northward from Pigage, 2004) that has an age range of 99 to 115 Ma (Pigage and Anderson, 1985; Rasmussen, 2013). Based on lithology and age it is part of the Selwyn plutonic suite (Gordey and Anderson, 1993).

The Anvil batholith, within the mapped area, has a contact metamorphic aureole approximately 2.5 km wide characterized by phyllitic and schistose Selwyn basin

rocks, and hornfelsed Late Paleozoic rocks. Southeast of this study area, previous workers documented up to amphibolite grade, coarse-grained schistose rocks within the Anvil batholith aureole, and peak metamorphism that occurred during intrusion at approximately 300 MPa pressure, and heated country rocks to between 600 and 620°C (Smith and Erdmer, 1990). The wide aureole comprising coarsely schistose and high grade metamorphosed rocks makes this mid-Cretaceous event atypical in this region (Smith and Erdmer, 1990).

STRUCTURE

Early Paleozoic strata (the southern half of the map area) constitute structural domain 1, and Late Paleozoic to Early Mesozoic strata (in the northern half of the map area; Fig. 9a) constitute structural domain 2. Domain 1 is characterized by a folded penetrative foliation defined by purple, beige, and green stripes in calc-silcate schist and hornfels, and by layers of biotite and mafic minerals in amphibolite schist (Fig. 10a,b). The Anvil batholith, where observed during this study, is undeformed and cuts all structures except one steep normal fault in the western part of the mapped area (Fig. 2).

Bedding is preserved locally within domain 1. The competent nature of the Menzie Creek volcanic rocks preserves beds of tuffaceous siltstone and sandstone between thick layers of volcanic breccia and basalt flows. Volcanic breccia commonly displays elongated clasts, and flows exhibit vesicles stretched parallel to the regional foliation. Bedding is also preserved in rare marble horizons that crop out within Vangorda calc-silicate schist.

In domain 1 outcrop-scale, tight to isoclinal folds deform the penetrative foliation and exhibit a closely spaced axial planar cleavage that is visible in hinges (Fig. 10c). The cleavage is generally steeply dipping to the south and northeast (Fig. 9b). Intersection between the foliation and the cleavage creates a prominent lineation in micaceous layers within calc-silicate schist and amphibolite. It plunges shallowly to the southeast throughout the map area (Fig. 9c).

Domain 2 encompasses Late Paleozoic to Early Mesozoic rocks that are faulted against the Early Paleozoic strata in the southern part of the map area (Fig. 2 and 9a). Primary textures are always preserved; in addition some pelitic rocks display moderately-developed foliation. These rocks are tight to isoclinally folded in outcrop and on a regional scale with folds becoming tighter and overturned to the NNE. Folds are asymmetric, and have a steeper north-dipping limb and a shallow south-dipping limb (Fig. 9d). Folds commonly display a well-developed axial planar cleavage that on average strikes southeast and dips shallowly to moderately SW (Fig.11a). Folding is kinematically linked to northeast-verging thrust faults (Fig. 11b). On Twopete Mountain closely spaced brittle fracture sets are oriented steeply east dipping and steeply southeast dipping (Fig. 11c). Within domain 2 several thrust faults (including western parts of Gordey's Twopete thrust) imbricate the Late Paleozoic rocks (Fig. 2, cross sections BB', CC', DD').

The thrust fault separating domain 1 from domain 2 is similar to Gordey's (2013b) Twopete thrust in that it separates Cambro-Ordovicain strata from Late Paleozoic strata; however, based on re-assignment of Cambro-Ordovician strata within the mapped area, this fault traces out further south than shown on Gordey's map. Studies on the geologic history that accounts for the structural and metamorphic differences in domain 1 and domain 2, and the timing and nature of their juxtaposition, are in progress.

Variably oriented normal faults cross cut folding and thrusting, and occur for the most part within domain 2. Offset along these structures varies from an estimated 30 to 1000 m. In the central part of the mapped area a normal fault separates domain 1 from domain 2, dropping the north side down and truncating a thrust fault that was the original domain 1-domain 2 boundary. Orientation and intersection of some of these normal faults create graben-like features in the eastern part of the map area suggesting extension followed fold-and-thrust deformation (Fig. 2, cross section D-D').

MINERAL OCCURRENCES AND EXPLORATION

The Keg occurrence (Yukon MINFILE 105K 078) is a bulk tonnage silver-polymetallic base metal deposit with an inferred resource of 38.8 million tonnes containing Ag, Zn, Pb, and Cu. It is modelled to be a 150–m-wide linear zone of mineralization that dips moderately to the southeast. The highest silver grades (>50 g/t) are at, or near the surface, and decrease at depth (*www.silverrangeresources.com*). This study postulates that the host unit closely resembles chert belonging to the Mount Christie Formation, structurally below and stratigraphically above limestone correlated with the Tay Formation (Fig. 2).

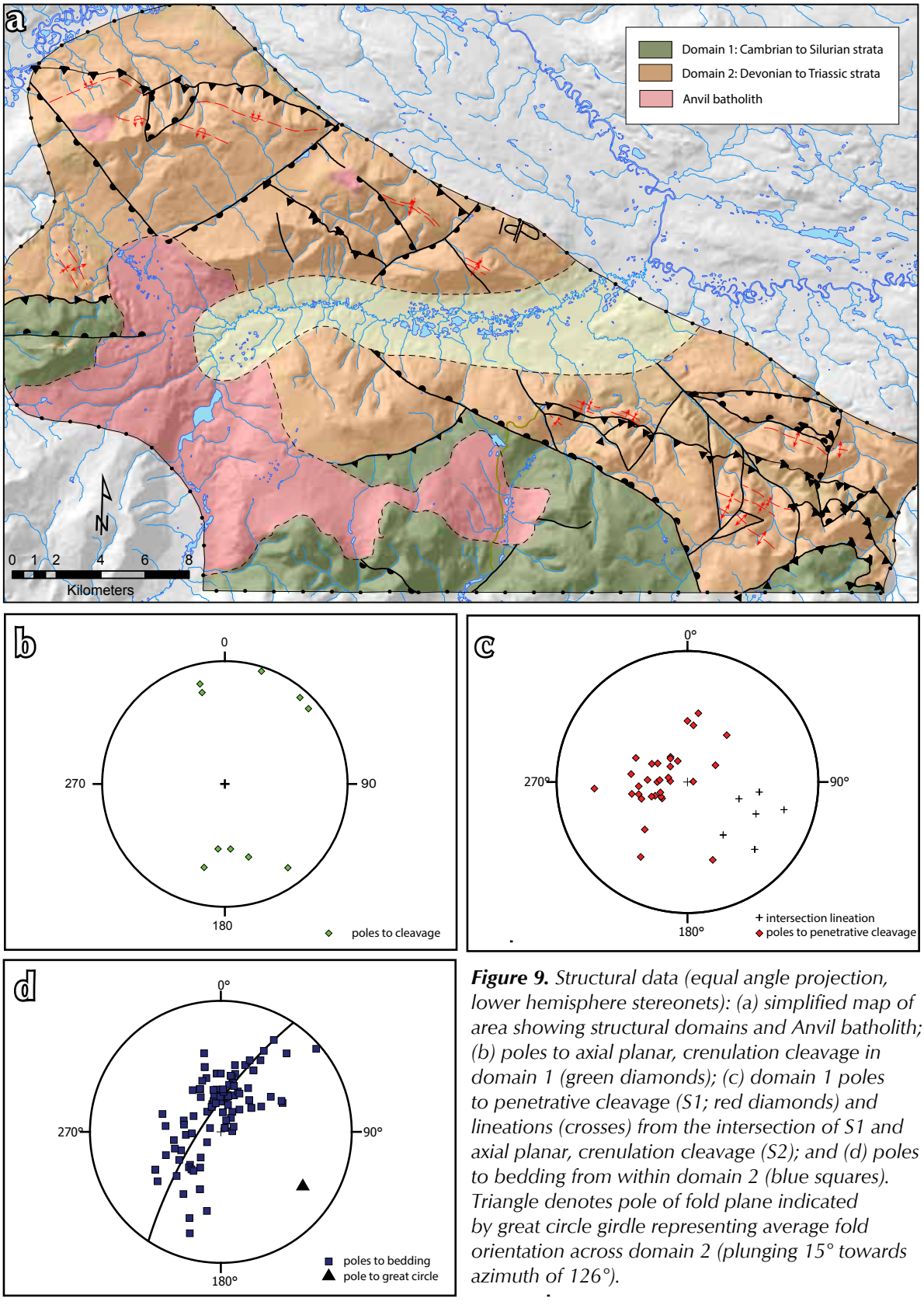

Figure 9. *Structural data (equal angle projection, lower hemisphere stereonets): (a) simplified map of area showing structural domains and Anvil batholith; (b) poles to axial planar, crenulation cleavage in domain 1 (green diamonds); (c) domain 1 poles to penetrative cleavage (S1; red diamonds) and lineations (crosses) from the intersection of S1 and axial planar, crenulation cleavage (S2); and (d) poles to bedding from within domain 2 (blue squares). Triangle denotes pole of fold plane indicated by great circle girdle representing average fold orientation across domain 2 (plunging 15° towards azimuth of 126°).*

A NW-trending zone of high-grade silver-bearing veins has been delineated based on the prospecting of numerous soil geochemistry anomalies (*www.silverrangeresources.com*) in 2011 and 2012. It is parallel to the structural grain and general trend of the upper Paleozoic units and includes the Keg deposit and several other mineralized occurrences. Silver veins commonly occur at both stratigraphic and structural contacts between Mount Christie Formation chert and Tay Formation limestone, where these rocks are tightly folded. Late normal faulting may also play a role in the location of mineralization.

Intermediate to felsic volcanics found within the Devono-Mississippian Earn Group suggest the area has potential for VMS style mineralization similar to the Marg deposit (Yukon MINFILE 106D 009) (Holbek *et al.*, 2001). Exposures of these volcanic rocks make up a small percentage of the eastern mapped area with rare exposures found in the north-central parts of the mapped area. No mineralization was found associated with them. Rare tuffs crop out within undifferentiated Earn Group in the central part of the mapped area and occur in an area of very little bedrock exposure.

The mapped area also includes a Pb-Zn skarn (Yukon MINFILE 105K 076) and a drilled SEDEX (Yukon MINFILE 105K 074) prospect (Fig. 2), although their locations may be incorrect (granitic rock is currently mapped at the given coordinates of the SEDEX prospect). Tay Formation limestone are intruded by a small granodiorite body east of Twopete Mountain, and thin marble horizons (COVm) occur within the contact aureole of the western edge of the Anvil batholith, both prospective areas for skarn mineralization. Shale within the lower Earn Group is the only host unit within the mapped area that has potential for SEDEX style mineralization.

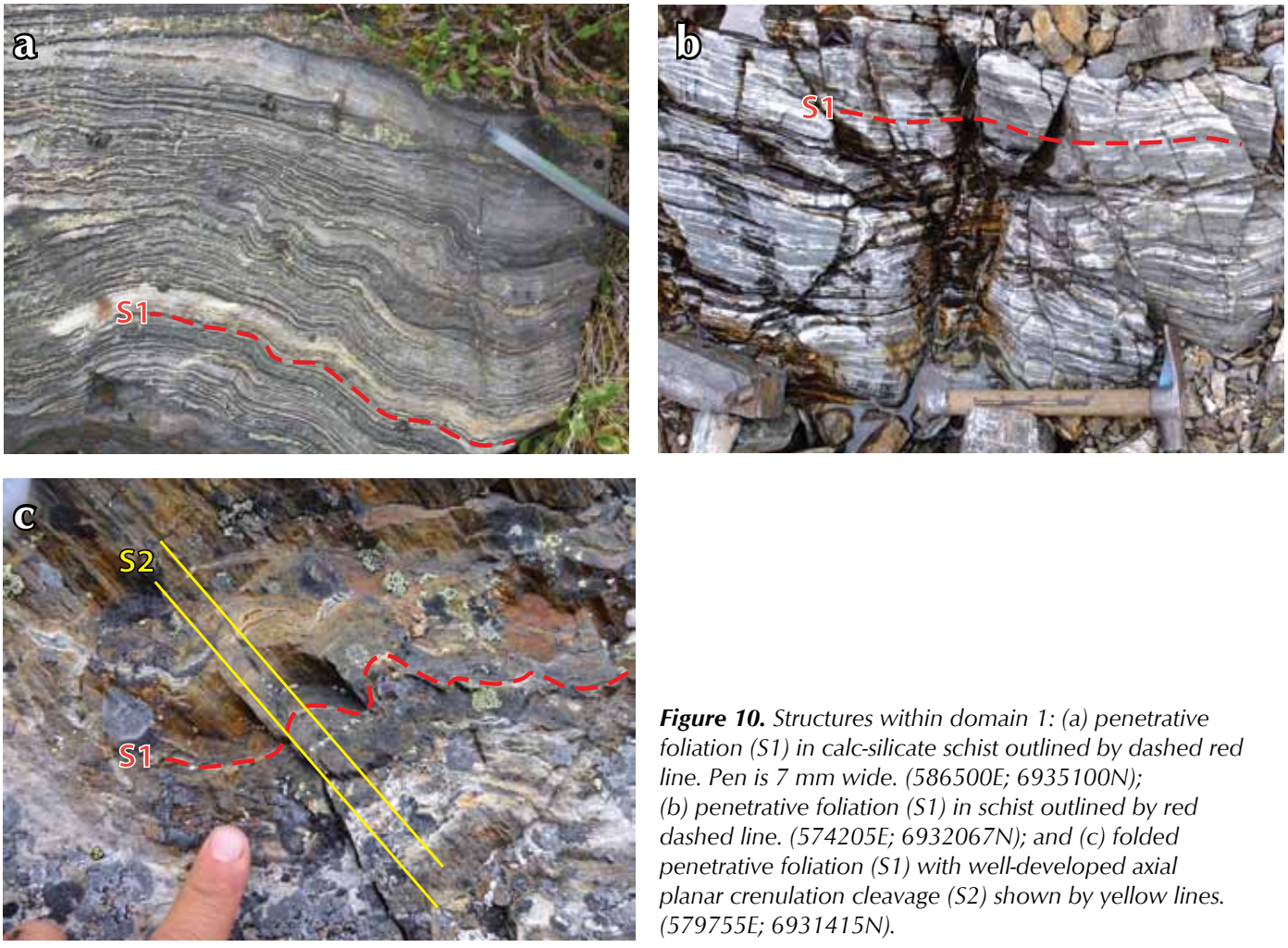

Figure 10. *Structures within domain 1: (a) penetrative foliation (S1) in calc-silicate schist outlined by dashed red line. Pen is 7 mm wide. (586500E; 6935100N); (b) penetrative foliation (S1) in schist outlined by red dashed line. (574205E; 6932067N); and (c) folded penetrative foliation (S1) with well-developed axial planar crenulation cleavage (S2) shown by yellow lines. (579755E; 6931415N).*

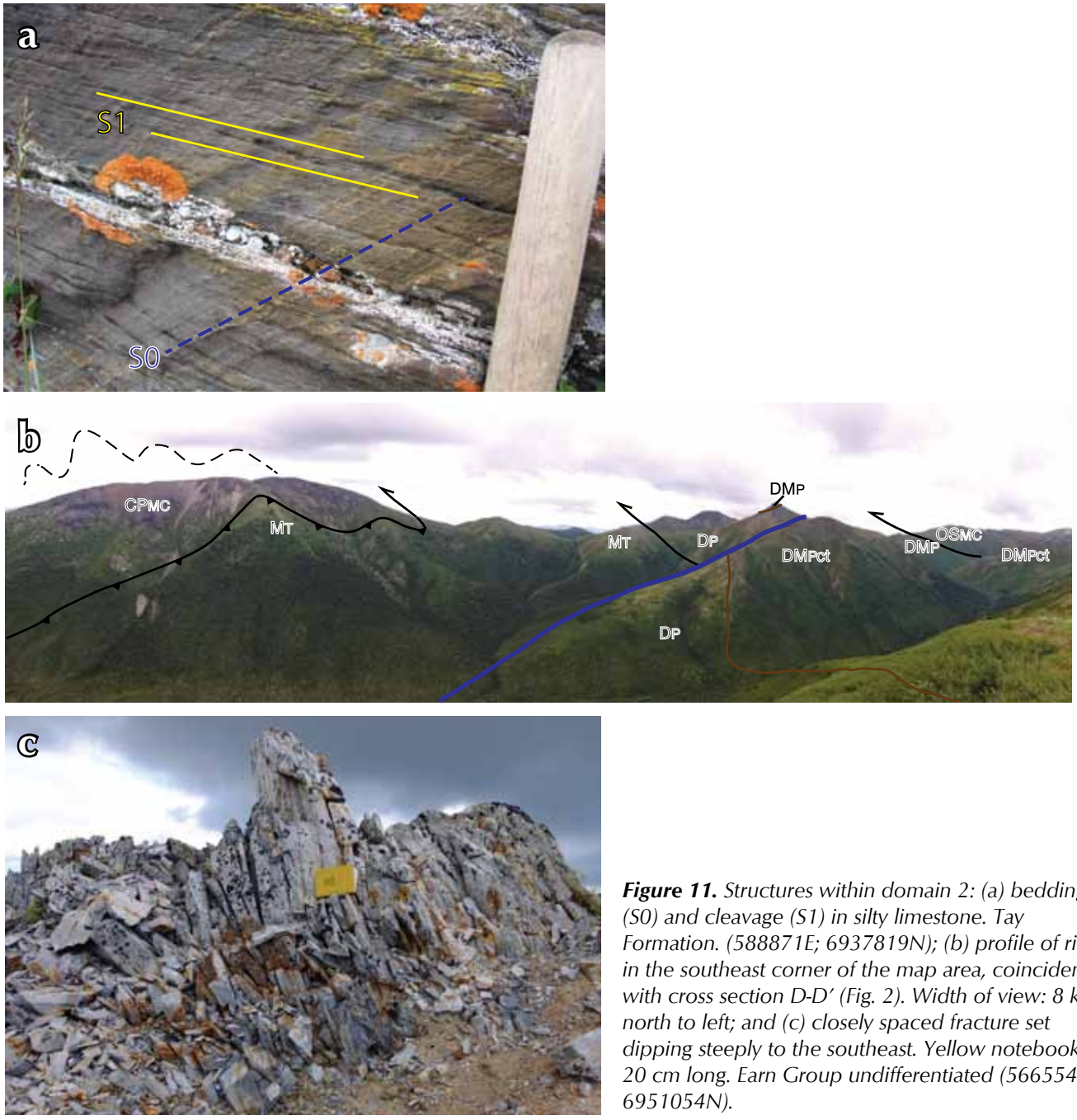

Figure 11. *Structures within domain 2: (a) bedding (S0) and cleavage (S1) in silty limestone. Tay Formation. (588871E; 6937819N); (b) profile of ridge in the southeast corner of the map area, coincident with cross section D-D′ (Fig. 2). Width of view: 8 km; north to left; and (c) closely spaced fracture set dipping steeply to the southeast. Yellow notebook is 20 cm long. Earn Group undifferentiated (566554E; 6951054N).*

CONCLUSIONS

The project area is underlain by Cambrian to Silurian Selwyn basin strata, thrust over Devonian to Triassic coarse and fine clastic, carbonate, and minor volcanic rocks. These are intruded by the mid-Cretaceous granitic Anvil batholith. A significant contact aureole surrounds the Anvil batholith, destroying primary textures in most Early Paleozoic rocks.

The area is deformed by pre mid-Cretaceous folding and north-verging thrusts and post mid-Cretaceous normal faults.

Several observations have been made based on field observations:

1. Previously mapped Rabbitkettle Formation (Cambro-Ordovician) are re-interpreted as an unnamed unit of probable Carboniferous age, possibly correlative with

quartzose strata recognized elsewhere in the Selwyn basin.

2. Intermediate to felsic volcanics found within the Devono-Mississippian Earn Group suggest the area has potential for VMS style mineralization
3. Prospective areas for high-grade silver veins occur where folded Mount Christie Formation chert is in structural or stratigraphic contact with Tay Formation limestone, subsequently dissected by normal faults.

ACKNOWLEDGEMENTS

Kane Keating provided capable field assistance. Don Murphy and Carolyn Relf instilled their knowledge of field geology and regional Selwyn basin stratigraphy. Silver Range Resources Ltd. and Archer Cathro and Associates shared geological insights from their long experience in the area and coordinated helicopter logistics. Trans North helicopters provided prompt and safe transportation.

Lee Pigage, Charlie Roots, and Don Murphy instilled their knowledge of the Anvil district and Selwyn basin stratigraphy; Don Murphy and Steve Israel discussed the structures. Preparation of this article was greatly assisted by Charlie Roots, with drafts reviewed by Lee Pigage; responsibility for the interpretations is mine. I am grateful to Karen MacFarlane and Monica Nordling for expediting its publication.

REFERENCES

Abbott, J.G., Gordey, S.P., and Tempelman-Kluit, D.J., 1986. Setting of stratiform, sediment-hosted lead-zinc deposits in Yukon and northeastern British Columbia. *In*: Mineral Deposits of Northern Cordillera, J.A. Morin (ed.), Canadian Institute of Mining and Metallurgy, special volume 37, p. 1-18.

Cecile, M.P., 2000. Geology of the northeastern Niddery Lake map area, east-central Yukon and adjacent Northwest Territories. Geological Survey of Canada, Bulletin 553, 120 p.

Colpron, M., Mortensen, J.K., Gehrels, G.E., and Villeneuve, M., 2006. Basement complex, Carboniferous magmatic arcs and Paleozoic deformation in Yukon-Tanana terrane of central Yukon: Field, geochemical, geochronological constraints from Glenlyon map area. *In:* Paleozoic evolution and metallogeny of pericratonic terranes at the ancient Pacific margin of North America, Canadian and Alaskan Cordillera, Geological Association of Canada, Special Paper 45.

Gabrielse, H., 1967. Tectonic evolution of the northern Canadian Cordillera. Canadian Journal of Earth Sciences, vol. 4, p. 271-298.

Gabrielse, H., Murphy, D.C., and Mortensen, J.K. 2006. Cretaceous and Cenozoic dextral orogeny-parallel displacement, magmatism, and paleogeography, north-central Canadian Cordillera. *In:* Paleogeography of the North American Cordillera: Evidence For and Against Large-Scale Displacements, J. Haggart, R.J. Enkin, and J.W.H. Monger (eds), Geological Association of Canada, Special Paper 46, p. 255-276.

Gordey, S.P., 2013a. Geology, central Tay River, Yukon. Geological Survey of Canada, Map 2150A, scale 1:100 000. doi: 10.4095/288983.

Gordey, S.P., 20013b. Geology, Selwyn Basin (105J and 105K), Yukon. Geological Survey of Canada, Open File 2149A, 2 maps at 1:250 000 scale and 1 sheet cross sections at 1:100 000 scale.

Gordey, S.P., in press. Evolution of the Selwyn Basin region, Sheldon Lake (105J) and Tay River (105K) map areas, central Yukon Territory. Geological Survey of Canada, Bulletin 599, 247 p.

Gordey, S.P. and Anderson, R.G., 1993. Evolution of the northern Cordilleran miogeocline, Nahanni Map area (105I), Yukon and Northwest Territories. Geological Survey of Canada, Memoir 428, 214 p.

Gordey, S.P. and Makepeace, A.J. (comps.), 2003. Yukon digital geology, version 2.0; Geological Survey of Canada Open File 1749 and Yukon Geological Survey Open File 2003-9(D), 2 CD-ROMs.

Hills, L.V., Sangster, E.V., and Suneby, L.B. (eds.), 2000. Lexicon of Canadian Stratigraphy, Volume 2, Yukon Territory and District of Mackenzie. Canadian Society of Petroleum Geologists, 471 p.

Holbek, P.M., Copeland, D.A., and Wilson, R.G., 2001. Structure and stratigraphy of the Marg volcanogenic massive sulphide deposit, north-central Yukon. *In:* Yukon Exploration and Geology 2000, Emond, D.S. and Weston, L.W. (eds.), Exploration and Geological Sciences Division, Yukon Region, Indian and Northern Affairs Canada, p. 319-333.

Jennings, D.S. and Jilson, G.A., 1986. Geology and sulphide deposits of Anvil Range, Yukon. *In*: Mineral Deposits of Northern Cordillera, J.A. Morin (ed.), Canadian Institute of Mining and Metallurgy, Special Volume 37, p. 319-361

Johnson, J.G. and Lane, N.G., 1969. Two new Devonian crinoids from central Nevada. Journal of Paleontology, vol. 43, no. 1, p. 69-73.

Mair, J.L., Hart, C.R.J., and Stephens, J.R., 2006. Deformation history of the northwestern Selwyn Basin, Yukon, Canada: implications for orogeny evolution and mid-Cretaceous magmatism. Bulletin of Geological Society of America, vol. 118 (3/4), p. 304-323.

Nelson, J.L. and Colpron, M., 2013. The Cordillera of British Columbia, Yukon and Alaska: Tectonics and Metallogeny. Society of Economic Geology, Inc., Special Publication 17, p. 53-109.

Pigage, L.C., 2004. Bedrock geology compilation of the Anvil District (parts of NTS 105K/2, 3, 5, 6, 7 and 11), central Yukon. Yukon Geological Survey, Bulletin 15, 103 p.

Pigage, L.C. and Anderson, R.G., 1985. The Anvil plutonic suite, Faro, Yukon Territory. Canadian Journal of Earth Sciences, vol. 22, p. 1204-1216.

Rasmussen, K.L., 2013. The timing, composition, and petrogenisis of syn- to post-accrectionary magmatism in the northern Cordilleran Miogeocline, eastern Yukon and southwestern Northwest Territories. Unpublished PhD theses, University of British Columbia, Vancouver, Canada, 788 p.

Roddick, J.A., 1967. Tintina Trench. Journal of Geology, vol. 75, p. 23-33.

Roots, C.F., 2003. Bedrock geology of the Lansing Range map area (NTS 105N), central Yukon. Yukon Geological Survey, Geoscience map 2003-1, 1:250000.

Smith, J.M. and Erdmer, P., 1990. The Anvil aureole, an a-typical mid-Cretaceous culmination in the northern Canadian Cordillera. Canadian Journal of Earth Sciences, vol. 27, p. 344-356.

Silver Ranges Resources, 2013. Silver Range Project. <*http://www.silverrangeresources.com/s/SilverRange.asp*> [accessed November 2013].

Templeman-Kluit, D.J., 1972. Geology and origin of the Faro, Vangorda, and Swim concordant zinc-lead deposits, central Yukon Territory. Geological Survey of Canada, Bulletin 208, 73 p.

Yukon MINFILE, 2013. Yukon MINFILE – A database of mineral occurrences. Yukon Geological Survey, <*http://data.geology.gov.yk.ca*>[accessed November 2013].

Field descriptions of the Middle-Upper Devonian Canol Formation on Trail River, east Richardson Mountains, Yukon

Tiffani Fraser[1]
Yukon Geological Survey

Fraser, T., 2014. Field descriptions of the Middle-Upper Devonian Canol Formation on Trail River, east Richardson Mountains, Yukon. *In:* Yukon Exploration and Geology 2013, K.E. MacFarlane, M.G. Nordling, and P.J. Sack (eds.), Yukon Geological Survey, p. 53-68.

ABSTRACT

The Middle–Upper Devonian Canol Formation is the focus of a new study by the Yukon Geological Survey in north Yukon. Fieldwork in summer 2013 involved locating, measuring, and sampling Canol Formation strata in the Richardson and northern Ogilvie mountains. In June, 229 m of Canol Formation strata were measured on the Trail River, eastern Richardson Mountains (NTS 106L/6). The Canol Formation at this location is entirely exposed, except for ~2 m at its upper contact with the overlying Imperial Formation. On Trail River, the Canol Formation is a resistant, silica-rich unit that is characterized by rhythmically bedded siliceous shale and chert comprising four lithofacies: 1) siliceous shale; 2) chert; 3) siliceous shale (>50%) and chert (10-50%); and 4) chert (>70%) and siliceous shale (10-30%). Siliceous shale is fissile, finely laminated in beds up to 10 cm thick, and may be either soft and recessive or hard and resistant. Chert exhibits conchoidal fracture and occurs in beds up to 16 cm thick. Both shale and chert are black in color on fresh surfaces, and weather grey to black, olive grey, brown with a distinct yellowish orange, dark red, and/or very minor apple-green weathering residue. The lower contact of the Canol Formation with Road River Group calcareous shale is sharp, and marked by a concretionary bed overlain by a thin (<1 m) weathered mineralized zone. This mineralized zone may be in-part correlative with the Ni-Zn-PGE "Nick" horizon observed in the region. A marked lithology change occurs from the Canol to the Imperial formation which consists of weathered mudstones with a significantly lower silica content. Concretions up to 2.5 m long were observed in the Canol Formation but possible fossils were only observed at two locations where unidentified impressions on a bedding surface could be biological (or mineralogical). Fine-grained pyrite occurs throughout the formation, either as disseminated grains, in thin laminations (mm-scale), and rarely in concretionary horizons. The sampling program involved spectral gamma-radiation readings at one-metre intervals, and chip samples through two-metre intervals for Rock-Eval/total organic carbon (RE/TOC) and inductively coupled plasma-emissions/mass spectroscopy lithogeochemistry (ICP-ES/MS). Targeted samples for microfossil biostratigraphy, vitrinite reflectance, and XRD mineralogy were also collected. Laboratory results are anticipated in 2014.

[1] *tiffani.fraser@gov.yk.ca*

INTRODUCTION

The Canol Formation is a Middle-Upper Devonian shale and chert unit that is present in Northwest Territories (NWT and Yukon. Previous studies have identified it as a potential hydrocarbon source rock, but its lithology, geochemistry, age, stratigraphic relationships, and distribution in Yukon have not been systematically described. This paper presents descriptions of a near-complete stratigraphic section of the Canol Formation in the eastern Richardson Mountains, measured in summer 2013. The section is part of a larger project to characterize and correlate the Canol Formation within Yukon and to assess the formation's regional hydrocarbon potential, both as a source rock and a shale reservoir. This study is timely as the Canol Formation is currently being explored as an unconventional hydrocarbon resource in NWT's central Mackenzie Valley.

SECTION LOCATION AND REGIONAL GEOLOGY

The Canol Formation outcrop described in this paper is situated on the north bank of the Trail River, a tributary of the Peel River, on the eastern flank of the southern Richardson Mountains (NTS 106L/6; start of section at UTM 477796 E; 7366173 N; all UTM locations in this paper are NAD 83 Zone 8W; Fig. 1).

The Richardson Mountains coincide with the location of the former early to middle Paleozoic Richardson trough (Lenz, 1972). The trough was a north-south oriented deep water sedimentary basin flanked by carbonate shelves, Mackenzie Platform to the east (Lenz, 1972), and Porcupine Platform to the west (Jeletzky, 1962), that existed from Cambrian to Devonian time. Early Paleozoic deposition in the trough is recorded by the Road River

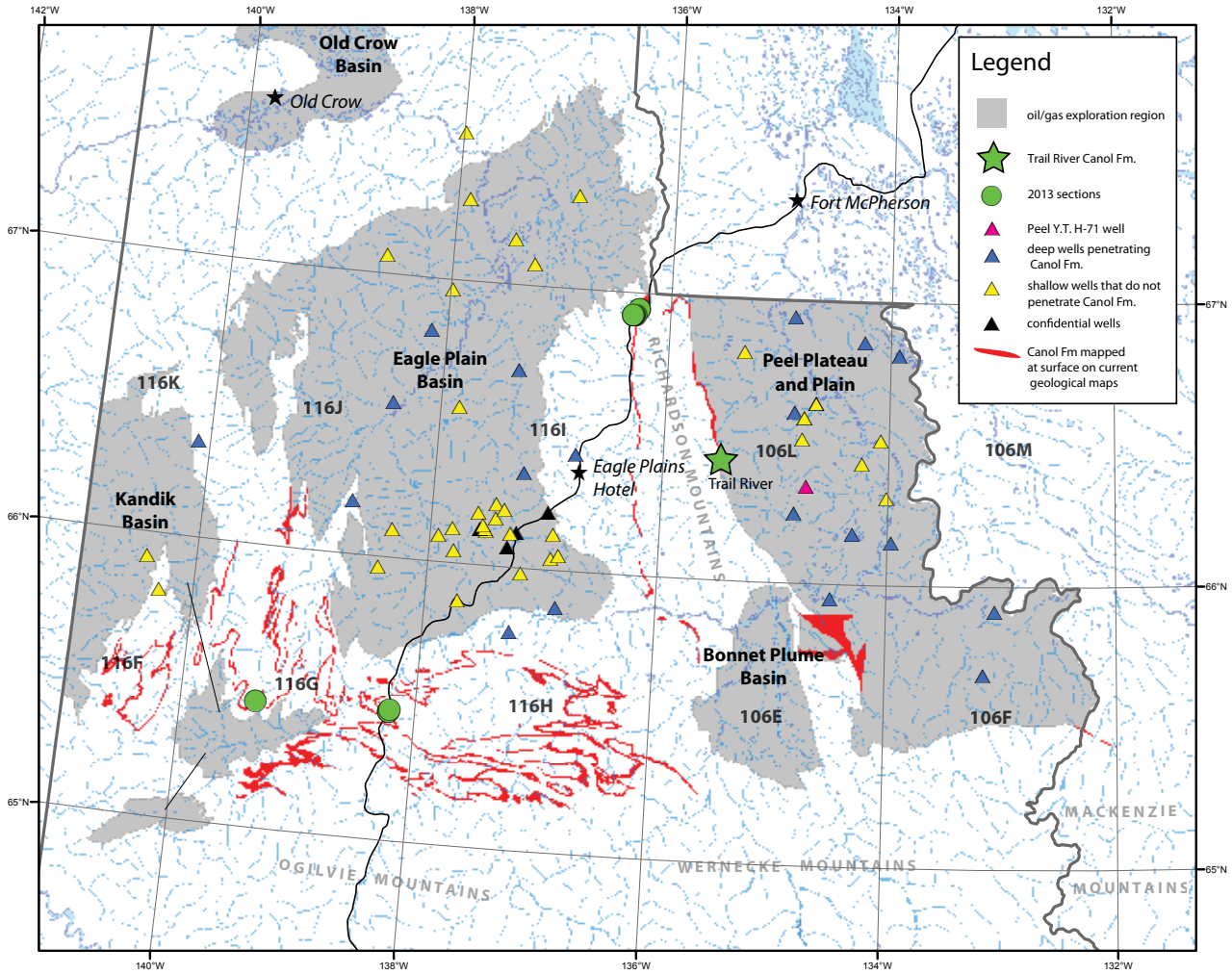

Figure 1. *Map of part of northern Yukon showing the location of 2013 measured sections with respect to the surface extent of Canol Formation (after Gordey and Makepeace, 2003), Yukon oil and gas exploration regions, and oil and gas exploration wells.*

Formation (Jackson and Lenz, 1962), a thick succession of graptolitic shale and argillaceous limestone. Post-Richardson trough deposits comprise the Middle-Upper Devonian Canol Formation basinal shale and chert, together with an overlying wedge of Upper Devonian–Mississippian, marine, siliciclastic strata of the Imperial, Tuttle, and Ford Lake Shale formations. Provenance for this succession was from a northern orogenic source area (Ellesmerian orogeny; Pugh 1983; Lane, 2007). The trough was inverted into a faulted, north-plunging anticlinorium by the reactivation of Paleozoic faults in Late Cretaceous and Tertiary time (Norris, D.K., 1997), resulting in the mountain range observed today.

THE CANOL FORMATION

TYPE SECTION

The Canol Formation was proposed by Bassett (1961) for black shale on the northeast flank of the Mackenzie Mountains in NWT that overlies either the Middle Devonian Ramparts or Hare Indian formations. The type section for the Canol Formation is at Powell Creek, NWT (65° 16′30″N; 128°46′30″W), where it comprises 23 m of grey to black, soft to hard, non-calcareous shale that is covered with a green and yellow weathering residue. The formation was named after Camp Canol, an abandoned military camp located on the shore of the Mackenzie River across from Norman Wells, which served as a supply camp for the construction of the Canol Road during World War II.

DISTRIBUTION AND THICKNESS

From the type section in NWT, the Canol Formation shale has been traced west-northwestwardly along the Mackenzie Mountain front to the Snake River area, along both flanks of the Richardson Mountains and westwardly along the northern Ogilvie Mountains to the Alaska border (Norris, A.W., 1997; Norris, 1981a,b; 1982a,b,c,d,e,f).

The Canol Formation has previously been mapped at surface in Yukon on NTS mapsheets 116 F, G, H, I, J, and 106 E, F, and L (Fig. 1); however, reconnaissance helicopter surveys as part of this study have determined that Canol surface exposures are rare. In the subsurface, Canol Formation strata were intersected in oil and gas exploration wells in and near Eagle Plain Basin, Peel Plateau and Plain, and northeast of Kandik Basin (Fraser and Hogue, 2007; Fig. 1). Subsurface interpretation of Yukon well logs suggests Canol strata range between 6 and 79 m thick in the Peel Plateau and Plain, and between 4 and 79 m thick in the subsurface of Eagle Plain. Canol Formation shale is inferred to be 271 m thick in one well northeast of Kandik Basin (Fraser and Hogue, 2007).

STRATIGRAPHY

In Yukon, the Canol Formation overlies either Middle Devonian carbonate of the Ogilvie and Hume formations (Norris, 1967; Norris, 1982a,b), or in the Richardson Mountains, by Road River Group limestone and shale (Cecile *et al.*, 1982; Morrow, 1999; Norris, 1982e; Fig. 2). The basal contact of the Canol Formation has been described as unconformable/disconformable (*e.g.*, Norris, 1985; Kunst, 1973; Bassett and Stout, 1967; Norris, 1968) or conformable (*e.g.*, Williams, 1983; Morrow, 1999). In Richardson Mountains, the contact between the Road River Group and Canol Formation is marked by metre-scale ironstone concretions and Ni-Zn-PGE mineralization called the "Nick" zone (Hulbert *et al.*, 1992). In north Yukon, Canol Formation is conformably overlain by clastic strata including the Imperial, Ford Lake Shale, and Nation River formations (Pugh, 1983; Churkin and Brabb, 1965; Norris, 1982a,b).

CORRELATIVE AND COEVAL STRATA

In Mackenzie Plains region, NWT, the Canol Formation is the uppermost formation of the Horn River Group, which also includes the older Ramparts Formation (Kee Scarp member) and the Hare Indian Formation with its basal Bluefish Member (Pugh, 1983). West of Richardson trough, the Canol Formation may be equivalent to, or form a part of, the 'unnamed shale unit' of Norris (1968) and the upper part of the McCann Hill Chert (Churkin and Brabb, 1965; Clough and Blodgett, 1984) of east-central Alaska (Fig. 2). The 'unnamed shale unit' does not appear on geological maps of north Yukon; it is mapped as Canol Formation, suggesting the term is no longer in use.

Coeval shale strata occur on Banks Island (Nanuk and Ibbett Bay Formations; Miall, 1976), in Selwyn Basin in central Yukon (Earn Group *e.g.*, Portrait Lake Formation (Gordey and Anderson, 1993) and Misfortune Formation (Cecile, 2000), Liard Basin (Besa River Formation; Pigage, 2009), and Horn River Basin, northeastern British Columbia (Muskwa Member, Horn River Formation; Pugh, 1983; Fig. 2).

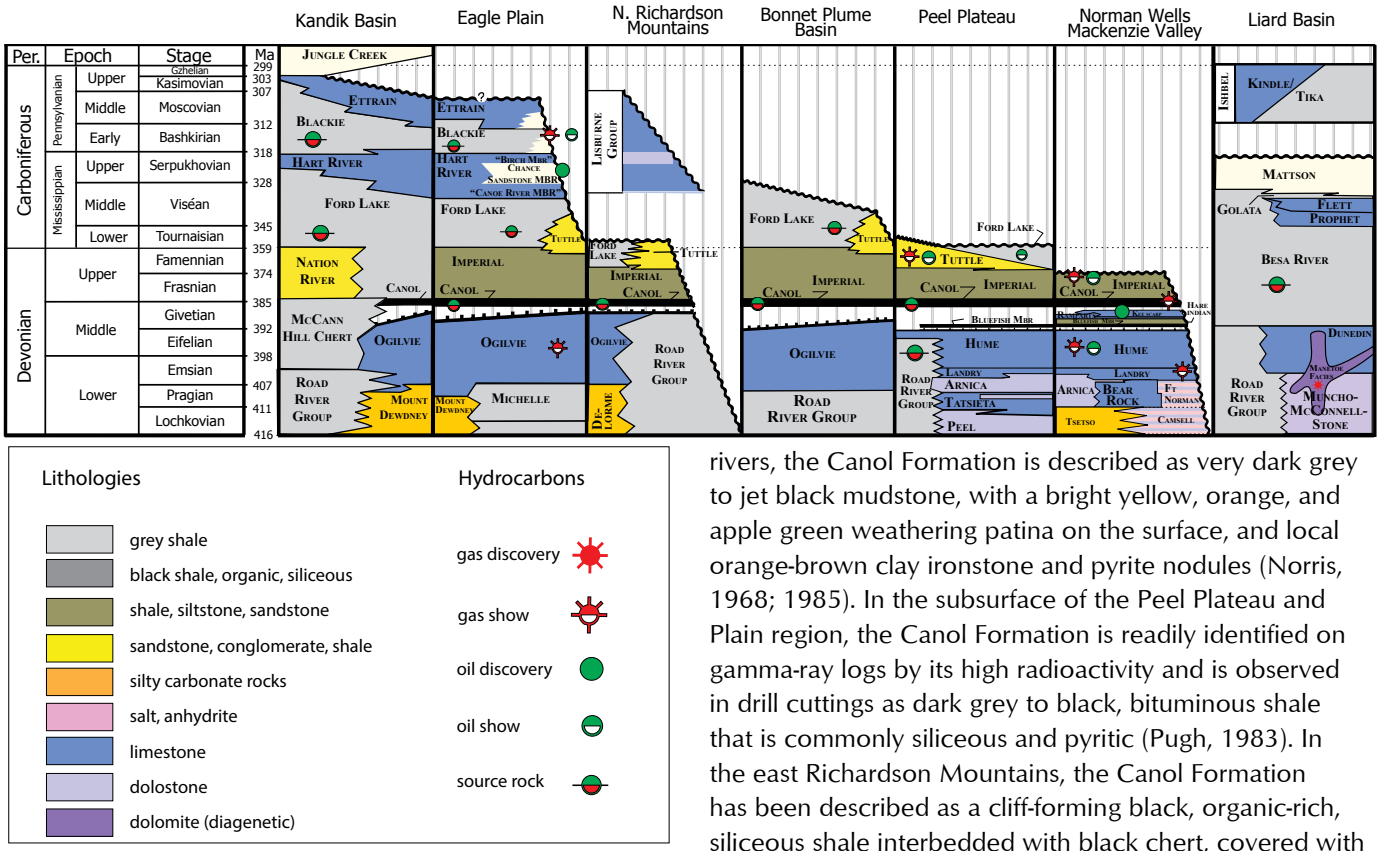

Figure 2. *Devonian-Carboniferous strata in northern Yukon, Mackenzie Plain, and Liard Basin. Modified from Pigage (2009) and Morrow et al. (2006).*

AGE

Fossils are rare in the Canol Formation; however, conodont, ostracod, and/or palynomorph identifications suggest that the Canol Formation is Middle–Upper Devonian in age (Givetian, Norris, 1985; late(?) Givetian to early Frasnian, Gal *et al.*, 2009). Palynomorphs collected from the Trail River section in Yukon described in this paper provide late Givetian or early Frasnian dates (Norris, 1985).

LITHOLOGY AND DEPOSITIONAL ENVIRONMENT

Near the type section in NWT, the Canol Formation is described as dark grey to black, soft to very hard, non-calcareous black shale and mudstone that weathers greenish, yellowish, and rusty brown (Bassett, 1961). It is organic-rich, siliceous, and may contain chert, mudstone with carbonate concretions, calcisiltite, and crinoidal grainstones (Muir and Dixon, 1984). Further west along the Mackenzie Mountains, between Arctic Red and Snake rivers, the Canol Formation is described as very dark grey to jet black mudstone, with a bright yellow, orange, and apple green weathering patina on the surface, and local orange-brown clay ironstone and pyrite nodules (Norris, 1968; 1985). In the subsurface of the Peel Plateau and Plain region, the Canol Formation is readily identified on gamma-ray logs by its high radioactivity and is observed in drill cuttings as dark grey to black, bituminous shale that is commonly siliceous and pyritic (Pugh, 1983). In the east Richardson Mountains, the Canol Formation has been described as a cliff-forming black, organic-rich, siliceous shale interbedded with black chert, covered with a distinctive apple-green to yellow patina (Allen and Fraser, 2008). The measured section described in this paper will expand on this definition.

The correlative 'unnamed shale unit' in the northern Ogilvie Mountains west of the Blackstone River (delineated as Canol Formation on bedrock geology maps) is described as a recessive unit comprising a variety of types of shale that overlie the Ogilvie Formation (Norris, 1967; 1968). Near the Blackstone and Hart rivers, it is a black, fissile, non-calcareous shale that may be burnt to a brick red or pink color. In Nahoni Range, southwest of Eagle Plain, it is a hard, highly fissile siliceous shale interbedded with soft, black shale which weathers to bluish grey or silvery grey. West of Miner River, the unit is composed of black, hard, non-calcareous, and, in part, silty and ferruginous shale, including minor interbeds of sandstone. Outcrops near the Yukon-Alaska border consist of medium brownish-grey shale in part burnt to a brick red colour.

Studies of organic matter carbon isotopes ($\delta^{13}C$), total organic content, and iron content in pyrite in Canol Formation shale in the Mackenzie Mountains, NWT, suggest that the sediments were deposited in anoxic, low energy conditions that persisted over relatively long, uninterrupted periods (Al-Aasm *et al.*, 1996).

HYDROCARBON POTENTIAL

The Canol Formation has been proven to be the source of oil for the Kee Scarp Formation reservoir in Norman Wells, NWT (Snowdon *et al.*, 1987). It has also been identified as a potential source rock in northern Yukon and northwestern Northwest Territories, with variable thermal maturity (*e.g.*, Pugh, 1983; Snowdon *et al.*, 1987; Link *et al.*, 1989; Gal *et al.*, 2009; Fraser *et al.* 2012).

Current exploration in the central Mackenzie Valley, NWT (Shell Canada Limited, MGM Energy Corporation, Husky Energy Incorporated, Imperial Oil Limited, and ConocoPhillips Canada Resources Corporation) is focussed on unconventional oil targets in the Canol Formation and the Middle Devonian Bluefish Member of the Hare Indian Formation. Since 2011, the play has resulted in work proposal bids totalling $645 million (Aboriginal Affairs and Northern Development Canada, 2013). Results from one well (East MacKay I-78) have been released: 140 barrels of fluid consisting of a mixture of frack fluid and formation hydrocarbons consisting of light, sweet crude and natural gas (Campbell, 2013).

TRAIL RIVER FIELD STUDIES 2013

A near-complete section of Canol Formation is exposed on the north side of Trail River, eastern Richardson Mountains (Fig. 3). This outcrop was measured over a five-day period in June, 2013. Access to the outcrop was by helicopter contracted from Dawson City via Eagle Plains Hotel. Flight distance to the outcrop from the hotel is approximately 55 km east.

Figure 3. *Aerial view of the near-complete exposure of Canol Formation on Trail River, east Richardson Mountains. The stratigraphic thickness of the Canol formation at this locality is 229 m. View is towards the northeast.*

At the Trail River location, the Canol Formation is 229.3 m thick and forms resistant, steep exposures and canyons. Strata generally strike north (000°) and dip 35-50° east. The basal contact with strata of the Road River Group is exposed (UTM 477805E; 7366765N) and the upper contact with the Imperial Formation underlies a ~2 metre covered interval (UTM 478181E; 7366563N). This section is the most complete Canol Formation section observed during reconnaissance studies in the region over the past eight years and thus presented a good opportunity for detailed sampling and description.

Four geologists measured, described, and sampled 261 m of section, including the underlying upper Road River Group (19.7 m), Canol Formation (229.3 m) and overlying Imperial Formation (12.0 m). Detailed lithological descriptions were made of the section and spectral gamma-radiation counts (SGR) of uranium, thorium, and potassium were measured with a handheld spectrometer at one-metre intervals. Shale/chert chip samples were collected through two-metre intervals for Rock-Eval/total organic carbon (RE/TOC) and inductively coupled plasma-emission/mass spectroscopy lithogeochemistry (ICP-ES/MS). Targeted samples for microfossil biostratigraphy (conodonts, radiolarians, pollen) and vitrinite reflectance (VR) were collected near formation contacts. All rock types were sampled for XRD mineralogy.

FIELD OBSERVATIONS

Presented here are the lithological descriptions and spectral gamma ray data from the Canol Formation outcrop on Trail River. Figure 4 displays a lithological log of the section, with sample locations indicated, and corresponding potassium, uranium, and thorium elemental concentrations and total API (derived using Schlumberger equation in Rider, 1996).

ROAD RIVER GROUP

The upper 19.7 m of the Road River Group observed at Trail River consists of recessive calcareous shale and mudstone, with ~10% resistant beds of bioclastic packstone (Fig. 5). Calcareous shale and mudstone are dark grey on fresh surfaces, weather grayish brown to brownish grey, are laminated, and occur in beds ~2–10 cm thick (Fig. 6). Fine-grained pyrite, both disseminated and laminated, is present. Bioclastic packstone beds are medium grey on fresh surfaces and weather medium to light grey, yellowish grey, and white (Fig. 7). Beds are up to 28 cm thick and have scoured lower and sharp upper contacts. Fossil debris includes crinoids, brachiopods, and

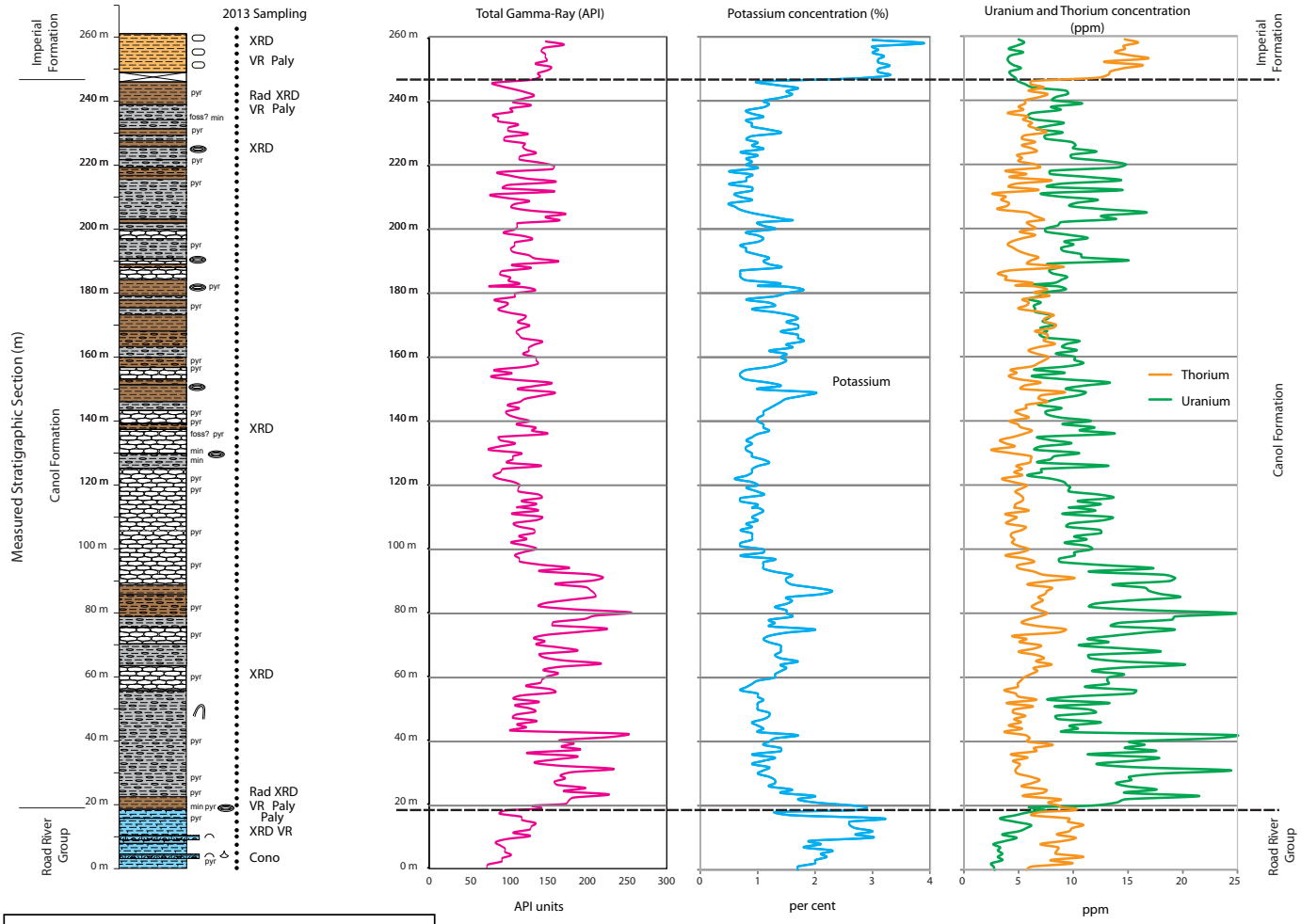

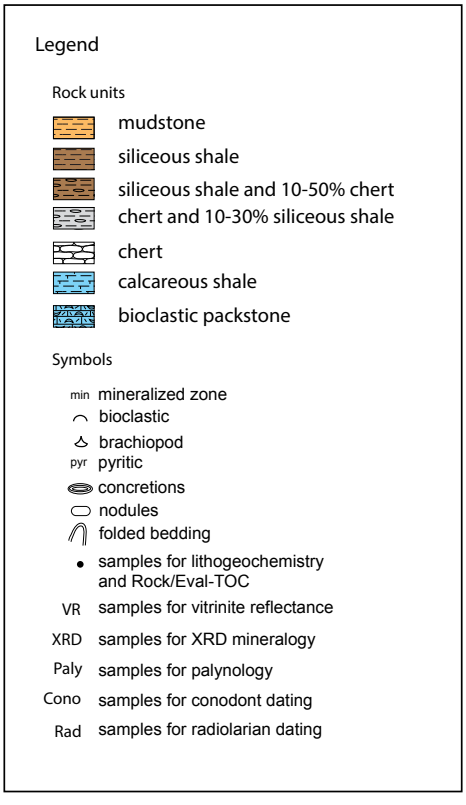

Figure 4. *Measured stratigraphic section and field-collected spectral gamma radiation logs of the Canol Formation on Trail River. Gamma-ray data were collected at one-metre intervals.*

Figure 5. *Upper 15 m of the Road River Group on Trail River. Strata of the Road River Group at this location consist of recessive calcareous shale and mudstone with minor resistant beds of bioclastic packstone. These resistant beds can be seen as continuous light grey horizons in the photograph. Orange flagging is placed at one-metre stratigraphic thicknesses.*

unidentified bivalves. Rare pyrite occurs as fine-grained disseminations or in fossil replacements. A ~10 cm thick channel-form bed made up of chert rip-up clasts in a limestone matrix was also observed (Fig. 8).

The uppermost Road River Group is characterized by concretions and highly weathered and mineralized shale/mudstone. A resistant, continuous, bed of concretions up to 30 cm thick occurs 2-3 m below the contact (Fig. 9). Concretions in this bed are light grey on fresh surfaces and weather beige, yellow, or powdery white. They are microcrystalline, slightly calcareous, and very dense, suggesting the presence of dolomite or barite. An iron-stained, highly weathered, elongate mudstone concretion at least 4.5 m long and up to 1 m thick was observed 1-2 m below the contact. The concretionary horizon is reminiscent of the "limestone ball" member immediately below the Ni-Zn-PGE mineralization identified at the Nick Property, approximately 190 km south of the Trail River location (Hulbert *et al.*, 1992). Geochemical samples to evaluate this correlation are currently being analysed.

The contact with the Canol Formation was placed at the first competent, bedded, siliceous shale bed above mineralized, weathered, recessive mudstone (Fig. 9). However, it has been suggested that the onset of Canol sedimentation may have occurred at the top of the last concretionary bed, immediately below the mineralized zone, approximately 1 m below the current placement (Rob Carnes, pers. comm). The placement of this contact will be reviewed when geochemical data are available.

Figure 6. *Calcareous shale/mudstone of the upper Road River Group. These rocks are laminated and occur in beds ~2–10 cm thick.*

Figure 7. *Bioclastic packstone of the upper Road River Group. These beds are commonly 5–10 cm thick, but were observed up to 28 cm thick.*

Figure 8. *Individual bed of chert rip-up clasts fining up to laminated limestone in the upper Road River Group.*

Figure 9. *Siliceous shale of the Canol Formation (right) overlying calcareous shale of the upper Road River Group. Note the large, rusty-colored ironstone concretion immediately to the right of the geologist (circled).*

CANOL FORMATION

Lithology

Overall, the Canol Formation is a resistant, silica-rich unit that is characterized by rhythmically bedded siliceous shale and chert (Fig. 10). Fifty-three separate lithological units were described in the field, based on the relative proportion of each of the rock types and changes in bedding thicknesses. These units were then grouped into the following lithofacies: siliceous shale; chert; siliceous shale (>50%) and chert (10-50%); and chert (>70%) and siliceous shale (10-30%).

Siliceous shale is black on fresh surfaces and weathers dark grey to black and olive grey, often with a distinctive pale and dark yellowish orange, dark red, light yellow, yellowish grey and/or very minor apple-green weathering residue (Fig. 11). A distinguishing characteristic about this lithofacies is the fissility of the shale that cleaves into wafers, sheets, or plates, depending on lamination/bed thickness (Fig. 12). Walking on the scree beneath an exposure of siliceous shale is akin to walking on broken glass, attesting to the high silica content of this formation. Bedding is planar and contacts are sharp. Two variants of this lithofacies are: 1) thin to medium bedded units, up to 10 cm thick, which require a hammer to break; and 2) recessive, finely laminated units, composed of beds up to 3 cm thick that are softer and easy to break by hand, and locally weathering to a soft clay-consistency. The siliceous shale lithofacies may include up to 10% chert beds.

Chert is black on fresh surfaces and weathers dark/medium grey to black, olive brown, light brown, and may have a distinctive pale and dark yellowish orange, dark red, and/or very minor apple-green weathering residue. Unlike the fissility of the shale, the chert exhibits conchoidal fracture and is very difficult to break with a hammer (Fig. 13). The chert weathers to irregular blocks.

Figure 10. *Typical outcrop of the Canol Formation on Trail River, showing consistent, rhythmic bedding of chert and siliceous shale.*

Figure 11. *Typical weathering colors of the Canol Formation on Trail River.*

Figure 12. *Fissile siliceous shale of the Canol Formation, 5.3 m above the basal contact (25 m stratigraphic level).*

Figure 13. *Conchoidally fractured chert of the Canol Formation, 90.3 m above the basal contact (110 m stratigraphic level).*

Laminations (mm-scale) can be observed on weathered surfaces; however, the rocks do not split along these surfaces, but will separate along certain bedding planes. Bed thicknesses are commonly 1–10 cm, but may be as thick as 16 cm. This unit may include up to 10% siliceous shale partings in intervals <5 cm thick.

Two additional lithofacies were identified in intervals where chert and siliceous shale were interbedded (Fig. 14). *Siliceous shale and chert* is characterized by ≥50% siliceous shale interbedded with 10-50% chert. Shale is more dominant overall and is more recessive than the chert-dominated lithofacies. *Chert and siliceous shale* is characterized by a ≥70% chert beds interbedded with 10-30% siliceous shale. For this lithofacies, the shale generally forms thinner partings between thicker chert beds.

In addition to stratigraphic variations in lithology, it can also vary along strike. For example, it is commonly observed that chert grades laterally into siliceous shale and vice versa. As well, the difference between chert and siliceous shale is sometimes difficult to determine in the field, as there were some beds that exhibited both conchoidal fracture and some fissility. Further refinement of what constitutes chert and siliceous shale and gradations thereof in the Canol Formation will be addressed in a future publication.

Concretions

Concretions (or nodules) of various sizes occur locally in the measured section. The term concretion is used in this study as many of these features were inaccessible, and as such it was difficult to determine with certainly whether they formed around an obvious nucleus. At 130 m and 151 m stratigraphic levels (Fig. 4), flat and elongate, orange and yellow-weathered concretions up to 2 m long and up to 0.15 m wide occur in continuous discrete iron-rich horizons.

More notable are the large concretions at 182 m, 190 m, and 227 m stratigraphic levels (Fig. 4). At 182 m, several non-calcareous mudstone concretions measuring 2.5 m-long and 0.75 m-wide occur in a discrete horizon. One located at river level is flat and elongate, internally planar laminated, dark grey on fresh surfaces, and weathers dark grey and reddish brown with a white chalky residue. This concretion occurs within beds of thin, fissile shale that appear to have been deformed by its growth, or compaction around it (Fig. 15). This is the only large concretion that was accessible for sampling and will be submitted for XRD mineralogy.

Isolated concretions occur at 190 m (1.5 m long and 0.90 m wide) and at 227 m stratigraphic levels (1.5 m long and 0.90 m wide; Fig. 4). These concretions have flat bases and appear mound-like (Fig. 16). These concretions were inaccessible for sampling or close inspection, but they weather reddish brown (190 m) or light grey (227 m) with a white chalky residue and appear to be composed of mudstone. Overlying strata are either deformed around these features due to compaction, or may be draped around what may have been a positive feature on the seafloor. The flat bases of these concretions suggest that they may have formed during deposition of the shale/chert, rather than post-deposition.

Figure 14. *Interbedded chert and siliceous shale of the Canol Formation, 20.7 m above the basal contact (40 m stratigraphic level).*

Figure 15. *Mudstone concretion in Canol Formation, 162.3 m above the basal contact (182 m stratigraphic level). The concretion is 2.5 m long, 0.75 m wide, and has planar laminations. Note the white chalky residue on the weathering surface.*

Fossils

With two possible exceptions, no macrofossils or trace fossils were observed in the Canol Formation at this section. At ~134 m and 236 m stratigraphic levels (Fig. 4), bedding surfaces were marked with small, semi-rounded, positive features <1 cm long that could be biological remnants (Fig. 17); however, they may also be interpreted as mineral casts.

Pyrite

Fine-grained pyrite is common in the Canol Formation and was found in the Trail River section concentrated along bedding planes or disseminated within shale. Coarse-grained pyrite was observed in a 35 cm long and 3 cm wide pyrite nodule (concretion?) at the 25 m stratigraphic level (Fig. 18). Continuous or semi-continuous horizons of red weathering, iron-rich concretionary or nodular horizons (up to 20 cm thick) occur but they are not a common feature.

Figure 16. *Isolated concretion (or mound?) in the Canol Formation; 207.3 m above the basal contact (227 m stratigraphic level). Note the flat base and the thinning of bedding around the top of the feature, suggesting it may have been a positive feature on the seafloor, having formed during the deposition of the shale/chert, rather than being a post-depositional feature. Like other concretions in the section, it has a white chalky residue on the weathering surface.*

Structure

The entire section is relatively undeformed, except for an area of ~14 m thick at the 43-57 m stratigraphic horizon where beds are tightly folded and locally fractured. This structure could result in the thickening of the section by ~7 m.

IMPERIAL FORMATION

Twelve metres of the lower Imperial Formation was measured. The Canol-Imperial contact is covered at this section, but its location is estimated to within ~2 m. Imperial strata at this location comprise weathered mudstone with continuous iron-rich nodular horizons

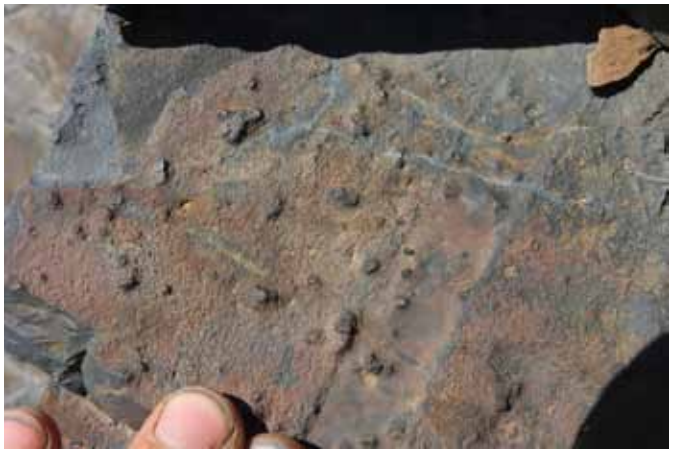

Figure 17. *Small, semi-rounded features on the bedding surface of Canol Formation siliceous shale at 236 m stratigraphic level (216.3 m above the basal contact). These may be biological remnants; alternatively, they may be casts of minerals.*

Figure 18. *Thirty-five cm-long pyrite concretion observed ~5 m above the basal contact of the Canol Formation, at the 25 m stratigraphic level. These concretions are rare in the section. Fine-grain disseminated or laminated pyrite is more common.*

(Fig. 19). The mudstone is dark grey on fresh surfaces, and weathers moderate brown, reddish brown, and minor yellowish brown. From a distance, the outcrop appears reddish brown or burgundy, which is diagnostic of the Imperial Formation in north Yukon. The mudstone is friable, weathering to small 1 cm angular shards (Fig. 20). Due to the degree of weathering, no sedimentary structures other than the continuous nodular horizons are apparent. Dense, microcrystalline and iron-rich nodules occur in continuous beds, 2-8 cm thick, every 2-50 cm throughout the unit; they are olive grey on fresh surfaces, weather reddish orange and smell sulphurous on fresh surfaces. In east Richardson Mountains, the nodules are comprised of 55% siderite (Allen *et al.*, 2011).

No macrofossils or trace fossils were observed in the Imperial Formation.

SPECTRAL GAMMA RADIATION (SGR)

Spectral gamma radiation data were collected using a Radiation Solutions RS-230 BGO gamma-ray spectrometer (Fig. 4). Potassium (K) was collected as a percentage (%), and uranium (U) and thorium (Th) as parts per million (ppm). The total gamma-ray, incorporating the gamma-radiation from U, Th, and K, is displayed as API units (American Petroleum Institute) which is the industry standard for the presentation of the gamma-ray curve and is useful for correlating to subsurface well logs (see next section). API was calculated using the following multiplier: 1ppm U = 8 API units; 1 ppm Th = 4 API units; and 1% K = 16 API units (Schlumberger NGT-A log in Rider, 1996).

A full analysis of the SGR data is not presented in this paper, but will be provided in future publications where geochemical and petroleum potential data can be incorporated for a more robust interpretation. General trends and statements about the relevance of the data are presented here.

GENERAL TRENDS

The total gamma-ray curve in Figure 4 shows that the upper Road River Group is less radioactive than the Canol and Imperial Formations, averaging 107 API. A marked increase in overall radioactivity appears at the Road River–Canol contact. The Canol Formation becomes less radioactive from the base to the top of the section. The most radioactive part of the exposure is the lower ~75 m of the Canol section, between the Canol-Road River contact and the 95 m stratigraphic level. A noticeable shift occurs at ~95 m, from an average of 165 API between 19.7 m and 95 m to an average of 115 API between 95 m and 247 m. The transition from the Canol to the Imperial formation results in a slight increase in average radioactivity to 145 API and the actual contact is marked by a sudden, sharp increase of over 50 API between the two formations.

URANIUM

The occurrence of uranium in sediments can result from chemical precipitation in acidic, reducing environments, by adsorption by organic matter or living plants and animals, or by chemical reactions in phosphate rich rocks (Rider, 1996). Because uranium is highly soluble, the most likely

Figure 19. *Typical exposure of Imperial Formation on Trail River. Here it consists of friable mudstone with continuous horizons of iron concretions spaced every 2–50 cm apart. The section has a reddish brown to burgundy weathering colour, distinctive of this formation in north Yukon.*

Figure 20. *Close-up of weathered mudstone and ironstone concretions of the Imperial Formation. Concretions in the Imperial Formation in west Richardson Mountains are comprised of 55% siderite.*

way it is incorporated into sediments is in association with organic matter, where loose bonds are formed between the uranyle ion ($U0_2$) and organic material. In hydrocarbon source rock studies, higher levels of uranium often correlate to higher levels of total organic content (TOC), and as a result, uranium concentration log curves are often used to predict the presence of potential source rock intervals from wireline data.

Uranium concentrations in the Road River Group and Imperial Formation are lower than in the Canol Formation, averaging 4.5 and 4.6 ppm respectively (Fig. 4). In the Canol Formation, uranium concentration decreases towards the top of the section from an average of 14.8 ppm between the lower contact and 95 m stratigraphic level, to an average of 9.4 ppm between 95 m and the upper contact. Notable are marked changes in uranium radiation at both the upper and lower contacts of the Canol Formation. Correlating organic content to uranium would suggest that the lower one-third of the Canol Formation is likely to contain the highest TOC values of the section and hence show the best source rock or shale gas prospectivity, with possibly slightly higher values between 190 m and 220 m stratigraphic levels. The Road River Group and the Imperial Formation are likely to be organically lean.

POTASSIUM AND THORIUM

Potassium readily forms chemical bonds and is common in rocks (Rider, 1996). It occurs variably in clay minerals and micas (*e.g.*, illite), feldspars, and in evaporites. The average shale has a potassium content of 2-3.5% (Rider, 1996 and references therein). Thorium is generally transported to sites of sediment deposition as clay fraction detrital grains and is chemically stable (Rider, 1996). Both potassium and thorium may be used as proxies for detrital clay influx.

Potassium concentration in the Road River Group and Imperial Formation are higher than in the Canol Formation, at 2.3% and 3.1% respectively (Fig. 4), falling within the average shale category. Potassium concentration in the Canol Formation varies from 0.5% to 2.0%, averaging 1.2%, which is lower than an average shale. Potassium concentrations in the Canol are cyclic, occurring in ~40–50 m thick cycles of either ~1% or 1.5% concentrations. Both upper and lower contacts of the Canol Formation are marked by strong shifts in potassium concentrations: a decrease from 3.2% in the Road River Group to 1.3% in the Canol at the lower contact, and an increase from 1.0% in the Canol to 2.7% in the Imperial at the upper contact.

Average thorium concentrations are highest in the Imperial Formation (14.5 ppm) followed by Road River Group (8.8 ppm), and the Canol Formation (5.8 ppm). There is a gradual decrease in thorium radiation from the Road River Group to the Canol Formation, and a marked increase from the Canol Formation to the Imperial Formation. Thorium levels within the Canol Formation are consistent, averaging 5.8 ppm, and do not show any significant trends.

Potassium and thorium concentration data suggest the Road River Group and Imperial Formations received more detrital input than the Canol Formation. There is evidence of very minor fluctuations in detrital input in the Canol Formation as shown in the potassium curve, but detrital input is interpreted as insignificant. This interpretation could also suggest that the silica and organic material in these sediments may be biogenic, sourced from local organisms, as opposed to detrital.

CORRELATION

The total gamma ray curve (API) is correlated to the closest well that penetrates the Canol Formation, Peel Y.T. H-71 (300G716630134300), drilled 35 km southeast of the outcrop section (Fig. 21). In older well logs, such as this one drilled in 1977, spectral gamma-radiation data is not available. The Canol section in the well is 79 m thick, compared with the outcrop section where it is 229 m thick. Despite the variation in thickness, the overall trend in gamma-radiation is comparable between the sections. The Road River Group shows the least radioactivity of all strata. At both locations, the Canol Formation is more radioactive in its lower part, although this accounts for two-thirds of the well section (between 1840 m and 1887 m below Kelly Bushing) and only one-third of the outcrop section (between 19.7 m and 95 m stratigraphic levels). The change from Canol to Imperial formation strata is marked at both locations by a sharp increase in gamma API.

SUMMARY AND FUTURE WORK

A near-complete stratigraphic section of Middle-Upper Devonian Canol Formation was measured on Trail River, east Richardson Mountains, in June, 2013. The section description is part of a larger study aimed at characterizing and correlating the Canol Formation within the Yukon, and assessing the formation's regional hydrocarbon potential, both as a source rock and an unconventional shale reservoir. The Canol Formation at this location

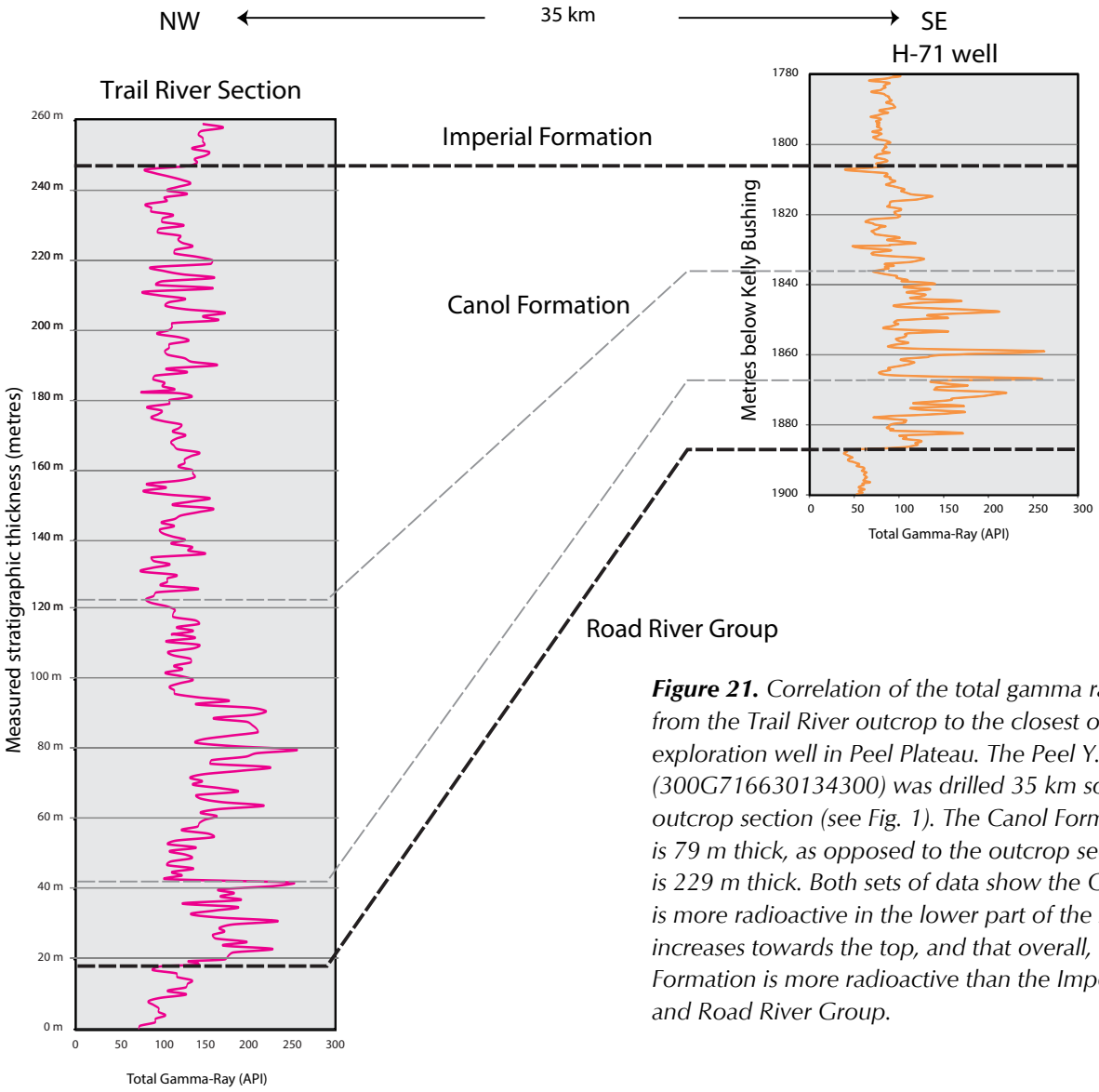

Figure 21. *Correlation of the total gamma ray curve (API) from the Trail River outcrop to the closest oil and gas exploration well in Peel Plateau. The Peel Y.T. H-71 well (300G716630134300) was drilled 35 km southeast of the outcrop section (see Fig. 1). The Canol Formation in the well is 79 m thick, as opposed to the outcrop section where it is 229 m thick. Both sets of data show the Canol Formation is more radioactive in the lower part of the section and increases towards the top, and that overall, the Canol Formation is more radioactive than the Imperial Formation and Road River Group.*

overlies the upper part of the Road River Group, and underlies the Devonian–Carboniferous Imperial Formation. In total, 261 m of section were measured and sampled for spectral gamma-radiation (U, K, Th), Rock-Eval/TOC, lithogeochemistry (ICP-ES/MS), XRD, VR, and microfossil biostratigraphy. A key part of this study is to collect data to assist in regional correlations in an attempt to differentiate shale packages in frontier areas. The spectral gamma-ray data collected in this study shows the effectiveness of this tool for surface to subsurface correlations.

This description of the Trail River section of the Canol Formation will be supplemented by lithogeochemical, RE/TOC, VR, XRD data and microfossil biostratigraphy. These data will provide further insight into questions about the Canol Formation, *e.g.*, the source of the silica in the shales and chert (biogenic or detrital); the formation's internal geochemical variability and its utility in correlating within and beyond the basin; the stratigraphic position of the "Nick" horizon and evaluating its extent in the Yukon; the extent, age, and variability of the Canol Formation throughout the Yukon; and ultimately, the hydrocarbon potential of Devonian shale, both as a source rock and a shale reservoir.

ACKNOWLEDGEMENTS

Tammy Allen, Patrick Sack, and Monica Nordling are acknowledged for field assistance. Bailey Staffen assisted with figures. Don Murphy and Matt Hutchison reviewed this manuscript, thanks! Discussions with YGS staff including Patrick Sack, Don Murphy, and Matt Hutchison are greatly appreciated. I am grateful to Trans North Helicopters for safe and competent flying this summer, and a special thanks to the staff at Eagle Plains Hotel for providing a variety of assistance with logistics.

REFERENCES

Aboriginal Affairs and Northern Development Canada, 2013. Central Mackenzie Valley Call. <*http://www.aadnc-aandc.gc.ca/eng/1100100036430/1100100036431*> [accessed December 15, 2013].

Al-Aasm, I.S., Morad, S., Durochyer, S., and Muir, I., 1996. C-S-Fe relationships and stable isotopic compositions in Devonian black mudrocks, Mackenzie Mountains, Northwest Territories, Canada. Sedimentary Geology, vol. 106, issues 3-4, p. 279-298.

Allen, T.L., Fraser, T.A., Lane, L.S., 2011. Preliminary results from a diamond drill hole study to assess shale gas potential of Devonian strata, Eagle Plain, Yukon. *In*: Yukon Exploration and Geology 2010, K.E. MacFarlane, L.H. Weston and C Relf (eds.), Yukon Geological Survey, p. 1-17.

Allen, T.L. and Fraser, T.A., 2008. Hydrocarbon potential of Upper Paleozoic strata, eastern Richardson Mountains, northern Mackenzie Mountains and Peel Plateau, Yukon. *In:* Yukon Exploration and Geology 2007, D.S. Emond, L.R. Blackburn, R.P. Hill, and L.H. Weston (eds.), Yukon Geological Survey, p. 91-114.

Bassett, H.G., 1961. Devonian stratigraphy, central Mackenzie River region, Northwest Territories, Canada. *In:* Geology of the Arctic, Raasch, G. (ed.), Alberta Society of Petroleum Geologists and University of Toronto Press, vol. 1, p. 481-498.

Bassett, H.G. and Stout, J.G., 1967. Devonian of Western Canada. *In:* International Symposium on the Devonian System, Calgary, 1967. Alberta Society of Petroleum Geologists, vol. 1, p. 717-752.

Campbell, D., 2013. Could the N.W.T's Canol shale be the next Bakken? Alberta Oil, <*http://www.albertaoilmagazine.com/2013/05/is-canol-shale-the-next-bakken/*> [accesssed December 6, 2013].

Cecile, M.P., 2000. Geology of the northeastern Niddery Lake map area, east-central Yukon and adjacent Nortwest Territories. Geological Survey of Canada, Bulletin 553, 120 p.

Cecile., M.P., Hutcheon, E.I., and Gardiner, D., 1982. Geology of the Northern Richardson Anticlinorium. Geological Survey of Canada, Open File 875, 1 map, 1:125 000.

Churkin, M. Jr., and Brabb, E.E., 1965. Ordovician, Silurian and Devonian biostratigraphy of east-central Alaska. Bulletin of the American Association of Petroleum Geologists, vol. 49, p. 172-185.

Clough, J.G. and Blodgett, R.G., 1984. Lower Devonian basin to shelf carbonates in outcrop from the western Ogilvie Mountains, Alaska and Yukon Territory. *In:* Carbonates in Subsurface and Outcrop, L. Eliuk (Chairperson), Canadian Society of Petroleum Geologists 1984 Core Conference, October 18-19, 1984, Calgary, Alberta, Canadian Society of Petroleum Geologists, p. 57-81.

Fraser, T.A., Allen, T.L., Lane, L.S., and Reyes, J.C., 2012. Shale gas potential of Devonian shale in north Yukon: Results from a diamond drillhole study in western Richardson Mountains. *In:* Yukon Exploration and Geology 2011, K.E. MacFarlane and P.J. Sack (eds.), Yukon Geological Survey, p. 45-74.

Fraser, T.A. and Hogue, B., 2007. List of wells and formation tops, Yukon Territory, version 1.0. Yukon Geological Survey, Open File 2007-05.

Gal, L.P., Pyle, L.J., Hadlari, T., and Allen, T.L., 2009. Chapter 6 – Lower to Upper Devonian Strata, Arnica-Landry Play, and Kee Scarp Play. *In:* Regional Geoscience Studies and Petroleum Potential, Peel Plateau and Plain, Northwest Territories and Yukon: Project Volume, L.J. Pyle and A.L. Jones (eds.), Northwest Territories Geoscience office, Open File 2009-02 and Yukon Geological Survey, Open File 2009-25, p. 187-289.

Gordey, S.P. and Anderson, R.G., 1993. Evolution of the northern Cordilleran miogeocline, Nahanni map area, Yukon and Northwest Territories. Geological Survey of Canada, Memoir 428, 214 p.

Gordey, S.P. and Makepeace, A.J. (comps.), 2003. Yukon digital geology, v. 2.0. Geological Survey of Canada, Open File D1749 and Yukon Geological Survey, Open File 2003-9(D), 2 CD-ROMs.

Hulbert, L.J., Gregoire, D.C., Paktunc, D., and Carnes, R.C., 1992. Sedimentary nickel, zinc, and platinum-group-element mineralization in Devonian black shales at the Nick Property, Yukon, Canada: a new deposit type. Exploration Mining Geology, vol. 1, p. 39-62.

Jackson, D.E. and Lenz, A.C., 1962. Zonation of Ordovician and Silurian graptolites of northern Yukon, Canada. American Association of Petroleum Geologists Bulletin, vol. 46, p. 30-45.

Jeletzky, J.A., 1962. Pre-Cretaceous Richardson Mountain trough: its place in the tectonic framework of Arctic Canada and its bearing on some geosynclinal concepts. Royal Society of Canada, Transactions, vol. LVI, Series III, Section III, p. 55-84.

Kunst, H., 1973. The Peel Plateau. *In:* The future petroleum provinces of Canada, R.G. McCrossan (ed.), Canadian Society of Petroleum Geologists, Memoir 1, p. 213-244.

Lane, L.S., 2007. Devonian-Carboniferous paleogeography and orogenesis, northern Yukon and adjacent Arctic Alaska. Canadian Journal of Earth Sciences, vol. 44, p. 679-694.

Lenz, A.C., 1972. Ordovician to Devonian history of northern Yukon and adjacent District of Mackenzie. Bulletin of Canadian Petroleum Geology, vol. 20, p. 321-361.

Link, C.M., Bustin, R.M., and Snowdon, L.R., 1989. Petroleum source potential and depositional setting of Phanerozoic strata in northern Yukon and northwestern district of Mackenzie. Bulletin of Canadian Petroleum Geology, vol., 37, p. 293-315.

Miall, A.D., 1976. Devonian geology of Banks Island, Arctic Canada, and its bearing on the tectonic development of the circum-Arctic region. Geological Society of America Bulletin, vol. 87, p. 1599-1608.

Morrow, D.W., 1999. Lower Paleozoic Stratigraphy of Northern Yukon Territory and Northwestern District of Mackenzie. Geological Survey of Canada, Bulletin 538, 202 p.

Muir, I. and Dixon, O.A., 1984. Facies analysis of a Middle Devonian sequence in the Mountain River-Gayna River. *In:* Contributions to the geology of the Northwest Territories, J.A. Brophy (ed.), vol. 1, p. 55-61.

Morrow, D.W., Jones, A.L., and Dixon, J., 2006. Infrastructure and resources of the northern Canadian mainland sedimentary basin. Geological Survey of Canada, Open File 5152, 59 p.

Norris, A.W., 1967. Devonian of northern Yukon Territory and adjacent District of Mackenzie. International Symposium on the Devonian System. Alberta Society of Petroleum Geologists, Calgary, Alberta, vol. 1, p. 753-780.

Norris, A.W., 1968. Reconnaissance Devonian stratigraphy of northern Yukon Territory and northwestern District of Mackenzie. Geological Survey of Canada, Paper 67-53, 287 p.

Norris, A.W., 1985. Stratigraphy of Devonian Outcrop Belts in Northern Yukon Territory and Northwestern District of Mackenzie (Operation Porcupine Area). Geological Survey of Canada, Memoir 410, 81 p.

Norris, A.W., 1997. Devonian. *In:* The Geology, Mineral and Hydrocarbon Potential of Northern Yukon Territory and Northwestern District of Mackenzie, D.K. Norris (ed.), Geological Survey of Canada, Bulletin 422, p. 163-200.

Norris, D.K., 1981a. Geology, Bell River, Yukon Territory-Northwest Territories. Geological Survey of Canada, "A" Series Map 1519A, 1981, 1 sheet, doi:10.4095/109696.

Norris, D.K., 1981b. Geology Eagle River, Yukon Territory. Geological Survey of Canada, "A" Series Map 1523A, 1981, 1 sheet, doi:10.4095/109352.

Norris, D.K., 1982a. Geology, Hart River, Yukon Territory. Geological Survey of Canada, "A" Series Map 1527A, 1982, 1 sheet, doi:10.4095/119039.

Norris, D.K., 1982b. Geology, Ogilvie River, Yukon Territory. Geological Survey of Canada, "A" Series Map 1526A, 1982, 1 sheet, doi:10.4095/119037.

Norris, D.K., 1982c. Geology, Porcupine River, Yukon Territory. Geological Survey of Canada, "A" Series Map 1522A, 1981, 1 sheet, doi:10.4095/119401.

Norris, D.K., 1982d. Geology, Snake River, Yukon-Northwest Territories. Geological Survey of Canada, "A" Series Map 1529A, 1982, 1 sheet, doi:10.4095/109233.

Norris, D.K., 1982e. Geology, Trail River, Yukon-Northwest Territories. Geological Survey of Canada, "A" Series Map 1524A, 1981, 1 sheet, doi:10.4095/119405.

Norris, D.K., 1982f. Geology, Wind River, Yukon Territory. Geological Survey of Canada, "A" Series Map 1528A, 1982, 1 sheet, doi:10.4095/119062.

Norris, D.K., 1997. Geological setting. *In:* The Geology, Mineral and Hydrocarbon Potential of Northern Yukon Territory and Northwestern District of Mackenzie, D.K. Norris (ed.), Geological Survey of Canada, Bulletin 422, p. 21-64.

Snowdon, L.R., Brooks, P.W., Williams, G.K., and Goodarzi, F., 1987. Coorelation of the Canol Formation source rock with oil from Norman Wells. Organic Geochemistry, vol. 11, p. 529-548.

Pigage, L.C., 2009. Yukon Table of Formations v3.2. Yukon Geological Survey and Oil and Gas Resources Branch, Government of Yukon, Canada.

Pugh, D.C., 1983. Pre-Mesozoic Geology in the Subsurface of Peel River Map Area, Yukon Territory and District of Mackenzie. Geological Survey of Canada, Memoir 401, 61 p.

Rider, M., 1996. The Geological Interpretation of Well Logs, second edition. Whittles Publishing, Roseleigh House, Latheronwheel, Caithness, Scotland, 280 p.

Williams, G.K., 1983. What does the term "Horn River Formation" mean? Bulletin of Canadian Petroleum Geology, vol. 31, p. 117-122.

Geology and jade prospects of the northern St. Cyr klippe (NTS 105F/6), Yukon

Sierra J. Isard[1] and Jane A. Gilotti
Department of Earth and Environmental Sciences, University of Iowa, Iowa City, Iowa, USA

Isard, S.J. and Gilotti, J.A., 2014. Geology and jade prospects of the northern St. Cyr klippe (NTS 105F/6), Yukon. *In:* Yukon Exploration and Geology 2013, K.E. MacFarlane, M.G. Nordling, and P.J. Sack (eds.), Yukon Geological Survey, p. 69-77.

ABSTRACT

Nephritic jade deposits have been found along faulted contacts between serpentinite and siliceous units at the King Arctic mine in southeastern Yukon. In the St. Cyr klippe near Quiet Lake south-central Yukon, serpentinite units of the Slide Mountain oceanic assemblage are thrust above phyllite units of the Cassiar terrane. This contact has the potential to contain jade deposits similar to the ones found at the King Arctic mine. However, bedrock mapping during the summer of 2013 failed to identify large jade deposits within the field area, but smaller jade deposits may have been overlooked. The absence of jade mineralization could be due to the lack of fluid migration through faults, but is more likely due to the low silica content of the phyllite.

[1] *sierra-isard@uiowa.edu*

INTRODUCTION

Jade deposits associated with suture zones have been found extending northward from the United States-Canada border, through British Columbia and into Yukon (Harlow and Sorensen, 2005). Jade refers to two different monomineralic rocks: nephrite and jadeitite. Jadeitite consists of pure jadeite, *i.e.*, the Na-pyroxene end member ($NaAlSi_2O_6$), while nephrite is the microcrystalline, amphibole (tremolite-actinolite) variety ($Ca_2(Mg, Fe)_5Si_8O_{22}(OH)_2$). Jade is most often used as gemstone for jewelry, sculpture, and ornamental stones. British Columbia accounts for three quarters the world's jade production. The world market for jade is estimated at 300 tonnes per year (Scott, 1996).

Nephritic jade throughout the Canadian Cordillera is associated with serpentinite in fault contact with metasedimentary or felsic igneous rocks (Simandl *et al.*, 2001). Nephrite deposits are uncommon in Yukon, but when present they are associated with Slide Mountain and Cache Creek ultramafic rocks. In southeast Yukon at the King Arctic mine (Fig. 1), nephrite occurs in layers up to 3 m thick along northwest-striking reverse faults that imbricate a serpentinite mélange of the Slide Mountain assemblage with basal chert conglomerate and sandstone of the Money Creek formation (Devine *et al.*, 2004). The serpentinite units have thicknesses ranging from <1 m to 150 m and are associated with talc-schist zones along the fault boundaries, which result from shearing and fluid flow. The faulted contacts are sealed by the jade mineralization indicating syn-faulting jade formation (Devine *et al.*, 2004). The suggested age of the D_4 faulting, based on regional tectonics, is Jurassic to Cretaceous, and is thought to be related to shortening of the Yukon–Tanana terrane (Murphy *et al.*, 2003).

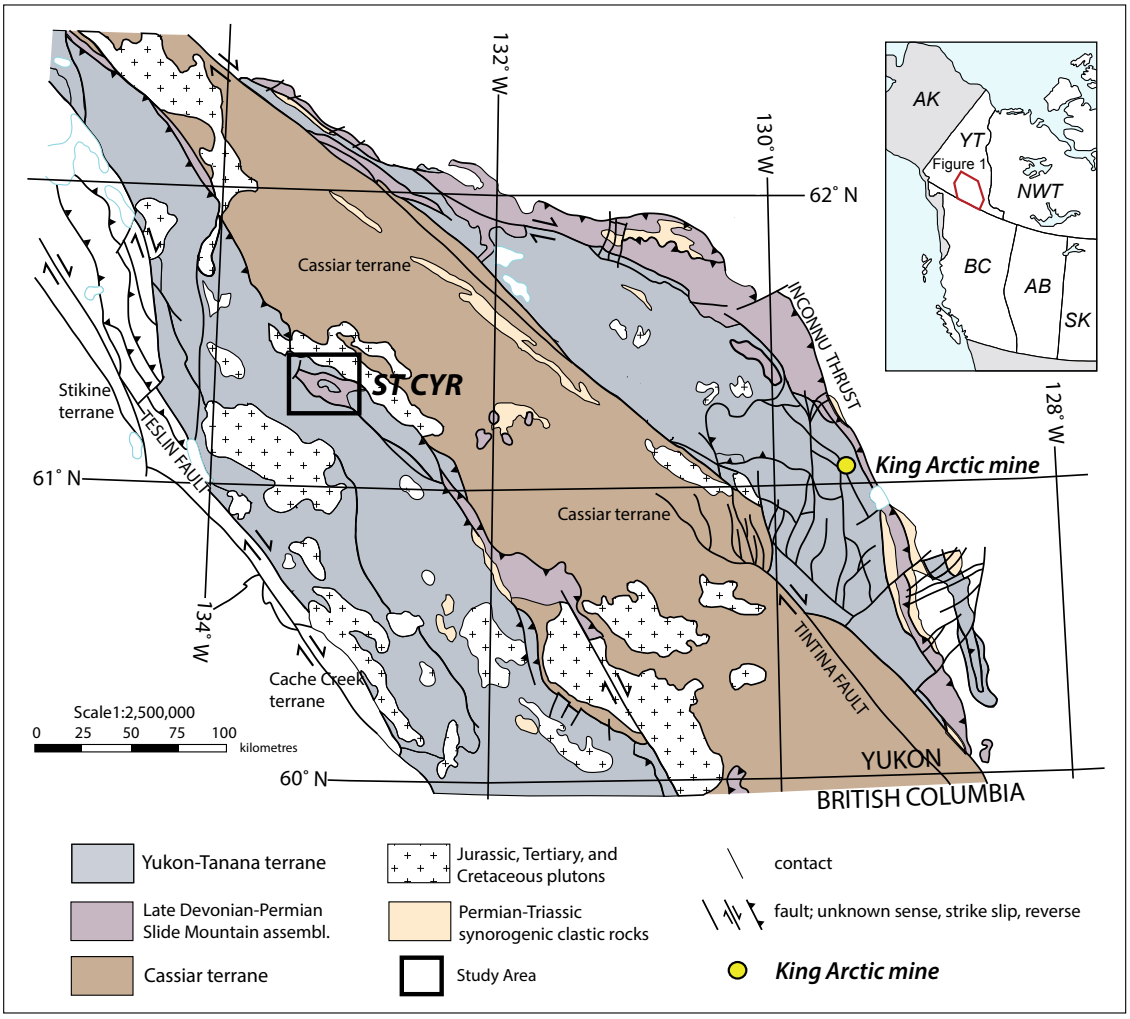

***Figure 1**. Simplified regional map of southeastern Yukon modified from Colpron et al., 2006. Study area is marked by a black box. King Arctic mine is marked by a yellow circle.*

In the northwest section of the St. Cyr klippe (Fig. 1), serpentinite units of the Slide Mountain assemblage are thrust above phyllite of the Cassiar terrane. These thrust contacts have the potential to host jade deposits similar to those found at the King Arctic mine. This contribution describes the lithology and structures of the northern part of the St. Cyr klippe, and the jade prospects of the area. Geological mapping at 1:20 000 and 1:50 000, conducted during the summer of 2013 in the southwest corner of NTS 105F/6, serves as the basis for this research.

REGIONAL SETTING

The Yukon-Tanana terrane (YTT), located in the northern Cordillera, is interpreted as a composite arc built on the rifted margin of North America that is associated with the opening of the Slide Mountain Ocean (SMO) during a Devonian, east-dipping subduction event (Murphy *et al.*, 2006; Nelson *et al.*, 2006). The YTT is composed of four main tectonic assemblages (Colpron *et al.*, 2006): Snowcap, Finlayson, Klinkit, and Klondike. The basal Snowcap assemblage contains Neoproterozoic to earliest Devonian sedimentary rocks derived from the Laurentian continental margin and forms the substrate of the Yukon-Tanana arc. The Finlayson assemblage is late Devonian-early Mississippian and represents a paired continental arc and extending back arc. The Klinkit units are attributed to a middle Mississippian to early Permian island arc assemblage. Lastly, the Klondike assemblage is middle to late Permian and represents continental arc material (Colpron *et al.*, 2006). Typically, the SMO assemblage occurs as a mixture of serpentinite, ultramafic rocks, gabbro, chert, and marble throughout the Canadian Cordillera (Mortensen, 1992b). Starting in the mid-Permian, the SMO was closed by west-dipping subduction beneath the YTT and by the early Triassic (Beranek *et al.*, 2011) the closure was complete. Shortening of the continental margin continued into the Jurassic resulting in the YTT and SMO occurring as thrust panels or klippen obducted onto North American strata, in this case the Cassiar terrane (Murphy *et al.*, 2006; Nelson *et al.*, 2006; Mortensen, 1992a&b). Re-accretion occurred in the Permo-Triassic as evidenced by the presence of YTT and SMO detrital zircons in Triassic units deposited on the continental margin (Beranek *et al.*, 2010). The Cassiar terrane represents a slice of the North American continental margin assemblage that is presently located southwest of the right-lateral, strike-slip Tintina fault (Fritz *et al.*, 1991). The Cassiar terrane generally contains siltstone, sandstone, shale, and limestone, and metamorphic equivalents of quartzite and muscovite-graphitic-quartz schist (Tempelman-Kluit, 2012).

ST. CYR KLIPPE

GEOLOGIC SETTING

The St. Cyr klippe is a 70-km long by 15-km wide, northwest-striking metamorphic unit that contains imbricated slices of YTT and SMO rocks. It lies in the region between the Tintina and Teslin faults (Fig. 1; Tempelman-Kluit, 2012). Previously all units in the St. Cyr klippe were mapped as the Slide Mountain oceanic terrane (Tempelman-Kluit, 1979; Erdmer, 1992; Fallas, 1999); however, to the southeast of the study area is an eclogite-bearing, quartzofeldspathic, high-pressure metamorphic unit. The eclogite occurs as lenses within coherent slices of quartzofeldpathic rocks with igneous and sedimentary protoliths that are part of the YTT arc (Gilotti *et al.*, 2013; Petrie *et al.*, 2012). To the northeast, rocks of the St. Cyr klippe are cut by the Cretaceous Nisutlin batholith.

Our study area (Fig. 2) is located in the northwest part of the St. Cyr klippe and contains units of the Cassiar terrane, Tower Peak assemblage, and Slide Mountain assemblage. The Tower Peak assemblage, described by Fallas (1999) as a greenschist-facies metavolcanic unit, has no age or provenance constraints. Results from sampling in the spring of 2014, including U/Pb geochronology, bulk rock, and trace element geochemistry will provide these constraints as part of Isard's MS thesis. The Slide Mountain assemblage occurs as a mafic-ultramafic unit with a MORB-like protolith that is related to the late Devonian to early Triassic SMO (Fallas, 1999; Gabrielse *et al.*, 1993; Mortensen, 1992a,b).

The Tower Peak assemblage is emplaced over the Slide Mountain assemblage, which in turn overlies the phyllite units of the Cassiar terrane forming a composite klippe. Both thrust faults are dipping shallowly to the south. A post-thrusting syncline is present that folds phyllite units of the Cassiar terrane, the Tower Peak assemblage, and Slide Mountain terrane.

LITHOLOGIC DESCRIPTIONS

The best prospect for jade mineralization is at the base of the klippe, provided the right rock types (*i.e.*, serpentinite and silica-rich rocks) are in contact. Therefore, units of the Cassiar terrane in the footwall of the St. Cyr klippe, and the Tower Peak and Slide Mountain Ocean slices in the klippe itself are described below.

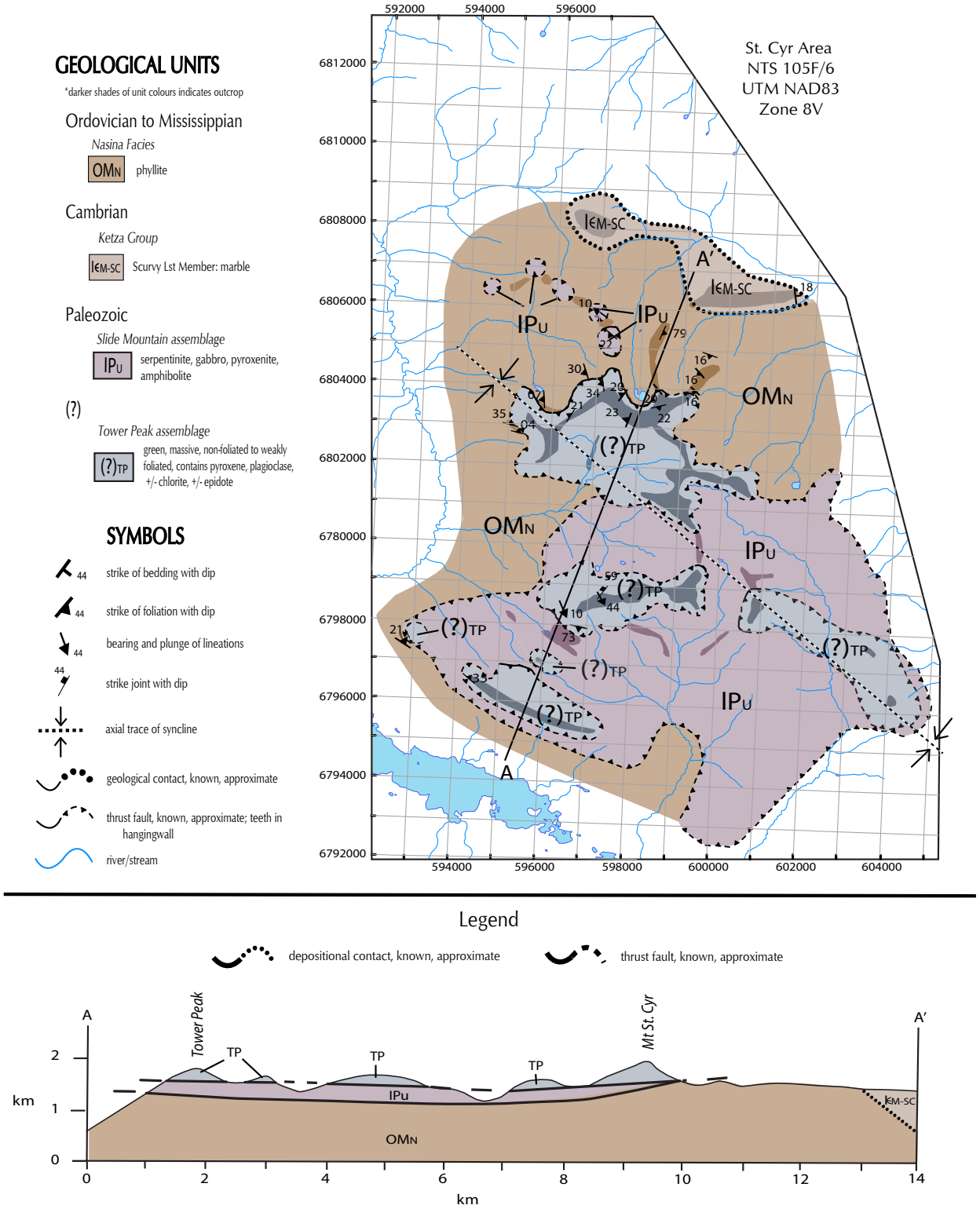

Figure 2. *Geological map of the NW St. Cyr klippe with cross section A-A′.*

Cassiar terrane

The Cassiar units in the St. Cyr area (Fig. 2) include phyllite and a panel of marble. The Cassiar terrane here is dominated by black to dark green, fine-grained phyllite consisting of quartz + biotite + muscovite ± chlorite (Fig. 3a). A >300 m-thick marble unit (Fig. 3b), correlating with the Scurvy limestone member of the Ketza group (Tempelman-Kluit, 2012), is exposed in the northern section of the map area. The marble is coarse-grained with ~0.5 to 5.0 cm thick alternating dark and light grey layers dipping 18° east. This unit is structurally higher than the phyllite, and the contact between the units dips approximately 45° to the east.

Tower Peak unit

The Tower Peak assemblage is grey to green, very fine to medium grained, and weakly foliated to massive (Fig. 3c). Cataclasite-ultracataclasite rocks containing secondary quartz and calcite veins occur adjacent to the fault zones (Fig. 3e). Many of these rocks have angular clasts within a very fine-grained groundmass; there is no evidence of rotation to determine fault movement. There are local occurrences of incohesive fault gouge at contacts with the Cassiar terrane. The Tower Peak rocks are mainly composed of feldspar and pyroxene (Fig. 3d). Epidote and chlorite are present as secondary metamorphic minerals while quartz and calcite are most likely derived from secondary fluids associated with brittle deformation. The occurrence of epidote and chlorite suggest greenschist facies or lower P-T conditions. Many of the feldspar grains are interlocking suggesting an igneous protolith, most likely a diabase or gabbro. The mafic mineralogy and igneous protolith suggests the Tower Peak assemblage may be part of the oceanic Slide Mountain assemblage. Prominent joints dip steeply to moderately northwest, while a weak, local foliation dips gently southwest.

Slide Mountain terrane

The Slide Mountain rocks are serpentinite, pyroxenite, and gabbro with rare amphibolite. Generally, the serpentinite is black to green, fine grained, massive, fibrous, and glassy (Fig. 4a,b). Powder XRD analysis using a D8 Advance Bruker instrument at the Department of Chemistry, University of Iowa indicates that lizardite is the serpentinite mineral. A unit of brecciated serpentinite, 2 to 3 m thick, weathering tan, and containing large, angular clasts approximately 1to 40 cm with a fine grained, fibrous serpentinite matrix (Fig. 4c), lies in the eastern part of the map area. In the same area, massive, tan-weathering ultramafic lenses occur within serpentinite that is approximately 3-5 m thick (Fig. 4d). The gabbro is black with undeformed plagioclase crystals, fine to coarse grained, and foliated to massive. Calcite veins commonly cut the serpentinite and gabbro. The veins are typically 1to 4 cm thick (Fig. 4e,f). A rare metagabbro (amphibolite) outcrops in one location. The amphibolite is black, coarse grained, massive, and approximately 1 to 2 m thick. Orange-weathering, serpentinized pyroxenite, with pseudomorphs after chromite, is massive to foliated. These ultramafic rocks are intercalated with the serpentinite and gabbro on a one meter to tens of meters scale.

JADE POTENTIAL

Jadeitite typically occurs in high pressure–low temperature metamorphic terranes, while nephrite occurs at greenschist-facies or lower conditions. The rock units in the northwest part of the St. Cyr klippe reached greenschist facies, and therefore, only have the potential to host nephrite. Since lizardite is the main serpentine mineral, metamorphic temperatures were probably <300°C (Evans *et al.*, 2013). Nephritic jade is produced by either Ca-metasomatism in serpentinite at contacts with silica-rich rocks, or replacement of dolomite by silicic fluids (Harlow and Sorensen, 2005). Replacement of dolomite by silicic fluids is an unlikely mechanism at St. Cyr because it requires post-magmatic fluids to be channeled by fissures and faults through dolomite (Sekerina, 1992).

At the King Arctic mine, jade mineralization was controlled by reverse faults that imbricated serpentinite with the basal conglomerate and sandstone of the Money Creek formation and limestone of the White Lake formation, together with fluid migration synchronous with D_4 faulting (Devine *et al.*, 2004). In the northwest section of the St. Cyr klippe, nephrite could have formed along thrust contacts between phyllite in the footwall and serpentinite in the hanging wall. However, no large nephrite deposits were found during our mapping along the basal thrust of the St. Cyr klippe.

The apparent absence of jade in the St. Cyr klippe could be explained if no fluid migration occurred during emplacement of the serpentinite. The presence of numerous calcite veins within the serpentinite suggests fluid migration did occur; however, the secondary calcite veins may have formed at a later time. The more likely explanation for the lack of jade is that the phyllite does not have a high enough silica content to facilitate metasomatic exchange—unlike the silica-rich chert conglomerate at the King Arctic mine. Similarly, nephrite is unlikely to form at

fault contacts between the serpentinite and the Tower Peak units because the Tower Peak has a brecciated mafic protolith, probably consisting of basalt, diabase, and gabbro. Although large jade deposits were not found in this study, the possibility exists for smaller occurrences of nephritic jade in the St. Cyr area. Elsewhere in southern Yukon, nephrite deposits may exist where serpentinite units of the Slide Mountain assemblage are in fault contact with silica-rich units.

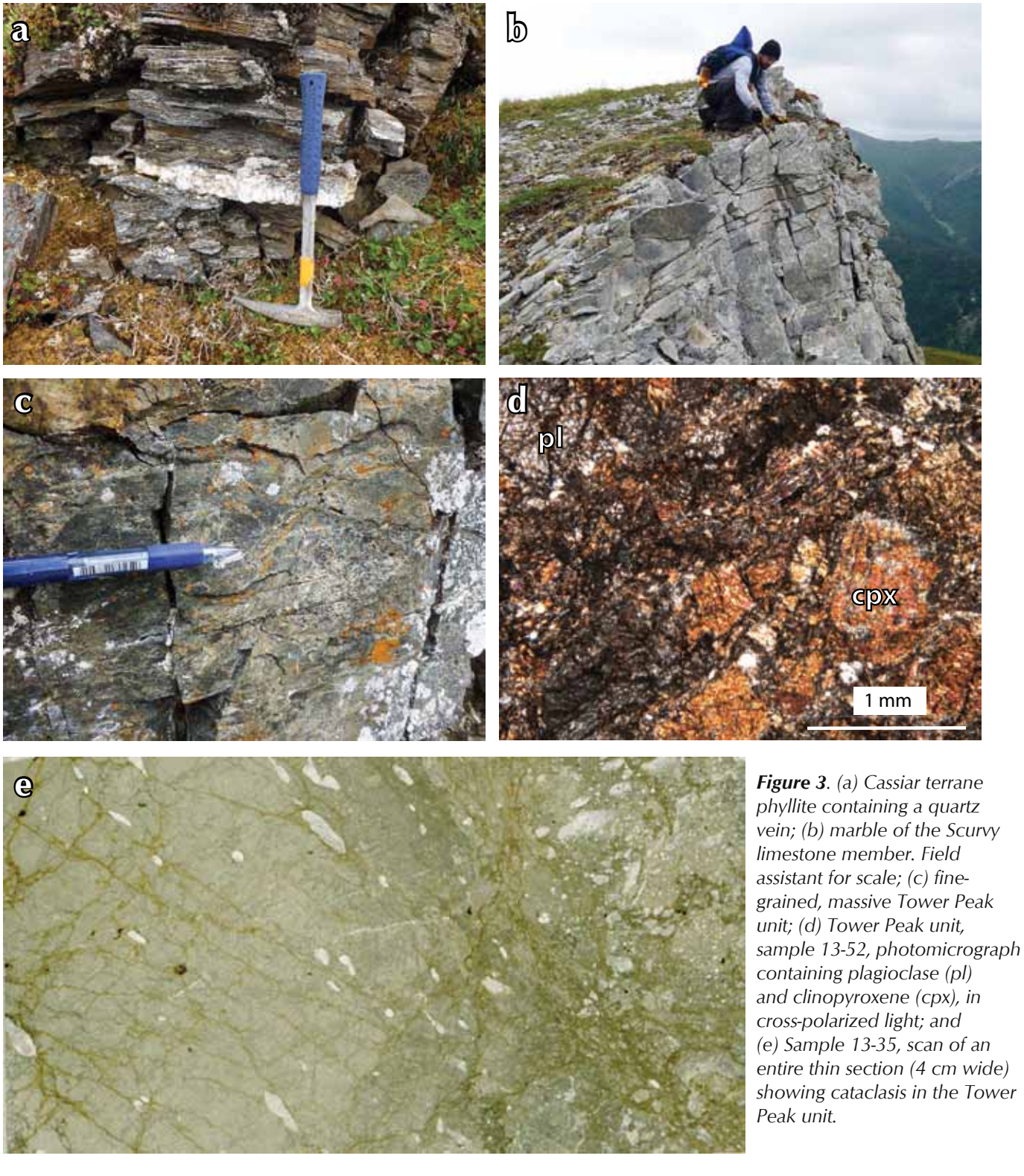

Figure 3. *(a) Cassiar terrane phyllite containing a quartz vein; (b) marble of the Scurvy limestone member. Field assistant for scale; (c) fine-grained, massive Tower Peak unit; (d) Tower Peak unit, sample 13-52, photomicrograph containing plagioclase (pl) and clinopyroxene (cpx), in cross-polarized light; and (e) Sample 13-35, scan of an entire thin section (4 cm wide) showing cataclasis in the Tower Peak unit.*

Figure 4. *Slide Mountain Assemblage: (a) massive serpentinite; (b) fibrous serpentinite; (c) brecciated serpentinite clasts with a fine-grain serpentinite matrix; (d) massive, orange weathering ultramafic rock; (e) calcite veins in a massive gabbro, white box indicates photograph f; and (f) close-up of area in (e).*

ACKNOWLEDGEMENTS

This study is part of a MS thesis in preparation by Sierra Isard. We are grateful to field assistant Nick Lamkey for his hard work. Everyone at the Yukon Geological Survey was extremely helpful throughout fieldwork and beyond, but we would particularly like to thank Carolyn Relf and Don Murphy for making this study possible. Funding for this project came from the Canadian Northern Economic Development Agency (CanNor) through the Yukon Geological Survey, National Science Foundation grant EAR1118834 (awarded to Jane Gilotti), a Geological Society of America Student Research Grant, and Department of Earth and Environmental Sciences, University of Iowa funds (awarded to Isard).

REFERENCES

Beranek, L., and Mortensen, J., 2011. The timing and provenance record of the Late Permian Klondike orogeny in northwestern Canada and arc-continent collision along western North America. Tectonics, vol. 30, no. 5, TC5017.

Beranek, L., Mortensen, J., Orchard, M., and Ullrich, T., 2010. Provenance of North American Triassic strata from west-central and southeastern Yukon: correlations with coeval strata in the Western Canada Sedimentary Basin and Canadian Arctic Islands. Canadian Journal of Earth Sciences, vol. 49, no. 1, p. 53-73.

Colpron, M., Nelson, J.L. and Murphy, D.C., 2006. A tectonostratigraphic framework for the pericratonic terranes of the northern Canadian Cordillera. In: Paleozoic Evolution and Metallogeny of Pericratonic Terranes at the Ancient Pacific Margin of North America, Canadian and Alaskan Cordillera, Colpron, M., and Nelson, J.L., (eds.), Geological Survey of Canada, vol. 45, p. 1-23.

Devine, F., Murphy, D.C., Kennedy, R., Tizzard, A.M. and Carr, S.D., 2004. Geological setting of retrogressed eclogite and jade in the southern Campbell Range: Preliminary structure and stratigraphy, Frances Lake area (NTS 105H), southeastern Yukon. *In:* Yukon Exploration and Geology 2003, Emond, D.S., and Lewis, L.L., (eds.), Yukon Geological Survey, p. 89-105.

Erdmer, P., 1992. Eclogitic rocks in the St. Cyr Klippe, Yukon, and their tectonic significance. Canadian Journal of Earth Sciences, vol. 29, p. 1296-1304.

Evans, B.W., Hattori, K., and Baronnet, A., 2013. Serpentinite: What, Why, Where? Elements, vol. 9, no. 2, p. 99-106.

Fallas, K., Erdmer, P., Creaser, R., Archibald, D., and Heaman, L., 1999. New terrane interpretation for the St. Cyr Klippe, south-central Yukon. Lithoprobe SNORCLE Transect Meeting Report, University of Calgary.

Fritz, W.H., Cecile, M.P., Norford, B.S., Morrow, D., and Geldsetzer, H.H.J., 1991. Cambrian to Middle Devonian assemblages. *In:* Geology of the Cordilleran Orogen in Canada, H. Gabrielse and C.J. Yorath (eds.), Geological Survey of Canada, no. 4, p. 151-218.

Gabrielse, H., Mortensen, J.K., Parrish, R.R., Harms, T.A., Nelson, J.L., and van der Heyden, P., 1993. Late Paleozoic plutons in the Sylvester Allochthon, northern British Columbia. *In:* Radiogenic Age and Isotopic Studies, Report 7, Geological Survey of Canada. Geological Survey of Canada, Report 93-2, p. 107-118.

Gilotti, J.A., McClelland, W.C., Petrie, M., and Van Staal, C.R., 2013. Interpreting subduction polarity from eclogite-bearing slices in accretionary orogens – a cautionary note from the Yukon-Tanana terrane. Geological Society of America, Program with Abstracts, vol. 45, no. 7, p. 442.

Harlow, G. and Sorensen, S., 2005. Jade (Nephrite and Jadeitite) and Serpentinite: Metasomatic Connections. International Geology Review, vol. 47, p. 113-146.

Mortensen, J.K., 1992a. Pre-mid-Mesozoic tectonic evolution of the Yukon-Tanana terrane, Yukon and Alaska. Tectonics, vol. 11, p. 836-853.

Mortensen, J.K., 1992b. New U-Pb ages for the Slide Mountain Terrane in southeastern Yukon Territory, Radiogenic Age and Isotopic Studies, Report 5. Geological Survey of Canada, Report 91-02, p. 167-173.

Murphy, D.C., Mortensen, J.K., Piercey, S.J., Orchard, M.J. and Gehrels, G.E., 2006. Mid-Paleozoic to early Mesozoic tectonostratigraphic evolution of Yukon-Tanana and Slide Mountain terranes and affiliated overlap assemblages, Finlayson Lake massive sulphide district, southeastern Yukon. *In:* Paleozoic Evolution and Metallogeny of Pericratonic Terranes at the Ancient Pacific Margin of North America, Canadian and Alaskan Cordillera, Colpron, M. and Nelson, J.L. (eds.), Geological Association of Canada, Special Paper 45, p. 75-105.

Murphy, D.C., Piercey, S.J., Mortensen, J.K., and Orchard, M.J., 2003. Mid to Late Paleozoic tectonostratigraphic evolution of Yukon-Tanana Terrane, Finlayson Lake massive sulphide district, southeastern Yukon. *In:* Geological Association of Canada–Mineralogical Association of Canada - Society of Economic Geologists Joint Annual Meeting, Vancouver, British Columbia, Abstracts vol. 28, p. 212, CD-ROM.

Nelson, J.L., Colpron, M., Piercey, S.J., Dusel-Bacon, C., Murphy, D.C., and Roots, C.F., 2006. Paleozoic tectonic and metallogenic evolution of the pericratonic terranes in Yukon, northern British Columbia and eastern Alaska. *In:* Paleozoic Evolution and Metallogeny of Pericratonic Terranes at the Ancient Pacific Margin of North America, Canadian and Alaskan Cordillera, Colpron, M. and Nelson, J.L. (eds.), Geological Association of Canada, Special Paper 45, p. 323-360.

Petrie, M., Gilotti, J., McClelland, W., and Van Staal, C., 2012. Age and tectonic setting of eclogites in the St. Cyr area, Yukon-Tanana Terrane, Canadian Cordillera. Geological Society of America, Program with Abstracts, vol. 44, no. 7, p. 494.

Scott, A., 1996. Jade a Mystical Mineral. Equinox, no. 89, p. 64-69.

Sekerina, N.V., 1992. Main regularities of nephrite formation. Russian Geology and Geophysics, vol. 33, no. 4, p. 31–36.

Simandl, G. J., Paradis, S., and Nelson, J., 2001. Jade and Rhodonite Deposits, British Columbia, Canada. *In:* Proceedings of the 35th Forum on the Geology of Industrial Minerals-Intermountain West Forum, Salt Lake City, vol. 1999, p. 163-172.

Tempelman-Kluit, D., 1979. Transported cataclasite, ophiolite and granodiorite in Yukon: evidence of arc-continent collision. Geological Survey of Canada, Open File 578.

Tempelman-Kluit, D.J., 2012. Geology of Quiet Lake and Finlayson Lake map areas, south-central Yukon – An early interpretation of bedrock stratigraphy and structure. Geological Survey of Canada, Open File 5487.

Preliminary investigation into the geologic relationships in the Granite Lake area, parts of NTS 115A/10, 11, 14, and 15, southwest Yukon

Steve Israel[1]
Yukon Geological Survey, Whitehorse, YT

Rachel Kim
Queen's University, Kingston, ON

Israel, S. and Kim, R., 2014. Preliminary investigation into the geologic relationships in the Granite Lake area, parts of NTS 115A/10, 11, 14, and 15, southwest Yukon. *In:* Yukon Exploration and Geology 2013, K.E. MacFarlane, M.G. Nordling, and P.J. Sack (eds.), Yukon Geological Survey, p. 79-91.

ABSTRACT

Bedrock mapping, during the summer of 2013, within the Granite Lake area was completed as part of the first year of a multi-year project to investigate the geological relationships in southwest Yukon. Several different tectonostratigraphic elements were identified including rocks of the Yukon-Tanana terrane, the Kluane schist, and the Bear Creek assemblage. These were tectonically juxtaposed into a northeast dipping structural stack with the Yukon-Tanana terrane occupying the highest structural level, followed by the Kluane schist and the Bear Creek assemblage. Two plutonic phases of probable mid-Cretaceous and Late Cretaceous age were identified to intrude the Kluane schist and the Yukon-Tanana terrane respectively. A large Paleocene aged batholithic intrusive suite, the Ruby Range suite, intrudes across all tectonic boundaries.

Tectonic and stratigraphic relationships observed in southwest Yukon are strikingly similar to those found in southeast Alaska, near Juneau. These similarities increase the potential for Juneau gold-belt type mineralizing systems extending into southwest Yukon.

[1] *steve.israel@gov.yk.ca*

INTRODUCTION

The Granite Lake area (parts of NTS 115A/10, 11, 14, and 15) is located east of Haines Junction and north of Dezadeash Lake (Fig. 1). The area was last mapped as part of a regional examination of the bedrock geology within the area of the Dezadeash map sheet (NTS 115A) in 1946 to 1950 by Kindle (1952). Since then few geological investigations have been conducted in the area and those that were included the Granite Lake area only as a small part of much larger regional studies. These studies include work on the relationships of metamorphic and plutonic rocks and overall tectonic synthesis of southwest Yukon (Erdmer and Mortensen, 1993; Mezger *et al.*, 2001; Johnston and Canil, 2006).

The current study builds on previous detailed 1:50 000 scale bedrock mapping to the north and northeast (Israel *et al.*, 2011a,b; Israel and Westberg, 2011, 2012). The goals of this project are to determine the geologic relationships between diverse lithotectonic elements in order to gain better insight into the overall tectonic and metallogenic understanding of southwest Yukon.

Exposure in the area ranges from excellent near high peaks and ridges, to very poor in the wide bush covered valleys. Access is restricted to helicopter or float plane, and very few useable roads or trails.

REGIONAL GEOLOGY

Southwest Yukon comprises several tectonic terranes, overlapped and intruded by younger stratigraphy and plutons (Fig. 1). In the east and north, the Yukon-Tanana terrane is characterized by Proterozoic to mid-Paleozoic metamorphic rocks. The Yukon-Tanana terrane continues both to the southeast, into northern British Columbia, and to the northwest into eastern Alaska. The terrane has been affected by multiple phases of deformation and metamorphism that resulted in transposition of original layering, isoclinal folding, and upper greenschist to amphibolite grade metamorphism. In southwest Yukon the Yukon-Tanana terrane appears to be thrust to the west/southwest over younger, metamorphic rocks of the Kluane schist; however, much of this contact has been intruded by post-deformation plutonic rocks, making it difficult to characterize.

The Kluane schist occupies much of the central part of southwest Yukon, overthrust to the east/northeast by the Yukon-Tanana terrane, faulted against rocks of the Insular terranes across the Tertiary Denali fault to the west/southwest, and juxtaposed next to the Jura-Cretaceous Dezadeash Formation and the enigmatic Bear Creek assemblage across an unnamed fault in the southwest (Fig. 1). The rocks of the Kluane schist are characterized mainly by biotite and muscovite schist that were likely part of a forearc assemblage sourced from the exhumation of the Yukon-Tanana terrane and its younger intrusions sometime in the Early to Late Cretaceous (Israel *et al.*, 2011b). Metamorphism within the Kluane schist appears to be two stage with a medium pressure and temperature burial phase, related to overthrusting of Yukon-Tanana terrane, overprinted by a low pressure and high temperature phase related to intrusion of the Ruby Range batholith (Mezger *et al.*, 2001). Peak metamorphism is likely concurrent with overgrowths on detrital zircons dated at ~82 Ma (Israel *et al.*, 2011b). The age of the Kluane schist is not well constrained, but must be older than the metamorphic age and younger than ~94 Ma, the age of the youngest detrital zircon (Israel *et al.*, 2011b).

The boundary between the Kluane schist and the Yukon-Tanana terrane is presumed to be a faulted contact; however, it is intruded by the Paleocene Ruby Range suite and therefore not exposed.

The Ruby Range suite is found as a northwest trending batholith of felsic to intermediate composition that continues into northern BC at its southeast end, and is cut off by the Denali fault at its northwest end (Fig. 1). Where exposed, the structural base of the batholith is foliated, passing upwards into more massive undeformed intrusive rock (Israel *et al.*, 2011b). The age of the Ruby Range batholith ranges from ~64 Ma to ~57 Ma (Israel *et al.*, 2011b; Israel and Westberg, 2011).

An unnamed fault, with unknown kinematics, separates the above rocks from a Jura-Cretaceous sedimentary unit, the Dezadeash Formation, and an enigmatic package of strongly metamorphosed and deformed rocks assigned to the informal Bear Creek assemblage (Fig. 1). The Dezadeash Formation has been correlated to other Jura-Cretaceous overlap assemblages found in east and southeast Alaska and British Columbia along the boundary between the outboard Insular terranes and the Intermontane terranes (McClelland *et al.*, 1992). The Bear Creek assemblage is found to structurally underlie the Dezadeash Formation. It is a unit composed of mainly metabasalt and meta-ultramafic rocks structurally interleaved with lesser metasedimentary rocks. Age and correlation of the assemblage is not constrained. Read and

Monger (1976) included it within the Taku-Skolai terrane, a terrane consisting largely of what is now referred to as Wrangellia. Gordey and Makepeace (2003) included the Bear Creek assemblage with the Nikolai formation, Triassic basalt of Wrangellia. It is most likely that the Bear Creek assemblage is part of the Paleozoic to early Mesozoic Taku terrane (Gehrels, 2002), found in southeast Alaska.

The Denali fault, with up to 400 km of dextral strike-slip offset, separates all of the above rocks from those of the Insular terranes to the south/southwest (Fig. 1). The Insular terranes include the Alexander terrane and Wrangellia, and were amalgamated to the margin of the Intermontane terranes during or before the Middle Jurassic (McClelland *et al.*, 1992; van der Heyden, 1992).

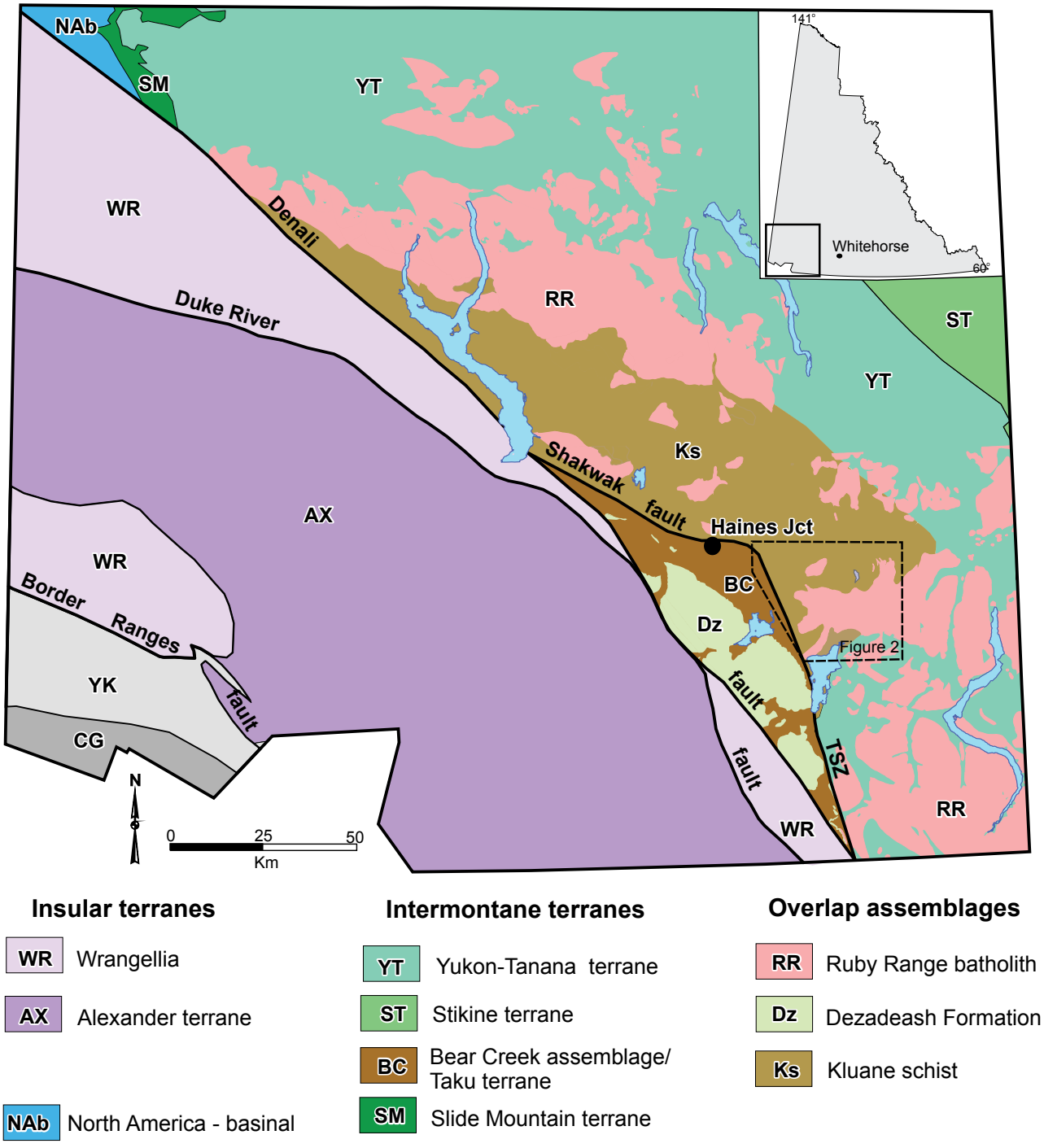

***Figure 1**. Regional tectonic framework of southwest Yukon with Granite Lake area outlined.*

LOCAL GEOLOGY

The Granite Lake area is underlain by rocks of the Kluane schist, the Ruby Range batholith, the Yukon-Tanana terrane, and the Bear Creek assemblage (Fig. 2). Contacts between the different units are generally located in the valley bottoms and are therefore not well exposed. It is assumed that most contacts are structural in nature, yet the nature of the structures are not well constrained.

a

LEGEND

QUATERNARY

Q — unconsolidated glacial, glaciofluvial and glaciolacustrine deposits; fluviatile silt, sand and gravel, and local volcanic ash, in part with cover of soil and organic deposits

OVERLAP ASSEMBLAGES

PALEOCENE

RUBY RANGE BATHOLITH (ca. 64-57 Ma):

PR — fine to coarse-grained, salt and pepper, hornblende +/- biotite, quartz diorite, rare garnets; medium-grained, light grey to pinkish biotite +/- hornblende granodiorite; fine- to medium-grained, beige to grey tonalite with distinctive smokey grey quartz; pinkish/grey, biotite granite; likely in part coeval with Rhyolite Creek volcanoplutonic complex

LATE CRETACEOUS (?)

LKgd — fine to coarse-grained, strongly foliated to massive hornblende, biotite granodiorite; white to beige weathered, salt and pepper fresh; garnets common

MID-CRETACEOUS (?)

mKgn — fine to coarse-grained, strongly to weakly foliated hornblende, biotite, quartz-diorite to granodiorite orthogneiss

JURASSIC TO MID-CRETACEOUS

KLUANE SCHIST:

KK — dark grey, brown to black weathered, dark grey to black fresh, fine-grained, biotite, quartz, feldspar schist; local feldspar porphyroblasts; blocky weathered appearance

KKgn — migmatitic paragneissic equivalents of Kluane Schist; medium to coarse-grained, dark grey to black weathered with orange to cream coloured leucocratic layers

TAKU TERRANE (?)

PERMIAN (?) TO TRIASSIC (?)

BEAR CREEK ASSEMBLAGE

PTKBu — light to dark green and black serpentinite, meta-dunite and meta-pyroxenite; strongly deformed; locally abundant asbestos

PTKB — strongly deformed and metamorphosed, mainly light to dark green and black basalt; lesser amounts of light grey/green andesite and dacite and dark grey to brown mudstone

YUKON-TANANA TERRANE

MISSISSIPPIAN (?) or PERMIAN (?)

MPgn — medium to coarse-grained hornblende-biotite quartz-diorite and diorite orthogneiss; dark grey, black to salt and pepper colour; abundant garnets found locally

UPPER DEVONIAN AND OLDER

SNOWCAP ASSEMBLAGE:

PDSs — polydeformed and metamorphosed dark grey to black biotite and amphibolite schist; minor garnets; locally contains thin light to dark grey banded quartzite layers

PDSc — light grey and cream weathered, fine to medium-grained calcsilicate schist; light grey to white, fine to medium-grained marble occurring as lenses and thick layers (up to several metres wide) within calcsilicate schist

PDSa — medium-grained, dark and light grey banded gneiss with abundant garnets, interlayered with fine-grained dark green to black garnet amphibolite

PDSqs — light to dark grey and brown weathered biotite, muscovite, quartz, garnet schist; locally abundant aluminosilicates (sillimanite, +/- kyanite); locally migmatitic

LEGEND EXPLANATION

PLUTONIC SUITES: grouping of plutonic rock units based on age, regional distribution and in some cases composition

LAYERED ROCK ASSEMBLAGES: regionally mappable units generally of Group or Formation rank

MINFILE Occurrences

Number	Name	Deposit Type	Commodity/Status
115A032	REX	Ultramafic-hosted asbestos	asbestos

SYMBOLS

geologic contacts (defined, approximate)

fault; movement not known (approximate, inferred)

thrust fault (inferred)

normal fault (approximate)

foliation (dominant) 83

elongation lineation 23

intersection lineation 54

crenulation lineation 23

fold axis (early, m-fold, s-fold, z-fold) 12 12 25 12

limited-use road or trail

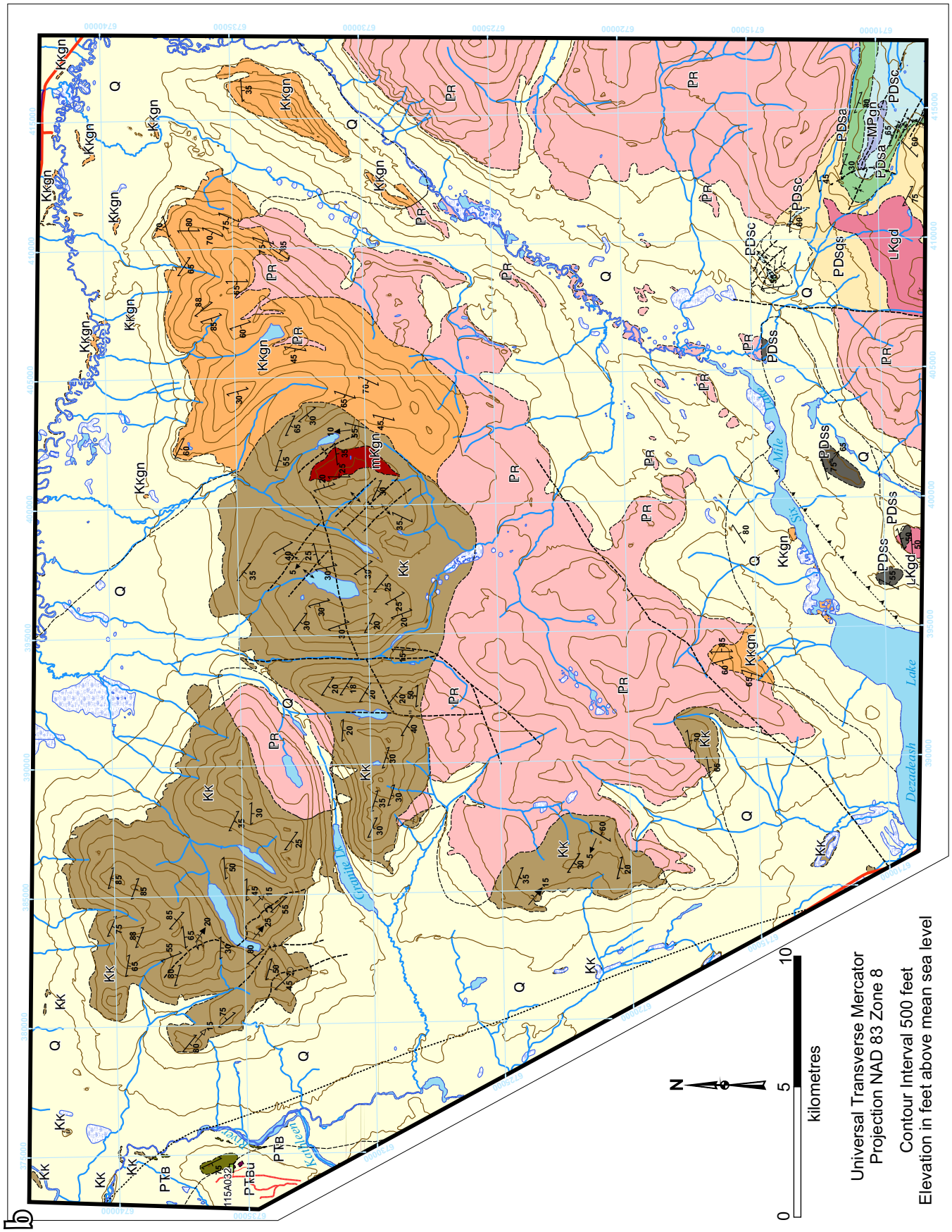

Figure 2. *(a) legend; and (b) generalized bedrock geology of the Granite Lake area. Modified from Israel and Kim (2013).*

STRATIGRAPHY

YUKON-TANANA TERRANE

The Yukon-Tanana terrane in the Granite Lake area is located mainly in the far southeast corner, where it is intruded by the Ruby Range batholith and apparently thrust over rocks of the Kluane schist (Fig. 2). Rocks assigned to the Yukon-Tanana terrane consist primarily of schist, orthogneiss, and calc-silicate that have been tentatively assigned to the Proterozoic to Devonian Snowcap assemblage. The assemblage has been subdivided into four mappable units, based mainly on lithologic composition. They occur in an upright, moderately to steeply, southeast plunging synform with tight antiform/synform pairs on its flanks (Fig. 2). This folding is likely a late phase of deformation as internally the units are more complexly deformed, showing evidence for multiple phases of deformation.

PDsqs

The structurally lowest unit of the Snowcap assemblage is a seemingly thick package of light to dark grey and brown weathered biotite, muscovite, quartz, garnet schist (Fig. 3a). Locally abundant sillimanite, (±) kyanite occurs within the schist. Limited field observations suggest sillimanite grew after kyanite, indicating fairly high temperatures and pressures were involved in metamorphism of this unit. Where intruded by Late Cretaceous (?) granitic rocks, the schist becomes migmatitic and in places almost completely recrystallized, giving the rock an igneous appearance (Fig. 3b).

PDsa

Structurally, and probably stratigraphically, overlying PDsqs is a package of medium to coarse-grained, dark and light grey banded orthogneiss, interlayered with fine-grained dark green to black garnet amphibolite (Fig. 3c). The thickness of this unit varies from several metres to tens of metres. The contact with the underlying schist is not exposed. At the upper contact, interlayering of amphibolite with calc-silicate schist may suggest a partial gradation between the two units. Much of PDsa appears to be meta-igneous in origin; however, some of the garnet amphibolite near the top of the unit may be metabasalt interlayered with the calc-silicate rocks. Garnet is abundant in all rock types within PDsa, in some places forming complete layers up to several centimetres thick (Fig. 3d). The orthogneiss is mainly diorite to quartz-diorite in composition with alternating layers of light coloured (quartz, plagioclase) and dark coloured (amphibole, ± biotite) minerals. Amphibolite is composed primarily of hornblende and plagioclase, with minor quartz and biotite. Age of this unit is not known.

PDsc

Overlying PDsa is a package of calc-silicate schist and marble (Fig. 2). Interlayering of amphibolite of unit PDsa and calc-silicate schist occurs at the lower contact of PDsc. A deformed intrusive contact defines the upper boundary of PDsc where it is next to a possible Mississippian to Permian orthogneiss unit (Fig. 2). No contact was observed between PDsc and PDss, the unit within the Yukon-Tanana terrane interpreted to be at the highest stratigraphic position (Fig. 2). The calc-silicate schist is light grey to beige and cream weathered and thinly to thickly layered (Fig. 3e). It is strongly deformed and metamorphosed but locally primary layering is preserved. The schist is fine to medium grained, and composed of calcite (± dolomite) and quartz. Locally, some layers are more psammitic in composition, being more quartz-rich with varying amounts of biotite. Thin light to dark grey quartzite layers are found within the more psammitic layers. The calc-silicate and quartz-rich schists pass up into strongly deformed, white to light grey weathered marble that can be up to several metres wide (Fig. 3f). The marble occurs as bands, interlayered within the calc-silicate rocks, at all levels within PDsc. It is difficult to determine if this is stratigraphic or reflecting internal structural complexities. The age of PDsc is unknown.

PDss

Rocks assigned to unit PDss include biotite and amphibolite schist. Their position within the stratigraphy of the Yukon-Tanana terrane is not well constrained, mainly because of the poor outcrop exposure of this unit, which occurs mainly as small, almost hidden exposures in the bush south of Six Mile Lake, and as small roof pendants within Late Cretaceous (?) plutons (Fig. 2). As interpreted it represents the highest level of Yukon-Tanana stratigraphy. This is based mainly on field observations that appear to show these rocks are the least metamorphosed, but until further analyses can be done this assignment is tenuous at best. The dominant rock type is a biotite, hornblende schist, and minor garnet (Fig. 3g). Locally the rock approaches garnet amphibolite with little to no biotite. The largest exposure of the unit shows interlayering of biotite, ± hornblende schist, quartz-rich psammitic schist, and thin (10 cm) dark grey quartzite layers (Fig. 3h). As with the other rocks assigned to the Yukon-Tanana terrane, the age of this unit is unknown.

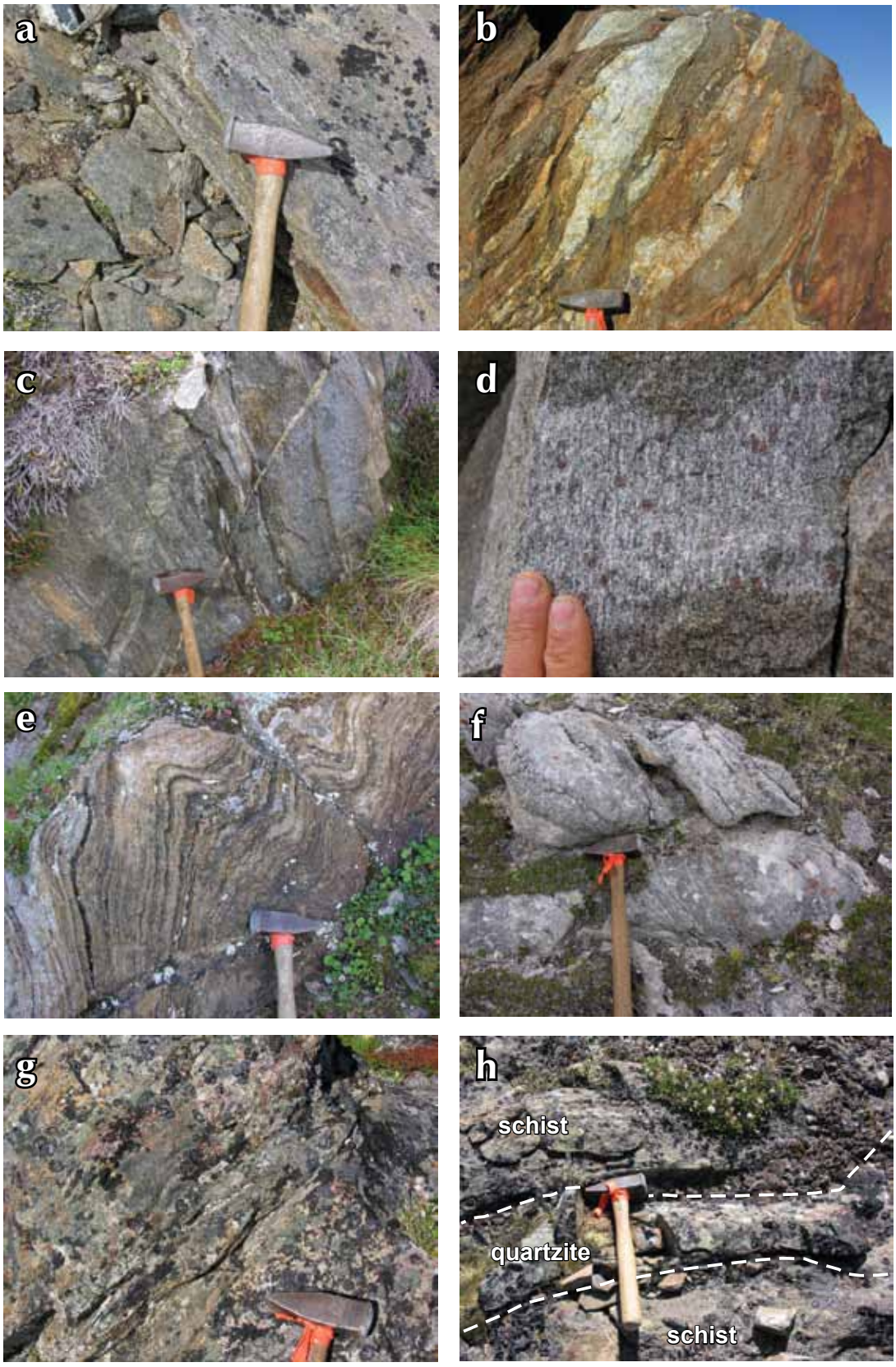

Figure 3. *Rocks assigned to the Yukon-Tanana terrane: (a) biotite, quartz, garnet schist of unit PDsqs; (b) migmatitic schist of unit PDsqs; (c) garnet amphibolite of unit PDSa; (d) abundant garnets within rocks of unit PDsa; (e) folded calc-silicates of unit PDSc; (f) strongly deformed marble of unit PDSc; (g) lichen covered outcrop of biotite, hornblende schist of unit PDSs; and (h) thin quartzite layer within biotite, hornblende schist of unit PDSs.*

BEAR CREEK ASSEMBLAGE (PTB)

Rocks of the Bear Creek assemblage are found at the western margin of the Granite Lake map area (Fig. 2). They comprise a small collection of outcrops just west of the Kathleen River. The Bear Creek assemblage is interpreted to be in fault contact with rocks of the Kluane schist and Ruby Range batholith to the east, and likely occur under thick quaternary cover as far south as Dezadeash Lake (Fig. 2). The assemblage is characterized by metabasalt and meta-ultramafic rocks that are strongly deformed and structurally interleaved. A limited use road into this area was established in order to gain access to asbestos showings related to the ultramafic rocks (Yukon MINFILE 115A 032; Fig. 2). The ultramafic rocks were not examined during this study, but elsewhere in the assemblage outside of the project area, are observed to comprise strongly deformed and metamorphosed pyroxenite, dunite, and peridotite, all intensely altered and serpentinite and epidote are common. Metabasalt is fine grained, dark and light green to black, and shows layering of these colours on the centimetre to metre scale (Fig. 4a). It is strongly deformed and the layering likely reflects this deformation rather than original depositional characteristics. The age of the Bear Creek assemblage is not known. If the correlation with the Taku terrane in southeast Alaska is correct, it would date these rocks as Late Paleozoic to early Mesozoic.

KLUANE SCHIST

By far the largest, non-intrusive, spatially represented unit in the Granite Lake map area is the Kluane schist (Fig. 2). The Kluane schist is faulted against the Bear Creek assemblage in the west and is interpreted to be overthrust by the Yukon-Tanana terrane in the southeast. The Ruby Range batholith intrudes across these boundaries and throughout the heart of the unit. Large outcrops of the schist occur in the northern and western halves of the project area comprising much of the higher peaks and ridges. In the Granite Lake area, two main mappable units of the schist are found, a lower unit of paragneiss and an upper unit of biotite schist.

Kkgn

The lowest, structurally and likely stratigraphically, unit of the Kluane schist is characterized by a banded paragneiss. It outcrops mainly in the northeast part of the project area, continuing to the west, just north of Dezadeash Lake (Fig. 2). The paragneiss is extensively intruded by the Ruby Range batholith concealing the contact between the gneiss and the Yukon-Tanana terrane to the south. Contact with the overlying schist of the Kluane schist is not very well exposed either, making the nature of this contact unclear. It appears from limited examination to be a gradational contact; however, elsewhere in southwest Yukon this contact is structural, characterized by a thrust fault that places the paragneiss over biotite schist (Israel *et al.*, 2011a,b).

The paragneiss is distinctly banded and weathers an orange to brown. It is medium to coarse grained, dominantly composed of quartz, biotite, and feldspar, and a minor local abundance of muscovite. The banding is defined by dark layers of mainly biotite and quartz, and the more leucocratic layers of plagioclase, ± potassium feldspar, and quartz (Fig. 4b). The layers range in thickness from less than one centimetre to several centimetres. Garnet was only rarely observed and only within pockets of what appears to be melt, comprising quartz, muscovite, feldspar, and garnet.

The age of Kkgn is not well constrained. Detrital zircon analyses from other parts of the unit in southwest Yukon suggest it could be as young as 94 Ma (Israel *et al.*, 2011b); however more work needs to be done to confirm this age.

Kk

The most prominent, rock type within the Kluane schist is quartz, biotite schist. It is distinct from the paragneiss and from other schist assigned to the Yukon-Tanana terrane. In the Granite Lake area, the schist is fairly monotonous, not changing its appearance very much from one area to another. It is characterized by blocky, brown to dark grey weathered outcrops comprising fine to medium-grained biotite, quartz, schist (Fig. 4c). Locally, abundant 1-2 mm feldspar porphyroblasts are present. Laterally discontinuous, foliation parallel quartz veins, 1-5 cm thick, are found throughout the schist. The schist has been deformed by at least two phases of folds. The dominant phase of folding resulted in tight, overturned, north to northeast verging structures having northwest to southeast, shallow to moderate plunging axes (Fig. 4d). These have been deformed by broad, open folds with shallow north plunges.

The age of the schist is thought to be Late Cretaceous, based on the youngest detrital zircons analyzed from rocks elsewhere in the belt (Israel *et al.*, 2011b).

Figure 4. *(a) Metabasalt of the Bear Creek assemblage; (b) strongly deformed paragneiss of the lower Kluane schist (Kkgn); (c) biotite, quartz schist of the Kluane schist (Kk); and (d) northeast verging, overturned folds within biotite schist of the Kluane schist.*

INTRUSIVE ROCKS

Several different intrusive units are found within the Granite Lake area, ranging in composition from granodiorite to diorite, and are strongly deformed to massive. The age assignments to the different units below are based upon field observations; to better constrain the age of emplacement of these bodies, and to determine relative ages of deformation that affected the area, samples of each were collected for U-Pb dating.

MID-CRETACEOUS (?) ORTHOGNEISS (MKGN)

A large body of granodioritic to quartz-dioritic orthogneiss is found in the central part of the Granite Lake map area, intruding into biotite schist of the Kluane schist (Fig. 2). It is characterized by light and dark grey banding that reflects the change in abundance of biotite and hornblende within a dominantly quartz, feldspar matrix (Fig. 5a). The foliation within the orthogneiss is parallel to the surrounding schist, and small dikes off the main body are seen to intrude along foliation and are folded with the schist. It is likely that this orthogneiss intruded during deformation, possibly in the mid to Late Cretaceous.

LATE (?) CRETACEOUS (LKGD)

A unit of garnet bearing, foliated to massive, granodiorite to gabbro is found south of Six Mile Lake where it intrudes exclusively into rocks of the Yukon-Tanana terrane (Fig. 2). These rocks consist of hornblende (± pyroxene), biotite, quartz, and feldspar with abundant 1-3 mm pink garnets.

Evidence for deformation within the unit is highly variable and ranges from a well-developed foliation near contacts with the country rock, to very weakly-developed away from the contact (Fig. 5b). The contacts of this intrusive unit and the Yukon-Tanana rocks appear to be both intrusive and structural, suggesting a syn-deformation timing for its emplacement.

RUBY RANGE SUITE

The most abundant rock unit in the Granite Lake area belongs to the Ruby Range suite. It outcrops across the project area and intrudes into all other rock units and across all ductile fabrics (Fig. 2). Regionally the Ruby Range suite ranges in composition from granodiorite to quartz-diorite and quartz-monzonite. In the Granite Lake area the suite is dominated by a medium-grained, light grey to beige weathered biotite, granodiorite to tonalite with distinctive smoky grey quartz crystals up to 3-4 mm (Fig. 5c). The suite shows no evidence of ductile fabrics and is only deformed by the latest stage of brittle faulting. Miarolitic cavities are found locally, suggesting a relatively high level of emplacement for the Ruby Range suite in the project area (Fig. 5d). The age of the Ruby Range suite is early Paleocene (~64 Ma) to early Eocene (~54 Ma).

DISCUSSION

TECTONIC IMPLICATIONS

Although it is early on in the investigation into the geological relationships of the southern Coast belt region of southwest Yukon, it is apparent that some fundamental

***Figure 5**. Intrusive rocks from the Granite Lake area: (a) orthogneiss intruding into the Kluane schist; (b) strongly foliated garnet bearing granodiorite found intruding the Yukon-Tanana terrane; (c) massive biotite granodiorite to tonalite of the Ruby Range suite; and (d) miarolitic cavities filled with quartz crystals observed within plutons of the Ruby Range suite.*

tectonic relationships are present. These relationships are centred on the nature of the boundaries between three distinct tectonostratigraphic units; the Yukon-Tanana terrane, the Kluane schist, and the Bear Creek assemblage. The timing and characteristics of these boundaries are important in determining the overall tectonic evolution of southwest Yukon.

Metamorphism within the Yukon-Tanana terrane in this region appears to coincide with high temperatures and pressures shown by the presence of sillimanite, kyanite, and migmatite in unit PDsqs. Metamorphism within the Kluane schist is not as dramatic. Mezger *et al.* (*2001*) suggest the Kluane schist underwent medium pressure and temperature metamorphism (upper greenschist to lowermost amphibolite) *ca.* 72 Ma. This is below the apparent sillimanite after kyanite upper amphibolite metamorphism observed within the Yukon-Tanana terrane, suggesting some kind of non-stratigraphic boundary between the two packages of rocks. Based on limited structural information (including stretching lineations and c-s fabrics noted in outcrops) a thrust fault is inferred to accommodate the juxtaposition of the higher-grade Yukon-Tanana rocks over the lower grade Kluane schist (Fig. 2). The timing of this structural stacking is not well-constrained but had to occur before the intrusion of the Ruby Range suite (*ca.* 64-57 Ma). It is likely that this deformation event occurred during the emplacement of the foliated garnet bearing granodiorite that intrudes the Yukon-Tanana terrane.

The boundary between the Bear Creek assemblage and the other rock units is somewhat ambiguous. Kindle (1952) interprets a structure that separates the Dezadeash Formation and metamorphic rocks that include the Kluane schist and the Yukon-Tanana terrane. Kindle (1952) shows this structure to continue south into northern British Columbia. Just north of the Yukon/British Columbia border, Lowey (2000) proposed that this fault (referred to as the Tatshenshini shear zone) had northeast dipping fabrics within it and suggested that the shear zone accommodated southwest directed thrusting of the Ruby Range suite over the Dezadeash Formation. Limited outcrop information hampers direct observation of the fault zone in the Granite Lake area, however if the interpretations along the Tatshenshini shear zone are correct, then the Kluane schist and Yukon-Tanana terrane (along with the Ruby Range suite) is thrust over rocks of the Bear Creek assemblage.

This northeast dipping structural stack of tectonic elements was proposed by Johnston and Canil (2006) to explain regional structural fabrics. The exact tectonic driver and timing of deformation for this crustal juxtaposition remains ambiguous.

METALLOGENIC IMPLICATIONS

Previous investigations into the geologic relationships of southwest Yukon have shown that the areas comprising the tectonic elements in the Granite Lake area are highly prospective with respect to both orogenic and intrusion related mineralizing systems (Israel *et al.*, 2011a,b; Israel and Westberg, 2012).

The high level of crustal emplacement for the Ruby Range suite, coupled with extensive coeval volcanic deposition, increases the potential for porphyry and epithermal style mineralization. Both porphyry and epithermal associated alteration and mineralization are found north of the Granite Lake area, near Aishihik Lake and are believed to be related to Ruby Range plutons and coeval Rhyolite Creek volcanic rocks (Israel *et al.*, 2011b; Israel and Westberg, 2012).

Orogenic related mineralization occurs within the Kluane schist near Killermun Lake, northwest of the Granite Lake area. This mineralization includes several vein hosted gold occurrences over several kilometres of strike length. The veins are found near the structural boundary between the Yukon-Tanana terrane, the Ruby Range batholith, and the Kluane schist, with veins formed in both the schist and the granitic rocks. Gold mineralization is also found within the Bear Creek assemblage just to the west of the Granite Lake area, near Bear Creek. The nature of this mineralization is not well documented but appears to be structurally controlled.

The regional geologic setting observed in southwest Yukon is the same as that found in the Juneau, Alaska area, where several orogenic related gold deposits occur. Comparing the Juneau area with southwest Yukon indicates that the two areas share both stratigraphic and intrusive relationships as well as structural architecture (Fig. 6). These parallels in geologic relationships increase the potential for similar style mineral systems within the Granite Lake area.

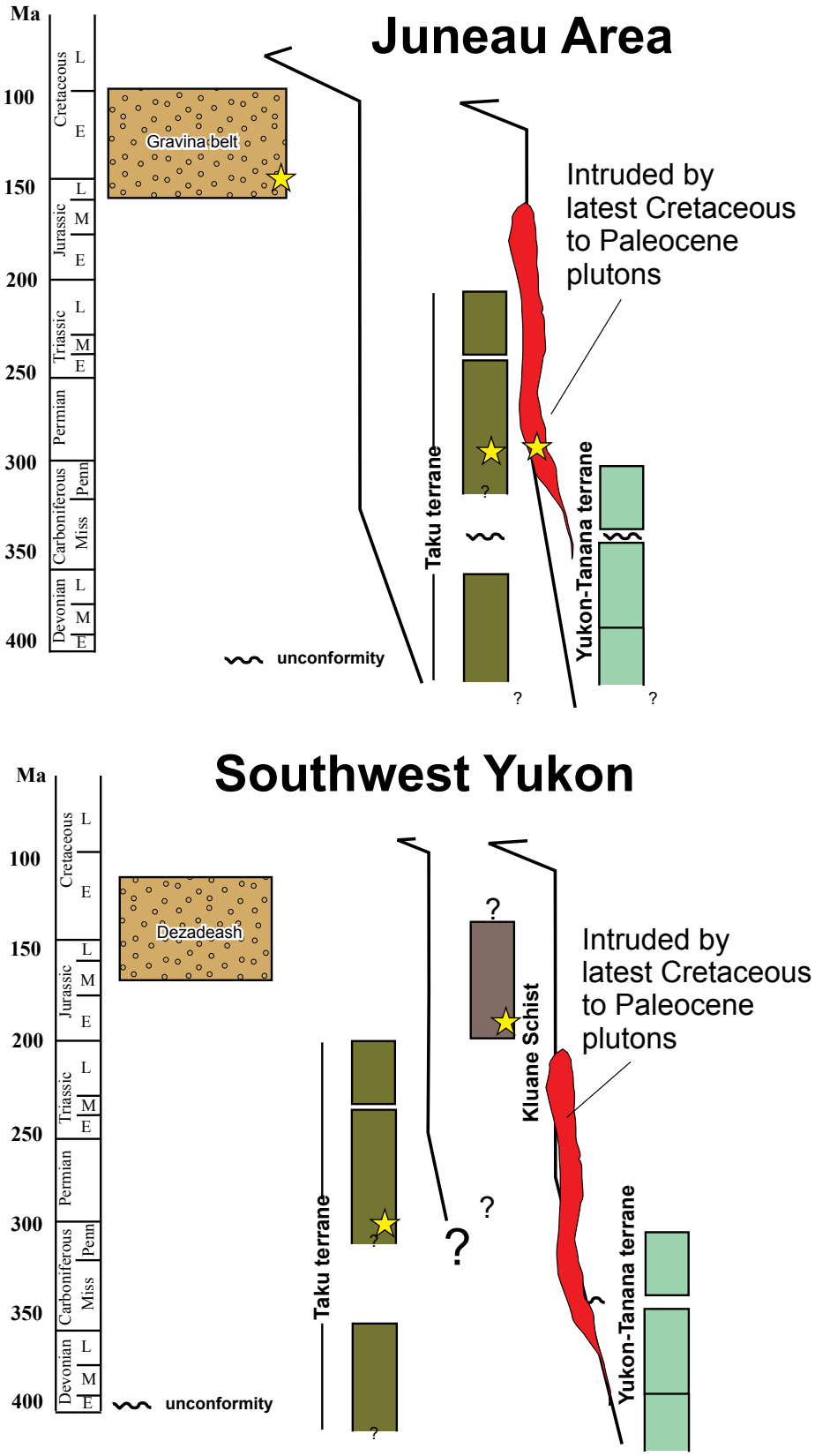

Figure 6. *Tectonostratigraphic diagrams for southwest Yukon and the Juneau areas. Gold stars indicate areas of known gold mineralization. Juneau stratigraphy modified from Goldfarb et al. (1988).*

ACKNOWLEDGEMENTS

The authors would like to thank Trans North Helicopters out of Haines Junction for excellent service and safe flying. We would also like to thank Don Murphy for comments, making this a better manuscript. Karen MacFarlane and Monica Nordling are thanked for final edits and comments.

REFERENCES

Erdmer, P. and Mortensen, J.K., 1993. A 1200-km-long Eocene metamorphic-plutonic belt in the northwestern Cordillera: Evidence from southwest Yukon. Geology, vol. 21, p. 1039-1042.

Gehrels, G.E., 2002. Detrital zircon geochronology of the Taku terrane, southeast Alaska. Canadian Journal of Earth Sciences, vol. 39, p. 921-931.

Goldfarb, R.J., Leach, D.L., Pickthorn, W.J., and Paterson, C.J., 1988. Origin of lode-gold deposits of the Juneau gold belt, southeastern Alaska. Geology, vol. 16, p. 440-443.

Gordey, S.P. and Makepeace, A.J., 2003. Yukon Digital Geology (version 2). Geological Survey of Canada, Open File 1749.

Israel, S., Cobbett, R., Westberg, E., Stanley, B., and Hayward, N., 2011a. Preliminary bedrock geology of the Ruby Ranges, southwest Yukon (Parts of NTS 115G, 115H, 115A and 115B) (1:150 000-scale). Yukon Geological Survey, Open File 2011-2.

Israel, S. and Kim, R., 2013. Preliminary geological map of the Granite Lake area, parts of NTS 115A/10, 11, 14, and 15 (1:50 000 scale). Yukon Geological Survey, Open File 2013-17.

Israel, S., Murphy, D.C., Bennett, V., Mortensen, J.K., and Crowley, J., 2011b. New insights into the geology and mineral potential of the Coast Belt in southwestern Yukon. *In:* Yukon Exploration and Geology, K.E. MacFarlane, L.H. Weston, and C. Relf (eds.), Yukon Geological Survey, p. 101-123.

Israel, S. and Westberg, E., 2011. Preliminary geological map of the northwestern Aishihik Lake area, parts of NTS 115H/12 and 13 (1:50 000-scale). Yukon Geological Survey Open File 2011-31.

Israel, S. and Westberg, E., 2012. Geology and mineral potential of the northwestern Aishihik Lake map area, parts of NTS 115H/12 and 13. *In:* Yukon Exploration and Geology 2011, K.E. MacFarlane and P.J. Sack (eds.), Yukon Geological Survey, p. 103-113.

Johnston, S.T. and Canil, D., 2006. Crustal architecture of SW Yukon, northern Cordillera: Implications for crustal growth in a convergent margin orogen. Tectonics, vol. 26, p. 18.

Kindle, E.D., 1952. Dezadeash Map-Area, Yukon Territory. Geological Survey of Canada Memoir 268, p. 68.

Lowey, G., 2000. The Tatshenshini shear zone (new) in southwestern Yukon, Canada: Comparison with the Coast shear zone in British Columbia and southeastern Alaska and implications regarding the Shakwak suture. Tectonics, vol. 19, p. 512-528.

McClelland, W.C., Gehrels, G.E., and Saleeby, J.B., 1992. Upper Jurassic-Lower Cretaceous basinal strata along Cordilleran margin: Implications for the accretionary history of the Alexander-Wrangellia-Peninsular terrane. Tectonics, vol. 11, p. 823-835.

Mezger, J.E., Chacko, T., and Erdmer, P., 2001. Metamorphism at a late Mesozoic accretionary margin: a study from the Coast Belt of the North American Cordillera. Journal of metamorphic Geology, vol. 19, p. 121-137.

Read, P.B. and Monger, J.W.H., 1976. Pre-Cenozoic volcanic assemblages of the Kluane and Alsek Ranges, southwestern Yukon Territory. Geological Survey of Canada, Open File 381, 96 p.

van der Heyden, P., 1992. A Middle Jurassic to early Tertiary Andean-Sierran arc model for the Coast Belt of British Columbia. Tectonics, vol. 11, p. 82-97.

Yukon MINFILE, 2013. Yukon MINFILE - A database of mineral occurrences. Yukon Geological Survey, <*http://data.geology.gov.yk.ca*> [accessed November 1, 2013].

The early Neoproterozoic Chandindu Formation of the Fifteenmile Group in the Ogilvie Mountains

Marcus Kunzmann[1], Galen P. Halverson, Malcolm Hodgskiss, Pierre D. Sansjofre, Dirk Schumann
Department of Earth & Planetary Sciences/GEOTOP, McGill University, Montreal, Quebec, Canada

Francis A. Macdonald
Department of Earth & Planetary Sciences, Harvard University, Cambridge, MA, USA

Robert H. Rainbird
Geological Survey of Canada, Ottawa, Ontario, Canada

Kunzmann, M., Halverson, G.P, Macdonald, F.A., Hodgskiss, M., Sansjofre, P.D., Schumann, D., and Rainbird, R.H, 2014. The early Neoproterozoic Chandindu Formation of the Fifteenmile Group in the Ogilvie Mountains. *In:* Yukon Exploration and Geology 2013, K.E. MacFarlane, M.G. Nordling, and P.J. Sack (eds.), Yukon Geological Survey, p. 93-107.

ABSTRACT

Studies of biogeochemical and evolutionary change in the Neoproterozoic require a detailed understanding of stratigraphic successions and their intrabasinal correlation to integrate those records into regional and global frameworks. The early Neoproterozoic Fifteenmile Group in the Ogilvie Mountains has previously been shown to archive important information on the evolution of the biosphere, including ocean redox and early evolution of eukaryotes. Here, we formally define the Chandindu Formation, a 150 to 420-m-thick siltstone-dominated mixed carbonate-siliciclastic succession of the lower Fifteenmile Group in the Coal Creek and Hart River inliers. We present ten sections of the Chandindu Formation and propose a type section and formalization to promote the development of a consistent stratigraphic framework for Proterozoic successions in northwest Canada.

The Chandindu Formation begins with muddy tidal flat facies, which are succeeded by shale-siltstone-sandstone coarsening-upward cycles deposited in a predominantly subtidal environment. However, carbonate occurrences throughout the entire unit suggest localized carbonate buildups, likely nucleated on fault-bound paleohighs where siliciclastic background sedimentation was low. These paleohighs originated from rift-inherited complex basin topography and syn-depositional faulting during deposition of the upper Chandindu Formation.

[1] *marcus.kunzmann@mail.mcgill.ca*

INTRODUCTION

Proterozoic strata in northwest Canada are exposed in erosional windows through Phanerozoic cover (Fig. 1a); from west to east, these are the Tatonduk, Coal Creek, and Hart River inliers of the Ogilvie Mountains, the Wernecke inlier in the Wernecke Mountains, and the Mackenzie Mountains. Broad stratigraphic correlation between Neoproterozoic successions in the Mackenzie Mountains and elsewhere in the Amundsen Basin in Arctic Canada is relatively straightforward (*e.g.*, Rainbird *et al.*, 1996), although new radiometric ages and chemostratigraphy (Jones *et al.*, 2010; Macdonald *et al.*, 2010b) motivate refinement of this correlation. Although broad stratigraphic similarities between Proterozoic inliers in northwest Canada were noticed decades ago (*e.g.*, Gabrielse, 1972; Eisbacher, 1978a; Young *et al.*, 1979), refined correlations on the formation scale have remained elusive. The difficulty in correlating between the inliers is due to many factors, including a paucity of radiometric dates, incomplete stratigraphic records, complex tectonostratigraphic evolution, and significant lateral facies changes, even within inliers (Macdonald *et al.*, 2012). Nonetheless, a detailed understanding of regional correlations based on mapping, stratigraphic analysis including the definition and introduction of new formations, geochronology, and geochemistry, is necessary both to reconstruct the tectonic setting and basin evolution, and also to calibrate records of biogeochemical change and biological evolution obtained from these strata.

The early Neoproterozoic Fifteenmile Group in Yukon was deposited during a time span characterized by globally increasing eukaryotic diversity (*e.g.*, Schopf *et al.*, 1973; Porter and Knoll, 2000; Butterfield, 2004; Knoll *et al.*, 2006) possibly facilitated by a non-sulphidic deep ocean (Canfield *et al.*, 2008; Johnston *et al.*, 2010; Sperling *et al.*, 2013). Recent studies of the Fifteenmile Group identified scale microfossils (Macdonald *et al.*, 2010a; Cohen *et al.*, 2011; Cohen and Knoll, 2012) of which some show the "earliest compelling evidence for biologically controlled eukaryotic biomineralization" (Cohen *et al.*, 2011, p. 541). A recent study of the Fifteenmile Group by Sperling *et al.* (2013) concluded that mostly ferruginous deep waters were overlain by oxygenated shelf waters and that the oxygen level in the surface mixed layer should have been high enough to support early metazoa.

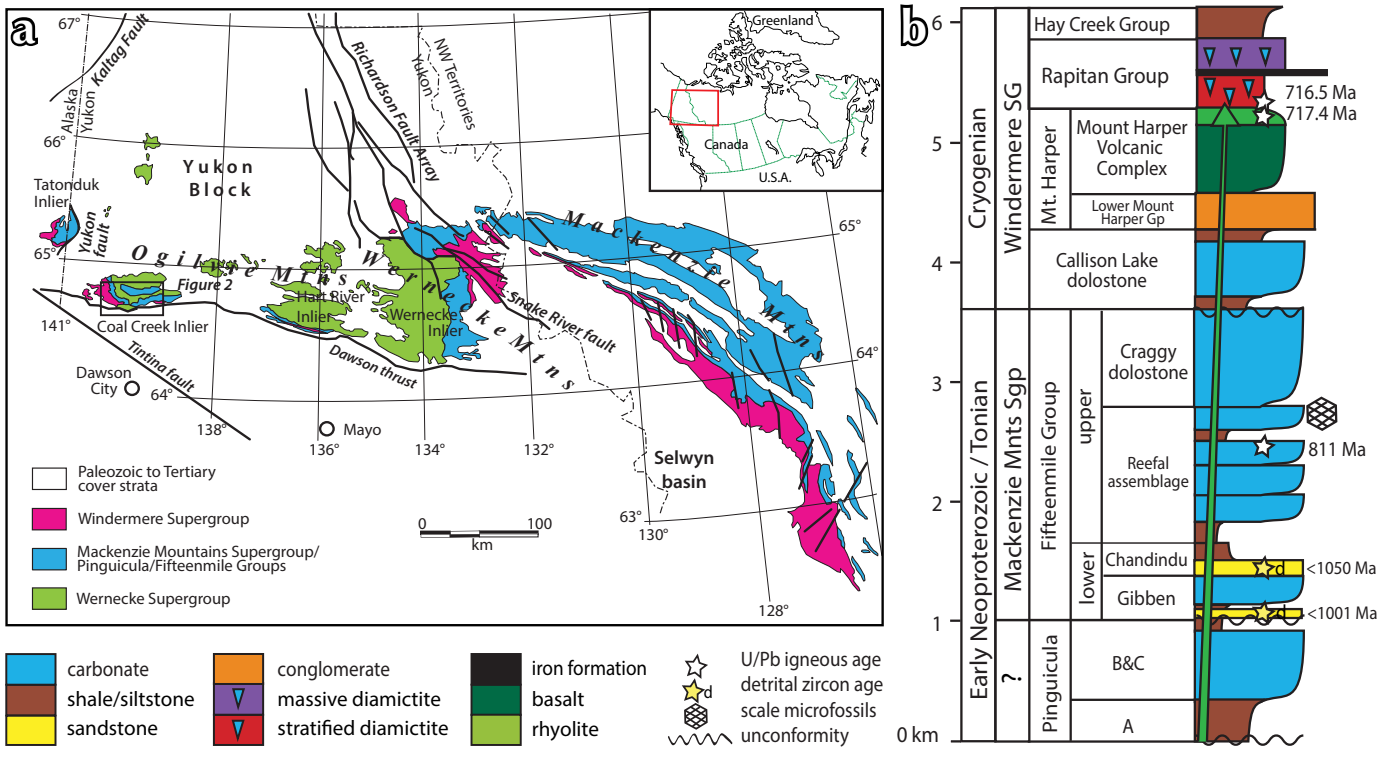

Figure 1. *Simplified geology and stratigraphy of the study area: (a) distribution of Proterozoic strata in inliers in Yukon and the Northwest Territories. Black box of the Coal Creek inlier indicates the area shown in Figure 2. Modified from Macdonald et al. (2011); and (b) lithostratigraphy of Tonian and Cryogenian strata in the Ogilvie Mountains. Modified from Macdonald et al. (2012).*

In this paper, we describe the sedimentology and lateral variation of the Chandindu Formation of the lower Fifteenmile Group in the Coal Creek and Hart River inliers, and also describe a proposed type section in detail. These data provide constraints on the depositional environment and basin topography, which in turn have implications for basin evolution, regional correlations, and biogeochemical data obtained from this succession.

FIFTEENMILE GROUP

The Fifteenmile Group (Fig. 1b; Thompson *et al.*, 1987; Roots and Thompson, 1992; Thompson *et al.*, 1994) in the Ogilvie Mountains is part of the early Neoproterozoic "Succession B" of northwestern Laurentia which also comprises the Mackenzie Mountains Supergroup in the Wernecke and Mackenzie mountains, and the Shaler Supergroup on Victoria Island (Young *et al.*, 1979; Eisbacher, 1981; Rainbird *et al.*, 1996; Long *et al.*, 2008). In the central Ogilvie Mountains, the Fifteenmile Group originally included all strata that unconformably rest on the late Paleoproterozoic Wernecke Supergroup (Delaney, 1981; Thorkelson, 2000; Thorkelson *et al.*, 2005) and unconformably underlie the mid-Neoproterozoic Callison Lake dolostone (Abbott, 1997; Macdonald and Roots, 2010) and Mount Harper Group (Mustard and Roots, 1997; Macdonald *et al.*, 2011; Cox *et al.*, 2013) of the Windermere Supergroup. Following initial subdivision of the Fifteenmile Group into five lower (PR1-PR5) and three upper (PF1-PF3) map units (Thompson *et al.*, 1994), Abbott (1993) introduced a fourth upper map unit (PF4) and extended the nomenclature to the Hart River inlier. Subsequently, Abbott (1997) renamed PF4 the "Callison Lake dolostone" and interpreted the entire succession between Wernecke Supergroup and Callison Lake dolostone to represent the Pinguicula Group in the Ogilvie Mountains. The Pinguicula Group is a mixed siliciclastic-carbonate unit and was originally defined in the Wernecke Mountains (Eisbacher, 1978b; 1981), where it was subdivided into five units (A-E). Young *et al.* (1979) subsequently correlated it with the Mackenzie Mountains and Shaler supergroups. Later, Thorkelson *et al.*, (2005) proposed that only the upper units correlate with the Mackenzie Mountains Supergroup. Following re-mapping, Macdonald *et al.* (2011) assigned the lower four map units (PR1-PR4) to the Pinguicula Group and the upper map units (PF1-PF3) to the Fifteenmile Group. Correlation of PR1 and PR2 with the Pinguicula Group was also suggested by Medig *et al.* (2010) based on stratigraphic similarities and contact relationships with the underlying Wernecke Supergroup. Medig *et al.* (2013) subsequently suggested that the base of the purported Pinguicula Group in the Coal Creek inlier (PR1, or PA in our mapping) is in fact an older unit. This raises the possibility that the Pinguicula Group does not occur in the Coal Creek inlier.

Recently, new radiometric ages coupled with chemostratigraphy motivated revised regional correlations of the Fifteenmile Group in the central Ogilvie Mountains with strata in other inliers in Yukon, the Mackenzie Mountains, and on Victoria Island (Macdonald *et al.*, 2010a,b; Macdonald and Roots (2010); Halverson *et al.*, 2012; Macdonald *et al.*, 2012). The first direct age constraint on the Fifteenmile Group came from a tuff in the upper half of the succession (Fig. 1b) that yielded a U-Pb zircon age of 811.51±0.25 Ma (Macdonald *et al.*, 2010b). A 717.43±0.14 Ma U-Pb zircon age from a rhyolite in the Mount Harper Volcanic Complex, upper Mount Harper Group, places a minimum age on the Fifteenmile Group. Subsequently, Macdonald and Roots (2010) correlated the Fifteenmile Group in the Coal Creek inlier with the Lower Tindir Group of the Tatonduk inlier and refined correlations with strata in the Hart River inlier. As a consequence, Macdonald *et al.* (2011) recommended abandonment of the term Tindir Group to simplify stratigraphic nomenclature across the inliers. Furthermore, they subdivided the Fifteenmile Group into a "Lower Assemblage" composed of mixed clastic rocks and dolostone, conformably followed by the "Craggy Dolostone" (Macdonald *et al.*, 2011). Most recently, Halverson *et al.* (2012) subdivided the Lower Assemblage into the "Gibben", "Chandindu", and "Reefal Assemblage" formations. They proposed correlation of a basal sandstone in the Gibben formation with map unit PPD1 in the Hart River inlier (Abbott, 1997), correlation of the remaining Gibben formation with PPD2, and correlation of the Chandindu formation with PPD3.

The basal sandstone unit in the Gibben formation unconformably overlies the Pinguicula Group (as mapped), and grades upward into shallow marine ooid and coated-grain packstone and grainstone, with microbial laminite and evidence of subaerial exposure increasing up section (Halverson *et al.*, 2012; Macdonald *et al.*, 2012). In the Hart River inlier, the Gibben formation, as currently defined, includes a basal interval of fine-grained siliciclastic rocks, which is succeeded by a shoaling upward carbonate sequence that is virtually identical to that described in the Coal Creek inlier. Due to syn-depositional extensional tectonics and deposition in fault-bound grabens, the thickness can vary from less than 20 m to 600 m (Halverson *et al.*, 2012; Macdonald *et al.*, 2012).

The Gibben formation is overlain by a prominent interval of mud-cracked, maroon shale and siltstone which grade into grey shale, and siltstone and sandstone with rare stromatolite bioherms and olistoliths. This mainly clastic unit comprises the up to 400-m-thick Chandindu Formation, as informally proposed by Halverson *et al*. (2012). The top of the Chandindu Formation is a prominent flooding interval.

The overlying 500 to 1700-m-thick Reefal Assemblage is mostly composed of thick, grey, stromatolitic boundstone, grainstone, ribbonite, and rhythmite interbedded with prominent black shale intervals representing maximum flooding surfaces (Halverson *et al*., 2012; Macdonald *et al*., 2012). The formation is marked by significant lateral facies changes controlled by early Fifteenmile Group syn-depositional, down-to-the-northwest, normal faulting that generated significant basin relief. Lateral facies variation is interpreted to represent NW-prograding reef systems that grade laterally into siliciclastic basinal deposits representing grabens or half-grabens (Halverson *et al*., 2012; Macdonald *et al*., 2012).

The following >500-m-thick Craggy Dolostone is mostly composed of light grey, strongly silicified and recrystallized, ridge-forming dolostone, consisting mostly of microbial laminite, ooid and coated-grain pack and grainstone, tabular clast conglomerate, and gravity flow breccia. Macdonald *et al*. (2012) concluded that the Craggy Dolostone represents the establishment of a broad stable carbonate platform and infilling of Reefal Assemblage sub-basins. However, more recent observations show significant lateral facies changes and large volumes of gravity flow breccia that imply more complex seafloor topography and may indicate continued extensional tectonism. The top of the Craggy Dolostone is truncated by the sub-Callison Lake Dolostone unconformity.

CHANDINDU FORMATION (NEW)

The proposed type section of the Chandindu Formation is M103, about 15 km northeast of Mount Harper (Fig. 2). A northeast-trending ridge provides continuous exposure of the unit, which is typically recessive weathering and slightly more vegetated than the grey-weathering rubble-covered slopes of the over and underlying units (Fig. 3). Here the Chandindu Formation is 249 m thick (Fig. 4), with clear lower and upper boundaries. The base of the section (N64°45′15.4″, W139°32′21.9″) is located on a north-facing slope and repeated by a fault. This fault causes a repetition of about 20 m of the uppermost underlying Gibben formation and the base of the Chandindu Formation (Fig. 5a).

The top of the underlying Gibben formation is composed of medium-grey and medium-bedded microbial laminite and minor grainstone indicating deposition in a peritidal environment. Secondary black chert bands, up to 5 cm thick, cut carbonate bedding in places. A sharp contact with a prominent mud-cracked (Fig. 5b), reddish siltstone with grey-brown shale interbeds marks the base of the Chandindu Formation. This distinct and laterally continuous mud-cracked interval makes identifying the base of the Chandindu Formation straightforward. In this section, the mud-cracked interval consists of 17 m of alternating fine-grained, grey-green (black-weathering), mostly thickly laminated to very thinly bedded, well-sorted sandstone with common mud cracks and grey-green siltstone. The mud-cracked interval is succeeded by 232 m of moderately well defined coarsening-upward cycles with no mud cracks. These cycles typically consist of dark grey to black, thinly laminated silty shale and shale between a few decimeters and a few meters thick at the base; a middle interval of tens of metres of grey-green, thickly laminated siltstone; and fine-grained, well sorted, very thinly bedded, grey sandstone ranging in thickness from 1 decimeter to 1-2 m at the top (Fig. 5c). Coarsening-upward cycles are typical for the Chandindu Formation and are observed in every section (Fig. 8). Sandstone beds commonly contain hummocky cross-stratification (*e.g.*, in section MY1301, Fig. 8), and locally other indications of a storm-dominated environment (Fig. 5d). Three beds of ribbonite-facies carbonate (facies types were described by Macdonald and Roots, (2010) and Macdonald *et al*., (2012)) also occur throughout this interval. A prominent feature of the uppermost Chandindu Formation in this section is the occurrence of olistoliths: a 2 m-thick block of stromatolite and a 6 m-thick block of grainstone and stromatolite. Following Halverson *et al*. (2012), we place the top of the Chandindu Formation at the base of the uppermost maximum flooding surface (that is an abrupt shift to finer grained rocks, typically black shale) which separates the siliciclastic-dominated Chandindu Formation from the overlying carbonate-dominated informal Reefal Assemblage. However, we note that in more siliciclastic-dominated sections, this boundary can be somewhat difficult to identify.

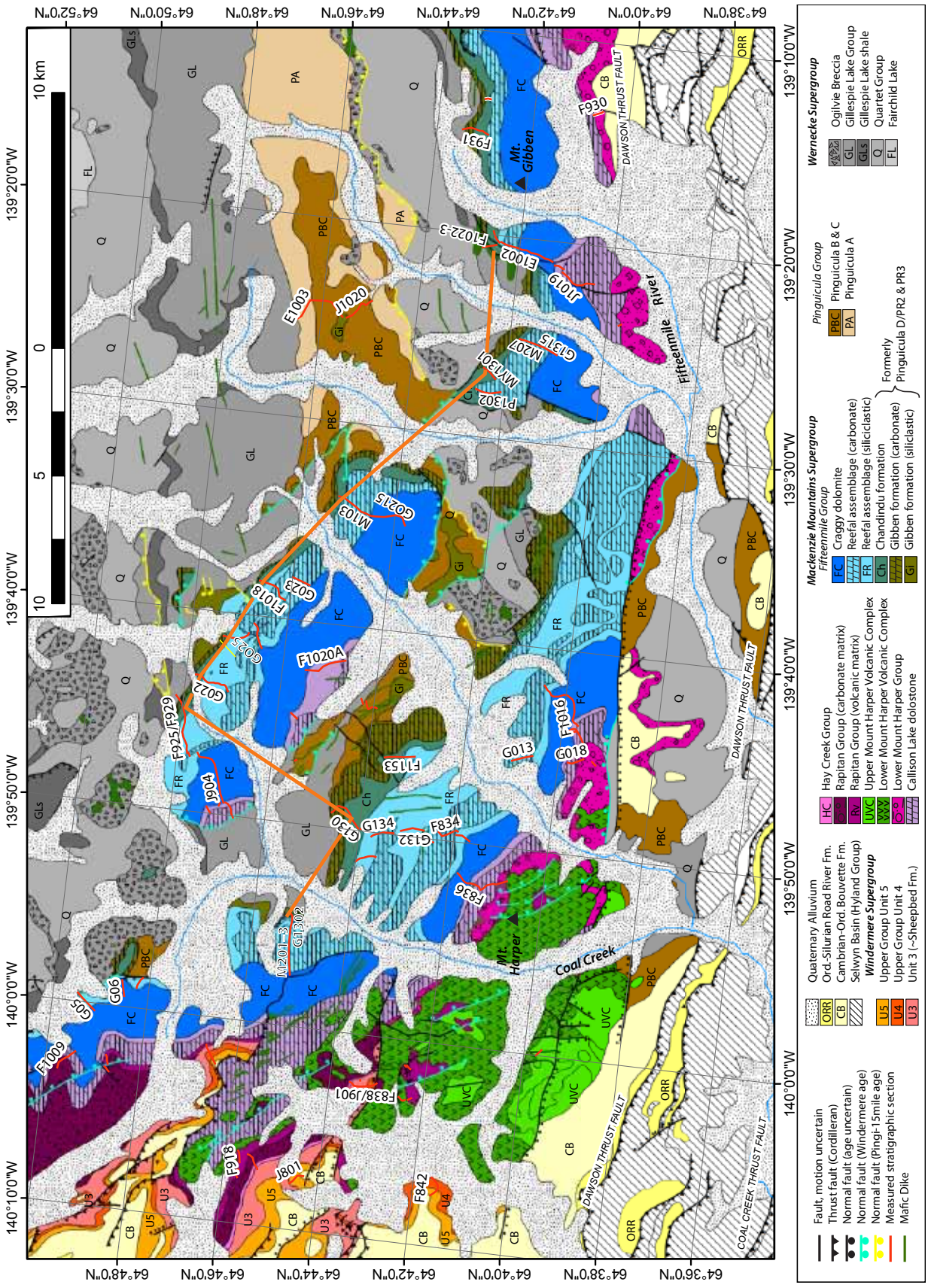

Figure 2. *Geological map of the Coal Creek inlier in the central Ogilvie Mountains. Orange line indicates the location of the Chandindu Formation transect shown in Figure 8.*

***Figure 3**. View northwestward of Fifteenmile Group including the well exposed type section of the Chandindu Formation. Field of view is about 3 km.*

PETROGRAPHY OF SILICICLASTIC ROCKS

To characterize the siliciclastic Chandindu Formation, we applied optical microscopy and scanning electron microscopy (SEM) on specimens of sandstone, siltstone, and shale collected from type section M103. Here, we describe one example from each type (Fig. 4). Petrographic thin sections were investigated with a Hitachi S-3000N Variable Pressure-SEM (VP-SEM) equipped with an Oxford INCA microanalytical system (energy dispersive X-ray spectrometry (EDS) detector). The samples were studied in backscattered electron (BSE) SEM mode at an acceleration voltage of 15 kV, an emission current of 64 µA, and a vacuum pressure of 20 Pa. Selected areas were analyzed with the SEM-EDS microanalytical system for approximately 15 to 20 minutes to obtain element distribution maps. Descriptions of the carbonate facies types can be found elsewhere (*e.g.*, Macdonald *et al.*, 2012).

Sandstone (M103.1.0): This sample comes from a 3.1 m-thick sandstone interval at the base of M103 (Fig. 4). The black-weathering, fine-grained sandstone is reddish-grey on fresh surfaces and breaks into laminae 0.5-1.0 cm thick. Siltstone interbeds, shale partings, mm-scale mud drapes, and mud cracks occur. In thin section, the rock is composed of about 90% quartz and 10% sericite. The mineralogically mature rock is very well sorted with up to 160 µm-large monocrystalline quartz crystals that show slight undulose extinction. Roundness and sphericity of quartz grains are difficult to evaluate due to compaction (Fig. 6a), which causes straight crystal boundaries and the undulose extinction. However, quartz grains seem to have a high sphericity. Porosity is estimated to be less than 1%. The sericite occurs in mud drapes up to 2 cm long and 2 mm thick and indicates alteration of primary phyllosilicates. Precise identification of minerals would require Transmission Electron Microscopy (TEM) and X-ray powder diffraction (XRD). The mud drapes show an internal parallel and continuous lamination caused by a material difference (Fig. 6a) and also include up to 100 µm-large, anhedral, round to elliptical opaque phases (Fig. 6a). Scanning electron microscopy shows that these phases are often composed of a concentric core of organic matter and an iron oxyhydroxide rim (Fig. 6b-d). The rim also contains small quartz and phyllosilicate crystals, which are likely inclusions that could suggest a secondary origin of the iron oxyhydroxide. These inclusions are also visible on element distribution maps (Fig. 6e-h). Alternatively, the iron oxyhydroxide could have precipitated early and quickly in association with the inclusions. These structures could be fragments of microbial mats preserved by the iron oxyhydroxide rim or even represent microfossils, but additional SEM and TEM studies are necessary to distinguish between these possibilities.

Siltstone (M103.143.2): This sample comes from the top of a 21.1-m-thick siltstone interval (Fig. 4). The grey to dark grey, partly rusty-weathering siltstone breaks into laminae ~ 0.5 cm thick. The sample was taken at the contact with overlying fine-grained sandstone (Fig. 7a,b). The rock is composed of about 50% quartz and 50% small phyllosilicate crystals, likely sericite resulting from alteration and low-grade metamorphism of clay minerals and mica. Individual quartz grains show undulose extinction and are up to 30 µm in diameter (Fig. 7c). The phyllosilicate crystals are <10 µm across (Fig. 7c,d). Organic matter mostly occurs as <50 µm-large irregular accumulations and is always mixed with quartz crystals (Fig. 7c,e). In contrast to organic matter occurrences in

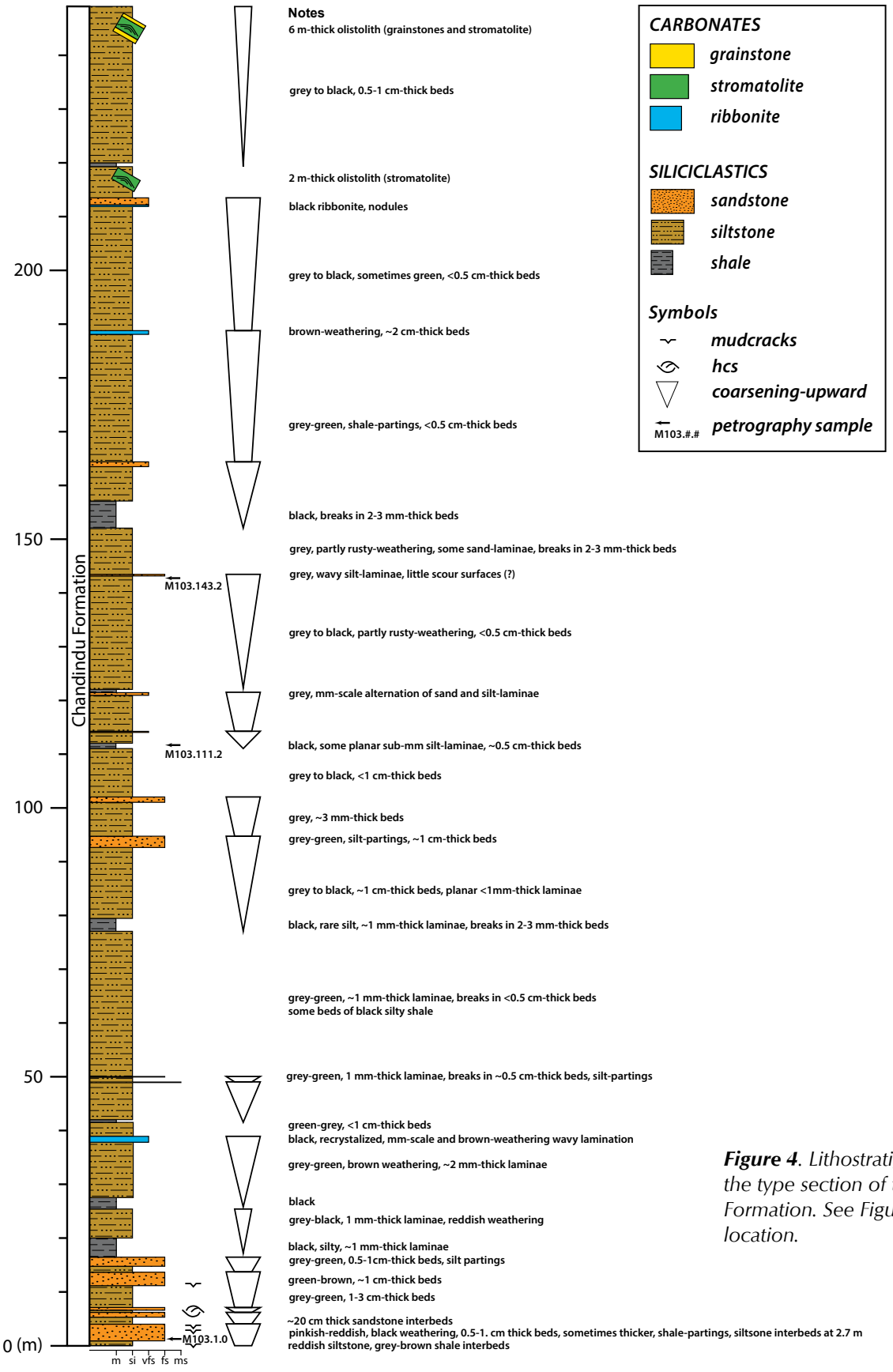

***Figure 4**. Lithostratigraphy of M103, the type section of the Chandindu Formation. See Figures 2 and 3 for location.*

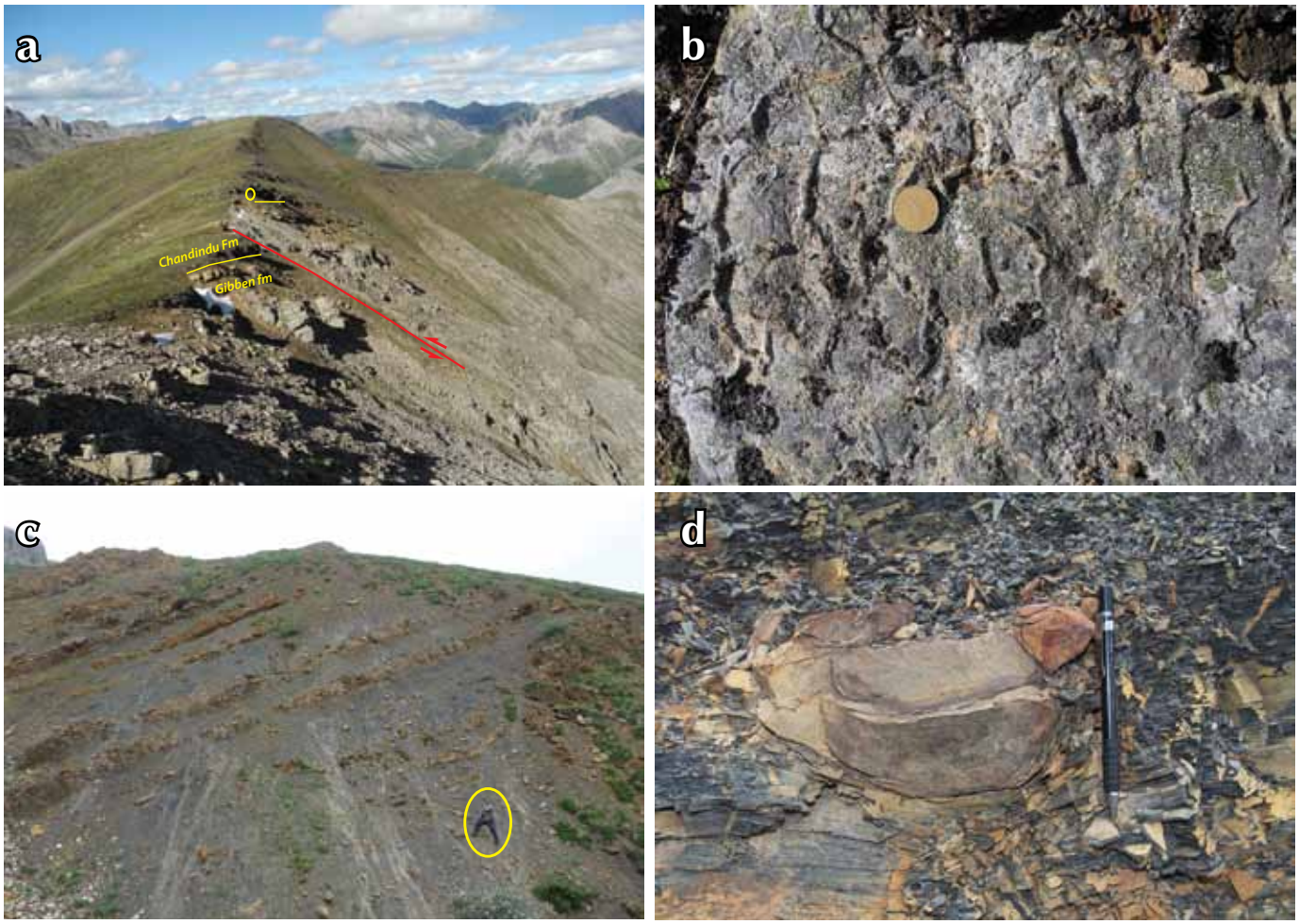

***Figure 5**. Outcrop photos of the Chandindu Formation. (a) Base of the Chandindu Formation in section M103 (yellow line) looking westward. The Gibben-Chandindu contact is repeated by a fault. Person (yellow ellipse) for scale. (b) Mud cracks of the basal Chandindu Formation in section M103. Coin for scale is 2.65 cm across. (c) Shale-siltstone-sandstone cycles in section MY1301 between 190 and 260 m above base. Person (yellow ellipse) for scale. (d) Cross section of sand-filled gutter cast in the lower Chandindu Formation in section MY1301. Pencil length is 15 cm.*

mud drapes of the sandstone sample M103.1.0, organic matter in siltstone does not occur as round structures and is not rimmed by iron oxyhydroxide (Fig. 7c,e). Organic matter accumulations in overlying fine-grained sandstone are also irregular but larger (<80 µm) and more common (Fig. 7b).

Shale (M103.111.2): The shale sample described here comes from a 1-m-thick interval in the middle of the Chandindu Formation (Fig. 4). The rock is dark-grey and contains some sub-millimeter-thick silt laminae. SEM study reveals that the rock consists of about 20% quartz and 80% phyllosilicates (Fig. 7f-h). The quartz crystals are less than 15 µm in diameter. Phyllosilicate crystals are less than 10 µm across (Fig. 7f). Element mapping helped to identify calcium-phosphorous-bearing minerals, likely apatite (Fig. 7g,h).

LATERAL VARIABILITY OF THE CHANDINDU FORMATION

Ten sections of the Chandindu Formation were logged in the central and eastern Ogilvie Mountains (Fig. 8). Nine were logged in the Coal Creek inlier, about 80 km north of Dawson City, and one section was logged in the Hart River inlier, about 120 km north of Mayo. In the western part of the Coal Creek inlier, near Mount Harper, the Chandindu Formation thickness is between 150 and 250 m. Further to the east, at Fifteenmile River and Mount Gibben, the thickness increases to 400-420 m (Fig. 8). In the Hart River inlier, the top of the Chandindu Formation is commonly truncated on a low-angle unconformity beneath the Callison Lake dolostone (Abbott, 1997; Macdonald *et al.*, 2011); however, in our measured section, it is

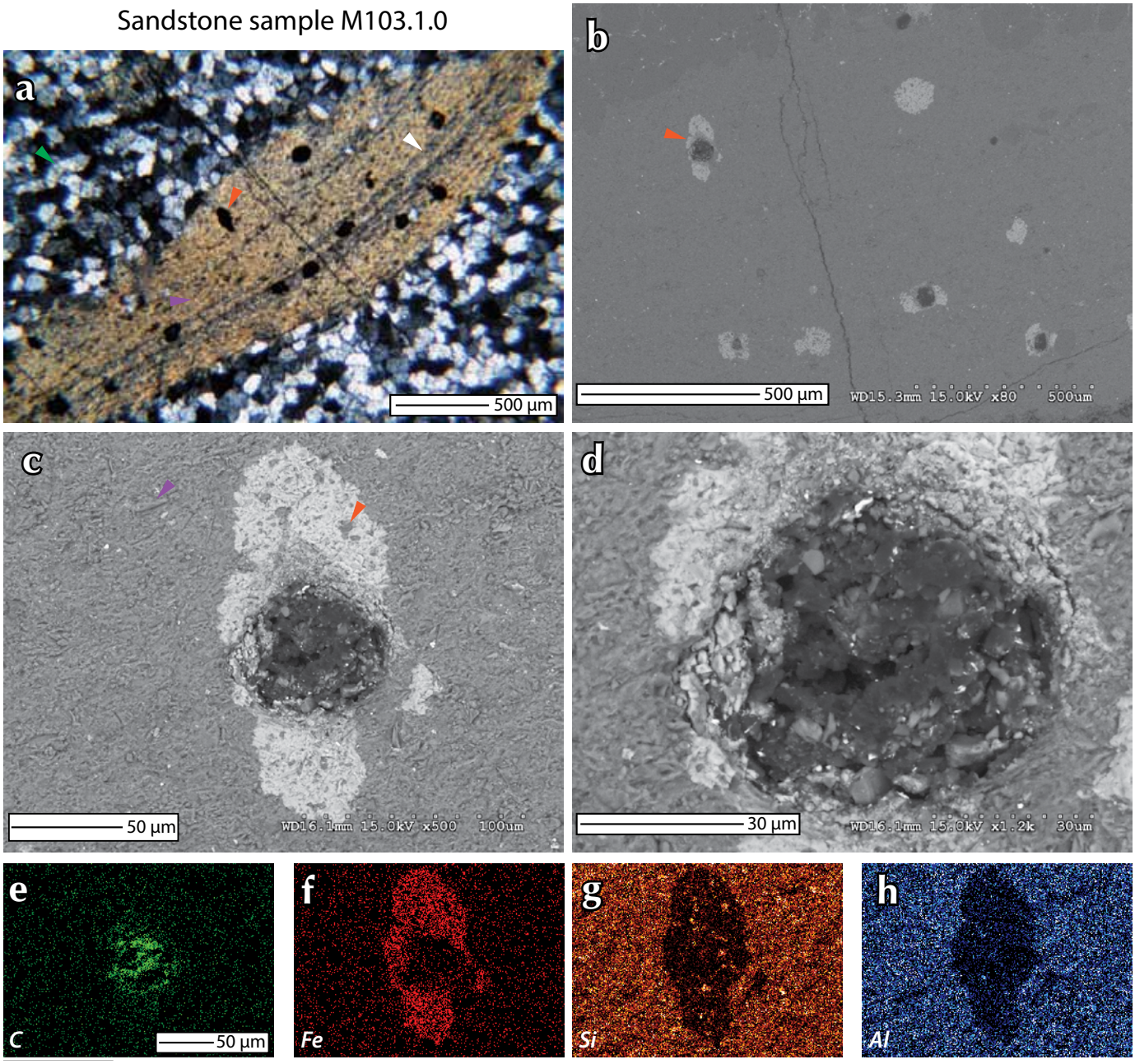

Figure 6. *Thin section and SEM-BSE images of the sandstone sample M103.1.0. (a) Sericitized mud drape (purple arrow, brown interval) floats in well-sorted quartz arenite (green arrow). The mud drape shows an internal parallel lamination (white arrow) and about 100 µm-large opaque phases (orange arrow). Cross-polarized light. (b) SEM imaging reveals that many opaque phases consist of a core of organic matter. The object shown in (c) is indicated by the orange arrow. (c) Higher magnification shows that <5 µm-large quartz crystals occur as inclusion in the rim (orange arrow). Note small crystal size (<10 µm, purple arrow) of sericite. (d) Close-up of organic matter in (c) that forms the core. (e to h) Element distribution maps of the area shown in (c) clearly distinguishes the carbon-rich core, iron-rich rim and aluminium and silica-rich phyllosilicates (sericite) of the surrounding material. Scale shown in (e) also applies to maps (f, g, and h) of other elements.*

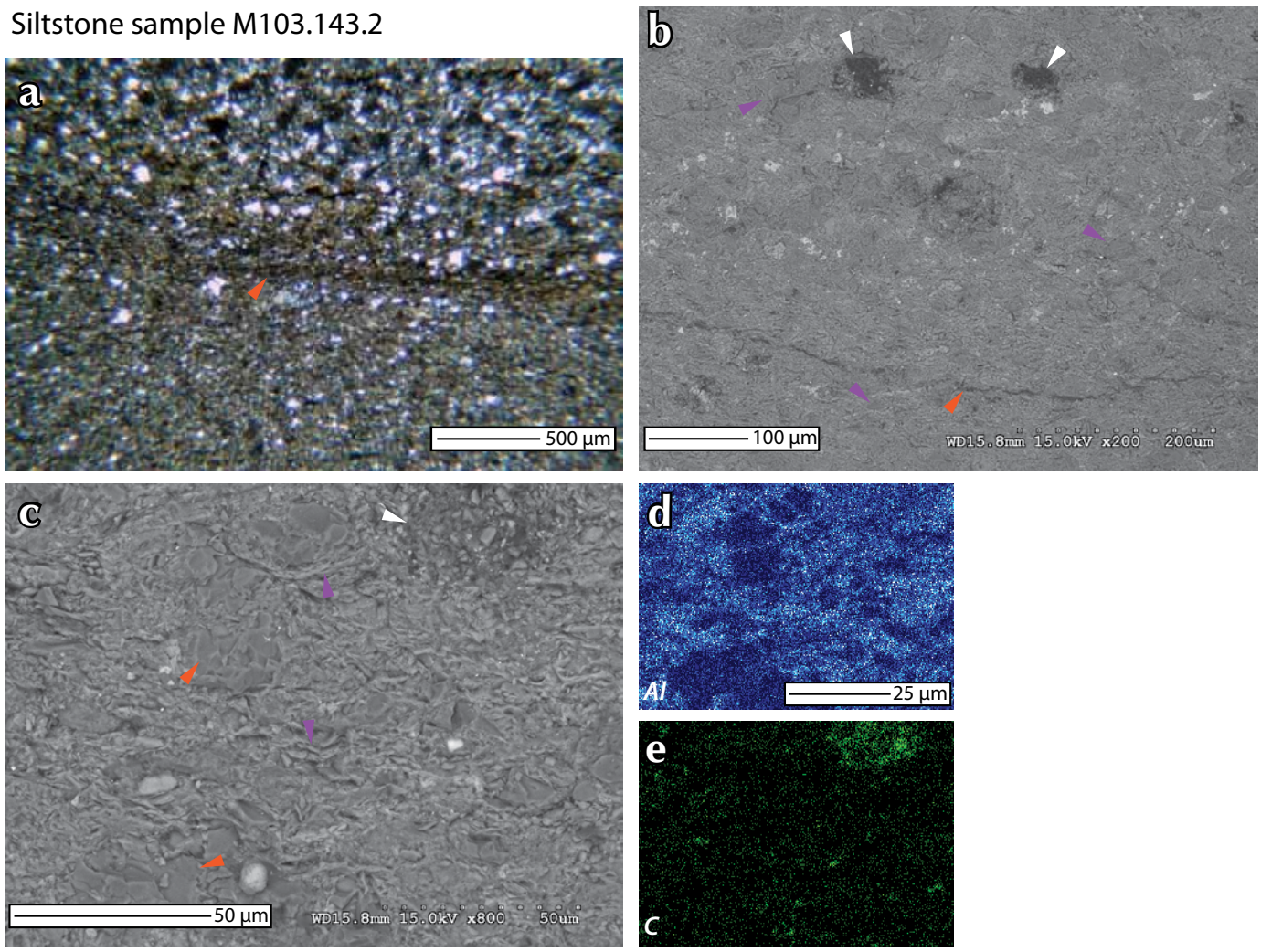

***Figure 7**. Thin section and SEM-BSE images of the siltstone sample M103.143.2 (a-e; this page) and shale sample M103.111.2 (f-h; next page). (a) Thin section photograph of the contact (orange arrow) between siltstone (below) and fine-grained sandstone (above). (b) SEM backscatter image of the siltstone-sandstone contact (orange arrow). Note significant larger size of quartz crystals (purple arrows) above the contact and larger accumulations of organic matter (white arrows, black clots). (c) Higher magnification of the siltstone part shows up to 30 µm-large quartz crystals (orange arrows), less than 10 µm-large phyllosilicates (purple arrows), and an irregular accumulation of organic matter (white arrow). (d) Aluminium distribution map shows dominance of phyllosilicates and occurrence of larger quartz crystals (lack of aluminium, dark areas). (e) Carbon distribution map helps to identify the concentration of organic matter in the upper right corner of photo. See (d) for scale.*

truncated by an unconformity at the base of the early Paleozoic Bouvette Formation, resulting in a partial thickness of the Chandindu Formation of < 200 m.

The dominant lithology in the Chandindu Formation is siltstone with minor shale and sandstone typically arranged in coarsening-upward cycles (for example in the type section M103 or in MY1301 about 190-260 m above base, Figs. 4 and 5c). However, carbonate rocks representing diverse depositional environments occur in every section.

DISCUSSION

The Chandindu Formation is conformably bound by the older Gibben formation and the younger Reefal Assemblage (Fig. 1b). The sharp base of the Chandindu Formation reflects an abrupt change of the depositional environment from a shallow marine carbonate environment dominated by microbial laminite formed on tidal flats and high-energy grainstone bars, to a muddy tidal flat where fine-grained siliciclastic sediments were deposited. The contact with the overlying Reefal

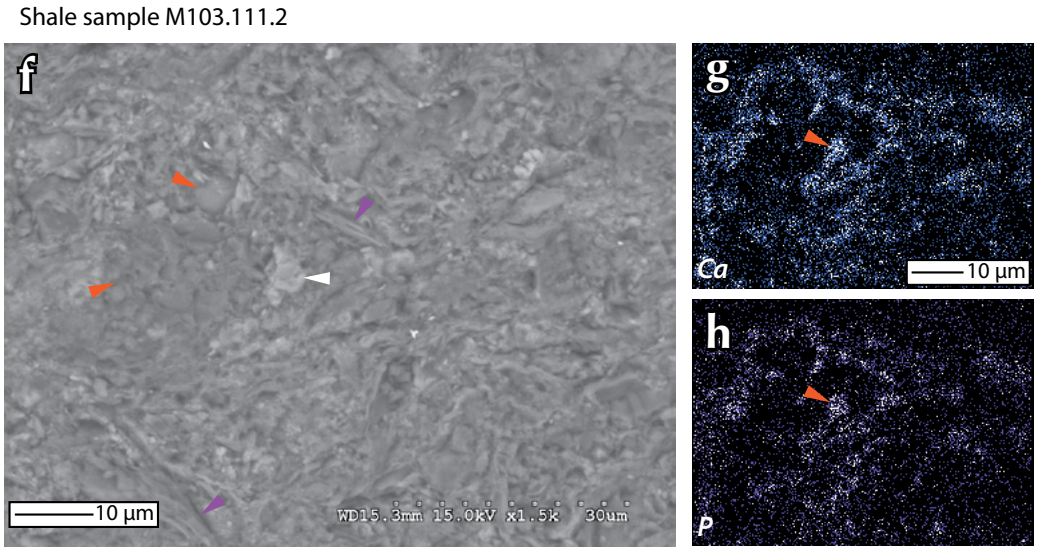

***Figure 7 con'd**. (f) SEM-BSE image of shale sample M103.111.2. Note occurrence of quartz crystals (orange arrows), phyllosilicates (purple arrows), and apatite (white arrow). (g and h) Distribution maps of calcium and phosphorous show correlation in some areas (for example orange arrow) indicating occurrence of apatite. Scale in (g) also applies to (h).*

Assemblage is marked by a prominent maximum flooding surface indicated by the occurrence of black shale. This flooding interval is usually overlain by the first reef deposits of the Reefal Assemblage. An exception is the section reported by Macdonald and Roots (2010) north of Mount Harper where deposition of black shale continued to dominate until deposition of the upper Reefal Assemblage.

The laterally extensive mud-cracked siliciclastic interval at the base of the Chandindu Formation (Fig. 8) suggests deposition on a large, partly exposed, muddy tidal flat. Base level rise up-section is indicated by the transition of this mud-cracked interval to coarsening-upward cycles of shale, siltstone, and sandstone, sporadically capped by carbonate, commonly stromatolitic (Halverson *et al.*, 2012). The coarsening-upward cycles indicate progradation and shallowing of the depositional environment. The occurrence of stromatolites at the top of some cycles points towards decreasing siliciclastic sedimentation rates and presages the eventual proliferation of stromatolite reef facies in the overlying Reefal Assemblage. Hummocky cross-stratification in sandstone of coarsening upward-cycles is evidence of common storm events and suggest deposition between storm and fair weather wave base (*e.g.*, Dott and Bourgeois, 1982; Duke, 1985; Leckie and Krystinic, 1989; Dumas and Arnott, 2006). Mild lateral thickness and facies variations, in particular in the lower part of the formation (Fig. 8), may indicate less extensional tectonic activity compared to the underlying Gibben formation. However, map relationships (Fig. 2) and the occurrence of large olistoliths in the upper part of the formation (for example in the type section, Fig. 4, see also Macdonald *et al.*, 2012) indicate syn-depositional faulting. Significant basin relief is also likely the reason why lithostratigraphic correlation of coarsening-upward cycles in the Chandindu Formation is not readily apparent. However, at least one flooding event (indicated by shale intervals) in the middle part of the unit is present in every section west of Mount Gibben.

One of the most striking features of the Chandindu Formation is the occurrence of different carbonate facies types throughout the formation in every section. The carbonate facies range from supratidal intraclast breccia to deep marine debris flow deposits and rhythmite (Fig. 8), and often forms laterally discontinuous mounds. Carbonate deposition was therefore not restricted to one depositional environment and the carbonate factory was never completely overwhelmed by the abundant siliciclastic input. What controlled carbonate versus siliciclastic deposition? A possible explanation is that a laterally extensive carbonate depositional environment, parallel to the shoreline, was interrupted by terrigenous input from a delta. Lateral migration of distributary channels could have controlled the spatial distribution of siliciclastic versus carbonate deposition. Another possible explanation is that rift-inherited complex basin topography, further enhanced by syn-depositional faulting, controlled the sedimentation regime. Carbonate deposition established in areas of low siliciclastic background sedimentation, for example, on paleohighs on fault-bound rift blocks. Here, stromatolite bioherms and grainstone bars (the two most common carbonate facies types in the Chandindu Formation) preferentially developed (Fig. 8), providing a source for olistoliths in the Chandindu Formation (*e.g.*, M103; Figs. 4 and 8).

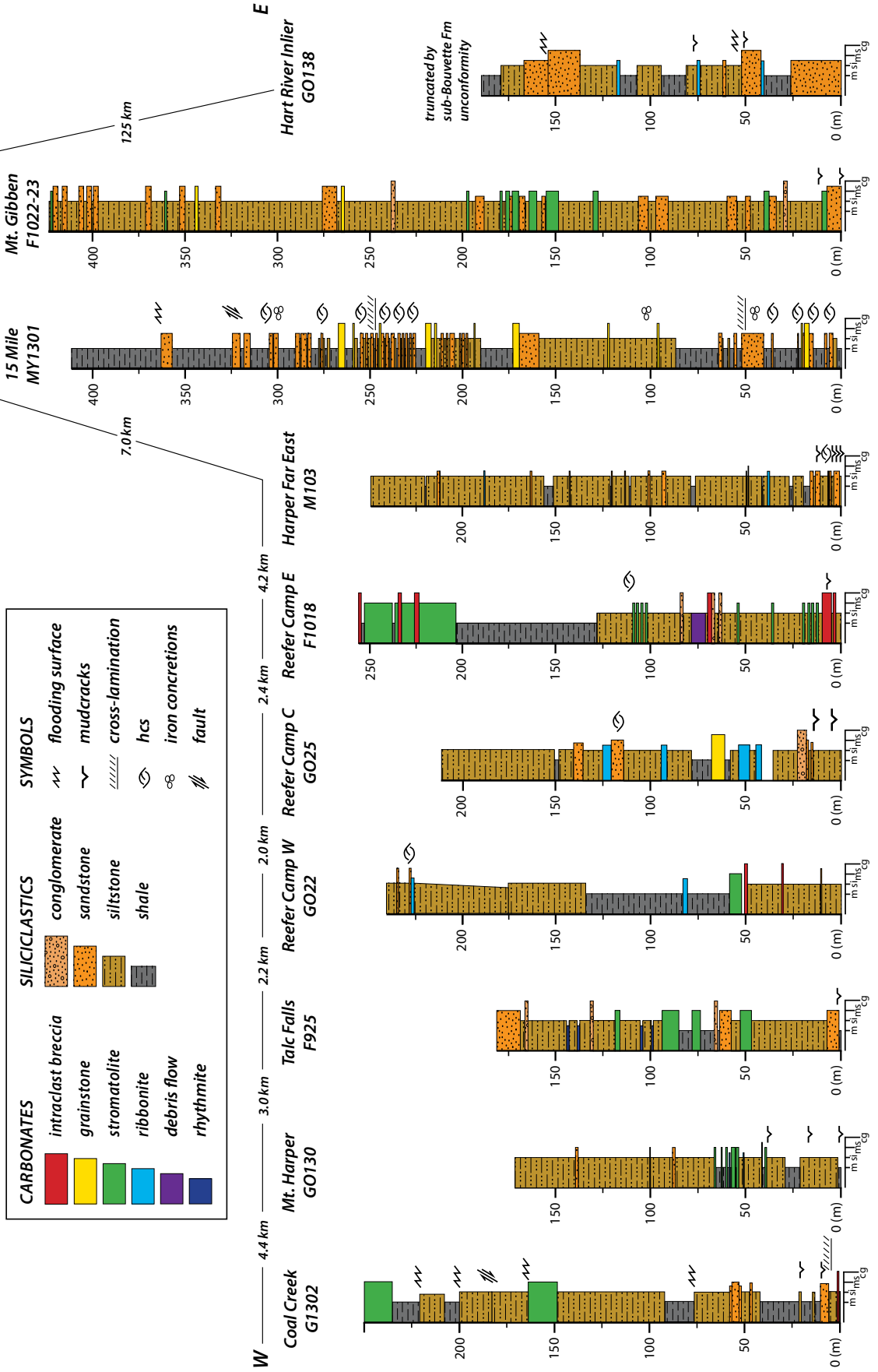

Figure 8. *West-east transect of the Chandindu Formation across the Coal Creek inlier (see Figure 2 for location of sections) plus additional section from the Hart River Inlier. Note dominance of siltstone and occurrence of carbonate (ranging from tidal flat to sub-storm wave base deposits) in every section.*

The Chandindu Formation in the Hart River inlier contains a significantly higher ratio of sandstone to siltstone, which is consistent with the occurrence of a deltaic system to the east (in present coordinates) and at least partial correlation of the Chandindu Formation with the Katherine Group. In the Wernecke and Mackenzie mountains, the Katherine Group is a thick succession of fluvial-deltaic quartz arenite and marine siltstone and sandstone (Eisbacher, 1978b, 1981; Thorkelson, 2000; Thorkelson *et al*., 2005; Turner, 2011; Long and Turner, 2012) that likely represents the proximal facies of a delta. Rainbird *et al*., (1997) previously postulated that the Katherine delta was fed by continent-scale, northwesterly migrating river systems that originated from the Grenvillian orogeny based on the predominance of *ca.* 1 Ga detrital zircons in the Katherine sands. The high degree of maturity of the sandstones in the Chandindu Formation (see petrographic description) is consistent with an interpretation of distal equivalent of parts of the Katherine Group, although documentation of Grenvillian-aged tectonothermal activity in the northern Cordillera (Thorkelson *et al*., 2005; Milidragovic *et al*., 2011) allows that the *ca.* 1 Ga zircons may have been more locally sourced. Correlation of the lower Fifteenmile Group in the Coal Creek and Hart River inliers with parts of the Katherine and Hematite Creek groups in the Wernecke Mountains (Turner, 2011; Macdonald *et al*., 2012) is still poorly understood and needs to be tested in future studies.

CONCLUSION

We describe the type section of the early Neoproterozoic Chandindu Formation. This overall deepening-upward unit represents diverse depositional regimes ranging from supra and intertidal to subtidal environments dominated by siliciclastic sedimentation. Deposition of carbonate most likely occurred on rift-related paleohighs where the site of deposition was protected from siliciclastic input. Parts of the fluvial-deltaic Katherine Group further to the east (present coordinates) are a possible source of the terrigenous material.

ACKNOWLEDGMENTS

We are grateful for financial support from the Yukon Geological Survey, NSERC, American Chemical Society Petroleum Research Fund, and the Polar Continental Shelf Program. MK acknowledges support by a GEOTOP scholarship and a J.B. Lynch Fellowship. Justin Strauss, Emily Smith, Eric Bellefroid, Thomas Maguire, Lyle Nelson, and Danielle Thomson helped in the field. Hojatollah Vali is thanked for access to the Facility for Electron Microscopy Research (FEMR) at McGill and Tanja Bosak for discussions. We sincerely thank Charlie Roots and his family for their hospitality and help with logistics. Charlie Roots is also thanked for a constructive and detailed review that improved the paper. We acknowledge logistical support by Don Francis. Finally, we thank Fireweed Helicopters for safe transportation.

REFERENCES

Abbott, J.G., 1993. Revised stratigraphy and new exploration targets in the Hart River region (NTS 116A/10, 116A/11), southeastern Ogilvie Mountains. *In:* Yukon Exploration and Geology 1992, Exploration and Geological Services Division, Yukon, Indian and Northern Affairs, Canada, p. 13-23.

Abbott, J.G., 1997. Geology of the Upper Hart River area, eastern Ogilvie Mountains, Yukon Territory (116A/10, 116A/11). Exploration and Geological Services Division, Yukon Region, Bulletin 9, 76 p.

Butterfield, N.J., 2004. A vaucheriacean algae from the middle Neoproterozoic of Spitsbergen: implications for the evolution of Proterozoic eukaryotes and the Cambrian explosion. Paleobiology, vol. 30 (2), p. 231-252.

Canfield, D.E., Poulton, S.W., Knoll, A.H., Narbonne, G.M., Ross, G., Goldberg, T., and Strauss, H., 2008. Ferruginous conditions dominated later Neoproterozoic deep-water chemistry. Science, vol. 321, p. 949-952.

Cohen, P.A. and Knoll, A.H., 2012. Scale microfossils from the mid-Neoproterozoic Fifteenmile Group, Yukon Territory. Journal of Paleontology, vol. 86 (5), p. 775-800.

Cohen, P.A., Schopf, J.W., Butterfield, N.J., Kudryavtsev, A.B., and Macdonald, F.A., 2011. Phosphate biomineralization in mid-Neoproterozoic protists. Geology, vol. 39 (6), p. 539-542.

Cox, G.M., Roots, C.F., Halverson, G.P., Minarik, W.G., Macdonald, F.A., and Hubert Théou, L., 2013. Mount Harper Volcanic Complex, Ogilvie Mountains: A far-flung occurrence of the Franklin Igneous Event? *In:* Yukon Exploration and Geology 2012, K.E. MacFarlane, M.G. Nordling, and P.J. Sack (eds.), Yukon Geological Survey, p. 19-36.

Delaney, D.G., 1981. The mid-Proterozoic Wernecke Supergroup, Wernecke Mountains, Yukon Territory. *In:* Proterozoic Basins of Canada, F.H.A. Campbell (ed.), Geological Survey of Canada, Paper 81-10, p. 1-24.

Dott, R.J. and Bourgeois, J., 1982. Hummocky stratification: Significance of its variable bedding sequences. Geological Society of America Bulletin, vol. 93, p. 663-680.

Duke, W.L., 1985. Hummocky cross-stratification, tropical hurricanes, and intense winter storms. Sedimentology, vol. 32, p. 167-194.

Dumas, S. and Arnott, R.W.C., 2006. Origin of hummocky and swaley cross-stratification – The controlling influence of unidirectional current and aggradation rate. Geology, vol. 34 (12), p. 1073-1076.

Eisbacher, G.H., 1978a. Redefinition and subdivision of the Rapitan Group, Mackenzie Mountains. Geological Survey of Canada, Paper 77-35, 21 p.

Eisbacher, G.H., 1978b. Two major Proterozoic unconformities, northern Cordillera. Geological Survey of Canada, Current Research Paper 78-1A, p. 53-58.

Eisbacher, G.H., 1981. Sedimentary tectonics and glacial record in the Windermere Supergroup, Mackenzie Mountains, northwestern Canada. Geological Survey of Canada, Paper 80-27, 40 p.

Gabrielse, H., 1972. Younger Precambrian of the Canadian Cordillera. American Journal of Science, vol. 272, p. 521- 536.

Halverson, G.P., Macdonald, F.A., Strauss, J.V., Smith, E. F., Cox, G.M, and Hubert-Théou, L., 2012. Updated definition and correlation of the lower Fifteenmile Group in the central and eastern Ogilvie Mountains. *In:* Yukon Exploration and Geology 2011, K.E. MacFarlane and P.J. Sack (eds.), Yukon Geological Survey, p. 75-90.

Johnston, D. T., Poulton, S.W., Dehler, C., Porter, S., Husson, J., Canfield, D.E., and Knoll, A.H., 2010. An emerging picture of Neoproterozoic ocean chemistry: Insights from the Chuar Group, Grand Canyon, USA. Earth and Planetary Science Letters, vol. 290, p. 64-73.

Jones, D.S., Maloof, A.C., Hurtgen, M.T., Rainbird, R.H., and Schrag, D.P., 2010. Regional and global chemostratigraphic correlation of the early Neoproterozoic Shaler Supergroup, Victoria Island, Northwestern Canada. Precambrian Research, vol. 181, p. 43-63.

Knoll, A.H., Javaux, E.J., Hewitt, D., and Cohen, P.A., 2006. Eukaryotic organisms in Proterozoic oceans. Philosophical Transactions of the Royal Society of Biological Sciences, vol. 361, p. 1023-1038.

Leckie, D.A. and Krystinic, L.F., 1989. Is there evidence for geostrophic current preserved in the sedimentary record of inner to middle-shelf deposits? Journal of Sedimentary Petrology, vol. 59, p. 862-870.

Long, D.G.F., Rainbird, R.H., Turner, E.C., and MacNaughton, R.B., 2008. Early Neoproterozoic strata (Sequence B) of mainland northern Canada and Victoria and Banks islands: a contribution to the Geological Atlas of the Northern Canadian Mainland Sedimentary Basin. Geological Survey of Canada, Open File 5700, p. 1-24.

Long, D.G.F. and Turner, E.C., 2012. Formal definition of the Neoproterozoic Mackenzie Mountains Supergroup (Northwest Territories), and formal stratigraphic nomenclature for terrigenous clastic units of the Katherine Group. Geological Survey of Canada, Open File 7113, 40 p.

Macdonald, F.A. and Roots, C.F., 2010. Upper Fifteenmile Group in the Ogilvie Mountains and correlations of early Neoproterozoic strata in the northern Cordillera. *In:* Yukon Exploration and Geology 2009, K.E. MacFarlane, L.H. Weston, and Blackburn L.R. (eds.), Yukon Geological Survey, p. 237-252.

Macdonald, F.A., Cohen, P.A., Dudás, F.Ö., and Schrag, D.P., 2010a. Early Neoproterozoic scale microfossils in the Lower Tindir Group of Alaska and the Yukon Territory. Geology, vol. 38 (2), p. 143-146.

Macdonald, F.A., Schmitz, M.D., Crowley, J.L., Roots, C.F., Jones, D.S., Maloof, A.C., Strauss, J.V., Cohen, P.A., Johnston, D.T., and Schrag, D.P., 2010b. Calibrating the Cryogenian. Science, vol. 327, p. 1241-1243.

Macdonald, F.A., Smith, E.F., Strauss, J.V., Cox, G.M., Halverson, G.P., and Roots, C.F., 2011. Neoproterozoic and early Paleozoic correlations in the western Ogilvie Mountains, Yukon. *In:* Yukon Exploration and Geology 2010, K.E. MacFarlane, L.H. Weston, and Relf, C. (eds.), Yukon Geological Survey, p. 161-182.

Macdonald, F.A., Halverson, G.P., Strauss, J.V., Smith, E.F., Cox, G.M., Sperling, E.A., and Roots, C.F., 2012. Early Neoproterozoic Basin Formation in Yukon, Canada: Implications for the make-up and break-up of Rodinia. Geoscience Canada, vol. 39, p. 77-99.

Medig, K.P.R., Thorkelson, D.J., Davis, W.J., Rainbird, R.H., Gibson, H.D., Turner, E.C., and Marshall, D.D., 2013. Evidence of the Laurentia-Australia connection? Detrital zircons from the Mesoproterozoic strata in Yukon, Canada. GAC-MAC 2013, Winnipeg, Program with abstracts, vol. 36, p. 143.

Medig, K.P.R., Thorkelson, D.J., and Dunlop, R.L., 2010. The Proterozoic Pinguicula Group: Stratigraphy, contact relationships and possible correlations. *In:* Yukon Exploration and Geology 2009, K.E. MacFarlane, L.H. Weston, and Blackburn, L.R. (eds.), Yukon Geological Survey, p. 265-278.

Milidragovic, D., Thorkelson, D.J., Davis, W.J., Marshall, D.D., and Gibson, H.D., 2011. Evidence for late Mesoproterozoic tectonism in northern Yukon and the identification of a Grenville-age tectonothermal belt in western Laurentia. Terra Nova, vol. 23, p. 307-313.

Mustard, P.S. and Roots, C.F., 1997. Rift-related volcanism, sedimentation, and tectonic setting of the Mount Harper Group, Ogilvie Mountains, Yukon Territory. Geological Survey of Canada Bulletin, vol. 492, 92 p.

Porter, S.M. and Knoll, A.H., 2000. Testate amoebae in the Neoproterozoic Era: evidence from vase-shaped microfossils in the Chuar Group, Grand Canyon. Paleobiology, vol. 26, p. 360-385.

Rainbird, R.H., Jefferson, C.W., and Young, G.M., 1996. The early Neoproterozoic sedimentary Succession B of northwestern Laurentia: Correlations and paleogeographic significance. Geological Society of America Bulletin, vol. 105, p. 454-470.

Rainbird, R.H., McNicoll, V.J., Thériault, R.J., Heaman, L.M., Abott, J.G., Long, D.G.F., and Thorkleson, D.J., 1997. Pan-continental River System Draining Grenville Orogen Recorded by U-Pb and Sm-Nd Geochronology of Neoproterozoic Quartzarenites and Mudrocks, Northwestern Canada. The Journal of Geology, vol. 105, p. 1-17.

Roots, C.F. and Thompson, R.I., 1992. Long-lived basement weak zones and their role in extensional magmatism in the Ogilvie Mountains, Yukon Territory. *In:* Basement Tectonics 8: Characterization and Comparison of Ancient and Mesozoic Continental Margins – Proceedings of the 8th International Conference on Basement Tectonics (Butte, Montana, 1988), M.J. Bartholomew, D.W. Hyndman, D.W. Mogk and R. Mason (eds.), Kluwer Academic Publishers, Dordrecht, The Netherlands, p. 359-372.

Schopf, W.J., Ford, T.D., and Breed, W.J., 1973. Microorganisms from the Late Precambrian of the Grand Canyon, Arizona. Science, vol. 179, p. 1319-1321.

Sperling, E.A., Halverson, G.P., Knoll, A.H., Macdonald, F.A., and Johnston, D.T., 2013. A basin redox transect at the dawn of animal life. Earth and Planetary Science Letters, vol. 371-372, p. 143-155.

Thompson, R.I., Mercier, E., and Roots, C.F., 1987. Extension and its influence on Canadian Cordilleran passive-margin evolution. *In:* Continental Extensional Tectonics, M.P. Coward, J.F. Dewey and P.L. Hancock (eds.), Geological Society of London Special Publication, vol. 28, p. 409-417.

Thompson, R.I., Roots, C.F., and Mustard, P.S., 1994. Dawson map area. Geological Survey of Canada, Open File 2849, scale 1: 50 000.

Thorkelson, D.J., 2000. Geology and mineral occurrences of the Slats Creek, Fairchild Lake and "Dolores Creek" areas. Wernecke Mountains (106D/16, 106C/13, 106C/14), Yukon Territory. Exploration and Geological Services Division, Yukon Region, Bulletin, vol. 10, 73 p.

Thorkelson, D.J., Abbott, J.G., Mortensen, J.K., Creaser, R.A., Villeneuve, M.E., McNicoll, V.J., and Layer, P.W., 2005. Early and Middle Proterozoic evolution of Yukon, Canada. Canadian Journal of Earth Sciences, vol. 42, p. 1045-1071.

Turner, E.C., 2011. Stratigraphy of the Mackenzie Mountains supergroup in the Wernecke Mountains, Yukon. *In:* Yukon Exploration and Geology 2011, K.E. MacFarlane, L.H. Weston, and C. Relf (eds.), Yukon Geological Survey, p. 207-231.

Young, G.M., Jefferson, C.W., Delaney, D.G., and Yeo, G.M., 1979. Middle and upper Proterozoic evolution of the northern Canadian Cordillera and Shield. Geology, vol. 7, p. 125-128.

A four stage evolution of the White Channel gravel: Implications for stratigraphy and palaeoclimates

Robert I. Lowther[1], Jeff Peakall, Robert J. Chapman
Placer Minerals Group, School of Earth and Environment, University of Leeds, Leeds

Matthew J. Pound
Department of Geography, Faculty of Engineering and Environment, Northumbria University, Newcastle upon Tyne

Lowther, R.I., Peakall, J., Chapman, R.J., and Pound, M.J., 2014. A four stage evolution of the White Channel gravel: Implications for stratigraphy and palaeoclimates. *In:* Yukon Exploration and Geology 2013, K.E. MacFarlane, M.G. Nordling, and P.J. Sack (eds.), Yukon Geological Survey, p. 109-118.

ABSTRACT

Although the White Channel gravel (WCG) of the Klondike district, Yukon, contains gold placers which have been exploited for over a century, few sedimentological studies have been undertaken. This study reports a four stage evolution of the WCG, comprising:

i. An initial downcutting period which preferentially retained gold particles on the base of the strath.
ii. An aggradational stage in which gold concentration occurred within sedimentary features.
iii. A lacustrine layer representing a depositional hiatus.
iv. A final, more rapidly aggrading fluvial stage.

Identification of the lacustrine layer has clarified the evolution of the WCG depositional fluvial systems. Architectural element analysis and detailed sedimentological observations have been synthesized to gain a clearer understanding of the spatial variations within the WCG. Additionally, the identification of plant species from pollen within the lacustrine layer provides irrefutable evidence that the Klondike district was at least 7°C warmer during the Pliocene compared to the present.

[1] *eeril@leeds.ac.uk*

INTRODUCTION

The gold placers of the Klondike district, Yukon Territory, Canada, have generated around 90% of the Territory's historic gold production, producing a recorded minimum of 10 million fine ounces of gold (Burke *et al.*, 2005). The 'White Channel gravel' (WCG) found within the drainages of the Klondike district are economically important auriferous high bench gravel deposits. Despite the economic importance of the WCG deposits, only limited study has been undertaken in order to establish their sedimentological and depositional history. A greater understanding of these deposits and their depositional history is desirable if the remaining placers contained within the WCG are to be utilized. Such knowledge will aid in exploration for similar placer deposits, not only within the Yukon, but worldwide. This study introduces a new methodology for recording the sedimentology of the WCG that allows for a greater comprehension of its formation, and presents an initial interpretation of observations made during recent fieldwork in the Bonanza and Hunker Creek drainages. These are the preliminary findings of an on-going study which will continue to characterize materials collected in the field and synthesize field data with information gained from physical modelling of river systems.

THE WHITE CHANNEL GRAVEL

The auriferous high bench WCG deposits studied in the present project are situated within the Klondike River drainage, located within an unglaciated area of west-central Yukon, Canada, immediately south of Dawson City (Fig. 1). The study areas are within the drainages of Bonanza and Hunker Creeks, both of which flow into the Klondike River. The WCG deposits sit uncomformably on the White Channel strath, an eroded bedrock surface composed mainly of Klondike Schist of the Yukon-Tanana terrane, at heights of 10 m to 200 m above the modern creeks (Lowey, 2004). The WCG deposits in Bonanza and Hunker Creeks are locally overlain by loess ('black muck') and colluviums. However, at the confluence of Bonanza and Hunker Creeks with the Klondike River the WCG is both over laid by, and interbedded with, the Klondike gravel, a glaciofluvial outwash deposit related to the pre-Reid glacial retreat (Morison and Hein, 1987). Deposits of the WCG have a length of several kilometres, a maximum width of 1 km, a maximum thickness of 46 m, and are composed predominantly of clast supported gravels with the presence of minor sand and mud horizons (McConnell, 1905; Lowey, 2004). An organic-rich mud, thought to be an overbank deposit, has been recorded within the WCG at Dago Hill on Hunker Creek (Durfresne

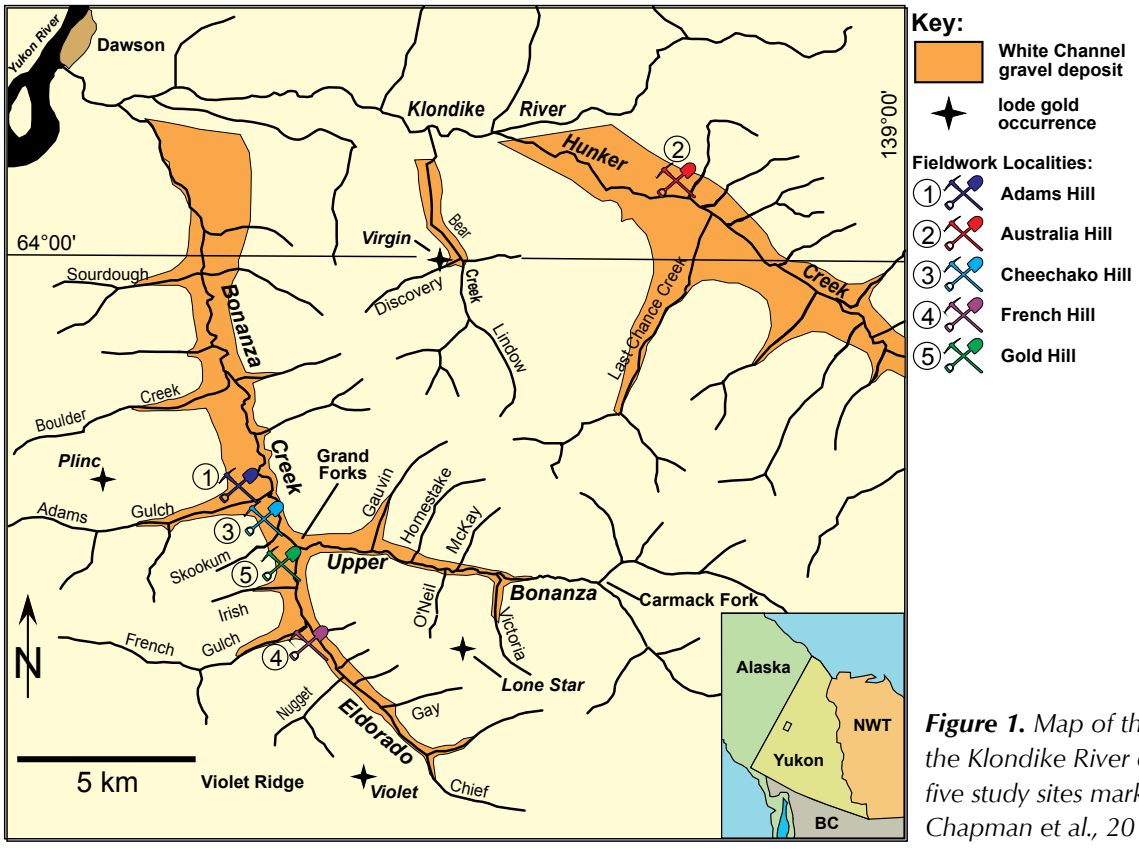

Figure 1. *Map of the study area in the Klondike River drainage with the five study sites marked, adapted from Chapman et al., 2010.*

and Morison, 1985), although no further investigations into it or its organic content were reported. Historically, the WCG has been divided into a lower 'white' and higher 'yellow' units, based on the corresponding colour difference, which was thought to represent separate deposition of the units (McConnell, 1905; 1907). However, later work has proposed that the WCG is one unit with no observed break in deposition and that the colour difference seen within the deposit is a result of staining caused by groundwater percolation (Morison, 1985). The WCG is Pliocene in age, the 'white' unit has been dated between 5 and 3 Ma (based on hornblende $^{40}Ar/^{39}Ar$ dating), whereas a date of 3 Ma was recorded for the yellow unit using glass fission track dating (Lowey, 2004). The overlying Klondike gravel has an age of 2.62 +0.21/-0.17 Ma based on terrestrial cosmogenic nuclide burial ages (Hidy *et al.*, 2013). Lowey (2004) reports that there is no mention of plant or animal remains in current descriptions of the WCG, though fossil pollens and spores have been reported. Fossil pollen samples were used by Morison (1985) to ascribe a Pliocene age to the lower 'white' unit of the WCG, through the presence of *Corylus* within the pollen assemblage and through comparison of the whole flora assemblage (*Abies*, *Corylus, Picea*, *Pinus* and *Poaceae*) with known dated flora assemblages within Alaska (Westgate *et al.*, 2003). However, to date there have been no palaeoenvironmental interpretations of these pollen samples and the current palaeoenvironment model for the north west of the Yukon is based on studies on gravel deposits in neighbouring Alaska (Ager *et al.*, 1994; White *et al.* 1999). These authors suggest a mean annual temperature of 3°C associated with a greater amount of precipitation than currently observed.

The present study focusses on five localities where WCG remains within the Bonanza Creek and Hunker Creek drainages. These localities represent proximal, medial, and distal proportions of the depositional system. The proximal sites are represented by mine sites at French Hill on Eldorado Creek and Gold Hill on Bonanza Creek, medial sites are represented by Cheechako Hill and Adams Hill on Bonanza Creek, and the distal site for this study is at Australia Hill on Hunker Creek (Fig. 1).

ORGANIC-RICH MUD HORIZON

An organic-rich mud horizon was found at French Hill (Eldorado Creek), Cheechako Hill, and Adams Hill (Bonanza Creek). The mud layer is black to dark black-brown in colour, 3 mm to 6 mm thick, and is laterally extensive when seen in outcrop. It was only observed within a small exposure at French Hill, in an outwash gully within the gravel face. At Adams Hill, there is evidence to suggest that this layer has been partially eroded and re-deposited within a sand horizon at approximately the same stratigraphic level, as the sand horizon contains fragments of organic mud. The organic-rich horizon typically overlays an inorganic mud that is 10 to 15 cm thick, light grey in colour, and varies from massive to finely laminated. Overlying the organic-rich horizon is a second inorganic mud layer with a similar grey colour, laminated to massive, and 11 to 14 cm thick, which in turn is overlain by a sequence of bedded sand, which is overlain by the upper unit of the WCG. The sand is observed at both Cheechako Hill and Adams Hill where they are 2 m and 30 cm in thickness respectively, containing beds that exhibit cross-bedding and trough cross-bedding, and have grain sizes that range from very fine sand to granular but have a mean grain size of medium coarse sand.

Analysis of the organic-rich horizon reveals a large quantity of diatoms, observed together with heavily fragmented ancient plant material. The presence of diatoms suggests that the horizon is aquatic in origin (Smol and Stoermer, 2010). The samples also contain an array of fossil pollen (Fig. 2). *Abies*, *Corylus, Picea*, *Pinus* and *Poaceae* have all been found that match those in samples from the WCG (Westgate *et al.*, 2003). In addition to this, *Alnus*, *Betula*, *Campanula*-type, Cyperaceae, Ericaceae, *Ilex,* Liguliflorae-type*, Quercus*, *Salix*, and *Sphagnum* have all been found within the organic-rich mud horizon, giving a detailed insight into the flora present during its deposition in the Pliocene. This initial analysis suggests the flora assemblage represents a cold needleleaf forest (taiga) biome, more taxonomically diverse than the modern high latitude forests and comparable to those reported from Circle, Alaska (Ager *et al.*, 1994). One sample shows a high Cyperaceae content, indicating the possibility of a local sedge swamp being present at the time of deposition. The flora assemblage found within the organic-rich mud horizon indicates that the study area was much warmer than today, with an estimated mean annual temperature of 3°C, in comparison to the Klondike region's present mean annual temperature of -4°C (Environment Canada, 2013), and would have also experienced greater precipitation than today. These pollen samples are important because understanding of Late Pliocene vegetation in Canada is currently restricted to islands in the Arctic Sea (Salzmann *et al.*, 2008). This means that the global state-of-the-art Late Pliocene vegetation reconstruction previously relied on

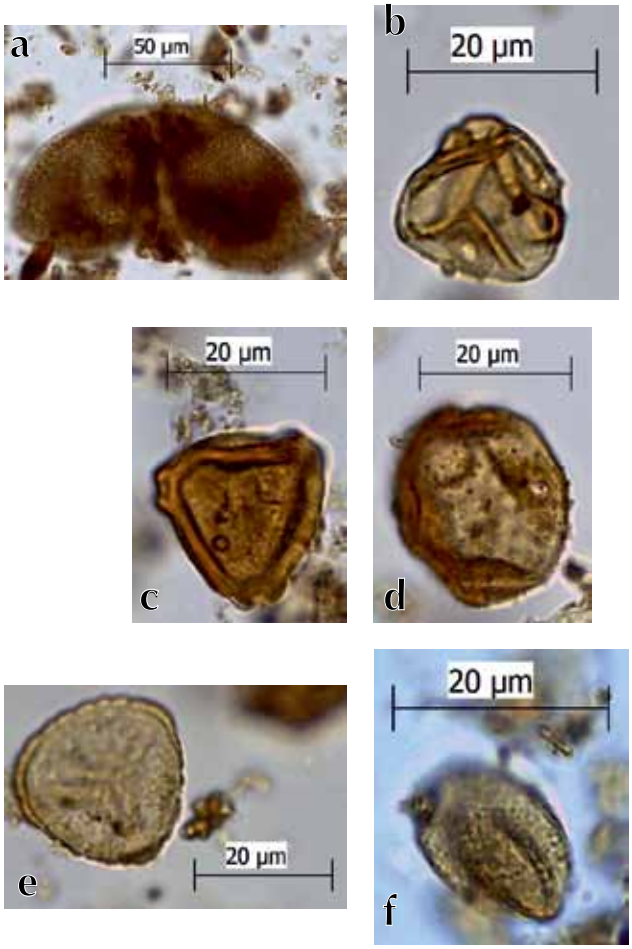

Figure 2. *Examples of the fossil pollen found within the organic-rich mud horizon. Pollen are as follows: (a) = Pinus; (b) = Alnus; (c) = Betula; (d) = Campanula-type; (e) = Sphagnum; and (f) = Quercus.*

predictions from an Alaskan vegetation model to cover much of Canada (Salzmann *et al.,* 2008). The organics preserved within this horizon in the WCG will provide data to ground-truth this region of the current global vegetation reconstruction used in the PlioMIP (Pliocene Model Inter-comparison Project), which aims to improve our understanding of terrestrial ecosystem dynamics during the most recent geological warm period.

CURRENT DEPOSITIONAL MODEL FOR THE WHITE CHANNEL GRAVEL

The current proposed mode of deposition for the WCG involves continuous deposition by shallow gravel-bed braided river systems in the palaeo-creeks (Morison, 1985; Morison and Hein, 1987; Lowey, 2004; 2006).

Morison and Hein (1987) divided the river systems into a crudely braided proximal system with a few main channels, and a medial to distal setting with well-defined braided sequences composed of channels and low relief bars. These authors also proposed that the upper 'yellow' unit was deposited in a less energetic fluvial regime. This depositional model has been developed by four sedimentological studies: Morison (1985), Morison and Hein (1987) and Lowey (2004, 2006), which have collectively applied three different lithofacies schemes to examine the WCG. Lithofacies schemes divide a deposit into a series of homogeneous components based on factors including structure, grain size, and texture that can be observed through the entirety of the deposit. Once a lithofacies scheme has been developed, it allows for stratigraphic sequences through the deposit to be recorded, enabling discussion and interpretation of the formation and evolution of the deposit. The first lithofacies scheme developed for the WCG (Morison, 1985) divided the deposit into 14 individual facies, the majority (80%) of these being gravel based. This approach was adapted and simplified by Morison and Hein (1987) who reduced the number of facies to nine through the combination of related units. Lowey (2004; 2006) used a single lithofacies scheme comprising eight facies types based on the ideas of Miall (1978). All of these lithofacies schemes have several features in common. Clast-supported gravels are a dominant feature present in two or more facies, either massive or containing crude planar or cross bedding, representing bars within the depositional environment. These lithofacies schemes were used to produce stratigraphic sections and panels of the deposits, allowing for the sedimentology of the WCG to be recorded and interpreted.

Nevertheless, the use of stratigraphic sections has its limitations within these deposits, primarily because they do not capture the wide range of variation that can occur laterally within a single exposure. Even when several sections are prepared within the same exposure, it is frequently challenging to characterize the sedimentary features and to cross-correlate them. When panels have been produced in an attempt to capture any spatial variation within an exposure (Lowey, 2004), the use of a lithofacies scheme has resulted in large areas being recorded as a single lithofacies, with none of the internal structures of the exposure being recorded. This means that, within the existing literature, details of variation within the sediments are not wholly represented. The stratigraphic sections and panels that have been produced

also provide little information on the sizes of the bars and channels within the braided river system that laid down the WCG, and any variation within them over the period of deposition.

ARCHITECTURAL ELEMENT ANALYSIS

This study introduces the use of an alternative methodology of recording the sedimentology of the WCG deposits. Architectural element analysis has been successfully used in a number of studies (e.g., Ashworth *et al.*, 1994; 1999; Peakall *et al.*, 1996) to record the varying depositional niches within a gravel deposit, such as gravel bars, channels, and overbank deposits (Fig. 3). This technique records the sedimentology of an entire exposure, as opposed to a single transect represented by a stratigraphic sequence, easily recognising and recording spatial variations within a deposit. The architectural elements represent those seen within modern gravel bed braided river systems (e.g., Ashworth *et al.*, 1999; Bridge and Lunt, 2009). The use of this method has provided data on the relative sizes of bars and channels within the river system that deposited the WCG. This method is also beneficial as it allows comparison of the WCG deposits with modern river systems, other ancient river systems, and experimentally produced model river systems. In the field, this method was implemented on 16 exposure faces over the five study sites. The sedimentary architecture was recorded onto detailed scaled photos of the outcrop, facilitating element shape, size, and inter-relationship to be precisely documented.

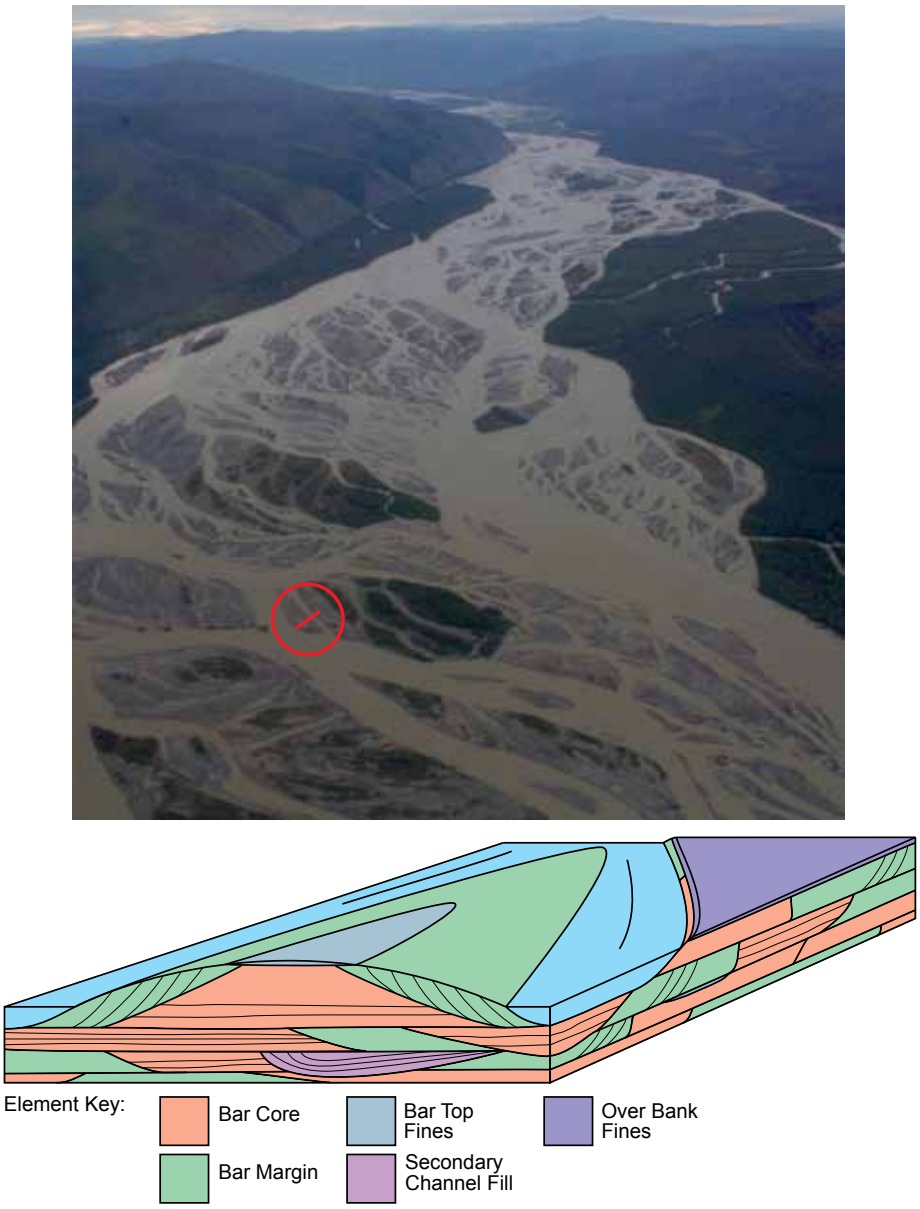

Figure 3. *The White River, Yukon, Canada; an example braided river system similar to that which deposited the White Channel gravels. The lower figure is a generic block model diagram of the architectural elements that are present within a braided river system (block model represents the circled red cross section line).*

The architectural element scheme utilized for the WCG is adapted from Ashworth *et al.* (1999), whose work examined the deposits of the Ashburton River, Canterbury Plains, New Zealand. This new scheme is composed of seven main elements (Fig. 3), descriptions of which are listed below. Due to the nature of working on both active and inactive mine sites, the size and exposure of the mine face outcrops vary from site to site.

WHITE CHANNEL GRAVEL ARCHITECTURAL ELEMENT SCHEME AND ANALYSIS

The WCG is analysed using seven architectural elements (examples illustrated in Fig. 3 and Fig. 4)

A. *Bar Core:* Coarse grained, laterally extensive gravel sheets that can be massive to laminated, typically lacks internal structure, but may contain low angle cross bedding. Predominantly clast supported gravel with moderate to poor sorting, however, some fining up may be seen. Bar cores are tabular with erosional bases and represent primary channel fill. Bar cores may laterally grade into bar margins and may be overlain by bar top fines. This is a primary element within the WCG.

B. *Bar Margin:* Coarse grained, although generally finer than bar cores, with lenses of finer grained material sometimes present. Largely cross-bedded and moderate to well sorted. Bar margins are tabular with erosional bases, but not as laterally extensive as bar cores. Bar margins may laterally grade into bar cores, may be overlain by bar top fines, and represent primary channel fill.

C. *Bar Top Fines:* Fine grained sheets of sand and silt that may be laterally extensive but are often eroded into discontinuous horizons. Bar top fines are found as thin beds overlying bar cores and bar margins. They are preserved only in relatively low energy conditions.

D. *Secondary Channel Fill:* Coarse gravel to fine sand in grain size and may be homogeneous or a mixture of sizes. Fill may be massive or show a range of internal stratification including grain size sorting that may be observed both laterally and vertically. Channel fills possess arcuate erosional bases which may contain a coarser lag deposit in the bottom of the channel fill. These fills represent the infilling of channels that have cut through the bar complexes within the braid plain of the ancient fluvial system.

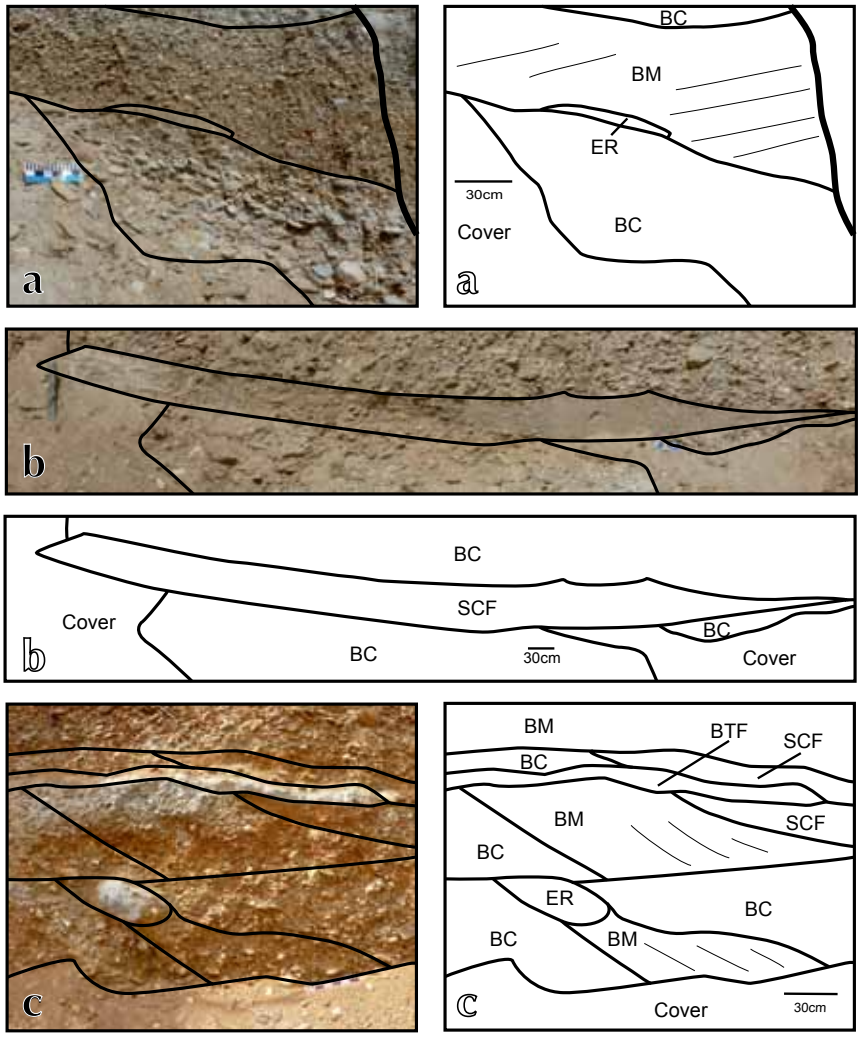

Figure 4. *Examples of the architectural elements seen within the White Channel gravels: (a) and (b) from Adams Hill and (c) from Cheechako Hill. Labels on figure are as follows: BC = Bar Core; BM = Bar Margin; BTF = Bar Top Fines; SCF = Secondary Channel Fill; OBF = Overbank Fines; and ER = Erosional Remains.*

E. *Overbank Fines:* Mud deposits that may be massive or laminated and in some cases may contain clasts (present as matrix supported gravel). They generally produce relatively tabular deposits which vary in size, dependent on subsequent erosion.

F. *Sand Horizon:* Coarse to fine grained sands which may contain granule to small pebble sized lags at their base. Sands are tabular when extensive lateral preservation has been achieved and may possess erosional bases. Sands may be planar, cross- or trough cross-bedded and can contain fining sequences.

G. *Erosional Remnants:* Areas where the initial depositional environment cannot be identified due to their small size within the outcrop and, therefore, a lack of distinguishing features.

The discovery of the organic layer provides the opportunity to study discrete depositional systems within the WCG, allowing for the palaeo-sedimentary systems evolution to be established. At the Cheechako Hill site the architectural element composition and element sizes (Table 1) can be compared for the upper and lower units. In the lower unit, all the elements present (with the exception of the erosional remains) are larger than in the upper unit based on mean height and width measurements. An example of this are the bar cores in the upper unit having an average width of 2.9 m compared to 4.5 m of the lower unit. Bar cores are the dominant sedimentary characteristic in both units (68% of total exposure), comprising a larger percentage of the sediment in the lower unit (74% of exposure) than the upper unit (58% of exposure). However, the upper unit contains a larger proportion of preserved bar margins, (27% versus 18% of exposure in the lower unit) and contains more fine sediment in the form of bar top fines and overbank fines, both of which are absent from preservation within the lower unit. This indicates that the braided river system that deposited the WCG was initially a larger river system with a low aggradation rate, which produced large gravel bars (Table 1) that were largely erosive as they migrated and stacked. In this environment, previously deposited bar top fines were removed by the succeeding fluvial flows. Fine sediment, muds and sands, immediately above this layer indicates the presence of a much smaller river system which preceded the reinstatement of gravel transport and deposition. In the upper unit, the smaller element sizes coupled with the preservation of fine sediment is interpreted as indicating the presence of a fully developed river system that was smaller and more highly aggradational than that which deposited the lower unit. This enhanced aggradation prevented the extensive reworking seen in the lower unit. This sequence can also be observed within the architectural element composition and element sizes of Adams Hill (Table 2).

Table 1. *Architectural element frequency and size data from the Cheechako Hill site.*

		Number of elements	Exposure (%)	Mean Height (m)	Mean Width (m)
Bar Core	Total	37	68	0.45	3.83
	Lower	21	74	0.47	4.51
	Upper	16	58	0.44	2.93
Bar Margin	Total	19	21	0.4	2.65
	Lower	8	18	0.43	3.25
	Upper	11	27	0.37	2.21
Bar Top Fines	Total	2	<1	0.11	1.8
	Lower	0	-	-	-
	Upper	2	1	0.11	1.8
Secondary Channel Fill	Total	15	9	0.26	2.15
	Lower	8	9	0.31	2.22
	Upper	7	9	0.2	2.07
Overbank Fines	Total	1	1	0.36	3.35
	Lower	0	-	-	-
	Upper	1	3	0.36	3.35
Erosional Remains	Total	5	<1	0.18	0.51
	Lower	1	<1	0.13	1.46
	Upper	4	1	0.19	1.52

HISTORY OF THE WHITE CHANNEL GRAVEL

The study demonstrates that there are two distinct phases of WCG deposition, separated by a system shut-down characterized by the rapid abandonment of a high-energy braided river system, and the development of a lake or swamp. The WCG below and above this stratigraphic marker are fundamentally different in nature. Architectural element analysis demonstrates that the lower WCG was formed by a large braided river system, associated with a relatively low aggradation rate. In contrast, the upper WCG is a smaller channel system with a considerably higher aggradation rate that results in the preservation of a greater percentage of the deposits. While dating of the WCG is limited, this analysis indicates that the lower WCG unit represents a much greater proportion of the total time of deposition, compared to the upper WCG unit.

Table 2. *Architectural element frequency and size data from the Adams Hill site.*

		Number of elements	Exposure (%)	Mean Height (m)	Mean Width (m)
Bar Core	Total	39	62	0.95	4.13
	Lower	19	59	0.97	4.54
	Upper	20	66	0.94	3.79
Bar Margin	Total	25	26	0.77	3.18
	Lower	12	25	0.67	3.79
	Upper	13	27	0.86	2.61
Bar Top Fines	Total	3	<1	0.29	1.48
	Lower	0	-	-	-
	Upper	3	1	0.29	1.48
Secondary Channel Fill	Total	9	11	0.68	4.73
	Lower	6	16	0.69	5.79
	Upper	3	4	0.65	2.6
Erosional Remains	Total	9	1	0.22	1.1
	Lower	4	<1	0.14	0.86
	Upper	5	2	0.29	1.48

The bipartite nature of the WCG, separated by fine grained, mud-rich sedimentation, and an organic-rich lacustrine horizon, suggests that a major event took place at this interface. At the WCG-bedrock interface there is very coarse gravel that represents a phase dominated by erosion into the bedrock prior to significant aggradation. Above this coarse basal gravel, there is no obvious decline in the gravel size or architectural element size with time in the lower WCG until the abrupt transition into the muddy sediments. This section examines the possible mechanism for the abandonment of coarse grained gravel deposition.

Large tectonic events involving the back tilting of the braided river system would have led to a reduction and eventual elimination of down-valley slope. Such an interpretation would fit with the development of a lake that was at least 5 km in length, which would not normally form in a system characterized by relatively steep gradients. An isolated phase of tectonism, during an otherwise reportedly tectonically quiet period (Duk-Rodkin *et al.,* 2001), would have been required to alter the braided river system, as mentioned, and allow for the formation of a lake. Given the regional setting of the deposit this tectonic phase may be related to the Tintina Fault, north of the study area, or the St. Elias orogeny to the south. Alternatively, damming of the river could have occurred, either by landslide, perhaps associated in turn with seismicity, or by an ice dam further down the system. In both cases, the development of a lake behind the dam would lead to a marked backwater effect, and any resultant gravity deposition would have been restricted to the head of the lake. However, analysis of the flora suggests that the climate at this time was relatively warm and consequently an ice dam is improbable. The marked difference between the channel systems represented by the lower and upper WCG does suggest, however, that some fundamental change has occurred to the system across this condensed section. This in turn militates against the suggestion of a landslide induced dam, since these are typically ephemeral events on a geological time scale, and would not be expected to lead to any significant re-organization of the system.

From the analysis provided above, a tectonically induced change appears the most likely (although it is noted that this hypothesis is inconsistent with that of Duk-Rodkin *et al.* (2001)). The new model suggested here proposes that the condensed section between the lower and upper WCG, represented by the fine grained sediment, was the product of a period of significant tectonic activity leading to the back tilting and ultimate abandonment of the braided river system. After a period of lacustrine activity, a new braided river system (the upper WCG) prograded over the lake deposits, but as a smaller system. The higher aggradation rate suggests that more accommodation space was available, presumably related to the re-grading of the down valley slope leading to significant localized aggradation rates.

IMPLICATIONS OF FLUVIAL SYSTEM SHUTDOWN FOR PLACER-LODE RELATIONSHIPS

The hypothesis of a four stage evolution for the WCG has implications for studies of placer-lode relationships. Placer mining activities generally concentrate on processing the lowest stratigraphic levels in the WCG and it is generally accepted that the highest gold grades are found at the bedrock contact. This observation is consistent with a prolonged erosional phase in which gold particles accumulated in bedrock imperfections, while most other clasts were swept through the system. The preservation of sedimentary architecture above this horizon indicates that the fluvial system then switched to an aggradational regime, during which gold particles could not penetrate down to the bedrock gutter. The sedimentary architecture of the lower WCG unit suggests the concentration of gold continued within a slowly aggrading system that processed a large amount of material, selectively retaining the coarse gold particles, therefore, producing high gold grades. In contrast, the placers which formed above the organic-rich layer accumulated in a rapidly aggrading system, and consequently gold grades are relatively low. However, the presence of gold within these sediments shows that particulate gold continued to enter the fluvial system, either as a consequence of on-going erosion of *in situ* gold mineralization or through the continued influx of elluvial gold. The analysis of the placer evolution, described above, suggests that the placer gold grades are primarily a function of the sedimentary environment rather than an indication of variation of gold grade within an eroding orebody. The gold-rich paystreaks at the base of the WCG probably contained only a fraction of the total gold eroded from the source, and consequently current estimates of the original size of the hypogene source may be under represented.

CONCLUSION

The detailed studies of the WCG presented above has established four stages of development. The initial stage involved downcutting and formation of a gold placer through winnowing in an aggressive fluvial regime. A second stage is defined by a change to an aggradational system, although gold placer formation continued within this sedimentary environment. A third stage, defined by an organic-rich mud horizon is interpreted as a lacustrine environment, established during a hiatus in deposition that was succeeded by a fourth stage, in which gravels aggraded rapidly in a new fluvial system.

The discovery of a widespread organic-rich mud horizon that acts as an important stratigraphic marker horizon has enabled the division of the WCG into a lower and an upper unit. Consideration of the size of the lake suggests that the most likely cause of formation is tectonic activity within the area rather than an ephemeral surficial control such as a landslide or ice dam. The newly established units of the lower and upper WCG both display some key differences that reflect changes in the depositing river system. The difference in architectural element sizes between the two units indicates that the lower unit was deposited by a larger river system than the upper unit. Consequently, the early river system would have been able to concentrate coarse gold more effectively than its later counterpart. Architectural analysis has also shown that the lower unit was deposited in an environment with a much lower aggradation rate than the upper unit, which would facilitate a higher degree of gold concentration within the sediments. Conversely, the upper unit underwent less reworking which may result in differing variations in gold grade through the lower and upper parts of the WCG section.

The gold present at the base of the WCG accumulated while most other material was transported away. Almost certainly, some gold was removed at the same time and, consequently, the gold present in the placers probably under represents the amount eroded from the original sources.

The study of the pollen within the organic-rich mud horizon has facilitated reconstruction of the Pliocene palaeo-flora. The species present indicate that the average annual temperature was at least seven degrees warmer than at present. These palaeo-flora data provide independent validation of data generated using state-of-the-art Late Pliocene global vegetation reconstructions, which are used in Pliocene climate modelling.

ACKNOWLEDGEMENTS

A special thanks is given to the placer miners of the Dawson area; namely, John Alton, the Christie family, Ivan Daunt, Daryl Fry, Doug Jackson, Mike McDougall, Erich Rauguth, Don Ruman, and Chuck Sigurdson, without whom the field work for this project would not have been possible.

Thanks are also given to the Natural Environmental Research Council, Yukon Geological Survey, Canadian Northern Development Agency, Society of Economic Geologists, and the International Association of Sedimentologists for providing funding for this project.

REFERENCES

Ager, T.A., Matthews Jr., J.V., and Yeend, W., 1994. Pliocene terrace gravels of the ancestral Yukon River near Circle, Alaska: Palynology, paleobotany, paleoenvironmental reconstruction and regional correlation. Quaternary International, vol. 22–23, p. 185-206.

Ashworth, P.J., Best, J.L., Leddy, J.O., and Geehan, G.W., 1994. The physical modelling of braided rivers and deposition of finer-grained sediment. *In:* Process Models and Theoretical Geomorphology, M.J. Kirkby (ed.), Wiley, Chichester, p. 115-139.

Ashworth, P.J., Best, J.L., Peakall, J., and Lorsong, J.A., 1999. The influence of aggradation rate on braided alluvial architecture: field study and physical scale-modelling of the Ashburton River gravels, Canterbury Plains, New Zealand. *In:* Fluvial Sedimentology VI: International Association of Sedimentologists, N.D. Smith and J. Rogers (eds.), Special Publication 28, p. 333-346.

Bridge, J.S. and Lunt, I.A., 2009. Depositional models of braided rivers. *In:* Braided Rivers: Processes, Deposits, Ecology and Management, International Association of Sedimentologists, G.H. Sambrook Smith, J.L. Best, C.S. Bristow, and G.E. Petts (eds.), Special Publication 36, p. 11-50.

Burke, M., Hart, C.J.R., and Lewis, L.L., 2005. Models for epigenetic gold exploration in the northern Cordillern orogen, Yukon, Canada, *In:* Mineral deposit research: Meeting the global challenge, J. Mao and F.P. Bierlein (eds.), Proceedings of the Eighth Biennial SGA Meeting, Beijing, China, p. 525-528.

Chapman, R.J., Mortensen, J.K., Crawford, E.C., and Lebarge, W., 2010. Microchemical studies of placer and lode gold in the Klondike District, Yukon, Canada: 1. Evidence for a small, gold-rich, orogenic hydrothermal system in the Bonanza and Eldorado Creek area. Economic Geology, vol. 105, p. 1369-1392.

Duk-Rodkin, A., Barendregt, R.W., White, J.M., and Singhroy, V.H., 2001. Geologic evolution of the Yukon River: implications for placer gold. Quaternary International, vol. 82, p. 5-31.

Dufresne, M.B. and Morison, S.R., 1985. Stratigraphy and alteration of the White Channel Gravel at Dago Hill, a progress report, Klondike area, Yukon. *In:* Yukon Exploration and Geology 1983, Exploration and Geological Services Division, Yukon Region, Indian and Northern Affairs Canada, p. 55-59.

Environment Canada, 2013. Canadian Climate Normals 1981-2010, Environment Canada, Government of Canada, <*ftp://ftp.tor.ec.gc.ca/Pub/Normals/English/*> [accessed November 5, 2013].

Hidy, A.J., Gosse, J.C., Froese, D.G., Bond, J.D., and Rood, D.H., 2013. A latest Pliocene age for the earliest and most extensive Cordilleran Ice Sheet in northwestern Canada. Quaternary Science Reviews, vol. 61, p. 77-84.

Lowey, G.W., 2004. Placer geology of the Stewart River (115N&O) and part of the Dawson (116B&C) map areas, west-central Yukon, Canada. Yukon Geological Survey Bulletin 14, Yukon Geological Survey, 275 p.

Lowey, G.W., 2006. The origin and evolution of the Klondike goldfields, Yukon, Canada. Ore Geology Reviews, vol. 28, p. 431-450.

McConnell, R.G., 1905. Report on the Klondike gold fields. Geological Survey of Canada, Annual Report (New Series), vol. 14, p. 1B-71B.

McConnell, R.G., 1907. Report on gold values in the Klondike high level gravels. Geological Survey of Canada, Report No. 979, 34 p.

Miall, A.D., 1978. Lithofacies types and vertical profile models in braided river deposits: A summary. *In:* Fluvial Sedimentology, A.D. Miall (ed.), Canadian Society of Petroleum Geologists, Memoir 5, p. 597-604.

Morison, S., 1985. Sedimentology of White Channel placer deposits, Klondike area, west-central Yukon. Unpublished MSc thesis, University of Alberta, Edmonton, Alberta, 149 p.

Morison, S.R. and Hein, F.J., 1987. Sedimentology of the White Channel Gravels, Klondike area, Yukon Territory: Fluvial deposits of a confined valley. *In:* Recent Developments in Fluvial Sedimentology, F.G. Ethridge, R.M. Flores, and M.D. Harvey (eds.), Society of Economic Paleontologists and Mineralogists, Special Publication 39, p. 205-215.

Peakall, J., Ashworth, P., and Best, J., 1996. Physical modelling in fluvial geomorphology: Principles, applications and unresolved issues. *In:* Scientific Nature of Geomorphology, B.L. Rhoads and C.E. Thorn (eds.), Proceedings of the 27th Binghamton Symposium in Geomorphology held 27–29 September 1996, Wiley, Chichester, p. 221-253

Salzmann, U., Haywood, A.M., Lunt, D.J., Valdes, P.J., and Hill, D.J., 2008. A new global biome reconstruction and data-model comparison for the Middle Pliocene. Global Ecology and Biogeography, vol. 17, p. 432-447.

Smol, J.P. and Stoermer, E.F., 2010. The diatoms: applications for the environmental and earth sciences. Cambridge University Press, Cambridge, 667 p.

Westgate, J.A., Sandhu, A.S., Preece, S.J., and Froese, D.G., 2003. Age of the gold-bearing White Channel Gravel, Klondike district, Yukon. *In:* Yukon Exploration and Geology 2003, D.S. Emond and L.L. Lewis (eds.), Exploration and Geological Services Division, Yukon Region, Indian and Northern Affairs Canada, p. 241-250.

White, J.M., Ager, T.A., Adam, D.P., Leopold, E.B., Liu, G., Jetté, H., and Schweger, C.E., 1999. Neogene and Quaternary quantitative palynostratigraphy and paleoclimatology from sections in Yukon and adjacent Northwest Territories and Alaska. Geological Survey of Canada, Bulletin 543, 30 p.

Structural controls on alteration and mineralization at the Coffee gold deposits, Yukon

Doug MacKenzie[1], Dave Craw
Geology Department, University of Otago, New Zealand

Craig Finnigan
Department of Earth Sciences, Western University, London, Canada

MacKenzie, D., Craw, D., and Finnigan, C., 2014. Structural controls on alteration and mineralization at the Coffee gold deposits, Yukon. *In:* Yukon Exploration and Geology 2013, K.E. MacFarlane, M.G. Nordling, and P.J. Sack (eds.), Yukon Geological Survey, p. 119-131.

ABSTRACT

The Coffee gold deposits are controlled by east and north-striking structures that initiated in the Jurassic and were re-activated in the Cretaceous. Cretaceous igneous rocks and Jurassic-altered Paleozoic rocks were overprinted by Late Cretaceous (or younger) gold mineralization and the paragenetic sequence for the main prospects has been established. Jurassic alteration is characterized by zones of pervasive quartz sericite alteration of metamorphic minerals and disseminated brassy pyrite. Jurassic pyrite is locally anomalous in gold, but is generally barren. Cretaceous gold mineralization overprints Jurassic sericite alteration and is characterized by veins and breccia infilled with gold-bearing, dark grey, 'sooty' arsenian pyrite. In biotite-rich host gneiss, disseminated arsenian pyrite extends outwards from fracture zones along biotite-rich metamorphic foliation and pre-existing Jurassic shears. In altered Late Cretaceous igneous rocks, gold-bearing arsenian pyrite replaces primary biotite. Compared to other nearby prospects, the Coffee gold project is most similar to the Boulevard trend but textures suggest it formed at shallower levels.

[1] *doug.mackenzie@otago.ac.nz*

INTRODUCTION

Heightened gold exploration activity in central Yukon from 2007 to 2010 yielded several significant new discoveries, such as the White Gold deposit and Boulevard trend (Fig. 1; MacKenzie and Craw, 2010; MacKenzie *et al.*, 2010; Bailey, 2013; McKenzie *et al.*, 2013). Deposits in the Coffee Creek area (Fig. 1; Wainwright *et al.*, 2011) were discovered during this time, and have been advanced since then with a major drilling program. A preliminary economic assessment is planned for early 2014. The drilling program was accompanied by detailed surface geochemical sampling and site-wide airborne geophysical surveying, yielding a large amount of new data on the geology of the area.

This paper reports on work from the 2013 summer season in which these large data sets were integrated with new mapping and examination of drill core to produce a new geological map for the mineralized area (Fig. 2). The geological structure of the Coffee Creek area has been placed into the context of the regional geology (Figs. 1, 2, and 3) in order to better understand the geological development of the immediate host rocks for the gold deposits. From this basis, the structure and alteration mineralogy of the Coffee gold deposits have been integrated into the framework of tectonic and structural evolution of basement rocks and hydrothermal systems of the wider Yukon-Tanana terrane.

GEOLOGICAL SETTING

The main prospects at the Coffee Gold Project (Coffee) are hosted in metamorphic basement rocks of the Yukon Tanana terrane (Mortensen, 1992, 1996; Ryan *et al.*, 2013; Fig. 1). South of Stewart River through to the Dawson Range, basement rocks consists of Paleozoic schist and gneiss that were intruded by a least three generations

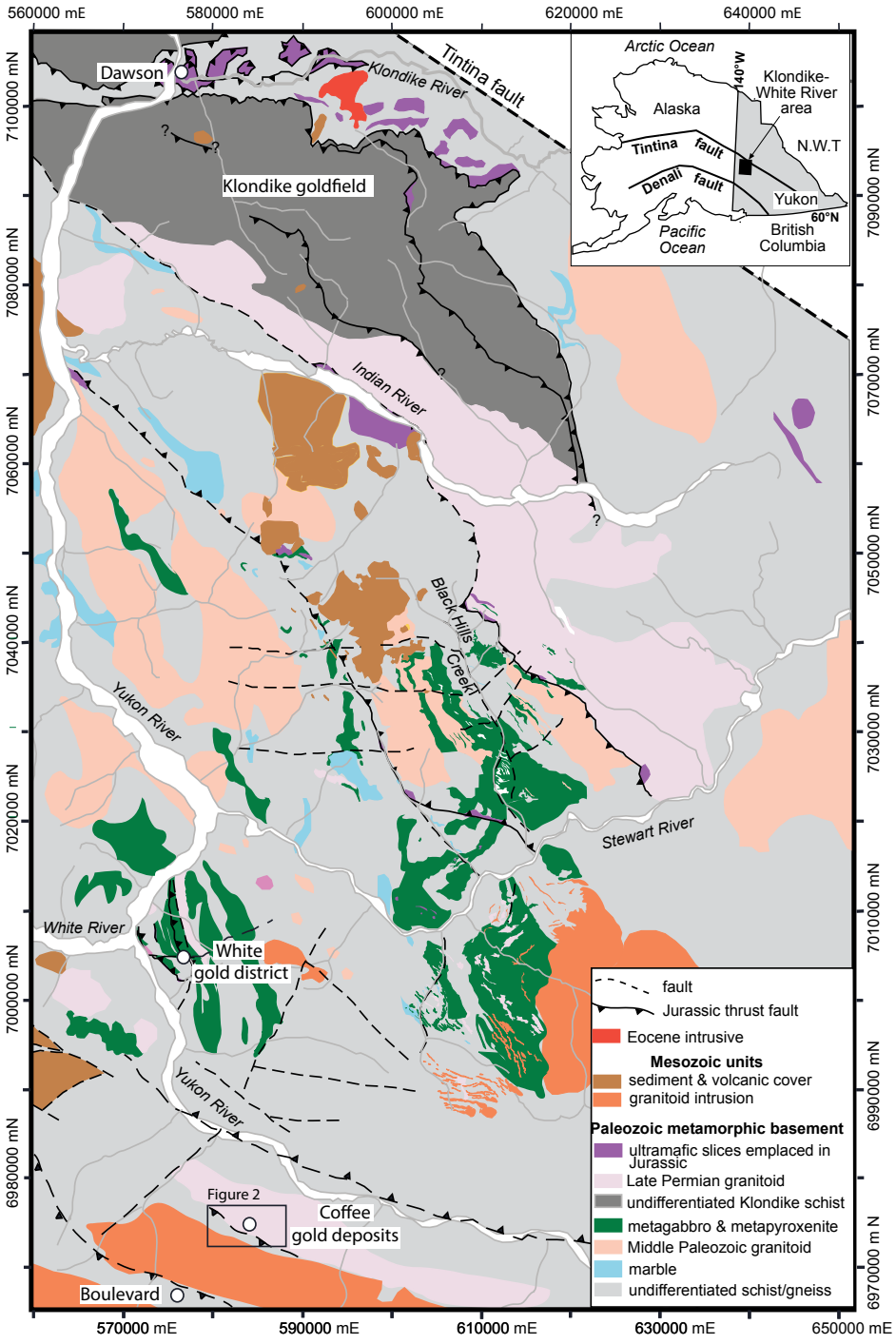

Figure 1. *Geological map of the Klondike – White River and Coffee Creek area, central western Yukon (modified after Ryan and Gordey, 2004; MacKenzie et al., 2008a,b, 2010, 2013; MacKenzie and Craw, 2010, 2012). Rectangular box shows the location of the area mapped in this study (Fig. 2).*

of pre and synmetamorphic granitic, gabbroic, and pyroxenite intrusions in the Devonian, Mississippian and Permian (Ruks *et al.*, 2006; MacKenzie and Craw, 2012). All of these rocks were subjected to Late Permian amphibolite facies metamorphism (Berman *et al.*, 2007; Beranek and Mortensen, 2011). The rocks were completely recrystallized and developed a pervasive metamorphic foliation. This foliation, designated S_2 (Table 1), is a composite feature made up of at least two almost completely transposed foliations (S_1+S_2). S_1 is rarely seen, as isolated, foliation-parallel, isoclinal folds along the foliation. S_2 foliation dominates in the Coffee Creek area and in most outcrops throughout the region.

Metamorphic basement rocks and the metamorphic foliation were deformed and folded in the Jurassic when kilometre-scale slices of rock were tectonically stacked along regional-scale thrust faults (F_3, Table 1; Mortensen, 1996). Thrust stacking incorporated lower grade, greenschist facies mafic and ultramafic rocks of the Slide Mountain Terrane (Mortensen, 1996; MacKenzie *et al.*, 2008b; Table 1). Greenschist facies shear zones and alteration developed at this time in zones of intense semi-ductile F_3 folding and accompanied regional-scale thrust faulting. Later stages of more brittle kink folding and fracturing (F_4, Table 1) subsequently developed in the region and these structures were locally infilled by orogenic quartz veins formed from fluids generated at depth within the thickened metamorphic pile (MacKenzie *et al.*, 2008a). Hydrothermal alteration and disseminated gold mineralization in the White Gold district is controlled by extensional fractures and E-W striking Jurassic faults and shear zones (MacKenzie *et al.*, 2010; Bailey, 2013).

Extensional tectonics dominated from Early to Late Cretaceous when granitoids of the Dawson Range batholith (Middle to Late Cretaceous age; McKenzie *et al.*, 2013) intruded along pre-existing fault zones in

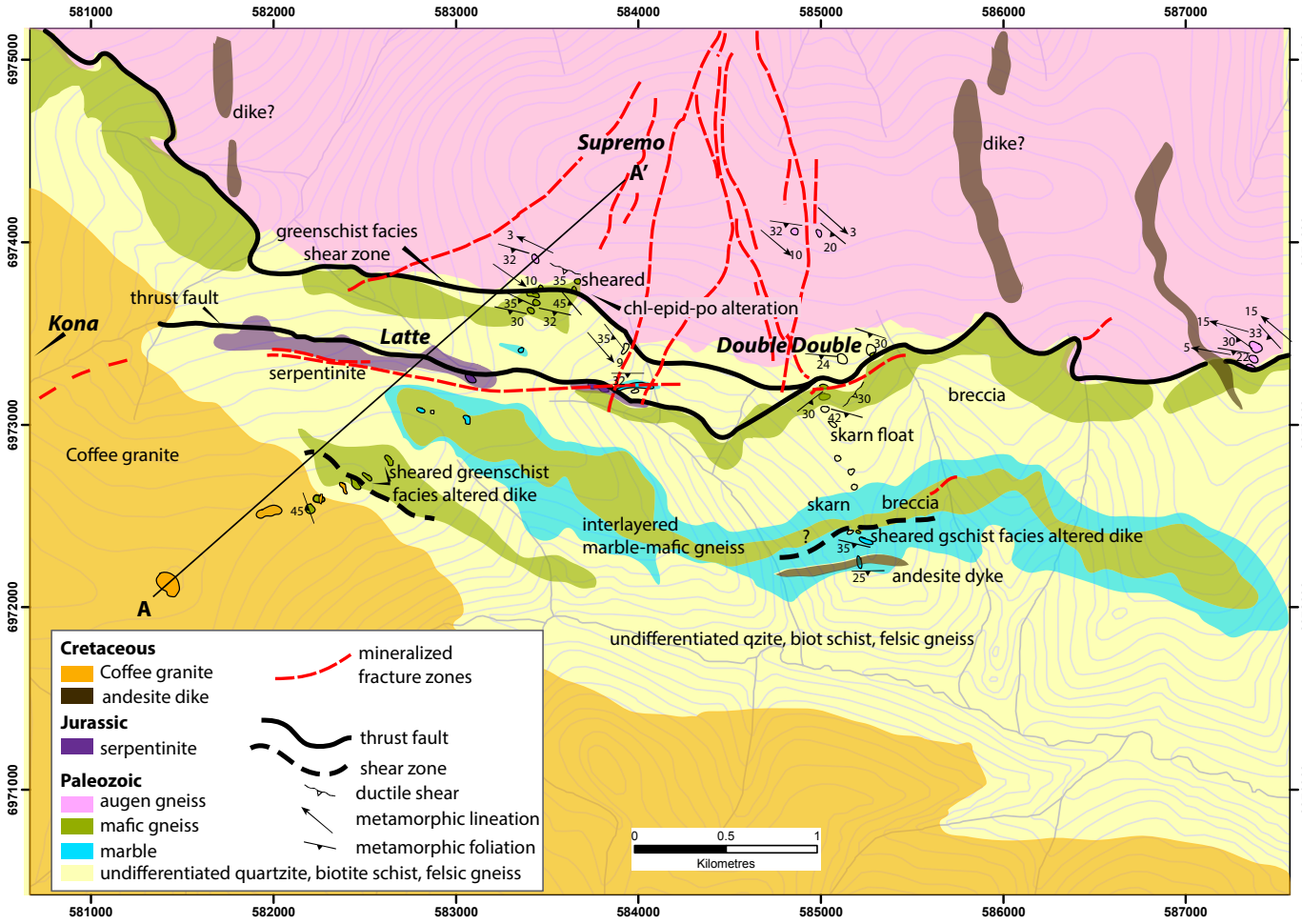

***Figure 2**. Geological map of the Coffee Creek area, showing the line of cross section A-A′ in Fig. 3. chl= chlorite, epid=epidote, po=pyrrhotite.*

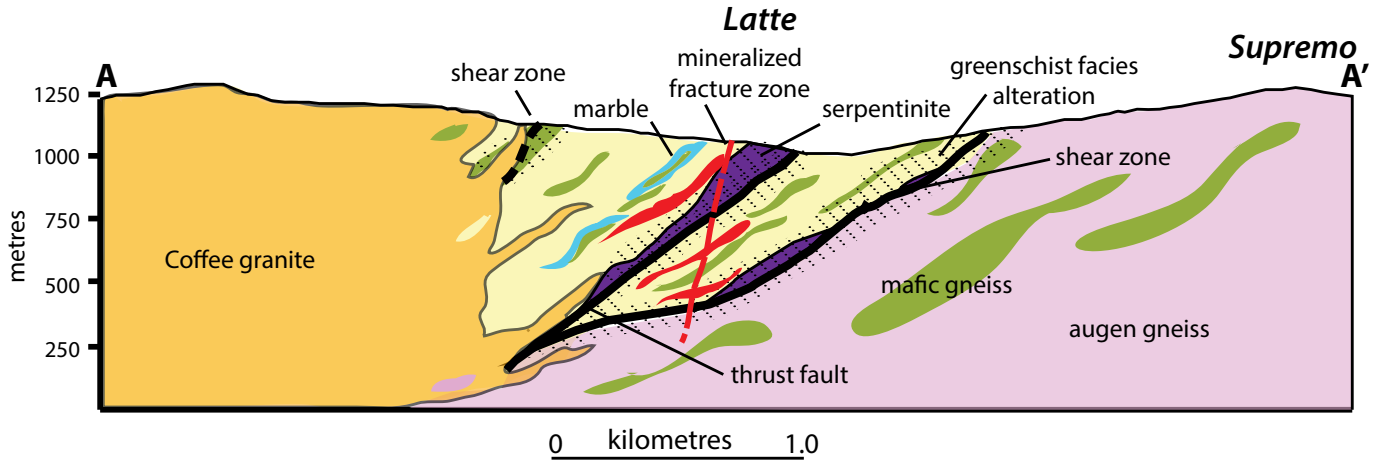

Figure 3. *Interpretive geological cross section through line A-A′ Fig. 2.*

the metamorphic package south of Coffee (Figs. 1 and 2). Extension continued through to the Eocene with the initiation of the Tintina fault as a major regional transcurrent structure (Gabrielse *et al.*, 2006).

COFFEE CREEK BASEMENT ROCKS

The metamorphic basement rocks in the Coffee Creek area (Figs. 2 and 3) include early Paleozoic clastic sedimentary rocks that are now amphibolite facies biotite schist and quartz-muscovite schist, and minor quartzite and marble. These are interlayered with middle to late Paleozoic hornblende-bearing mafic orthogneiss, biotite-quartz-feldspar gneiss, and Late Permian granitoid orthogneiss (locally with K-feldspar augen; Ryan *et al.*, 2013). The Paleozoic rocks are cut by a series of east-trending faults and shear zones that locally contain Paleozoic greenschist facies ultramafic and mafic rocks that were tectonically emplaced in the Jurassic (Figs. 2 and 3). Cretaceous granitoids cut the sequence and a large Cretaceous granite (99 Ma; McKenzie *et al.*, 2013), the Coffee Creek granite, intrudes the metamorphic rocks in the south (Figs. 1,2, and 3).

A greenschist facies shear foliation has been superimposed on, but locally obliquely crosscuts, the pervasive amphibolite facies foliation. The shear foliation (S_3, Table 1) occurs in narrow (100 m scale) east-trending zones, north and south of the Latte prospect, and in another subparallel zone in the metamorphic rocks just north of the Coffee Creek granite (Figs. 2 and 3). In the basement gneiss, the shear foliation consists of highly deformed zones rich in epidote, actinolite ± tremolite, and chlorite. These minerals have been derived by retrogressive alteration of pre-existing amphibolite facies minerals such as hornblende and biotite. The shear foliation is locally crosscut by apophyses of the Coffee Creek granite. Retrograde greenschist alteration, associated with the shear foliation, does not extend into any of the Cretaceous igneous rocks. Magnetite-bearing skarn occurs where greenschist facies shear zones cut through Paleozoic marble.

The ultramafic bodies are generally 5 to 50 m across and occur as irregularly shaped pods (Figs. 2 and 3). Two or more such pods can occur along a zone that lies parallel or subparallel to the adjacent amphibolite facies foliation. The pods are variably deformed internally, and parts of some pods retain their primary mineralogy and texture. Zones of deformed rocks within the ultramafic pods have a characteristic phacoidal texture on the outcrop scale, where anastomosing, pervasively serpentinized and foliated rock surround lenses of less-deformed rock. Serpentinized rock contains serpentine, chlorite, actinolite, talc, and magnesite; serpentinization also produced abundant magnetite.

Open folding and related fractures (D_4, Table 1) are relatively rare in the limited amount of outcrop that has been mapped in the Coffee Creek area, but this style of folding is commonly observed in drill core as small-scale kink and chevron folds. The folds have rounded to angular hinges and have steeply dipping fold axial surfaces relative to the metamorphic foliation. A steeply dipping fracture, subparallel to the axial surface F_4, is common and this is locally infilled with white orogenic quartz veins (discussed below).

Table 1. *Paragenetic sequence for the main minerals and structures in the Coffee Creek area.*

Age	Early Paleozoic	Late Paleozoic	Permian	Jurassic		Jurassic to Late Cretaceous	Late Cretaceous				Pliocene - Recent
Event	Host rock sedimentation	Pre-syn metamorphic intrusions	Late metamorphic intrusions	Slide Mountain terrane collision and thrusting			main gold event (Supremo, Latte)		high grade zones in Latte	late breccia	oxidation, weathering
Regional tectonics		Assembly of Yukon -Tanana terrane (D1-D2)		Orogenic collision, uplift, thrust stacking (D3-D4)	early silicification and pervasive sericite alteration		dark grey fine grained sulphides, veins and breccia infill	euhedral quartz, carbonate, translucent quartz	Fe(Mg) carbonate veinlets and breccia infill	late fractures calcite, hematite	regional uplift & erosion
Metamorphism		Amphibolite facies		localized Greenschist facies							groundwater alteration
gold	syn-depositional enrichment?			white quartz veins			Au in solid solution				Au liberated
arsenian pyrite					replace Hb, cubic, brassy blebs & masses along foliation		fine breccia; sooty py	local realgar			altered to limonite
pyrite		metamorphic brassy cubes		white quartz veins							
chalcopyrite		metamorphic in mafic rocks		white quartz veins							
hematite									specular hematite	fractures in mafic rocks	
sericite ± fuchsite					sericite, local fuchsite		minor sericite				
chlorite-epidote-actinolite				disseminated in shears, alteration							
Fe(Mg) carbonate											altered to limonite
calcite		metamorphic		remobilized in shears				multiple phases euhedral, banded vuggy carbonate		late white cc fractures	
quartz		quartz segregations		early white quartz veins; silicification of fold hinges	pervasive silicification		grey quartz	euhedral vuggy quartz			
dacite dikes, andesite dikes											
Coffee Granite											
serpentinite, talc schist				tectonically emplaced							
cataclasite, gouge							mineralized breccia	mineralized breccia	non-mineralized	non-mineralized	
ductile shears				S3							
folds			intrafolial F2	asymmetric F3	chevron kink F4						
foliation		S2	local crenulation cleavage								

COFFEE GOLD DEPOSITS

EARLY (JURASSIC) ALTERATION

Sericitic alteration is a common feature in core from the Coffee gold deposits and occurs in irregular patches or zones (cm to m-scale) that overprint the metamorphic host rocks, and in narrow vein selvages on the margins of early quartz veins. The alteration is characterized by pervasive quartz-sericite-hematite alteration that overprints the foliation in biotite-bearing orthogneiss rocks (Fig. 4). This sericitic alteration occurs in metamorphic rocks throughout the region but is most intense near regional scale, east-striking D_3 shears and thrust faults at Latte and Double Double and north-trending fault zones at Supremo. The alteration zones are mineralized with brassy coloured subhedral pyrite (Fig. 4a), and are generally barren, however, with little or no gold, unless overprinted by later sericitic alteration and arsenian pyrite (As-pyrite), discussed below.

Some of the early sericitic alteration zones are spatially associated with cm-scale, early white orogenic quartz veins (Table 1). Sericite + pyrite haloes extend (5 to 15 mm) outwards from some vein margins into host rock and locally contain elevated As. Some of these veins are folded and locally contain S_3 shear fabric and other veins infill brittle fractures associated with F_4 axial surface fractures. This generation of veins also appears to be barren and predates the main phase of overprinting Cretaceous gold mineralization.

CRETACEOUS GOLD MINERALIZATION

The main phase of gold mineralization at Coffee is associated with relatively high angle fractures and breccia that overprint earlier, Jurassic shear fabrics (D_3 to D_4) and sericitic alteration zones (Table 1; Fig. 4b). These mineralized brittle structures cut across all of the mapped rock types on the property, including the 99 Ma Coffee Creek granite (McKenzie *et al.*, 2013). Gold mineralization is therefore Late Cretaceous or younger. The main paragenetic stages of Coffee gold mineralization are listed in Table 1.

Much of the mineralized Coffee core is oxidised and paragenetic relationships are difficult to distinguish. Where oxidation has been limited, however, by low permeability (Fig. 5), early dark grey, 'sooty', arsenian pyrite (As-pyrite) replaces biotite along the metamorphic foliation. The Cretaceous mineralization is distinct from earlier sulphides deposited during Jurassic alteration (Figs. 4 and 5). The As-pyrite is relatively finer grained (typically <100 µm) than Jurassic 'brassy' pyrite (Fig. 6) and concentrated along micaceous layers, replacing biotite. Earlier generations of pyrite (metamorphic and Jurassic pyrite) are more euhedral, often cubic, and can be enclosed in quartz segregations and veins (Fig. 6).

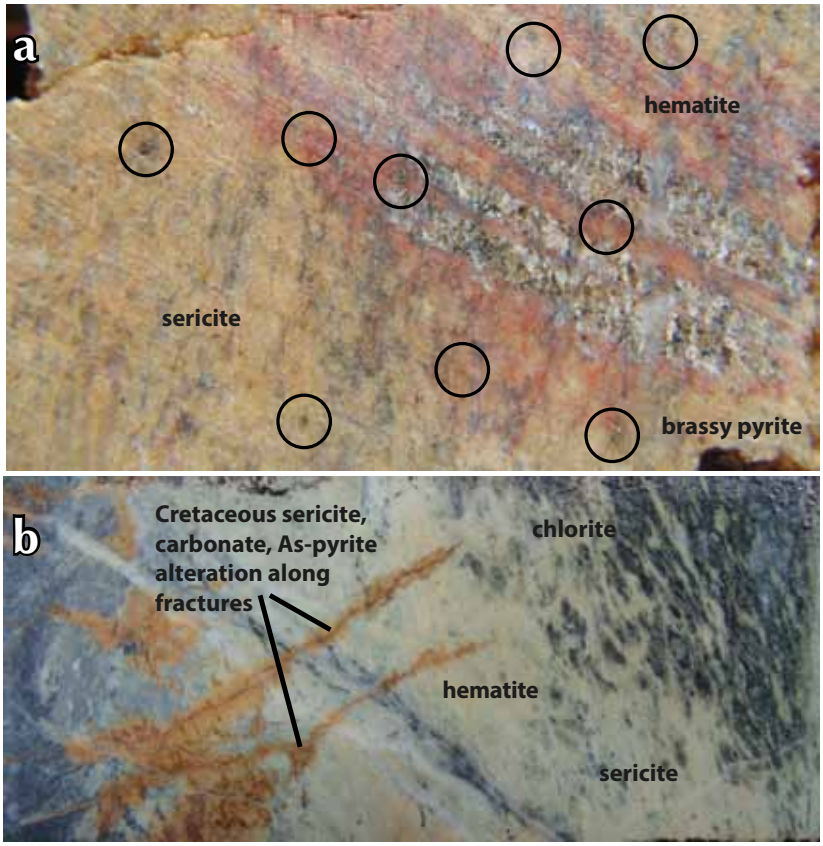

Figure 4. *Coffee core samples showing Jurassic sericitic alteration of granitoid orthogneiss from Supremo prospect: (a) unmineralized sericitic alteration zone (pale brown) and relict biotite-bearing host rock (centre right). A zone of red hematite-rich weak sericitic alteration occurs near the boundary between the relict host rock and the main sericitized zone. Brassy pyrite with little or no associated gold is scattered through the alteration zone (larger grains in black circles); and (b) unmineralized disseminated sericitic alteration and variable hematite staining is overprinted by fracture-controlled Cretaceous gold-bearing alteration. Cretaceous carbonate and As-pyrite is variably oxidised along the fractures.*

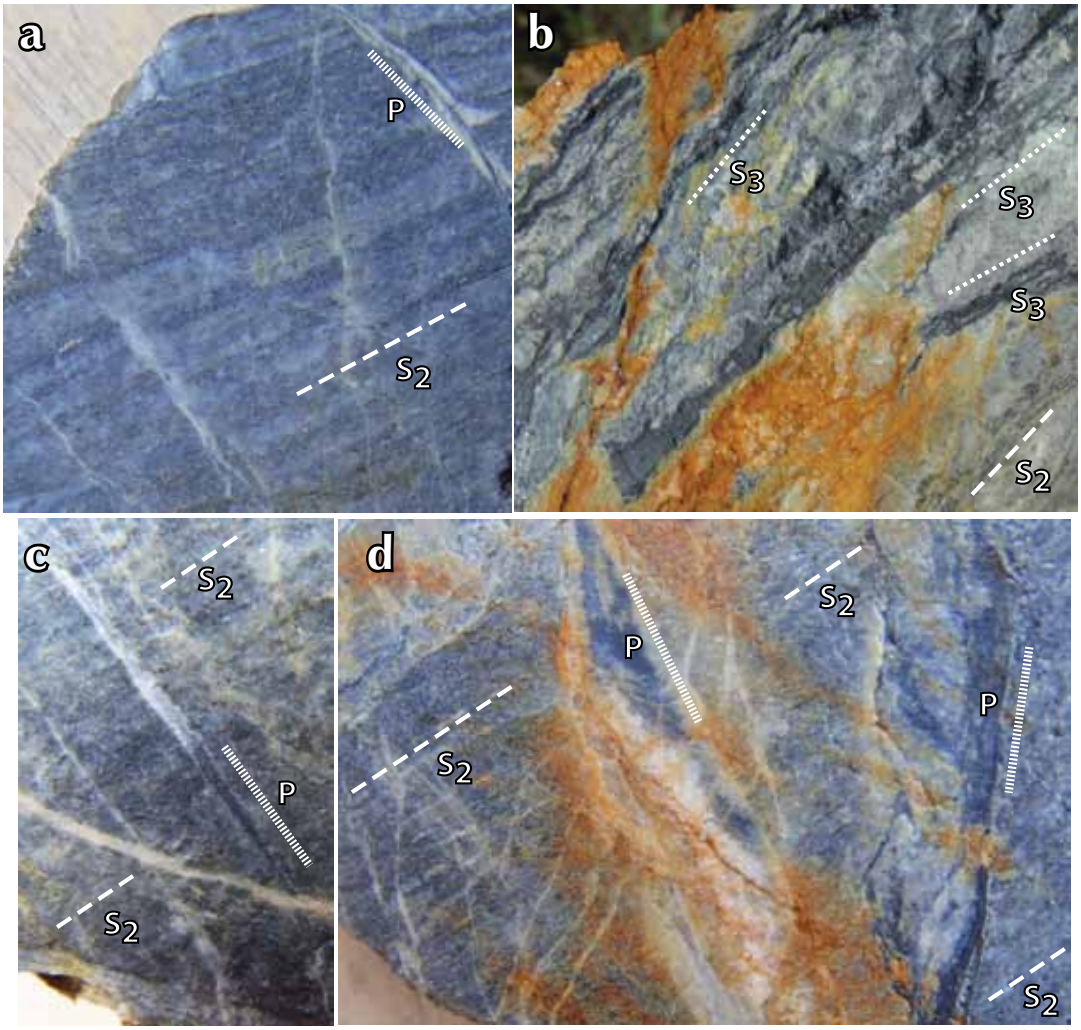

Figure 5. *Core photographs of mineralized biotite gneiss from the Latte prospect at Coffee, in samples where oxidation has been limited by low permeability. Biotite has been largely replaced by As-pyrite (dark grey) along foliation (S_2 in all images); pyrite-rich zones occur along Jurassic shears (S_3 in b) and crosscutting microveinlets (P in a, c, d).*

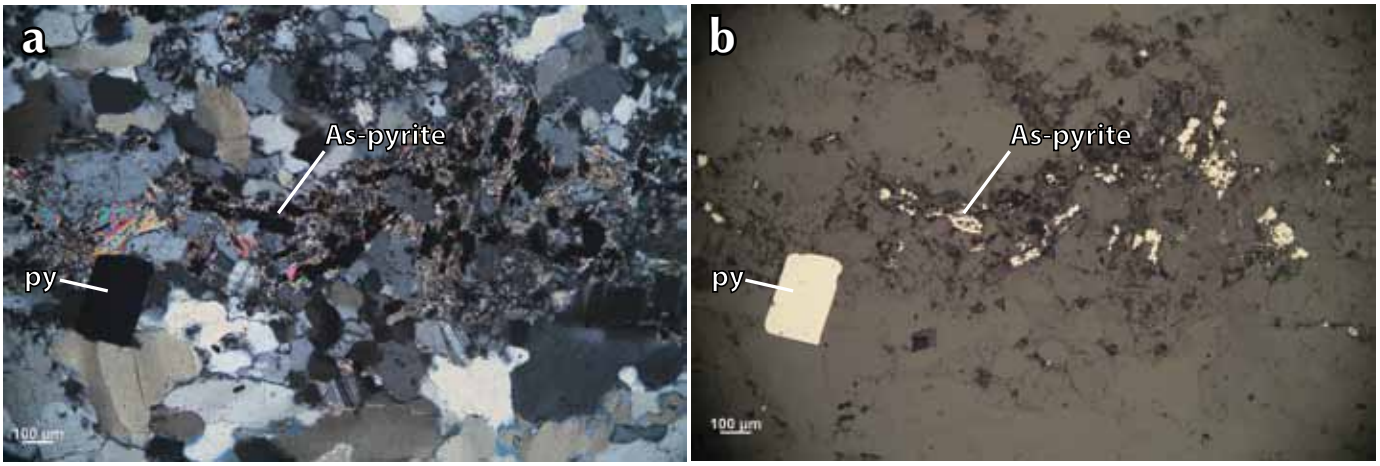

Figure 6. *Photomicrographs of early euhedral pyrite (py) and Cretaceous arsenian pyrite (As-pyrite): (a) transmitted light, crossed polars; and (b) Reflected light. The early pyrite is intergrown with relatively coarse quartz grains. The As-pyrite is finer grained, anhedral, and occurs in the micaceous layers replacing biotite.*

The presence of As-pyrite gives the Coffee gold deposits a strong As signature (Fig. 7) that is distinct from most Yukon gold deposits (MacKenzie *et al.*, 2008a, 2010, 2013). Typical As concentrations in mineralized samples are >> 100 ppm, and strongly altered samples contain between 1000 and 10 000 ppm, the upper analytical limit to this ICP assay method (Fig. 7a). Many mineralized samples contain several % As, as detected by portable XRF.

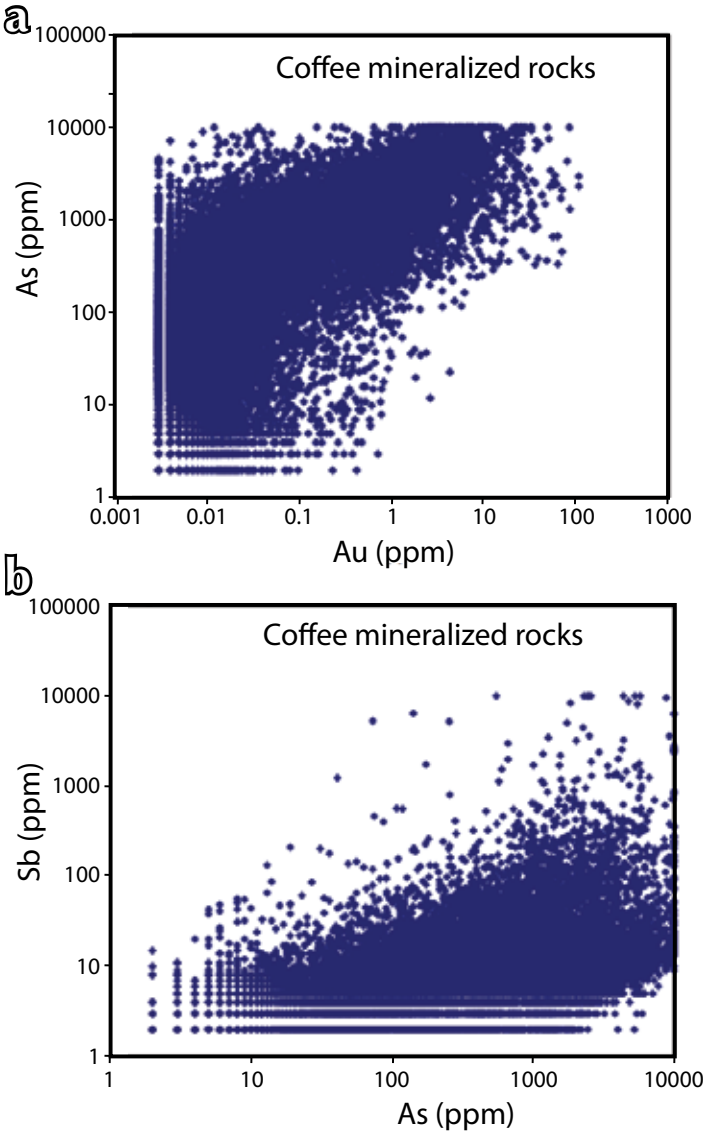

***Figure 7**. Arsenic and antimony concentrations in relation to gold contents for Coffee mineralized rocks (1 m core segments): (a) measured arsenic concentrations. The upper limit of 1 wt% to As contents is an analytical limit for the method used (ICP), not a real limit, and As contents >3 wt% are commonly measured with portable XRF; and (b) Measured antimony concentrations.*

As-pyrite occurs in both high angle mm-scale veins and as fine disseminations concentrated along micaceous layers in gneiss, and along pre-existing Jurassic shears (Fig. 5). The As-pyrite is generally dark grey, anhedral, and sooty in appearance, and associated with titanite where the two minerals have replaced metamorphic biotite. The greatest concentrations of sulphide occur where mineralized rocks have been brecciated and infilled with this As-pyrite. Grey, translucent quartz occurs with As-pyrite in microveinlets, and minor sericite extends (mm-scale) into wallrock (Table 1). Breccia dominates in mineralized rocks at Supremo and good gold grades (>1 ppm) correlate well with the 'sooty' As-pyrite-rich zones. The paragenetic sequence is more complex at Latte and Double Double where As-pyrite bearing rock and breccia are locally crosscut by additional phases of mm-scale prismatic quartz veins and banded carbonate veins (Table 1). These overprinting veins contain 'sooty' As-pyrite as well, and have locally enriched the gold grades (>3 ppm). Volumetrically, however, the bulk of the mineralized rock at all prospects is composed of the earlier As-pyrite that infills veins and breccia. Crosscutting Fe(Mg) carbonate veins and breccia cut the mineralized rocks (Table 1) but these phases are generally barren, as are other late-stage vein generations (Table 1).

Alteration and mineralization of the Coffee Creek granite is evident in zones of bleaching that extend outwards from high angle fractures (Fig. 8). Biotite in these zones is altered to sericite and the primary feldspars are albitized and sericitized. Where alteration is most intense, the biotite has been completely replaced by As-pyrite (Figs. 8c and 9).

High angle mineralized fractures and pyrite-bearing veins and breccia (with high As contents measured by bench top XRF) crosscut a variety of rock types at Latte (Fig. 10) including the ultramafic rocks emplaced along Jurassic thrust faults (Figs. 10d,e). Tectonically emplaced serpentinite is generally a poor host for gold but Cretaceous mineralized fractures locally extend into these ultramafic rocks, particularly in areas where they have been deformed and altered by Jurassic shears (S_3)

COMPARISONS TO OTHER YUKON TANANA TERRANE GOLD DEPOSITS

The style of mineralization at Coffee has some important similarities to, and differences from, other gold-bearing deposits in this part of the Yukon Tanana terrane (Table 2). The main difference between deposits at Coffee and the

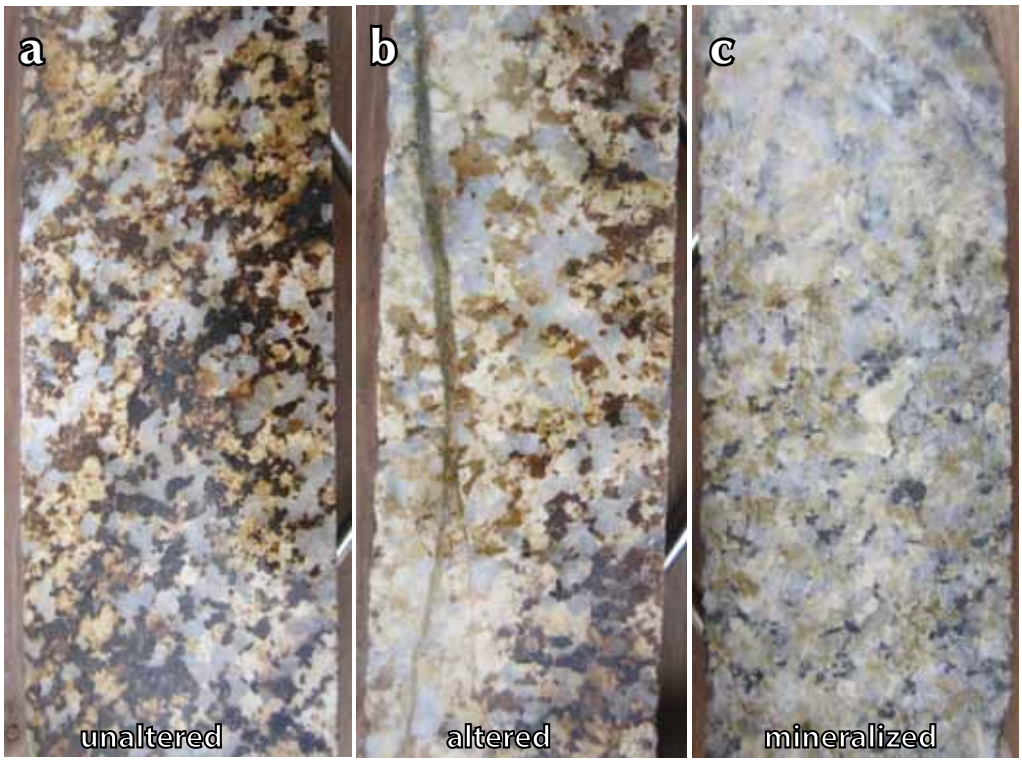

***Figure 8**. Progressively altered and mineralized core from the Kona prospect: (a) unaltered Cretaceous Coffee Creek granite containing quartz, feldspar, and biotite; (b) altered Coffee Creek granite. Biotite is sericitized and feldspars are albitized; and (c) Mineralized and altered Coffee Creek granite. Feldspars are sericitized and biotite has been replaced by As-pyrite.*

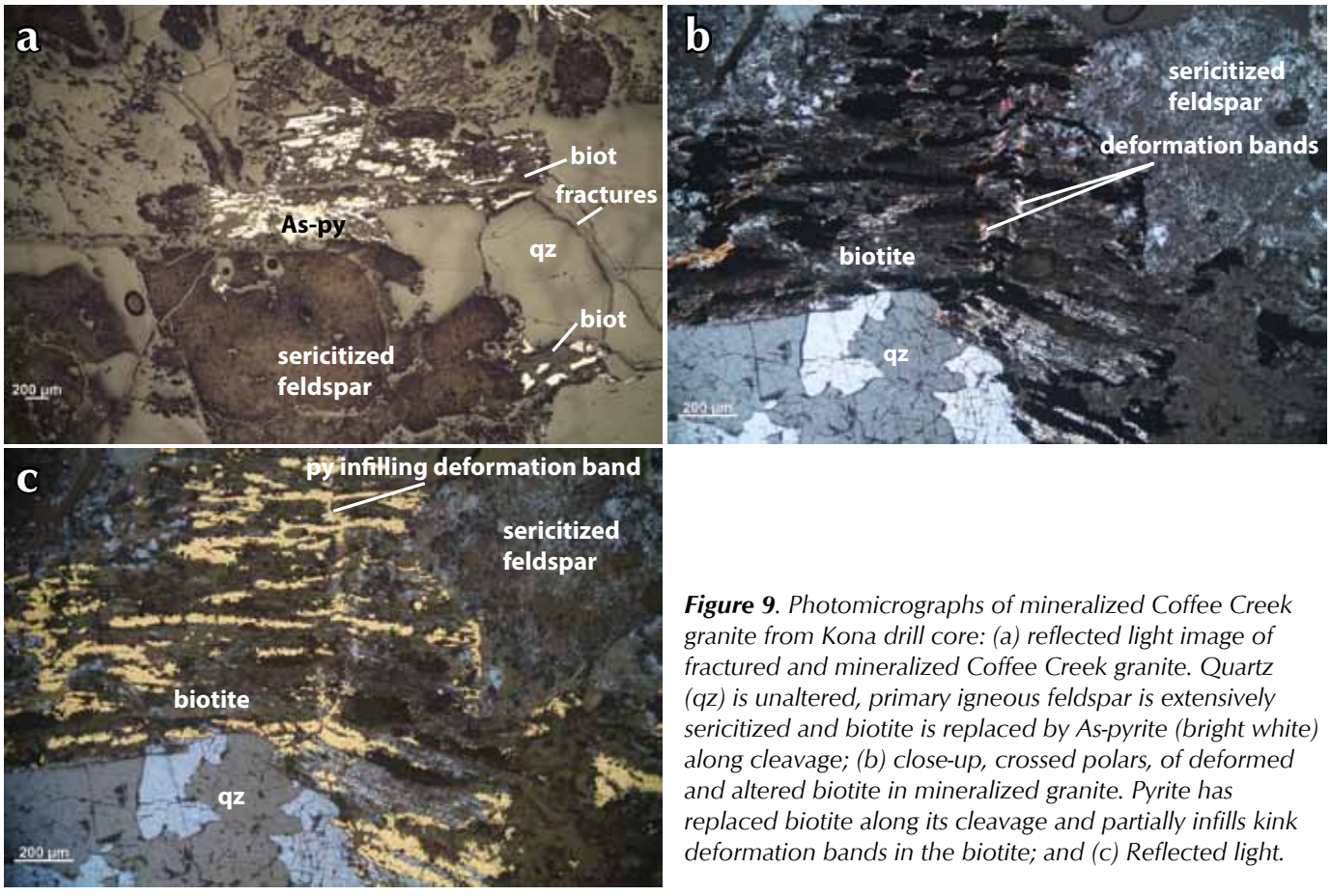

***Figure 9**. Photomicrographs of mineralized Coffee Creek granite from Kona drill core: (a) reflected light image of fractured and mineralized Coffee Creek granite. Quartz (qz) is unaltered, primary igneous feldspar is extensively sericitized and biotite is replaced by As-pyrite (bright white) along cleavage; (b) close-up, crossed polars, of deformed and altered biotite in mineralized granite. Pyrite has replaced biotite along its cleavage and partially infills kink deformation bands in the biotite; and (c) Reflected light.*

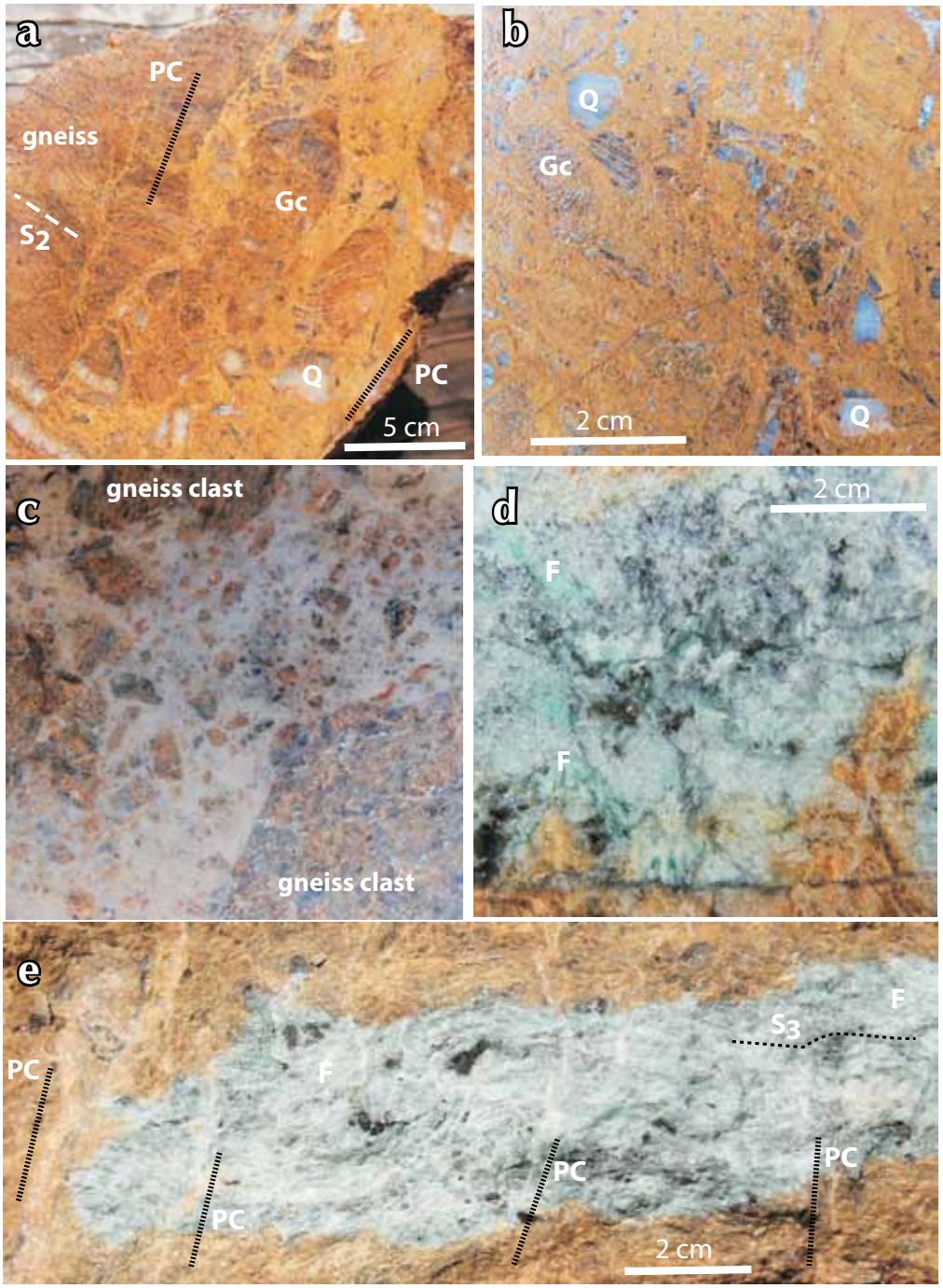

Figure 10. *Photographs of samples of fracture-controlled and brecciated mineralized zones in the Latte prospect at Coffee: (a) slabbed boulder of biotite gneiss (relict S_2 foliation preserved on margins) cut by steeply dipping brecciated zones with clasts of gneiss (Gc) and quartz (Q). Fractures with hydrothermal As-pyrite and carbonate (PC) cut the rock in the indicated steep orientations, and both clasts and host rock have been impregnated by disseminated As-pyrite and carbonate; (b) cut slab of a boulder more intensely brecciated than in (a); (c) core photograph of quartz-dominated mineralized breccia; (d) Boulder of serpentinite altered to talc, chlorite, carbonate, and fuchsite (F) with As-pyrite (dark seams) along numerous fractures; and (e) boulder of altered serpentinite (as in d) with steeply crosscutting fractures containing carbonate and As-pyrite (PC).*

nearby White Gold district is that mineralization at Coffee is superimposed on White Gold-style alteration. Gold mineralization at Coffee is characterized by gold-bearing As-pyrite that overprints earlier sericitic alteration. The early sericitic alteration is associated with Jurassic D_3 and D_4 structures and minor local orogenic quartz veins. In the White Gold district, this stage of alteration is accompanied by gold-bearing disseminated pyrite and little or no As (in orthogneiss rocks). At Coffee, this stage of alteration is accompanied by brassy pyrite that looks similar to the pyrite at White Gold but is generally barren. The main stage of gold mineralization at White Gold is thought to be Jurassic (Bailey, 2013) whereas gold mineralization at Coffee is no older than Late Cretaceous (McKenzie *et al.*, 2013). Mineralization in both areas is hosted in regional scale east and north-trending structures. These structures probably initiated in the Jurassic and were reactivated in the Cretaceous. Molybdenite associated with gold-bearing pyrite veins and sericite alteration in fault rocks at the Golden Saddle deposit on the White Gold property has been dated Late Jurassic (Re-Os ages, 163-155 Ma; Bailey, 2013). However, additional Early Cretaceous dates were obtained from hydrothermal altered rocks containing illite and fuchsite at Golden

Table 2. *Summary of mineralization characteristics of the Coffee hydrothermal gold system, in comparison to some other known gold deposits in the Yukon region (partly after Johnston et al., 1996; Baker and Lang, 2001; MacKenzie et al., 2008a, 2010; McKenzie et al., 2013,).*

Deposit:	Coffee gold deposits	Boulevard	White Gold district	Klondike goldfield	Tintina Au belt Intrusion-related	Carmacks	Casino
Metal(loids)	Au, As, Sb	Au, As, Sb	Au (Mo, As)	Au	Au, Bi, As, Te (W, Mo)	Au, Cu, Ag	Cu, Au, Mo, Ag
Age	Cretaceous?	mid-Cretaceous	Jurassic	Jurassic	mid-Cretaceous	Late Cretaceous	Late Cretaceous
Principal host rocks	Granitoid orthogneiss, biotite gneiss; Coffee Ck granite	Mafic schist	Granitoid orthogneiss, graphitic quartzite	Felsic schist, mafic schist	Felsic-intermediate intrusive rocks	Gneiss, hypabyssal intrusive rocks	Gneiss, Dawson Range & Casino complex felsic intrusive rocks
Primary structural control	Jurassic extensional fractures, faults, reactivated in Cretaceous	Cretaceous faults	Jurassic extensional fractures, faults	Jurassic extensional fractures in fold axial surfaces	Extensional fractures	Normal faults	Cretaceous faults
Secondary structural controls	Paleozoic foliation; Jurassic foliation-parallel shears	Fault-related extensional fractures	Paleozoic foliation, Jurassic foliation-parallel shears	Localised extensional fracture sets	Extensional fractures	Fractures	Intrusive breccia
Alteration	Biotite replacement, sericitization, silicification, carbonation; overprints Jurassic sericitization	Sericitization, silicification	Sericitization, silicification, graphitisation	Minor carbonate	Minor muscovite, carbonate, feldspar, sulphide zones; skarns	Sericitization, clay alteration	Potassic core, phyllic, weak argillic and propylitic
Mineralization style	Breccia, disseminated	Quartz veins, breccia	Breccia, disseminated	Quartz veins	Sheeted quartz veins	Veins, disseminated	Disseminated
Gold	Solid solution in arsenian pyrite	Microparticulate in sulphides	Free grains, microparticulate in sulphides	Free grains	Free grains; microparticulate in sulphides	Disseminated, with pyrite	Disseminated with sulphides
Inferred mineralization type	Epizonal orogenic	Mesozonal orogenic	Mesozonal orogenic (local epizonal signatures)	Mesozonal orogenic	Intrusion-related	Epithermal	Porphyry, breccia pipe
Inferred metal source	External, regional tectonic processes	External, regional tectonic processes	Local, lithologically controlled	Local, lithologically controlled	Magmatic	Magmatic	Magmatic

Saddle (Ar/Ar ages, 139-114 Ma; Bailey, 2013). So timing of hydrothermal alteration minerals at White Gold suggests mineralization extended from the Jurassic to at least mid-Cretaceous. The main phase of gold mineralization at Coffee is associated with Late Cretaceous (or younger) As-pyrite that overprints the earlier Jurassic White Gold-style alteration.

There are other deposits in the region that were mineralized in the Cretaceous. Mineralization at the Casino deposit is related to an intrusive breccia pipe and is dated as Late Cretaceous (75-74 Ma; Selby and Creaser, 2001). Geochemically, structurally, and mineralogically this deposit is very different from the deposits at Coffee. Similarly, the magmatic-related deposits at Carmacks, and the intrusion-related gold systems in the Tombstone plutonic suite in the Tintina gold belt are characterized by very different mineralogical and metal associations (Table 2). Furthermore, mineralization at Coffee is dominated by disseminated mineralization and breccia, not epithermal-style or intrusion-related veins.

Coffee gold deposit rocks have been affected by some of the same structural features that host gold in the Klondike goldfield (MacKenzie *et al.*, 2008a). Coffee core contains some orogenic-style quartz veins hosted in F_4 fold axial surface fractures, but these are relatively minor and, unlike coeval veins in the Klondike, the Coffee orogenic veins contain little or no gold.

Gold mineralization at Coffee is most similar to the deposits along the Boulevard trend in the Independence Creek area (McKenzie *et al.,* 2013; Table 2). These occurrences are dated as Cretaceous and mineralization is hosted in similar rocks. Mineralization at Coffee is characterized by more brittle structures, lacks abundant Mo, and is likely a shallower (epizonal) deposit. In contrast, the deposits in the Independence Creek area are mesozonal, and the Toni Tiger showing contains abundant quartz molybdenite veins.

CONCLUSIONS

Mineralized rocks at Coffee record a succession of biotite replacement, sericitization, silicification, and carbonatization events that overprint earlier Jurassic sericitic alteration (Table 1). Au, As, and Sb-bearing fluids (Fig. 7) were structurally controlled along regional-scale Jurassic faults and shear zones that were reactivated in the Late Cretaceous. Mineralization, in primarily Paleozoic gneiss but also Cretaceous igneous rocks, was focused along high angle fracture systems and breccia.

Disseminated mineralization extended outwards from brecciated zones in biotite-rich host rocks. Disseminated mineralization in these rocks was controlled and enhanced by pre-existing biotite within metamorphic foliation and Jurassic shears. As-pyrite replaced metamorphic biotite in gneiss and igneous biotite in Cretaceous granitoid rocks.

Cretaceous mineralization superimposed over Jurassic alteration can be distinguished on the basis of pyrite colour and morphology. Jurassic pyrite is generally brassy coloured and euhedral, and is commonly disseminated as isolated grains or clusters throughout sericitic alteration zones. Cretaceous As-pyrite is typically darker grey ('sooty') and more anhedral (Fig. 6). As-pyrite generally occurs as breccia infill, narrow veinlets, or as fine-grained aggregates disseminated along micaceous layers replacing biotite.

Coffee mineralized rocks show a strong positive correlation between Au and As, and Au and Sb (Fig. 7). As values are several orders of magnitude higher than As concentrations in mineralized rocks from orogenic gold occurrences in the Klondike goldfield and mineralized orthogneiss at Golden Saddle in the White Gold district (<100 ppm; MacKenzie *et al.*, 2008a, 2010). Sb contents are similarly elevated in Coffee mineralized rocks compared to mineralized rocks from the Klondike goldfield and the White Gold district (MacKenzie *et al.*, 2008a, 2010), but the Sb/As ratios are broadly similar.

ACKNOWLEDGEMENTS

This research was supported financially by Kaminak Gold Corporation, the New Zealand Ministry for Science and Innovation, and the University of Otago. Geological discussions with Tim Smith, Rory Kutluoglu, Geoff Newton, Adam Fage, Hannah Grimson, and Joe Currie were very helpful. A constructive review of the manuscript by Murray Allan was much appreciated.

REFERENCES

Bailey, L., 2013. Late Jurassic fault-hosted gold mineralization of the Golden Saddle deposit, White Gold district, Yukon Territory. Unpublished MSc Thesis, University of British Columbia, Vancouver, Canada.

Baker, T. and Lang, J.R., 2001. Fluid inclusion characteristics of intrusion-related gold mineralization, Tombstone-Tungsten magmatic belt, Yukon Territory, Canada. Mineralium Deposita, vol. 36, p. 563-582.

Beranek, L.P. and Mortensen, J.K., 2011. The timing and provenance record of the Late Permian Klondike orogeny in northwestern Canada and arc-continent collision along western North America. Tectonics, vol. 30, TC5017.

Berman, R.G., Ryan, J. J., Gordey, S.P., and Villeneuve, M., 2007. Permian to Cretaceous polymetamorphic evolution of the Stewart River region, Yukon-Tanana terrane, Yukon, Canada: P-T evolution linked with insitu SHRIMP monazite geochronology. Journal of Metamorphic Geology, vol. 25, p. 803-827.

Gabrielse, H., Murphy, D.C., and Mortensen, J.K., 2006. Cretaceous and Cenozoic dextral orogen-parallel displacements, magmatism, and paleogeography, north-central Canadian Cordillera. *In:* Paleogeography of the North American Cordillera: Evidence For and Against Large-Scale Displacement, J.W. Haggart, R.J. Enkin, and J.W.H. Monger (eds.), Geological Association of Canada, Special Paper 46, p. 255-276.

Johnston, S.T., Mortensen, J.K., and Erdmer, P., 1996. Igneous and metaigneous age constraints on the Aishihik metamorphic suite, SW Yukon. Canadian Journal of Earth Sciences, vol. 33, p. 1543-1555.

MacKenzie, D.J. and Craw, D., 2010. Structural controls on hydrothermal gold mineralization in the White River area, Yukon. *In:* Yukon Exploration and Geology 2009, K.E. MacFarlane, L.H. Weston, and L.R. Blackburn (eds.) Yukon Geological Survey, p. 253-263.

MacKenzie, D. and Craw, D., 2012. Contrasting structural settings of mafic and ultramafic rocks in the Yukon-Tanana terrane. *In:* Yukon Exploration and Geology 2011, K.E. MacFarlane and P.J. Sack (eds.), Yukon Geological Survey, p. 115-127.

MacKenzie, D., Craw, D., Brodie, C., and Fleming, A., 2013 Foliation development and hydrothermal gold emplacement in metagabbroic rocks, central Yukon, Canada. *In:* Yukon Exploration and Geology 2012, K.E. MacFarlane, M.G. Nordling, and P.J. Sack (eds.), Yukon Geological Survey, p. 47-64.

MacKenzie, D.J., Craw, D., Cooley, M., and Fleming, A., 2010. Lithogeochemical localisation of disseminated gold in the White River area, Yukon, Canada. Mineralium Deposita vol. 45, p. 683-705.

MacKenzie, D.J., Craw, D., and Mortensen, J., 2008a. Structural controls on orogenic gold mineralisation in the Klondike goldfield, Canada. Mineralium Deposita, vol. 43, p. 435-448.

MacKenzie, D., Craw, D., and Mortensen, J. K., 2008b. Thrust slices and associated deformation in the Klondike goldfields, Yukon. *In:* Yukon Exploration and Geology 2007, D.S. Emond, L.R. Blackburn, R.P. Hill, and L.H. Weston (eds.), Yukon Geological Survey, p. 199-213.

McKenzie, G.G., Allan, M.M., Mortensen, J.K., Hart, C.J.R., Sanchez, M., and Creaser, R.A., 2013. Cretaceous orogenic gold and molybdenite mineralization in the Independence Creek area, Dawson Range, parts of NTS 115J/13 and 14. *In*: Yukon Exploration and Geology 2012, K.E. MacFarlane, M.G. Nordling, and P.J. Sack (eds.), Yukon Geological Survey, p. 73-97.

Mortensen, J.K., 1992. Pre-mid-Mesozoic tectonic evolution of the Yukon-Tanana Terrance, Yukon and Alaska. Tectonics, vol. 11, p. 836-853.

Mortensen, J.K., 1996. Geological compilation maps of the northern Stewart River map area, Klondike and Sixtymile Districts (115N/15, 16: 115O/13, 14; and parts of 115O/15, 16). Exploration and Geological Services Division, Yukon Region, Indian and Northern Affairs Canada, Open File 1996-1(G), 43 p.

Ruks, T.W., Piercey, S.J., Ryan, J.J., Villeneuve, M.E., and Creaser, R.A., 2006. Mid to Late Paleozoic K-feldspar augen granitoids of the Yukon-Tanana Terrance, Yukon, Canada: Implications for crustal growth and tectonic evolution of the northern Cordillera. GSA Bulletin, vol. 118, p. 1212-1231.

Ryan, J.J. and Gordey, S.P., 2004. Geology, Stewart River Area (Parts of 115N/1,2,7,8 and 115-O/2-12), Yukon Territory. Geological Survey of Canada, Open File 4641, scale 1:100 000.

Ryan, J.J., Zagorevski, A., Williams, S.P., Roots, C., Ciolkiewicz, W., Hayward, N., and Chapman, J.B., 2013. Geology, Stevenson Ridge (northwest part), Yukon. Geological Survey of Canada, Canadian Geoscience Map 117 (2nd edition, preliminary), scale 1:100 000.

Selby, D. and Creaser, R. A., 2001. Late and mid-Cretaceous mineralization in the Northern Canadian Cordillera: constraints from Re-Os Molybdenite Dates. Economic Geology, vol. 96, p. 1461-1467.

Wainwright, A.J., Simmons A.T., Finnigan, C.S., Smith, T.R., and Carpenter, R.L., 2011. Geology of new gold discoveries in the Coffee Creek area, White Gold District, west-central Yukon. *In:* Yukon Exploration and Geology 2010, K.E. MacFarlane, L.H. Weston, and C. Relf (eds.) Yukon Geological Survey, p. 233-247.

U-Pb age, whole-rock geochemistry and radiogenic isotopic compositions of Late Cretaceous volcanic rocks in the central Aishihik Lake area, Yukon (NTS 115H)

G.A. Morris
Geological Survey of Sweden, Uppsala, Sweden

J.K. Mortensen[1]
University of British Columbia, Vancouver BC

S. Israel
Yukon Geological Survey, Whitehorse YT

Morris, G.A., Mortensen, J.K., and Israel, S., 2014. U-Pb age, whole-rock geochemistry and radiogenic isotopic compositions of Late Cretaceous volcanic rocks in the central Aishihik Lake area, Yukon (NTS 115H). *In:* Yukon Exploration and Geology 2013, K.E. MacFarlane, M.G. Nordling, and P.J. Sack (eds.), Yukon Geological Survey, p. 133-145.

ABSTRACT

Geochemical, isotopic and U-Pb dating studies of volcanic rocks of the Tlansanlin Formation in central Aishihik Lake map area (115H) show that these are Late Cretaceous (75.8±0.4 Ma to 77.3±1.3 Ma), relatively primitive magmas that were emplaced in a continental arc setting. Intrusive rocks in the immediate area, associated with the Hopper porphyry and skarn and Sato porphyry occurrences (Yukon MINFILE 115H 019, 021, respectively), are similar in age and composition to the Tlansanlin Formation rock units, confirming the presence of a significant Late Cretaceous igneous and mineralizing event in the area. Significant porphyry and skarn occurrences associated with the Late Cretaceous intrusions in the Aishihik Lake area, as well as the important mineral deposits and occurrences associated with this magmatic event in the Dawson Range to the northeast (*e.g.*, Casino, Revenue-Nucleus, Sonora Gulch), underscore the metallogenic potential of this previously poorly recognized magmatic event.

[1] *jmortensen@eos.ubc.ca*

INTRODUCTION

At least seven separate suites of volcanic rocks of Late Cretaceous to Paleocene age have been recognized northeast of the Denali fault system in southwestern Yukon (Fig. 1). The Bennett Lake and Mount Skukum volcanic complexes in the southwestern Whitehorse map area (Morris and Creaser, 2003) and the Rhyolite Creek volcanoplutonic complex in the northwestern Aishihik Lake map area (Fig. 1; Israel *et al.*, 2011a,b; Israel and Westberg, 2011, 2012) have given Paleocene to Eocene emplacement ages. The Sifton Range volcanic complex in the eastern Aishihik Lake map area (Fig. 1) is undated but is also inferred to be Paleocene in age by Miskovic and Francis (2004) based on the age of Paleocene intrusive rocks that crosscut the complex. The Donjek Volcanics in the central Stevenson Ridge map area (Fig. 1; Templeman-Kluit, 1974; Murphy, 2007) have yielded preliminary Late Cretaceous crystallization ages (D. Murphy and J.K. Mortensen, unpublished data). The small Mount Creedon volcanic complex on the western side of Aishihik Lake in central Aishihik Lake map area (Fig. 1) is undated but has been inferred to be of Paleocene age in most recent map compilations (Johnston and Timmerman, 1997a; Israel *et al.*, 2011a). Finally, volcanic units immediately east of Aishihik Lake in the central part of the Aishihik Lake map area (Fig. 1) were previously assigned to the Carmacks Group (Tempelman-Kluit, 1974) and subsequently to a newly named Tlansanlin Formation with an assumed Late Cretaceous age by Johnston and Timmerman (1997b).

In this study we present previously unpublished major, trace and rare earth element data, as well as measured Nd and Sr isotopic compositions and two U-Pb zircon ages, for a suite of samples from the Tlansanlin Formation in the central Aishihik Lake area. We then use these results to better constrain the nature and timing of magmatism and discuss metallogenic implications for this part of southwestern Yukon.

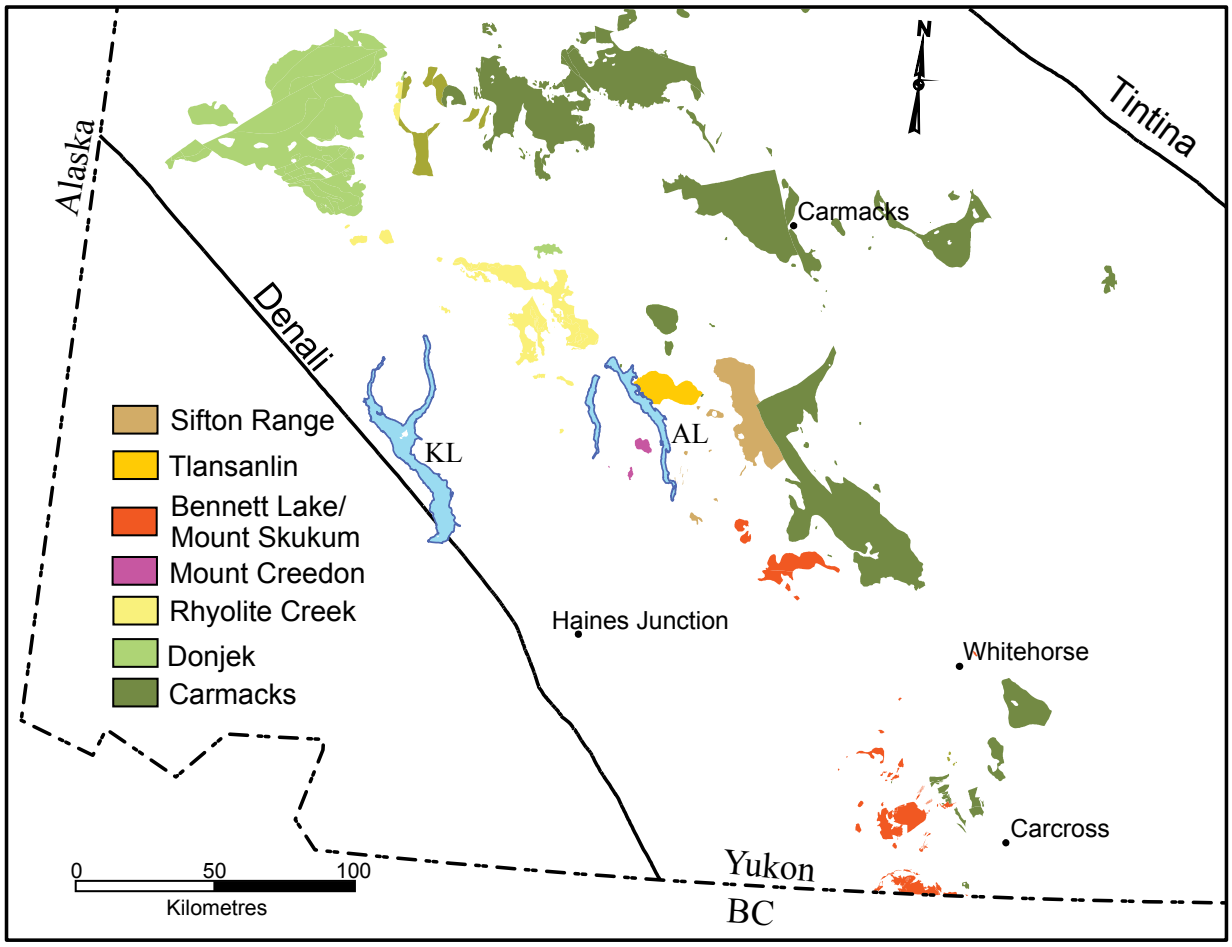

Figure 1. *Map showing the locations of the various Paleocene/Eocene and Late Cretaceous volcanic and plutonic assemblages in southwestern Yukon. Geology from Colpron (2013). AL = Aishihik Lake, KL = Kluane Lake.*

REGIONAL GEOLOGY OF THE AISHIHIK LAKE AREA

A simplified version of the geology of the Aishihik Lake map area is shown in Figure 2.

Metamorphic rocks assigned to the Yukon-Tanana Terrane (Snowcap and Finlayson assemblages; Israel *et al.*, 2011b) occur within a northwest-trending belt across the centre of the map area (Fig. 2). These rocks comprise metasedimentary and metavolcanic rocks, including quartz-muscovite ± garnet schist, carbonaceous biotite ± garnet schist and quartzite, garnet amphibolite and marble, as well as rare intermediate composition metaplutonic rocks. The metasedimentary units are undated in this area, but are assumed to be Mississippian and older based on correlations with well-dated rock units elsewhere in Yukon. Samples of granitic orthogneiss and possible metavolcanic units in the immediate vicinity of Aishihik Lake have given U-Pb crystallization ages of 352-344 Ma (Johnston *et al.*, 1996).

Plutonic rocks underlie much of the Aishihik Lake map area (Fig. 2). These include intermediate to felsic intrusions of the Early Jurassic Aishihik and Long Lake plutonic suites (Johnston *et al.*, 1996), which underlie large portions of the eastern half of the map area, together with felsic intrusive rocks of the mainly Paleocene Ruby Range batholith, which forms a northwest-trending belt across the southern and western part of the map area (*e.g.*, Israel *et al.*, 2011a; Israel and Westberg, 2011; Fig. 2). Numerous smaller intrusions that crosscut the Early Jurassic intrusions and their metamorphic wall rocks northeast of the Ruby Range batholith have in the past been mainly assumed to be related to the batholith itself. Several of these intrusions, however, have yielded Late Cretaceous crystallization ages. A small body of hornblende diorite that hosts the Sato porphyry copper occurrence (Yukon MINFILE 115H 021; Fig. 2) yielded two conventional U-Pb zircon ages of 78.2 ± 0.1 Ma and 78.8 ± 0.2 Ma (Lewis and Mortensen, 1998). Another small stock immediately east of Hopkins Lake (the "Hopper intrusion"; Johnston and Timmerman, 1997b; Blumenthal, 2010) gave U-Pb zircon ages by laser ablation ICP-MS methods at 77.2 ± 1.2 Ma and 76.0 ± 1.1 Ma (Blumenthal, 2010; a third sample gave a calculated age of 83.7 ± 1.9 Ma; however, the analytical data from this sample shows a high degree of scatter and the significance of the calculated age is uncertain). Johnston and Timmerman (1997b) describe scattered outcrops of volcanic rocks in the northeastern part of the Hopkins Lake map area (115H/7) as comprising "heterogeneous grey, green and maroon, poorly consolidated, intermediate to felsic, feldspar and hornblende-feldspar porphyritic tuff, flow breccia and volcaniclastic rocks". These volcanic units overlie a package of conglomerate, sandstone and mudstone that contains a large proportion of reworked volcanic rocks as well as minor tuff. Collectively these two units are called the Tlansanlin Formation (Johnston and Timmerman, 1997b), named for a type locality along the Tlansanlin Creek on the east side of Aishihik Lake (Fig. 2). In the vicinity of the Sato occurrence, in the northeastern Hopkins Lake map area, the upper Tlansanlin Formation volcanic rocks are interpreted to unconformably overlie Early Jurassic Long Lake suite intrusive rocks, but to be crosscut by the ~78 Ma diorite body that hosts the Sato porphyry-style mineralization. This interpreted relationship implies a probable Late Cretaceous age for the Tlansanlin Formation volcanic rocks (Johnston and Timmerman, 1997b).

Intermediate to felsic volcanic rocks interlayered with volcaniclastic units underlies part of the northeastern Hopkins Lake map sheet and areas farther to the north and east (Fig. 2). Although Johnston and Timmerman (1997b) included these units in their Tlansanlin Formation, Miskovic and Francis (2004) include them in the Sifton Range complex.

Johnston and Timmerman (1997b) also included a number of narrow, north-south trending, fine grained mafic dikes that are widespread in the Hopkins Lake map area (115H/7) as part of the Late Cretaceous magmatic suite. None of these dikes have been dated thus far. North-south trending quartz-feldspar porphyry dikes are also widespread in the southern Hopkins Lake and adjacent Aishihik Lake map areas; these dikes are also undated but are inferred by Johnston and Timmerman (1997a) and Israel *et al.* (2011a) to be Paleocene or Eocene in age.

TLANSANLIN FORMATION VOLCANIC UNITS IN THE CENTRAL AISHIHIK LAKE AREA

Volcanic rock units that comprise the upper part of the Tlansanlin Formation of Johnston and Timmerman (1997b) underlie an area of approximately 200 km^2 to the east of Aishihik Lake (Fig. 2). The volcanic sequence consists of extensive, flat-lying basalt, basaltic andesite, andesite and dacite lava flows, lapilli and welded pyroclastic flows. Basalt and basaltic andesite are generally fine-grained with

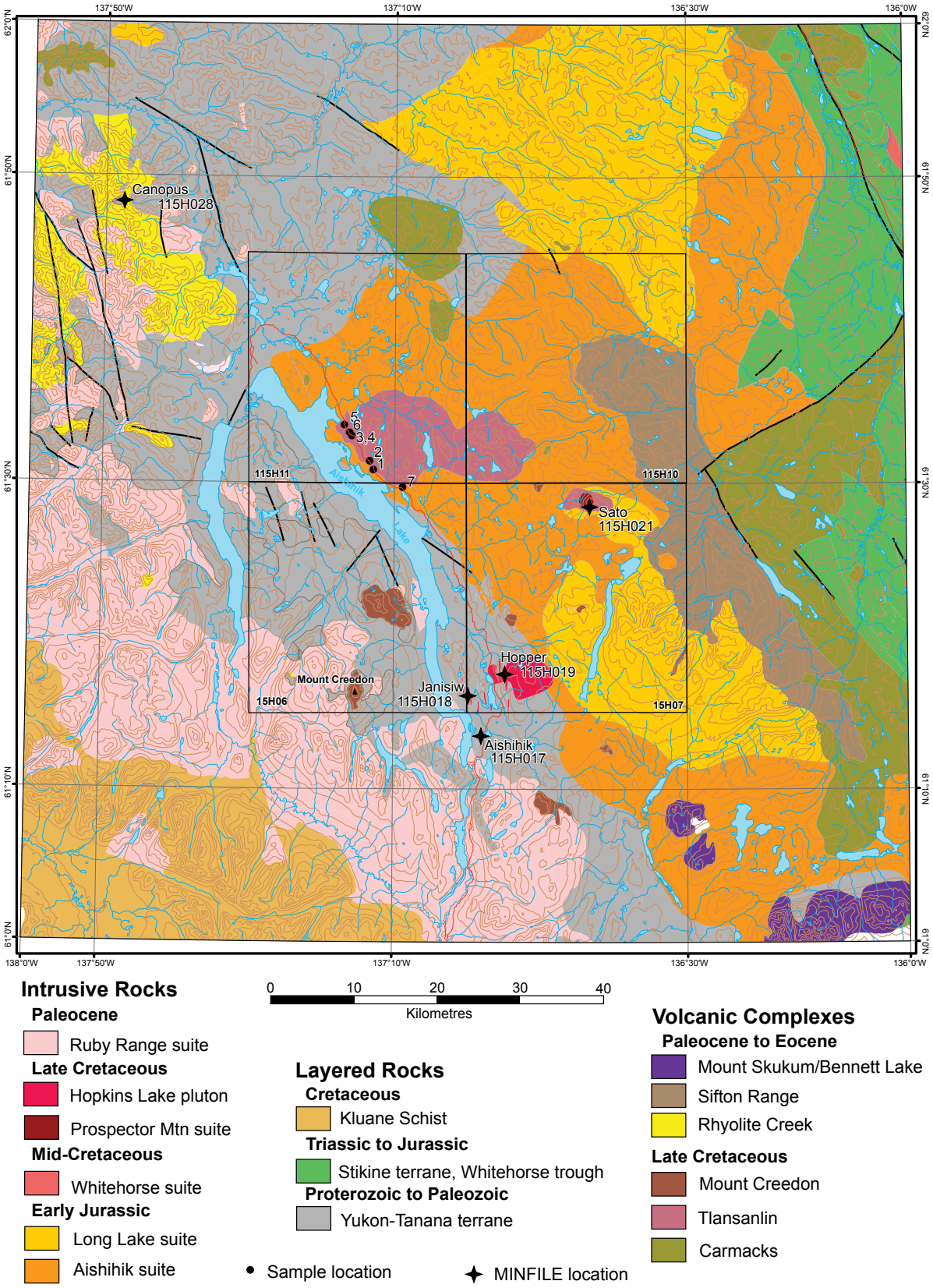

Figure 2. *Simplified geology of the Aishihik Lake map area. Sample location numbers correspond to those in Table 1. Geology is modified from Johnston and Timmerman (1997a,b), Israel and Westberg (2011), and Israel et al. (2011a).*

microphenocrysts of olivine and pyroxene in a groundmass dominated by calcic plagioclase. Andesite and dacite contain phenocrysts of plagioclase, hornblende and, rarely, pyroxene up to 5 mm in size, in a fine-grained to devitrified glass matrix. Plagioclase phenocrysts commonly display fine scale cyclic zoning and are generally broken. Mafic phenocryst phases commonly show reaction rims of oxide minerals.

Volcanic rocks in the study area were originally mapped by Cockfield (1927) as "Jurassic (?) to Triassic (?) older volcanics" but were subsequently mapped by Templeman-Kluit (1974) as the "varicoloured acid tuff." They were later incorporated into the Mount Creedon Volcanic Suite of Johnston and Timmerman (1994), which were thought to correlate with the Mount Nansen Group and/or the Carmacks Group, as defined farther to the northeast in the Dawson Range. More recent geochronological studies have shown that the Mount Nansen and Carmacks groups are middle and Late Cretaceous in age, respectively (Allan *et al*., 2013, and references therein). Johnston and Timmerman (1997b) subsequently included the volcanic rocks into their Tlansanlin Formation, tentatively assigned to the Late Cretaceous. Due to the flat lying and undeformed nature of lava flows, they were, however, thought to have been erupted following uplift of the Palaeocene-Eocene Ruby Range batholith and the associated Aishihik and Kluane metamorphic assemblages. The earliest date for this uplift has been put at ~55 Ma (Erdmer and Mortensen, 1993). Clasts that were thought to have been derived from the Ruby Range batholith have also been identified within the volcanic strata at Aishihik Lake (Johnson and Timmerman, 1994). This evidence suggested a Paleocene or Eocene age rather than an association with any Cretaceous magmatic event, including the Carmacks Group volcanics (which in any case do not generally contain dacite) or the Mount Nansen volcanics (Morris and Creaser, 1998).

SAMPLE DESCRIPTIONS

Whole-rock geochemistry, together with Sr and Nd isotopic compositions and U-Pb zircon age, were determined for a suite of six samples of massive dikes and volcanic flows and domes of the Tlansanlin Formation that were collected during a reconnaissance level investigation of this sequence by the first author. Sample locations and brief descriptions are given in Table 1.

Sample GM97 A94 was collected from a partially weathered and well fractured dike and is basaltic or trachybasaltic in composition (see below). Sample GM97 A95 is an andesite collected from a poor exposure of what is thought to be a dike, and is also moderately weathered. Sample GM97 A96 is a basaltic andesite, also from a moderately weathered and poorly exposed dike whereas sample GM97 A97 is a much less weathered basaltic andesite collected from a sub-aerial flow with well-developed columnar joints. Sample GM97 A98 is a dacite which shows two well mixed but distinct components, probably as a result of magma mingling. In outcrop it was unclear if this was a small high-level intrusion or a sub-aerial dome. Sample GM97 A99 is also dacitic, appears unaltered and was clearly emplaced as a flow. Both dacite samples contain numerous feldspar phenocrysts (30-40%).

Table 1. *Locations and field-based lithological descriptions of Tlansanlin Formation igneous rocks in the central Aishihik Lake map area.*

Sample	Number on Fig. 2	Lithological Description	Latitude	Longitude	UTM (NAD83)		
					Zone	Northing	Easting
GM 97 A94	1	Fractured and variably weathered basaltic dike	61 30′53.4″	137 12′52.6″	8V	6822135	382180
GM 97 A95	2	Moderately weathered andesite dike(?)	61 31′28.9″	137 13′32.5″	8V	6823253	381629
GM 97 A96	3	Moderately weathered basaltic andesite dike	61 33′07.5″	137 15′50.3″	8V	6826373	379699
GM 97 A96R	4	Moderately weathered basaltic andesite dike	61 33′07.5″	137 15′50.3″	8V	6826373	379699
GM 97 A97	5	Fine-grained basaltic andesite flow with well-developed columnar joints	61 33′52.0″	137 16′57.2″	8V	6827784	378760
GM 97 A98	6	Highly weathered plagioclase-phyric dacite intrusion or dome	61 33′20.9″	137 16′16″	8V	6826802	379334
GM 97 A99	7	Massive unaltered plagioclase-phyric dacite flow	61 29′43.5″	137 09′05.5″	8V	6819862	385464

WHOLE-ROCK GEOCHEMISTRY AND RADIOGENIC ISOTOPES

ANALYTICAL METHODS

Major and trace elements were analysed by X-ray fluorescence (XRF) spectrometry at Washington State University's Peter Hooper Geoanalytical Laboratory in Pullman, Washington, USA. (Table 2). Analytical procedures, accuracy, and precision for data are reported in Johnson *et al*. (1999). Rare-earth elements (REE) and selected trace elements were also analysed by inductively coupled plasma – mass spectrometry (ICP–MS) (Table 3) at the Peter Hooper Geoanalytical Laboratory following procedures given in Knaack *et al*. (1994). Of the trace elements analysed, Ba, Rb, Sr, Th, Nb, Y, Pb, La, Ce, and Sc duplicate the XRF analysis to provide a certain degree of internal monitoring. Of these, the Ba, Sr, Th, Nb, Sc, and Pb values by ICP–MS are preferred, particularly at lower abundances, whereas the XRF values for Rb and Y are considered more precise (Knaack *et al*. 1994; Johnson *et al*. 1999). For the REE, La and Ce are also duplicated and the ICP–MS data are preferred, particularly at the low abundances observed here.

Table 2. *Major and selected trace element data by X-ray Fluorescence. Major element data is presented as weight percent oxide normalised to 100%.*

Sample	GM97 A94	GM97 A95	GM97 A96	GM97 A97	GM97 A98	GM97 A99	GM 97A96	GM97 A96R
Major Elements. normalized (wt%)								
SiO_2	52.6	62.42	55.47	56.25	67.4	65.24	55.47	55.47
Al_2O_3	18.15	17.07	17.46	16.37	15.83	16.72	17.46	17.41
TiO_2	1.12	0.87	1.05	0.93	0.61	0.5	1.05	1.04
FeO*	7.15	5.41	7.54	7.01	4.5	3.56	7.54	7.65
MnO	0.14	0.1	0.14	0.13	0.04	0.09	0.14	0.14
CaO	10.19	6.88	10.66	7.94	2.73	5.24	10.66	10.67
MgO	4.57	2.39	2.89	6.12	0.72	2.18	2.89	2.91
K_2O	1.9	1.42	1.29	1.12	1.93	1.36	1.29	1.29
Na_2O	3.7	3.14	3.14	3.81	5.96	4.96	3.14	3.06
P_2O_5	0.48	0.3	0.36	0.32	0.28	0.15	0.36	0.36
Original total	94.62	96.35	94.21	97.9	99.66	98.56	94.21	94.22
Trace Elements (ppm)								
Ni	93	26	69	98	16	22	69	68
Cr	241	123	255	281	50	69	255	255
Sc	27	16	25	25	9	11	25	25
V	190	135	168	159	100	74	168	168
Ba	1195	1342	945	1965	1034	1709	945	922
Rb	40	28	14	25	39	17	14	13
Sr	763	743	663	775	480	573	663	664
Zr	152	156	142	139	136	120	142	141
Y	22	18	18	18	14	15	18	19
Nb	21	9	10	10	8	6	10	10
Ga	19	18	19	15	14	18	19	19
Cu	27	25	30	38	15	10	30	28
Zn	89	77	115	81	42	59	115	107
Pb	3	4	5	8	15	10	5	6
La	42	18	21	23	25	11	21	21
Ce	71	49	31	40	31	25	31	56
Th	9	6	3	3	7	4	3	1

***Table 3**. Rare earth and selected trace element data by ICP-MS (in ppm).*

Sample	GM 97 A97	GM 97 A98	GM 97 A99
La	21.66	25.08	14.73
Ce	41.63	41.7	26.37
Pr	4.89	4.49	3.03
Nd	21.08	17.69	12.26
Sm	4.78	3.61	2.95
Eu	1.56	1.12	1.05
Gd	4.55	3.29	3.03
Tb	0.66	0.49	0.45
Dy	3.73	2.72	2.63
Ho	0.73	0.51	0.54
Er	1.9	1.4	1.45
Tm	0.27	0.2	0.21
Yb	1.61	1.23	1.33
Lu	0.27	0.2	0.21
Ba	1918	870	1616
Th	4.16	7.99	4.45
Nb	10.01	7.35	5.2
Y	20.08	14.71	15.51
Hf	3.1	3.03	2.7
Ta	0.59	0.55	0.39
U	1.39	2.79	1.72
Pb	7.44	16.71	12.08
Rb	23.7	30.1	17.4
Cs	8.55	0.54	0.28
Sr	772	432	543
Sc	26.3	12.2	12.8

Three samples were analysed for Rb–Sr and Sm–Nd isotopes at the Radiogenic Isotope Facility of the University of Alberta, Edmonton, Alberta (Table 4). Samples were totally spiked and dissolved in a 10:2 mix of concentrated HF:concentrated HNO_3 acid at approximately 120°C for 5 days. Samples were then converted to chloride salts using concentrated HCl. Rb, Sr, and the REE were separated from the whole sample by passing through standard cation exchange columns. Rb and Sr separates were passed through a second ion exchange column before isotopic analysis. Sm and Nd were separated from the other REE by being passed through HDEHP-coated (Di(2-ethylexyl) orthophosphoric acid coated) BioBead columns, then analysed isotopically. Rb and Sm samples were analysed on a VG Micromass 30 single- collector mass spectrometer. Sr and Nd were analysed on a VG Micromass 354 fully automated 5-collector mass spectrometer. Rb and Sr data were standardised to NBS-987, while Sm and Nd data were standardised to an internal standard, then corrected to the La Jolla standard. During the period of these analyses, an average $^{87}Sr/^{86}Sr$ ratio of 0.710213 (1SD (standard deviation) = 0.000032, n = 22) was recorded for NBS 987. To facilitate comparisons with other laboratories, a correction factor of +0.000032 was applied to all data that are reported relative to an NBS 987 ratio of 0.710245. Likewise a $^{143}Nd/^{144}Nd$ ratio of 0.511839 (1SD = 0.000011, n = 4 determinations) was recorded for the La Jolla standard. A correction factor of 0.000011 was added to all analyses that are reported relative to an expected value for La Jolla of 0.511850. An age of 76 Ma was used to calculate Sr_i (initial Sr ratio) and Nd_i (initial Nd ratio).

RESULTS

Major and trace element compositions for six samples (together with one replicate analysis) are shown in Table 2, and additional high field strength (HFS) and rare earth elements (REE) for three of the samples are shown in Table 3. The analyses are plotted on a variety of petrological discriminant diagrams in Figure 3, and tectonic discriminant diagrams and spider diagrams depicting ratios of HFSE and REE compositions to average values for primitive mantle and chondrites in Figure 4. Fields for whole rock compositions from the variably altered diorite and quartz monzonite that hosts the Sato Cu-Mo porphyry occurrence (from Lewis, 1997), and

***Table 4**. Results of Rb Sr and Sm Nd isotopic analyses. Analysed data corrected to an expected value of 0.710213 for NBS 987 (Rb Sr) and 0,511839 for the La Jolla standard (Sm Nd). Initial ratios calculated assuming an age of 76 Ma based upon data presented in this paper.*

2σ error	$Sr_{i(76Ma)}$	Sm ppm	Nd ppm	$^{147}Sm/^{144}Nd$	$^{143}Nd/^{144}Nd$	$^{143}Nd/^{144}Nd$ corrected	2σ error	$Nd_{i(76Ma)}$	εNd_{76}
0.00001	**0.705**	4.46	21.91	0.1241	0.512678	0.512689	0.000009	0.512627	**1.7**
0.00001	**0.70531**	3.56	19.19	0.1127	0.512678	0.512689	0.000008	0.512633	**1.8**
0.00002	**0.70563**	2.73	12.99	0.1278	0.512607	0.512618	0.000009	0.512574	**0.1**

altered and unaltered granodiorite of the Hopper intrusion on the east side of Hopkins Lake (Fig. 2) are shown for reference where this information is available.

Particular note should be made of the low totals obtained from the more basic dikes that were analysed in this study. This, combined with the generally altered appearance of some of the sampled outcrops, suggests that significant alteration of samples has taken place. Classification and tectonic discrimination diagrams that rely on the more mobile elements should therefore be treated with caution.

Samples range in silica content from 52.6 to 67.4 wt% SiO_2. The sample suite plots as calcic, according to the classification of Peacock (1931), or calc-alkaline according to Peccerillo and Taylor (1976; Fig. 3b). On plots of total alkalis vs. SiO_2 and K_2O vs. SiO_2 (Le Bas *et al.*, 1986, and Peccerillo and Taylor, 1976 respectively; Figs. 3a,b) all but one of the samples plot as subalkaline (Fig. 3b), and range in composition from basaltic andesite to dacite/trachydacite. On immobile element ratio plots such as Zr/TiO_2 vs Nb/Y (Winchester and Floyd, 1977; Fig. 3c), however, the analyses show much less scatter, falling mainly in the basalt and basaltic andesite fields. This suggests that at least some of the observed range of SiO_2 contents, and potentially also the alkali-metals contents, may be a result of element mobility related to hydrothermal alteration or surface weathering.

Incompatible trace element concentrations for the sample suite (Tables 2 and 3) are comparable to similar rock types in present day subduction related volcanic arcs (Ni >90 ppm in basalt and basaltic andesite to ~20 ppm in dacite (*e.g.*, Bacon *et al.*, 1997). Most incompatible trace element concentrations (*e.g.*, Ba, Rb, Zr and Y) are relatively low although there is a somewhat higher concentration of Sr at equivalent silica contents compared with arc volcanic rocks. All rocks analysed show the distinctive decoupling of HFS and large ion lithophile (LIL) elements associated with arc magmatism, or reactivation of such rocks. There is a slight decrease in the concentrations of REEs with increasing silica, particularly evident in the heavy REEs, but there is a negligible Eu anomaly, even at the highest silica values suggesting that the fractionation of plagioclase was not a key factor in the evolution of this suite.

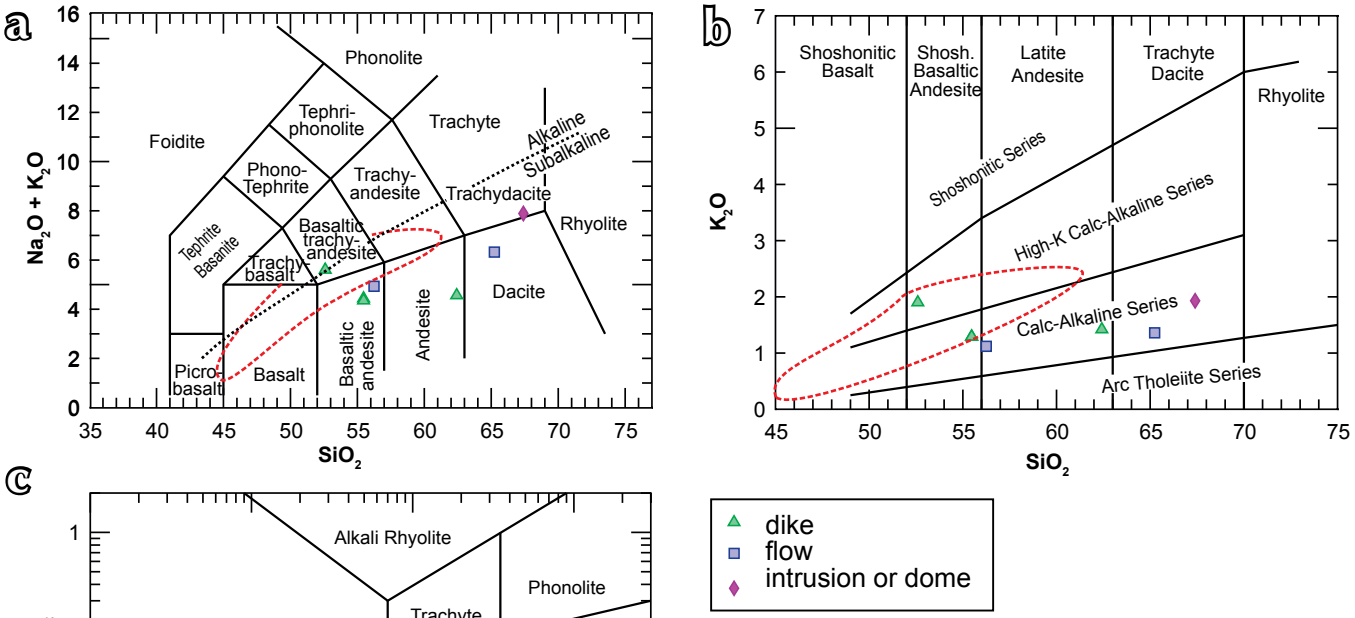

***Figure 3**. Plots of whole rock geochemical analyses of volcanic and intrusive rocks from the study area: (a)total alkalis vs. SiO_2 plot from Le Bas et al. (1986); fields for subalkaline vs. alkaline compositions from Irvine and Baragar (1971); (b) K_2O vs. SiO_2 from Pecarrillo and Taylor (1976); (c) immobile element ratio plot from Winchester and Floyd (1977) as revised by Pearce et al. (1996). Red dashed field shows the range of compositions for altered and unaltered intrusive rocks that host the Sato porphyry Cu-Mo occurrence (115 H/7) (data from Lewis, 1997).*

Extended plots of HFSE and REE ratios to model primitive mantle (Sun and McDonough, 1989; Fig. 4a) show Nb and Ti depletions typical of subduction-related magmatism. On a tectonic discriminant plot of Y+Nb vs. Rb (Pearce *et al.*, 1986; Fig. 4c) all of the samples fall well within the "volcanic arc" field (although it is possible that there may have been some post-crystallization mobility of Rb; see above discussion). One basaltic andesite sample returns a Sr_i ratio of 0.70500 and an ε_{Ndi} value of +1.7 whereas dacite from the same area return Sr_i ratios of 0.70531 to 0.70563 and ε_{Ndi} of +1.8 to +0.1 (Table 4). Such values are typical for fairly young and primitive continental arc rocks.

Taken together, the measured whole rock geochemical and isotopic compositions of the sample suite are typical of continental arc volcanic rocks. The slightly elevated K and lower compatible element concentrations at the basaltic end of the range when compared to typical arc volcanic rocks from the Cascade Range (Bacon *et al.*, 1997) could be attributed to the observed alteration and weathering of these rocks, but nothing that could not be argued to be the result of assimilation and fractional crystallization (AFC) processes, possibly together with minor crustal contamination in a continental arc setting. The fairly primitive isotopic values argue against remobilisation or significant assimilation of older continental crust.

U-PB AGE DETERMINATIONS

ANALYTICAL METHODS

U-Pb dating of two samples of dacite from the sample suite was carried out using isotopic dilution-thermal ionization mass spectrometry (ID-TIMS) methods. Zircons were separated from ~3 kg samples using conventional crushing, grinding, wet shaking table, heavy liquids and magnetic methods. U-Pb ID-TIMS analyses were carried out at the Pacific Centre for Isotopic and Geochemical Research at the University of British Columbia, using methods as described by Mortensen *et al.* (2008). Multigrain zircon samples were analysed, and all of the zircons were strongly air-abraded prior to analysis in an attempt to minimize the effects of post-crystallization Pb-loss. Errors on calculated ages are given at the 2σ level (95% confidence interval).

RESULTS

Zircons recovered from the two samples consisted of euhedral, clear, colorless, stubby to elongate, euhedral prismatic grains containing rare clear colorless inclusions, and exhibiting vague concentric growth zoning but no obvious inherited cores. Four multigrain fractions were analysed from each sample. Results are listed in Table 5 and are plotted on conventional concordia diagrams in Figure 5.

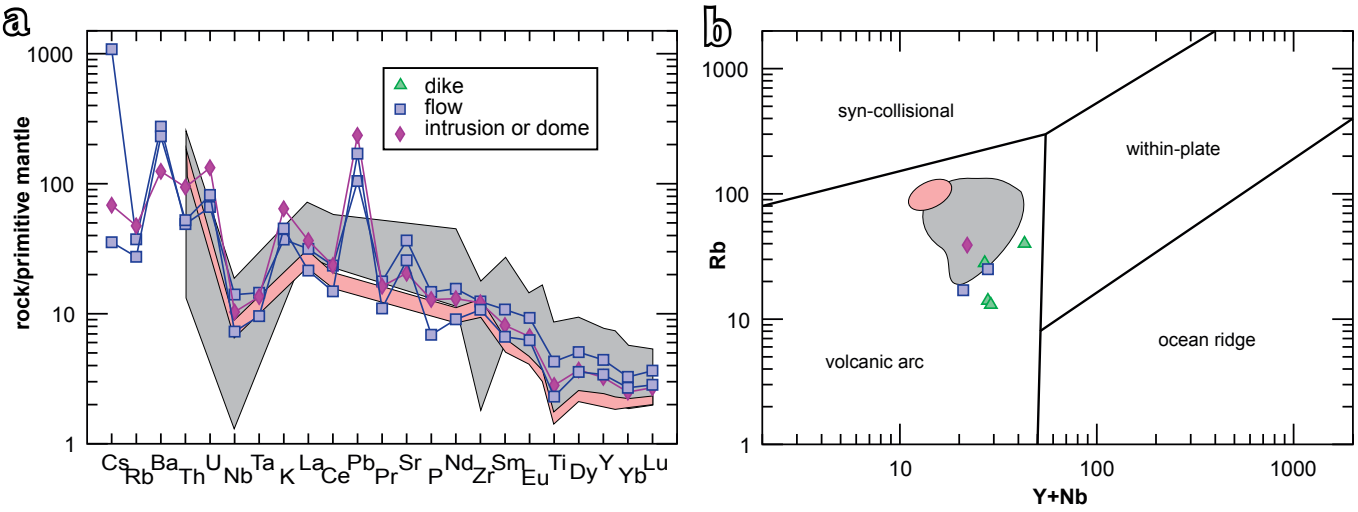

***Figure 4**. (a) extended plot of HFSE and REE ratios of Tlansanlin Formation volcanic and intrusive rocks from this study to model primitive mantle values (from Sun and McDonough, 1989); (b) tectonic discriminant plot for Tlansanlin Formation volcanic and intrusive rocks (from Pearce et al., 1984). Shaded fields in (a) is for altered and unaltered granodiorites from the Hopper intrusion (grey), and quartz-feldspar porphyry dike cutting the Hopper intrusion (pink), from Blumenthal (2010).*

***Table 5**. U-Pb isotopic analyses of zircons from two Tlansanlin Formation dacite samples from the central Aishihik Lake map area.*

Sample	Wt	U	Pb[2]	$^{206}Pb/^{204}Pb$	total common	%	$^{207}Pb/^{235}U$[4]	(±% 1σ)	$^{206}Pb/^{238}U$[4]	(±% 1σ)	Rho	$^{207}Pb/^{206}Pb$[4]	(±% 1σ)	$^{206}Pb/^{238}U$ age	(±2σ)	$^{207}Pb/^{235}U$ age	(±2σ)	$^{207}Pb/^{206}Pb$ age	(±2σ)
Description[1]	(mg)	(ppm)	(ppm)	(meas.)[3]	Pb (pg)	^{208}Pb[2]								Ma		Ma		Ma	
97GM A98 (dacite intrusion or dome)																			
A: N10,+134	0.06	461	5.8	449	46	14.6	0.0778	1.3	0.01182	0.12	0.52	0.04784	1.24	75.8	0.2	76.2	1.9	91.6	58.1
B: N10,+134	0.055	365	4.6	369	41	15.2	0.07777	0.74	0.01176	0.21	0.67	0.04796	0.63	75.4	0.3	76.1	1.1	97.1	29.5
C: N10,+134	0.056	440	5.4	1866	10	13.3	0.0781	0.2	0.01186	0.08	0.46	0.04777	0.18	76	0.1	76.4	0.3	87.7	8.5
D: N10,+134	0.057	428	5.3	1669	11	14.2	0.07766	0.21	0.01181	0.09	0.39	0.04769	0.19	75.7	0.1	75.9	0.3	84.1	9.2
97 GM A99 (dacite flow)																			
A: N10,+134	0.056	411	5.1	350	55	7.4	0.08524	0.67	0.01279	0.31	0.50	0.04835	0.58	81.9	0.5	83.1	1.1	116.5	27.1
B: N10,+134	0.041	331	3.9	207	54	8	0.07976	1.24	0.01208	0.32	0.67	0.04789	1.05	77.4	0.5	77.9	1.9	93.6	49.5
C: N10,+134	0.049	476	5.6	279	66	9	0.07799	0.88	0.01194	0.25	0.67	0.04738	0.73	76.5	0.4	76.3	1.3	68.4	34.8
D: N10,+134	0.047	466	5.5	313	56	7.6	0.07962	0.68	0.01213	0.2	0.66	0.0476	0.56	77.7	0.3	77.8	1	79.5	26.7

1 N10 = non-magnetic at 10 degrees side slope on Frantz magnetic separator; grain size given in microns

2 radiogenic Pb; corrected for blank, initial common Pb, and spike

3 corrected for spike and fractionation

4 corrected for blank Pb and U, and common Pb

Four fractions of zircon were analysed from each of the two samples. Four analyses for sample GM97 A98 (dacite intrusion or dome) fall on or near concordia, with some scatter. A weighted average of the $^{206}Pb/^{238}U$ ages for three of the analyses gives 75.8±0.4 Ma, which is interpreted to be the best estimate for the crystallization age of the sample. A fourth zircon fraction yields a slightly younger $^{206}Pb/^{238}U$ age, probably reflecting minor post-crystallization Pb-loss that was not completely eliminated by the air abrasion.

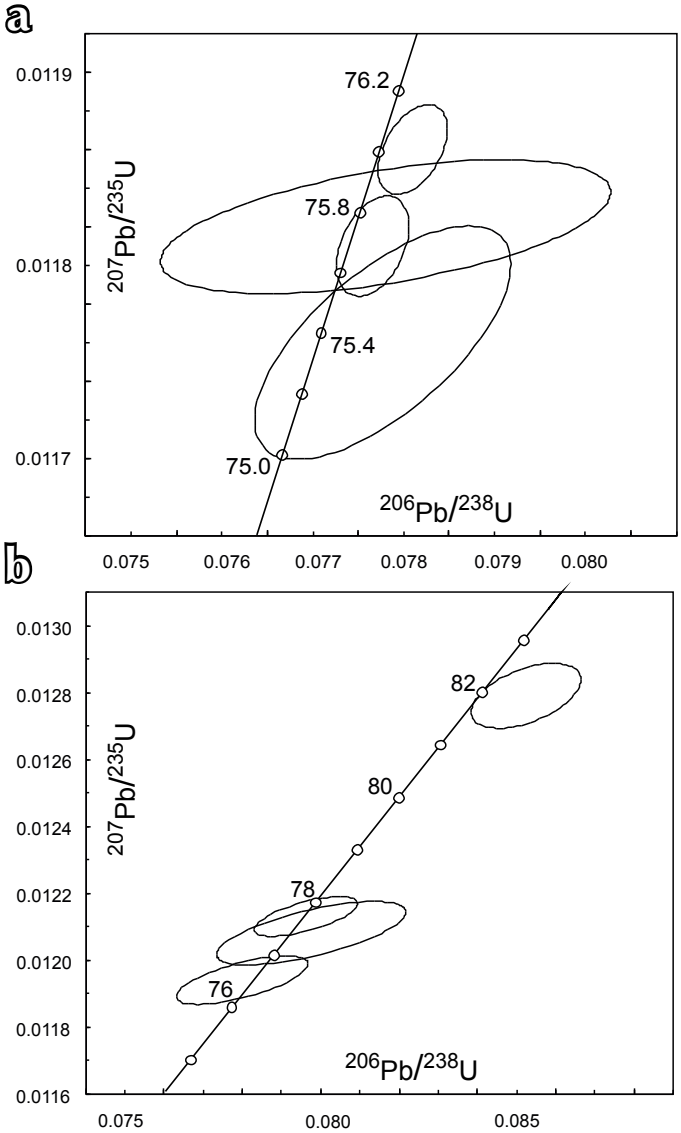

***Figure 5**. Conventional U-Pb concordia plot for zircons from the Tlansanlin Formation volcanics: (a) sample GAM97-A98 (dacite intrusion or dome); (b) sample 97GAM-A99 (dacite flow).*

Four analyses from sample GM97 A99 (dacite flow) also scatter along concordia. One analysis gives a distinctly older $^{206}Pb/^{238}U$ age than the others (81.2 Ma) and is interpreted to have contained an older zircon component, probably as one or more somewhat older xenocrysts that were entrained from underlying rock units. The other three analyses give $^{206}Pb/^{238}U$ ages in the range of 76.5±0.4 Ma to 77.7±0.3 Ma (Table 3, Fig. 5b). The two older of these give a weighted average $^{206}Pb/^{238}U$ age of 77.3±1.3 Ma, which gives the best estimate of the crystallization age of the sample. The fourth zircon fraction has likely suffered very minor post-crystallization Pb-loss.

DISCUSSION

Johnston and Timmerman (1997b) report crosscutting relationships which indicate that plutons at the Sato porphyry occurrence (78.2±0.1 Ma and 78.8±0.2 Ma; Lewis and Mortensen, 1998) intrude Tlansanlin Formation volcanic rocks in the northern Hopkins Lake area. Taken together with ages of 75.8±0.4 Ma and 77.3±1.3 Ma reported here for a dacite flow and an associated flow or dome, respectively, from within the Tlansanlin Formation suggests an age range of at least 3 m.y. for Tlansanlin magmatism in this area. Ages of 77.2±1.2 Ma and 76.0±1.1 Ma reported by Blumenthal (2010) for two samples of the Hopper intrusion in the southwestern Hopkins Lake map area indicate that this intrusion is likely also part of this same magmatic event.

Major element geochemical compositions from the Sato and Hopper intrusions (Lewis and Mortensen, 1998; Blumenthal, 2010) indicate that these bodies are also calc-alkaline and generally overlap with our measured compositions for volcanic rocks in the Tlansanlin Creek area (Figs. 3a,b). HFSE and REE compositions from the Hopper intrusion (fields from Blumenthal, 2010) are also very similar to the Tlansanlin Formation volcanic rocks (Figs. 4a,b). It is interesting to note that two samples of undated, north-south trending quartz-feldspar dikes that cut the Hopper intrusion give compositions (including HFSE and REE; Blumenthal, 2010; Figs. 4a,b) that are also very similar to the Tlansanlin Formation volcanic rocks. These dikes are typical of a suite of north-south trending quartz-feldspar dikes that area widespread throughout the central and western Aishihik Lake map area, and have been interpreted by previous workers to be Paleocene or Eocene in age (Johnston and Timmerman, 1997a,b; Israel *et al.*, 2011a; Israel and Westberg, 2012). Blumenthal's (2010) data indicates that the porphyry dikes were derived by similar igneous processes as the Late Cretaceous magmatism, and also suggest that some or all of the porphyry dikes may actually be Late Cretaceous in age rather than Paleocene or Eocene. The Late Cretaceous magmatism may be considerably more widespread than previously thought, and possibly includes the presently undated Mount Creedon and Sifton Range volcanic complexes, as well as some of the volcanic and intrusive rocks presently mapped as the Paleocene or Eocene Rhyolite Creek volcanic complex farther to the west, as well as some phases of the Ruby Range batholith and associated dikes in that area.

Recent regional studies throughout the Dawson Range have led to the recognition of two distinct pulses of Late Cretaceous magmatism in this region (Allan *et al.*, 2013). An early phase of magmatism ("early Late Cretaceous"; 79-71 Ma) is represented by relatively small volume intrusions that form a belt along the trend of the Dawson Range, and yield compositions that are consistent with having formed in a continental magmatic arc. A slightly later magmatic event ("late Late Cretaceous"; 72-67 Ma) includes both small intrusions as well as the aerially extensive volcanic rocks of the Carmacks Group. This younger phase of magmatism is present throughout the Dawson Range but also extends far to the northeast, and reflects magmatic processes that are not thought to be directly subduction-related (Allan *et al.*, 2013). Although a significant number of porphyry, vein and other styles of mineralization have been shown to be related to the "late Late Cretaceous" magmatism, the "early Late Cretaceous" event appears to host larger and economically more important mineral deposits (*e.g.*, Casino, Revenue/Nucleus, Cyprus). The recognition of the potentially widespread occurrence of "early Late Cretaceous" volcanic rocks and high level intrusions in the central Aishihik Lake area therefore considerably enhances the mineral deposit potential of that region. Several porphyry Cu-Mo occurrences are already known in the area (*e.g.*, Sato - 115H 021, and Hopper - 115H 019), as well as Cu and Cu-Mo-W skarns (*e.g.*, Hopkins - 115H 019, and Janisiw - 115H 018) (Fig. 2). Israel *et al.* (2011b) and Israel and Westberg (2012) noted that the observed transition from high level intrusions along the northeastern margin of the Paleocene Ruby Range batholith into coeval volcanic rocks and associated hypabyssal intrusions of the Rhyolite Creek volcanoplutonic complex suggested high potential for porphyry and epithermal vein deposits (the "porphyry-to-epithermal transition") in that area. It is interesting to note that a slightly older (Late Cretaceous; ~78-75 Ma)

"porphyry-to-epithermal transition" occurs in exactly the same area, and is also known to be associated with porphyry and skarn mineralization.

Results of our study highlight the uncertainty that presently exists regarding the age and extent of Late Cretaceous and Paleocene magmatism in southwestern Yukon, and tectonic setting(s) in which the various magmatic events occurred and their mineral potential. More focused work is required to resolve this and to provide a more robust metallogenic framework for this highly prospective region.

ACKNOWLEDGMENTS

Fieldwork for this study as well as whole rock geochemistry and tracer isotope analysis was partially funded by a Lithoprobe University Supporting Geoscience grant to GM. GM acknowledges Rob Creaser (University of Alberta) for guidance and advice regarding the radiogenic isotope data. JM thanks the staff of the Pacific Centre for Isotopic and Geochemical Research (University of British Columbia) for assistance in the U-Pb analytical work. A critical review of the manuscript was provided by Don Murphy.

REFERENCES

Allan, M.M., Mortensen, J.K., Hart, C.J.R., Bailey, L.A., Sanchez, M.G., Ciolkiewicz, W., McKenzie, G.G., and Creaser, R.A., 2013. Magmatic and metallogenic framework of west-central Yukon and eastern Alaska. Society of Economic Geologists, Special Publication 17, p. 111–168.

Bacon, C.R., Bruggman, P.E., Christiansen, R.L., Clynne, M.A., Donnelly-Nolan, J.M., and Hildreth, W., 1997. Primitive magmas at five Cascade volcanic fields: Melts from hot heterogeneous sub-arc mantle. Canadian Mineralogist, vol. 35, p. 397-423.

Blumenthal, V.H., 2010. A geochemical study of the mineralization at the Hopper property, Yukon: A case study of an atypical copper occurrence. Unpublished MSc thesis, University of Waterloo, 119 p.

Cockfield, W.E., 1927. Aishihik Lake District, Yukon. Geological Survey of Canada, Summary Report, 1926, part A, p. 1-13.

Colpron, M., 2013. Yukon bedrock geology map (digital). <*http://ygsftp.gov.yk.ca/YGSIDS/compilations/Yukon_Geology_update_Nov2013.gdb.zip*>.

Erdmer, P. and Mortensen, J.K., 1993. A 1200 km long Eocene metamorphic-plutonic belt in the northwestern Cordillera: evidence from southwestern Yukon. Geology, vol. 21, p. 1039-1042.

Irvine, T.N., and Baragar, W.R.A., 1971. A guide to the chemical classification of the common volcanic rocks. Canadian Journal of Earth Sciences, vol. 8, p. 523-548.

Israel, S., Cobbett, R., Westberg, E., Stanley, B., and Hayward, N., 2011a. Preliminary bedrock geology of the Ruby Ranges, southwest Yukon (Parts of NTS 115G, 115H, 115A and 115B) (1:150 000-scale). Yukon Geological Survey, Open File 2011-2.

Israel, S., Murphy, D.C., Bennett, V., Mortensen, J.K., and Crowley, J., 2011b. New insights into the geology and mineral potential of the Coast Belt in southwestern Yukon. *In:* Yukon Exploration and Geology, K.E. MacFarlane, L.H. Weston, and C. Relf (eds.), Yukon Geological Survey, p. 101-123.

Israel, S. and Westberg, E., 2011. Preliminary geological map of the northwestern Aishihik Lake area, parts of NTS 115H/12 and 13 (1:50 000-scale). Yukon Geological Survey Open File 2011-31.

Israel, S. and Westberg, E., 2012. Geology and mineral potential of the northwestern Aishihik Lake map area, parts of NTS 115H/12 and 13. *In:* Yukon Exploration and Geology 2011, K.E. MacFarlane and P.J. Sack (eds.), Yukon Geological Survey, p. 103-113.

Johnson, D.M., Hooper P.R., and Conrey, R.M., 1999. XRF analysis of Rocks and Minerals for Major and Trace Elements on a single low dilution Li-tetraborate fused bead. Advances in X-ray Analysis, vol. l 41, p. 843-867.

Johnston, S.T., 1993. Geological evolution of Nisling Assemblage and Stikine Terrane in the Aishihik Lake area, southwest Yukon. Unpublished PhD thesis, University of Alberta, 336 p.

Johnston, S.T., Mortensen, J.K., and Erdmer, P., 1996. Igneous and meta-igneous age constraints for the Aishihik metamorphic suite, southwest Yukon. Canadian Journal of Earth Sciences, vol. 33, p. 1543-1555.

Johnston, S.T. and Timmerman, J.R., 1994. Geology of the Aishihik Lake and Hopkins Lake map areas (115H6/7), southwestern Yukon. *In:* Yukon Exploration and Geology 1993, S.R. Morison (ed.), Indian and Northern Affairs Canada, Exploration and Geological Services Division, p. 93-110.

Johnston, S.T. and Timmerman, J.R., 1997a. Geology of Aishihik Lake map area, Yukon (NTS 115 H/6). Exploration and Geological Services Division, Yukon, Indian and Northern Affairs Canada. Geoscience Map 1997-8.

Johnston, S.T. and Timmerman, J.R., 1997b. Geology map of the Hopkins Lake area, Yukon (115H/7) (1:50 000 scale). Exploration and Geological Services Division, Yukon, Indian and Northern Affairs Canada. Geoscience Map 1997-9.

Knaack, C.M., Cornelius, S., and Hooper, P.R. 1994. Trace element analysis of rocks and minerals by ICP–MS. Washington State University, Geology Department, Open File Report.

Le Bas, M.J., LeMaitre, R.W., Streckeisen, A., and Zanettin, B., 1986. A chemical classification of volcanic rocks based on the total alkali silica diagram. Journal of Petrology, vol. 27, p. 745-750.

Lewis, J., 1997. Geology, alteration, and mineralization of the Sato copper porphyry property, southwestern Yukon Territory, Canada. Unpublished directed study report for J.K. Mortensen, 68 p.

Lewis, J. and Mortensen, J.K., 1998. Geology, alteration, and mineralization of the Sato porphyry copper prospect, southwestern Yukon. *In:* Yukon Exploration and Geology 1997, Roots, C.F. (ed.), Indian & Northern Affairs Canada/Department of Indian & Northern Development: Exploration & Geological Services Division, p. 153-160.

Miskovic, A. and Francis. D., 2004. The Early Tertiary Sifton Range volcanic complex, southwestern Yukon. *In:* Yukon Exploration and Geology 2003, D.S. Edmond and L.L. Lewis (eds.), Yukon Geological Survey, p. 143-155.

Morris G.A. and Creaser, R.A., 1998. Petrogenesis of the Eocene Mt. Skukum and Bennett Lake igneous complexes, southwest Yukon Territory, Canada. Abstracts with Programs, Geological Society of America, vol. 30, p. 55-56.

Morris G.A. and Creaser R.A., 2003. Crustal recycling during subduction at the Eocene Cordilleran margin of North America: a petrogenetic study from the southwestern Yukon. Canadian Journal of Earth Sciences, vol. 40, p. 1805-1821.

Mortensen J.K., Hall, B.V., Bissig, T., Freidman R.M., Danielson, T., Oliver, J., Rhys, D.A., Ross, K.V., and Gabites, J.E., 2008. Age and paleotectonic setting of massive sulphide deposits in the Guerrero terrane of central Mexico: Constraints from U-Pb Age and Pb isotope studies. Economic Geology, vol. 103, p. 117-140.

Murphy, D.C. 2007. The three "Windy KcKinley" terranes of Stevenson Ridge (115jk), western Yukon. *In:* Yukon Exploration and Geology 2006, D.S. Emond, L.L. Lewis, and L.H. Weston (eds.), Yukon Geological Survey, p. 223-236.

Peacock, M.A., 1931. Classification of igneous rock series. Journal of Geology, vol. 39, p. 54-67.

Pearce, J.A., 1996. A user's guide to basalt discrimination diagrams. *In:* Trace element geochemistry of volcanic rocks; applications for massive sulphide exploration, A.H. Bailes, E.H. Christiansen, A.G. Galley, G.A. Jenner, J.D. Keith, R. Kerrich, D.R. Lentz, C.M. Lesher, S.B. Lucas, J.N. Ludden, J.A. Pearce, S.A. Peloquin, R.A. Stern, W.E. Stone, E.C. Syme, H.S. Swinden, and D.A. Wyman (eds.), Short Course Notes, Geological Association of Canada, vol. 12, p. 79-113.

Pearce, J.A., Harris, B.W., and Tindle, A.G., 1984. Trace element discrimination diagrams for the tectonic interpretation of granitic rocks. Journal of Petrology, vol. 25, p. 956-983.

Peccerillo, A. and Taylor, S.R., 1976. Geochemistry of Eocene calc-alkaline volcanic rocks from the Kastamonu area, Northern Turkey. Contributions to Mineralogy and Petrology, vol. 58, p. 63-81.

Sun S., and McDonough, W.F., 1989. Chemical and isotopic systematics of oceanic basalts: implications for mantle composition and processes. *In:* Magmatism in the Ocean Basins, A.D. Saunders and M.J. Norry (eds.), Geological Society Special Publication, no. 42, p. 313-345.

Tempelman-Kluit, D.J., 1974. Reconnaissance geology of the Aishihik Lake, Snag and part of the Stewart River map areas, west-central Yukon (115A, 115F, 115G and 115K). Geological Survey of Canada Paper 73-41, 97 p.

Winchester, J.A. and Floyd, P.A., 1977. Geochemical discrimination of different magma series and their differentiation products using immobile elements. Chemical Geology, vol. 20, p. 325-343.

Yukon MINFILE, 2013. Yukon MINFILE - A database of mineral occurrences. Yukon Geological Survey, <*http://data.geology.gov.yk.ca*> [accessed November 1, 2013].

Bedrock Geology of NTS 106B/04, Eastern Rackla Belt

David Moynihan[1]
Yukon Geological Survey, Whitehorse, YT

Moynihan, D., 2014. Bedrock Geology of NTS 106B/04, Eastern Rackla Belt. *In:* Yukon Exploration and Geology 2013, K.E. MacFarlane, M.G. Nordling, and P.J. Sack (eds.), Yukon Geological Survey, p. 147-167.

ABSTRACT

The NTS 106B/04 map area straddles the upper reaches of the Stewart River in east-central Yukon. The area north of the Stewart River is underlain by Ediacaran clastic and carbonate continental slope deposits of the uppermost Windermere Supergroup, and by Ediacaran-Cambrian rocks of the Hyland Group (Selwyn basin). The area south of the Stewart River is dominated by the Cambrian Gull Lake Formation and Cambrian (-Silurian?) volcanic rocks of the Old Cabin Formation. The main structures in 106B/04 define an arcuate pattern; they are oriented NW-SE in most of the area, but are approximately E-W in the westernmost part of the map area. These structures include upright, gently-plunging folds and steeply-dipping, axial-planar cleavage. Folding was locally accompanied by thrusting. Late structures include a steeply-dipping sinistral fault that transects the central part of the map area and a number of NW-WNW-striking normal (±dextral) faults. Stratigraphic relationships suggest correlation of the upper Yusezyu, Algae, and Narchilla formations of the Hyland Group (Selwyn basin) with the upper Blueflower, Risky, and Ingta formations of the Windermere Supergroup (Ogilvie and Mackenzie platforms). Gold mineralization has recently been discovered in the Algae Formation, which has also been explored for Mississippi Valley-type lead-zinc-silver mineralization elsewhere in the area.

[1] *david.moynihan@gov.yk.ca*

INTRODUCTION

In 2010, the Yukon Geological Survey began a 1:50 000-scale bedrock mapping project focused on the northern margin of Selwyn basin in east-central Yukon (NTS 106D and 106C; Fig. 1). The project area covers a narrow region approximately parallel to the east-striking Dawson thrust, which marks the northern margin of Selwyn basin in this region. The area, which includes the headwaters of the Rackla and Nadaleen rivers, is informally known as the Rackla belt.

The Rackla belt contains numerous mineral occurrences (Fig. 2) and continues to attract exploration activity following recent discoveries of gold mineralization. Of particular interest is the recognition of sediment-hosted gold mineralization similar to that in the Carlin area of Nevada (Tucker *et al.*, 2013, Arehart *et al.*, 2013). With the exception of NTS 106D/01, which was mapped by Abbott (1990a,b), the only regional geological information available prior to 2010 was contained in 1:250 000 reconnaissance level maps (Green, 1972; Blusson, 1974). The YGS mapping program was established to document the regional stratigraphic and structural characteristics of this geological and metallogenic belt.

Following their work in the summer of 2012, Colpron *et al.* (2013) combined their mapping with all recent work (Abbott, 1990a,b; Chakungal and Bennett, 2011; Colpron, 2012a,b) and released a compilation map of most of the belt (5 contiguous 1:50 000 sheets) with a common legend (Figs. 1 and 2). In the summer of 2013, mapping was extended eastward to include NTS sheet 106B/04 (Figs. 2 and 3). This report describes the bedrock geology of this area and accompanies a new 1:50 000-scale open file map (Moynihan, 2014).

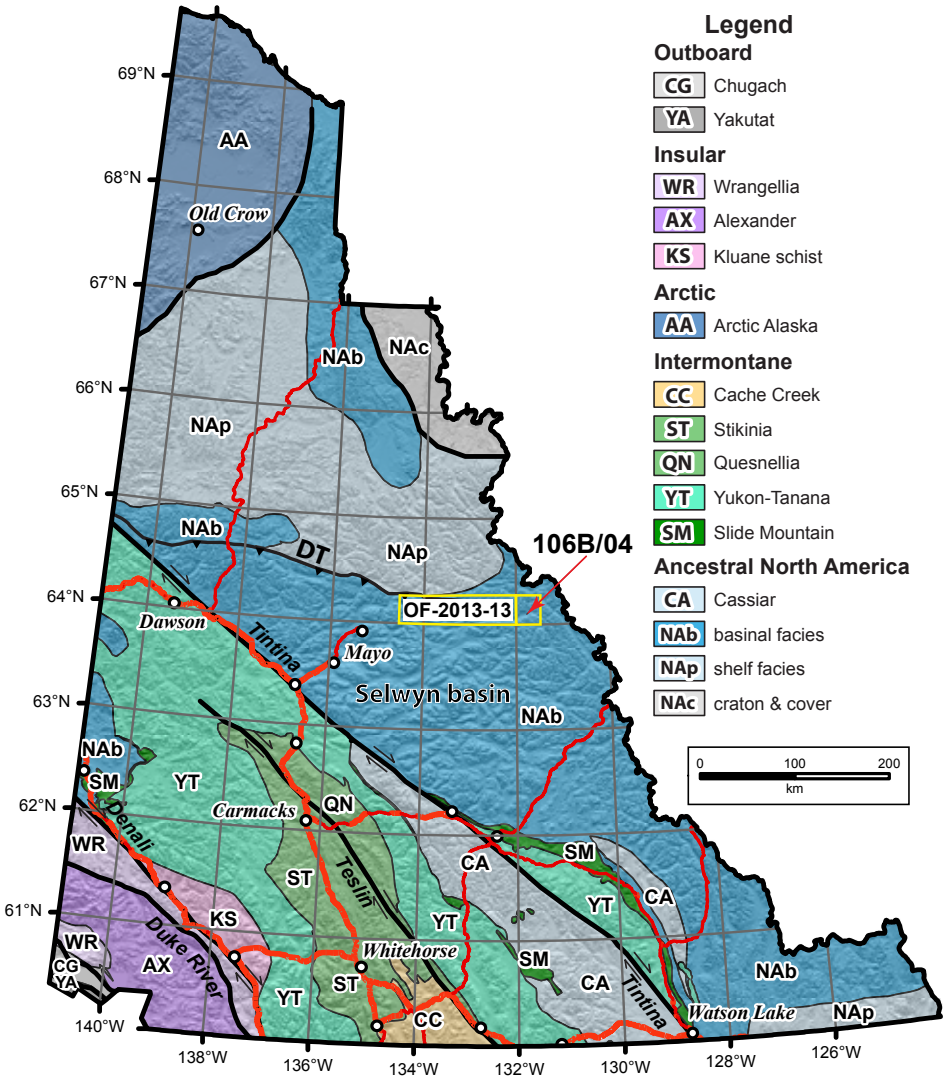

Figure 1. *Terrane map of Yukon, showing the location of the Rackla project area. The yellow boxes show the extent of the compilation map of Colpron et al. (2013) and the area mapped in 2013 (NTS 106B/04). DT = Dawson thrust.*

GEOLOGICAL BACKGROUND

The northern margin of Selwyn basin is marked by the Dawson thrust, which was active during Mesozoic (probably mid-Cretaceous) shortening associated with the Cordilleran orogeny. The Mesozoic thrust coincides with the location of an antecedent structure that influenced depositional/intrusion patterns over a number of intervals since the Neoproterozoic (Abbott, 1997).

In the western part of the Rackla belt the Dawson thrust juxtaposes Neoproterozoic-Cambrian rocks of the Selwyn basin (Hyland Group; Gordey and Anderson, 1993) against Proterozoic-Paleozoic shelf and

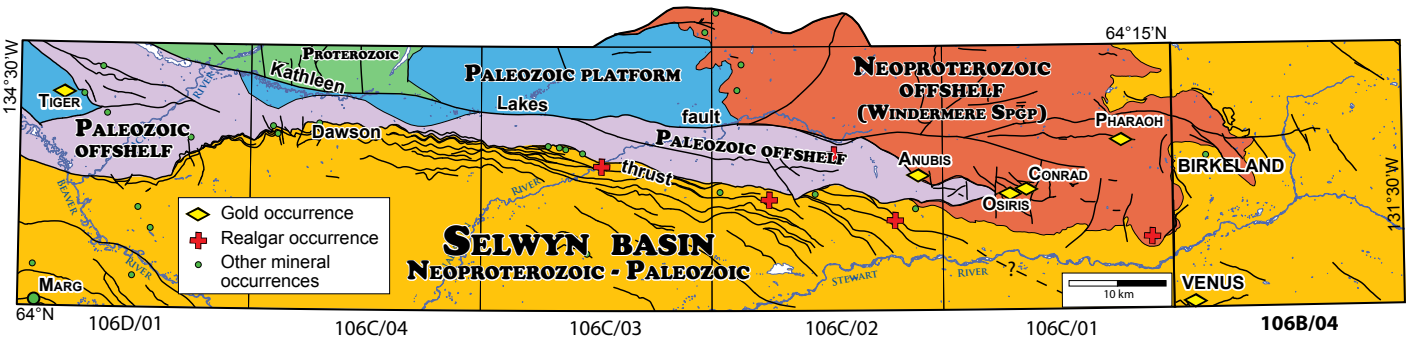

***Figure 2**. Summary of facies domains, major structures, and mineral occurrences in the Rackla belt, after Colpron et al. (2013). The northern margin of Selwyn basin is marked by the Dawson thrust in the western and central Rackla belt; however, the fault dies out towards its eastern end of the Rackla belt.*

slope rocks of the Ogilvie platform (Fig. 2). The thrust is not a single structure but rather a highly imbricated zone with several closely-spaced thrust faults that strike east and dip at moderate angles to the south (Chakungal and Bennett, 2011; Colpron, 2012a,b).

Towards the eastern end of the belt the fault zone steepens, its strike changes to a SSE orientation, and the distances between splays of the fault increase (Fig. 2; Colpron *et al.*, 2013), implying a decrease in the amount of shortening across the zone. This diffuse fault zone projects into the NE corner of the Lansing area, where Roots (2003) mapped NE-verging thrusts and folds.

In the eastern Rackla belt, upper parts of the Hyland Group - represented by the carbonate Algae and mudstone-dominated Narchilla formations - occur within, and on either side of the diffuse fault zone. Whereas these formations are exposed throughout the area, the nature of the rocks they overlie varies. South of the Dawson thrust zone the Algae-Narchilla formations succeed coarse clastic rocks of the Yusezyu Formation (lower Hyland Group), whereas in the region to the north they form the upper part of a sequence dominated by fine clastic and carbonate rocks of the Windermere Supergroup. The information contained within this report illustrates the primary stratigraphic relationships between these contrasting sequences.

STRATIGRAPHY

WINDERMERE SUPERGROUP

The oldest units in the area, which are exposed north of the Stewart River, are correlated with the unnamed "upper group" of the Windermere Supergroup. The stratigraphy, sedimentology, and paleontology of these units have been documented extensively elsewhere in the Mackenzie and Wernecke mountains (Aitken, 1989; Narbonne and Aitken, 1995; Pyle *et al.* 2004; MacNaughton *et al.* 2000; Macdonald *et al.*, 2013). Colpron *et al.* (2013) provisionally correlated Neoproterozoic stratigraphy north of the Dawson thrust with the Windermere Supergroup, but did not use Windermere Supergroup formation names; instead, they divided the sequence into informal "assemblages". Correlation with the upper group of the Windermere Supergroup is substantiated by detailed lithostratigraphic, paleontological, and chemostratigraphic data collected by the author and J. Strauss during the summer of 2013, and formation names are used in this report. These data, and a discussion of their broader significance, are beyond the scope of the current article and will be presented elsewhere.

NADALEEN FORMATION

The oldest rocks in NTS 106B/04 belong to the upper part of a unit that is here informally termed the Nadaleen formation. This unit, which will be formally defined in the future, is correlative with the "June beds" of Macdonald *et al.* (2013), which were previously considered part of the Sheepbed Formation (Gabrielse *et al.*, 1973). The Nadaleen formation is equivalent to the "Nadaleen assemblage" of Colpron *et al.* (2013).

The Nadaleen formation comprises two members in the map area. The *lower member* consists of thickly-bedded quartz arenite and brown shale ("lower Nadaleen assemblage" of Colpron *et al.*, 2013). This is overlain by rhythmically-layered green to grey, thinly-bedded mudstone, siltstone, and sandstone of the *Stenbraten member*. Graded bedding is evident, sandstones layers are commonly cross-bedded, and some display sole marks, suggesting deposition by turbidity currents. The Stenbraten member was referred to as the "upper Nadaleen assemblage" by Colpron *et al.* (2013).

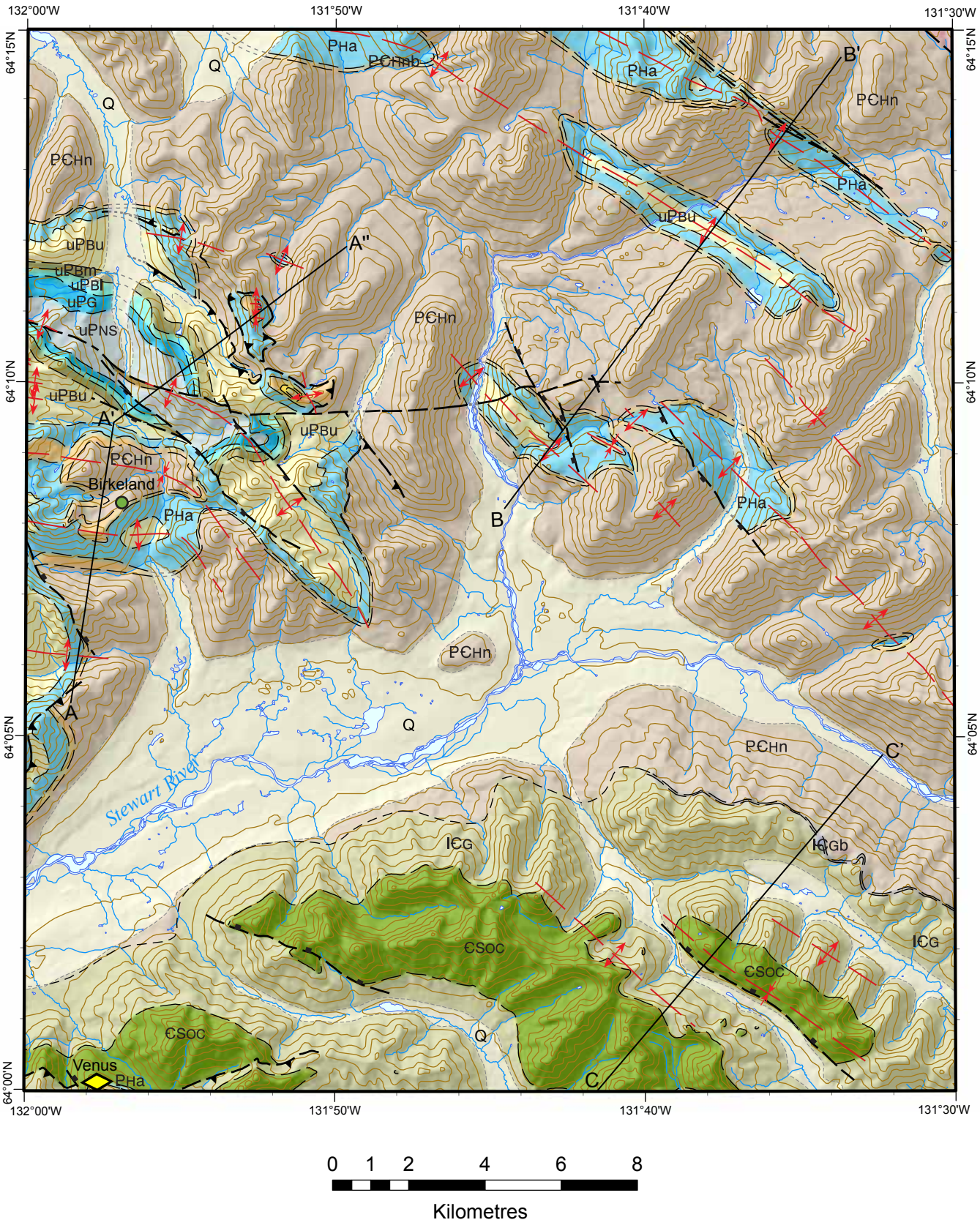

Figure 3. *Preliminary geological map and cross sections of NTS 106B/04 at 1:150 000 scale.*

QUATERNARY

Q — **QUATERNARY:** *unconsolidated alluvial, colluvial, fluvial and glacial deposits*

MIDDLE CAMBRIAN-SILURIAN

ЄSOc — **OLD CABIN FORMATION:** *mafic volcanic breccia and conglomerate, interbedded with argillite, siltstone and sandstone; minor diabase intrusions.*

LOWER TO MIDDLE CAMBRIAN

lЄs — **SEKWI FORMATION:** *thinly-bedded silty limestone*

lЄG — **GULL LAKE FORMATION:** *white, brown and orange-weathering, olive-green argillite, siltstone and fine sandstone; maroon, black and lime green shale; interbedded shale and quartz arenite; minor silty limestone and limestone-clast conglomerate*

lЄGb — **GULL LAKE FORMATION, BASAL MEMBER:** *boulder conglomerate with archaeocyathid-bearing limestone clasts; brown-weathering, green lithic sandstone and conglomerate, quartz arenite*

SYMBOLS

stratigraphic contact (approximate, covered)

fault (normal, thrust, sinistral movement not known)

fold axial trace (anticline, syncline)

gold occurrence

Zn/Pb occurrence

NEOPROTEROZOIC-CAMBRIAN HYLAND GROUP

EDIACARAN TO LOWER CAMBRIAN

PЄHnq — **NARCHILLA FORMATION:** *quartzite, quartz pebble conglomerate*

PЄHn — **NARCHILLA FORMATION:** *pale brown, green and maroon shale; well-cleaved, rhythmically-bedded mudstone and siltstone, locally bioturbated; white-weathering sandstone*

PЄHnb — **NARCHILLA FORMATION, BASAL MEMBER:** *limestone-clast conglomerate; quartz arenite and grit; limestone; calcareous siltstone/sandstone; green, brown and maroon shale*

NEOPROTEROZOIC (EDIACARAN)

PHa — **ALGAE FORMATION:** *dark grey, light grey and buff-coloured limestone and dolostone, variably dolomitized and variably silty/sandy; commonly graded and cross-bedded; minor grey and/or maroon shale; limestone pebble to cobble breccia and conglomerate; equivalent to Risky Formation of the Windermere Supergroup*

NEOPROTEROZOIC WINDERMERE SUPERGROUP

EDIACARAN

uPBu — **BLUEFLOWER FORMATION, UPPER MEMBER:** *brown-weathering, shale, siltstone and sandstone; pale grey-pink sandstone and grit; calcareous shale; limestone. Equivalent to Yusezyu Formation of the Hyland Group*

uPBm — **BLUEFLOWER FORMATION, MIDDLE MEMBER:** *green or grey, rhythmically-bedded mudstone, siltstone, and fine sandstone*

uPBl — **BLUEFLOWER FORMATION, LOWER MEMBER:** *buff, grey and pale yellow-weathering limestone interbedded with green shale. Limestone is planar and cross-bedded*

uPG — **GAMETRAIL FORMATION:** *grey, yellow and orange weathering dolostone, dolomitic siltstone/sandstone and limestone, commonly planar and/or cross laminated; calcareous shale and siltstone; maroon shale; carbonate-clast breccia and conglomerate*

uPNS — **NADALEEN FORMATION, STENBRATEN MEMBER:** *grey to greenish-brown rhythmically bedded fine-grained sandstone, siltstone, mudstone; maroon siltstone-mudstone*

uPN — **NADALEEN FORMATION, LOWER MEMBER:** *brownish-grey siltstone, mudstone, limestone; limestone conglomerate; rhythmically, thin to medium bedded mudstone and limestone; local pink-grey quartz sandstone and quartzite; calcareous grit and sandstone*

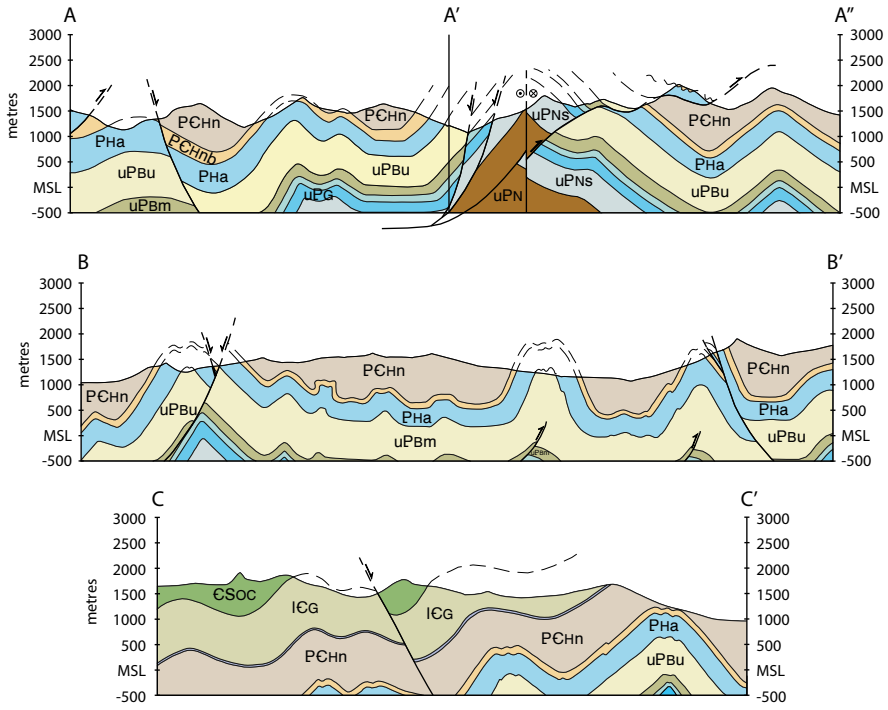

GAMETRAIL FORMATION

The Gametrail Formation (Aitken, 1989) forms a distinctive resistant marker unit that is approximately 200 m thick. It comprises deep yellow-orange weathering, thin to thickly bedded dolomitic sandstone, siltstone and shale, grey or yellow ribbon-bedded limestone/dolostone, thin to medium-bedded silty limestone, and massive carbonate breccia. Silty limestone is typically planar and/or cross-bedded and exhibits sole structures indicative of deposition by turbidity currents. The top of the Gametrail Formation is marked by a boulder breccia consisting of large grey and orange limestone/dolostone clasts in a grey limestone matrix (Fig. 4a). In 106C/01, the formation contains a number of maroon shale intervals in a sequence that is generally paler coloured, with a higher proportion of grey limestone; these maroon intervals are not present in 106B/04. Colpron *et al.* (2013) referred to the Gametrail Formation as the "lower Stenbraten assemblage".

BLUEFLOWER FORMATION

The Blueflower Formation (Aitken, 1989) is here divided into three map units, termed the lower, middle, and upper members. The combined thickness of these units approaches 1 km. The Blueflower Formation was referred to as the "upper Stenbraten assemblage" by Colpron *et al.* (2013).

The *lower member* comprises approximately 100 m of medium-bedded silty limestone interbedded with green to grey mudstone (Fig. 4b). Silty limestone beds, interpreted as limestone turbidite deposits, are generally 2-20 cm thick, grey to pale yellow, and are typically planar and/or cross-bedded. They are interbedded with thin green to grey mudstone partings and layers <1 mm to several centimetres thick. On mountain slopes, the lower contact of the Blueflower Formation is marked by an obvious colour change, from pale tones of the lower member to the bright yellow/orange of the Gametrail Formation.

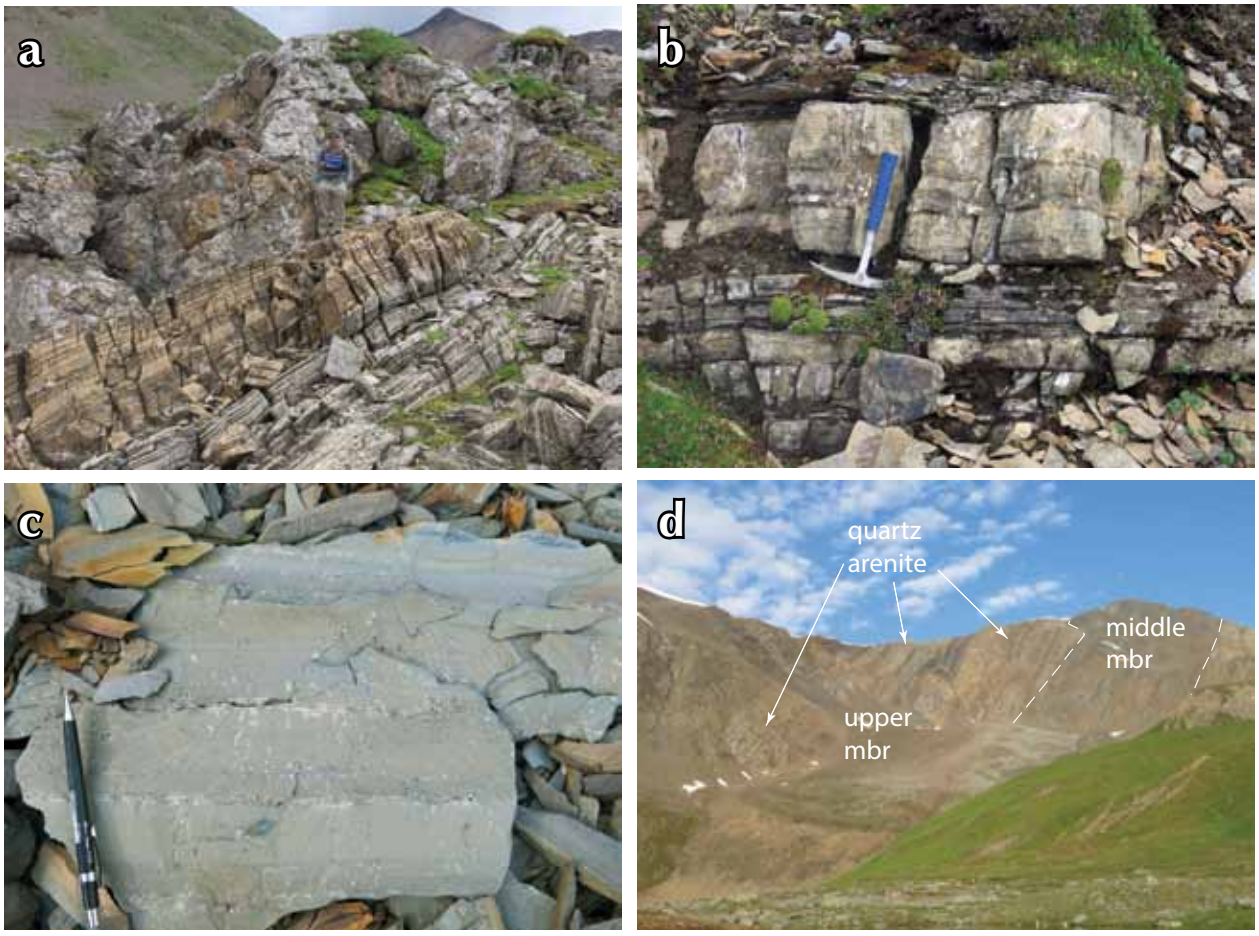

Figure 4. *(a) Ribbon-bedded limestone and dolostone overlain by carbonate-clast breccia; uppermost Gametrail Fm; (b) planar and cross-laminated limestone interbedded with grey-green mudstone; Blueflower Fm, lower mbr; (c) green mudstone and siltstone with graded bedding; Blueflower Fm, middle mbr; (d) view across steeply-dipping section of Blueflower Fm. The upper member contains thick, resistant intervals of quartz arenite and grit; relief is ~400 m.*

The *middle member* is approximately 200 m of olive green to grey, very thinly bedded mudstone, siltstone, and fine sandstone; graded bedding is common and the rocks are rhythmically-layered (Fig. 4c). The boundary between this and the underlying member is gradational. This member is similar to the Stenbraten member of the Nadaleen formation and is likewise interpreted to have been deposited by turbidity currents.

The *upper member* comprises a varied mixture of variably calcareous clastic rocks. It includes intervals of very thickly bedded quartz arenite/grit with abundant limonite spots, brown shale, black shale and sandstone, calcareous grit and conglomerate, silty/sandy limestone, and limy mudstone (Fig. 4d). The top of the unit comprises an interval of brown shale. This member has a total thickness of approximately 500 m. The rock types in the upper member are similar to those in the upper part of the Yusezyu Formation of the Hyland Group (Gordey and Anderson, 1993; Colpron, 2012a,b) south of the Dawson thrust.

In Windermere Supergoup sequences of the Mackenzie and Wernecke mountains, the Blueflower Formation is overlain by the Risky and Ingta formations, which are dominated by carbonate and green/maroon shale, respectively. Similar units overlie the Blueflower Formation in the Rackla area, but are referred to as the Algae and Narchilla formations of the Hyland Group (Selwyn basin; Fig. 3). Windermere Supergroup-Hyland Group stratigraphic nomenclature has evolved independently and clear relationships have not been reported elsewhere. The Risky-Ingta and Algae-Narchilla sequences are considered direct correlatives, but Hyland Group nomenclature is used here based on historical precedent, continuity with mapped sequences in the Selwyn basin, and proximity to the type section of one of the units (Algae Formation). Hyland Group-Windermere Supergroup stratigraphic relationships are discussed further in a later section.

HYLAND GROUP

ALGAE FORMATION

The Algae Formation (Cecile, 2000) consists of pale to dark grey, thinly to medium-bedded cliff-forming limestone and dolostone (Fig. 5a,b). Most of the rocks are limestone (micrite and grainstone, locally oolitic) and silty/sandy limestone, with minor intraclast floatstone/rudstones. Some shaly intervals are interbedded with grainstone near the top of the formation, and the formation also includes minor chert. The base of the formation includes a fetid interval that emits a strong sulphurous smell when walked over or hammered. Silty/sandy limestone is commonly cross-bedded, and in some cases display an upward transition from planar to cross-lamination within individual beds (Fig. 5c). This is interpreted to represent deposition by sediment gravity flows (Bouma B-C sequences). Dolomitized intervals have a coarse-grained, sugary texture, and are coloured white, beige, pink, and light grey. Zebra texture is locally developed. Dolomitization is most widespread and pervasive in the upper part of the formation (Fig. 5b). The Algae Formation is approximately 250-350 m thick in the area; at least part of this variation is due to the presence of an irregular erosional surface between it and the overlying Narchilla Formation.

CONTACT BETWEEN THE ALGAE AND NARCHILLA FORMATIONS

The contact between the Algae Formation and the Narchilla Formation is marked by an erosional surface of varying character. The contact zone commonly includes 1-5 m of clast-supported, brecciated limestone, and varying amounts of a brown sandy matrix (Fig. 5d). In places, this brecciated limestone can be traced downwards into intact bedded limestone with sand-filled cracks. Elsewhere, the brecciated limestone has been reworked and is in sharp contact with intact limestone. Relief on the erosional surface is visible in mountainside exposures in the western part of the area (Fig. 6). Here, the matrix to the limestone breccia is stained bright red. This red matrix is interpreted as a "Terra Rosa" (Merino and Banerjee, 2008) that developed during terrestrial weathering of the limestone.

NARCHILLA FORMATION

The Narchilla Formation (Gordey and Anderson, 1993) is dominated by fine-grained clastic rocks with a cumulative present-day (deformed) thickness of almost 1 km in 106B/04. In the Niddery Lake area, Cecile (2000) divided the formation into two members. The lower Senoah Member (~400 m thick) consists of grey-black, grey-blue, and minor mauve siltstone and shale, and some quartzite/grit and minor limestone, while the overlying Arrowhead Lake Member (~120 m) comprises maroon and lime green argillite and minor quartzite. The contact between the two members is described as "distinct and marked by a generally abrupt change from maroon, lime green or blue-grey argillite typical of the Arrowhead Lake Member, into more drab siltstone or coarser clastic rocks of the Senoah Member" (Cecile, 2000, p. 20). This subdivision, with its discrete colour-change, was not recognized in the map area; instead, a thin basal member is distinguished from the remainder of the formation.

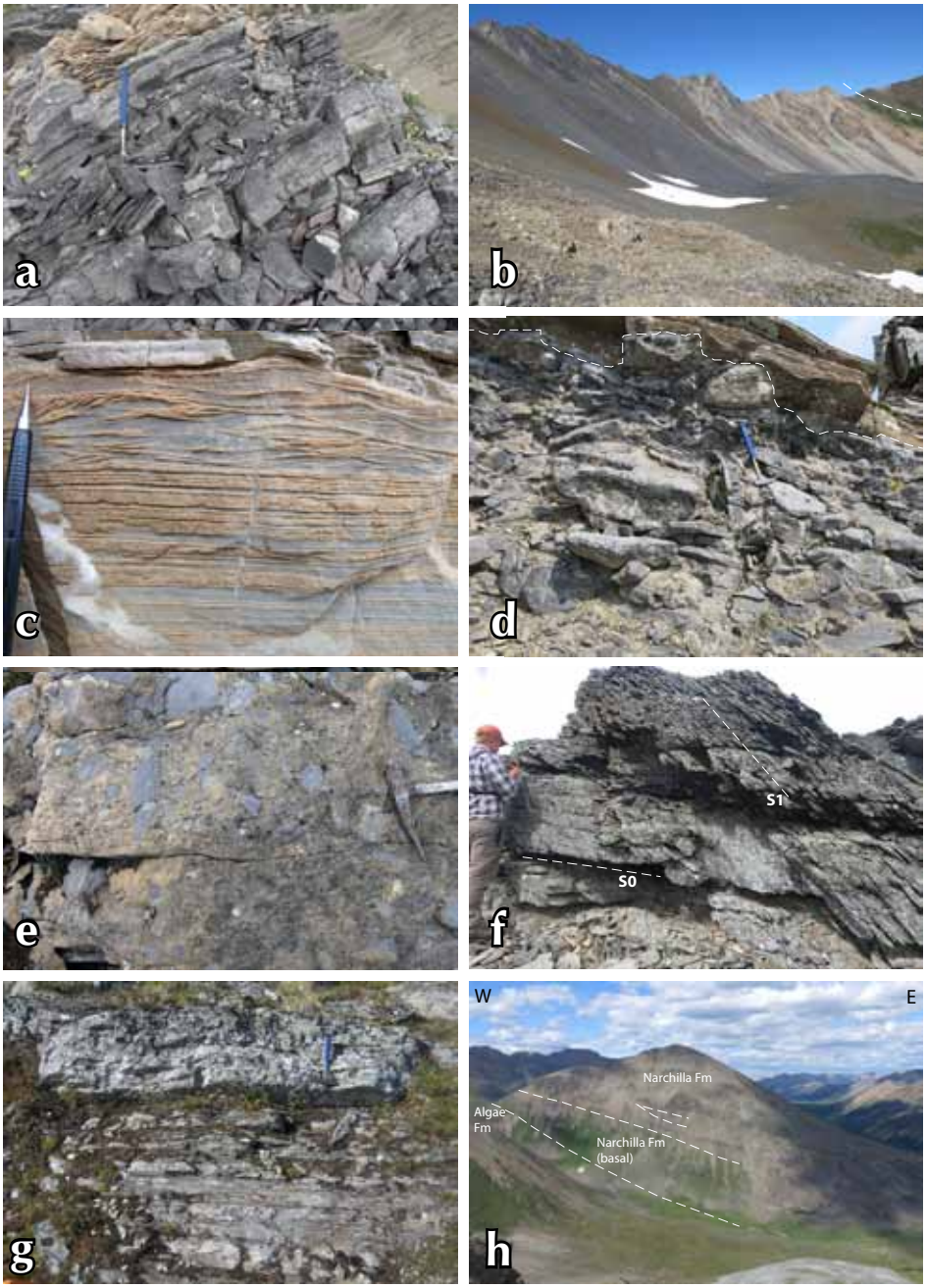

***Figure 5**. (a) Thinly-bedded grey limestone of Algae Fm. The buff-coloured layers at the top of the photograph are dolostone; (b) view across tilted section of Algae Fm. The upper part is pale grey as a result of dolomitization. The upper boundary with the Narchilla Fm is marked. Relief is ~200 m; (c) upward transition from planar to cross-bedding in sandy limestone of the Algae Fm; (d) limestone breccia at the top of the Algae Fm, overlain by pale brown sandstone (Narchilla Fm); (e) conglomerate at base of Narchilla Fm comprising grey limestone clasts in a brown, slightly calcareous sand/grit matrix; (f) high angle between bedding and cleavage in mudstone of the Narchilla Fm; (g) white-weathering sandstone beds ranging from 5-50 cm; sandstone beds display upwards transitions from planar to cross-lamination. Narchilla Fm; (h) lower part of the Narchilla Fm. Sandstone-rich basal member is overlain by maroon and green mudstone with some discontinuous sandstone intervals (wedge outlined in white). Relief is ~500 m.*

The *basal member* of the Narchilla Formation (~10 to 100 m) is highly variable in terms of lithology and thickness. Rock types include medium to thickly bedded quartz arenite, brown sandstone, conglomerate/breccia, green shale, thinly interbedded limestone and shale, medium to thickly-bedded limestone and silty limestone, calcareous sandstone, and grit. The most characteristic rock type is a brown-weathering conglomerate/breccia with a poorly-sorted sandstone or grit matrix and abundant clasts of grey limestone derived from the underlying Algae Fm (Fig. 5e). In areas that contain several conglomerate horizons, there is generally an upward increase in the matrix to clast ratio.

The remainder of the Narchilla Formation is dominated by thinly-bedded, well-cleaved mudstone (Fig. 5f), siltstone, and shale, with some sandstone-rich intervals. Mudstone and siltstone are very thinly bedded, and graded bedding is common. Thin, white-weathering sandstone layers are widely distributed and commonly cross-bedded (Fig. 5g). Rocks of the Narchilla Formation are bioturbated, and simple horizontal trace fossils are preserved on the base of sandy beds (Fig. 7a,b). Mudstones and siltstones are mostly pastel shades of beige and brown, but are also commonly lime green, mauve, or maroon (Fig. 5h). Green and mauve/maroon intervals are stratiform or patchy, and form particularly fine-grained shaly slopes. Colour variations within the Narchilla Fm are interpreted as a secondary characteristic rather than having any regional stratigraphic significance.

***Figure 6**. Erosional unconformity between the Algae Fm and overlying Narchilla Fm. Note the irregular shape of the contact, which truncates bedding in the limestone, and the bright red colour (interpreted as 'Terra Rosa'). The cliff is approximately 300 m high.*

Sandstone-rich intervals contain abundant sandstone layers from 1 cm to 1 m thick. These beds typically weather white and contain abundant detrital white mica; orange limonite spots are also common on fresh surfaces. Sandstone typically displays a mixture of planar and cross-lamination, and flute casts are developed on the bottom of some beds, suggesting deposition by turbidity currents. A thick unit (~10 to 15 m) of quartzite and grit is present in some locations near the bottom of the main part of the formation.

CAMBRIAN-SILURIAN

GULL LAKE FORMATION

The Gull Lake Formation (Gordey and Anderson, 1993), which is exposed south of the Stewart River (Fig. 3), is dominated by fine-grained clastic rocks.

The thin *basal member* comprises a variable mix of limestone-clast conglomerate (Fig. 8a), lithic sandstone and grit, quartz arenite, and argillite. Lithic sandstone and granule-pebble conglomerate weathers orange, and is commonly green on fresh surfaces. It is poorly sorted and contains a mixture of subrounded quartz grains and lithic clasts. It is interfingered with a cobble to boulder matrix-supported conglomerate of variable thickness (2-10 m) that contains predominantly limestone clasts and, locally, with medium to thickly bedded white quartz arenite. Limestone clasts in the conglomerate are pale grey and mostly subrounded; some clasts contain archaeocyathids (Fig. 8b), and less commonly, oolites. Other clast types include blocky quartz arenite and dark sandstone. The conglomerate matrix consists of pale beige to brown, slightly calcareous sandstone with abundant granules of quartz and subangular to subrounded chert clasts.

Most of the Gull Lake Formation is dominated by argillite, siltstone, and fine sandstone. The argillite is typically olive green (Fig. 8c), very thinly bedded, and blocky. Beds are commonly graded and are extensively bioturbated by horizontal burrows (Fig. 7c). The argillite weathers brown,

orange, or white in mountain exposures; where a white weathering rind is most intensely developed it has a porcelaneous character (Fig. 8d). Argillite is also coloured lime green, black, and red-maroon in places. Fine-grained clastic rocks of the Gull Lake Formation are extensively altered to a red-maroon colour near the southern margin of the map area (Fig. 8e).

The upper part of the formation includes a number of intervals, each tens of metres thick, characterized by rhythmic interbeds of sandstone and shale/argillite. Sandstone layers are white-grey, 2 to 40 cm thick, and display basal flute casts (Fig. 8f). Other minor rock types in this part of the section include rare silty limestone layers that display upward transitions from massive bedding to planar lamination to cross-lamination (Bouma A-C), and carbonate clast conglomerate. A small amount of black shale and blue chert are also present near the top of the formation.

A number of occurrences of the trace fossil *Oldhamia* were encountered in the upper part of the formation (Fig. 7d). As *Oldhamia* does not appear in the fossil record above Stage 5 of the Cambrian System (Herbosch and Verniers, 2011), this places a lower age limit on most of the Gull Lake Formation. An upper limit is imposed by the presence of archaeocyathid-bearing clasts at the base of the formation. As archaeocyathids are restricted to the interval covered by Stages 2-4, most, and possibly all of the formation was deposited during Stages 2 to 5 of the Cambrian (~528-506 Ma; Babcock and Peng, 2007).

In the Niddery Lake map area, Cecile (2000, p. 25) described the contact between the Arrowhead Member of the Narchilla Formation and the Gull Lake Formation as being "distinct and conformable and defined by a colour change". In 106B/04, the formations cannot be distinguished based on their colour as each includes intervals of brown, maroon, and green shale/argillite.

***Figure 7**. (a) Pale green wispy lenses indicative of bioturbation of graded beds in rhythmically-layered mudstone-siltstone; Narchilla Fm; (b) casts of horizontal burrows on the base of a sandstone bed in green mudstone; Narchilla Fm; (c) cast of sinuous horizontal burrows on sandstone bed; Gull Lake Fm; (d) radiating traces of Oldhamia in green mudstone; Gull Lake Fm.*

Some of the rocks on the southern boundary of the map area that were included by Cecile (1998) in the Arrowhead Member of the Narchilla Formation are here assigned to Gull Lake Formation. The thickness of the Gull Lake Formation is comparable to that in its type area (~1 km) but exceeds that (~400 m) reported by Cecile (2000) in the Niddery Lake area.

OLD CABIN FORMATION

The Old Cabin Formation (Cecile, 2000) is dominated by green volcanic breccia and conglomerate composed of mafic volcanic clasts and matrix (Fig. 8g). The top of the Old Cabin Formation is not exposed in the area, but regionally it forms a separate unit above the Gull Lake Formation, or is intertongued with it (Cecile, 2000).

Clasts are typically lapilli to boulder size and sit in a matrix that is compositionally similar. Mafic clasts contain phenocrysts of black clinopyroxene and less commonly phlogopite in a fine-grained green matrix; some are also amygdaloidal. Locally, clasts are cemented together by coarsely crystalline, space-filling calcite, or more rarely, bluish opal/chalcedony. In addition to clasts of mafic volcanic rock, white to pale grey barren limestone clasts are common. These are generally 2 to 10 cm, but some clasts are up to 5 to 10 m in maximum dimension. Breccia and conglomerate are interbedded with thinly-bedded, orange, brown, or white-weathering siltstone and sandstone. Some sandstone beds are rich in clinopyroxene fragments. Breccia is generally massive, and locally form channelized bodies that are incised into finer grained layers. The base of the formation was drawn at the bottom of the first massive breccia layer overlying thinly-bedded siltstone and sandstone of the Gull Lake Formation. Thin units of siltstone and sandstone (Fig. 8h) are found throughout the Old Cabin Formation, but are most abundant in its lowest part. The formation also includes minor dolerite; a single small body, which probably represents a sub-volcanic feeder dike or sill, was encountered in the area.

While volcanic breccia and conglomerate are generally coloured green, maroon clasts are present in some places, and a small volume of the formation is maroon in its entirety. Some siltstone-sandstone sequences are also maroon or bright green. Locally, relatively unaltered green, coloured breccia can be traced laterally into maroon-red shaly material. This is not true shale but rather an alteration product of the mafic volcanic rocks. Areas that are altered in this manner locally define linear trends, suggesting fluids responsible for the alteration were channeled along steeply-dipping structures.

The Old Cabin Formation conformably overlies the Cambrian Gull Lake Formation, but there are no further age constraints in the map area. In its type area the Old Cabin Formation sits between Gull Lake Formation and the Silurian-Devonian Steel Formation of the Road River Group (Cecile, 2000). Elsewhere in the region, similar rocks are intercalated with Cambrian and Ordovician rocks, including the Gull Lake Formation. The Old Cabin Formation is one of a series of alkalic and potassic volcanic centres in the Selwyn basin that are associated with episodic lower Paleozoic rifting (Goodfellow *et al.*, 1995).

STRUCTURAL GEOLOGY

The mapped area forms part of the Selwyn fold belt, which developed during Jura-Cretaceous shortening associated with the Cordilleran orogeny (Gordey and Anderson, 1993). There are no plutonic rocks in the NTS 106B/04 map sheet area, but elsewhere in the region a lower limit on the age of deformation is provided by mid-Cretaceous plutons that overprint folds and faults (Cecile, 2000; Roots, 2003; Abbott, 2013). Structures are colour coded according to their relative age in Figure 9.

NW-SE TO E-W TRENDING FOLDS

The dominant structures in 106B/04 define an arcuate pattern; they are oriented NW-SE in most of the area, but are approximately E-W in the westernmost part of the map sheet area (major folds are coloured red in Fig. 9). These structures include folds at a range of scales and steeply-dipping axial-planar cleavage, which is variably developed.

Folds are typically upright, open to close, and plunge at shallow angles to the W-NW or E-SE (Figs. 3 and 10). Exceptions to this trend were observed in the hinge zones of major folds, where pelitic rocks are affected by tight, steeply-plunging folds, and in the vicinity of faults. Minor folds are best developed in strongly layered mudstone/siltstone-sandstone sequences, particularly those of the Narchilla Formation (Fig. 11a). Major folds generally have wavelengths of 2-3 km and amplitudes of approximately 500-750 m. These folds commonly have complex hinge zones characterized by abundant chevron and box folding of competent units (*e.g.*, carbonate of the Algae Formation; Fig. 11b-d). The axial traces of major folds are curved around the "strike-swing" in the west-central part of the map area (Fig. 11e).

A penetrative cleavage is developed in fine-grained clastic rocks (mudstone, siltstone) throughout the area, with the exception of argillite in parts of the Gull Lake Formation. In these rocks, a scaly, semi-penetrative cleavage is developed instead. Semi-penetrative foliation is also locally developed in impure carbonate units, but is largely absent from pure carbonate and quartz arenite.

SW-DIPPING THRUST FAULT

The oldest rocks in the area are exposed in the core of a large anticline in the western part of the area, the northeastern flank of which is cut by a SW-dipping thrust fault (coloured red in Fig. 9; Fig. 12a,b). The fault plane is affected by open folds, and intersection of the thrust with topography has produced a klippe of Algae Formation and lowermost Narchilla Formation (Fig. 12a). Offset on the fault, which reaches a maximum of ~1.5 km in its central part, diminishes rapidly along strike. Folding of the fault plane and truncation of the NE limb of the major anticline suggests there was temporal overlap between folding and thrusting.

Folds of the Algae Formation and lowermost Narchilla Formation in the hanging wall of the fault are tight chevrons and box folds (Fig. 12a). Fold axes trend E or W in the klippe, whereas folds in the hanging wall further south trend approximately NNW or SSE. The contact between the Algae Formation (hanging wall) and Narchilla Formation (footwall) is sharp, but there is a 5-15m thick zone below the contact characterised by highly disrupted bedding with abundant disarticulated blocks of quartzite; a crenulation cleavage is locally developed in pelitic rocks in this zone.

EAST-STRIKING THRUST FAULT IN THE SOUTH-WEST CORNER OF THE MAP AREA

An east-striking, north-verging fault extends into the SW corner of the map sheet area, where it separates Gull Lake Formation from underlying mafic volcaniclastic rocks of

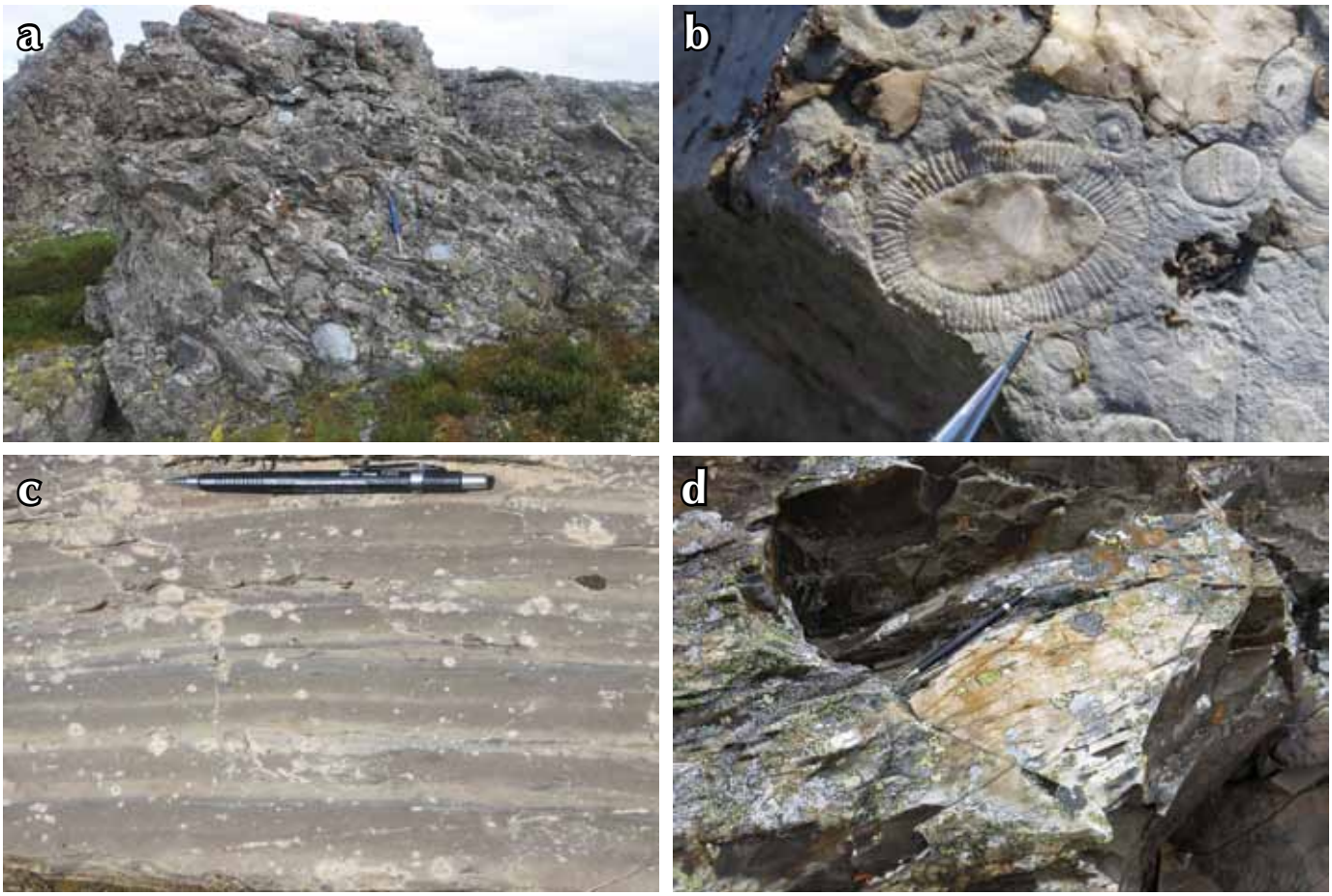

Figure 8. *(a) Conglomerate containing abundant grey limestone clasts; Gull Lake Fm, basal mbr; (b) clasts in the conglomerate shown in (a) contain archaeocyathids; (c) graded bedding in green-brown argillite. Dark lenses indicate bioturbation; Gull Lake Fm; (d) white and orange weathering rind is typical of Gull Lake Fm argillite in mountain exposures;*

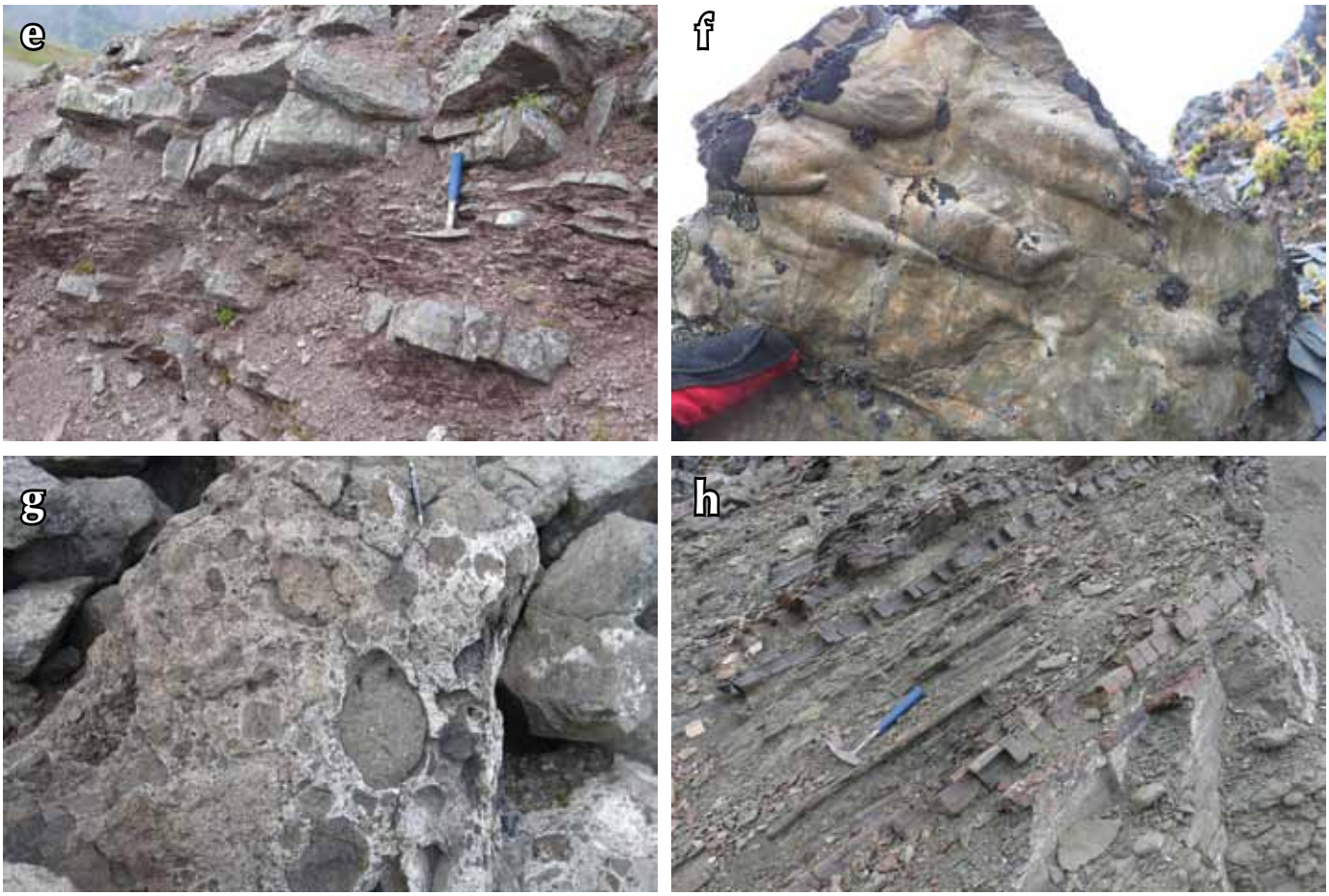

***Figure 8 con'd**. (e) white-grey sandstone beds interbedded with maroon shale; upper part of Gull Lake Fm; (f) Sole markings on the base of turbiditic sandstone beds; upper part of Gull Lake Fm; (g) breccia that comprises porphyritic mafic volcanic clasts in matrix composed of mafic volcanic detritus; Old Cabin Fm; (h) green, thinly-bedded siltstone and sandstone interbedded with mafic volcanic breccia/conglomerate; Old Cabin Fm.*

the Old Cabin Formation (coloured red in Fig. 9). Thrust-sense displacement of approximately 400 m is indicated by offset of the Gull Lake-Old Cabin formation contact close to the eastern limit of its mapped extent. Turbidite sequences of the Gull Lake Formation in the hanging wall of the fault are tightly folded and contain numerous small-scale faults.

The fault plane dips approximately 40° to the south and displays prominent ridges and grooves spaced at ~5 cm intervals that plunge approximately down the dip of the fault. Slickenlines with sub-horizontal or down-dip orientations are locally developed on polished fault surfaces. Overprinting relationships between the two sets of slickenlines were not observed, but as the down-dip grooves are the dominant structures it is likely the main phase of displacement was dip-slip, with some strike-slip reactivation.

NE-TRENDING FOLDS AND NW-VERGENT THRUST

Outcrop-scale upright, chevron folds (F2) whose axes plunge to the NE or SW are developed close to the western boundary of the map sheet area (Fig. 11f). Map-scale deflections that have NE or SW trending axes are also evident on the NE limb of the major antiform in the western part of the area. The axial planes of these folds are parallel to that of the strike-swing and are located in the vicinity of its hinge region. A NW-vergent thrust fault also formed on the western edge of the map area immediately north of the Stewart River (coloured green in Fig. 9).

EAST-STRIKING SINISTRAL FAULT

A steeply-dipping, east-striking fault extends approximately half-way across the central region of the map area (coloured blue in Fig. 9; Fig. 12c). This fault merges

with, or is a splay of the Kathleen Lakes fault, a major structure that separates facies domains along the length of the Rackla belt (Fig. 2). In 106/C01, the fault has approximately 3 km of apparent sinistral offset. A slightly smaller offset (~2 km) of steeply-dipping stratigraphy is apparent in the western part of 106B/04, where it transects the major NW-SE to E-W-trending anticline. Displacement further decreases to the east, where the fault dies out. This fault is younger than the NW/W-trending folds and cleavage, and is unaffected by the strike-swing, but is offset by NW-trending faults.

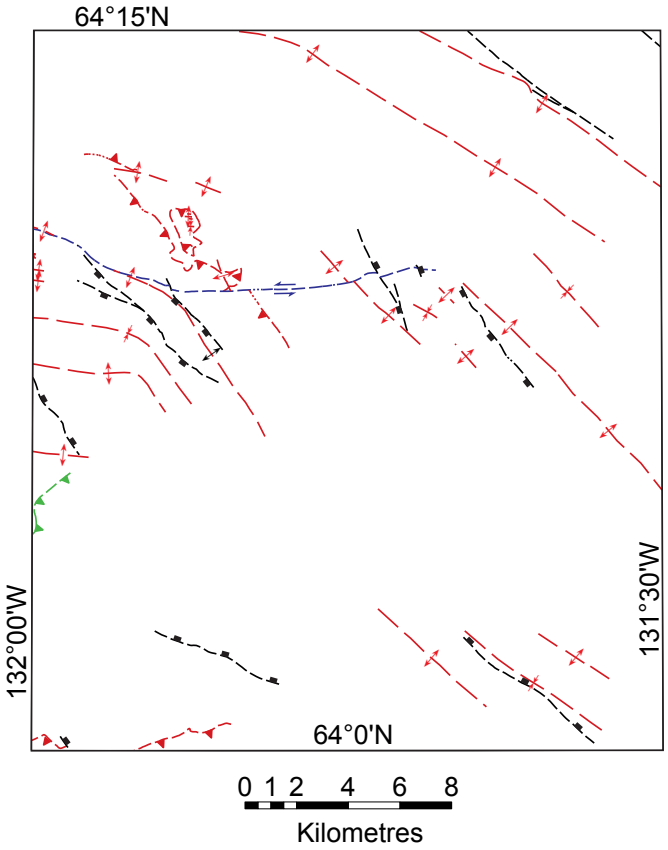

***Figure 9**. Map-scale structures in 106B/04. Early structures are shown in red. These are cut by an east-trending sinistral fault (blue), which is offset by the latest regional structures, NW to WNW- striking faults (black).*

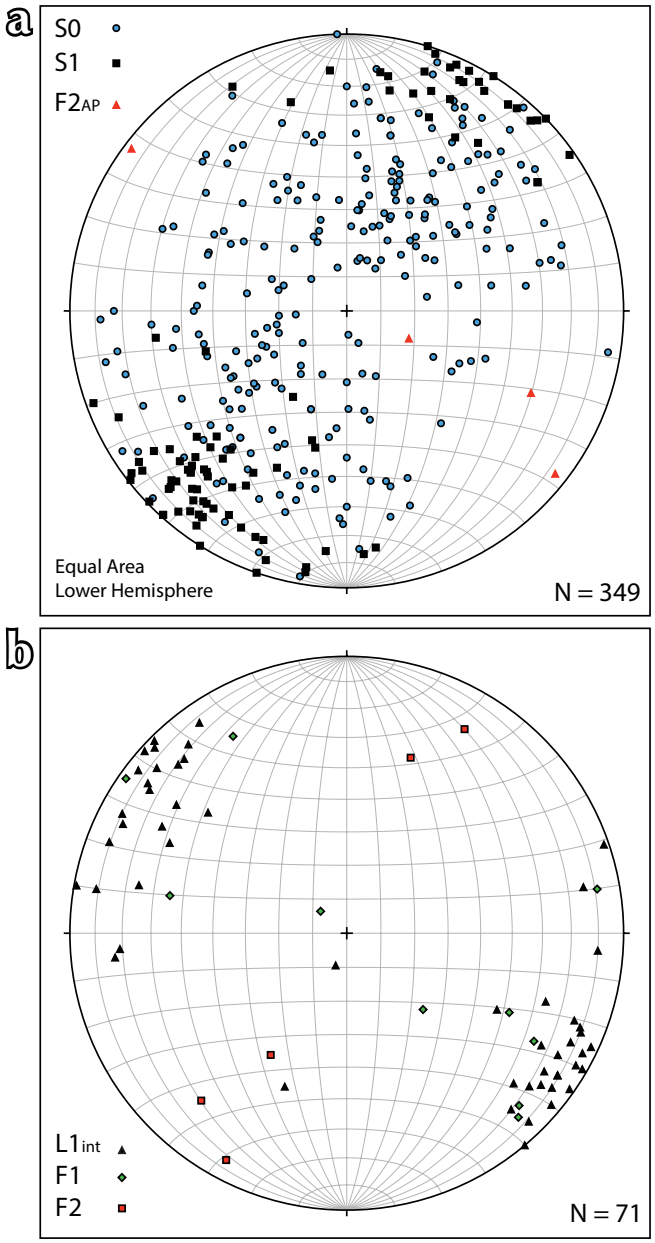

***Figure 10**. Equal area lower hemisphere stereographic projections of (a) planar and (b) linear structures in 106B/04. $F2_{AP}$=F2 axial plane; and $L1_{int}$=Intersection lineation.*

NW-STRIKING FAULTS

The youngest structures that affect the map pattern are steeply-dipping faults that strike NNW to WNW (Figs. 12d and 13; coloured black on Fig. 9). These faults, which occur throughout the area, have strike lengths of approximately 3-10 km. Where observed, areas adjacent to these faults are characterized by disrupted bedding and anomalous fold orientations; a fault-parallel foliation is also locally developed. Most of these faults have normal-sense offsets of hundres of metres (up to a maximum of approximately 1 km in the case of the fault illustrated in Fig. 13); however in some cases a component of dextral displacement is also required to account for the offset of markers. The sense of displacement on the steeply-dipping fault in the NE corner of the map is unclear (Fig. 12e); duplication of the Algae - Narchilla formation contact is compatible with thrusting, but could also be a result of strike-slip (dextral) faulting.

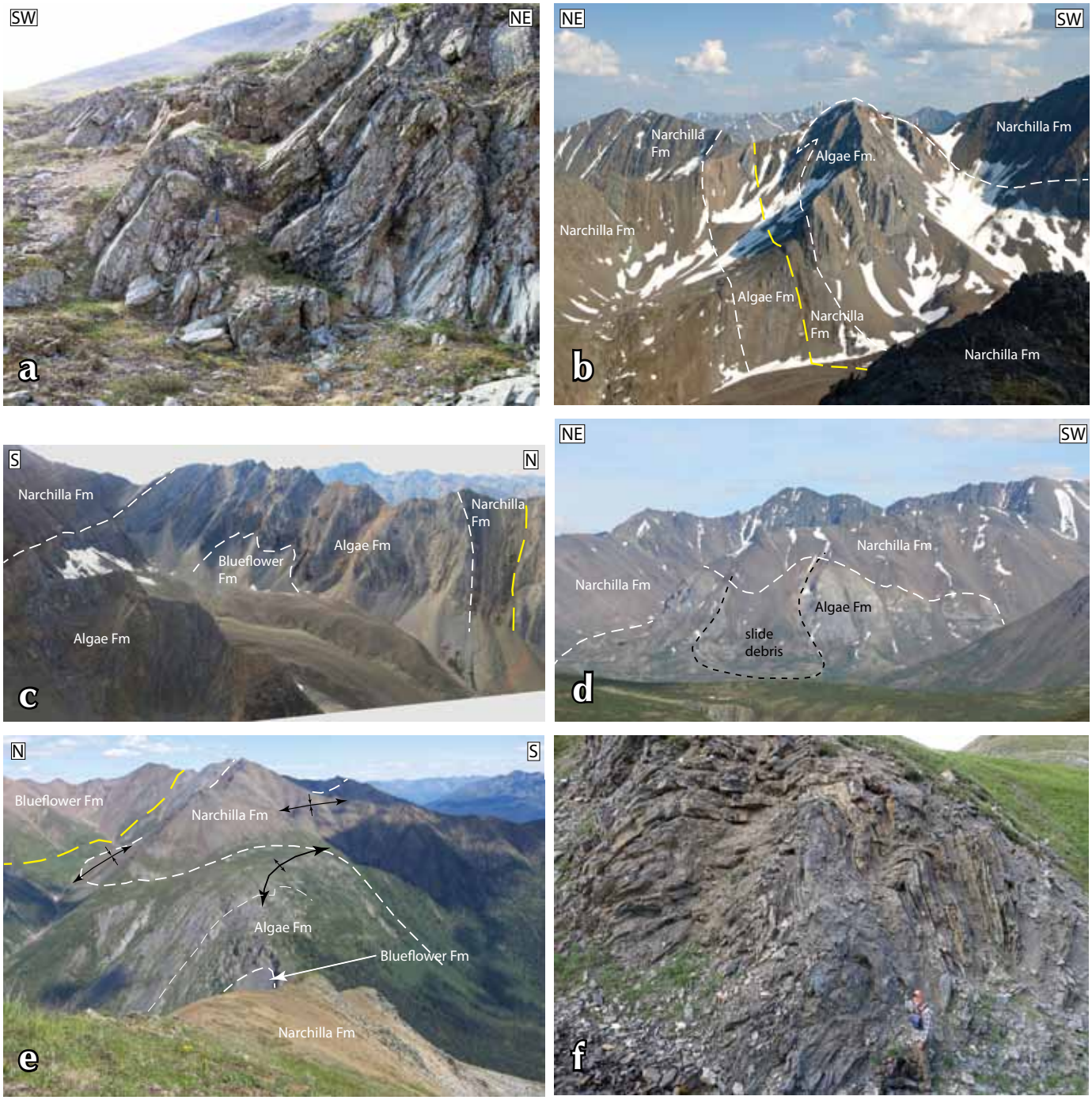

Figure 11. *(a) Minor upright folding of sandstone beds in the Narchilla Fm; (b) hinge region of large anticline in the NE corner of the map area. The Algae Fm on the NW limb is repeated across a steep fault; relief is ~400 m; (c) the same anticline as shown in b) viewed in the opposite direction from the air. Note the steep limbs and complex hinge zone with abundant chevron folding; relief is ~450 m; (d) anticline cored by Algae Fm in NE part of the area (west of the anticline shown in parts b,c). This anticline also has a folded hinge zone with sub-horizontal enveloping surface; relief is ~600 m; (e) anticline cored by Blueflower Fm and adjacent syncline in the western part of the area. Orientation of structures changes from E-W (foreground) to NW-SE (background); relief is ~950 m; (f) NE-plunging (F2) chevron folds in Algae Fm limestone.*

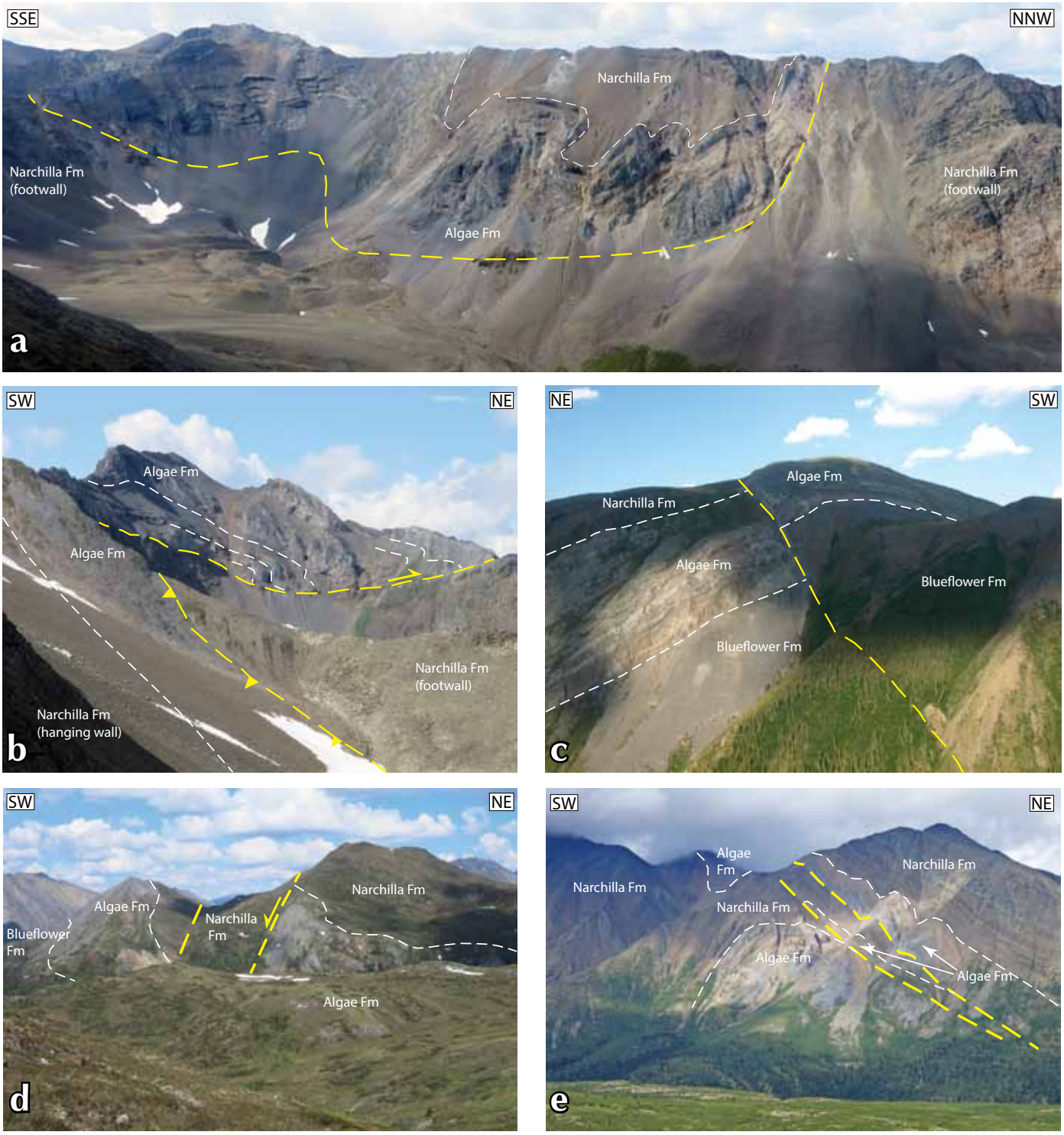

Figure 12. (a) Oblique view of the SW-dipping thrust fault in the western part of the area. The thrust (shown in yellow) is gently folded, but tighter folds are developed in the Algae and Narchilla formations in its immediate hanging wall; relief is ~400 m; (b) truncation of bedding in the Algae Fm along a sub-horizontal portion of the SW-dipping thrust fault; (c) offset of the Blueflower-Algae-Narchilla formation contacts by the east-striking, steeply-dipping fault in the centre of the map area. Displacement on the fault is small near its tip zone; relief is ~400 m; (d) Algae Fm offset by SE-striking normal fault in the central part of the area; relief is 300 m; (e) repetition of the Algae Fm-Narchilla Fm contact across steeply-dipping faults that truncate the flanks of the antiform in the NE corner of the area; relief is ~700 m.

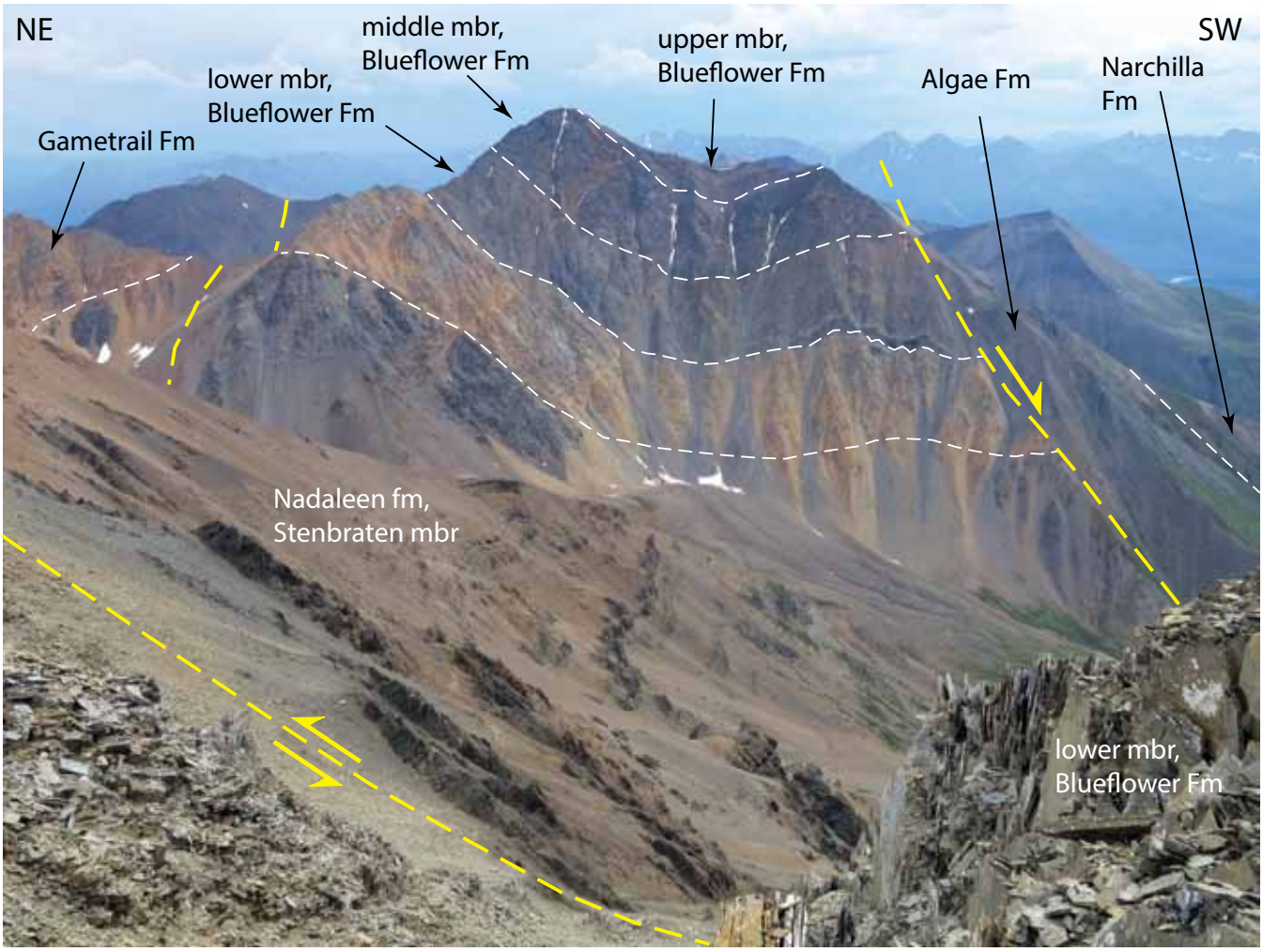

***Figure 13**. Down-plunge view across the crestal region of the large antiform in the western part of the area. The antiform is cut by a SW-dipping normal fault that juxtaposes Algae Fm limestone against the Gametrail Fm, which forms a distinctive yellow-weathering layer. The sinistral fault that runs across the foreground offsets the axial plane and here juxtaposes the lower member of the Blueflower Fm against the oldest rocks that are exposed in the area (Nadaleen fm); relief is ~600 m.*

WEDGE-SHAPED PANEL OF ALGAE AND NARCHILLA FORMATIONS IN THE SW CORNER OF THE MAP AREA

The isolated, wedge-shaped panel of Algae and Narchilla formations in the SW-corner of the map area is in an anomalous structural position. The panel, which comprises the upper part of the Algae Formation and lowermost Narchilla Formation, dips gently south, and is truncated along its steeply-dipping southern boundary (Fig. 14). The gently-dipping base and the steeply-dipping southern boundary are in contact with mafic volcaniclastic rocks of the Old Cabin Formation, whereas the SW boundary is in contact with Gull Lake Formation across a NW-trending fault. The east-striking thrust runs ~350 m south of the Algae-Narchilla wedge, and is separated from it by a narrow belt of Old Cabin Formation.

The observed geometry could have been produced by out-of-sequence thrusting. In this interpretation, a low-angle thrust separating the Algae and Old Cabin formations is cut by a steeper fault that defines the southern boundary of the wedge; this fault is itself cut by, or is a splay of the east-striking thrust. A problem with this interpretation is that the low-angle "thrust" contact between Algae Formation and Old Cabin Formation is not exposed to the south, where it would be expected to intersect the surface. No north-verging thrust faults have been mapped in the area to the south (Cecile, 1998), where structures (folds, faults) are instead oriented NNW-SSE.

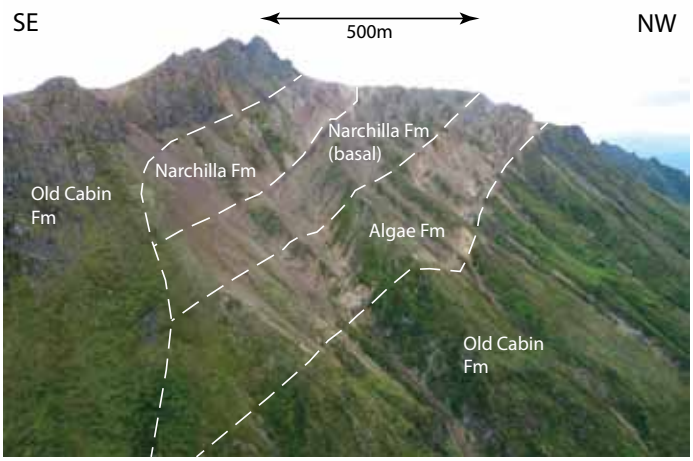

***Figure 14**. Aerial view of the small isolated panel of Algae Fm-Narchilla Fm in the SW part of the area. The Algae-Narchilla panel dips gently south and is truncated along a steeply-dipping surface at its southern end.*

An alternative interpretation is that the Algae Formation-Narchilla Formation wedge is an isolated block (an olistolith) that slid into its current position during deposition of the Old Cabin Formation. Although blocks of this magnitude were not observed elsewhere in the Old Cabin Formation, barren limestone clasts are common, and clasts up to 10 m in maximum dimension were observed.

MINERALIZATION

The map area lies to the east of recent discoveries of "Carlin-type" gold mineralization (Arehart *et al.*, 2013; Tucker *et al.*, 2013) by ATAC Resources (*www.atacresources.com*). Mineralization is structurally controlled and is hosted by arsenic-rich pyrite in calcareous rocks of widely varying age (Conrad zone – Ediacaran Nadaleen formation; Osiris zone – Ediacaran Gametrail Formation; Anubis zone – Devonian limestone).

Within the map area, gold mineralization has recently been discovered at the Venus zone in the SW part of the area (Anthill resources; *www.anthillresources.com*). Mineralization is located in the upper part of the Algae Formation, which is dolomitized and variably silicified. The Algae Formation in this area forms part of the isolated wedge-shaped panel discussed in the previous section.

Given the widespread presence of dolomitized limestone and its position close to the margin of the Selwyn basin, the area may also be prospective for Mississippi Valley-type mineralization. The Birkeland drilled prospect (originally staked as the Tom and Mom claims) was explored for Pb-Zn-Ag mineralization in the 1970's (Shearer, 1976). Mineralization is located in the upper part of the Algae Formation, where lead-zinc showings are associated with zebra dolomite.

DISCUSSION

STRATIGRAPHIC RELATIONSHIPS BETWEEN THE WINDERMERE SUPERGROUP AND HYLAND GROUP

The Algae and Narchilla formations were deposited throughout the eastern Rackla belt, but the nature of the rocks they overlie varies. North of the Dawson thrust they overlie the Blueflower Formation (Windermere Supergoup) whereas they succeed Yusezyu Formation (Hyland Group) in Selwyn basin (Fig. 15).

In NTS 106C/02 and the western part of 106C/01 (Colpron *et al.*, 2013), the Blueflower Formation is dominated by fine-grained clastic rocks and carbonate turbidites, with some carbonate-clast diamictites (debris-flow deposits). To the east, increasing amounts of quartz arenite and grit appear in its upper part, and in 106B/04, form a large proportion of an upper member that is lithologically comparable to the upper part of the Yusezyu Formation of the Hyland Group. These relationships imply equivalence of the Algae and Narchilla formations with the Risky and Ingta formations, and of the upper member of the Blueflower Formation with the Yusezyu Formation (Fig. 15). The upper Blueflower Formation-Yusezyu Formation comprises a clastic wedge that thickens into Selwyn basin, where it is estimated to have a stratigraphic thickness of approximately 3 km (Gordey and Anderson, 1993).

An erosional unconformity is developed between the Algae and Narchilla formations in the eastern Rackla belt and the Risky-Ingta formations on the Mackenzie and Ogilvie platforms. At the Algae Formation type section, located ~15 km south of the southern boundary of the map area, Cecile (2000) reported conglomerate with limestone clasts at the base of the Narchilla Formation but interpreted the contact to be conformable. It appears, therefore, that the Algae-Narchilla/Risky-Ingta unconformity passes basinward into a conformable surface.

FORMATION OF THE "STRIKE-SWING"

The dominant structures in the area define an arcuate trend, with a change in orientation from E-W around the western boundary of the map area (106B/04) to NW-SE in its remainder. The formation of this arcuate pattern is attributed to the position of the area in the "corner" between south and southwest-facing segments of the Selwyn basin margin (Fig. 1). The strike curvature is interpreted to have been acquired progressively as strata were shortened against the non-parallel basin margins. Continuity of major fold axes around the strike swing suggests that fold axes were originally approximately linear, as folds that initiated on either limb of the strike swing are unlikely to have propagated around a pre-existing bend. Tight folds in the hanging wall of the SW-dipping thrust trend ~E or W in the klippe and ~NNW or SSE in the region to its south. These folds exhibit a higher degree of obliquity across the axis of the strike swing than do regional-scale structures; this may reflect primary curvature arising from displacement gradients during thrusting. Although NE-trending structures around the hinge of the "strike-swing" ostensibly represent a second phase of deformation, these may have formed during the latter stages of the main deformation period as tightening of the strike swing gave rise to NW-SE-directed shortening around its hinge zone.

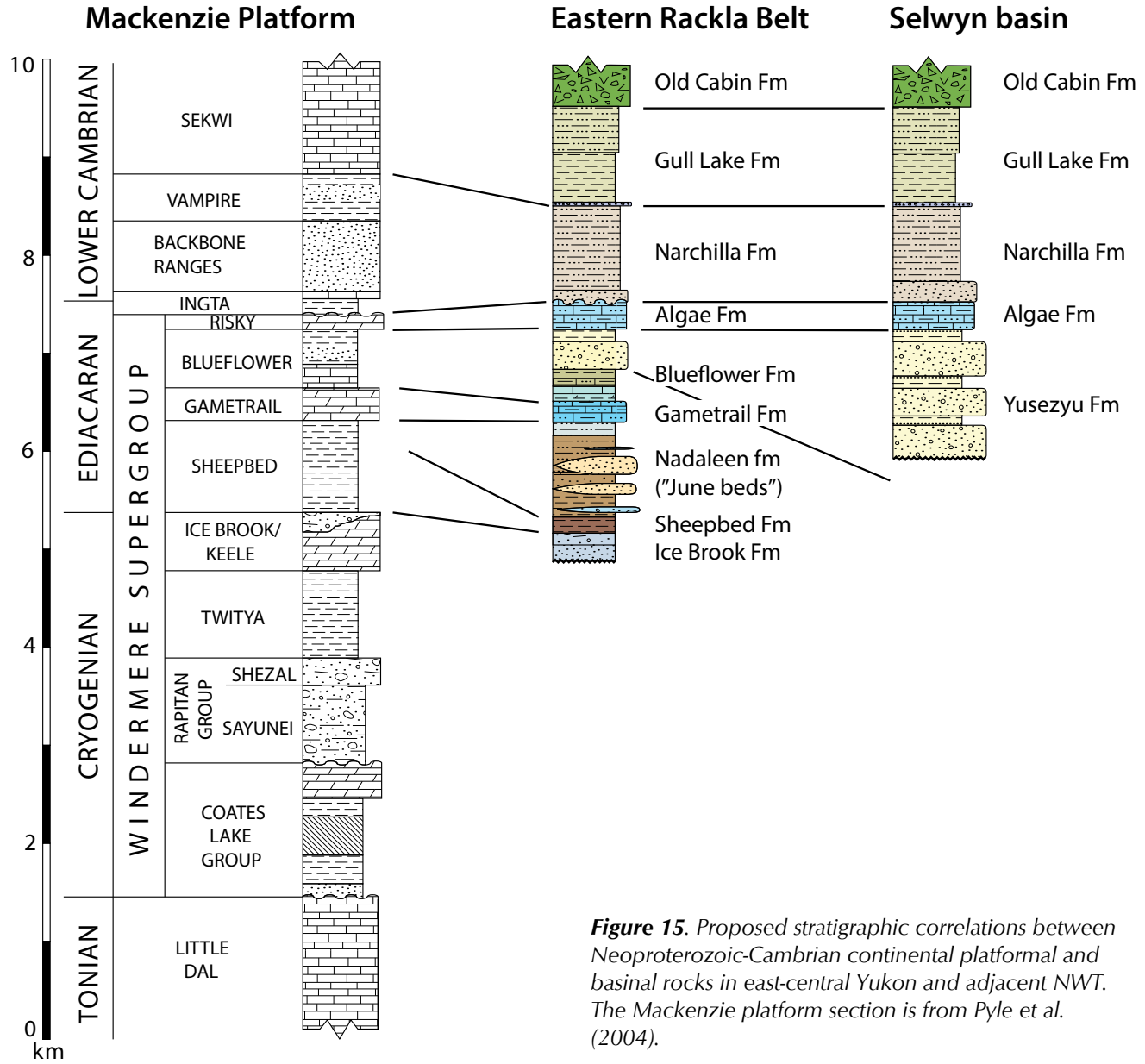

***Figure 15**. Proposed stratigraphic correlations between Neoproterozoic-Cambrian continental platformal and basinal rocks in east-central Yukon and adjacent NWT. The Mackenzie platform section is from Pyle et al. (2004).*

ACKNOWLEDGEMENTS

Thanks to Colin Paget, Ellen Hunter-Perkins, and Chad Bustin for assistance in the field, and to Justin Strauss for geological discussions. Anthill Resources Ltd. gave logistical assistance and access to helicopter support, which was provided by Horizon Helicopters. Maurice Colpron provided a critical review and suggested improvements to the manuscript.

REFERENCES

Abbott, G., 1990a. Geological map of Mt. Westman map area (106D/01). Yukon Geological Survey, Open File 1990-1, 1:50000.

Abbott, G., 1990b. Preliminary results of the stratigraphy and structure of the Mt. Westman map area, central Yukon. *In:* Current Research, Part E, Geological Survey of Canada, Paper 90-1E, p. 15-22.

Abbott, G., 1997. Geology of the upper Hart River area, eastern Ogilvie Mountains, Yukon Territory (116A/10, 116A/11). Yukon Geological Survey, Bulletin 9, 92 p.

Abbott, G., 2013. Bedrock Geology of the MacMillan Pass Area. Yukon Geological Survey, Geoscience Map 2013-1.

Aitken, J.D., 1989. Uppermost Proterozoic formations in central Mackenzie Mountains, Northwest Territories. Geological Survey of Canada Bulletin 368, 26 pages.

Arehart, G.B., Ressel, M., Carne, R., and Muntean, J., 2013. A comparison of Carlin-type deposits in Nevada and Yukon. *In*: Society of Economic Geologists special publication 17, M. Colpron, T. Bissig, B.G. Rusk, and J.F.H. Thompson (eds.), p. 389-401.

Babcock, L.E. and Peng, S., 2007. Cambrian chronostratigraphy: current state and future plans. Palaeogeography, Palaeoclimotology, Palaeoecology, vol. 254, p. 62-66.

Blusson, S.L., 1974. Five geological maps of northern Selwyn Basin (Operation Stewart), Yukon Territory and District of Mackenzie, N.W.T. Geological Survey of Canada, Open File 205, 1:250000.

Cecile, M.P., 1998. Geology and structure cross-section, Einarson Creek, Yukon territory. Geological Survey of Canada, Map 1944A, 1:50000.

Cecile, M.P., 2000. Geology of the northeastern Niddery Lake map area, east-central Yukon and adjacent Northwest Territories. Geological Survey of Canada, Bulletin 553, 120 p.

Chakungal, J. and Bennett, V., 2011. New bedrock geology of Mount Mervyn map sheet (106C/04) and mineral potential for the South Wernecke mapping project. *In:* Yukon Exploration and Geology 2010, K.E. MacFarlane, L.H. Weston, and C. Relf (eds.), Yukon Geological Survey, p. 55-87.

Colpron, M., 2012a. Preliminary geological map of the Mount Ferrell area (106C/3), central Yukon. Yukon Geological Survey, Open File 2012-11, 1:50000.

Colpron, M., 2012b. Preliminary observations on the geology of the Rackla belt, Mount Ferrell map area (NTS 106C/3), central Yukon. *In:* Yukon Exploration and Geology 2011, K.E. MacFarlane, M.G. Nordling, and P.J. Sack (eds.), Yukon Geological Survey, p. 27-43.

Colpron, M., Moynihan, D., Israel, S., and Abbott, G., 2013. Geological map of the Rackla belt, east-central Yukon (NTS 106C/1-4, 106D/1). Yukon Geological Survey, Open File 2013-13, 1:50000 scale, 5 maps and legend.

Gabrielse, H., Blusson, S.L., and Roddick, J.A., 1973. Geology of Flat River, Glacier Lake and Wrigley map areas, District of Mckenzie and Yukon Territory. Geological Survey of Canada Memoir 366.

Goodfellow, W.D., Cecile, M.P. and Leybourne, M.I., 1995. Geochemistry, petrogenesis, and tectonic setting of lower Paleozoic alkalic and potassic volcanic rocks, Northern Canadian Cordilleran Miogeocline. Canadian Journal of Earth Sciences, vol. 32, p.1236-1254.

Gordey, S.P. and Anderson, R.G., 1993. Evolution of the northern Cordilleran miogeocline, Nahanni map area (105I), Yukon and Northwest Territories. Geological Survey of Canada, Memoir 428, 214 p.

Green, L.H., 1972. Geology of Nash Creek, Larsen Creek, and Dawson map-areas, Yukon Territory. Geological Survey of Canada, Memoir 364, 157 p.

Herbosch, A. and Verniers, J., 2011. What is the biostratigraphic value of the ichnofossil *Oldhamia* for the Cambrian: a review. Geologica Belgica, vol. 14, p. 229-248.

MacNaughton, R.B., Narbonne, G.M. and Dalrymple, R.W., 2000. Neoproterozoic slope deposits, Mackenzie Mountains, northwestern Canada: implications for passive-margin development and Ediacaran faunal ecology. Canadian Journal of Earth Sciences, vol. 37, p. 997-2000.

Macdonald, F.A., Strauss, J.V., Sperling, E.A., Halverson, G.P., Narbonne, G.M., Johnston, D.T., Kunzmann, M., Schrag, D., and Higgins, J.A., 2013. The stratigraphic relationship between the Shuram carbon isotpe excursion, the oxygenation of Neoproterozoic oceans, and the first appearance of the Ediacaran biota and bilaterian trace fossils in northwestern Canada. Chemical Geology, vol. 362, p. 250-272.

Merino, E. and Banerjee, A., 2008. Terra Rosa genesis, implications for karst, and Eolian dust: a geodynamic thread. Journal of Geology, vol. 116, p. 62-75.

Moynihan, D., 2014. Preliminary geological map of NTS 106B/04, central Yukon. Yukon Geological Survey, Open File 2014-1, 1:50 000.

Narbonne, G.M. and Aitken, J.D., 1995. Neoproterozoic of the Mackenzie Mountains, northwestern Canada. Precambrian research, vol. 73, 101-121.

Pyle, L.J., Narbonne, G.M., James, N.P., Dalrymple, R.W., and Kaufman, A.J., 2004. Integrated Ediacaran chronostratigraphy, Werneck Mountains, northwestern Canada. Precambrian Research, vol. 132, p. 1-27.

Roots, C.F., 2003. Bedrock geology of Lansing Range map area (NTS 105N), central Yukon. Yukon Geological Survey, Geoscience Map 2003-1, 1:250 000; also Geological Survey of Canada, Open File 1616.

Shearer, J.T., 1976. Geological and geochemical report on the Tom and Mom claims, North Stewart River area, Mayo mining division. Assessment report # 090080.

Tucker, M.J., Hart, C.J.R., and Carne, R.C., 2013. Geology, alteration, and mineralization of the Carlin-type Conrad zone, Yukon. *In:* Yukon Exploration and Geology 2012, K.E. MacFarlane, M.G. Nordling, and P.J. Sack (eds.), Yukon Geological Survey, p. 163-178.

Geochemistry and U-Pb zircon geochronology of mid-Cretaceous Tay River suite intrusions in southeast Yukon

Lee C. Pigage[1]
Yukon Geological Survey

Jim L. Crowley
Department of Geosciences, Boise State University

Charlie F. Roots
Geological Survey of Canada

J. Grant Abbott
Yukon Geological Survey

Pigage, L.C., Crowley, J.L., Roots, C.F., and Abbott, J.G., 2014. Geochemistry and U-Pb zircon geochronology of mid-Cretaceous Tay River suite intrusions in southeast Yukon. *In:* Yukon Exploration and Geology 2014, K.E. MacFarlane, M.G. Nordling, and P.J. Sack (eds.), Yukon Geological Survey, p. 169-194.

ABSTRACT

Reconnaissance geological mapping in the Coal River map area of southeastern Yukon investigated several small mid-Cretaceous plutons. The intrusions are composed of unfoliated or incipiently foliated, fine to coarse-grained, equigranular and porphyritic, biotite ± hornblende quartz monzodiorite to granodiorite. They are metaluminous to peraluminous and have reduced to oxidized geochemical characteristics. The composition of selected samples is consistent with magma formation from partial melting of infracrustal source rocks.

U-Pb ages were obtained for nine plutons from five or six zircon single-grain analyses by the isotope dilution thermal ionization mass spectrometry method with chemical abrasion (CA-TIMS). All interpreted ages are concordant within statistical uncertainty. The plutons range in age from 99.80 ± 0.03 to 97.70 ± 0.03 Ma. Given the primarily unfoliated nature of the plutons, contractional, fabric-forming deformation within the Cordilleran orogeny must therefore have largely ceased at the present level of exposure in the Coal River area by the time of intrusion (*ca.* 98 Ma).

The ages and compositions of the plutons in Coal River map area are consistent with their being part of the Tay River plutonic suite, a northwest-trending belt of coeval and compositionally similar plutons and local volcanic rocks (South Fork volcanic suite) that, when augmented by the addition of the Coal River plutons, extends approximately 465 km with a width of up to 150 km.

[1] *lee.pigage@gov.yk.ca*

INTRODUCTION

Several metallogenic belts of mid to late-Cretaceous intrusions extend from central Alaska across to southeast Yukon. Informally termed the Tintina gold belt (Smith, 2000), these intrusive belts have been a major impetus for recent exploration in Alaska and Yukon. Intrusions in the Coal River map area (NTS 95D) of southeastern Yukon (Fig. 1) define the most southern exposures of these mid to Late Cretaceous felsic plutons (Northern Cordilleran mid-Cretaceous plutonic province of Hart *et al.*, 2004) northeast of the Tintina fault in Yukon. The intrusions have been classified primarily in terms of age and composition (Pigage and Anderson, 1985; Gordey and Anderson, 1993; Mortensen *et al.*, 1995; 2000; Hart *et al.*, 2004; Heffernan, 2004; Rasmussen *et al.*, 2007; Rasmussen, 2013); these attempts have produced a complex and partially conflicting terminology that includes the Selwyn, Tombstone, Mayo, Tungsten, Tay River, transitional Tungsten-Tay River, Anvil, and Hyland suites.

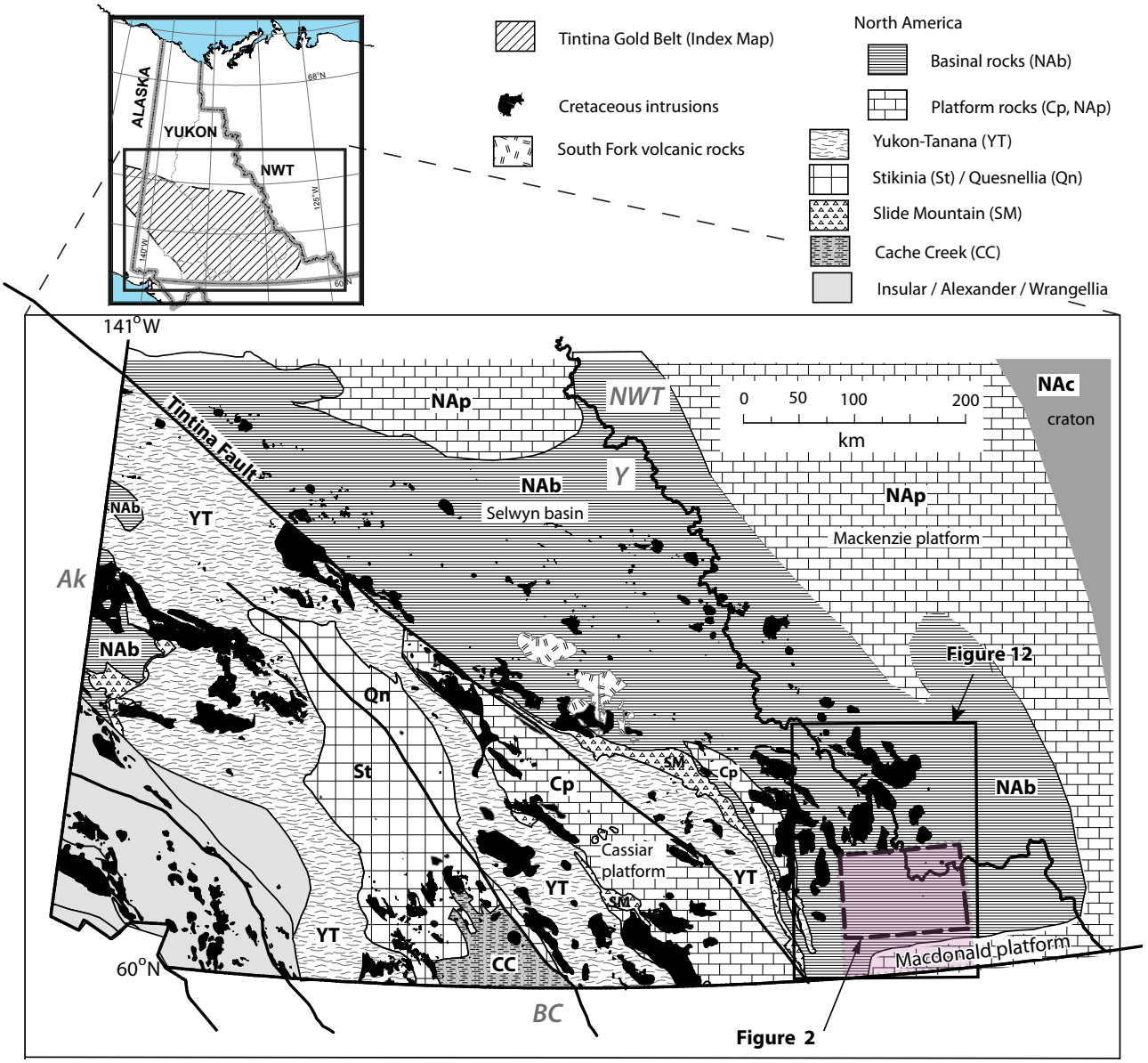

Figure 1. *Cretaceous plutonic rocks in south and central Yukon. The extent of the informal Tintina gold belt (hachured in inset map) is modified from Smith (2000). Distribution of terranes is from Colpron and Nelson (2011) and intrusions from Gordey and Makepeace (2003). Locations of figures 2 (Coal River map area shaded in pink) and 12 are indicated. Abbreviations are: Y=Yukon; NWT=Northwest Territories; BC=British Columbia.*

Bedrock geological mapping (1:250 000 scale) in 2009 and 2010 in the Coal River map area identified several small, previously unrecognized granitoid intrusions. In this paper we document the compositions and ages of many of these intrusions and use these new data to assign them to one of the regionally defined age/composition belts.

REGIONAL GEOLOGY

Southeastern Yukon is mainly underlain by a succession of Proterozoic to upper Eocene sedimentary rocks with a combined thickness of more than 14 000 m (Gabrielse and Blusson, 1969; Long and Sweet, 1994; Pigage, 2004; 2006; 2008; 2009; Pigage *et al.*, 2011). Coal River map area, centered 150 km northeast of the town of Watson Lake, contains Proterozoic siliciclastic rocks deposited during early rifting of the supercontinent Rodinia, lower Paleozoic carbonate strata of the Macdonald platform and marine shales of Selwyn basin, constituting the west-facing, passive continental miogeocline of Laurentia (Cecile *et al.*, 1997). Upper Paleozoic and lower Mesozoic siliciclastic and carbonate rocks were deposited in a shallow marine basin. Significant depositional hiatuses or subsequent erosion occurred in southeast Yukon during this time interval. Upper Eocene to Oligocene sedimentary rocks occur in a north-trending, extensional, half-graben (Pigage, 2008).

The age of contractional deformation and metamorphism is poorly constrained between early Triassic and late Eocene (Pigage, 2008; 2009), broadly correlative with the Cordilleran orogeny (Nelson and Colpron, 2007). It is manifested as northwest to northeast-trending, east-verging, asymmetric folds and reverse faults (Fig. 2). Metamorphic grade ranges from muscovite-chlorite to biotite-staurolite-garnet zones; with metamorphic grade generally decreasing from west to east. Extensional faults offset the late Eocene-Oligocene sediments, suggesting that at least some movement on normal faults is post-Oligocene.

Cretaceous and younger granitoid plutons intrude both the basinal marine siliciclastic rocks and the platformal carbonate rocks of southeast Yukon.

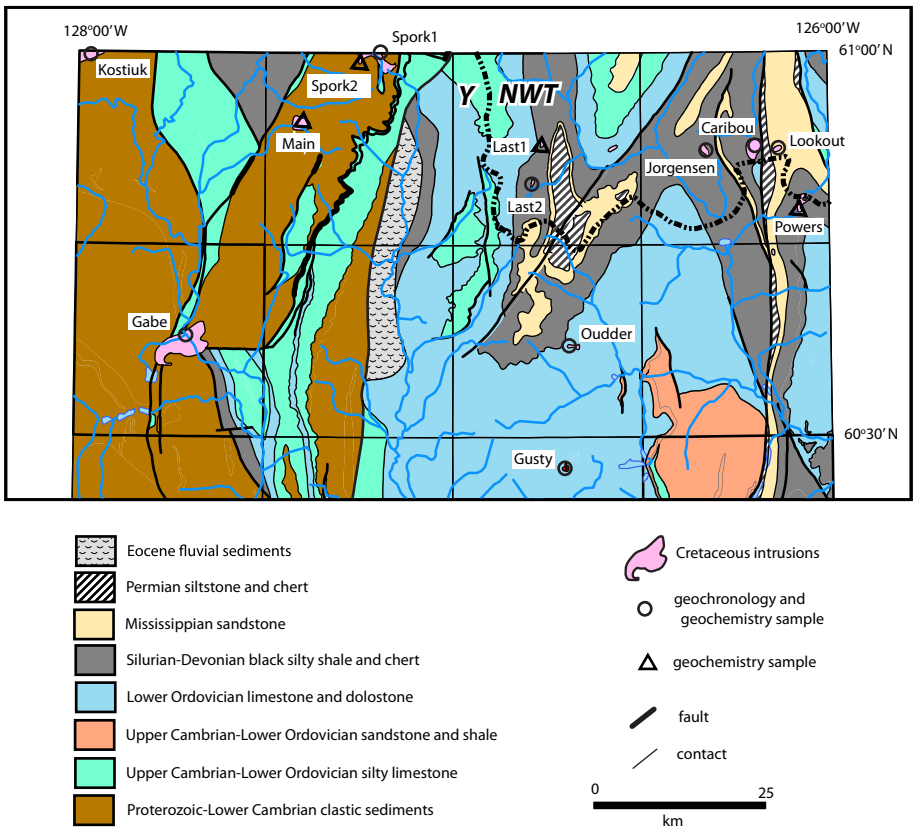

Figure 2. *Locations of samples (coordinates in Table 1) with respect to bedrock geology of northern Coal River map area, modified from Pigage et al. (2011).*

PREVIOUS WORK

Gabrielse and Blusson (1969) completed the first systematic regional mapping program in the Coal River area (based on fieldwork completed in 1967). Subsequent mapping occurred mainly in map areas farther north (e.g., Gabrielse *et al.*, 1973). Pigage and Anderson (1985) and Gordey and Anderson (1993) provided an early framework for defining igneous suites in Selwyn basin and Mackenzie platform of central Yukon. All intrusions were considered to be part of the Selwyn Plutonic Suite (Gordey and Anderson, 1993) or Anvil plutonic suite (Pigage and Anderson, 1985). Mortensen *et al.* (2000) described distinct plutonic suites in central and western Yukon, differentiating them according to spatial distribution, age, lithology, mineralogy and metallogeny. Hart *et al.* (2004) identified 25 Early and mid-Cretaceous plutonic suites and belts extending across Alaska and

Yukon; intrusions in southeast Yukon were assigned to the Anvil-Hyland-Cassiar belt. Regional studies by Heffernan (2004), Rasmussen *et al.* (2007), and Rasmussen (2013) included previously-mapped intrusions in the northeastern corner of the Coal River map area and completed petrological, geochemical, and geochronological analyses. They correlated southeastern Yukon intrusions with several plutonic suites identified in central Yukon, including Tay River, Tombstone, Mayo, and Tungsten suites.

PLUTONIC ROCKS IN COAL RIVER MAP AREA

Field work to update the earlier reconnaissance geology was completed in 2009 and 2010 (Pigage *et al.*, 2011). Several plutons intruding Neoproterozoic through Mississippian carbonate and siliciclastic strata in northern Coal River map area were investigated. All are poorly to moderately exposed and inferred from the extents of their positive aeromagnetic response to be subcircular, ranging from 0.3 to 8.4 km in diameter (Fig. 3).

The exposed plutonic rocks are grey-weathering and unfoliated to slightly foliated. They range in grain size and texture from fine to coarse-grained and equigranular to (dominantly) porphyritic. Biotite ± hornblende are the predominant primary mafic minerals. Coarse-grained, equigranular variants locally have anhedral to subhedral K-feldspar grains. Porphyritic variants are unfoliated and typically crowded with equant plagioclase phenocrysts up to 5 mm across in a fine-grained, grey matrix. Hornblende, biotite, and minor quartz also occur as phenocrysts in the porphyritic phases. Some of the intrusions are compositionally variable, but internal contacts were not mapped because visits were reconnaissance only. Composite intrusive bodies north of the Coal River map area have been identified (Gordey and Anderson, 1993; Pigage and Anderson; 1985). The appendix provides brief descriptions of the mineralogy and fabric of granitoid samples selected for geochemical analysis and geochronology.

Many of the intrusions are weakly to strongly altered, with chlorite replacing hornblende and biotite and very fine sericite replacing feldspar. Epidote and calcite are locally abundant within the matrix.

The Main pluton is unique in containing primary muscovite. It is a medium-grained, equigranular, foliated, medium gray, plagioclase-quartz-muscovite-tourmaline-garnet granitoid rock.

Details of their full extent, contact relationships and metamorphic effects such as hornfelsing, skarn formation, or alteration remain obscure because the intrusions are poorly exposed.

Average magnetic susceptibility readings (MS) for the various plutons range from 0 to 17.8 (10^{-3} SI units; Table 1). The plutons with high MS values contain fine-grained magnetite and correlate closely with large positive anomalies in the first vertical derivative of the regional aeromagnetic field (Fig. 3). Aeromagnetic anomalies associated with several plutons (*e.g.*, Jorgensen, Last2) do not overlap with the surface extent of the plutons. In this case the anomalies may represent pyrrhotite hornfels, magnetite skarns, or a magnetic portion of the pluton extending into the subsurface. The small and sub-circular aeromagnetic anomalies provide a proxy for the size and shape of the poorly exposed plutons and/

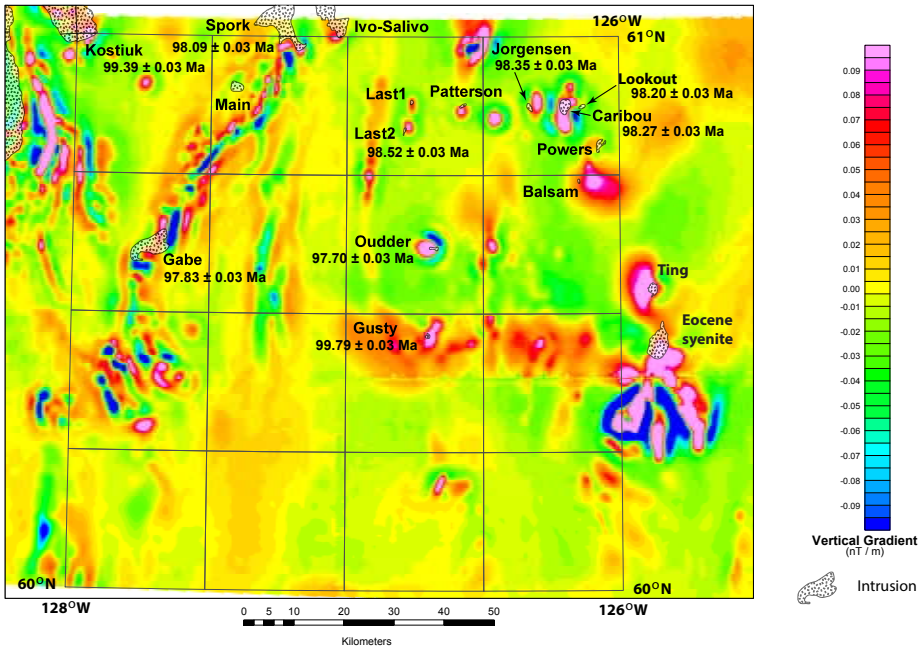

Figure 3. *First vertical derivative of regional aeromagnetic survey, intrusions in Coal River map area are labeled and described in this report. The age labels for the dated plutons have an analytical error of 2 sigma, as described in the text.*

Table 1. *Rock type, texture, magnetic susceptibility, location, and geochemistry of plutons in Coal River map area (NTS 95D). All coordinates NAD83 UTM, Zone 09N.*

Igneous Body		**Powers**	**Jorgensen**	**Last 2**	**Gabe**	**Kostiuk**	**Oudder**	**Lookout**	**Caribou**	**Last 1**	**Spork 1**	**Spork 2**	**Main**	**Gusty**
Sample #		09RAS137	09RAS136	09LP098	09LP048	09RAS062	09TOA135	09TOA179	09TOA180	09TOA185	10TOA014	10TOA016	10TOA019	Gusty Lake
UTM E		658,872	645,250	620,192	570,761	555,895	625,672	655,673	652,311	621,360	597,672	594,775	586,791	626,261
UTM N		6,743,596	6,751,550	6,745,800	6,722,414	6,762,820	6,723,074	6,752,196	6,752,434	6,751,642	6,764,282	6,762,834	6,754,152	6,704,777
Rock (Fig. 3)		quartz Monzodiorite	quartz monzodiorite	granodiorite	granodiorite	granodiorite	granodiorite	granodiorite	granodiorite	granodiorite	granodiorite	quartz diorite	granite	tonalite
Texture		porphyritic	porphyritic	porphyritic	equigranular	porphyritic	equigranular	porphyritic	porphyritic	porphyritic	equigranular	equigranular	equigranular	porphyritic
Age Date (this paper)		no	yes	yes	yes	yes	yes	yes	yes	no	yes	no	no	yes
M.S.*		0.4	0.2	14.2	1.0	12.1	14.0	0.2	17.8	11.8	5.1	3.3	0.0	0.4
	Anal. Method													
SiO_2 (%)	Fus-ICP	62.65	59.98	61.87	65.83	66.47	65.73	63.28	61.33	65.48	68.22	50.78	74.37	63.87
Al_2O_3 (%)	Fus-ICP	16.90	15.99	16.83	15.86	15.95	15.88	16.09	16.53	16.20	14.97	16.90	14.44	16.53
FeO (%)	Titration	3.65	3.93	3.01	2.69	3.65	2.65	3.44	2.22	2.80	2.49	8.09	0.23	3.00
Fe_2O_3 (%)	calculated	1.36	1.49	1.76	0.47	0.10	1.41	0.70	2.65	0.96	0.66	2.07	1.04	1.11
$Fe_2O_3^t$ (%)	Fus-ICP	5.42	5.86	5.11	3.46	4.16	4.36	4.52	5.12	4.07	3.43	11.06	1.30	4.44
MnO (%)	Fus-ICP	0.086	0.079	0.097	0.075	0.044	0.066	0.086	0.098	0.080	0.067	0.160	0.100	0.054
MgO (%)	Fus-ICP	2.25	2.89	1.92	1.30	1.36	1.68	2.22	2.35	1.77	1.21	3.76	0.07	2.00
CaO (%)	Fus-ICP	3.53	4.55	4.04	3.38	3.50	3.78	3.44	4.49	4.10	3.02	7.63	0.72	5.71
Na_2O (%)	Fus-ICP	4.01	3.77	3.47	2.94	3.36	3.05	3.90	3.46	3.71	3.05	2.89	4.11	2.81
K_2O (%)	Fus-ICP	2.34	2.33	2.29	3.84	3.23	3.91	2.25	2.52	2.50	3.77	1.60	3.79	2.56
TiO_2 (%)	Fus-ICP	0.600	0.840	0.544	0.373	0.537	0.452	0.525	0.553	0.440	0.448	2.526	0.022	0.514
P_2O_5 (%)	Fus-ICP	0.14	0.16	0.15	0.16	0.20	0.29	0.14	0.14	0.13	0.13	0.38	0.07	0.15
L.O.I. (%)	Fus-ICP	2.54	2.53	2.26	0.87	0.83	0.59	4.13	2.62	1.80	1.30	0.98	0.44	1.30
Total		100.06	98.54	98.24	97.79	99.23	99.49	100.20	98.96	99.97	99.34	97.77	99.40	99.61
Au (ppb)	INAA	< 2	< 2	< 2	< 2	< 2	< 2	< 2	< 2	2				
As (ppm)	INAA	< 0.5	< 0.5	1.6	< 0.5	< 0.5	< 0.5	1.3	1.8	< 0.5				
Br (ppm)	INAA	< 0.5	< 0.5	< 0.5	< 0.5	1.6	< 0.5	1.3	< 0.5	< 0.5				
Cr (ppm)	INAA	14	83	15	< 5	9	73	22	35	12				
Ir (ppb)	INAA	< 5	< 5	< 5	< 5	< 5	< 5	< 5	< 5	< 5				
Sc (ppm)	INAA	9.4	12.4	8.6	6.1	7.2	9.3	9.4	10.9	8.0				
Se (ppm)	INAA	< 3	< 3	< 3	< 3	< 3	< 3	< 3	< 3	< 3				
Sb (ppm)	INAA	0.4	< 0.2	0.4	< 0.2	< 0.2	0.2	0.4	0.4	< 0.2				
Sc (ppm)	Fus-ICP	11	13	9	7	8	10	11	12	9	8	29	3	11
Be (ppm)	Fus-ICP	2	2	2	2	2	3	2	2	2	2	1	11	2
V (ppm)	Fus-ICP	106	121	86	59	60	94	90	104	75	60	326	<5	96
Cr (ppm)	Fus-MS	< 20	80	< 20	< 20	< 20	70	< 20	30	< 20	<20	<20	<20	20
Co (ppm)	Fus-MS	9	13	8	5	4	7	8	9	6	5	25	<1	8
Ni (ppm)	Fus-MS	< 20	30	< 20	< 20	< 20	< 20	< 20	< 20	< 20	<20	30	<20	<20
Cu (ppm)	Fus-MS	< 10	10	< 10	< 10	10	< 10	< 10	< 10	< 10	<10	10	<10	50
Zn (ppm)	Fus-MS	110	70	270	40	30	< 30	50	60	40	40	100	50	40
Ga (ppm)	Fus-MS	19	19	18	16	17	17	17	18	17	17	22	21	21
Ge (ppm)	Fus-MS	1.5	1.3	1.5	1.4	1.4	1.7	1.5	1.5	1.5	1.9	2.0	5.2	1.6
As (ppm)	Fus-MS	< 5	< 5	< 5	< 5	< 5	< 5	< 5	< 5	< 5	<5	<5	<5	<5
Rb (ppm)	Fus-MS	71	76	75	135	102	131	68	83	84	136	57	310	71
Sr (ppm)	Fus-ICP	724	622	509	450	344	1064	572	564	502	310	393	17	451
Y (ppm)	Fus-MS	16.9	15.2	18.4	15.3	18.2	22.2	15.3	16.6	16.2	19.1	29.8	20.3	17.5
Zr (ppm)	Fus-MS	160	156	155	167	219	202	147	131	148	160	187	42	141
Nb (ppm)	Fus-MS	16.8	23.0	16.1	16.3	17.7	35.4	15.1	13.0	13.2	16.6	22.8	47.5	10.2
Mo (ppm)	Fus-MS	< 2	< 2	< 2	< 2	< 2	< 2	< 2	< 2	< 2	<2	<2	<2	<2
Ag (ppm)	Fus-MS	< 0.5	< 0.5	< 0.5	< 0.5	0.6	0.5	< 0.5	< 0.5	< 0.5	<0.5	<0.5	<0.5	<0.5

Table 1. *contined.*

Igneous Body		Powers	Jorgensen	Last 2	Gabe	Kostiuk	Oudder	Lookout	Caribou	Last 1	Spork 1	Spork 2	Main	Gusty
Sample #		09RAS137	09RAS136	09LP098	09LP048	09RAS062	09TOA135	09TOA179	09TOA180	09TOA185	10TOA014	10TOA016	10TOA019	Gusty Lake
UTM E		658,872	645,250	620,192	570,761	555,895	625,672	655,673	652,311	621,360	597,672	594,775	586,791	626,261
UTM N		6,743,596	6,751,550	6,745,800	6,722,414	6,762,820	6,723,074	6,752,196	6,752,434	6,751,642	6,764,282	6,762,834	6,754,152	6,704,777
Rock (Fig. 3)		quartz monzodiorite	quartz monzodiorite	granodiorite	granodiorite	granodiorite	granodiorite	granodiorite	granodiorite	granodiorite	granodiorite	quartz diorite	granite	tonalite
Texture		porphyritic	porphyritic	porphyritic	equigranular	porphyritic	equigranular	porphyritic	porphyritic	porphyritic	equigranular	equigranular	equigranular	porphyritic
Age Date (this paper)		no	yes	yes	yes	yes	yes	yes	yes	no	yes	no	no	yes
M.S.*		0.4	0.2	14.2	1.0	12.1	14.0	0.2	17.8	11.8	5.1	3.3	0.0	0.4
	Anal. Method													
In (ppm)	Fus-MS	< 0.1	< 0.1	< 0.1	< 0.1	< 0.1	< 0.1	< 0.1	< 0.1	< 0.1	<0.1	<0.1	<0.1	<0.1
Sn (ppm)	Fus-MS	1	1	2	2	3	2	1	1	2	3	3	7	1
Sb (ppm)	Fus-MS	< 0.2	< 0.2	0.4	< 0.2	< 0.2	< 0.2	< 0.2	< 0.2	< 0.2	<0.2	<0.2	<0.2	<0.2
Cs (ppm)	Fus-MS	2.1	2.7	1.1	3.9	1.2	1.8	1.6	3.6	2.3	2.9	2.2	13.6	2.2
Ba (ppm)	Fus-ICP	892	1077	1093	1303	1164	2050	1530	779	750	766	514	8	623
La (ppm)	Fus-MS	28.7	36.0	33.3	60.8	49.1	81.0	31.1	32.8	32.9	42.7	31.0	6.4	25.4
Ce (ppm)	Fus-MS	55.6	64.7	65.6	109.0	91.1	144.0	58.8	66.3	64.1	77.9	62.7	12.1	49.2
Pr (ppm)	Fus-MS	5.96	7.30	7.08	10.60	9.15	13.90	6.08	7.14	6.82	8.29	7.38	1.29	5.39
Nd (ppm)	Fus-MS	22.1	27.2	25.9	35.8	31.4	47.4	21.9	26.7	24.5	28.6	29.8	4.3	20.5
Sm (ppm)	Fus-MS	4.30	4.30	4.82	5.60	5.19	7.49	3.96	4.88	4.44	5.00	6.28	1.49	3.95
Eu (ppm)	Fus-MS	0.929	1.230	0.954	0.913	0.973	1.280	0.715	1.080	0.928	0.969	1.670	0.078	1.060
Gd (ppm)	Fus-MS	3.64	3.72	3.88	3.99	3.93	5.44	3.26	3.78	3.57	3.53	6.04	1.64	3.56
Tb (ppm)	Fus-MS	0.52	0.55	0.58	0.53	0.57	0.76	0.48	0.56	0.52	0.57	0.98	0.46	0.57
Dy (ppm)	Fus-MS	2.98	3.09	3.36	2.81	3.20	4.06	2.74	3.07	2.92	3.16	5.53	3.14	3.08
Ho (ppm)	Fus-MS	0.58	0.58	0.65	0.53	0.62	0.77	0.54	0.60	0.57	0.63	1.08	0.60	0.63
Er (ppm)	Fus-MS	1.68	1.69	1.90	1.56	1.87	2.26	1.57	1.73	1.65	1.82	3.06	1.89	1.79
Tm (ppm)	Fus-MS	0.253	0.252	0.289	0.232	0.284	0.330	0.241	0.259	0.252	0.276	0.458	0.381	0.283
Yb (ppm)	Fus-MS	1.68	1.62	1.95	1.52	1.95	2.21	1.58	1.69	1.72	1.94	2.94	3.25	1.95
Lu (ppm)	Fus-MS	0.273	0.259	0.312	0.240	0.322	0.349	0.246	0.259	0.267	0.31	0.46	0.63	0.32
Hf (ppm)	Fus-MS	3.6	3.5	3.7	3.7	4.7	4.4	3.5	3.1	3.6	3.9	3.9	2.1	3.4
Ta (ppm)	Fus-MS	1.46	1.14	1.36	1.43	1.66	2.72	1.50	1.41	1.32	1.62	1.88	11.40	0.82
W (ppm)	Fus-MS	< 0.5	< 0.5	2.7	< 0.5	< 0.5	< 0.5	< 0.5	< 0.5	< 0.5	1.3	0.5	0.9	0.9
Tl (ppm)	Fus-MS	0.27	0.27	0.29	0.61	0.44	0.39	0.31	0.29	0.33	0.66	0.27	1.71	0.48
Pb (ppm)	Fus-MS	212	9	29	19	10	14	15	19	13	19	11	33	7
Bi (ppm)	Fus-MS	< 0.1	< 0.1	< 0.1	< 0.1	< 0.1	< 0.1	< 0.1	< 0.1	< 0.1	<0.1	<0.1	2.3	0.3
Th (ppm)	Fus-MS	9.0	9.2	10.1	23.9	16.8	25.4	11.6	12.3	11.2	19.6	6.6	3.7	8.1
U (ppm)	Fus-MS	2.76	2.51	2.70	5.25	2.82	4.64	2.59	2.72	2.71	4.18	1.80	1.36	2.43

whole rock analyses completed at Activation Laboratories Ltd., Ancaster, Ontario in 2009 and 2010

FeO determined by titration

M.S. = magnetic susceptibility (10^{-3} S.I. units)

or hornfelsed sediments adjacent to the intrusions. Steep intrusive contacts are suggested by the rapid lateral change in magnetic intensity. Areas with similar positive aeromagnetic patterns in Figure 3 are inferred to mark unmapped or buried intrusions because sedimentary rocks in the map area have low magnetic susceptibilities (MS <1 x 10^{-3} SI units).

A north to northeast-trending, variable but generally positive aeromagnetic anomaly in the western part of the map area (Fig. 3) incorporates the Gabe, Main and Spork plutons. This linear trend is generally coincident with a topographic ridge exposing Neoproterozoic pelites with biotite ± garnet ± staurolite metamorphic assemblages, in contrast to the regional chlorite-muscovite metamorphic grade. Samples from the Gabe and Main intrusions (see Table 1), higher grade metamorphic rocks, and lower grade sedimentary rocks all have weak magnetic susceptibility (≤1 x 10^{-3} SI units). We suggest that this magnetic anomaly trend is likely related to intrusive rocks at depth, either directly as intrusion phases containing magnetite, or indirectly as associated pyrrhotite-bearing hornfels.

Another linear positive magnetic anomaly extends easterly from the Gusty pluton (Fig. 3) to beyond the eastern boundary of the map area where it terminates with a magnetite-bearing, Eocene biotite syenite (described by Pigage, 2009). Scant rock exposure along this aeromagnetic trend are siliciclastic and carbonate rock with little to no magnetic expression. Beneath these strata may be a linear array of unexposed granitoid plutons and associated hornfels. A similar east-trending "string" of magnetic plutons is exposed between the Last1/Last2 and Lookout/Powers plutons.

GEOCHEMISTRY

Thirteen whole rock compositions were determined for 12 plutons within the Coal River map area (Fig 2). Samples are predominantly granodiorite with minor granite, quartz monzodiorite and quartz diorite, based on the proportions of normative minerals (Table 1; Fig. 4a). The common porphyritic texture with a fine-grained, locally extensively altered matrix precludes systematic use of modal compositions (Streckeisen, 1976) to classify many of the intrusions. Samples were examined in thin section; offcuts from the thin sections were etched with HF and stained with sodium cobaltinitrite to estimate the occurrence of K-feldspar (see rock sample descriptions in the Appendix). Rock names were checked where appropriate against approximate mineral modes of stained samples from the particular pluton. Using the MALI classification scheme discussed by Frost *et al.* (2001), the plutons fall within the calc-alkalic suite (Fig. 4b).

SiO_2 (Figs. 5 and 6) for most of the intrusions varies from approximately 60 to 68%; only one sample is mafic (51%), and only the Main pluton is strongly felsic (74%). The Al_2O_3, MgO, $Fe_2O_3^T$ (total iron as Fe_2O_3), and CaO contents decrease approximately linearly with increasing SiO_2. In contrast, K_2O increases with increasing SiO_2, and Na_2O, TiO_2, and P_2O_5 do not show any systematic variation with SiO_2. Trace elements and rare earth elements (Fig. 6) are more scattered, with only V and Sc illustrating linear variation with increasing SiO_2.

Using Shand's index (Fig. 7) the intrusion samples are metaluminous to slightly peraluminous; only the Main

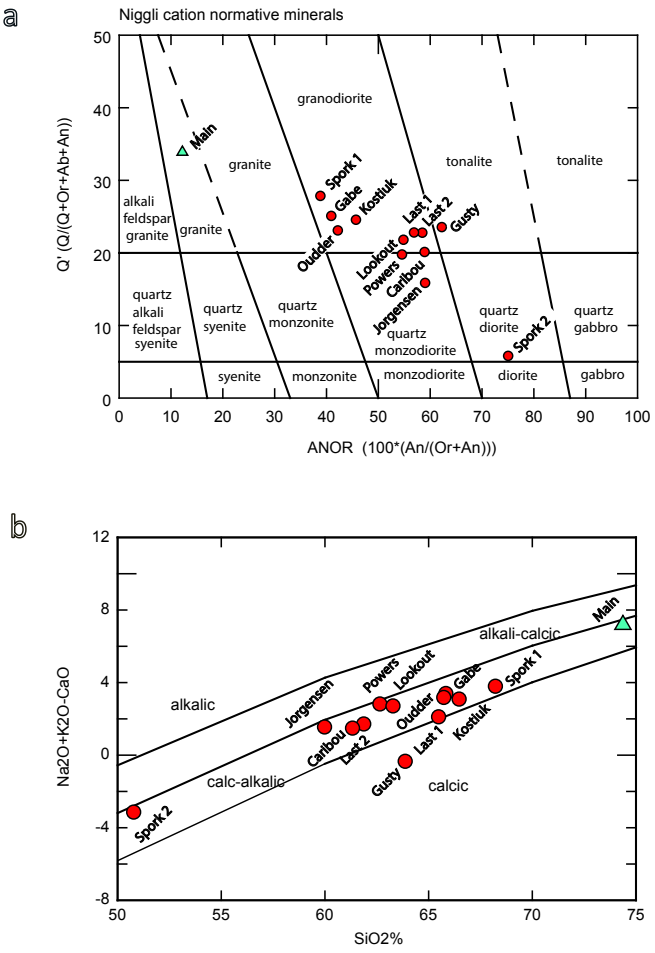

Figure 4. *(a) Compositional classification of igneous plutonic rocks (Streckeisen and Le Maitre, 1979). (b) MALI compositional plot (Frost et al., 2001). The Main intrusion is indicated with a triangle; other intrusions are indicated with circles.*

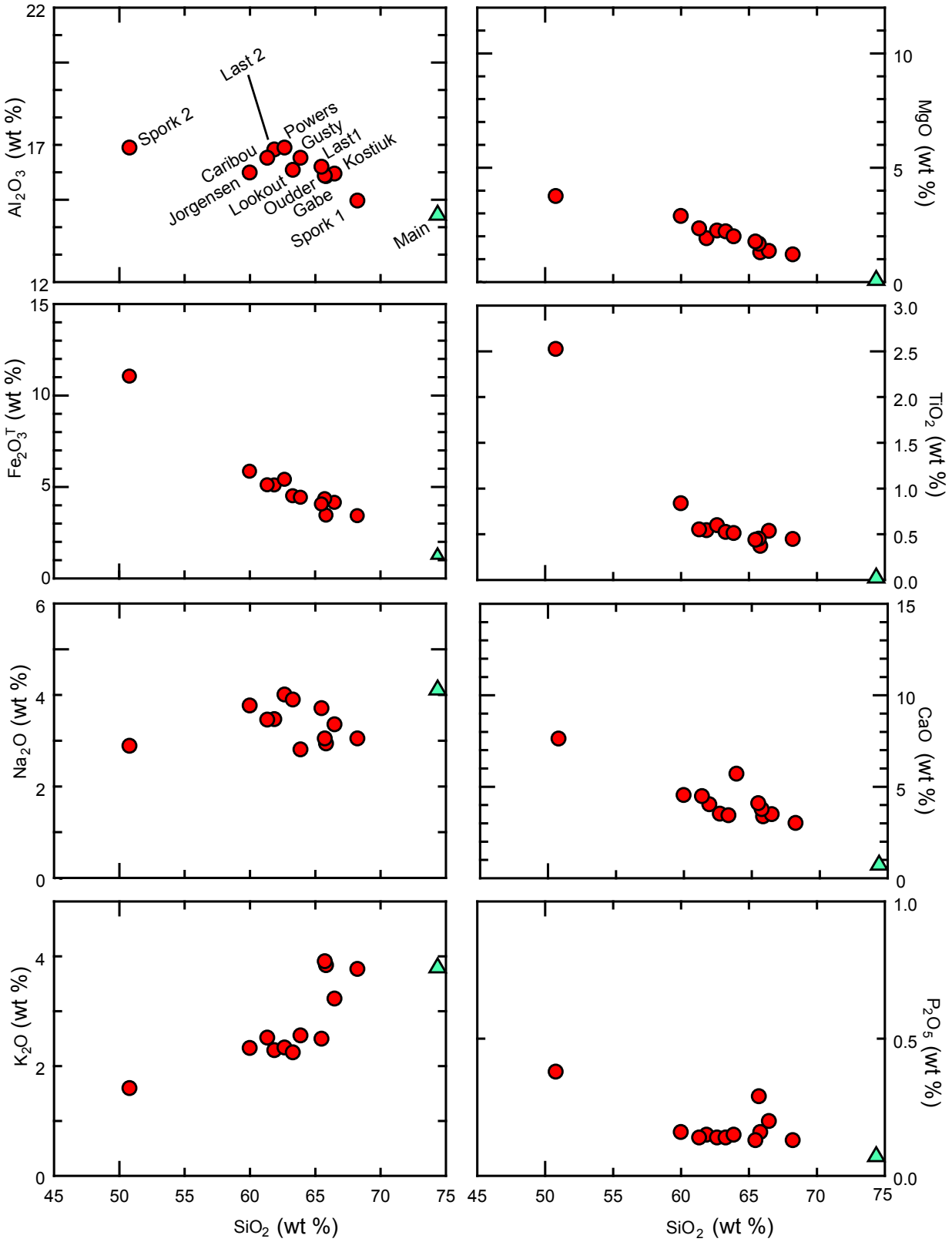

Figure 5. *Major element Harker diagrams for intrusion samples.*

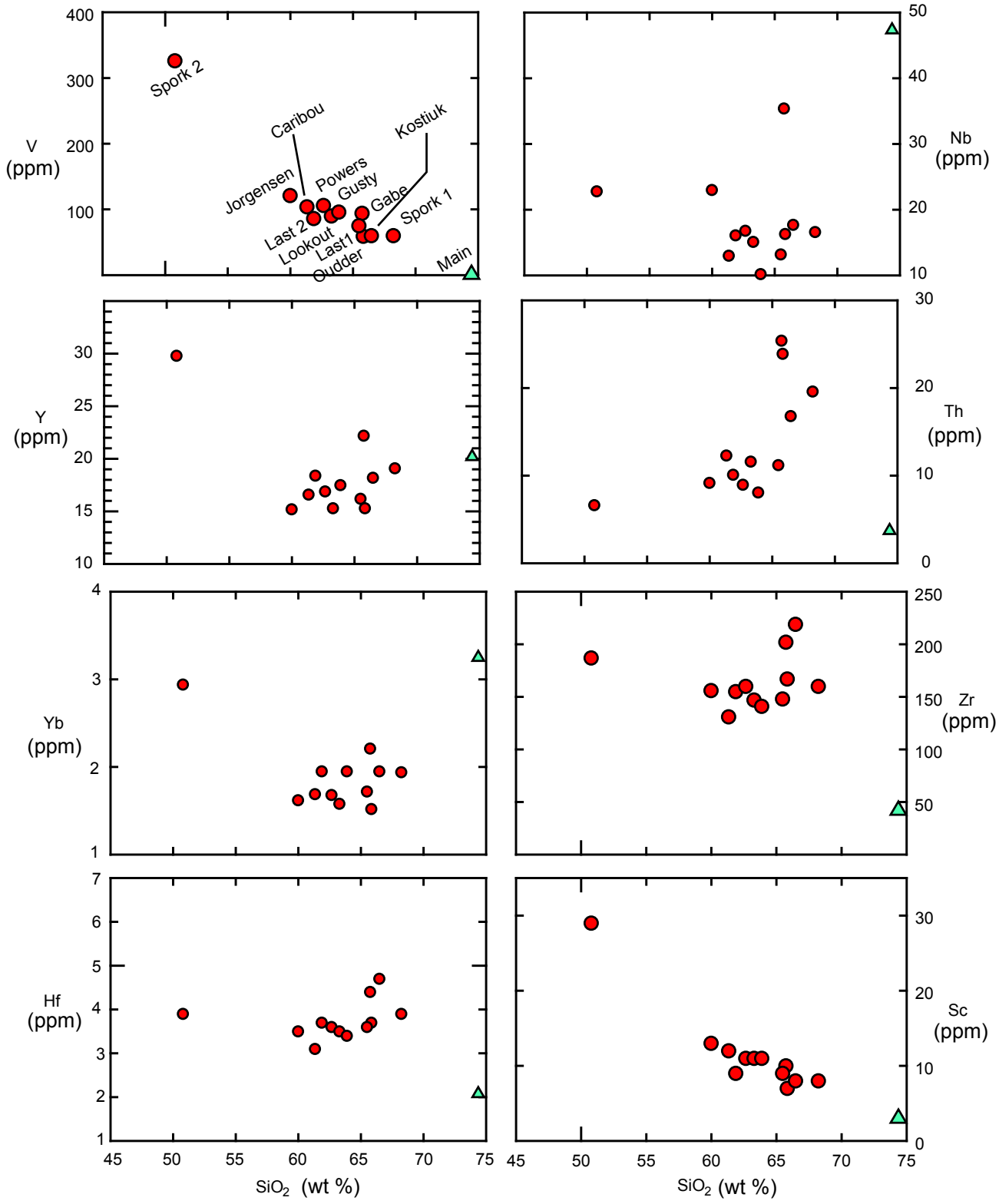

Figure 6. *Harker diagrams for selected trace elements.*

sample is clearly peraluminous. Porphyritic and magnetic samples do not display strong separation in Figure 7. The metaluminous character is fully consistent with modal occurrence of biotite and hornblende as the primary mafic minerals. Most of the samples also straddle the magnetite-ilmenite boundary (Fig. 8); only the sample of the Kostiuk pluton plots clearly within the ilmenite series domain, and Main pluton within the magnetite series domain. For the Kostiuk sample, classification in the ilmenite series is problematic given its very high measured magnetic susceptibility which implies large modal magnetite. No systematic correlation seems to exist between magnetic susceptibility and molar Al content or ferric/ferrous iron ratios. Similarly no apparent relation seems to exist between oxidation ratio in Figure 8 and porphyritic or equigranular texture.

Intrusion compositions normalized to primitive mantle are enriched in all elements except for V and Sc (Fig. 9a). Many of the samples have pronounced depletions in Nb and Ti and a slight depletion in Eu. Intrusion compositions normalized to upper continental crust have element ratios close to 1 (Fig 9b). Elements plotted along the x-axis in both figures are considered immobile under low temperature conditions (Jenner 1996), which is relevant considering the alteration noted in many of the samples. Many of these elements have high field strengths and are incompatible with typical differentiation processes; they are therefore thought to be indicative of their abundance in the source rocks. Normalized concentrations for the Main pluton in Figure 9a,b are significantly different from

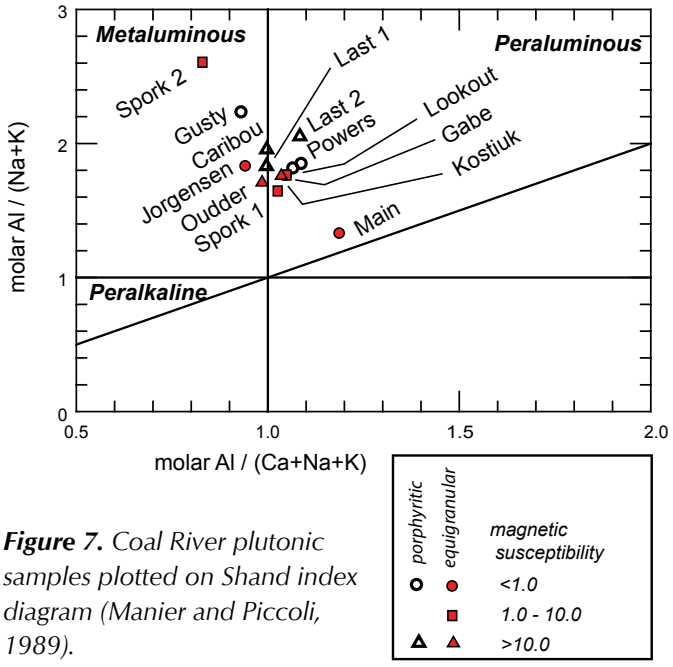

Figure 7. *Coal River plutonic samples plotted on Shand index diagram (Manier and Piccoli, 1989).*

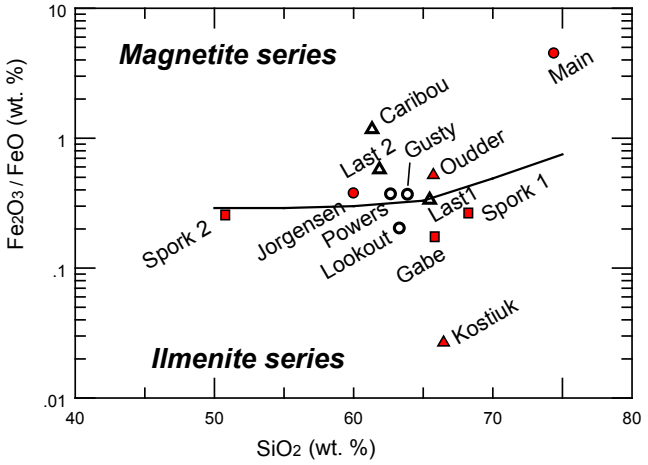

Figure 8. *Coal River plutonic samples on magnetite-ilmenite intrusive fields as illustrated in Hart et al. (2004).*

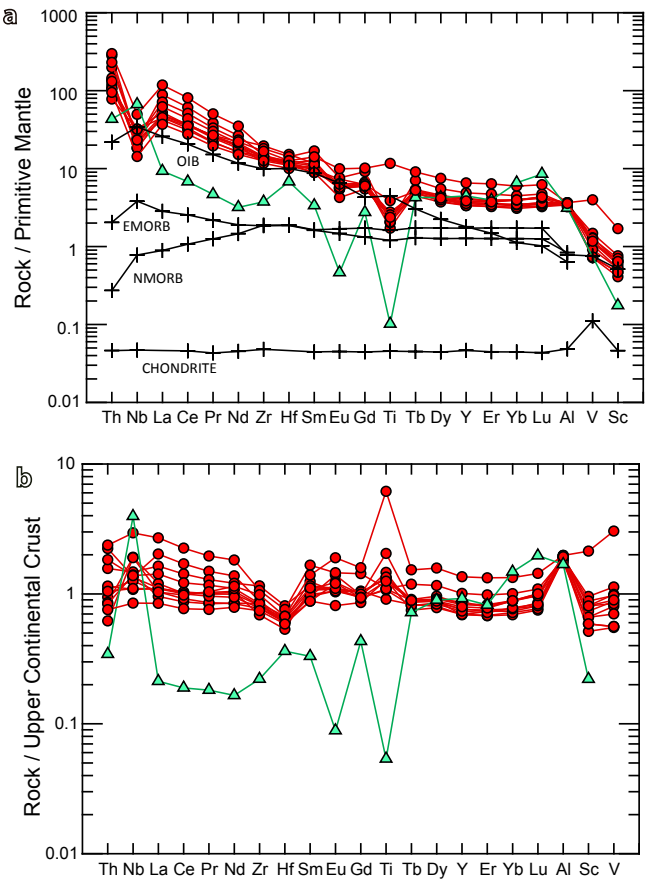

Figure 9. *Intrusion compositions normalized to: (a) primitive mantle composition (from Kerrich and Wyman, 1996); (b) upper continental crust composition (from McLennan, 2001). Triangle for sample 10TOA019 (Main intrusion); circles for all other samples.*

the other intrusions, raising the possibility that the Main pluton is not part of the same plutonic suite as the other intrusive bodies.

In tectonic discriminant diagrams (Fig. 10a,b,c; Pearce *et al.*, 1984) the intrusions are consistent with syn-collisional (S-type) and volcanic arc (I-type) granite, but the sample from the Main pluton plots in the field for within-plate granite. Most intrusions plot within the volcanic arc or I-type granite (Fig. 10c); however Rb is known to be mobile under many conditions, and the significance of this discriminant is suspect.

In summary, all of the intrusions except for the Main pluton form a chemically coherent plutonic suite. The plutons are generally weakly altered, but immobile elements can be used to determine their chemical affinity. They range from metaluminous to slightly peraluminous, oxidizing to reducing, and plot predominantly within the tectonic discriminant field of volcanic arc-related (or I-type) granites. This chemistry supports the presence of biotite and hornblende as the primary mafic minerals and the general absence of muscovite as a primary mineral. The mineralogy and chemistry of the Main pluton is distinct from the other intrusions. Either it is a more extensively evolved member of this plutonic suite, or it belongs to a different plutonic suite.

U-PB GEOCHRONOLOGY METHODS AND RESULTS

U-Pb ages (Table 2) for nine samples were obtained at Boise State University by the chemical abrasion isotope dilution thermal ionization mass spectrometry (CA ID-TIMS) method from analyses of single zircon grains or fragments of grains following methods described in Pigage *et al.* (2012) as modified from Mattinson (2005). Cathodoluminescent images were used to select zircon grains for dating, based upon zoning patterns and lack of apparent inherited cores (Appendix images A1-A9).

From each sample five or six grains were dated (Table 2; Appendix Figs. A1-A9). Weighted mean $^{206}Pb/^{238}U$ ages for each sample were calculated from equivalent ages using Isoplot 3.0 (Ludwig, 2003) and are interpreted as being the igneous crystallization ages for these plutons. U-Pb dates and uncertainties were calculated using the algorithms of Schmitz and Schoene (2007), $^{235}U/^{205}Pb$ of 77.93 and $^{233}U/^{235}U$ of 1.007066 for the Boise State University tracer solution, and U decay constants recommended by Jaffey *et al.* (1971). $^{206}Pb/^{238}U$ ratios and dates were corrected for initial ^{230}Th disequilibrium using a Th/U[magma]=3

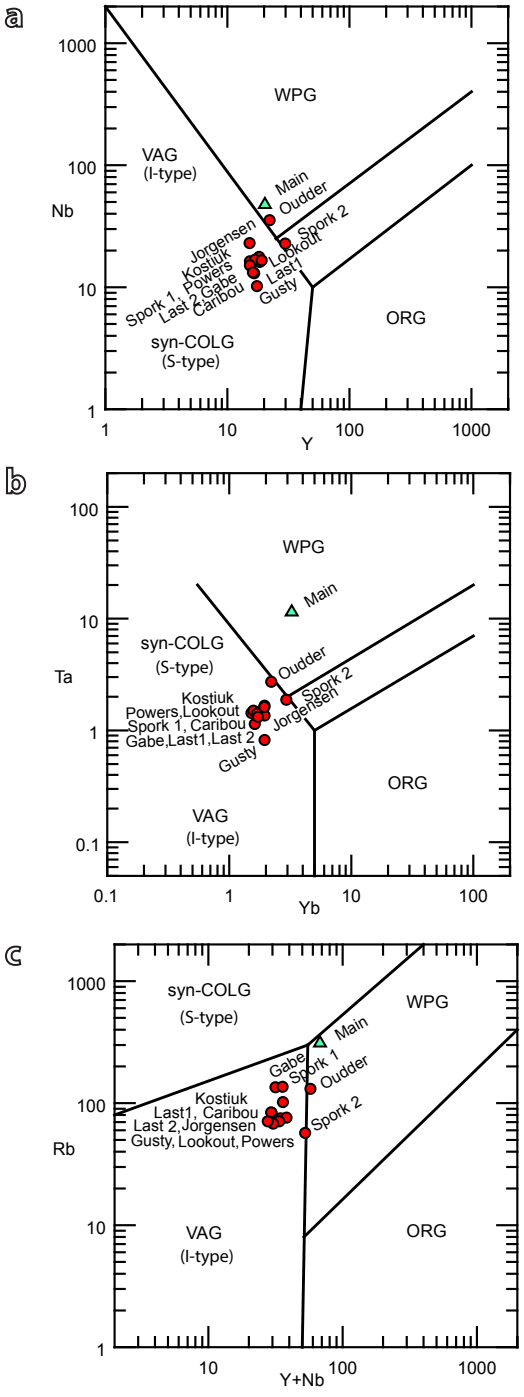

Figure 10. *Tectonic discriminant diagrams for intrusion samples in Coal River map area (from Pearce et al., 1984). Sample 10TOA019 (Main pluton) is indicated by the filled triangle; all other samples indicated with filled circles. (a) Nb vs Y; (b) Ta vs Yb; and (c) Rb vs (Y + Nb); VAG=volcanic arc granite, WPG=within plate granite, COLG=syn-collisional granite, ORG=ocean ridge granite.*

Table 2. *Uranium-lead isotopic CA-TIMS zircon data. Sample locations are in Table 1.*

							Radiogenic Isotope Ratios								Isotopic Dates					
Sample	Th/ U	$^{206}Pb^*$ x10^{-13} mol	mol % $^{206}Pb^*$	Pb^*/Pb_c	Pb_c (pg)[c]	$^{206}Pb/^{204}Pb$	$^{208}Pb/^{206}Pb$	$^{207}Pb/^{206}Pb$	% err	$^{207}Pb/^{235}U$	% err	$^{206}Pb/^{238}U$	% err	corr. coef.	$^{207}Pb/^{206}Pb$	±	$^{207}Pb/^{235}U$	±	$^{206}Pb/^{238}U$	±
(a)	(b)	(c)	(c)	(c)	(c)	(d)	(e)	(e)	(f)	(e)	(f)	(e)	(f)		(g)	(f)	(g)	(f)	(g)	(f)
Gusty		Gusty Lake																		
z1	0.252	1.9619	99.85%	193	0.24	12587	0.081	0.048072	0.107	0.103374	0.161	0.015596	0.070	0.863	102.82	2.53	99.89	0.15	99.76	0.07
z2	0.239	0.9393	99.75%	112	0.19	7346	0.076	0.047988	0.185	0.103209	0.229	0.015598	0.073	0.711	98.68	4.38	99.73	0.22	99.78	0.07
z3	0.235	1.1511	99.79%	135	0.20	8851	0.075	0.048014	0.176	0.103257	0.218	0.015597	0.075	0.675	99.98	4.17	99.78	0.21	99.77	0.07
z4	0.229	2.8010	99.86%	207	0.31	13553	0.073	0.048037	0.105	0.103333	0.158	0.015601	0.069	0.863	101.11	2.48	99.85	0.15	99.80	0.07
z5	0.264	1.1166	99.66%	84	0.31	5449	0.084	0.048085	0.220	0.103510	0.260	0.015613	0.073	0.655	103.44	5.19	100.01	0.25	99.87	0.07
z6	0.258	1.8928	99.78%	128	0.34	8342	0.083	0.048526	0.140	0.105236	0.189	0.015729	0.072	0.786	124.99	3.29	101.60	0.18	100.60	0.07
							weighted mean $^{206}Pb/^{238}U$ date for 5 zircon grains of 99.79 ± 0.03 Ma (MSWD = 1.4)											
Kostiuk		09RAS062																		
z1	0.613	1.6703	99.67%	95	0.45	5604	0.196	0.048010	0.195	0.102842	0.238	0.015536	0.072	0.704	99.76	4.60	99.40	0.23	99.38	0.07
z2	0.655	0.8859	99.45%	57	0.40	3357	0.210	0.048038	0.303	0.102921	0.346	0.015539	0.073	0.646	101.14	7.17	99.47	0.33	99.40	0.07
z3	0.661	1.7171	99.64%	87	0.51	5067	0.211	0.048011	0.213	0.102872	0.254	0.015540	0.072	0.664	99.80	5.03	99.42	0.24	99.41	0.07
z4	0.645	1.2771	99.66%	93	0.35	5473	0.206	0.047989	0.247	0.102786	0.284	0.015534	0.076	0.592	98.71	5.83	99.34	0.27	99.37	0.07
z5	0.639	1.2416	99.29%	44	0.73	2580	0.204	0.048023	0.380	0.102887	0.422	0.015539	0.077	0.613	100.39	8.99	99.44	0.40	99.40	0.08
z6	0.660	0.9236	99.11%	35	0.69	2057	0.211	0.047922	0.472	0.102664	0.518	0.015537	0.075	0.647	95.44	11.18	99.23	0.49	99.39	0.07
							weighted mean $^{206}Pb/^{238}U$ date for 6 zircon grains of 99.39 ± 0.03 Ma (MSWD = 0.1)											
Last2		09LP098																		
z1	0.340	4.2532	99.84%	178	0.57	11318	0.109	0.048037	0.110	0.102019	0.162	0.015403	0.070	0.838	101.08	2.60	98.64	0.15	98.54	0.07
z3	0.331	2.7269	99.85%	189	0.34	12025	0.106	0.048030	0.107	0.101959	0.160	0.015396	0.069	0.858	100.76	2.53	98.58	0.15	98.49	0.07
z4	0.381	2.6510	99.85%	194	0.33	12183	0.122	0.048073	0.138	0.102118	0.182	0.015406	0.072	0.733	102.88	3.26	98.73	0.17	98.56	0.07
z5	0.350	3.1374	99.84%	183	0.41	11604	0.112	0.048086	0.104	0.102067	0.159	0.015395	0.069	0.869	103.49	2.47	98.68	0.15	98.48	0.07
z6	0.361	2.1651	99.76%	122	0.42	7736	0.116	0.048026	0.142	0.101988	0.189	0.015402	0.070	0.778	100.54	3.35	98.61	0.18	98.53	0.07
							weighted mean $^{206}Pb/^{238}U$ date for 5 zircon grains of 98.52 ± 0.03 Ma (MSWD = 0.8)											
Jorgensen		09RAS136																		
z1	0.225	1.3220	99.65%	81	0.38	5310	0.072	0.047981	0.199	0.101727	0.242	0.015377	0.070	0.706	98.32	4.70	98.37	0.23	98.37	0.07
z2	0.229	1.6987	99.79%	130	0.30	8538	0.073	0.048015	0.135	0.101783	0.184	0.015374	0.070	0.799	99.99	3.18	98.42	0.17	98.36	0.07
z3	0.244	2.1815	99.83%	161	0.31	10510	0.078	0.048071	0.118	0.101885	0.170	0.015372	0.070	0.843	102.78	2.78	98.51	0.16	98.34	0.07
z4	0.284	0.6361	99.22%	36	0.41	2338	0.091	0.048118	0.438	0.102048	0.485	0.015381	0.082	0.623	105.10	10.35	98.67	0.46	98.40	0.08
z5	0.367	0.6939	99.39%	48	0.35	3021	0.117	0.047938	0.351	0.101547	0.393	0.015363	0.076	0.623	96.21	8.31	98.20	0.37	98.29	0.07
z6	0.289	1.0974	99.28%	39	0.66	2553	0.092	0.048043	0.381	0.101847	0.424	0.015375	0.074	0.627	101.41	9.02	98.48	0.40	98.36	0.07
							weighted mean $^{206}Pb/^{238}U$ date for 6 zircon grains of 98.35 ± 0.03 Ma (MSWD = 1.0)											
Caribou		09TOA180																		
z1	0.272	3.7709	99.87%	221	0.40	14321	0.087	0.048048	0.097	0.101759	0.152	0.015360	0.069	0.876	101.61	2.29	98.40	0.14	98.27	0.07
z3	0.313	2.3406	99.84%	174	0.32	11133	0.100	0.048077	0.113	0.101861	0.165	0.015366	0.069	0.846	103.04	2.66	98.49	0.15	98.31	0.07
z4	0.351	2.5384	99.61%	74	0.82	4706	0.112	0.048024	0.212	0.101713	0.253	0.015361	0.071	0.674	100.47	5.02	98.36	0.24	98.27	0.07
z5	0.420	2.4326	99.79%	139	0.43	8650	0.134	0.048014	0.134	0.101665	0.182	0.015357	0.071	0.780	99.98	3.17	98.31	0.17	98.24	0.07
z6	0.563	1.9651	99.76%	129	0.38	7744	0.180	0.048032	0.157	0.101699	0.201	0.015356	0.072	0.718	100.85	3.72	98.34	0.19	98.24	0.07
							weighted mean $^{206}Pb/^{238}U$ date for 5 zircon grains of 98.27 ± 0.03 Ma (MSWD = 0.6)											
Lookout		09TAO179																		
z2	0.393	5.1848	99.91%	336	0.37	21012	0.126	0.048013	0.082	0.101592	0.141	0.015346	0.069	0.917	99.91	1.94	98.24	0.13	98.18	0.07
z3	0.349	4.4313	99.90%	281	0.38	17787	0.112	0.048006	0.093	0.101648	0.148	0.015357	0.070	0.873	99.59	2.20	98.30	0.14	98.24	0.07
z4	0.456	7.1048	99.92%	358	0.49	21766	0.154	0.052448	0.079	0.183004	0.150	0.025306	0.090	0.898	304.98	1.81	170.64	0.24	161.11	0.14
z5	0.393	3.5271	99.71%	102	0.84	6381	0.126	0.048065	0.170	0.101698	0.213	0.015346	0.070	0.710	102.45	4.03	98.34	0.20	98.17	0.07
z6	0.666	4.2218	99.87%	248	0.44	14464	0.213	0.048052	0.085	0.101678	0.145	0.015347	0.069	0.931	101.84	2.01	98.32	0.14	98.18	0.07
z7	0.381	4.0498	99.88%	253	0.39	15877	0.122	0.048026	0.092	0.101669	0.148	0.015354	0.070	0.889	100.53	2.17	98.32	0.14	98.22	0.07
							weighted mean $^{206}Pb/^{238}U$ date for 5 zircon grains of 98.20 ± 0.03 Ma (MSWD = 0.9)											

Table 2. *continued.*

							Radiogenic Isotope Ratios								Isotopic Dates					
Sample	Th/U	$^{206}Pb^*$ x10^{-13} mol	mol % $^{206}Pb^*$	Pb^*/Pb_c	Pb_c (pg)	$^{206}Pb/^{204}Pb$	$^{208}Pb/^{206}Pb$	$^{207}Pb/^{206}Pb$	% err	$^{207}Pb/^{235}U$	% err	$^{206}Pb/^{238}U$	% err	corr. coef.	$^{207}Pb/^{206}Pb$	±	$^{207}Pb/^{235}U$	±	$^{206}Pb/^{238}U$	±
(a)	(b)	(c)	(c)	(c)	(c)	(d)	(e)	(e)	(f)	(e)	(f)	(e)	(f)		(g)	(f)	(g)	(f)	(g)	(f)
Spork1		10TOA014																		
z1	0.462	6.0370	99.95%	656	0.23	40238	0.148	0.048020	0.070	0.101516	0.133	0.015332	0.070	0.951	100.28	1.65	98.18	0.12	98.09	0.07
z2	0.452	1.9876	99.85%	201	0.24	12397	0.145	0.048038	0.128	0.101513	0.176	0.015326	0.071	0.787	101.16	3.03	98.17	0.17	98.05	0.07
z3	0.504	2.2253	99.90%	289	0.19	17547	0.161	0.048041	0.096	0.101521	0.151	0.015326	0.070	0.877	101.31	2.27	98.18	0.14	98.05	0.07
z4	0.417	3.6900	99.90%	294	0.31	18288	0.134	0.048033	0.089	0.101581	0.147	0.015338	0.071	0.897	100.90	2.10	98.23	0.14	98.12	0.07
z5	0.458	3.3013	99.91%	346	0.24	21246	0.147	0.048044	0.102	0.101606	0.154	0.015338	0.070	0.841	101.43	2.41	98.26	0.14	98.13	0.07
z6	0.577	2.3570	99.84%	197	0.30	11751	0.185	0.047974	0.112	0.101418	0.164	0.015332	0.069	0.840	97.98	2.66	98.08	0.15	98.09	0.07
							weighted mean $^{206}Pb/^{238}U$ date for 6 zircon grains of 98.09 ± 0.03 Ma (MSWD = 1.0)											
Gabe		09LP048																		
z1	0.236	6.4116	99.95%	517	0.29	33773	0.076	0.048039	0.072	0.101323	0.134	0.015297	0.070	0.939	101.21	1.71	98.00	0.13	97.87	0.07
z2	0.233	9.4835	99.83%	167	1.31	10987	0.075	0.048070	0.096	0.101365	0.151	0.015294	0.072	0.871	102.69	2.26	98.04	0.14	97.84	0.07
z3	0.284	3.6880	99.87%	215	0.40	13893	0.091	0.047990	0.103	0.101206	0.156	0.015295	0.070	0.855	98.77	2.44	97.89	0.15	97.85	0.07
z4	0.210	4.5338	99.87%	217	0.48	14312	0.067	0.048049	0.093	0.101280	0.149	0.015288	0.070	0.885	101.66	2.21	97.96	0.14	97.80	0.07
z5	0.252	4.4302	99.89%	253	0.41	16503	0.081	0.048001	0.095	0.101174	0.150	0.015287	0.070	0.869	99.33	2.26	97.86	0.14	97.80	0.07
z6	0.200	6.9512	99.89%	261	0.61	17272	0.064	0.048049	0.087	0.101280	0.145	0.015288	0.072	0.891	101.67	2.07	97.96	0.14	97.80	0.07
							weighted mean $^{206}Pb/^{238}U$ date for 6 zircon grains of 97.83 ± 0.03 Ma (MSWD = 0.7)											
Oudder		09TOA135																		
z1	0.448	11.5824	99.95%	638	0.45	39298	0.144	0.048018	0.068	0.101138	0.131	0.015276	0.071	0.950	100.13	1.60	97.83	0.12	97.73	0.07
z2	0.406	5.0870	99.90%	307	0.40	19168	0.130	0.048038	0.078	0.101181	0.138	0.015276	0.069	0.933	101.13	1.84	97.87	0.13	97.73	0.07
z3	0.303	4.7393	99.89%	268	0.42	17201	0.097	0.048019	0.083	0.101129	0.142	0.015274	0.069	0.916	100.22	1.97	97.82	0.13	97.72	0.07
z4	0.353	2.6732	99.82%	164	0.39	10408	0.113	0.048030	0.114	0.101101	0.166	0.015267	0.069	0.841	100.74	2.70	97.79	0.15	97.67	0.07
z5	0.357	2.5063	99.63%	79	0.76	5016	0.115	0.048058	0.210	0.101154	0.251	0.015266	0.071	0.667	102.10	4.97	97.84	0.23	97.67	0.07
z6	0.327	2.2775	99.73%	106	0.51	6759	0.105	0.048067	0.158	0.101213	0.203	0.015272	0.070	0.745	102.58	3.74	97.90	0.19	97.70	0.07
							weighted mean $^{206}Pb/^{238}U$ date for 6 zircon grains of 97.70 ± 0.03 Ma (MSWD = 0.7)											

(a) z1, z2, *etc*. are labels for analyses composed of single zircon grains that were annealed and chemically abraded (Mattinson, 2005).
Fraction labels in bold denote analyses used in the weighted mean calculations.

(b) Model Th/U ratio calculated from radiogenic $^{208}Pb/^{206}Pb$ ratio and $^{207}Pb/^{235}U$ date.

(c) Pb* and Pbc are radiogenic and common Pb, respectively. mol % $^{206}Pb^*$ is with respect to radiogenic and blank Pb.

(d) Measured ratio corrected for spike and fractionation only. Fractionation correction is 0.15 ± 0.03 (1 sigma) %/amu (atomic mass unit) for single-collector Daly analyses, based on analysis of EARTHTIME 202Pb-205Pb tracer solution.

(e) Corrected for fractionation, spike, common Pb, and initial disequilibrium in $^{230}Th/^{238}U$. Common Pb is assigned to procedural blank with composition of $^{206}Pb/^{204}Pb$ = 18.35 ± 1.50%; $^{207}Pb/^{204}Pb$ = 15.60 ± 0.75%; $^{208}Pb/^{204}Pb$ = 38.08 ± 1.00% (1 sigma). $^{206}Pb/^{238}U$ and $^{207}Pb/^{206}Pb$ ratios corrected for initial disequilibrium in $^{230}Th/^{238}U$ using Th/U [magma] = 3.

(f) Errors are 2 sigma, propagated using algorithms of Schmitz and Schoene (2007) and Crowley *et al.* (2007).

(g) Calculations based on the decay constants of Jaffey *et al.* (1971). $^{206}Pb/^{238}U$ and $^{207}Pb/^{206}Pb$ dates corrected for initial disequilibrium in $^{230}Th/^{238}U$ using Th/U [magma] = 3.

using the algorithms of Crowley *et al.* (2007), resulting in an increase in the $^{206}Pb/^{238}U$ dates of ~0.09 Ma. All common Pb in analyses was attributed to laboratory blank and subtracted based on the measured laboratory Pb isotopic composition and associated uncertainty. U blanks are difficult to precisely measure, but are estimated at 0.07 pg.

Errors are the internal errors given at the 2 sigma confidence interval based on analytical uncertainties only, including counting statistics, subtraction of tracer solution, and blank and initial common Pb subtraction. These errors should be considered when comparing our dates with $^{206}Pb/^{238}U$ dates from other laboratories that used the same Boise State University tracer solution or a tracer solution that was cross-calibrated using EARTHTIME gravimetric standards. When comparing our dates with those derived from other geochronological methods using the U-Pb decay scheme (*e.g.*, laser ablation ICP-MS), a systematic uncertainty in the tracer calibration should be added to the internal error in quadrature; this error is ±0.10 Ma for all samples, resulting in a 2 sigma error of ±0.13 Ma. When comparing our dates with those derived from other decay schemes (*e.g.*, $^{40}Ar/^{39}Ar$, $^{187}Re^{187}Os$), systematic uncertainties in the tracer calibration and ^{238}U decay constant (Jaffey *et al.*, 1971) should be added to the internal error in quadrature. This error is ± 0.15 Ma for all samples, resulting in a combined 2 sigma error of ±0.18 Ma.

The $^{206}Pb/^{238}U$ weighted mean ages for zircon grains from the nine plutons range from 99.79±0.03 Ma to 97.70±0.03 Ma (Fig. 11). One zircon grain from the Gusty Lake sample (grain z6, Table 2) yielded an older date of 100.60±0.07 Ma and it was not used in calculating the weighted mean. Also, one grain from the Lookout sample (grain z4; Table 2) that yielded an older, discordant date of 161 Ma (Table 2) was not used in the calculation of the weighted mean date. Unfortunately the sample from the Main stock (sample10TOA019) yielded such poor quality zircon that isotopic dating was not attempted. The agreement of the high-precision single-grain dates within each sample and the simple CL zoning patterns (*cf.* Appendix) indicate this range reflects the timing of intrusion rather than Pb loss or inheritance.

The age range of nine plutons spread across a 100 x 30 km area is only 2.1 Ma. No systematic change in age across the map is apparent (Fig. 3). The three plutons (Jorgensen, Caribou, Lookout) in the northeast corner of the map area have an age spread of less than 0.1 Ma.

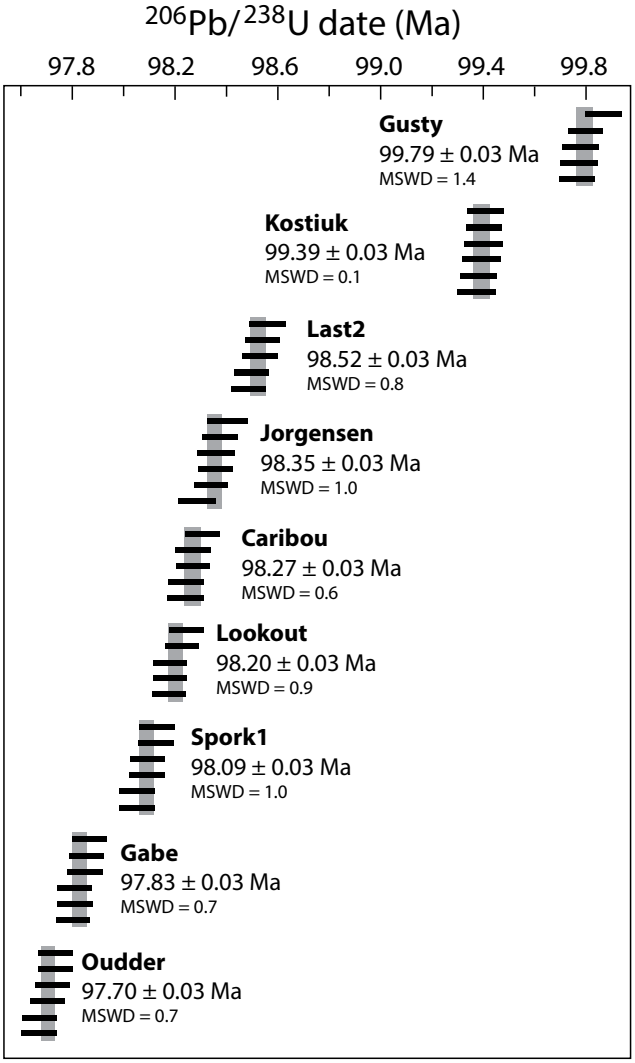

Figure 11. *Plot of new $^{206}Pb/^{238}U$ dates from single zircon grains from plutons in Coal River map area. Plotted with Isoplot 3.0 (Ludwig, 2003). Solid horizontal bars are 2 sigma internal errors. Weighted mean date is represented by the grey box behind the error bars.*

DISCUSSION

Our geochronological results are comparable to those completed by Heffernan (2004), Rasmussen *et al.* (2007), and Rasmussen (2013) in the region. Previous U-Pb ID-TIMS dating of the Patterson pluton (Fig. 3) used a single, abraded fraction of poor to moderate quality zircon to interpret an age of 97.5±0.5 Ma (Heffernan, 2004). Discordant dates from other fractions were deemed the result of inheritance. ID-TIMS dating of two fractions of monazite from a felsic dyke near the Patterson pluton yielded an age of 98.3±1.6 Ma (Heffernan, 2004). These

relatively imprecise dates complement ages from the same area reported here. U-Pb dating of zircon from the Powers pluton by the laser ablation inductively coupled plasma mass spectrometry (LA-ICP-MS) method yielded an age of 98.2 ± 1.3 Ma (Rasmussen *et al.*, 2007). This date is similar to those from the same area reported here. U-Pb dating of zircon from the Jorgensen pluton by Rasmussen *et al.* (2007, sample KR-05-08, mistakenly listed in their Table 2 as the Powers pluton) yielded an age of 102.4 ± 2.3 Ma; a more recent re-analysis of this sample resulted in an age of 95.9 ± 0.8 Ma (Rasmussen, 2013). ^{40}Ar ^{39}Ar dating of biotite from this sample yielded an age of 101.4 ± 0.6 Ma (Rasmussen *et al.*, 2007). These ages do not agree with the age of 98.35 ± 0.03 Ma from the Jorgensen pluton reported here, which is a robust age based on six high-precision CA-TIMS ages.

With the exception of the undated Main pluton, the similar chemistry and crystallization ages for all plutons dated in this study indicate they constitute a single plutonic suite. The compositions, mineralogy and crystallization ages of the dated Coal River intrusions support their logical inclusion in the Tay River plutonic suite as defined by Mortensen *et al.* (2000) and discussed further by Heffernan (2004), Rasmussen *et al.* (2007), and Rasmussen (2013).

Heffernan (2004) and Rasmussen *et al.* (2007) reported whole rock geochemistry for the Patterson, Jorgensen and Power plutons. Trace element plots normalized to primitive mantle for their samples fall within the envelope of plutonic samples reported in this study. High initial $^{87}Sr/^{86}Sr$ and epsilon Nd (εNd) values (Heffernan, 2004) and ^{18}O signatures (Rasmussen and Arehart, 2010) for these samples are consistent with the parental melts for the intrusions being sourced primarily, if not completely, from crustal rocks. Our element plots normalized to upper continental crust (Fig. 9b) are fully consistent with the sampled intrusions arising from partial melting of continental crust.

The overall limited geochemical variation in the granitoid samples implies a homogenous source material for the intrusions. Trends shown by the Harker diagrams reflect a liquid line of descent from a single magmatic source, with the possible exception of the Main pluton. The petrology of the samples, their metaluminous character and distribution on the tectonic discriminant diagrams further imply that the intrusions correlate best with I-type granites. For similar reasons Rasmussen (2013) considered these intrusions to be sourced from a homogenous, infracrustal source.

Immediately north of the Coal River map area coeval Tay River suite intrusions (including the Mount Kostiuk pluton, Coal River batholith, Spork pluton, and Ivo-Salivo pluton) are more extensively exposed, and not circular in plan (Heffernan, 2004; Rasmussen *et al.*, 2007; Fig. 12).

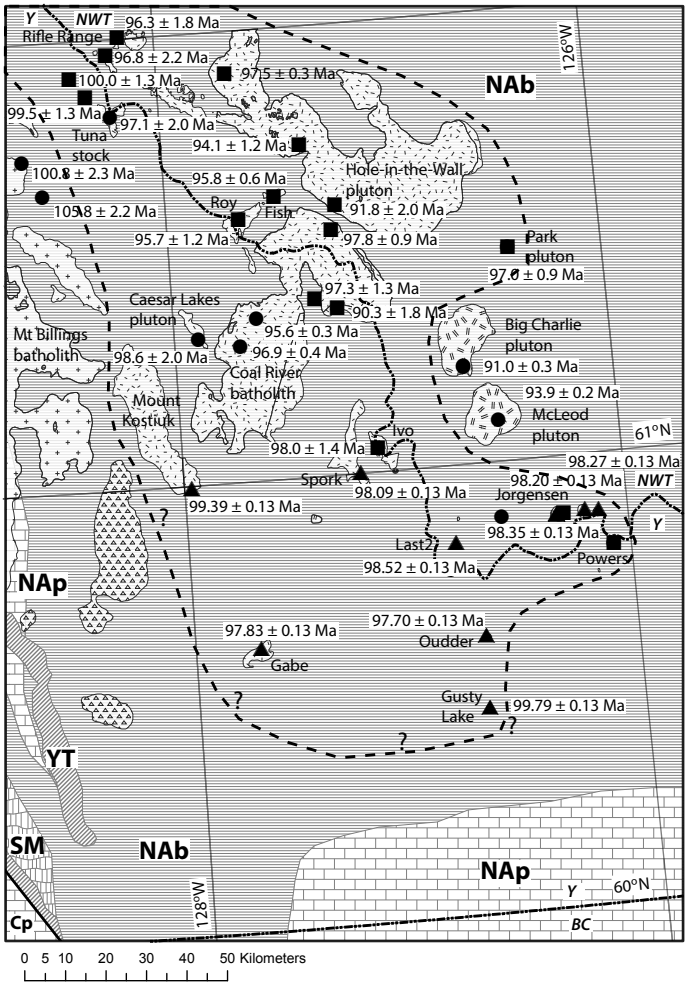

Figure 12. *Cretaceous intrusions in southeast Yukon and southwest Northwest Territories superimposed on the distribution of terranes and igneous bodies (from Colpron and Nelson, 2011; Gordey and Makepeace, 2003). Filled circles are ages from Heffernan (2004); filled squares are ages from Rasmussen et al. (2007); filled triangles are ages reported here. Error limits on ages from this paper are ± 2 sigma, including analytical error and uncertainty in the tracer calibration. Large plutons of the Anvil suite indicated by the cross pattern; Tay River plutonic suite denoted with random single line pattern (and encircled by the heavy dashed line); Tombstone plutonic suite indicated with random double line pattern; intrusions with unknown affiliation indicated with triangle pattern. NAb: basinal strata of North America; NAp: platformal strata of North America; Y: Yukon; NWT: Northwest Territories, BC: British Columbia.*

Crystallization ages for these intrusions are similar or slightly younger than the ages in our study area (Heffernan, 2004; Rasmussen *et al.*, 2007; Rasmussen, 2013). This apparent exposure difference has an approximate easterly orientation and appears to define the gradational southern edge of Tay River suite intrusions in Yukon. No apparent fault or plunging fold structures have been mapped to indicate that the transition from large, irregular to small, circular plan view exposures might be related to exposure of different structural levels.

The intrusions are almost entirely unfoliated (in a few localities incipiently foliated), indicating late syntectonic to post-tectonic crystallization. The interpreted map pattern for the slightly foliated Gabe intrusion suggests that intrusion post-dated significant offset on the reverse, normal and strike-slip faults traced into the area (Pigage *et al.*, 2011). Regional fabric-forming deformation at the exposed structural level therefore ceased before *ca.* 98 Ma.

Plutons of the 99-95 Ma Tay River suite occur in a 70-150 km wide belt that extends ~465 km northwest from the Coal River area in southeast Yukon to northwest of Faro (Mortensen *et al.*, 2000; Rasmussen, 2013). This belt is a subset of an arcuate belt of plutons of early and mid-Cretaceous age (Woodsworth *et al.*, 1991; Mortensen *et al.*, 1995; 2000; Hart *et al.*, 2004; Rasmussen, 2013) on the northeast side of Tintina fault (Fig. 13). When the 430 km of dextral offset is restored (Gabrielse *et al.*, 2006), the aggregate plutonic belt extends westward to include the Livengood and Fairbanks-Salcha suites in central Alaska, and southward to link with coeval plutons in the Pelly and Cassiar mountains of south-central Yukon and adjacent British Columbia.

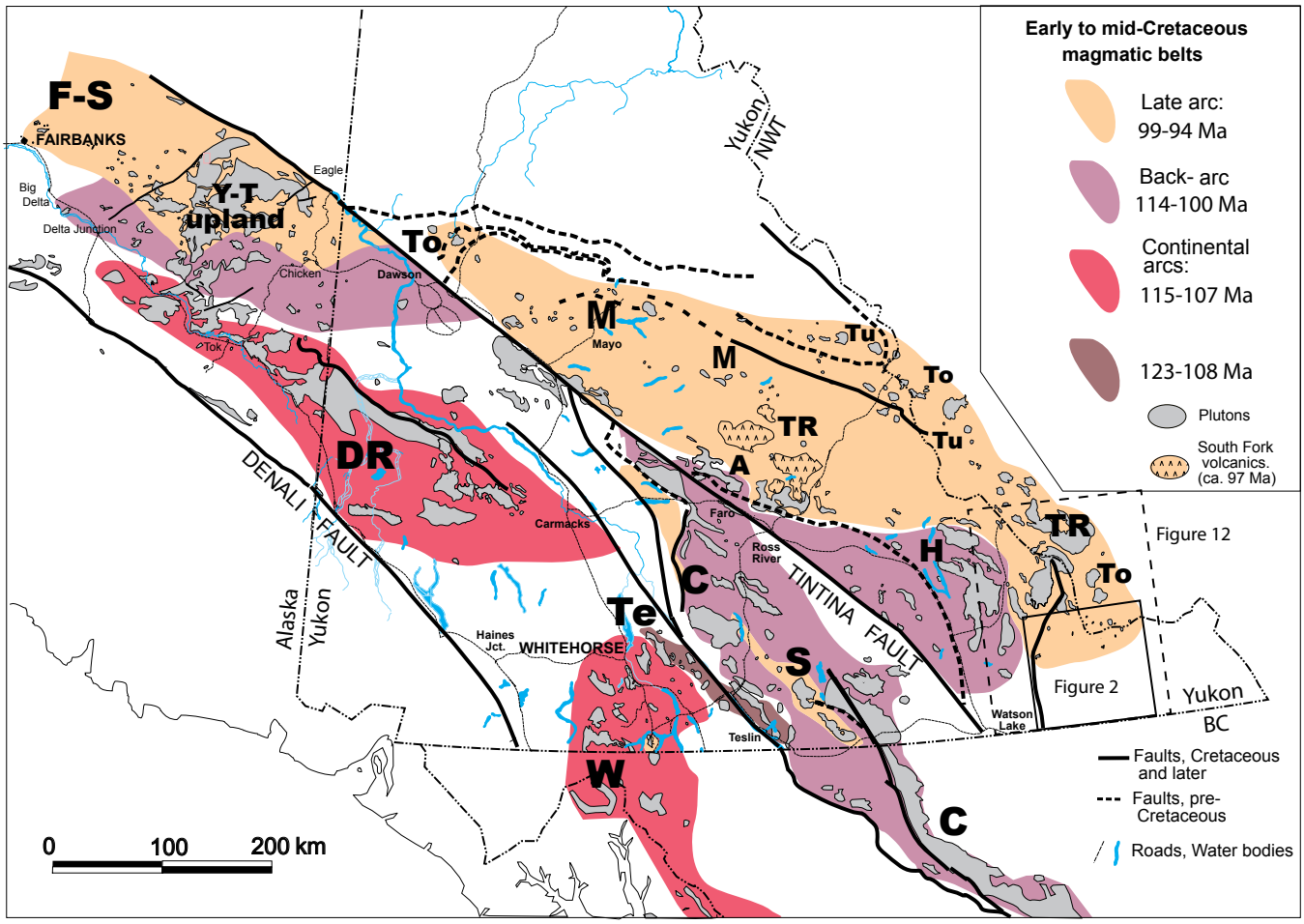

Figure 13. *Distribution of Early to mid-Cretaceous plutons and volcanic rocks (from Hart et al., 2004a) and their generalized magmatic belts reflecting geochronology by Rasmussen (2013), Heffernan (2004) and Mortensen et al. (2000). The approximate locations of plutonic suites are labeled: A = Anvil, C = Cassiar, DR = Dawson Range, F–S = Fairbanks–Salcha, H = Hyland, M = Mayo, S = Seagull–Thirtymile, Te = Teslin, To = Tombstone, TR = Tay River, Tu = Tungsten, W = Whitehorse, and Y-T upland = Yukon–Tanana Upland (modified from Rasmussen, 2013; Figure 1.4a).*

The composition and isotopic systematics of the late Early Cretaceous plutons are consistent with an arc setting, and the concept of a continental arc and inboard back-arc is widely accepted (*e.g.*, Woodsworth *et al.*, 1991; Mortensen *et al.*, 1995, 2000; Hart *et al.*, 2004; Rasmussen, 2013). They are interpreted to be the product of northeastward subduction of the Gravina ocean crust beneath the northwestward drifting North America continent in Early and mid-Cretaceous time (Engebretson *et al.*, 1985; Nelson *et al.*, 2013). Magmatism peaked within the northern Cordillera between 115 to 100 Ma with the voluminous intrusion of the Whitehorse-Coffee Creek suite (arc), and the Cassiar, Anvil and Hyland suites (back-arc; Hart *et al.*, 2004; Rasmussen, 2013).

Following Early to mid-Cretaceous arc and back-arc plutonism, mid-Cretaceous magmatism northeast of Tintina Trench resulted in successive broadly northwest-trending belts of plutons constituting the Tay River (99-96 Ma), Tungsten (98-95 Ma), Mayo (98-93 Ma), and Tombstone (94-89 Ma) plutonic suites and South Fork volcanism (112-93.7 Ma; Table 5a in Gordey, in press). All of the suites form convex bands extending easterly from the Tintina fault and curving to a more southerly trend near the Yukon-NWT border (Fig. 13). All are east (farther inboard) of the earlier Anvil and Hyland suite back-arc intrusions. The locus of plutonism moved east and north with progressively younger plutonic suites (Rasmussen, 2013). Geochemistry comparison (Rasmussen, 2013) of the different suites suggests that all but the Tungsten suite are I-type and formed as partial melts of infracrustal igneous source rocks. In contrast the Tungsten suite has been identified as a mixed suite with both S-type and I-type affinity, depending on location.

The arc magmatism interpretation for these mid-Cretaceous plutonic suite belts is problematic in that the northeast-facing subduction zone would have been located at least 400 km southwest (outboard) of the present location of the plutons. Rasmussen (2013) suggested that the occurrence of I-type magmatism hundreds of kilometres northeast (inboard) from the subduction trench may have been related to flattening of the subducting slab, moving the zone of mantle hydration farther inland. Higher heat flow leading to magma genesis could have been related to mantle convection around the descending slab, although slab break-off is unlikely or possibly occurred later (as indicated by the relative inhomogeneity of the Tombstone and Tungsten suites).

The termination in a southward direction of the Tay River suite plutons in the Coal River map area suggests that the geometry of the subducting slab changed southward, resulting in displacement or cessation of arc magmatism along strike to the south.

CONCLUSIONS

Intrusions in the Coal River map area of southeastern Yukon are predominantly equigranular or porphyritic, biotite ± hornblende granodiorite with lesser tonalite, granite quartz monzodiorite and quartz diorite. They are characterized by a range of magnetic susceptibilities from 0.0 to 17.8 (10^{-3} SI units), consistent major and trace element compositions corresponding to magnetite to ilmenite series intrusions and largely metaluminous to slightly peraluminous affinities. Their whole rock geochemical character and age suggests that they belong to the Tay River plutonic suite (except for the Main pluton) which was sourced from partial melting of a homogenous, infracrustal, igneous parent.

Most of the intrusions are approximately subcircular with steep to vertical intrusive contacts. Regional aeromagnetic surveys were helpful for locating intrusions in areas of poor bedrock exposure.

U-Pb CA ID-TIMS zircon crystallization ages from nine plutons range from 99.79 ± 0.03 to 97.70 ± 0.03 Ma, a spread of only 2.1 Ma. The plutons are late syntectonic to post-tectonic, putting an upper age restriction on deformation of the Cordilleran orogeny in the Coal River area at the exposed structural level.

The Tay River plutonic suite in Yukon and Northwest Territories is part of a northwest-trending belt of relatively homogeneous plutons that represent an intermediate phase (in both location and time) of the continental arc response to subduction and accretion along the Cordilleran margin.

ACKNOWLEDGEMENTS

This project was initiated under the Geoscience for Energy and Minerals (GEM) program of the Geological Survey of Canada and was continued by the Yukon Geological Survey. Field assistants Martina Bezzola, Casey Cardinal, Gavin Clarkson, Kristy Long, and Sarah Shoniker were uncomplaining in a surprisingly vegetated field area. Helicopter assistance was provided by HeliDynamics Ltd. (2009) and Trans North Helicopters (2010). Beth Hunt kept everyone well fed during the 2009 fieldwork. Geochronology in both years was funded by Geological

Survey of Canada. Michael Burns and Bev Quist of McEvoy Geosciences Ltd. kindly collected a granitic sample from near Gusty Lake.

This manuscript is a joint Yukon Geological Survey and Earth Sciences Sector (20120369) contribution. David Moynihan (Yukon Geological Survey) and Bob Anderson (Geological Survey of Canada) improved an earlier version, and we also thank reviewer Don Murphy and editor Patrick Sack.

REFERENCES

Cecile, M.P., Morrow, D.W., and Williams, G.K., 1997. Early Paleozoic (Cambrian to Early Devonian) tectonic framework, Canadian Cordillera. Bulletin of Canadian Petroleum Geology, vol. 45, p. 54-74.

Colpron, M. and Nelson, J.L., 2011. A digital atlas of terranes for the Northern Cordillera. Accessed online from: Yukon Geological Survey <*www.geology.gov.yk.ca*> [accessed July 15, 2012].

Crowley, J.L., Schoene, B., and Bowring, S.A., 2007. U-Pb dating of zircon in the Bishop Tuff at the millennial scale: Geology, vol. 35, p. 1123-1126.

Engebretson, D.C., Cox, A., and Gordon, R.G., 1985. Relative motions between oceanic and continental plates in the Pacific basin. Geological Society of America, Special Paper 206, 59 p.

Frost, B.R., Barnes, C.G., Collins, W.J., Arculus, R.J., Ellis, D.J., and Frost, C.D., 2001. A geochemical classification for granitic rocks. Journal of Petrology, vol. 42, p. 2033-2048.

Gabrielse, H. and Blusson, S., 1969. Geology of Coal River map-area, Yukon Territory and District of Mackenzie (95D). Geological Survey of Canada, Paper 68-38, 22 p.

Gabrielse H., 1973. Geology of Flat River, Glacier Lake and Wrigley Map-Areas, District of Mackenzie and Yukon Territory. Geological Survey of Canada, Memoir 366, Part I, 153 p.

Gabrielse, H., Murphy, D.C., and Mortensen, J.K., 2006. Cretaceous and Cenozoic dextral orogeny-parallel, displacements, magmatism, and paleogeography, north-central Canadian Cordillera. *In:* Paleogeography of the North American Cordillera: Evidence for and against large-scale displacements. J.W. Haggart, R.J. Enkin, and J.W.H. Monger (eds.), Geological Association of Canada, Special Paper 46, p. 255-276.

Gordey, S.P., 1988. The South Fork volcanics: mid-Cretaceous caldera fill tuffs in east central Yukon. *In:* Current Research, part E: Cordillera and Pacific margin, Geological Survey of Canada, Paper no. 88-1E, p. 13-18.

Gordey, S.P., in press. Evolution of the Selwyn basin region, Sheldon Lake (105J) and Tay River (105K) map areas, central Yukon Territory. Geological Survey of Canada, Bulletin 599, 274 p.

Gordey, S.P. and Anderson, R.J., 1993. Evolution of the northern Cordilleran miogeocline, Nahanni map area (105I), Yukon and Northwest Territories. Geological Survey of Canada, Memoir 428, 214 p.

Gordey, S.P. and Makepeace, A.J., 2003. Yukon digital geology, version 2.0. Geological Survey of Canada, Open File 1749 and Yukon Geological Survey, Open File 2003-9 (D), 2 CD-ROMs.

Hart, C.J.R., Goldfarb, R.J., Lewis, L.L., and Mair, J.L., 2004. The Northern Cordilleran mid-Cretaceous plutonic province: Ilmenite/Magnetite-series granitoids and intrusion-related mineralization. Resource Geology, vol. 54, p. 253-280.

Heffernan, R.S., 2004. Temporal, geochemical, isotopic, and metallogenic studies of mid-Cretaceous magmatism in the Tintina Gold Province, southeastern Yukon and southwestern Northwest Territories, Canada. Unpublished MSc thesis, University of British Columbia, 83 p.

Jaffey, A.H., Flynn, K.F., Glendenin, L.E., Bentley, W.C., and Essling, A.M., 1971. Precision measurements of half-lives and specific activities of ^{235}U and ^{238}U. Physical Review C, vol. 4, p. 1889-1906.

Jenner, G.A., 1996. Trace element geochemistry of igneous rocks: geochemical nomenclature and analytical geochemistry. *In:* Trace Element Geochemistry of Volcanic Rocks: Applications for massive sulphide exploration, D.A. Wyman (ed.), Geological Association of Canada, Short Course Notes, vol. 12, p. 51-77.

Kerrich, R. and Wyman, D.A., 1996. The trace element systematics of igneous rocks in mineral exploration: an overview. *In:* Trace Element Geochemistry of Volcanic Rocks: Applications for massive sulphide exploration. D.A. Wyman (ed.), Geological Association of Canada, Short Course Notes, vol. 12, p. 1-50.

Long, D.F. and Sweet, A.F., 1994. Age and depositional environment of the Rock River coal basin, Yukon Territory, Canada. Canadian Journal Earth Sciences, vol. 31, p. 865-880.

Ludwig, K.R., 2003. User's Manual for Isoplot 3.00. Berkeley Geochronology Center: Berkeley, CA.

Mair, J.L., Hart, C.R.J., and Stephens, J.R., 2006. Deformation history of the northwestern Selwyn Basin, Yukon, Canada: implications for orogeny evolution and mid-Cretaceous magmatism. Bulletin of Geological Society of America, vol. 118, p. 304-323.

Maniar, P.D. and Piccoli, P.M., 1989. Tectonic discrimination of granitoids. Bulletin of Geological Society of America, vol. 101, p. 635-643.

Mattinson, J.M., 2005. Zircon U-Pb chemical abrasion ("CA-TIMS") method: combined annealing and multi-step partial dissolution analysis for improved precision and accuracy of zircon ages. Chemical Geology, vol. 220, p. 47-66.

McLennan, S.M., 2001. Relationships between the trace element composition of sedimentary rocks and upper continental crust. Geochemistry, Geophysics, Geosystems, vol. 2, p. 1021.

Mortensen, J.K., Hart, C.J.R., Murphy, D.C., and Heffernan, S., 2000. Temporal evolution of early and mid-Cretaceous magmatism in the Tintina Gold Belt. *In:* The Tintina Gold Belt: Concepts, Exploration, and Discoveries. T. Tucker and M.T. Smith (eds.). British Columbia and Yukon Chamber of Mines, Special Volume 2, p. 49-58.

Mortensen, J.K., Murphy, D.C., Hart, C.J.R., and Anderson, R.G., 1995. Timing, tectonic setting, and metallogeny of Early and mid-Cretaceous magmatism in Yukon Territory. Geological Society of America Program Abstracts, vol. 27, p. 65.

Natural Resources Canada, 2009. Canadian Aeromagnetic Data Base, Geoscience Data Repository; Geological Survey of Canada, <*http://gdrdap.agg.nrcan.gc.ca/geodap/home/Default.aspx?lang=e*> [accessed April 1, 2009]

Nelson, J. and Colpron, M., 2007. Tectonics and metallogeny of the British Columbia, Yukon and Alaskan Cordillera, 1.8 Ga to the present. *In:* Mineral Deposits of Canada: A synthesis of major deposit-types, district metallogeny, the evolution of geological provinces, and exploration methods, W.D. Goodfellow (ed.), Geological Association of Canada, Mineral Deposits Division, Special Publication No. 5, p. 755-791.

Nelson, J.L., Colpron, M., and Israel, S., 2013. The Cordillera of British Columbia, Yukon, and Alaska: Tectonics and Metallogeny. *In:* Tectonics, Metallogeny, and Discovery: The North American Cordillera and Similar Accretionary Settings, M. Colpron, T. Bissig, B.G. Rusk, and J.F.H. Thompson (eds.), Society of Economic Geologists, Special Publication Number 17, p. 53-109.

Pearce, J.A., Harris, N.B.W., and Tindle, A.G., 1984. Trace element discrimination diagrams for the tectonic interpretation of granitic rocks. Journal of Petrology, vol. 25, p. 956-983.

Pigage, L.C., 2004. Preliminary geology of NTS 95D/8 (north Toobally Lakes area), southeast Yukon (1:50 000 scale). Yukon Geological Survey, Open File 2004-19.

Pigage, L.C., 2006. Stratigraphy summary for southeast Yukon (95D/8 and 95C/5). *In:* Yukon Exploration and Geology 2005. D.S. Emond, G.D. Bradshaw, L.L. Lewis, and L.H. Weston (eds.), Yukon Geological Survey, p. 267-285.

Pigage, L.C., 2008. Preliminary bedrock geology for NTS 95D/6 (Otter Creek area), southeast Yukon. *In:* Yukon Exploration and Geology 2007, D.S. Emond, L.R. Blackburn, R.P. Hill, and L.H. Weston (eds.), Yukon Geological Survey, p. 237-255.

Pigage, L.C., 2009. Bedrock geology of NTS 95C/5 (Pool Creek) and NTS 95D/8 map sheets, southeast Yukon. Yukon Geological Survey, Bulletin 16.

Pigage, L.C., Abbott, J.G., and Roots, C.F., 2011. Bedrock geology of Coal River map area (NTS 95D), Yukon (1:250 000 scale). Yukon Geological Survey, Open File 2011-1.

Pigage, L.C. and Anderson, R.G., 1985. The Anvil plutonic suite, Faro, Yukon Territory. Canadian Journal of Earth Sciences, vol. 22, p. 1204-1216.

Pigage, L.C., Crowley, J.L., Pyle, L.J., Abbott, J.G., Roots, C.F., and Schmitz, M.D., 2012. U-Pb zircon age of an Ordovician tuff in southeast Yukon: implications for the age of the Cambrian-Ordovician boundary. Canadian Journal of Earth Sciences, vol. 49, p. 732-741.

Rasmussen, K.L., 2013. The timing, composition, and petrogenesis of syn- to post-accretionary magmatism in the northern Cordilleran miogeocline, eastern Yukon and southwestern Northwest Territories. Unpublished PhD thesis, University of British Columbia, 788 p.

Rasmussen, K.L. and Arehart, G.B., 2010. Preliminary O-S isotopic compositions of Cretaceous granitoids in the Cassiar Platform and Selwyn Basin, Yukon and Northwest Territories. *In:* Yukon Exploration and Geology 2009. K.E. MacFarlane, L.H. Weston, and L.R. Blackburn (eds.), Yukon Geological Survey, p. 279-292.

Rasmussen, K.L., Mortensen, J.K., and Arehart, G.B., 2010. Radiogenic and stable isotopic compositions of mid--Cretaceous intrusions in the Selwyn basin, Yukon and Northwest Territories. Geo-Canada 2010 - Working with the Earth. Canadian Society of Petroleum Geologists, Joint annual convention, Calgary Alberta. Extended abstract. <*www.cspg.org/documents/Conventions/Archives/Annual/2010/0730_GC2010_Radiogenic_and_Stable_Isotopic_Compositions.pdf*> [accessed May 9, 2012]

Rasmussen, K.L., Mortensen, J.K., and Falck, H., 2006. Geochronological and lithogeochemical studies of intrusive rocks in the Nahanni region, southwestern Northwest Territories and southeastern Yukon. *In:* Yukon Exploration and Geology 2005. D.S. Emond, G.D. Bradshaw, L.L. Lewis, and L.H. Weston (eds.). Yukon Geological Survey, p. 287-298.

Rasmussen, K.L., Mortensen, J.K., Falck, H., and Ullrich, T.D., 2007. The potential for intrusion-related mineralization within the South Nahanni MERA area, Selwyn and Mackenzie Mountains, Northwest Territories. *In:* Mineral and energy resource assessment of the Greater Nahanni Ecosystem under consideration for the expansion of the Nahanni National Park Reserve, Northwest Territories. Geological Survey of Canada, Open File 5344, p. 203-278.

Schmitz, M.D. and Schoene, B., 2007. Derivation of isotope ratios, errors and error correlations for U-Pb geochronology using ^{205}Pb-^{235}U-(^{233}U)-spiked isotope dilution thermal ionization mass spectrometric data. Geochemistry, Geophysics, Geosystems, vol. 8, p. Q08006, doi:10.1029/2006GC001492.

Smith, M., 2000. The Tintina gold belt: an emerging gold district in Alaska and Yukon. *In:* The Tintina Gold Belt: Concepts, Exploration, and Discoveries. British Columbia and Yukon Chamber of Mines, Cordilleran Roundup, Special Volume 2, Vancouver, BC, p. 1-3.

Streckeisen, A., 1976. To each plutonic rock its proper name. Earth-Science Reviews, vol. 12, p. 1-33.

Streckeisen, A. and Le Maitre, R.W., 1979. A chemical approximation to the modal QAPF classification of the igneous rocks. Neues Jarbuch fuer Mineralogie Abhandlungen, vol. 136, p. 169-206.

Woodsworth, G.J., Anderson, R.G., and Armstrong, R.L., 1991. Plutonic regimes. *In*: Geology of the Cordilleran Orogen in Canada, H. Gabrielse and C.J. Yorath (eds.), Geological Survey of Canada, vol. 4, p. 491-531.

APPENDIX

SAMPLE DESCRIPTIONS

GUSTY (SAMPLE GUSTY LAKE)

The sample is an unfoliated, medium to fine-grained, porphyritic hornblende-biotite tonalite. Euhedral biotite, hornblende, plagioclase and quartz phenocrysts and glomerocrysts are disseminated in a fine-grained matrix. K-feldspar occurs only in the matrix, constituting up to 20% of the matrix.

KOSTIUK (SAMPLE 09RAS062)

The sample is an unfoliated biotite-hornblende-plagioclase-quartz granodiorite. It is medium grained with a slightly porphyritic to equigranular texture. Staining suggests that the matrix contains 30-40% interstitial K-feldspar. Locally it is extensively altered and contains sericite, epidote and chlorite.

LAST 2 (SAMPLE 09LP098)

The sample is an unfoliated, porphyritic, plagioclase-hornblende granodiorite. Subhedral plagioclase phenocrysts are up to 2 mm across. Rare subrounded and embayed quartz phenocrysts are also present. The matrix consists of a fine-grained mixture of opaques, chlorite, plagioclase, quartz and minor interstitial K-feldspar.

JORGENSEN (SAMPLE 09RAS136)

Texturally the sample is porphyritic with subhedral to euhedral plagioclase, biotite, hornblende, and rare quartz phenocrysts in a fine-grained, unfoliated, interstitial matrix. Compositionally the sample is a quartz monzodiorite. Very minor K-feldspar occurs only in the matrix. Quartz phenocrysts are locally embayed. Locally primary minerals are replaced by epidote, chlorite, sericite and carbonate.

CARIBOU (SAMPLE 09TOA180)

The sample is porphyritic with abundant euhedral to subhedral phenocrysts of plagioclase, biotite, hornblende, and minor quartz in a fine-grained, equigranular matrix. Phenocrysts constitute 50% of the sample. Quartz phenocrysts are rounded and locally embayed. The sample is extensively altered with alteration minerals including sericite, chlorite and epidote. K-feldspar is not present in the sample.

LOOKOUT (SAMPLE 09TOA179)

The sample is a porphyritic granodiorite with euhedral to subhedral biotite and plagioclase phenocrysts in a fine-grained, light grey matrix. The matrix is a mixture of quartz, chlorite and sericite. It is extensively altered; plagioclase is replaced by carbonate, and biotite is replaced by chlorite and carbonate. K-feldspar was not noted in the sample.

SPORK 1 (SAMPLE 10TOA014)

The sample is a coarse-grained, slightly foliated, medium grey, biotite granodiorite. K-feldspar forms large, irregular grains with well-developed microcline grid twinning. In some areas K-feldspar grains have a perthitic texture. The mafic mineral is biotite partially replaced by chlorite-epidote-sphene aggregates, constituting approximately 15% of the mode.

SPORK 2 (SAMPLE 10TOA016)

The sample is a coarse-grained, unfoliated, equigranular, hornblende-biotite quartz diorite. Dark green, subhedral hornblende is intergrown with lesser biotite. Biotite is preferentially replaced by chlorite. Minor quartz occurs as small interstitial grains. K-feldspar is not present, and plagioclase is not altered.

GABE (SAMPLE 09LP048)

The sample is a slightly foliated, equigranular, coarse-grained biotite-muscovite granodiorite. Biotite is intergrown with lesser muscovite; these aggregates partly to completely enclose euhedral to subhedral epidote.

OUDDER (SAMPLE 09TOA135)

The sample is a medium-grained, equigranular to slightly porphyritic, biotite-hornblende granodiorite. Plagioclase forms large subhedral phenocrysts and glomerocrysts in a matrix of interstitial plagioclase and K-feldspar. The rock is fresh with no deuteric alteration.

MAIN (SAMPLE10TOA019)

The sample is a medium-grained, equigranular, foliated, medium grey, muscovite-tourmaline-garnet granite. The feldspar is exclusively plagioclase. Subhedral plagioclase and interstitial quartz constitute approximately 90% of the mode. Staining reveals very minor, fine-grained, interstitial K-feldspar.

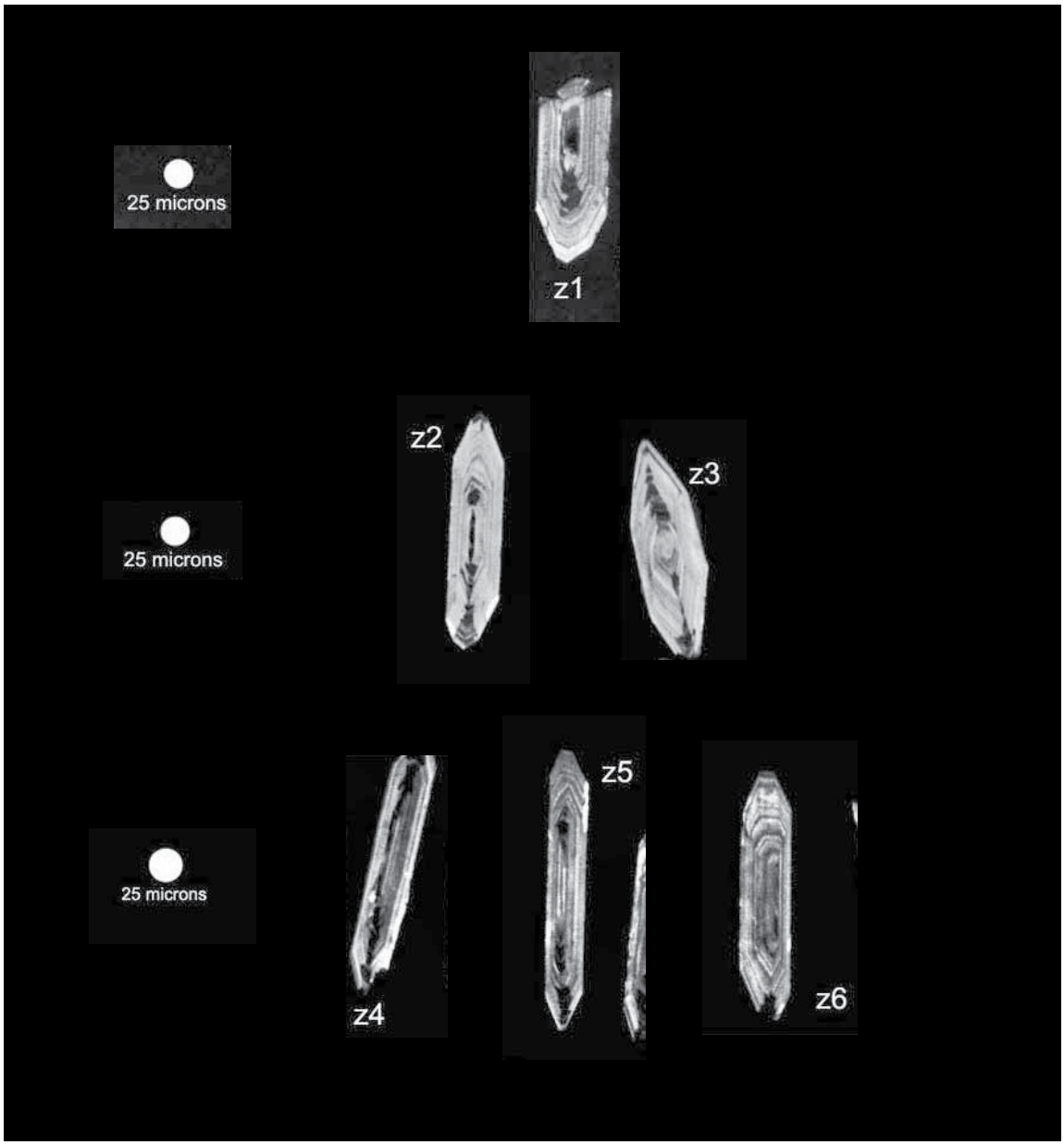

Figure A1. *Cathodoluminescent(CL) images of zircon grains from Jorgensen intrusion (sample 09RAS136).*

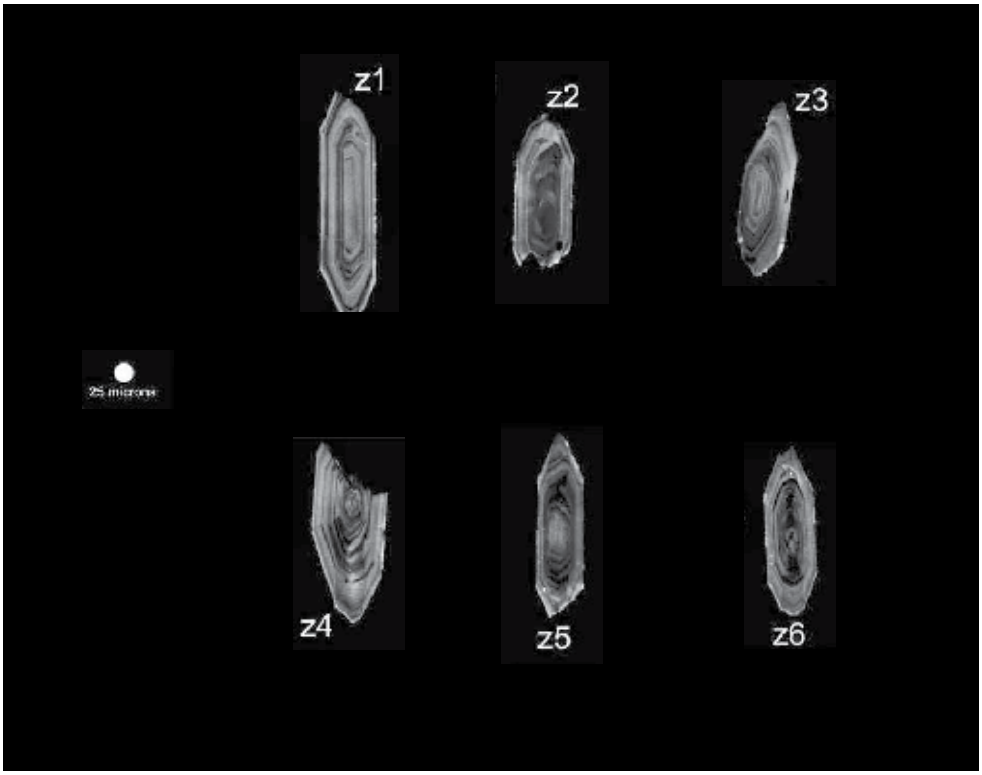

Figure A2. *CL images of zircon grains from Last 2 intrusion (sample 09LP098).*

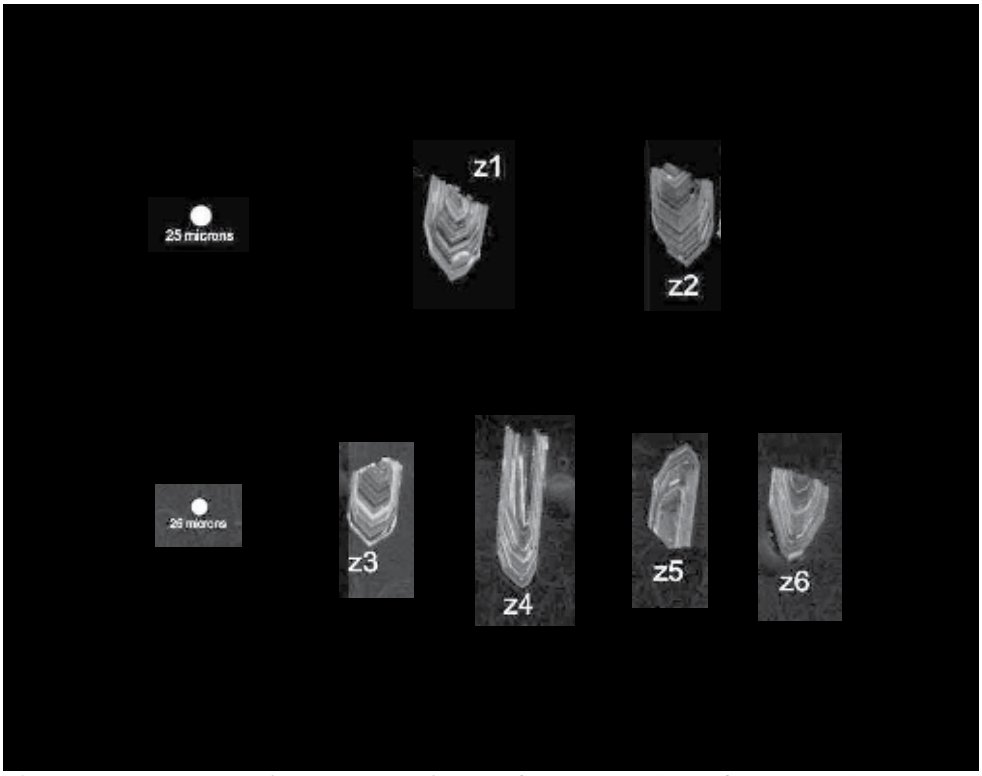

Figure A3. *CL images of zircon grains from Gabe intrusion (sample 09LP048).*

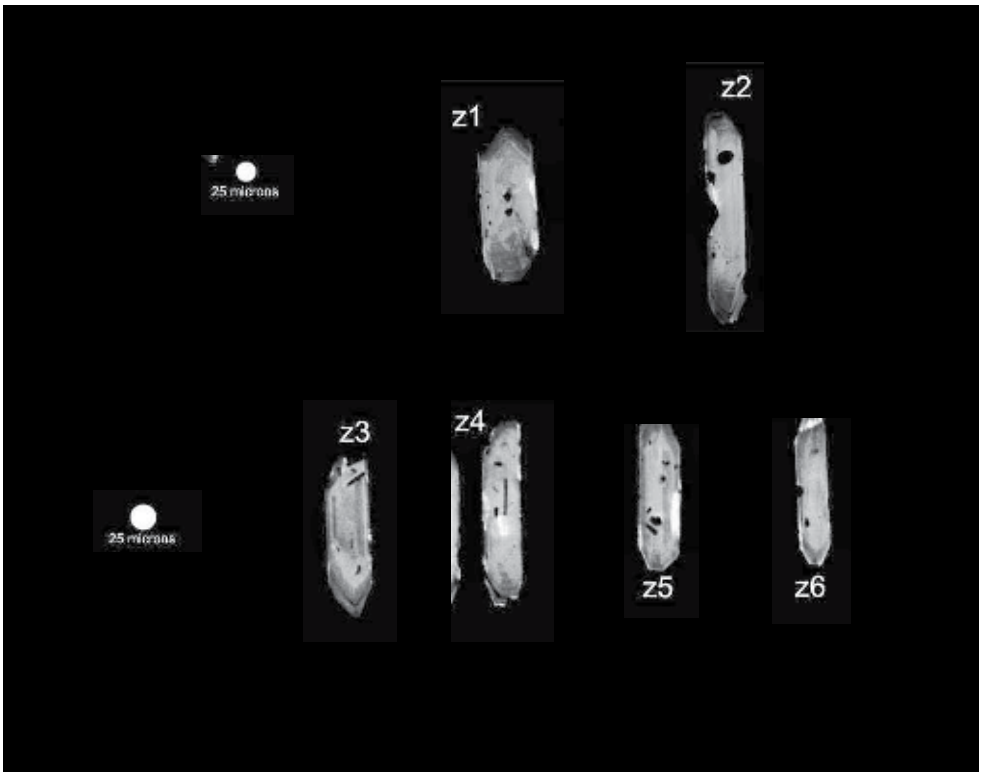

Figure A4. *CL images of zircon grains from Kostiuk intrusion (sample 09RAS062).*

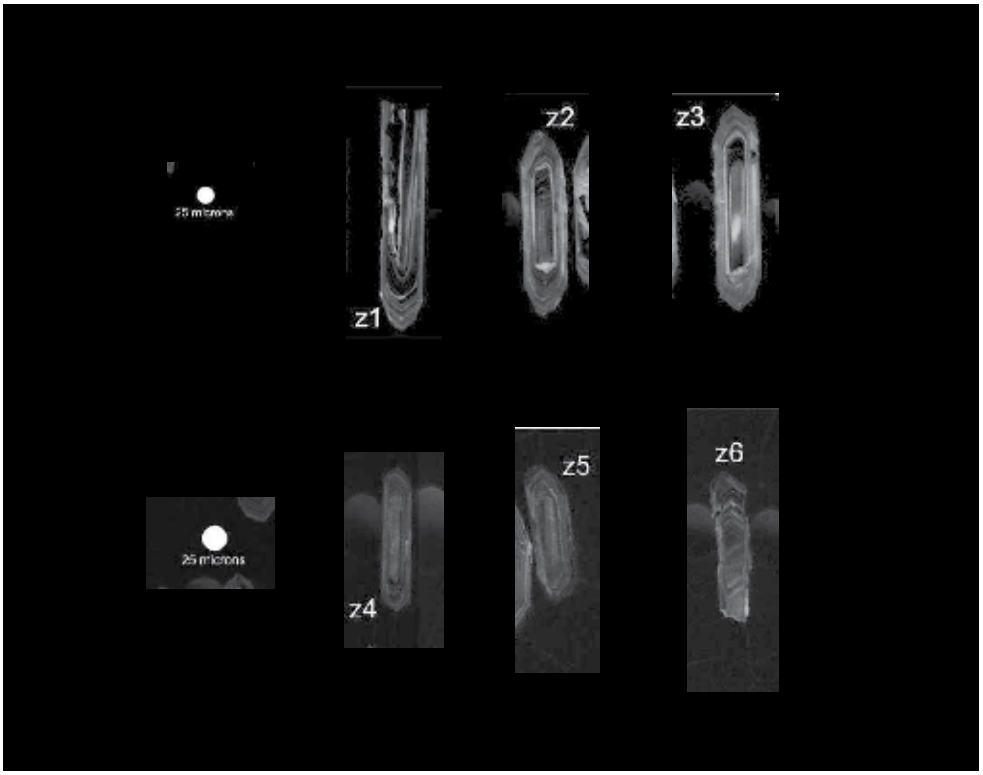

Figure A5. *CL images of zircon grains from Oudder intrusion (sample 09TOA135).*

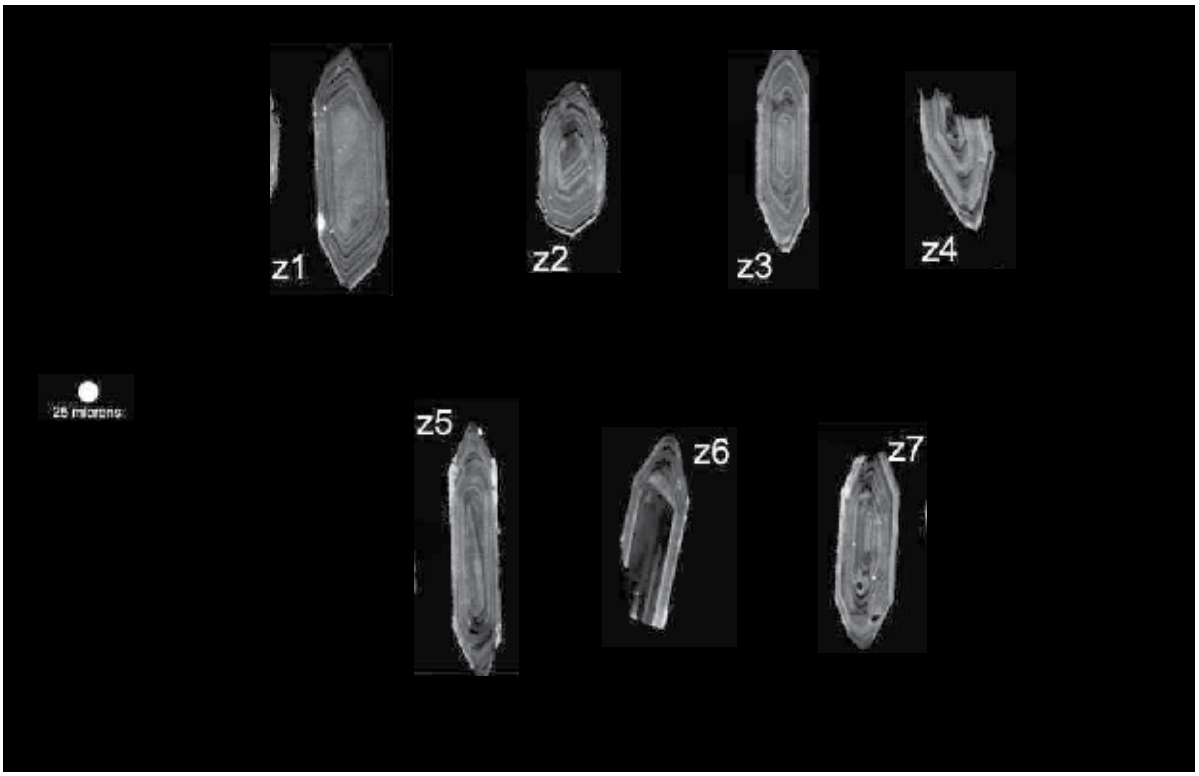

Figure A6. *CL images of zircon grains from Lookout intrusion (sample 09TOA179).*

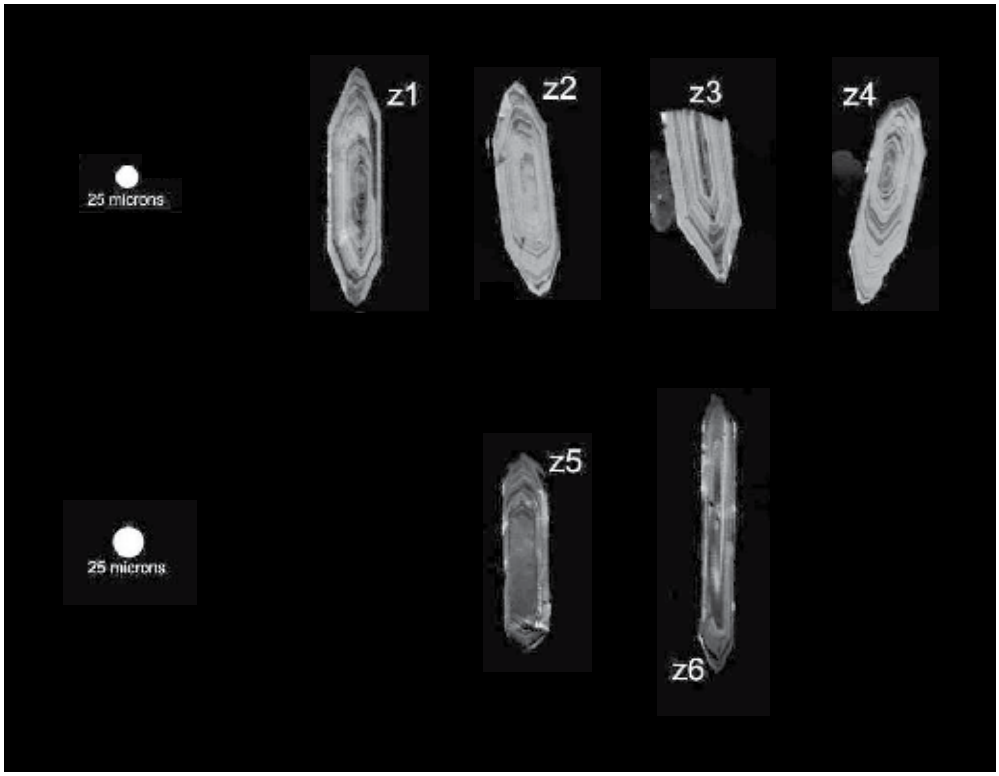

Figure A7. *CL images of zircon grains from Caribou intrusion (sample 09TOA180).*

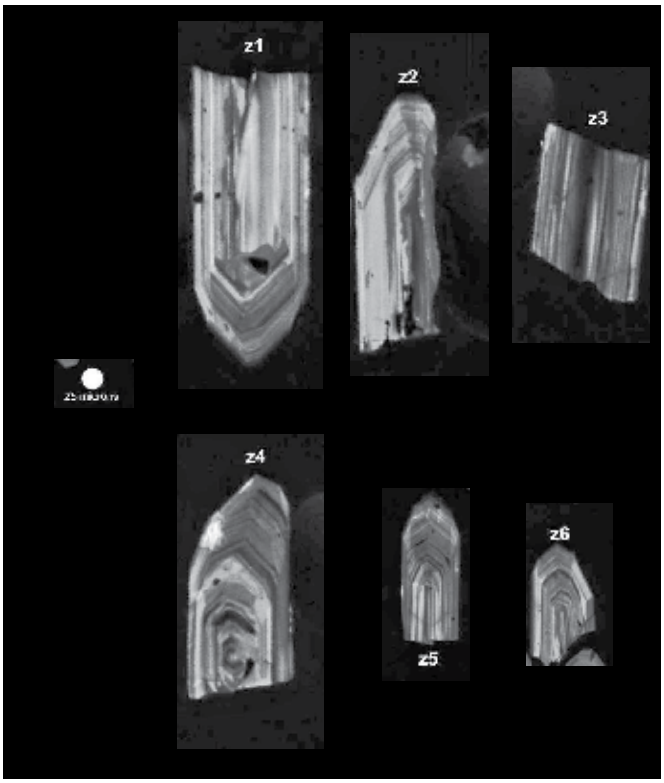

Figure A8. *CL images of zircon grains from Spork 1 intrusion (sample 10TOA014).*

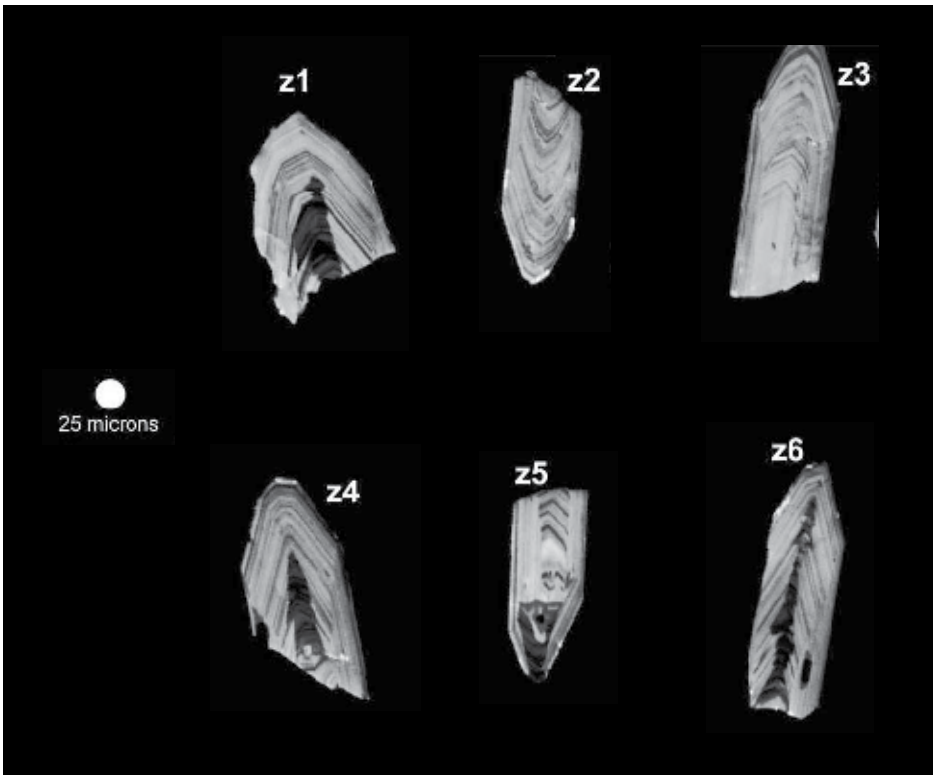

Figure A9. *CL images of zircon grains from Gusty intrusion (sample Gusty Lake).*

Sedimentary pyrite as a gold-source in sediment-hosted gold occurrences in the Selwyn basin area, eastern Yukon

Patrick J. Sack[1]
Yukon Geological Survey

L.V. Danyushevsky, R.R. Large, S. Gilbert, and D. Gregory
CODES, ARC Centre of Excellence in Ore Deposits, University of Tasmania, Australia

Sack, P.J., Danyushevsky, L.V., Large, R.R., Gilbert, S., and Gregory, D., 2014. Sedimentary pyrite as a gold-source in sediment-hosted gold occurrences in the Selwyn basin area, eastern Yukon. *In:* Yukon Exploration and Geology 2013, K.E. MacFarlane, M.G. Nordling, and P.J. Sack (eds.), Yukon Geological Survey, p. 195-220.

ABSTRACT

Intrabasinal sedimentary pyrite has recently been proposed as a potential gold source for sediment-hosted gold deposits. To evaluate this concept in the Selwyn basin area of eastern Yukon, we use laser ablation-inductively coupled plasma-mass spectrometry (LA-ICP-MS) to analyse pyrite from the Carlin-type Conrad, and orogenic gold 3Ace occurrences. This paper texturally and chemically characterizes four generations of pyrite in grey to black mudstones and siltstones, but focuses 83% of the analyses on early and late diagenetic pyrite. Diagenetic pyrite from the Conrad occurrence is trace element poor with respect to deposit-proximal pyrite from shales in the Northern Carlin Trend of Nevada, but is similar in composition to distal diagenetic pyrite in these Nevada shales. Diagenetic pyrite from the 3Ace occurrence is very similar in composition to pyrite around the giant Sukhoi Log deposit in eastern Russia. It can be preliminarily concluded that the trace element composition of diagenetic pyrite from the Conrad and 3Ace occurrences is permissive of a locally derived intrabasinal sedimentary pyrite gold source.

[1] *patrick.sack@gov.yk.ca*

INTRODUCTION

The Selwyn basin area of eastern Yukon has seen significant discoveries of sediment-hosted gold (*i.e.*, Carlin-type and orogenic gold deposit styles) in recent years. Carlin-type gold was discovered in 2010 on the northern margin of the Selwyn basin area (*e.g.*, Tucker *et al.*, 2013), and a recent review of these occurrences indicates they share many similarities with deposits found in Nevada (Arehart *et al.*, 2013). 3Ace, an orogenic gold occurrence in the SE part of the basin (Hart and Lewis, 2006), is another of these discoveries, returning multi-gram gold intercepts (*e.g.*, Northern Tiger Resources, October 25, 2011 news release). These recent gold discoveries mark newly identified metallogenic events for the Selwyn basin area, an area historically known for sedimentary exhalative (SEDEX) base metal deposits (Goodfellow, 2007). Most of what is known about the Selwyn basin area comes from the base metal exploration boom between the mid-1970's and early-1990's (*e.g.*, Abbott *et al.*, 1990; Goodfellow *et al.*, 1995; Goodfellow and Jonasson, 1987; Gordey and Anderson, 1993; Lydon *et al.*, 1979; Pigage, 1990). The notable exception to this is work done on reduced intrusion related gold systems in the northwest portion of the Selwyn basin area (*e.g.*, Hart, 2007; Lang and Baker, 2001). Another phase of research in Selwyn basin area geology is underway with the recent gold discoveries stimulating regional mapping (Chakungal and Bennett, 2011; Colpron, 2012; Colpron *et al.*, 2013; Moynihan, 2013) (Moynihan, 2014)and deposit research (Arehart *et al.*, 2013; Sack *et al.*, 2013; Tucker *et al.*, 2013; Whelan *et al.*, 2013).

Concurrent with, and slightly preceding, the recent surge in sediment-hosted gold exploration interest in the Selwyn basin area, have been technical advances in micro-analytical techniques allowing higher quality, faster, and less expensive studies of mineral chemistry, specifically on sulphides such as pyrite. Mineral petrogenesis coupled with laser ablation-inductively coupled plasma-mass spectrometer (LA-ICP-MS) pyrite studies have led to a new source-rock model using sedimentary pyrite, in local carbonaceous sedimentary rocks, as a gold, and associated trace element, source for sediment-hosted gold deposits (Large *et al.*, 2011). This model has subsequently been supported by fluid inclusion data (Gaboury, 2013), as well as additional pyrite chemistry data from other gold systems (*e.g.*, Large *et al.*, 2012). From a regional exploration perspective, this model is significant because it posits that regionally extensive sedimentary rocks, which host gold deposits, are likely to be the source of gold for these deposits. Furthermore, given that gold in these rocks is dominantly within pyrite, analyses of the sedimentary pyrite from intrabasinal strata may allow evaluation of the gold fertility of a basin. This is much different than most accepted sediment-hosted gold models that source gold from outside the basin (*e.g.*, metamorphic and/or magmatic fluids, Cline *et al.*, 2005; far travelled metamorphic fluids, Groves *et al.*, 1998). If this new model is correct, it potentially provides a powerful, first order discriminant of sedimentary basin (or specific strata within a basin) gold productivity, that is, does the sedimentary pyrite contain enough gold to produce economic sediment-hosted gold deposits? In this paper, we characterize predominantly sedimentary pyrite from two sediment-hosted gold occurrences in the Selwyn basin area, and compare these data against published pyrite data from near analogue deposits.

STUDY LOCATIONS

To investigate the potential of sedimentary pyrite as a gold-source in the Selwyn basin area, we sampled diamond drill core from two of the better known sediment-hosted gold occurrences, the Carlin-type Conrad occurrence (Tucker *et al.*, 2013) and the orogenic gold 3Ace occurrence (Hart and Lewis, 2006; Fig. 1). Neither occurrence has a defined resource, and only preliminary research has been completed (*e.g.*, Sack *et al.*, 2013; Tucker *et al.*, 2013; Whelan *et al.*, 2013), but both have been diamond drilled and a simple geological characterization of them is possible. A preliminary comparison between the Yukon Carlin-type occurrences (*e.g.*, Osiris, Conrad, and Isis) and the Carlin-type deposits in Nevada determined that they share many similarities, however more detailed research on the Yukon occurrences is needed (Arehart *et al.*, 2013). The main difference noted was the lack of Tertiary extension and magmatism near the Yukon examples (Arehart *et al.*, 2013). Initial work on the Conrad occurrence has demonstrated drill intercepts in the 1 g/t to 10 g/t Au range over 10's of metres, with the best intercept to date being 42.93 m of 18.44 g/t Au; including 16.73 m of 30.85 g/t Au (J. Lane, written comm.), which is comparable to the grade of Carlin-type deposits in Nevada (Cline *et al.*, 2005).

The 3Ace occurrence is found within the southeastern portion of the Tintina Gold Belt (Hart *et al.*, 2002), and was originally thought to be intrusion-related in origin, but a preliminary review of occurrences in the area by Hart and Lewis (2006) determined that the 3Ace occurrence shares more similarities with the orogenic gold deposit

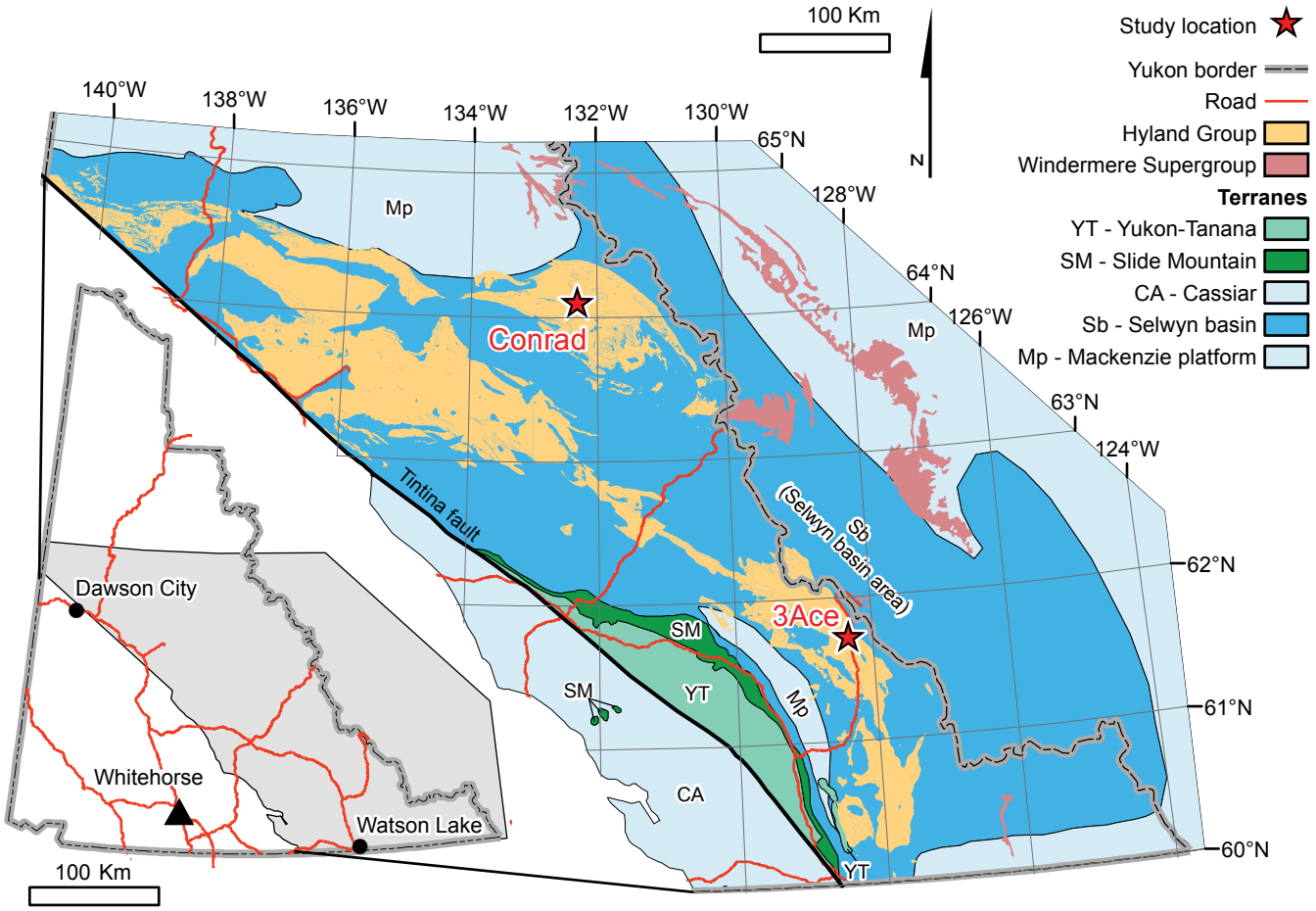

Figure 1. *Generalized geological map showing extent of the Selwyn basin area and distribution of Neoproterozoic strata in the northern Canadian Cordillera. The regional distribution of Windermere Supergroup is from Wheeler and McFeely (1991), and Hyland Group is from Gordey and Makepeace (2001). Note that the Conrad occurrence is shown as being hosted within the Hyland Group, but recent mapping by Colpron et al. (2013) places it within the Windermere Supergroup. Inset at bottom left shows extent of this map with respect to the Yukon Territory.*

style. The nearby Justin property, approximately 5 km to the east, has potential intrusion-related gold mineralization and preliminary fluid inclusion data on the Main Zone vein at the 3Ace are permissive of either magmatic or metamorphic fluid sources (Whelan *et al.*, 2013). Orogenic gold deposits tend to have a slightly higher, but less consistent, Au grade compared to Carlin-type deposits, with orogenic grades typically ranging from 3 g/t to 15 g/t Au (Goldfarb *et al.*, 2005). The best intercept, to date, from the 3Ace occurrence is 4.6 g/t Au over 35 m with several other intercepts between 1.4 g/t and 3.8 g/t Au over 10s of metres (Northern Tiger Resources, September 26 and October 25, 2011 news releases), similar in grade to known orogenic gold deposits. Both occurrences have mineralized diamond drill intercepts over several hundreds of metres of strike length and intercept grades comparable to known deposit grades. From the point of view of this study, the Conrad occurrence is a reasonable example of Carlin-type mineralization (Tucker *et al.*, 2013) and the 3Ace occurrence of orogenic gold mineralization (Hart and Lewis, 2006); where they sit exactly in their respective deposit-type spectrums is not currently known.

REGIONAL GEOLOGY

Eastern Yukon, north of the Tintina fault, is primarily made up of sedimentary and minor volcanic rocks of western Laurentian affinity that are Paleoproterozoic and younger (Nelson *et al.*, 2013). In broad terms, these can be divided into a 'basement', composed of rocks approximately

1.6 Ga to 0.78 Ga, and overlying Neoproterozoic–Paleozoic basinal sedimentary rocks (Gordey and Anderson, 1993; Fig. 2). The oldest of the 'basement' rocks, the 1.64 Ga to 1.60 Ga Wernecke Supergroup, comprises a sequence of sedimentary rocks that were deposited in a broadly subsiding marine basin, presumably floored by crystalline basement (Thorkelson *et al.*, 2001). These are intruded, and overlain by, mafic volcanic rocks of the Hart River sills and basalts (Abbott, 1997). Siliciclastic and carbonate rocks of the Pinguicula Group were deposited unconformably on the Hart River basalts in a slope to basin environment, and preliminary detrital zircon data suggest they are younger than approximately 1.15 Ga (Medig *et al.*, 2012). The youngest 'basement' rocks are the Mackenzie Mountain Supergroup, a thick succession of shallow marine limestone, evaporite, and fluvial sedimentary rocks deposited in an extensional basin, possibly as an early product of the breakup of Rodinia (Turner and Long, 2008). Collectively, these four units make up the 'basement' for post-0.78 Ga rift-related sedimentary rocks belonging to the Windermere Supergroup (Abbott, 1997; Eisbacher, 1981), the uppermost strata of which is broadly time-equivalent with the lowermost Selwyn basin stratigraphy, the Hyland Group (Moynihan, 2014).

SELWYN BASIN AREA

The term 'Selwyn basin' has seen several uses since its creation by Gabrielse (1967), and is thoroughly discussed in Gordey and Anderson (1993). The commonly accepted definition of Gordey and Anderson (1993, p. 14-15) which defines Selwyn basin as *"a region of deeper water offshelf sedimentation that persisted from the late Precambrian to Middle Devonian"* is used in this study. In the study area, the late Precambrian Hyland Group through to the Ordovician-Devonian Road River Group make up the basin stratigraphy; the overlying Devono-Mississippian Earn Group is not part of the basin stratigraphy (Gordey and Anderson, 1993). Though the upper Windermere Supergroup and lower Hyland Group are broadly age-equivalent, the majority of Windermere rocks are much older and thus not part of Selwyn basin (Moynihan, this volume). When referring to the geographical area roughly delineated by the Paleozoic carbonate-shale boundary, an area that includes both Windermere Supergroup and Hyland Group rocks, the term Selwyn basin area is used, as outlined in Figure 1.

The recently discovered, disseminated, Carlin-type gold occurrences (*e.g.*, Conrad, Osiris, and Isis zones) are predominantly found in fine-grained siliciclastic and carbonate rocks of the Neoproterozoic Windermere Supergroup, in the eastern part of the Rackla belt, north of the Dawson fault (Figs. 1 and 2; Colpron *et al.*, 2013; Tucker *et al.*, 2013). This belt straddles the Dawson fault, which defines the northern margin of Selwyn basin (Abbott, 1997). To the south of the Dawson fault, hanging wall stratigraphy consists of coarse-grained Hyland Group rocks, unconformably overlain by fine-grained Earn Group shale, chert, and sandstone, which are capped by Carboniferous to Triassic strata (Colpron *et al.*, 2013). Stratigraphy of the upper Windermere Supergroup in the footwall, to the north of the Dawson

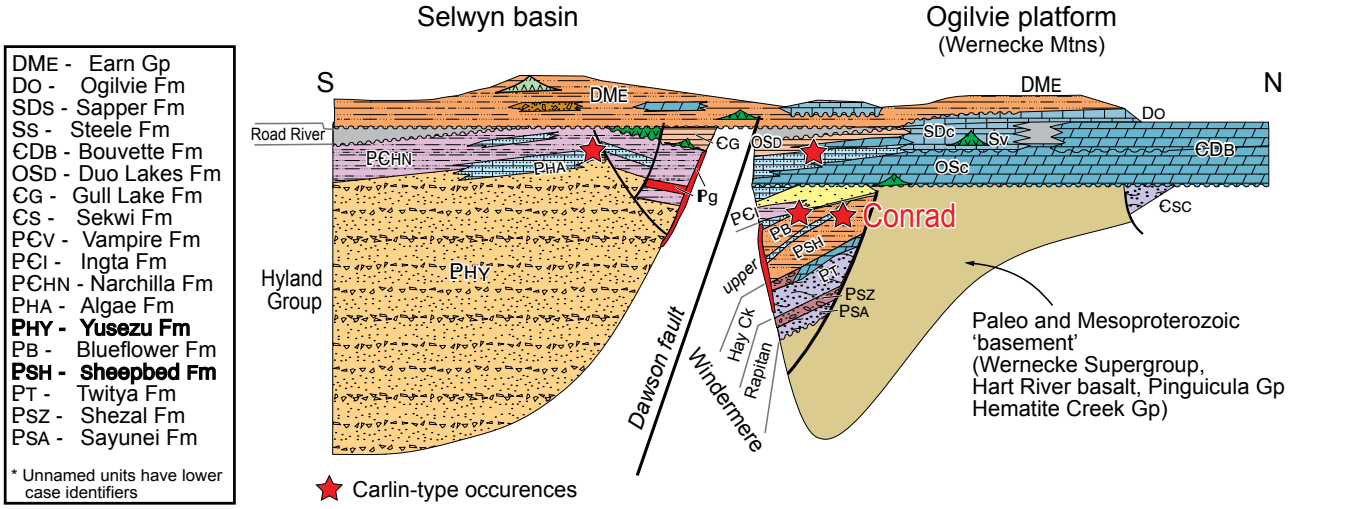

Figure 2. *Schematic north-south cross-section of the study area near the Conrad occurrence in east-central Yukon showing stratigraphic relationships for Neoproterozoic and younger strata of the Ancestral North American margin from Nelson et al. (2013) after Abbott (1997).*

fault, is generally correlative, but of very different facies (Colpron *et al.*, 2013). These upper Windermere rocks in the Rackla belt are slope deposits and lateral facies variations of Windermere Supergroup, as seen in the Wernecke Mountains and Mackenzie Mountains to the north (Colpron *et al.*, 2013). These upper Windermere slope deposits pass southward into deeper-water basinal deposits of the Hyland Group (Yusezyu Formation) (Moynihan, 2014). The regional metamorphic grade of the rocks in the Rackla belt is prehnite-pumpellyite (Read *et al.*, 1991).

The 3Ace occurrence is located in the upper Hyland River valley of eastern Yukon (Hart and Lewis, 2006; Whelan *et al.*, 2013; Fig. 1), an area of poorly understood regional geology that was last mapped in the 1960's (Blusson, 1966). The most recent regional mapping nearby is NTS map sheet 105I, the map sheet directly to the north of the 3Ace occurrence (Gordey and Anderson, 1993). The 3Ace occurrence is hosted by quartz veins best developed in coarse-grained sandstone of the Yusezyu Formation of the Hyland Group. Regionally, the Hyland Group is characterized by coarse-grained siliciclastic rocks (Yusezyu Formation), overlain by a thin discontinuous limestone (Algae Formation), and capped by maroon and green shale (Narchilla Formation) (Cecile, 2000; Gordey and Anderson, 1993). Approximately 5 km to the northeast of the 3Ace occurrence is the March fault, a fundamental geologic structure that separates Hyland Group basinal facies rocks from slope facies rocks of the Vampire Formation (Gordey and Anderson, 1993; Fig. 3). This thrust fault may be southwest dipping, and likely began life as a synsedimentary Neoproterozoic structure, possibly a normal fault, which controlled regional facies distributions until at least the early-Cambrian; it was later reactivated as a thrust fault during regional Cretaceous deformation (Gordey and Anderson, 1993; Hart and Lewis, 2006). The regional metamorphic grade of rocks in the Hyland River valley area is sub-greenschist to lower greenschist facies (chlorite zone); rocks directly adjacent to intrusions have been contact metamorphosed up to amphibolite facies (Moynihan, 2013; Read *et al.*, 1991).

PROPERTY-SCALE GEOLOGY

CONRAD OCCURRENCE

The Conrad deposit is hosted by a limestone unit which cores a doubly plunging antiform trending north-northeast (Tucker *et al.*, 2013). This limestone unit is found within a southward-younging sedimentary package that can be divided into lower stratigraphy, that hosts the Conrad occurrence (Nadaleen formation), and upper stratigraphy, which hosts the Osiris occurrence (Gametrail Formation; Colpron *et al.*, 2013). In the vicinity of the Conrad occurrence, the Nadaleen formation consists of silty limestone with siltstone and sandstone as well as large carbonate debris flows interbedded with black shale and siltstone, all overlain by maroon and green siltstone (Tucker *et al.*, 2013). Locally, the Gametrail Formation consists of a main limestone package, capped by a sequence of silty limestone and siltstone, diamictite, and dolomite (Tucker *et al.*, 2013).

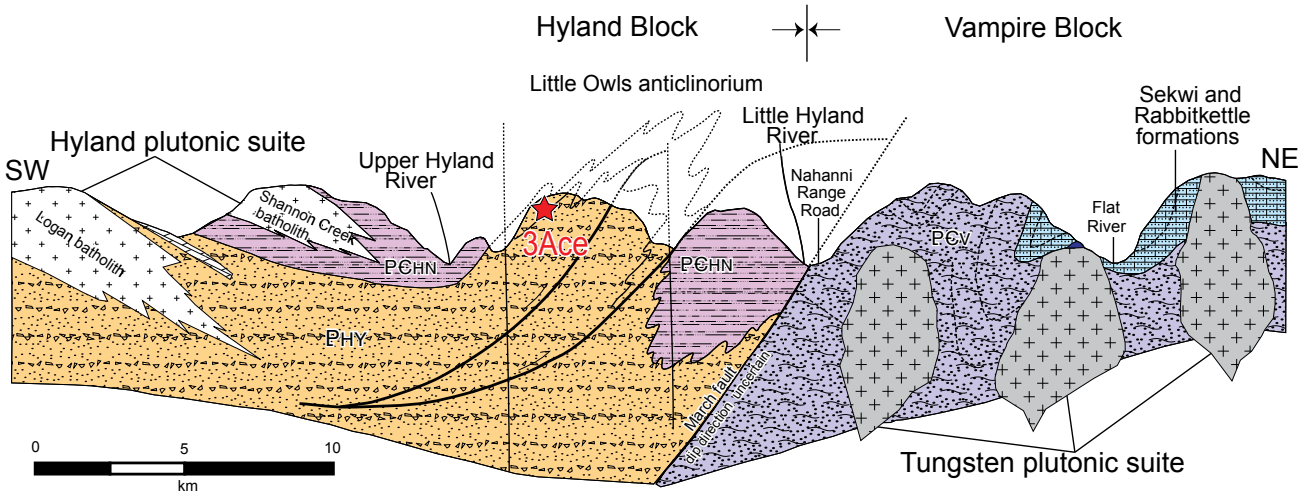

Figure 3. *Northeast-southwest schematic structural section of the upper Hyland River valley area (modified from Hart and Lewis, 2006); 3Ace occurrence projected approximately 20 km from the southeast. Unit abbreviations same as Figure 2.*

SUMMARY OF DIAMOND DRILL CORE LOGGING

Detailed logging of the mudstone-siltstone dominated intervals from two diamond drill holes into the Conrad occurrence was done in July 2012. Diamond drill hole OS11-74 is located in the middle of the Conrad occurrence with the best gold intersection starting at 245.97 m and consisting of 33.11 m of 2.67 g/t Au (ATAC Resources, November 23, 2011 news release). Diamond drill hole OS11-70 is located approximately 300 m west, on the western flank of the occurrence with several gold intersections (Fig. 4), the best of which is 15.24 m of 7.51 g/t Au starting at 243.84 m (ATAC Resources, November 23, 2011 news release).

Diamond drill hole OS11-74 has core recovery starting at 3.2 m depth and the hole ending at 639.17 m, but is heavily faulted in the upper 92 m; the interval from 3.2 m to 248.72 m was logged for this study and is shown graphically in Figure 4. The interval from 3.2 m to 25.47 m consists of a heavily faulted dark brown to black limestone breccia with a calcareous matrix, from 25.47 m to 92.0 m is also heavily faulted but with short (<2 m) unfaulted sections, the core is dominantly thinly laminated, dark grey to black, very fine-grained sandstone and siltstone with variable carbonate content (Fig. 5). The interval from 92.0 m to 102.0 m consists of dolomite with realgar and orpiment veins. From 102.0 m to 155.83 m are a series of thin (1-3 m) normally graded, polymictic pebble to coarse

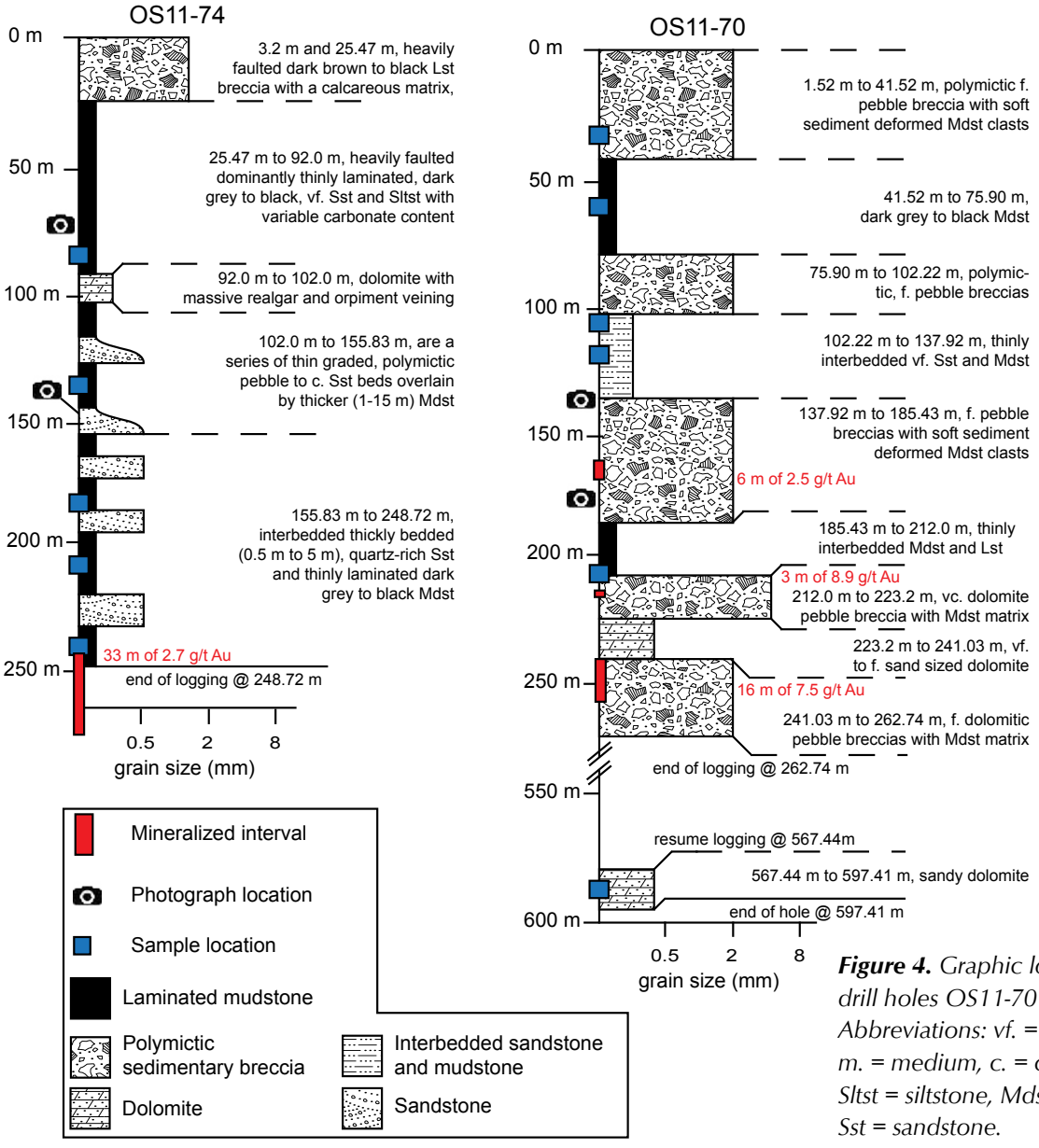

Figure 4. *Graphic logs of diamond drill holes OS11-70 and OS11-74. Abbreviations: vf. = very fine, f. = fine, m. = medium, c. = coarse; Lst = limestone, Sltst = siltstone, Mdst = mudstone, Sst = sandstone.*

sandstone beds overlain by thick intervals (1-15 m) of thinly laminated mudstone that is variably calcareous. The interval from 155.83 m to 248.72 m (end of logging) is made up of thickly bedded (0.5 m to 5 m), coarse-grained quartz sandstone interbedded with thinly laminated dark grey to black mudstone (Fig. 5). Sandstone-dominated intervals vary from 1 m to 10 m in apparent thickness and mudstone-dominated intervals are slightly thicker, varying between 1 m and 15 m.

Diamond drill hole OS11-70 is 597.41 m long with recovery starting at 1.52 m; 1.52 m to 262.74 m and 567.44 m to 597.41 m were logged for this study and are shown graphically in Figure 4. The core in this hole is less faulted than that in OS11-74, but does have short (<1 m to 10 m) faulted intervals. The interval from 1.52 m to 41.52 m is a weakly stratified to unstratified, poorly sorted, polymictic fine pebble breccia with soft sediment deformed mudstone clasts, white quartz clasts, light grey dolomite clasts and pale green mudstone clasts. The pale green clasts are likely of upper Nadaleen formation origin. Within this interval are several interlaminated mudstone and sandstone sequences up to 8 m in apparent thickness, some with highly irregular and contorted bedding suggesting soft sediment deformation. The interval from 41.52 m to 75.90 m is dominantly dark grey to black mudstone but includes thin dolomitic beds from 53.15 m to 59.0 m and complex, soft sediment deformed beds between 59.0 m and 75.90 m; the upper 11.63 m is intensely faulted. Between 75.90 m and 102.22 m, are normally graded, polymictic, fine pebble breccias with angular to subrounded limestone clasts and minor black mudstone clasts. Several short intervals within these breccias are intensely altered, displaying noticeable decalcification and minor realgar (Fig. 5). The interval between 102.22 m and 137.92 m is dominated by thinly interbedded very fine-grained sandstone and mudstone that is weakly dolomitic; some mudstone sections show evidence of both brittle and ductile (soft sediment) deformation. From 137.92 m to 185.43 m are several thick (up to 20 m) horizons of normal and reverse graded, fine pebble breccias with soft sediment deformed mudstone clasts (Fig. 5). The interval between 185.43 m and 212.0 m is thinly interbedded mudstone and limestone with faulted intervals from 185.43 m to 193.0 m and 198.12 to 206.0 m. The interval from 212.0 m to 223.2 m is a reversely graded, very coarse dolomitic pebble breccia with a mudstone matrix. From 223.2 m to 241.03 m is a very fine to fine-grained, weakly bedded dolomite. The interval from 241.03 m to 262.74 m (end of continuous logging) consists of several fine dolomitic pebble breccias with white quartz and dolomitic clasts within a dolomitic mudstone matrix; the breccias are separated by very fine grained dolomite intervals <5 m in apparent thickness. The interval at the bottom of the hole, 567.44 m to 597.41 m, is composed of weakly bedded fine to medium-grained dolomite including two reversely graded and one normally graded, coarse sandstone to fine pebble conglomerate beds approximately 75 cm thick.

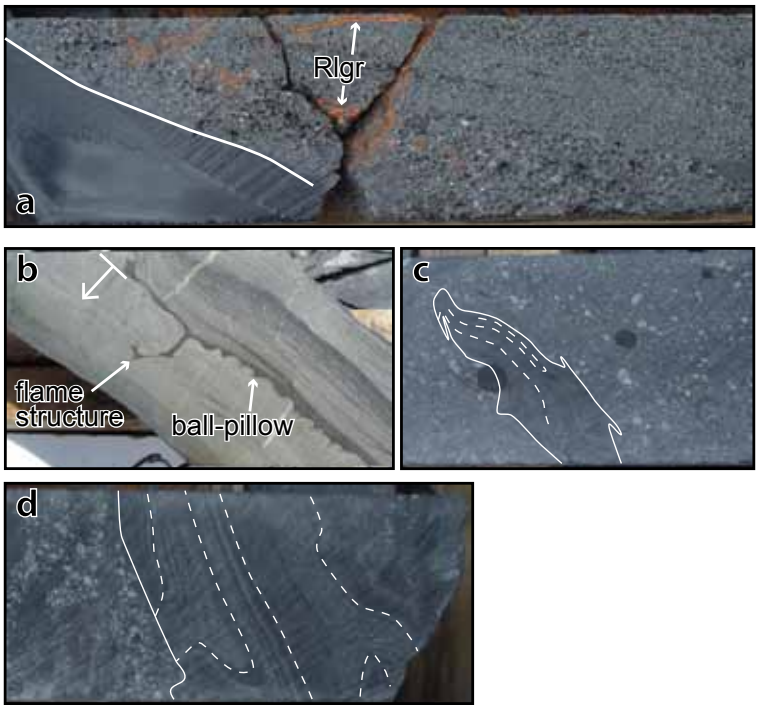

Figure 5. *Representative rocks from the Conrad occurrence, location of photos shown on Figure 4. (a) OS11-74 at 76.90 m: decalcified and silicified fine pebble conglomerate with realgar (Rlgr) in veins and on fractures. (b) OS11-74 at 146.70 m: load structures in fine sandstone and mudstone, way-up indicated by flat-bottomed arrow. (c) OS11-70 at 177.66 m: deformed mudstone clast (outlined in solid white) within pebble conglomerate. (d) OS11-70 at 139.0 m: base of a fine pebble conglomerate bed eroding complexly deformed, siltstone-mudstone beds. All photos of NQ diamond drill core; approximately 5 cm in diameter.*

The abundance of coarse-grained, graded beds and polymictic, pebble breccias with soft sediment deformed, mudstone clasts are interpreted as slump or debris flow deposits. Intervening periods of quiet water sedimentation were deposited as the thicker mudstone sequences. These interpretations are consistent with an overall slope, or near slope depositional environment as suggested by other researchers (*e.g.*, Arehart *et al.*, 2013; Colpron *et al.*, 2013; Tucker *et al.*, 2013).

3ACE OCCURRENCE

Property-scale mapping (1:10 000) at the 3Ace occurrence has documented a series of imbricated, north-dipping, thrust stacks of Hyland Group rocks (Buchanan and Oullette, 2013). Most of the mapped lithologies are consistent with the Yusezyu Formation as described by Gordey and Anderson (1993). At 3Ace the Yusezyu Formation consists of coarse-grained, arkosic sandstone and coarse to medium-grained quartz pebble conglomerate containing approximately 30% black and grey phyllites (Buchanan and Oullette, 2013). Near the northern limit of property mapping, and continuing further north, a series of calcareous lithologies have been tentatively correlated with the Algae Formation (Buchanan and Oullette, 2013), as noted elsewhere, stratigraphically above the Yusezyu Formation (*e.g.*, Cecile, 2000; Colpron, 2012; Colpron *et al.*, 2013). The lower greenschist (chlorite zone) regional metamorphism (Read *et al.*, 1991) has not recrystallized the rocks and is best seen in the fine-grained, carbonaceous, siliciclastic-dominated intervals that are now fine-grained, carbonaceous, black phyllites; sedimentary features such as grain size, bedding, grading, and load structures are easily recognizable. Due to the generally intimate laminations between mudstone and very fine-grained sandstone in the carbonaceous phyllite intervals, the overall low metamorphic grade, and the easily seen sedimentary structures, the terms mudstone and sandstone are used as opposed to phyllite to emphasize the protolith grain size difference; it is recognized that the rocks are weakly metamorphosed. Two sets of strike-slip faults cross-cut the stratigraphy; the Main Zone, where the holes used in this study were drilled, is along a north-striking fault. There are several east-striking faults on the property as well.

SUMMARY OF DIAMOND DRILL CORE LOGGING

Five hundred and ninety-one metres of core from two holes into the Main Zone at Northern Tiger Resources' 3Ace property were logged in late July and early August 2012. Diamond drill hole 3A11-15A is located in the centre of the Main Zone with the best gold intersection being 2.51 g/t Au over 27.2 m, starting at 83.30 m depth (Northern Tiger Resources, October 25, 2011 news release). Diamond drill hole 3A11-24A was collared 139 m to the south and did not intersect significant amounts of gold.

Diamond drill hole 3A11-15A, is 386.0 m long with recovery starting at a depth of 3.0 m; the entire hole was logged for this study and is shown graphically in Figure 6. The top interval from 3.0 m to 83.50 m is dominantly (~75%) very fine sandstone and lesser (~25%) interbedded mudstone. The sandstone is medium grey and thickly laminated to thinly bedded, with bed thicknesses ranging from 5 mm to 50 mm; the mudstone is black and thinly laminated, with bed thicknesses between 1 mm and 5 mm. The interval from 83.50 m to 103.10 m contains the best gold grades in the hole and is predominantly made up of massive, medium to coarse-grained sandstone with Au carried in cross-cutting, white quartz veins (Fig. 7); the upper approximately 3 m is a fine pebble, clast-supported conglomerate fining downhole into coarse-grained sandstone. The interval from 103.10 m to 257.72 m consists of alternating intervals (10-30 m) of coarse-grained sandstone to fine pebble conglomerate, and thinly laminated very fine sandstone and mudstone. Contacts between the fine and coarse-grained lithologies typically show depositional features such as loading (Fig. 7). The interval from 257.72 m to 343.50 m is a series of thick (0.5-7 m), normally graded beds with intervals (10 m or less) of medium to coarse-grained quartz sandstone. The remaining interval from 343.50 m to 386.0 m (end of hole) is heavily faulted, thinly interlaminated mudstone and medium-grained sandstone.

Diamond drill hole 3A11-24A was drilled to a depth of 205.0 m with recovery starting at 10.5 m. The interval between 10.50 m and 141.65 m is made up of alternating, thick sections (5-15 m) of dark grey to black, interbedded fine-grained sandstone and mudstone, and medium grey, coarse-grained, graded, and thickly bedded to massive quartz sandstone (Fig. 7). A bottom interval between 141.65 m and 205.0 m (end of hole) is composed of black, laminated mudstone (~90%) and very fine-grained dark grey sandstone (~10%).

Both holes logged from the 3Ace occurrence contain abundant, thick (up to 30 m) intervals of thickly-bedded to massive, coarse-grained sandstone (*e.g.*, 3A11-15A, 103.10 m to 257.72 m). There are also thick intervals of

fine-grained siliciclastic rocks (*e.g.*, 3A11-24A, 141.65 m to 205.0 m). The coarse grain size and thick-bedded nature of these rocks suggest they were deposited proximal to their source. This is consistent with deposition in submarine fan deposits proximal to the basin margin, but within the basin proper, as suggested by previous researchers (Gordey and Anderson, 1993; Hart and Lewis, 2006).

LA-ICP-MS ANALYTICAL METHODS

Two types of laser ablation-inductively coupled-mass spectrometer (LA-ICP-MS) instruments were used in this study to obtain quantitative spot data and semi-quantitative element image maps. These data were determined using a New Wave UP-213 Nd:YAG Laser Ablation System, coupled with either an Agilent 7500a ICP-QMS or an Agilent 7700s ICP-MS at the ARC Centre of Excellence in Ore Deposits at the University of Tasmania. The choice of ICP-MS was determined by availability, however both generated comparable datasets. Depending on the size of pyrite being ablated, the beam diameter was between 20 µm and 50 µm with most of the analyses done at 31 µm and 35 µm. All ablation was completed in an ultra-high purity He atmosphere, and the resulting aerosol was mixed with an Ar carrier gas before introduction to the ICP-MS. Laser energy of ~3.5 J cm^{-2} and a repetition rate of 5 Hz were used for all analyses. Data was collected over 70-90 s intervals, with a 30 s pre-ablation acquisition (background) interval and a 40-60 s acquisition interval. Generally 20 s of the laser-on data, equivalent to approximately 10 µm depth using a penetration rate of 0.5 µm/s, was used for data reduction. In most cases this was sufficient time to produce analyses with adequate detection limits (Table 1). However in the case of thin hydrothermal rims observed at the Conrad occurrence (1 µm to 5 µm; Tucker *et al.*, 2013), only seven analyses of rims were obtained.

Semi-quantitative element maps of pyrite were collected with the same analytical set-up as spot acquisition but using the technique described by Large *et al.* (2009). This technique consists of ablating sets of parallel lines in a grid pattern (rastering) across the sample and combining the data into false colour images of individual isotopes. Beam diameters of 15 µm to 25 µm with an ablation depth of approximately 1-2 µm were used in the creation of element maps. Lines were ablated with a repetition rate of 10 Hz, moving horizontally at 15 µm to 25 µm/s, making the effective spatial resolution of each pixel between one and two

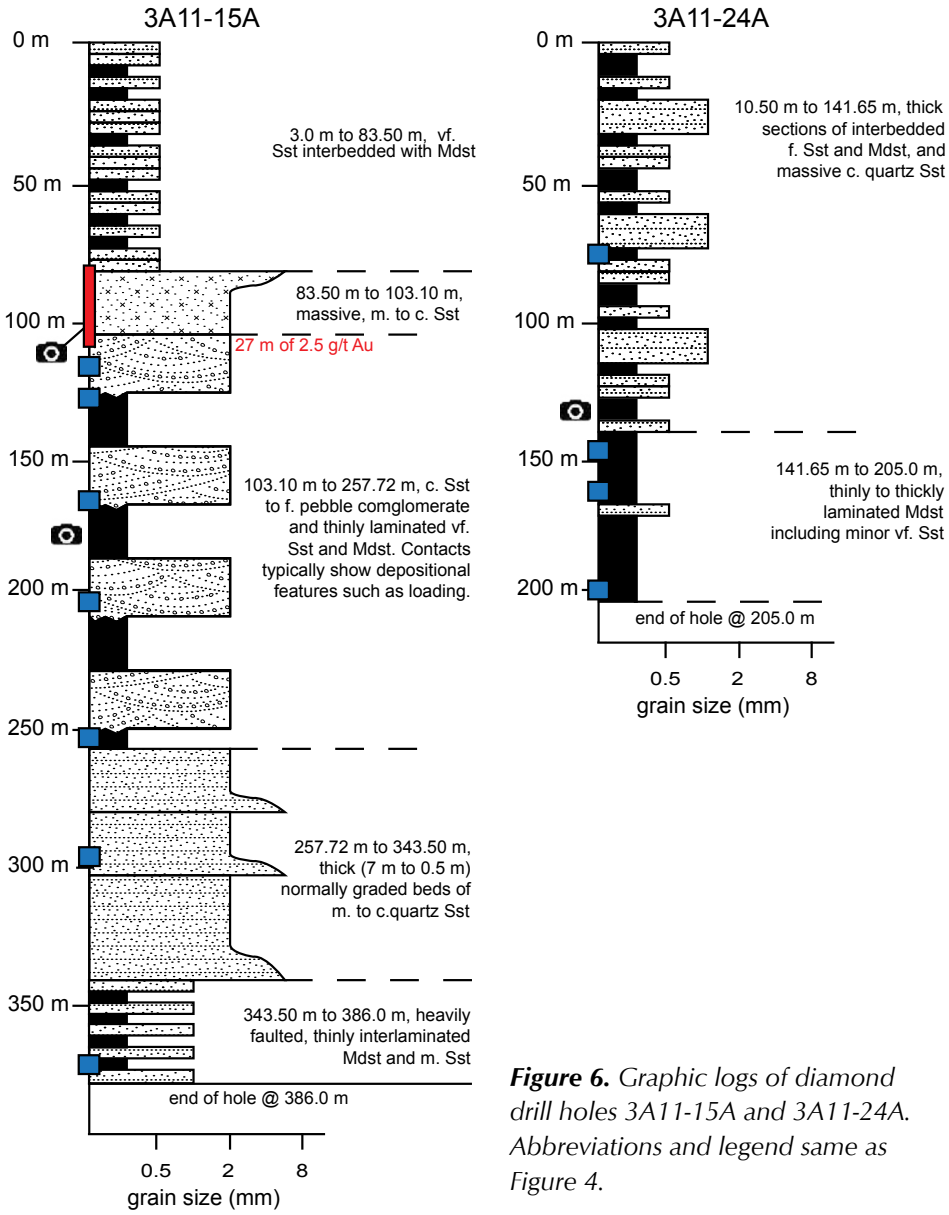

Figure 6. *Graphic logs of diamond drill holes 3A11-15A and 3A11-24A. Abbreviations and legend same as Figure 4.*

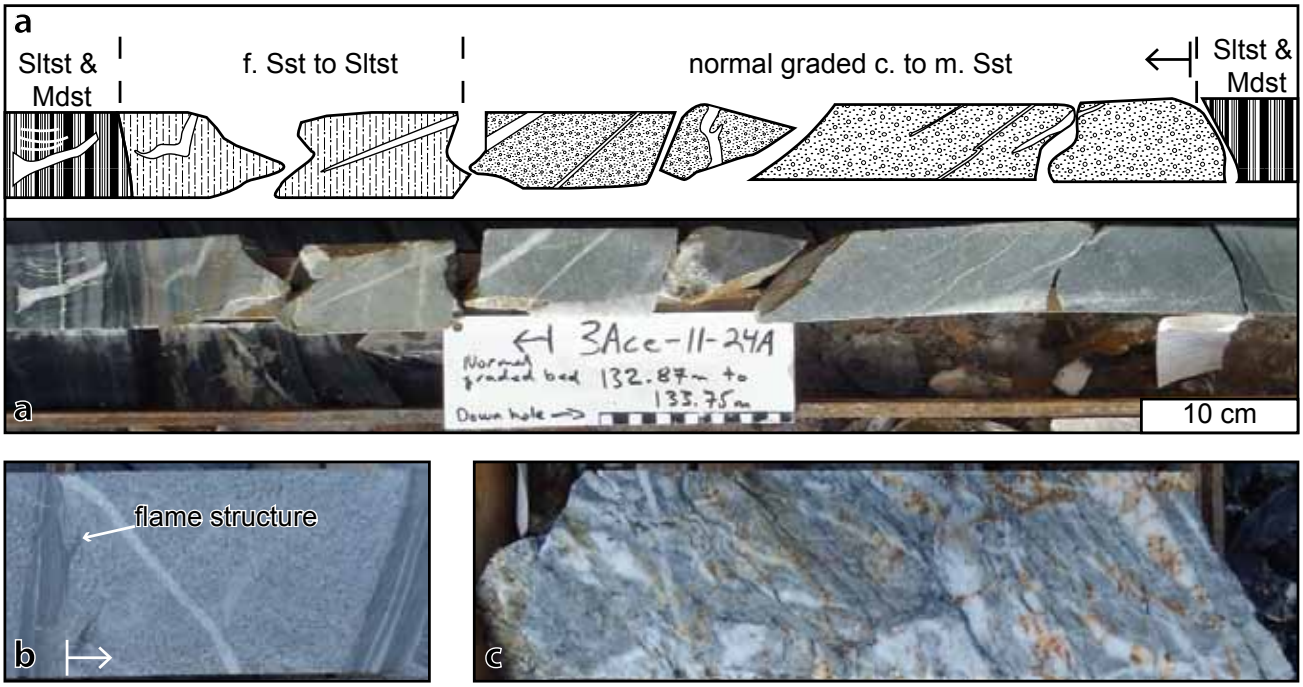

Figure 7. *Representative rocks from the 3Ace occurrence, location of photos shown on Figure 6. (a) 3A11-24A at 133.0m: approximately 1.1 m of core showing a 97 cm graded sandstone bed with mudstone above and below, way-up indicated by flat bottomed arrow. (b) 3A11-15A at 173.67 m: load structures in sandstone and mudstone, way-up indicated by flat bottomed arrow. (c) 3A11-15A at 101.28 m: strongly silicified and quartz veined sample of sandstone in the mineralized interval for this hole. All photos of NQ diamond drill core approximately 5 cm in diameter. Abbreviations same as Figure 4.*

times the beam diameter, depending on the chemical gradient (sharper gradients are easier to see). Processed images are displayed using a logarithmic colour scale corresponding to the signal intensities (counts per second) and not absolute abundance (*e.g.*, ppm). Changes in signal intensities greater than one order of magnitude can be confidently assigned to large changes in element content. Variations smaller than one order of magnitude may reflect subtler variations in element contents.

The calibration standard STDGL2b-2 was used to calculate contents and correct for instrument drift. STDGL2b-2, a certified reference material, is a lithium-borate fused disc of ore concentrate powder doped with certified element solutions (Danyushevsky *et al.*, 2011). Sulphide analyses calibrated on this standard yield an error of less than 15% for most elements. During spot analyses, the standards were analysed twice at the beginning and end of each session, before and after each sample change, and every one to two hours of analysis time. During imaging, the standard was analysed at the beginning and end of data acquisition. Iron was used as an internal standard to correct for differences in laser yield (Danyushevsky *et al.*, 2011). All spot analyses were corrected for linear drift and data reduction was undertaken following the methodology developed by Longerich *et al.* (1996); image data were corrected and reduced according to Large *et al.* (2009). Analyses of Hg concentrations of pyrite cannot be absolutely quantified due to the lack of suitable calibration standards. However, a ratio of Hg to Fe signal intensities can be calculated and used as a measure of relative variations in Hg contents. This ratio acts as a proportional proxy for the Hg content of pyrite. To enable a comparison between Hg/Fe values measured in different analytical sessions, the Hg/Fe values are normalized to Pb/Fe intensity ratios obtained in the same sessions.

RESULTS

PYRITE MORPHOLOGIES

Fine-grained pyrite morphologies (≤50 µm) include sooty microcrystalline aggregates and small anhedra to euhedra (Fig. 8) that are interpreted as having grown early in diagenesis (Large *et al.*, 2007; Raiswell and Plant, 1980). Framboidal pyrite of all sizes is also interpreted as early diagenetic, though under euxinic conditions, fine-grained

syngenetic examples may form within the water column (Large *et al.*, 2007; Raiswell and Plant, 1980; Wilkin *et al.*, 1996). Syngenetic and early diagenetic pyrites contain similar chemical information (Large *et al.*, in press) and for simplicity, we use the term early diagenetic to identify both types. Coarser grained morphologies (>50 µm to 200 µm) include nodular, and large anhedral to euhedral pyrite (Fig. 8) that are interpreted to have formed late in diagenesis at greater depths in the unconsolidated sediments where the nucleation rate is slower (Butler and Rickard, 2000). The formation of these coarser textures may involve some degree of recrystallization (Large *et al.*, 2011). Hydrothermal pyrite from the Conrad occurrence consists mostly of thin (1 µm to 5 µm), arsenian pyrite rims on precursor sedimentary pyrite (Fig. 8), though thicker anhedral to euhedral overgrowths also occur (Tucker *et al.*, 2013). Hydrothermal pyrite from the 3Ace occurrence is generally coarse-grained (>200 µm), and is either associated with quartz veins or as overgrowths on pre-existing sedimentary pyrite (Fig. 8). These four generations

Table 1. *Elements included in the LA-ICP-MS analytical suite. Elements shaded dark grey are used for quality control purposes, elements shaded light grey are primarily found with matrix material or are generally near or below detection in our results (†) and are not discussed. Elements without shading are found primarily within pyrite (focus of this paper). *results for the three isotopes of Pb show similar results, this study uses Pb(206). LA detection limits are a function of spot size, integration duration, and trace element concentration. Detection limits quoted here are mostly the median values calculated for the 31 µm spot size and can be considered a representative average. For full detection limits at all spot sizes used in this study (20 µm, 31 µm, 35 µm, and 50 µm) see the digital Appendices.*

Element (isotope) - 31 µm detection limit in ppm	Element (isotope) - 31 µm detection limit in ppm
Na(23) - 6.22	Mo(95) - 0.021
Mg(24) - 0.104	Ag(107) - 0.022
Al(27) - 0.300	Cd(111) - 0.070
Si(29) - 106	Sn(118) - 0.107
S(34) - 2436	Sb(121) - 0.075
K(39) - 2.61	Te(125) - 0.111
Ca(43) - 116	Ba(137) - 0.02
Ti(49) - 1.26	Gd(157)† - 0.02
V(51) - 0.067	Hf(178)† - 0.009
Cr(53) - 1.18	Ta(181)† - 0.003
Mn(55) - 0.478	W(182) - 0.009
Fe(57) - 5.17	Pt(195)† - 0.01
Co(59) - 0.018	Au(197) - 0.008
Ni(60) - 0.081	Tl(205) - 0.006
Cu(65) - 0.270	Pb(206)* - 0.017
Zn(66) - 0.365	Pb(207)* - 0.021
As(75) - 1.17	Pb(208)* - 0.011
Se(77) - 0.969	Bi(209) - 0.021
Rb(85) - 0.020	Th(232) - 0.004
Sr(88) - 0.003	U(238) - 0.004
Zr(90) - 0.006	

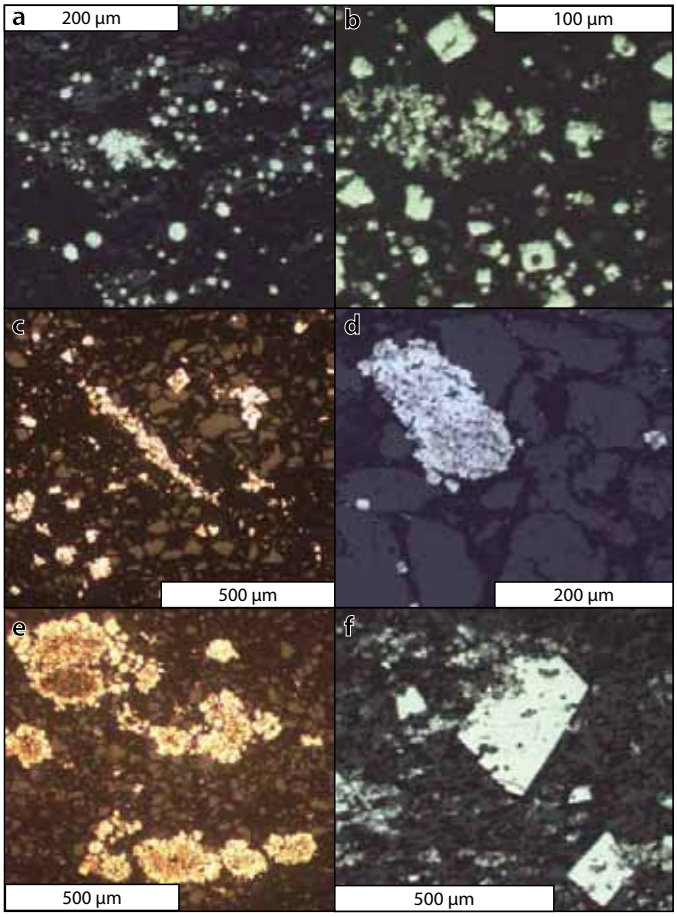

Figure 8. *Reflected light photomicrographs of various pyrite textures. (a) 3A11-24A at 199.30 m: framboidal pyrite. (b) OS11-74 at 76.90 m: early diagenetic fine-grained subhedra to euhedra. (c) OS11-74 at 216.0 m: late diagenetic pyrite nodule and coarse-grained subhedra. (d) OS11-70 at 207.90 m: late diagenetic subhedral pyrite. (e) OS11-70 at 57.25 m: early diagenetic fine-grained sooty microcrystalline core overgrown by cleaner hydrothermal pyrite rim 20 to 30 µm thick. (f) 3A11-15A at 169.97 m: fine-grained diagenetic anhedra overgrown by coarse-grained metamorphic pyrite.*

of pyrite: early diagenetic, late diagenetic, hydrothermal, and vein associated are the textural interpretations upon which our geochemical pyrite characterization are based.

The focus of sampling for this study was on sedimentary pyrite, specifically syngenetic pyrite and diagenetic pyrite; a small number of analyses were done on paragenetically late generations of hydrothermal and vein pyrite (Table 2). Our diagenetic sampling bias does not reflect the relative abundance of pyrite types in the samples, but rather where our analytical interests lie. Nearly half of the pyrite analysed in this study (46%) is fine-grained (≤50 µm) early diagenetic or syngenetic pyrite that occurs as both individual or aggregated framboidal and microcrystalline pyrite. Slightly coarser grained (>50 µm to 200 µm) euhedral to anhedral late diagenetic pyrite, commonly associated with nodules, made up 37% of the analyses. Secondary pyrite, commonly overgrowing diagenetic pyrite, was identified either as thin hydrothermal rims (Conrad) or coarse-grained metamorphic euhedra (3Ace), this population made up 13% of the analyses. A small number of analyses (4%) were done on coarse-grained pyrite associated with veins, but were not studied in detail.

Table 2. *Summary of pyrite morphologies and interpreted paragenesis for each occurrence.*

Pyrite morphology	Paragenetic class	Conrad	3Ace
microcrystalline aggregates, framboidal and small anhedral to subhedral	early diagenetic	47	68
nodular, and large anhedral to euhedral	late diagenetic	56	36
small anhedral overgrowths	hydrothermal	7	26
large euhedral overgrowths			
small to large euhedral	vein	7	2
	Total	**117**	**132**

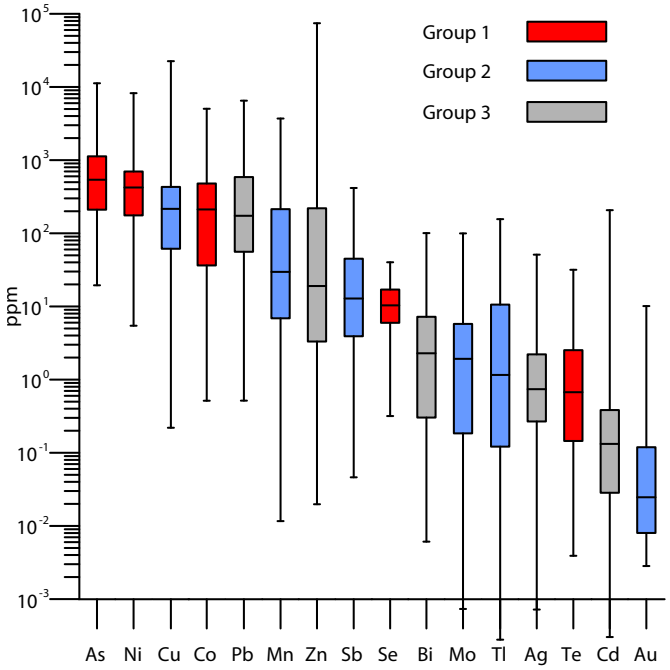

Figure 9. *Range of selected elements using all pyrite data; elements order according to decreasing median values and grouped according to distribution within pyrite as described in the text.*

GENERALITIES OF THE DATA

Data for 41 elements were collected for 249 spot analyses from 22 samples. Twelve of these samples were also image mapped for 41 elements. These data are available digitally in Appendices I and II. The suite of elements collected with the LA-ICP-MS can be broken down into: 1) elements used for internal quality control, 2) elements residing primarily in matrix minerals, and 3) elements primarily associated with pyrite (Table 1). Sulphur and Fe are used for internal quality control purposes, S data are used during processing to ensure results are stoichiometrically feasible for pyrite and Fe is used as the internal standard as described above; these elements are not discussed further. Data from 18 elements that are mostly hosted in matrix, either surrounding pyrite or as inclusions in the pyrite, are used to determine the phase being ablated. When plotted against Al, these matrix associated elements mostly have coefficients of determination (R^2 values) greater than 0.6 (*e.g.*, Na, Mg, Si, K, Ca, V, Cr, Rb, Sr, Zr, Sn, Ba) or are present in concentrations near or below detection limits (*e.g.*, Gd, Hf, Ta, Pt, Th). The remaining 19 elements are associated with pyrite and are the focus of this paper (Table 1).

Following the approach of previous researchers, trace elements are organized according to how they are distributed within pyrite. To accommodate the analytical suite used, the groupings of Huston *et al.* (1995) and Gregory *et al.* (in prep) are modified into the following:

- Group 1 elements (Ni, Co, As, Hg, Se, and Te): stoichiometrically substitute into the lattice of pyrite for Fe and S (Huston *et al.*, 1995), and typically have elevated and consistent LA signals across all element contents.
- Group 2 elements (Cu, Mn, Tl, Sb, Mo, and Au): have consistent LA signals at low element contents where they may be incorporated non-stoichiometrically into the lattice or be held as a uniform distribution of nano-inclusions. At higher element contents, the LA signal for these elements is highly variable, suggesting that they may occur as micro-inclusions (Gregory *et al.*, in prep).
- Group 3 elements (Pb, Zn, Ag, Bi, and Cd): typically have highly variable LA signals at all element contents and are thought to be held primarily within micro-inclusions (Gregory *et al.*, in prep).

Based on the study's entire data set, three generalities are noted. Firstly there are three ranges of trace element data (Fig. 9), in order of decreasing abundance these are: the main trace element constituents of pyrite, As, Ni, Cu, Co, and Pb (typically in the 100s to 1000s ppm range); minor trace element constituents of pyrite, Mn, Zn, Sb, Se, Bi, Mo, Tl, Ag, and Te (typically in the ppm to 10s ppm range); the ultra-trace element constituents of pyrite, Cd and Au, are typically sub-ppm. Secondly, pyrite that is interpreted as early diagenetic has the greatest trace element enrichment, followed by late diagenetic pyrite, hydrothermal, and vein-related pyrite (Fig. 10). Finally, pyrites from the 3Ace occurrence are generally more trace element-rich than those from the Conrad occurrence (Fig. 10).

CONRAD

Eleven samples from the Conrad occurrence were investigated with all four paragenetic classes of pyrite identified and analysed; 103 analyses were done on diagenetic pyrite with seven analyses each on hydrothermal and vein pyrite (Table 2). Besides cursory examination and noting that vein pyrite is depleted in trace elements compared to diagenetic pyrite (Fig. 10), the present study does not examine vein pyrite, and it is not discussed further. Results for elements primarily associated with pyrite are summarized in Table 3.

Early diagenetic and syngenetic pyrites at the Conrad occurrence are typically found as individual or amalgamated framboids or microcrystals; Figure 11 shows early diagenetic pyrite rimmed by hydrothermal pyrite with corresponding select element maps and downhole spectra. Group 1 elements (Ni, Co, As, Hg, Se, and Te) have median values that range from 357 ppm for Ni to 0.4 ppm for Te; Ni has the maximum value of 8347 ppm. The Conrad sedimentary pyrites have very elevated Hg/Fe*1000 ratios, varying from >0.1 to <4.0 with a mean of 0.52 and a median of 0.30. Group 2 elements (Cu, Mn, Tl, Sb, Mo, and Au) have median values that range between 283 ppm for Cu and 20 ppb for Au, Mn has the highest value of 3019 ppm. Group 3 elements (Pb, Zn, Ag, Bi, and Cd) have median values between 174 ppm for Pb and 190 ppb for Cd, Pb also has the maximum value of 2265 ppm.

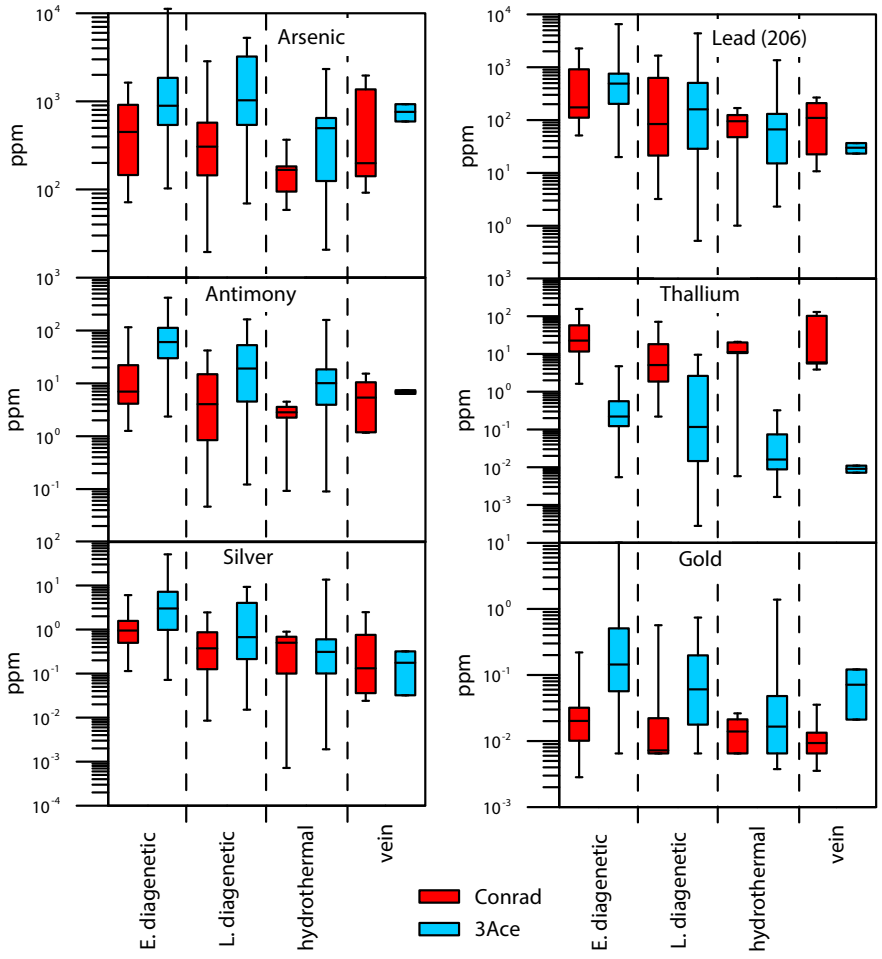

Figure 10. *Box-whisker plots of selected elements showing overall decrease in trace element concentrations between successive generations of pyrite.*

Table 3. *Summary statistics for the Conrad and 3Ace occurrences for elements associated with pyrite. Min. = minimum value, Med. = median value, and Max. = maximum value.*

		Group 1						Group 2						Group 3				
Conrad		**Ni**	**Co**	**As**	**Hg/Fe*1000**	**Se**	**Te**	**Cu**	**Mn**	**Tl**	**Sb**	**Mo**	**Au**	**Pb**	**Zn**	**Bi**	**Ag**	**Cd**
E. diagenetic	Min.	12	3	72	0.014	0.3	0.0	46	1	1.62	1.3	0.07	-0.002	51	2	0.10	0.11	-0.003
	Med.	357	303	449	0.491	7.0	0.4	283	74	22.59	7.0	2.46	0.020	174	26	1.66	0.95	0.190
	Max.	8347	1955	1632	4.051	21.7	5.6	1423	3019	155.95	115.4	63.94	0.219	2265	1116	14.27	6.03	2.211
L. diagenetic	Min.	6	1	19	0.000	0.7	0.0	3	0	0.22	0.0	0.01	-0.003	3	0	0.02	0.01	-0.019
	Med.	179	53	306	0.101	5.7	0.1	150	15	5.09	4.0	0.95	0.007	84	5	0.20	0.37	0.039
	Max.	3224	1162	2851	1.714	32.6	4.4	1689	682	71.03	41.9	25.03	0.566	1657	620	22.27	2.45	1.638
hydrothermal	Min.	6	1	59	0.014	2.7	0.0	16	0	0.01	0.1	0.00	0.000	1	0	0.01	0.00	-0.027
	Med.	106	172	167	0.805	5.2	0.8	247	982	11.23	2.8	2.10	0.014	95	86	1.19	0.50	0.124
	Max.	261	252	367	2.040	18.3	1.5	449	3718	20.96	4.5	3.53	0.026	169	258	2.28	0.89	0.479
3Ace		**Ni**	**Co**	**As**	**Hg/Fe*1000**	**Se**	**Te**	**Cu**	**Mn**	**Tl**	**Sb**	**Mo**	**Au**	**Pb**	**Zn**	**Bi**	**Ag**	**Cd**
E. diagenetic	Min.	170	1	103	-0.010	4.6	0.1	4	5	0.01	2.4	0.03	0.003	20	0	0.44	0.07	-0.330
	Med.	707	339	891	0.022	10.7	2.6	773	327	0.22	60.5	5.92	0.144	490	336	8.09	3.00	0.484
	Max.	2386	5006	11235	0.127	32.5	31.7	22639	3715	4.73	417.6	99.79	10.112	6534	40429	100.68	50.99	29.606
L. diagenetic	Min.	74	10	69	-0.008	8.5	0.0	0	0	-0.01	0.1	-0.03	-0.002	1	-1	0.03	-0.02	-0.326
	Med.	377	251	1028	0.014	18.4	2.5	45	9	0.12	19.1	0.17	0.061	160	8	3.59	0.67	0.086
	Max.	1092	5063	5259	0.075	36.2	19.1	2135	909	9.55	162.5	60.73	0.741	4371	74639	76.29	9.28	207.002
hydrothermal	Min.	47	1	21	-0.006	6.5	0.0	0	0	-0.01	0.1	-0.02	-0.003	2	-1	0.01	0.00	-0.238
	Med.	472	54	496	0.005	15.5	0.6	18	4	0.02	10.1	0.04	0.017	67	3	1.80	0.31	0.023
	Max.	1445	702	2329	0.066	40.4	8.4	10938	546	0.32	158.4	68.76	1.382	1356	32783	44.14	13.57	29.732

Late diagenetic pyrite at the Conrad occurrence is typically coarser grained (50 µm to 200 µm) euhedra to anhedra and the composition is more variable than that of the other paragenetic classes of pyrite. Group 1 elements have median values between 179 ppm for Ni and 0.4 ppm for Te, Ni has the maximum value of 3224 ppm. Group 2 elements median values vary between 150 ppm for Cu and 7 ppb for Au (~detection limit), the maximum value is 1689 ppm for Cu. Group 3 element median values vary between 84 ppm for Pb and 39 ppb for Cd, the maximum value is 1657 ppm for Pb.

Due to the thin (1 µm to 5 µm) rim morphology of most hydrothermal pyrite at the Conrad occurrence (Tucker *et al.*, 2013) only seven analyses were done and these were on ~20 µm thick rims (Fig. 11). Thin rims can be seen in many analyses, but the quality of data obtained from them is too low to be interpreted. The hydrothermal pyrite at the Conrad occurrence is trace element-poor: Group 1 elements have median values between 106 ppm for Ni and 0.8 ppm for Te, maximum value is 261 ppm for Ni; Group 2 median values vary between 982 ppm for Mn and 14 ppb for Au, with 3718 ppm for Mn the maximum value. Group 3 element median values vary between 95 ppm for Pb and 124 ppb for Cd, with a maximum of 258 ppm for Zn.

3ACE

Eleven samples from the 3Ace occurrence were investigated with all four paragenetic types of pyrite analysed; the majority of analyses were done on diagenetic pyrite with 26 analyses of hydrothermal pyrite (Table 2). Two analyses of vein pyrite were also done, but we do not discuss them further. Results for elements primarily associated with pyrite are summarized in Table 3.

Early diagenetic pyrite from the 3Ace occurrence is mostly framboidal; Figure 12 shows early diagenetic pyrite overgrown by hydrothermal pyrite with select element maps and downhole spectra. Group 1 median values vary between 891 ppm for As and 2.6 ppm for Te with 11 235 ppm As the highest value. Hg/Fe*1000 ratios are within the range of normal sedimentary pyrite, varying from <0.004 to 0.13 with a mean of 0.03 and a median of 0.02. Group 2 elements have median values ranging from 773 ppm for Cu to 144 ppb for Au, and a maximum value of 2.2% Cu. Group 3 median values range from 490 ppm for Pb to 484 ppb for Cd, with a maximum value of 4.0% Zn.

Late diagenetic pyrite are mostly 60 µm to 100 µm euhedra or microcrystalline nodules that generally have lower trace element contents than early diagenetic pyrite. Group 1 element median

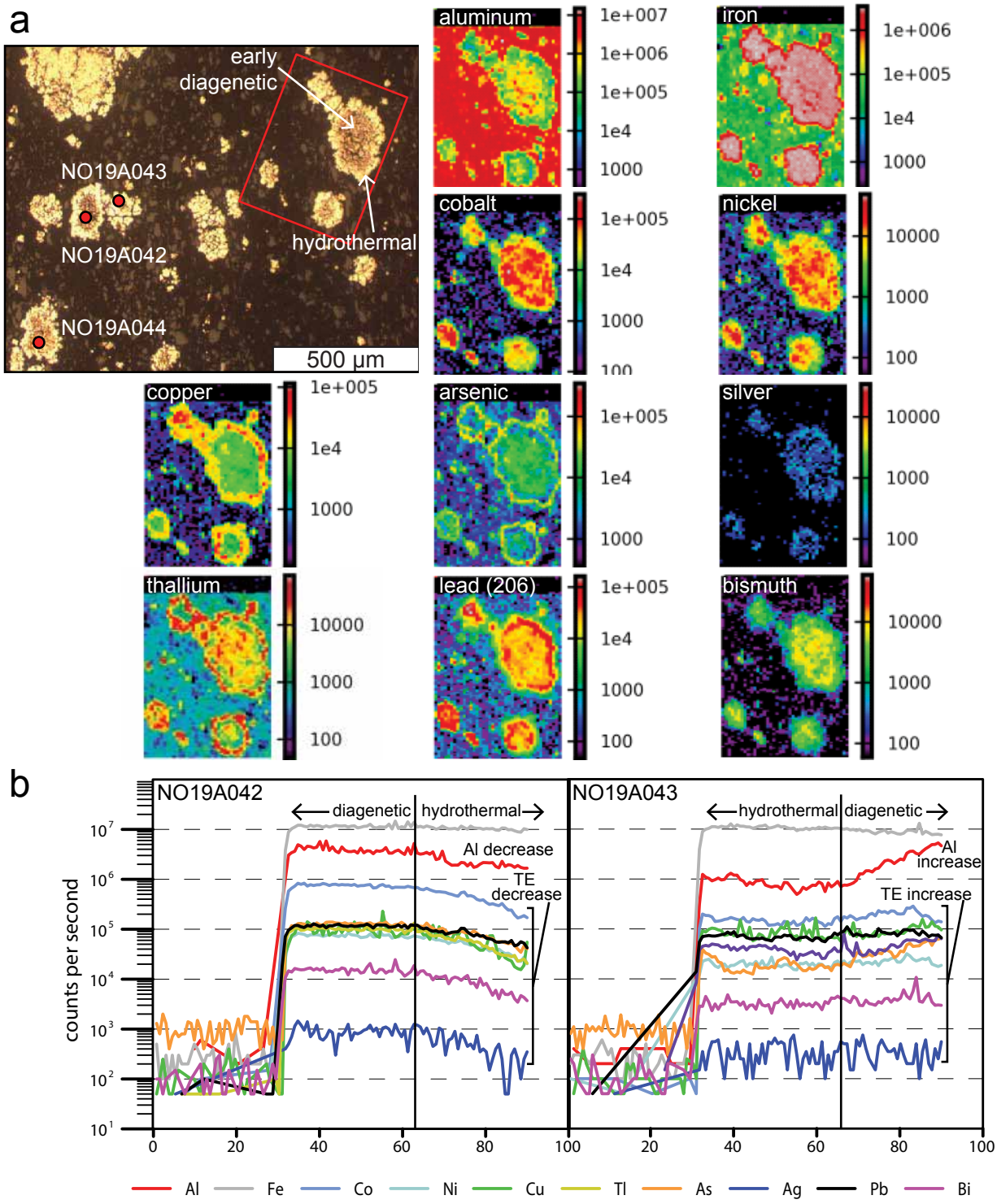

Figure 11. *Representative examples of: (a) element maps; and (b) downhole spectra from OS11-70 at 57.25 m. (a) the red box on the photomicrograph outlines the area mapped using the LA-ICP-MS technique of Large et al. (2009). Selected element maps show distribution of each element within the mapped area. Red circles represent LA-ICP-MS spot ablation sites labelled by analysis number. (b) Selected downhole LA-ICP-MS data for two of the analysis sites shown in a). TE = trace elements.*

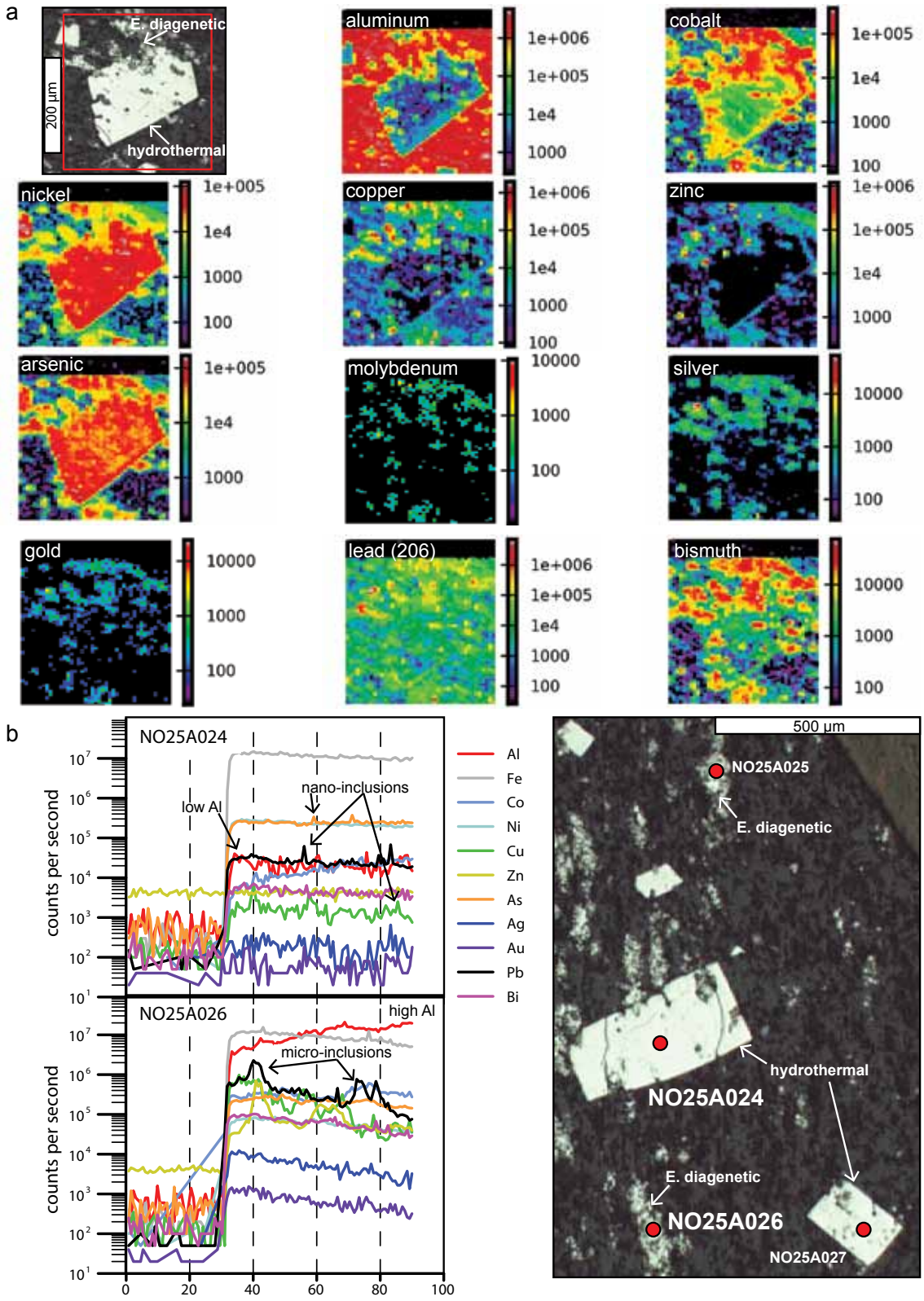

Figure 12. *Representative examples of: (a) element maps; and (b) downhole spectra from 3A11-15A-169.30 m. (a) Red box on the photomicrograph outlines the area mapped using the LA-ICP-MS technique of Large et al. (2009). Selected element maps show distribution of each element within the mapped area. (b) Red circles represent LA-ICP-MS spot ablation sites labelled with the analysis number; selected downhole LA-ICP-MS data for two of the analysis sites are shown.*

values range from 1028 ppm for As to 2.5 ppm for Te, 5259 ppm As is the maximum value. Group 2 elements have median values between 45 ppm for Cu and 61 ppb for Au, reaching a maximum of 2135 ppm Cu. Group 3 elements median values range from 160 ppm for Pb to 86 ppb for Cd, 7.5% Zn is the maximum. Hydrothermal pyrite at 3 Ace is typically coarse-grained (≥200 µm) euhedra overgrowing early diagenetic pyrite. Median values of Group 1 elements range between 496 ppm for As and 0.6 ppm for Te with a maximum value of 2329 ppm As. Group 2 elements have median values between 18 ppm for Cu and 17 ppb for Au, up to a maximum of 1.1% Cu. Group 3 median values range from 67 ppm for Pb to 23 ppb for Cd, with a maximum value of 3.3% Zn.

DISCUSSION

Our samples from the Carlin-type Conrad and orogenic gold 3Ace occurrences are from variably pyritic and calcareous, dark coloured siltstones and mudstones located near the ancient basin to slope transition of Selwyn basin; they are broadly age equivalent with Neoproterozoic (Ediacaran) depositional ages. The Conrad occurrence is hosted by unmetamorphosed mixed carbonate and siliciclastic strata deposited in a continental slope environment, whereas the 3Ace occurrence is hosted entirely within weakly metamorphosed, thick-bedded sequences of siliciclastics likely deposited further into the basin. Our samples share significant similarities (*e.g.*, lithology, age), but they also have significant differences (*e.g.*, depositional facies, style of mineralization, and metamorphic grade).

Ratios of Co/Ni, combined with Ni and Co contents, in pyrite are useful for determining the fluid source for pyrite formation (*e.g.*, Bajwah *et al.*, 1987; Bralia *et al.*, 1979; Clark *et al.*, 2004; Loftus-Hills and Solomon, 1967). Cobalt and Ni are incorporated into the pyrite lattice, and thus these elements are relatively immobile during recrystallization (Huston *et al.*, 1995), retaining their original signature under low intensity hydrothermal and metamorphic conditions, such as those experienced by the samples in our study. Conrad pyrite has a wide range of Ni contents, between 6 ppm and 8347 ppm, but a consistent Co/Ni ratio between 2 and 0.1 (Fig. 13). 3Ace pyrite has consistently high Ni values, mostly between 200 and 2386 ppm, but a wide variation in Co/Ni, ranging from 0.015 in hydrothermal pyrite to 30 in late diagenetic pyrite (Fig. 13). At the Conrad occurrence, the low ratio of Co/Ni suggests a sedimentary fluid source for all generations of pyrite, though the lower Ni content of hydrothermal pyrite may suggest other influences as well (*e.g.*, Campbell and Ethier, 1984; Loftus-Hills and Solomon, 1967). The 3Ace Co and Ni data show a much different pattern with consistently high Ni, but varying Co content (Fig. 13). The preferred explanation for this is that the early diagenetic pyrites at 3Ace, which mostly have Co/Ni values between 2 and 0.1, were formed from sedimentary fluids. The spread in Co data for late diagenetic and hydrothermal pyrite is more ambiguous and may represent an increasing metamorphic or magmatic input but this is poorly understood.

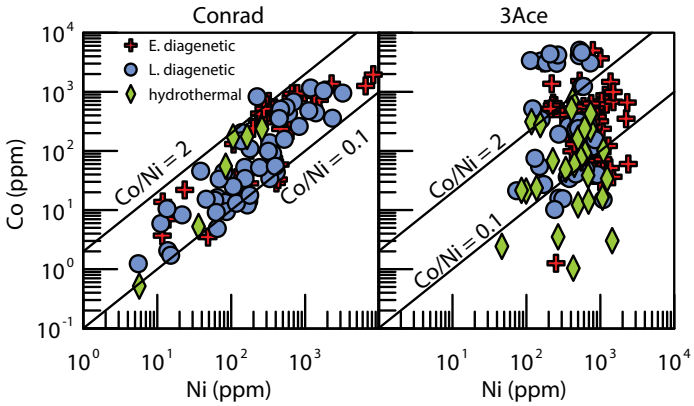

Figure 13. *Ni vs. Co plots of pyrite analyses from Conrad and 3Ace occurrence samples. Co/Ni boundaries from Gregory et al. (in prep).*

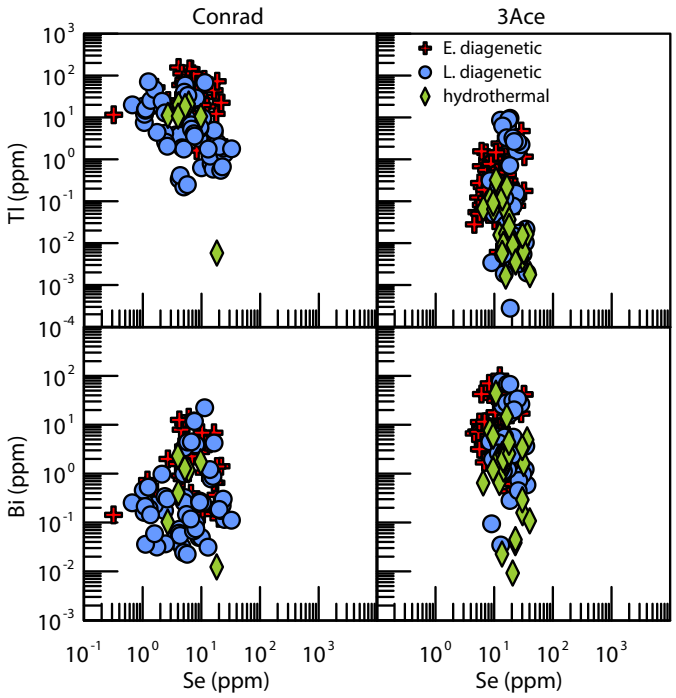

Figure 14. *Se vs. Tl and Bi plots of pyrite analyses from Conrad and 3Ace occurrence samples.*

Thallium is commonly associated with low temperature (<300 °C) hydrothermal fluids associated with syngenetic sulphide deposits (*e.g.*, Gifkins *et al.*, 2005; Goodfellow and Lydon, 2007) and epigenetic gold deposits, such as Carlin-type (*e.g.*, Cline *et al.*, 2005). Bismuth and Te are also associated with hydrothermal fluids, though typically those with higher temperatures (>250 °C), and are common trace elements in orogenic gold systems (Groves *et al.*, 2003). For all stages of pyrite from the Conrad occurrence, elevated Tl in the 1 ppm to >100 ppm and Bi values mostly <1 ppm, (Fig. 14) suggest that hydrothermal fluid temperatures were low through all stages of pyrite formation. Carlin-type deposits form at low temperatures (Cline *et al.*, 2005), and thus this is not an unusual finding for the hydrothermal pyrite. It is uncommon however that the early diagenetic pyrite have such high Tl values (Gregory *et al.*, in prep), up to 156 ppm. These elevated values in early diagenetic pyrite suggest the presence of a synsedimentary hydrothermal fluid. This may support preliminary observations by Gongora and Gleeson (2011) who suggest early, disseminated base metal, sulphide mineralization is present at the Osiris occurrence approximately 2 km to the west of the Conrad. Thallium and Bi levels in pyrite from the 3Ace show an opposite relationship, with 3Ace pyrite typically low in Tl and high in Bi and Te (Fig. 14), which is consistent with mineralization forming at higher temperatures, as would be expected in an orogenic gold deposit.

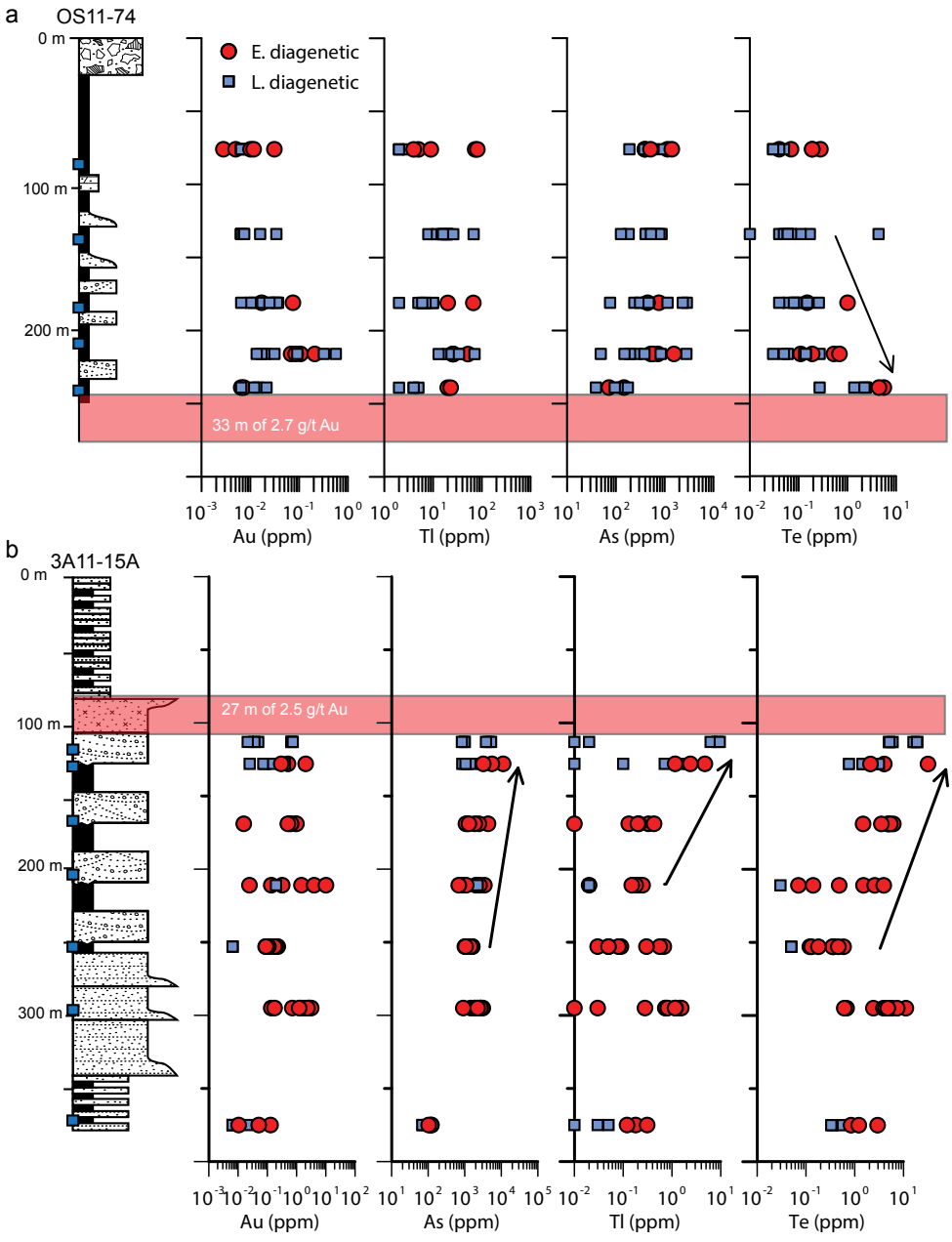

Figure 15. *Downhole plots of selected trace elements for the, (a) Conrad, and (b) 3Ace occurrences. Graphic logs same as in Figure 4 and Figure 6, respectively.*

Preliminary investigation of downhole geochemical vectors in pyrite is inconclusive for the Conrad occurrence where As decreases towards the mineralized interval, Au and Te increase slightly, and Tl remains unchanged (Fig. 15). Mercury is anomalous throughout the stratigraphy surrounding the Conrad occurrence, suggesting that pyrite further from the occurrence is required to determine the full extent of the Hg/Fe*1000 halo and the significance of Hg/Fe as a property-scale vector. In contrast, the downhole pyrite data from 3A11-15A at the 3Ace property show clear property-scale vectors provided by Tl and Te over a drilled length of 100 m to 150 m approaching mineralization (Fig. 15). Arsenic also shows a weak increasing trend over the same interval and Hg/Fe does not show a trend.

COMPARISON WITH OTHER DEPOSITS AND BASINS

The trace element chemistry of sedimentary pyrite has been shown to vary secularly (Large *et al.*, in press), by tectonic setting (Gregory *et al.*, in prep), and by gold productivity of a basin (Large *et al.*, 2011). To simplify comparison between data collected in this study and those from potential analogues, deposits hosted in Neoproterozoic strata deposited near the margin of continental basins have been chosen. Economic Carlin-type deposits are primarily found in slope facies rocks of the Great Basin in Nevada, a similar Neoproterozoic tectonic setting to that of the Conrad occurrence (Arehart *et al.*, 2013), and thus our Conrad pyrite data are best compared to data from some Nevada deposits (*e.g.*, Emsbo *et al.*, 1999; Large *et al.*, 2011; Large *et al.*, 2009). Orogenic gold deposits are found in most orogenic belts; the closest analogue with available pyrite chemistry is the Sukhoi Log gold deposit in eastern Siberia, hosted by continental slope to basinal facies of the Neoproterozoic Patom Group (Large *et al.*, 2007). For a global diagenetic pyrite context, a database compiled at CODES is used, with over 1800 sedimentary pyrite analyses (Large *et al.*, in press). The samples in the Large *et al.* (in press) database range in age from 3600 Ma to present, and are from black shales in both gold productive and unproductive basins. The black shale samples from productive sedimentary basins are distal to known deposits, and show no evidence of hydrothermal alteration. The analyses in this database can be considered representative of background diagenetic pyrite.

Emsbo *et al.* (1999) and Large *et al.* (2009) report the trace element composition of Carlin-type pyrite as having 12 000 ppm to 400 ppm As, 310 ppm to 0.01 ppm Au, and 100s of ppm to <1 ppm of Sb, Tl, Ag, Se, and Te. Conrad data are mostly within these ranges, though a significant number of analyses are below them, with only a few analyses above the preliminary thresholds defined by Large *et al.* (2011; Fig. 16). The Au, As, and Hg/Fe contents of the Conrad diagenetic pyrite are similar to that of distal sedimentary pyrite from the Popovich Formation in the North Carlin Trend (Fig. 16), overlapping with a similar range, but typically having lower median values. Mercury is commonly anomalous in the ore zone and halo of sediment-hosted gold deposits (Boyle, 1979), and recent research by Large (2013) demonstrated that pyrite in the along strike host shales of some of the largest

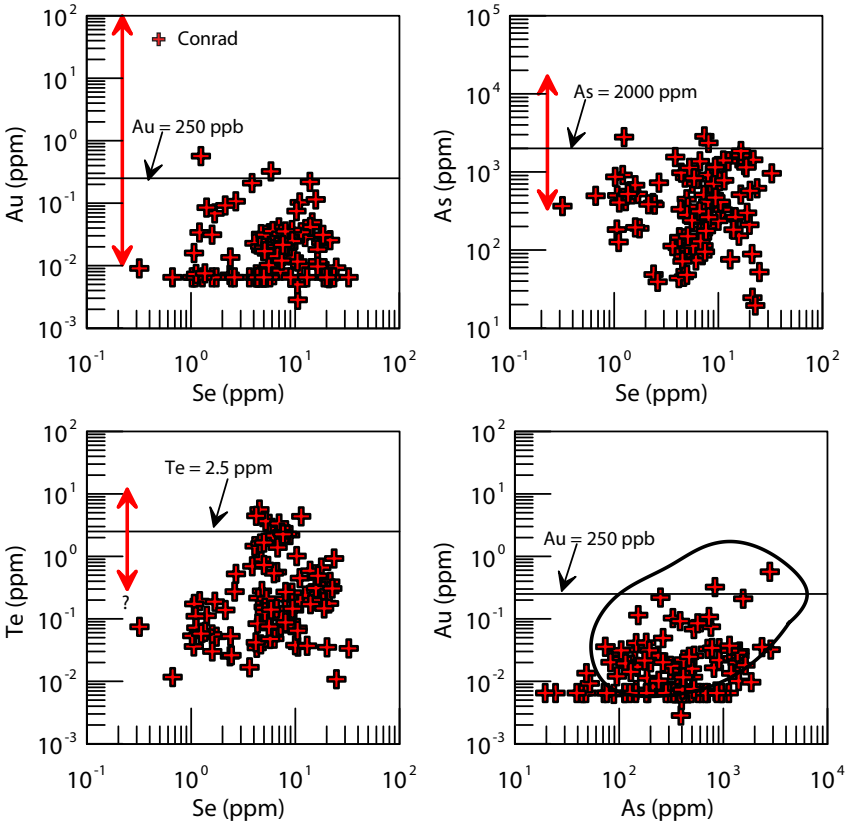

Figure 16. *Diagenetic pyrite (early and late) data for Se vs. Au, As, and Te from the Conrad occurrence and As vs. Au for Conrad with field of distal Popovich Formation diagenetic pyrite from Nevada (Large et al., 2011) outlined in heavy black. Red arrows show the elements range of pyrite from Carlin-type deposits from Emsbo et al. (1999) and Large et al. (2011).*

deposits in the world also contain anomalous levels of Hg. Conrad sedimentary pyrite has a 10 to 20 times larger Hg/Fe ratio than the 3Ace sedimentary pyrite (Fig. 17), and comparison with the Large *et al.* (in press) global database shows that Conrad sedimentary pyrites are at the upper percentile of Hg/Fe*1000 values, with a median of 0.30 (0.11 in the global database). Sedimentary pyrites in black shales from the Popovich Formation of the North Carlin Trend Nevada are the most Hg-rich of those measured in the database, having a median Hg/Fe*1000 value of 0.35. The Hg-enriched diagenetic pyrite at Conrad is a potential regional exploration vector for targeting Carlin-type deposits and prospective host strata. 3Ace pyrite has lower Hg/Fe*1000 values with a median of 0.02 and does not appear to be a regional exploration vector.

Several explanations for the generally low (excluding Hg) trace element content of Conrad diagenetic pyrite are possible: 1) Conrad diagenetic pyrite are trace element-poor compared to those near deposits in Nevada; 2) the upper limit for the ranges of most of the Nevada data is from Emsbo *et al.* (1999), which did not distinguish between generations of pyrite, thus the higher grade analyses may be from ore-stage pyrite; and 3) though the samples for this study were collected from drill holes which contain gold mineralization, they are from intervals that do not carry significant Au grade (Fig. 4). Geochemically, the Conrad sedimentary pyrite appears to be more analogous to the unmineralized, distal Popovich, sedimentary pyrite than sedimentary pyrite collected proximal to the ore shells of deposits.

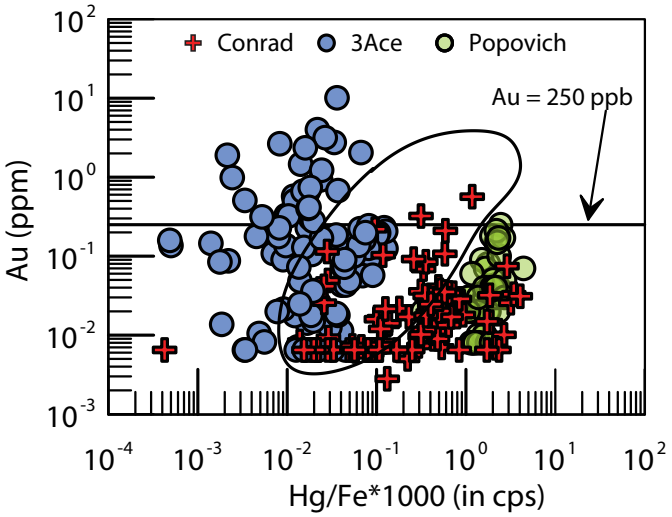

Figure 17. *Hg/Fe*1000 vs. Au plot for Conrad and 3Ace diagenetic pyrite. Distal diagenetic pyrite data from the Popovich Formation in Nevada (Large et al., 2011). Analyses from the sedimentary pyrite database of Large et al. (in press) outlined in black for context. X-axis is a ratio of counts per second (cps), not absolute abundance.*

Large *et al.* (2007) characterize the trace element composition of diagenetic pyrite from Sukhoi Log (referred to as Py1 and Py2) as having Au contents between 13 ppm and 0.002 ppm, and As contents between 13 000 ppm and 159 ppm. The remaining trace elements, Sb, Tl, Ag, and Te range from 175 ppm to <1 ppm (Large *et al.*, 2007). Comparative Se *vs.* Au, As, and Te plots and a Au-As plot show that sedimentary pyrite surrounding Sukhoi Log forms a similar overlapping field to the sedimentary pyrite adjacent to the 3Ace deposit (Fig. 18); approximately 30% of the 3Ace data plots above the preliminary thresholds of Large *et al.* (2011) for Au, As, and Te. Approximately 10% to 30% of the sedimentary pyrite analyses from 3Ace have anomalous chemistry, compared with less than 1% of Conrad analyses (Fig. 19) suggesting that the 3Ace black shales represent a more favourable gold source-rock. This assessment is strengthened by the positive linear relationship between Au-Te and Au-Ag for the sedimentary pyrites at 3Ace (Fig.19). These Au, Te, and Ag correlations in sedimentary pyrite are typical of source rocks that produce moderate to high-grade gold telluride

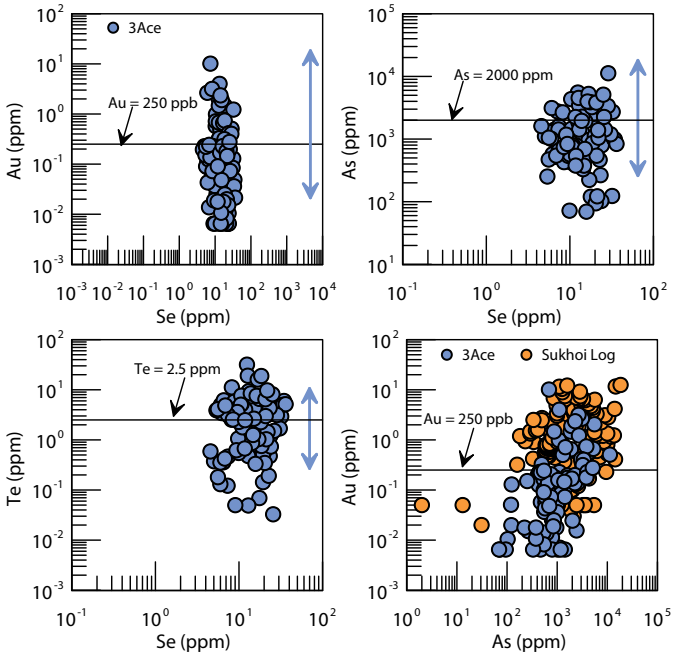

Figure 18. *Diagenetic pyrite (early and late) data for Se vs. Au, As, and Te from the 3Ace occurrence, and As vs. Au for 3Ace diagenetic pyrite and Sukhoi Log diagenetic pyrite. Blue arrow showing the diagenetic pyrite Au, As and Te ranges and Au-As data are from the Sukhoi Log deposit (Large et al., 2007).*

deposits (*e.g.*, Kumtor deposit, Central Asia; Large and Maslennikov, 2011). The Au-Te, Au-Ag plots (Fig. 19), and Te-Bi plot (Fig. 20) show systematic positive trends which suggest that the gold in sedimentary pyrite at both 3Ace and Conrad is present as nano inclusions of Bi-Ag-Au tellurides.

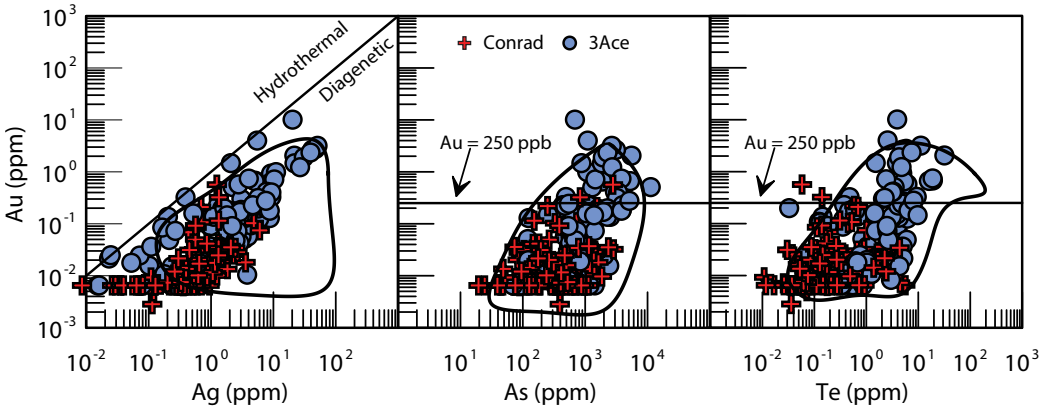

Figure 19. *As, Ag, and Te vs. Au data from Conrad and 3Ace. Analyses from the sedimentary pyrite database of Large et al. (in press) outlined in black for context. Ag vs. Au hydrothermal-sedimentary division from Large et al. (in press), Au = 250 ppb defining potential gold source rocks from Large et al. (2011).*

Large *et al.* (2011) discriminate between gold productive and unproductive basins using data from the Sukhoi Log, Bendigo, and Northern Carlin Trend deposits to represent productive basins and data from the Barney Creek Formation and Rock Cape Group in Australia, and Alum shale in Sweden to represent unproductive basins. There is considerable overlap between these two groups with the division at approximately Au = 250 ppb (Large *et al.*, 2011). On a Au-As plot, diagenetic pyrite from Conrad is mostly confined to the unproductive field whereas approximately 30% of the 3Ace data plots above the 250 ppb Au threshold well into the productive field (Fig. 21). Based on this plot and the overall lower trace element content of the Conrad diagenetic pyrite, it is tempting to infer that the strata around Conrad aren't gold productive. However, the chemistry of the Conrad diagenetic pyrite appears to match quite well with the distal Popovich Formation, diagenetic pyrite of Nevada, which is from within a gold productive basin, and diamond drilling at Conrad has returned some very respectable grades to date indicating significant amounts of Au are present. It appears that gold productive basins have significant amounts of diagenetic pyrite with <250 ppb Au, while unproductive basins rarely have diagenetic pyrite with >250 ppb Au. The diagenetic pyrite data collected suggest the Neoproterozoic stratigraphy of the Selwyn basin area may be productive and that stratigraphy near the 3Ace occurrence has higher Au in diagenetic pyrite than that near the Conrad occurrence.

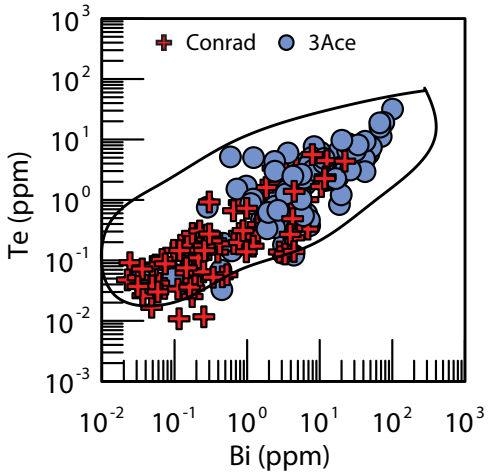

Figure 20. *Bi vs. Te data from Conrad and 3Ace. Analyses from the sedimentary pyrite database of Large et al. (in press) outlined in black for context.*

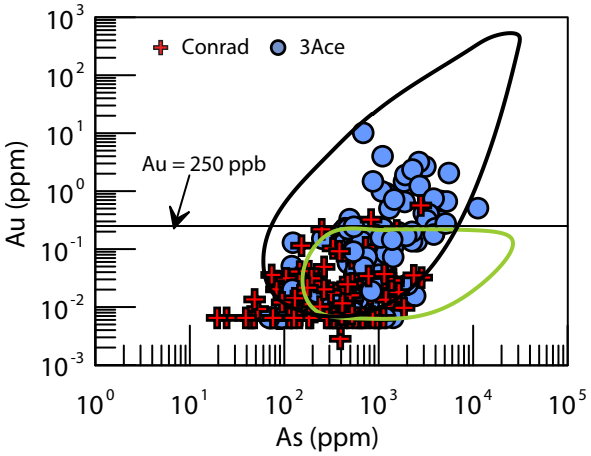

Figure 21. *As vs. Au plot for diagenetic pyrite (early and late) from Conrad and 3Ace occurrences. Productive (black) and unproductive (green) basin fields are from Large et al. (2011).*

CONCLUSIONS

Preliminary observations concerning diagenetic pyrite from two sediment-hosted gold occurrences in the Selwyn basin area are:

CONRAD

- Sedimentary pyrite in the vicinity of the Conrad occurrence has anomalously high Hg (measured as the Hg/Fe ratio by LA-ICP-MS); this elevated Hg content may be a stratigraphic marker for Neoproterozoic stratigraphy favourable for Carlin-like gold deposits in the Selwyn Basin area;
- With the exception of Hg, Conrad diagenetic pyrites are within the lower end of the compositional range of analyses from known Carlin-type deposits, and are more similar to distal sedimentary pyrite from the Popovich Formation in Nevada. The significance of Hg/Fe needs further investigation;
- Elevated Tl, and to a lesser extent Cu and Pb, in early diagenetic pyrite suggest the presence of a synsedimentary hydrothermal fluid near the Conrad occurrence;

3ACE

- At 3Ace the chemistry of sedimentary pyrite appears to be a potential vector to ore over 150 m as highlighted by Te and Tl;
- 3Ace diagenetic pyrite is within the range of analyses from the Sukhoi Log deposit for most trace elements, but is above the range for Te;

OVERALL

- With the exception of Hg, diagenetic pyrite from the Conrad occurrence has lower trace element contents than that from the 3Ace occurrence;
- At both occurrences, early diagenetic pyrite typically has higher trace element contents with successive generations having lower trace element contents;
- Both Conrad and 3Ace sedimentary pyrite show a Bi-Te-Ag-Au relationship indicative of nano particles of gold-bearing bismuth-silver tellurides within the pyrite; and
- Diagenetic pyrite from the Selwyn basin area plot within the field of productive basins on an As vs. Au diagram, but in an area of the diagram that partially overlaps with the unproductive field.

This study characterizes sedimentary pyrite from two of the more prospective sediment-hosted gold occurrences in the Selwyn basin area. The purpose of this characterization is to enable a preliminary comparison between Selwyn basin area sedimentary pyrite and sedimentary pyrite from analogue deposits and basins. This comparison provides an opportunity to apply the Large *et al.* (2011) source-rock model in a truly greenfields setting, as sediment-hosted gold exploration is in its infancy in the Selwyn basin area. Though no economic sediment-hosted gold ore body has been defined in the Selwyn basin area to date, and thus it is not known definitively if the Selwyn basin area is a productive gold basin, the preliminary data suggest that sedimentary pyrite has comparable levels of Au, Te, As, and associated trace elements to known productive basins elsewhere in the world. From this, one can preliminarily conclude that the trace element composition of diagenetic pyrite is permissive of the gold in these occurrences having been sourced, at least in part, locally. That is, the gold in these deposits can be explained using the Large *et al.* (2011) source-rock model. If this model is applicable, then based on the trace element composition of diagenetic pyrite, the Selwyn basin area and Hyland Group stratigraphy, in particular, should be prospective for future sediment-hosted gold exploration.

FURTHER WORK

This study is preliminary in nature and there is much work to be done to further the characterization of sedimentary pyrite and understanding of the significance of pyrite chemistry, both in general and in the Selwyn basin area specifically. Pyrite chemistry as a vector to ore, at both regional and property scales, has only been briefly touched on and several elements appear to be useful. Further study of other elements and relationship of samples to veining and alteration may increase the power of pyrite as a vectoring tool. Arehart *et al.* (2013) describe several other mineral occurrences as sharing similarities with deposits in the Carlin district of Nevada, including the past-producing Brewery Creek mine, which is associated with Cretaceous intrusions, and the Brick-Neve occurrence. Neither of these has been investigated from a Carlin-type perspective and evaluation of the sedimentary pyrite around them could prove interesting. The data collected on sedimentary pyrite do not convincingly demonstrate whether the anomalous Hg at Conrad is a halo effect related to the ore-forming event, or an early Hg-enrichment in pyrite during sedimentation and diagenesis. This important question may be resolved by detailed Pb-isotope measurement of the sedimentary pyrites and hydrothermal pyrites at Conrad. Lastly, this study focussed on diagenetic pyrite at the expense of later pyrite generations, these late generations, particularly those related to mineralization,

may prove interesting, and further study of their chemistry could inform genetic models and possibly add new exploration vectors.

ACKNOWLEDGMENTS

Thank you to ATAC Resources and Northern Tiger Resources for access to their core, education on the property geology, and permission to publish our results. Thank you to Dan Layton-Mathews for reviewing the entire manuscript and to Maurice Colpron and David Moynihan for help with the rapidly changing regional geologic picture. Funding for the analytical portion of this study was provided by the Canadian Northern Economic Development Agency (CanNor) from the Strategic Investment in Northern Economic Development fund (SINED). Finally, the lead author wishes to thank the CODES research group for conducting the analyses, helping with interpretation of results, and contributing to this manuscript.

REFERENCES

Abbott, G., 1997. Geology of the Upper Hart River area, eastern Ogilvie Mountains, Yukon Territory (116A/10, 116A/11). Exploration and Geological Services Division, Department of Indian and Northern Affairs Canada, Bulletin 9, 92 p.

Abbott, J.G., Gordey, S.P., and Tempelman-Kluit, D.J., 1990. Setting of stratiform, sediment-hosted lead-zinc deposits in Yukon and northeastern British Columbia. *In:* Field Trip Guidebook, 8th IAGOD Symposium: Mineral Deposits of the Northern Canadian Cordillera, Yukon-Eastern British Columbia, Abbott, J.G. and Turner, R.J.W. (eds.), Geological Survey of Canada, Open File 2169, p. 69-98.

Arehart, G.B., Ressel, M., Carne, R.C., and Muntean, J., 2013. A comparison of Carlin-type deposits in Nevada and Yukon. *In:* Tectonics, Metallogeny and discovery: The North American Cordillera and similar accretionary setttings, M. Colpron, T. Bissig, B.G. Rusk, and J.F.H. Thompson (eds.), Society of Economic Geologists, Special Publication No. 17, p. 389-401.

Bajwah, Z.U., Seccombe, P.K., and Offler, R., 1987. Trace element distribution, Co:Ni ratios and genesis of the Big Cadia iron-copper deposit, New South Wales, Australia. Mineralium Deposita, vol. 22, p. 292-300.

Blusson, S.L., 1966. Geology, Frances Lake, YukonTerritory and District of Mackenzie. Geological Survey of Canada, Preliminary Map 6-1966, scale 1:253 440.

Boyle, R.W., 1979. The geochemistry of gold and its deposits (together with a chapter on geochemical prospecting for the element). Geological Survey of Canada, GSC Bulletin 280, 584 p.

Bralia, A., Sabatini, G., and Troja, F., 1979. A revaluation of the Co/Ni ratio in pyrite as geochemical tool in ore genesis problems. Mineralium Deposita, vol. 14, p. 353-374.

Buchanan, C. and Oullette, D., 2013. Assessment Report on 2012 Diamond Drilling on the 3Ace Property, Little Hyland River Area, YT., Northern Tiger Resources.

Butler, I.B. and Rickard, D., 2000. Framboidal pyrite formation via the oxidation of iron (II) monosulfide by hydrogen sulphide. Geochimica et Cosmochimica Acta, vol. 64, p. 2665-2672.

Campbell, F.A. and Ethier, V.G., 1984. Nickel and cobalt in pyrrhotite and pyrite from the Faro and Sullivan orebodies. Canadian Mineralogist, vol. 22, p. 503-506.

Cecile, M.P., 2000. Geology of the northeastern Niddery Lake map area, east-central Yukon and adjacent Northwest Territories. Geological Survey of Canada, Bulletin 553, 122 p.

Chakungal, J. and Bennett, V., 2011. New bedrock geology of Mount Mervyn map sheet (106C/04) and mineral potential for the South Wernecke mapping project. *In:* Yukon Exploration and Geology 2010, MacFarlane, K.E., Weston, L.H., and Relf, C. (eds.), Yukon Geological Survey, p. 55-87.

Clark, C., Grguric, B., and Mumm, A.S., 2004. Genetic implications of pyrite chemistry from the Palaeoproterozoic Olary Domain and overlying Neoproterozoic Adelaidean sequences, northeastern South Australia. Ore Geology Reviews, vol. 25, p. 237-257.

Cline, J.S., Hofstra, A., Muntean, J., Tosdal, R., and Hickey, K., 2005. Carlin-type gold deposits in Nevada: Critical geologic characteristics and viable models. *In:* Economic Geology: One Hundreth Anniversary Volume, Hedenquist, J.W., Thompson, J.F.H., Goldfarb, R.J., and Richards, J.P. (eds.), Society of Economic Geologists, p. 451-484.

Colpron, M., 2012. Preliminary observations on the geology of the Rackla belt, Mount Ferrell map-area (NTS 106C/3), central Yukon. *In:* Yukon Exploration and Geology 2011, MacFarlane, K.E. and Sack, P.J. (eds.), Yukon Geological Survey, p. 27-43.

Colpron, M., Moynihan, D., Israel, S., and Abbott, G., 2013. Geological map of the Rackla belt, east-central Yukon (NTS 106C/1-4, 106D/1). Yukon Geological Survey, 5 maps and legend, scale 1:50 000.

Danyushevsky, L., Robinson, P., Gilbert, S., Norman, M., Large, R., McGoldrick, P., and Shelley, M., 2011. Routine quantitative multi-element analysis of sulphide minerals by laser ablation ICP-MS: Standard development and consideration of matrix effects. Geochemistry: Exploration, Environment, Analysis, vol. 11, p. 51-60.

Eisbacher, G.H., 1981. Sedimentary tectonics and glacial record in the Windermere Supergroup, Mackenzie Mountains, northwestern Canada. Geological Survey of Canada, Paper 80-27, 40 p.

Emsbo, P., Hutchinson, R.W., Hofstra, A., Volk, J.A., Bettles, K.H., Baschuk, G.J., and Johnson, C.A., 1999. Syngenetic Au on the Carlin trend: Implications for Carlin-type deposits. Geology, vol. 27, p. 59-62.

Gaboury, D., 2013. Does gold in orogenic deposits come from pyrite in deeply buried carbon-rich sediments?: Insight from volatiles in fluid inclusions. Geology, vol.41, p. 1207-1210.

Gabrielse, H., 1967. Tectonic evolution of the Northern Canadian Cordillera. Canadian Journal of Earth Sciences, vol. 4, p. 271-298.

Gifkins, C., Herrmann, W., and Large, R., 2005. Altered volcanic rocks: A guide to description and interpretation. Centre for Ore Deposit Research (CODES), University of Tasmania, 275 p.

Goldfarb, R.J., Baker, T., Dube, B., Groves, D.I., Hart, C.J.R., and Patrice, G., 2005. Distribution, character, and genesis of gold deposits in metamorphic terranes. *In:* Economic Geology: One Hundredth Anniversary Volume, Hedenquist, J.W., Thompson, J.F.H., Goldfarb, R.J., and Richards, J.P. (eds.), Society of Economic geologists, p. 407-450.

Gongora, P.A. and Gleeson, S.A., 2011. Petrographic and scanning electron microscope study of ore samples from Osiris, Nadaleen Trend, Yukon.

Goodfellow, W.D., 2007. Base metal metallogeny of the Selwyn Basin, Canada. *In:* Mineral Resources of Canada: A Synthesis of Major Deposit-types, District Metallogeny, the Evolution of Geological Provinces, and Exploration Methods, Goodfellow, W. D. (ed.), Mineral Deposits Division, Geological Association of Canada, Special Publication 5, p. 553-579.

Goodfellow, W.D., Cecile, M.P., and Leybourne, M.I., 1995. Geochemistry, petrogenesis, and tectonic setting of lower Paleozoic alkalic and potassic volcanic rocks, Northern Canadian Cordilleran Miogeocline Canadian Journal of Earth Sciences, vol. 32, p. 1236-1254.

Goodfellow, W.D. and Jonasson, I.R., 1987. Environment of formation of the Howards Pass (XY) Zn-Pb deposit, Selwyn Basin, Yukon. *In:* Proceedings Mineral Deposits of Northern Cordillera Symposium, Whitehorse, Yukon, Canada, 1987, Canadian Institute of Mining and Metallurgy, Special Volume 37, p. 19-50.

Goodfellow, W.D. and Lydon, J.W., 2007. Sedimentary exhalative (SEDEX) deposits. *In:* Mineral Deposits of Canada: A synthesis of major deposit types, district metallogeny, the evolution of geological provinces, and exploration methods, Goodfellow, W. D. (ed.), Geological Association of Canada, Special Publication No. 5, p. 163-183.

Gordey, S.P. and Anderson, R.G., 1993. Evolution of the northern Cordilleran miogeocline, Nahanni map area (105I), Yukon and Northwest Territories. Geological Survey of Canada, Memoir 428, 214 p.

Gordey, S.P. and Makepeace, A.J. (comps.), 2001. Bedrock geology, Yukon Territory. Geological Survey of Canada, Open File 3754 and Exploration and Geological Services Division, Yukon Indian and Northern Affairs Canada, Open File 2001-1, scale 1:1 000 000.

Gregory, D., Large, R., Bull, S., Halpin, J., Lounejeva, E., Maslennikov, V.V., Lyons, T., and Sack, P., in prep.

Groves, D.I., Goldfarb, R.J., Gebre-Mariam, M., Hagemann, S.G., and Robert, F., 1998. Orogenic gold deposits: A proposed classification in the context of their crustal distribution and relationship to other gold deposit types. Ore Geology Reviews, vol. 13, p. 7-27.

Groves, D.I., Goldfarb, R.J., Robert, F., and Hart, C.J.R., 2003. Gold deposits in metamorphic belts; overview of current understanding, outstanding problems, future research, and exploration significance. Economic Geology and the Bulletin of the Society of Economic Geologists, vol. 98, p. 1-29.

Hart, C., 2007. Reduced Intrusion-related gold systems. *In:* Mineral Deposits of Canada: A Synthesis of Major Deposit-types, District Metallogeny, the Evolution of Geological Provinces, and Exploration Methods, Goodfellow, W.D. (ed.), Geological Association of Canada, Special Publication 5, p. 95-112.

Hart, C.J.R. and Lewis, L.L., 2006. Gold mineralization in the upper Hyland River area: A nonmagmatic origin. *In:* Yukon Exploration and Geology 2005, D.S. Emond, G.D. Bradshaw, L.L. Lewis, and L.H. Weston (eds.), Yukon Geological Survey, p. 109-125.

Hart, C.J.R., McCoy, D.T., Goldfarb, R.J., Smith, M., Roberts, P., Hulstein, R., Bakke, A.A., and Bundtzen, T.K., 2002. Geology, exploration and discovery in the Tintina Gold Province, Alaska and Yukon. *In:* Global Exploration 2002: Integrated Methods for Discovery, E.E. Marsh, R.J. Goldfarb, and W.C. Day (eds.), Society of Economic Geologists, p. 25-26.

Huston, D.L., Sie, S.H., Suter, G.F., Cooke, D.R., and Both, R.A., 1995. Trace elements in sulfide minerals from eastern Australian volcanic-hosted massive sulfide deposits; Part I, Proton microprobe analyses of pyrite, chalcopyrite, and sphalerite, and Part II, Selenium levels in pyrite; comparison with delta 34 S values and implications for the source of sulfur in volcanogenic hydrothermal systems. Economic Geology, vol. 90, p. 1167-1196.

Lang, J.R. and Baker, T., 2001. Intrusion-related gold systems: the present level of understanding. Mineralium Deposita, vol. 36, p. 477-489.

Large, R., Thomas, H., Craw, D., Henne, A., and Henderson, S., 2012. Diagenetic pyrite as a source for metals in orogenic gold deposits, Otago Schist, New Zealand. New Zealand Journal of Geology and Geophysics, vol. 55, p. 137-149.

Large, R.R., 2013. Orogenic gold deposits through time: A two-stage process. *In:* Proceedings Mines and Wines, Orange, New South Wales, 2013, SMEDG.

Large, R.R., Bull, S.W., and Maslennikov, V.V., 2011. A Carbonaceous Sedimentary Source-Rock Model for Carlin-Type and Orogenic Gold Deposits. Economic Geology, vol. 106, p. 331-358.

Large, R.R., Danyushevsky, L., Hollit, C., Maslennikov, V., Meffre, S., Gilbert, S., Bull, S., Scott, R., Emsbo, P., Thomas, H., Singh, B., and Foster, J., 2009. Gold and trace element zonation in pyrite using a laser imaging technique: Implications for the timing of gold in orogenic and Carlin-style sediment-hosted deposits. Economic Geology, vol. 104, p. 635-668.

Large, R.R., Halpin, J.A., Danyushevsky, L.V., Maslennikov, V.V., Bull, S.W., Long, J.A., Gregory, D.D., Lounejeva, E., Lyons, T.W., Sack, P.J., McGoldrick, P., and Calver, C.R., in press. Trace element content of sedimentary pyrite as a new proxy for deep-time ocean-atmosphere evolution. Earth and Planetary Science Letters.

Large, R.R. and Maslennikov, V., 2011. Pyrite textures, composition and isotopic features at the Kumtor gold deposit, Kyrgyzstan: New data to improve the genetic model. *In:* Conference Proceedings, Society for Geology of Ore Deposits, Antofagasta, Chile, 2011, SGA.

Large, R.R., Maslennikov, V.V., Robert, F., Danyushevsky, L.V., and Chang, Z., 2007. Multistage sedimentary and metamorphic origin of pyrite and gold in the giant Sukhoi Log deposit, Lena Gold Province, Russia. Economic Geology, vol. 102, p. 1233-1267.

Loftus-Hills, G. and Solomon, M., 1967. Cobalt, nickel and selenium in sulphides as indicators of ore genesis. Mineralium Deposita, vol. 2, p. 228-242.

Longerich, H.P., Jackson, S.E., and Gunther, D., 1996. Laser ablation inductively coupled plasma-mass spectrometric transient signal data acquisition and analyte concentration calculation. Journal Analytical Atomic Spectrometry, vol. 11, p. 899-904.

Lydon, J.W., Lancaster, R.D., and Karkkainen, P., 1979. Genetic controls of Selwyn Basin stratiform barite/sphalerite/galena deposits; an investigation of the dominant barium mineralogy of the Tea Deposit, Yukon, Current Research, Part B. Geological Survey of Canada, Paper 79-1B, p. 223-229.

Medig, K.P.R., Thorkelson, D.J., Turner, E.C., Davis, W.J., Gibson, H.D., Rainbird, R.H., and Marshall, D.D., 2012. The Proterozoic Pinguicula Group, Wernecke Mountains, Yukon: A siliciclastic and carbonate slope to basin succession with local and exotic sediment provenance. *In:* Yukon Exploration and Geology 2011, K.E. MacFarlane and P.J. Sack (eds.), Yukon Geological Survey, p. 129-149.

Moynihan, D.P., 2013. A preliminary assessment of low pressure, amphibolite-facies metamorphism in the upper Hyland River area (NTS 105H), southeast Yukon. *In:* Yukon Exploration and Geology 2012, K.E. MacFarlane, M.G. Nordling, and P.J. Sack (eds.), Yukon Geological Survey, p. 99-114.

Moynihan, D.P., 2014 (this volume). Bedrock Geology of NTS 106B/4, Eastern Rackla Belt. *In:* Yukon Exploration and Geology 2013, K.E. MacFarlane, M.G. Nordling, and P.J. Sack (eds.), Yukon Geological Survey, p. 147-167.

Nelson, J.L., Colpron, M., and Israel, S., 2013. The Cordillera of British Columbia, Yukon, and Alaska: Tectonics and metallogeny. *In:* Tectonics, Metallogeny and discovery: The North American Cordillera and similar accretionary setttings, M. Colpron, T. Bissig, B.G. Rusk, and J.F.H. Thompson (eds.), Society of Economic Geologists, Special Publication No. 17, p. 53-109.

Pigage, L.C., 1990. Field guide Anvil Pb-Zn-Ag district Yukon Territory, Canada. *In:* Field Trip Guidebook, 8th IAGOD Symposium: Mineral Deposits of the Northern Canadian Cordillera, Yukon-Eastern British Columbia, J.G. Abbott and R.J.W. Turner (eds.), Geological Survey of Canada, Open File 2169, p. 283-308.

Raiswell, R. and Plant, J., 1980. The incorporation of trace elements into pyrite during diagenesis of black shales, Yorkshire, England. Economic Geology, vol. 75, p. 684-699.

Read, P.B., Woodsworth, G.J., Greenwood, H.J., Ghent, E.D., and Evenchick, C.A., 1991. Metamorphic map of the Canadian Cordillera.Geological Survey of Canada, Map 1714A, scale 1:2 000 000.

Sack, P.J., Danyushevsky, L.V., Gilbert, S.E., Large, R., and Gregory, D., 2013. Diagenetic pyrite, a source of gold in sediment-hosted gold deposits? Examples from the Selwyn basin, Yukon. *In:* Proceedings GAC-MAC Winnipeg 2013, Geological Association of Canada, vol. 36, p. 173.

Thorkelson, D.J., Mortensen, J.K., Creaser, R.A., Davidson, G.J., and Abbott, J.G., 2001. Early Proterozoic magmatism in Yukon, Canada: constraints on the evolution of northwestern Laurentia. Canadian Journal of Earth Sciences, vol. 38, p. 1479-1494.

Tucker, M.J., Hart, C.J.R., and Carne, R.C., 2013. Geology, alteration, and mineralization of the Carlin-type Conrad zone, Yukon. *In:* Yukon Exploration and Geology 2012, K.E. MacFarlane, M.G. Nordling, and P.J. Sack (eds.), Yukon Geological Survey, p. 163-178.

Turner, E.C. and Long, D.G.F., 2008. Basin architecture and syndepositional fault activity during deposition of the Neoproterozoic Mackenzie Mountains supergroup, Northwest Territories, Canada. Canadian Journal of Earth Sciences, vol. 45, p. 1159-1184.

Wheeler, J.O. and McFeely, P., 1991. Tectonic assemblage map of the Canadian Cordillera and adjacent parts of the United States of America. Geological Survey of Canada, Map 1712A, scale 1:2 000 000.

Whelan, S.C., Gleeson, S.A., Stern, R.A., and Buchanan, C., 2013. Au mineralization at 3Ace, south-east Yukon. *In:* Proceedings GAC-MAC Winnipeg 2013, Geological Association of Canada, vol. 36, p. 197.

Wilkin, R., Barnes, H., and Brantley, S., 1996. The size distribution of framboidal pyrite in modern sediments: An indicator of redox conditions. Geochimica et Cosmochimica Acta, vol. 60, p. 3897-3912.

Bathymetric and geophysical surveys of the southern end of Kluane Lake, Yukon

Dan H. Shugar[1]
Department of Geography, University of Victoria, Victoria, BC

Shugar, D.H., 2014. Bathymetric and geophysical surveys of the southern end of Kluane Lake, Yukon. *In:* Yukon Exploration and Geology 2013, K.E. MacFarlane, M.G. Nordling, and P.J. Sack (eds.), Yukon Geological Survey, p. 221-231.

ABSTRACT

Initial observations of lakebed geomorphology and morphodynamic processes operating at the southern end of Kluane Lake are presented here. In August 2013, multibeam and parametric echo sounders were used to map, with high resolution, the bathymetry and sub-bottom stratigraphy of the lakebed, and an acoustic Doppler current profiler and laser grain size analyser were used to measure flow and sediment transport over the Slims River delta. A series of low-angle asymmetric sediment waves were observed on the delta top, as well as buried within the delta sediments. These older bedforms were buried as the delta prograded into the lake over the past three centuries. Other delta surface features include small scarps and channels. Drowned terraces observed on the eastern margin of the lake indicate that lake level was stable and lower than present at least four times during the Holocene, to a maximum of 47 m below present datum.

[1] *dshugar@uvic.ca*

INTRODUCTION

Glacier-fed Kluane Lake, the largest lake in Yukon, has undergone significant hydrological changes in the past 1000 years. The most dramatic change resulted from the Little Ice Age advance of Kaskawulsh Glacier, south of Kluane Lake. Throughout most of the Holocene, Kaskawulsh Glacier terminated far short of the Slims River valley, which formerly drained south from Kluane Lake. However, during the Little Ice Age the glacier advanced into this valley and blocked the southerly drainage of the lake. As a result, Kluane Lake water levels rose to 12 m above current levels and a new drainage was created out the north end of the lake via the Kluane River (Bostock, 1969; Clague *et al.*, 2006). Discharge of high volumes of fine-grained sediment and meltwater from Kaskawulsh Glacier over the past three centuries has caused the Slims River delta to extend north into Kluane Lake. The high suspended sediment load in the Slims River generates continuous turbidity currents and upstream-migrating sediment waves on the delta clinoform, which is currently prograding north at a rate of 18 m a^{-1} into the lake (Gilbert and Crookshanks, 2009). Despite some recent work (Brahney *et al.*, 2008; Crookshanks and Gilbert, 2008; Gilbert and Crookshanks, 2009; Brahney *et al.*, 2010), the detailed dynamics of water level variation through the Holocene and the morphodynamic processes of the delta clinoform advance into the lake remain poorly understood.

In August 2013, geoscientists from University of Victoria (Dan Shugar), Simon Fraser University (John Clague and Ray Kostaschuk), University of Illinois, Urbana-Champaign, USA (Jim Best), and University of Hull, UK (Dan Parsons) completed field studies to further investigate sedimentary dynamics operating at the Slims River delta and examine late Holocene lake-level fluctuations via quantification of detailed bathymetry, subsurface sediment characteristics, and flow over the delta. This report describes the datasets collected, methods applied, and some preliminary results from this study.

STUDY AREA

Kluane Lake (Fig. 1) lies within the Shakwak Trench, a Cenozoic fault-bounded basin at the east margin of the St. Elias Mountains in southwestern Yukon. The lake has a surface area of approximately 432 km^2, is 65 km long, averages 4 km in width, and is up to about 78 m deep (Clague *et al.*, 2006). The Denali fault crosses the southern end of the Lake (Fig. 1). The Duke River fault crosses the Slims River valley south of Kluane Lake. Between 1897 and 2009, many earthquakes have occurred in the region, including a moment magnitude (M_w) 4.9 event on the Denali fault in 2009, a M_w5.1 event on the Duke River fault in 1995, and a M_w5.7 event between the Denali and Duke River faults in 1956 (Bird, 2004).

The watershed of Kluane Lake is approximately 5400 km^2 and, with the exception of Kaskawulsh Glacier which covers approximately 1100 km^2 (Foy *et al.*, 2011), is currently largely ice-free. However, the watershed was covered by glaciers at the maximum of the Late Wisconsinan Kluane (McConnell) Glaciation (Rampton, 1981). Kaskawulsh Glacier is one of the large outlet glaciers flowing from the Icefield Ranges of the St. Elias Mountains. Many small streams flow into the lake, but the main source of water is the Slims River. Only a portion of the meltwater flowing from Kaskawulsh Glacier reaches Kluane Lake via the Slims River; the remainder discharges to the south via the Kaskawulsh River to the Pacific Ocean (Gilbert and Crookshanks, 2009).

METHODS

A suite of instruments was deployed to document high resolution bathymetry, three-dimensional flow and sediment transport, and sub-bottom stratigraphy of the southern part of Kluane Lake. Bathymetric surveying was conducted with a RESON 7125 multibeam echo sounder (MBES) coupled to a POS-MV inertial motion sensor. We used the MBES to produce bathymetric elevation maps with 25-cm resolution. We measured 3D flow velocity with a Teledyne 1200 kHz RDInstruments RioGrande acoustic Doppler current profiler (aDcp), with a bin spacing of 0.25 m over the full water column. Time series of suspended sediment concentration and particle size were determined with a Sequoia laser *in situ* scattering transmissometer (LISST-SL). The LISST-SL data can also be used to calibrate the acoustic backscatter from the aDcp, effectively providing concurrent 3D flow and suspended sediment flux information from the same instrument and for the entire water column (*e.g.*, Shugar *et al.*, 2010). Sediment samples were also collected at the bed and at various depths in the water column using a a small Van Veen type grab and a Van Dorn sampler respectively.

An Innomar SES-2000 Parametric Echo Sounder (PES) was used to image and quantify the internal sedimentary structure of Slims River delta clinoform sediments. The instrument is uniquely suited for fine-grained sediments (Sambrook Smith *et al.*, 2013), making it ideal for use in Kluane Lake, and decimeter resolution of subsurface

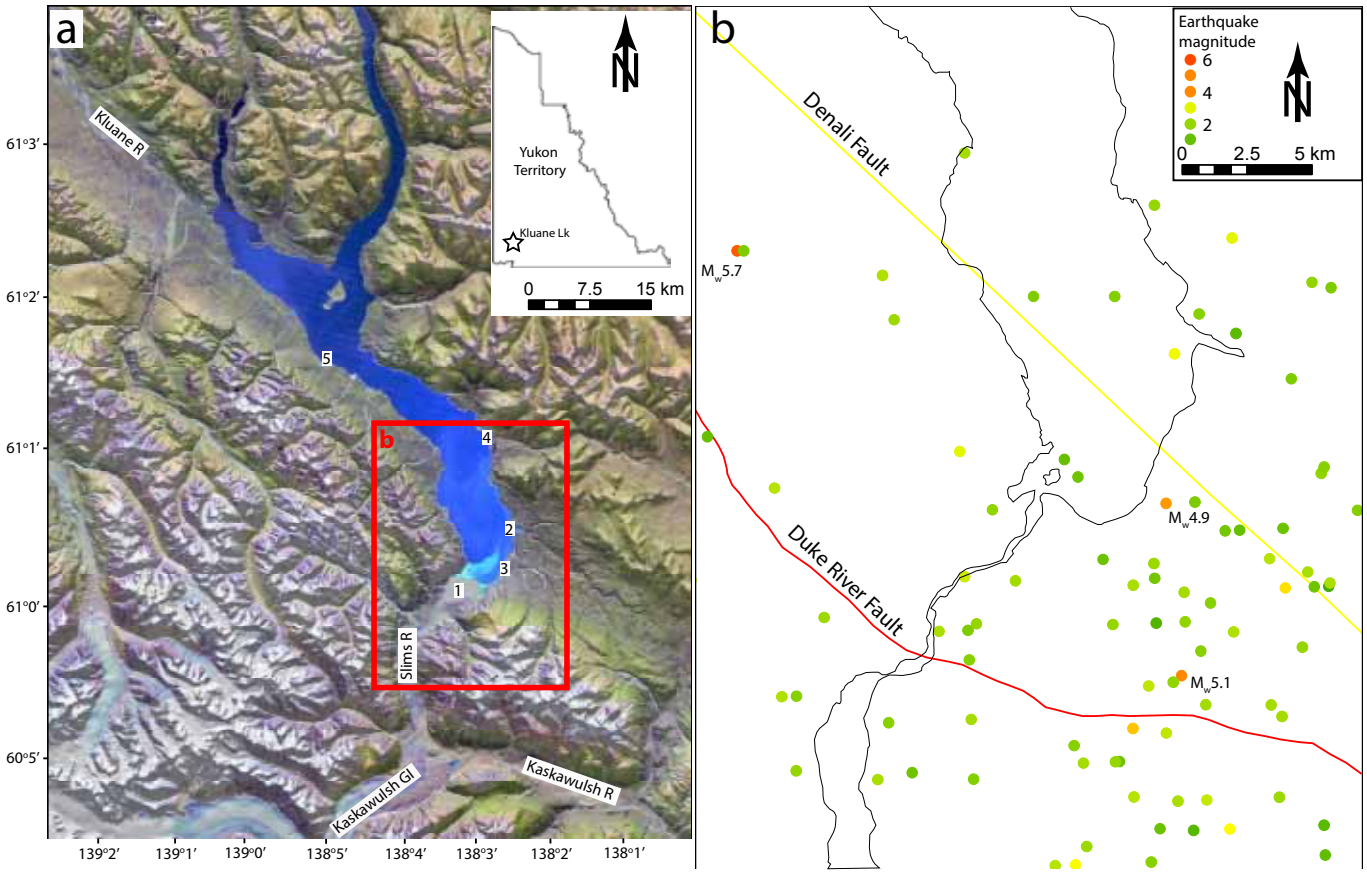

Figure 1. *(a) Map of the study area, showing Kluane Lake and its watershed; red box indicates extent of panel (b). Yukon Landsat mosaic with shaded relief underlay (Geomatics Yukon, 2004). Numbered locations refer to Slims River delta (1); Christmas Bay (2); Kluane Lake Research Station (3); Cultus Bay (4); and Destruction Bay (5). (b)Major faults and earthquake epicenters (1897-2009; Bird, 2004).*

sedimentary structure was achieved to depths of approximately 4x the water depth. For example, in 20 m of water, approximately 80 m of sediment could be imaged.

The MBES, PES, and aDcp were mounted, using pivoting brackets, to the side of a small aluminum-hulled research vessel (*RV Matthews*). The brackets allowed the instruments to be rotated out of the water when not in use. The LISST-SL was lowered into the water on a cable and trailed behind the vessel. All the instruments were tied spatially and temporally to a dGPS system, with a temporary RTK base station located at Kluane Lake Research Station during the entire survey. The RTK rover unit on the vessel was linked to the base unit via PDL radio for real-time corrections. Surveys were completed from Aug 7-13, 2013, during stationed moorings and while the vessel was under way. Significant volumes of data, totaling 1.8 TB were collected. At the time of writing, data processing was in progress.

RESULTS AND DISCUSSION

Approximately 12 km^2 of the floor of Kluane Lake was mapped using the MBES and a total of 48 km of PES line collected in three areas: the subaqueous portion of the Slims River delta; west of Christmas Bay; and west Cultus Bay (Fig. 2). Below, we discuss the historic (1899-present) evolution of the Slims River delta, describe the stratigraphy and bedforms on the delta, and examine drowned lake terraces off Christmas and Cultus bays.

HISTORIC DELTA MORPHOLOGY, 1899-PRESENT

The Slims River flows 19 km from the terminus of Kaskawulsh Glacier to Kluane Lake, where it is currently rapidly extending its delta. Historic rates of delta growth are high compared to other glaciolacustrine deltas in western Canada (Gilbert and Crookshanks, 2009).Rates have been decreasing steadily over the past century, from

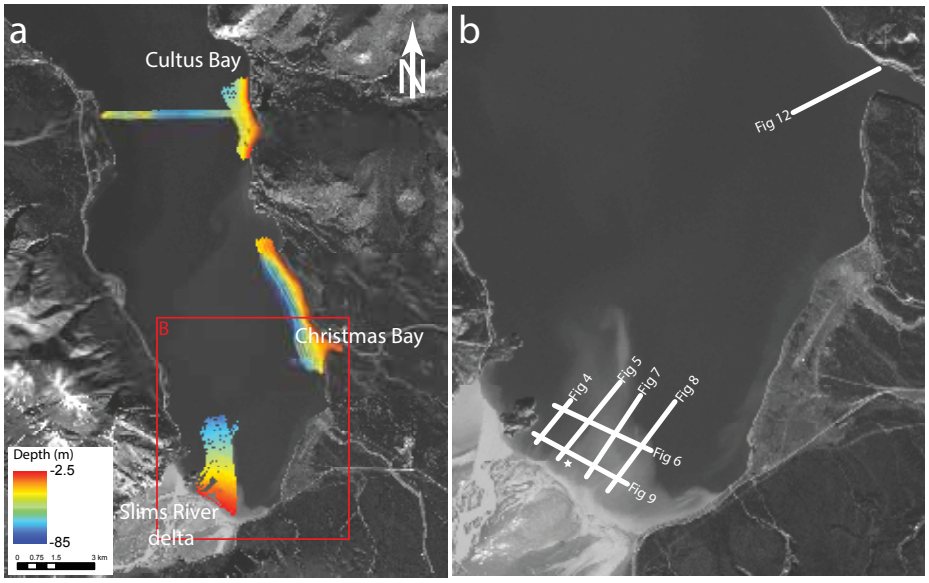

Figure 2. *(a) Multibeam echo sounding coverage; red box indicating extent of panel (b). (b) locations of PES survey lines and corresponding figure numbers. White star indicates location of sediment samples shown in Fig. 10, and aDcp profiles shown in Fig. 11.*

a high of 74 m a^{-1} between 1899 and 1914, to 48 m a^{-1} between 1914 and 1947, to 27 m a^{-1} between 1947 and 1970, and to about 18 m a-1 between 1970 and 2006 (Gilbert and Crookshanks, 2009). The decreasing rate of delta growth is due, in part, to construction of the Alaska Highway across the outwash plain in 1942 and relocation of the road and bridge in 1956. These engineering works confined flow to a single channel, trapping much of the coarser sediment upstream of the structures. Only the finer sediment fraction (silt and fine to very fine sand) is currently transported into the lake. Another factor in the decreasing rate of delta growth may be the greater width of the valley where Slims River is currently discharging into the lake. This assertion however, remains to be tested. As the delta progrades into the lake, it also aggrades vertically. Between 1970 and 2004, the delta aggraded approximately 15 m (0.45 m a^{-1}, Fig. 3) in thickness.

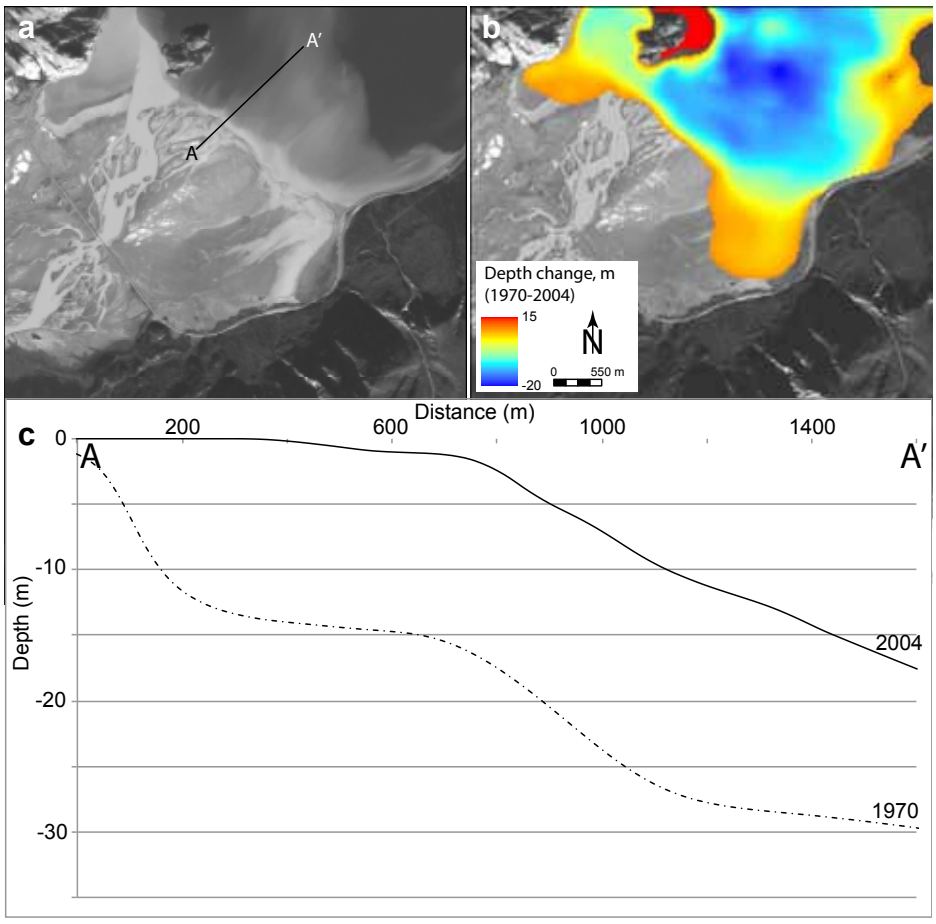

Figure 3. *(a) Orthophoto of southern Kluane Lake and Slims River delta with location of transect shown in panel C. (b) Lake depth difference map between 1970 (Bryan, 1970) and 2004 (Gilbert and Crookshanks, 2009), based on digitized bathymetric contours. Cool colours indicate a decrease in lake depth (e.g., sediment aggradation) while hot colours indicate an increase (e.g., erosion). Note that apparent scour in lee of the island may be a data artefact. (c). Change in depth of Kluane Lake along transect A-A′ between 1970 and 2004.*

DELTA STRATIGRAPHY

The Parametric Echo Sounder (PES) profiles from the Slims River delta show a range of surface and subsurface features that typify sedimentation in a fine-grained, actively prograding delta. The features identified in our survey support the earlier work of Gilbert and Crookshanks (2009), who found the delta surface to be populated by a series of large sediment waves that migrate upslope (*e.g.*, Fig. 4). Those authors also describe small, buried sediment waves, which initially formed at the distal end of the advancing sediment wedge. The sediment waves are seen in several of the PES profiles (Figs. 4, 5, and 6) that extend from the delta top into deeper water to the north. They are low-angle (1-2°) asymmetric features with heights of 1-3 m. The delta topset also appears to be cut by a number of small scarps (Fig. 7), which were interpreted by Gilbert and Crookshanks (2009) to be the result small sediment gravity flows from the delta top. Potential evidence for larger scale instabilities is shown by several large scarps that appear to cut through the delta sediment package (Figs. 7 and 8). These scarps are associated with underlying disturbance of sediment and appear to be products of longer-term gravitational instability and soft-sediment deformation on the delta slope. In addition to these larger scarp features, our surveys also reveal small channels, 1-3 m deep, that are cut into the delta top (Figs. 4 and 9).

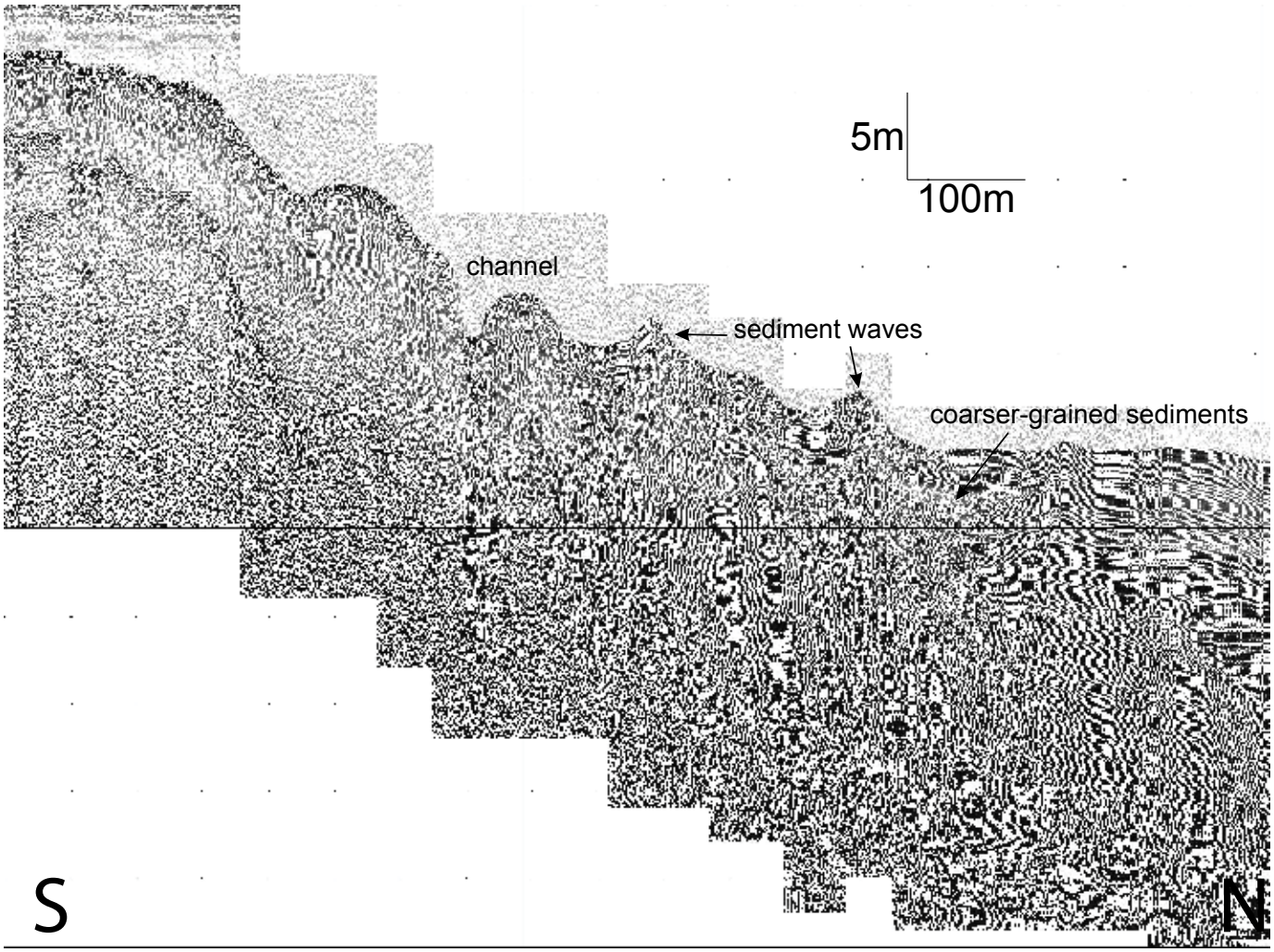

Figure 4. *Parametric echo sounder (PES) profile of Slims River delta showing lake bottom morphology and sediment stratigraphy; see Figure 2 for location.*

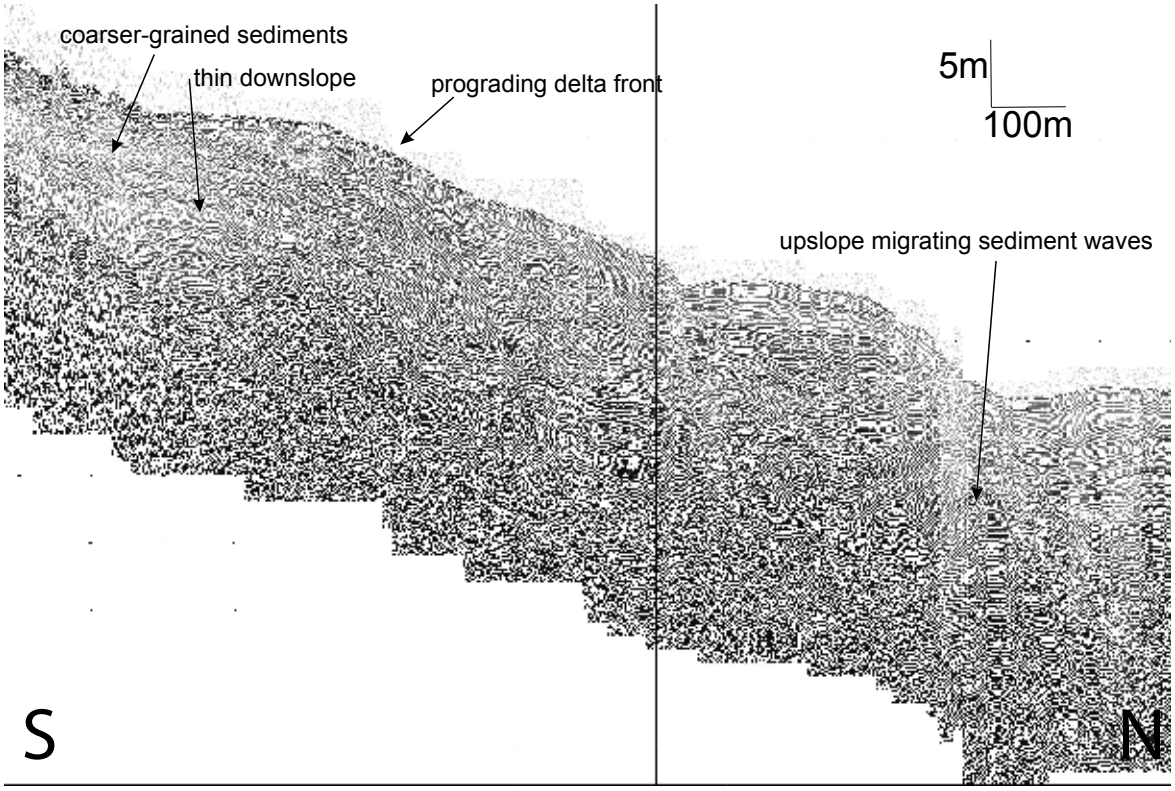

Figure 5. *Parametric echo sounder (PES) profile of Slims River delta showing lake bottom morphology and sediment stratigraphy; see Figure 2 for location.*

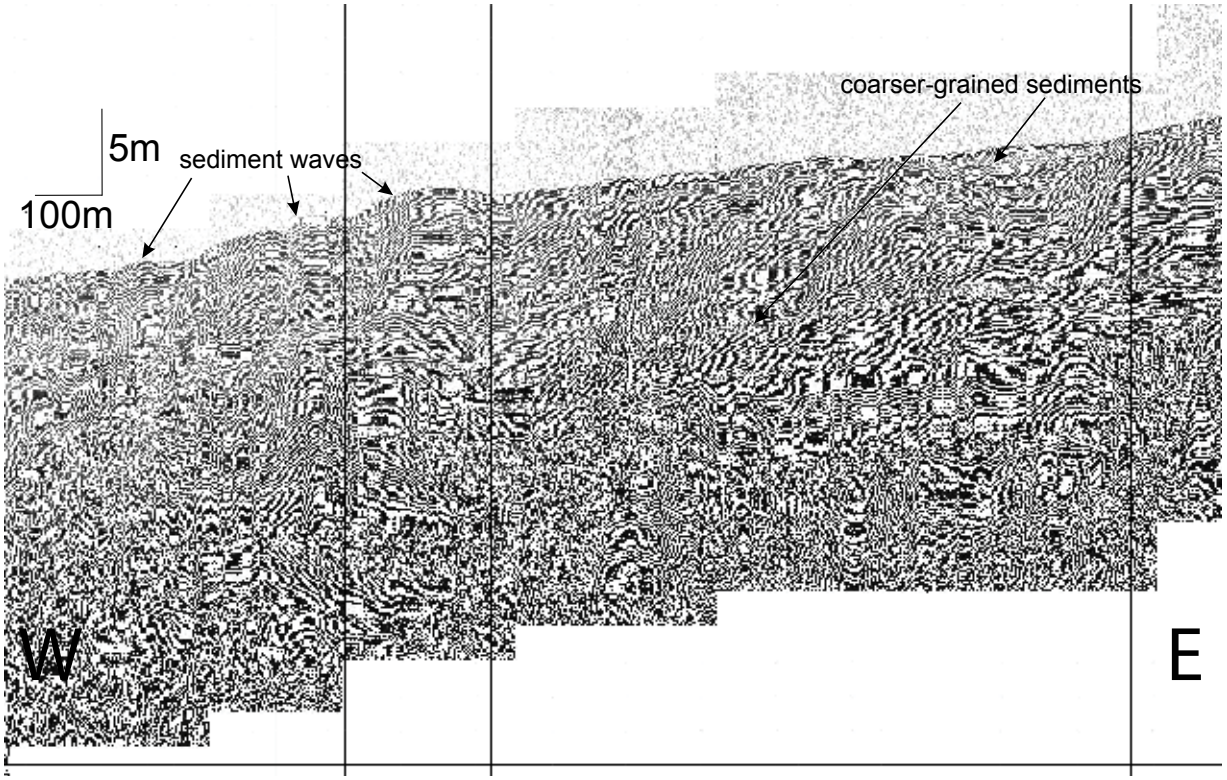

Figure 6. *Parametric echo sounder (PES) profile of Slims River delta showing lake bottom morphology and sediment stratigraphy; see Figure 2 for location.*

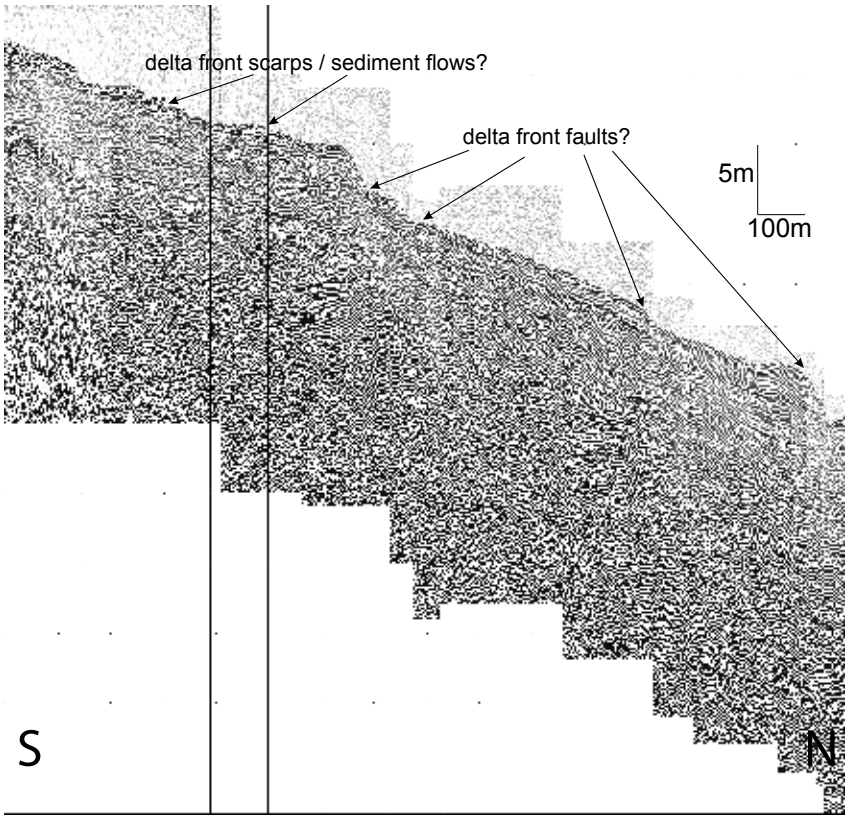

Figure 7. *Parametric echo sounder (PES) profile of Slims River delta showing lake bottom morphology and sediment stratigraphy; see Figure 2 for location.*

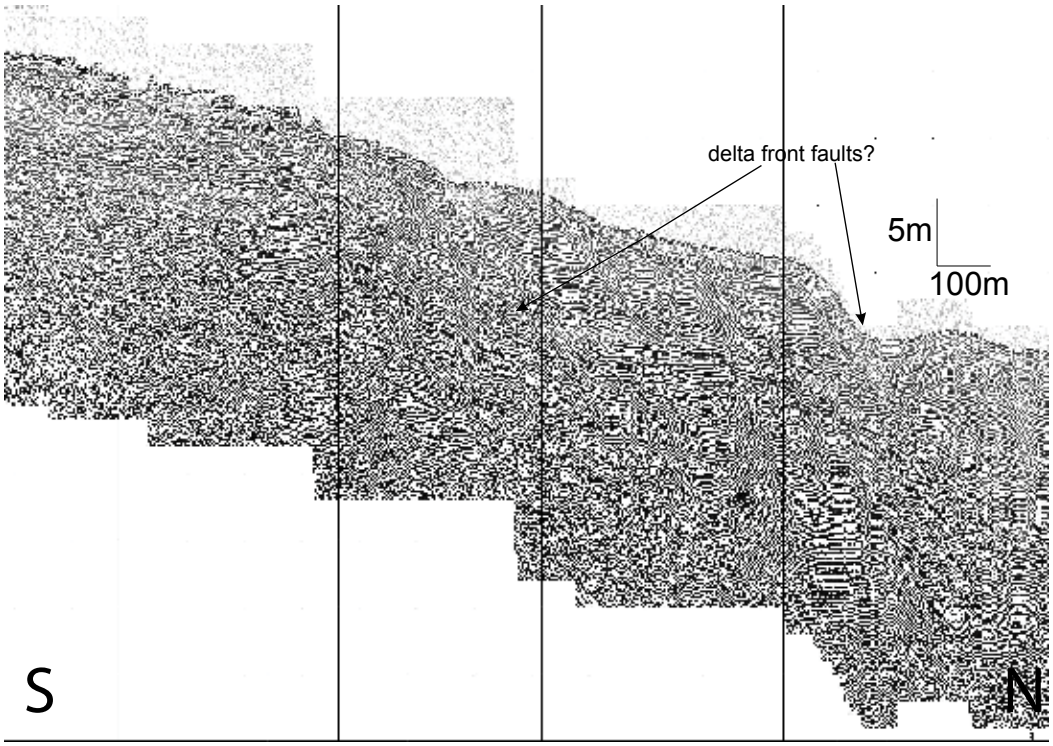

Figure 8. *Parametric echo sounder (PES) profile of Slims River delta showing lake bottom morphology and sediment stratigraphy; see Figure 2 for location.*

The strong reflections in the PES data indicate that most of the deltaic sediment sequence is fine-grained (silt to fine sand) (*e.g.*, Sambrook Smith *et al.*, 2013). Opaque structureless reflectors (Figs. 4, 5, 6, and 9) likely record episodic transport and deposition of coarser sand. Figure 5, for example, shows packets of sandy sediment that thin down the delta front and are bounded by strong reflectors that represent finer grained sedimentation. Coarser sediment is more abundant in the proximal region of the delta (Figs. 5 and 6) and is gradually replaced downslope by finer grained sediments. In other sections (*e.g.*, Figs. 8 and 9), lenses of opaque structureless sediment are nested within finer sediments. These may be evidence of occasional transport of coarser sediment during periods of high river discharge onto the delta slope, whereby the coarser sediments accumulate in depressions or swales and are then later covered by fine-grained sediments transported during lower velocity flows. Delta-front faults are evident (*e.g.*, Figs. 7, 8) although it is not clear whether or not these are co-seismically triggered.

FLOW AND SEDIMENT TRANSPORT OVER THE SLIMS RIVER DELTA

The mean grain size of suspended sediment reaching the Slims River delta is 5-10 µm (very fine to fine silt), with little difference from the lake floor to the water surface. Time-averaged suspended sediment concentrations (SSC), however, decrease logarithmically from a maximum of 0.96 g L^{-1} near the bed (0.85 m above the bed), to only 0.02 g L^{-1} near the surface (7.13 m above the bed; Fig. 10). These values are at the lower end of the "normal" range of 1-2 g L^{-1} reported by Crookshanks and Gilbert (2008). Those authors recorded a maximum SSC of 4.8 g L-1 during a flood on June 30-July 1, 2007. Bed sediments (based on one sample) have a median grain size (D_{50}) of approximately 78 µm (Fig. 10). Bryan (1970) observed somewhat finer bed sediments (D_{50} 3-30 µm) in samples further from the Slims River delta than ours.

An aDcp was used to quantify 3D velocity and backscatter (proxy for suspended sediment concentration) within the turbidity current on the Slims River delta. A 180-minute moored-station aDcp measurement obtained on the delta clinoform starting at 14:00hrs on August 12, 2013, indicates that flow plunges to the bed, with velocities up to 0.3 m s^{-1}, and is internally stratified. Flow was relatively steady through the period of measurements with variation in both velocity (0.1 to 0.3 m s^{-1}) and thickness of the underflow (varying in thickness by about 1.5 m) evident (Fig. 11). Previous work on turbidity driven flow dynamics have identified large variations in velocity (*e.g.*, Best *et al.*, 2005). However, the variations identified in Figure 11 indicate lower frequency pulsing of the current on the Slims River delta. Crookshanks and Gilbert (2008) found no dominant frequency in their velocity records from Kluane Lake in the summer of 2007. The backscatter record (Fig. 11) indicates a positive correlation of suspended sediment concentration with streamwise velocity. Calibration of the backscatter to suspended sediment concentrations is ongoing (see below).

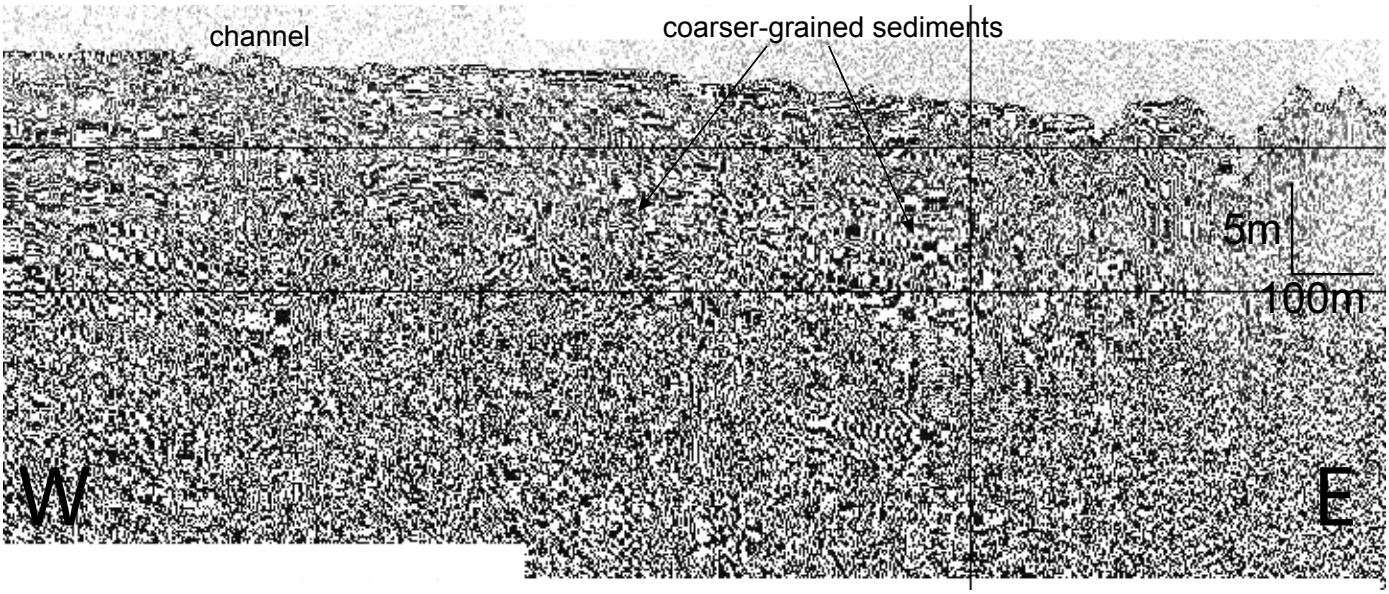

Figure 9. *Parametric echo sounder (PES) profile of Slims River delta showing lake bottom morphology and sediment stratigraphy; see Figure 2 for location.*

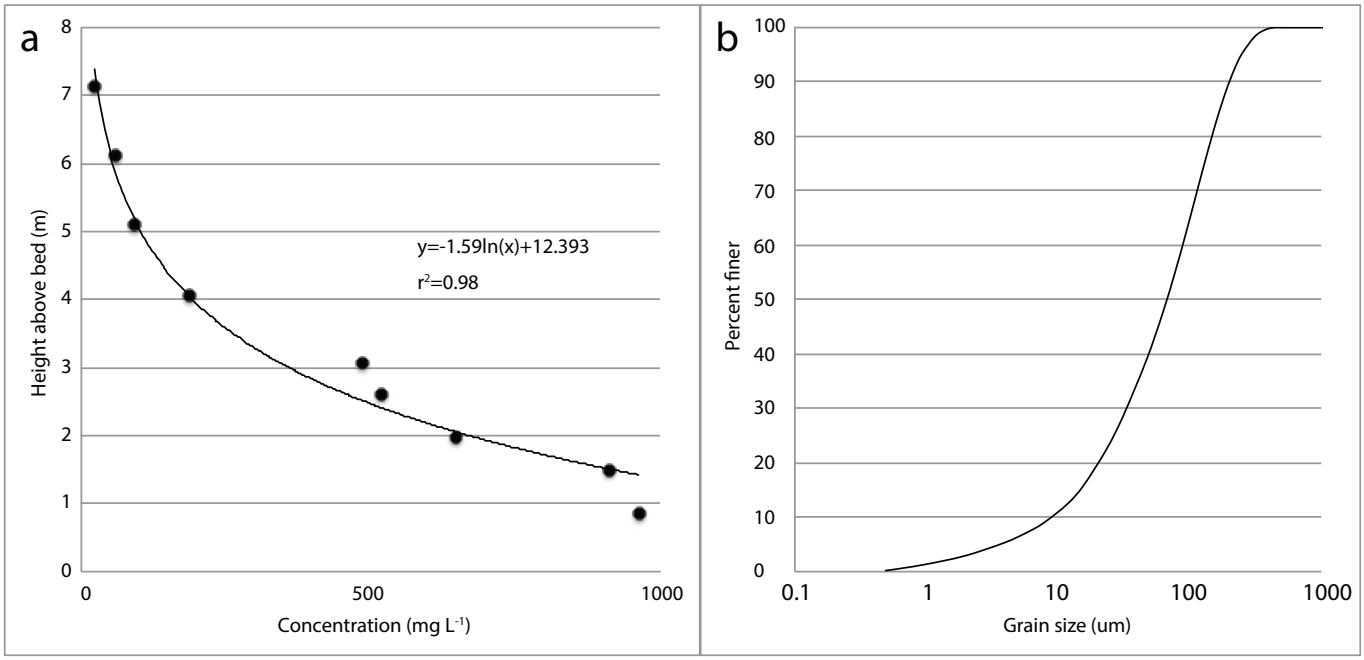

Figure 10. *(a) Profile of suspended sediment concentrations near the front of the Slims River delta. (b) Grain-size distribution of a sample of bed sediment collected from the Slims River delta.*

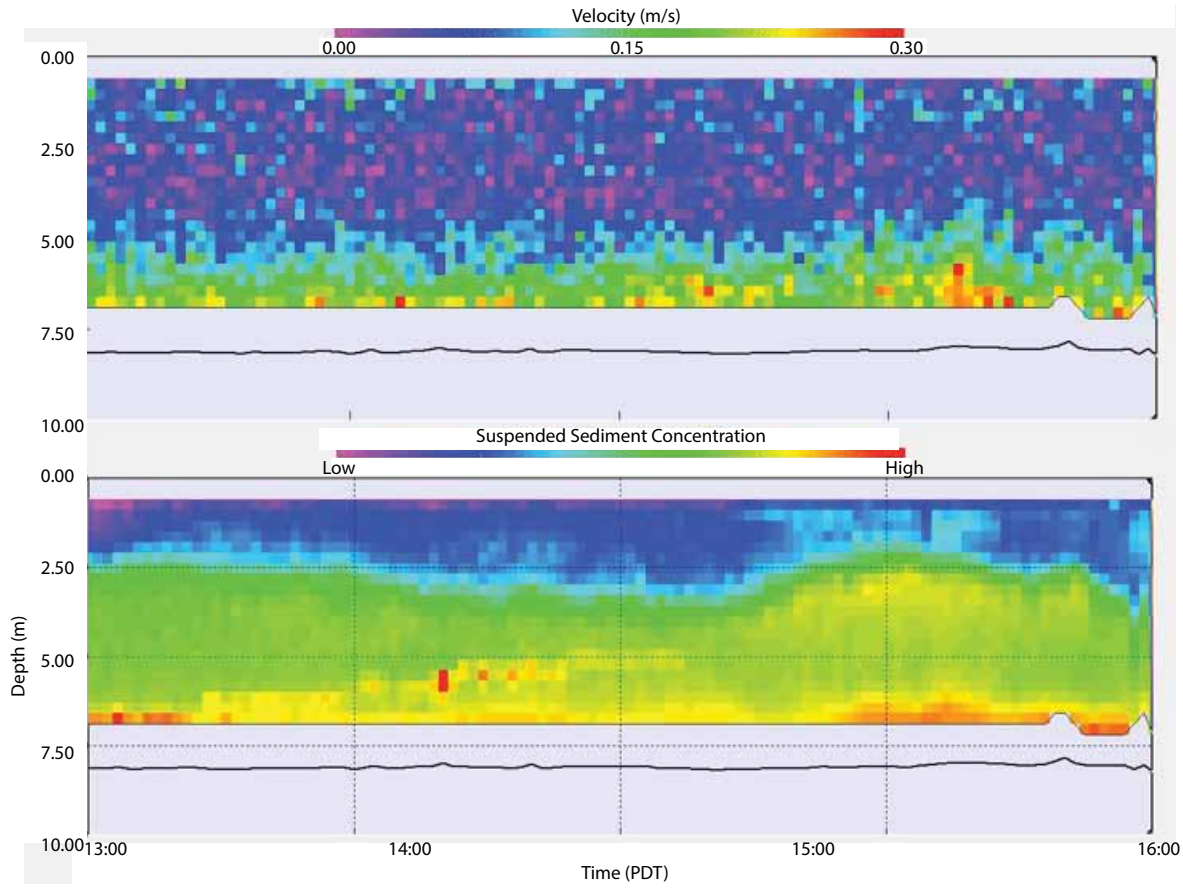

Figure 11. *Velocity and (uncalibrated) suspended sediment concentration record from 3-hr time series while moored near the front of the Slims River delta.*

HOLOCENE TERRACES

Drowned terraces (Fig. 12) are evident in the PES data west of Cultus and Christmas bays. The most well defined drowned terraces are approximately 25, 30, 37, and 47 m below the lake surface. The terraces range in width from approximately 50 m to more than 200 m, and are either flat or slope at a very low angle (<1°) toward deeper water. The drowned terraces appear to be eroded surfaces that are draped by younger sediments, some of which dip more steeply lakeward than the surfaces on which they lie. PES penetration in these sediments is poorer than in the fine-grained deltaic sediments, suggesting that the terrace sediments are sand and/or gravel.

Our preliminary interpretation of the terraces is that they are wave-cut benches that developed when Kluane Lake was lower than present. Clague *et al*. (2006) presented evidence that the lake was lower than at present prior to the seventeenth century, although by how much was uncertain. Brahney *et al*. (2007; 2008; 2010) interpreted late Holocene lake levels of -20 to -30 m based on sediment cores collected from the lake. If the terraces that we have mapped are wave-cut benches, Kluane Lake at some time during the Holocene was at least 47 m lower than today and the entire northern half of the lake basin at that time was subaerial.

CONCLUSIONS AND FUTURE WORK

The preliminary results presented here include detailed visualization of surface and subsurface features on the Slims River delta, as well as of Holocene-era drowned terraces on the eastern margin of the lake. Buried sediment waves seen in Parametric Echo Sounding profiles (*e.g.*, Fig. 5), and bathymetric data (*e.g.*, Fig. 3) indicate that the delta has been rapidly prograding and aggrading in the past decades to centuries. Drowned lake terraces on the eastern margin of the lake (*e.g.*, Fig. 12) indicate at least four periods of relative lake-level stability lower than the present level and the +12 m level previously described by Clague *et al*. (2006).

The 2013 field data are currently being processed and a 3D model of the surface and subsurface structure of the Slims River delta is being constructed from the MBES and PES data. The focus of future work will be on obtaining a higher-density grid of the delta, extending our survey further into the lake, quantifying annual changes to lake-bed topography in the vicinity of the delta, and mapping the Denali fault where it crosses the lake. Initial results indicate that the Denali fault was imaged by PES in 2013, but these data are not yet processed. This study intends to core through the lacustrine sediment sequence at the Kluane Lake Research Station to obtain samples for radiocarbon dating and paleo-ecological analysis in an effort to further elucidate the low-stand history of the lake. It is expected that coring will occur in summer 2014, while further MBES, PES, and aDcp surveys will occur in summers 2015 and 2016, subject to funding. Findings are expected to be published in peer-reviewed journals beginning in 2014.

ACKNOWLEDGEMENTS

We thank the Kluane First Nation and White River First Nation for their enthusiastic support of this research, which was licensed under the Yukon Scientists and Explorers Act. Fieldwork was facilitated by a Yukon Geological Survey research grant, and Geomatics Yukon provided satellite data. Logistical support from the Kluane Lake Research

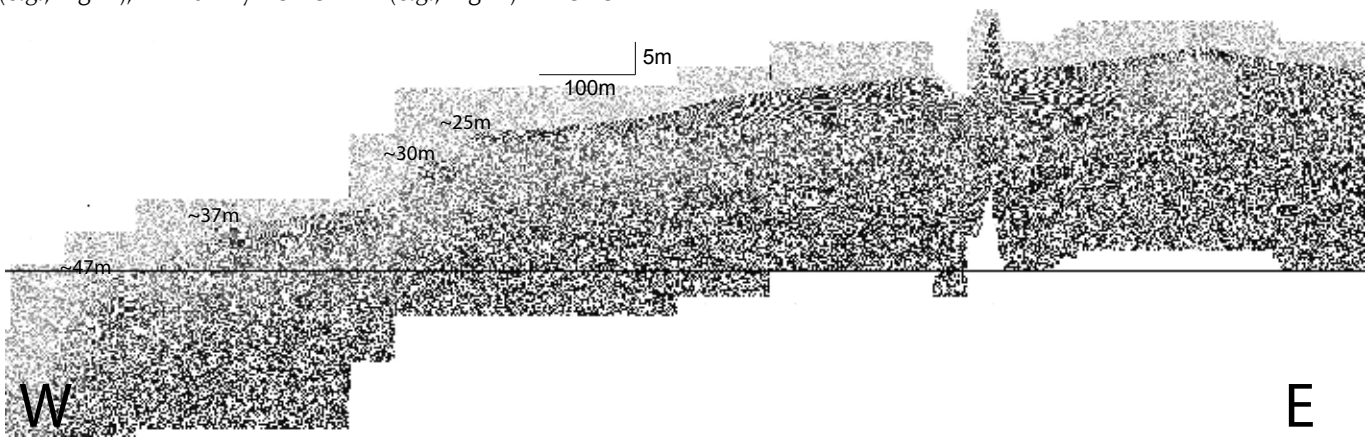

Figure 12. *Parametric echo sounder (PES) profile showing lake bottom morphology and sediment stratigraphy from Christmas Bay showing at least four drowned terraces, with depths below lake level indicated.*

Station, in particular Sian Williams and Lance Goodwin, was much appreciated. This research would not have been possible without the participation of Professors Jim Best, John Clague, Dan Parsons, and Ray Kostaschuk, as well as the assistance of Jamie Hizzett, Dr. Francis Gauthier, and Leila Ertolahti. This paper benefited from conversations with Professor David Hik and Dr. Eddy Carmack, and from comments by Dr. Tobi Gardner, Panya Lipovsky, and YEG editor Karen MacFarlane.

REFERENCES

Best, J.L., Kostaschuk, R.A., Peakall, J., Villard, P.V., and Franklin, M., 2005. Whole flow field dynamics and velocity pulsing within natural sediment-laden underflows. Geology, vol. 33, p. 765-768. doi: 10.1130/g21516.1.

Bird, A.L., 2004. Yukon earthquake data 1897-2009. Digital data accessed <*http://www.geomaticsyukon.ca/data/datasets*> [accessed January 20, 2014].

Bostock, H.S., 1969. Kluane Lake, Yukon Territory, its drainage and allied problems. Geological Survey of Canada, Paper 69-28.

Brahney, J., Clague, J.J., Edwards, T.W.D., and Menounos, B., 2010. Late Holocene paleohydrology of Kluane Lake, Yukon Territory, Canada. Journal of Paleolimnology, vol. 44, p. 873-885. doi: 10.1007/s10933-010-9459-8.

Brahney, J., Clague, J.J., Menounos, B., and Edwards T.W.D., 2007. Geochemical reconstruction of late Holocene drainage and mixing in Kluane Lake, Yukon Territory. Journal of Paleolimnology, vol. 40, p. 489-505. doi: 10.1007/s10933-007-9177-z.

Brahney, J., Clague, J.J., Menounos, B., and Edwards, T.W.D., 2008. Timing and cause of water level fluctuations in Kluane Lake, Yukon Territory, over the past 5000 years. Quaternary Research, vol. 70, p. 213-227. doi: 10.1016/j.yqres.2008.05.001.

Bryan, M.L., 1970. Sedimentation in Kluane Lake, Yukon Territory, Canada. Proceedings of the Association of American Geographers, vol. 2, p. 31-35.

Clague, J.J., Luckman, B.H., Van Dorp, R.D., Gilbert, R., Froese, D., Jensen, B.J.L., and Reyes, A.V., 2006. Rapid changes in the level of Kluane Lake in Yukon Territory over the last millennium. Quaternary Research, vol. 66, p. 342-355. doi: 10.1016/j.yqres.2006.06.005.

Crookshanks, S. and Gilbert, R., 2008. Continuous, diurnally fluctuating turbidity currents in Kluane Lake, Yukon Territory. Canadian Journal of Earth Sciences, vol. 45, p. 1123-1138. doi: 10.1139/e08-058.

Foy, N., Copland, L., Zdanowicz, C., Demuth, M., and Hopkinson, C., 2011. Recent volume and area changes of Kaskawulsh Glacier, Yukon, Canada. Journal of Glaciology, vol. 57, p. 515-525. doi: 10.3189/002214311796905596.

Geomatics Yukon, 2004. Yukon Landsat Mosaic with Shaded Relief. Geomatics Yukon <*www.geomaticsyukon.ca*> [accessed July 16, 2013].

Gilbert, R. and Crookshanks, S., 2009. Sediment waves in a modern high-energy glacilacustrine environment. Sedimentology, vol. 56, p. 645-659. doi: 10.1111/j.1365-3091.2008.00990.x.

Rampton, V., 1981. Surficial materials and landforms of Kluane National Park, Yukon Territory. Geological Survey of Canada, Paper 79-24, 37 p.

Sambrook Smith, G.H., Best, J.L., Orfeo, O., Vardy, M.E., and Zinger, J.A., 2013. Decimeter-scale in situ mapping of modern cross-bedded dune deposits using parametric echo sounding: A new method for linking river processes and their deposits. Geophysical Research Letters, vol. 40, p. 3883-3887. doi: 10.1002/grl.50703.

Shugar, D.H., Kostaschuk, R., Best, J.L., Parsons, D.R., Lane, S.N., Orfeo, O., and Hardy, R.J., 2010. On the relationship between flow and suspended sediment transport over the crest of a sand dune, Rio Parana, Argentina. Sedimentology, vol. 57, p. 252-272. doi: 10.1111/j.1365-3091.2009.01110.x.